IMPACT FACTOR
10.057

#1 NUCLEAR MEDICINE, MOLECULAR IMAGING AND MOLECULAR RADIOTHERAPY JOURNAL

Vol. 62 ▪ No. 10 ▪ October 2021

JNM
The Journal of Nuclear Medicine

FEATURED ARTICLE

A Prospective, Randomized, Double-Blind Study to Evaluate the Safety, Biodistribution, and Dosimetry of ^{68}Ga-NODAGA-LM3 and ^{68}Ga-DOTA-LM3 in Patients with Well-Differentiated Neuroendocrine Tumors. Wenjia Zhu et al. See page 1398.

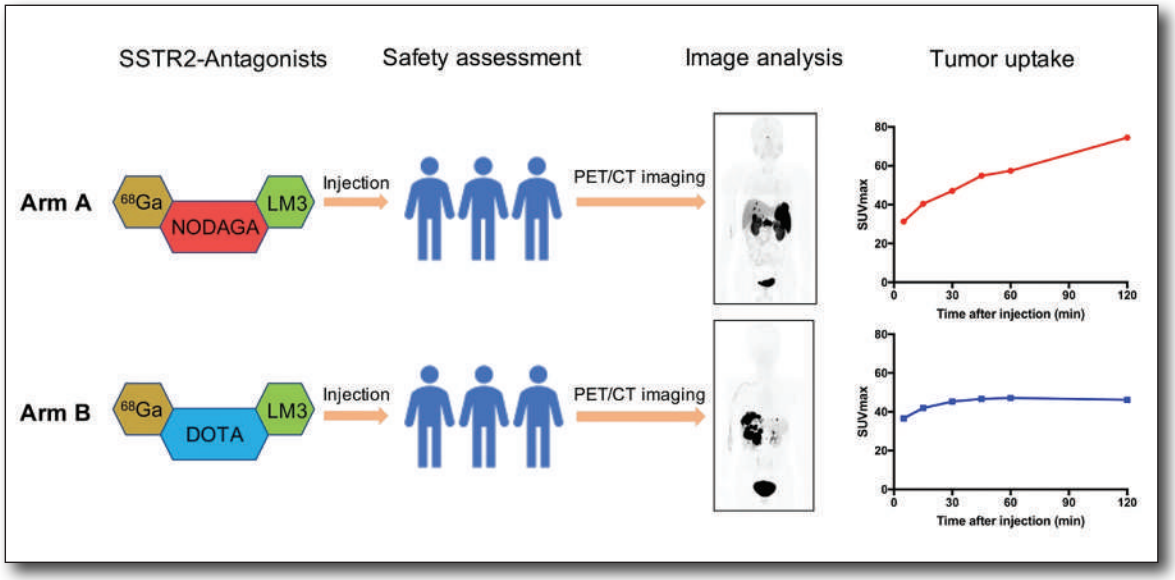

PSMA hybrid molecules: creating a second generation of PSMA-11 agents with enhanced pharmacokinetics and imaging capabilities. Ann-Christin Eder et al. See page 1461.

SNMMI Value Initiative
SOCIETY OF NUCLEAR MEDICINE & MOLECULAR IMAGING

CALL FOR ABSTRACTS

If you are a young professional in the field, we invite you to a submit clinical or scientific abstract for the **2022 ACNM Annual Meeting** on one of the following topics:

- Aspects of Clinical and Basic Science in Nuclear Medicine
- Correlative Imaging in Nuclear Medicine and Radiology
- Nuclear Pharmacy and Physics
- Nuclear Cardiology
- Theranostics
- Quality and Safety in Nuclear Medicine

2022 ACNM Annual Meeting Abstract AWARDS

Learn more about award opportunities available when you submit your abstract for the 2022 ACNM Annual Meeting.

ABSTRACT SUBMISSION DEADLINE:

NOVEMBER 18, 2021

www.snmmi.org/MWM2022

January 27-29

2022 SNMMI MID-WINTER & ACNM ANNUAL MEETING

HILTON ORLANDO LAKE BUENA VISTA
ORLANDO, FLORIDA

SNMMI 2022 Mid-Winter Meeting | ACNM ANNUAL MEETING

RadQual

Quality Radioactive Sources;
It's in our name!

Siemens Auto QC

Ge-68 PET cylinders & Transmission Rods

RADQUAL
Global Sources

Vials & Rod Sources

Flood Phantoms

www.radqual.com

info@radqual.com

Don't Make This Your LAST Issue of The Journal of Nuclear Medicine

Renew your SNMMI membership.

SNMMI members receive a complimentary subscription to *The Journal of Nuclear Medicine (JNM)*. Keep access to this world renowned publication by renewing your SNMMI membership for the coming year!

This past year, *The Journal of Nuclear Medicine* has achieved the highest impact factor ever in its 60+ year history, ranking among the top medical imaging journals worldwide. Your subscription includes access to continuing education articles approved for AMA/PRA and SAM credit, VOICE-approved articles, and SNMMI Annual Meeting Abstracts.

By renewing now, you'll ensure uninterrupted access to your monthly JNM issues, as well as continued online access to years of archived research!

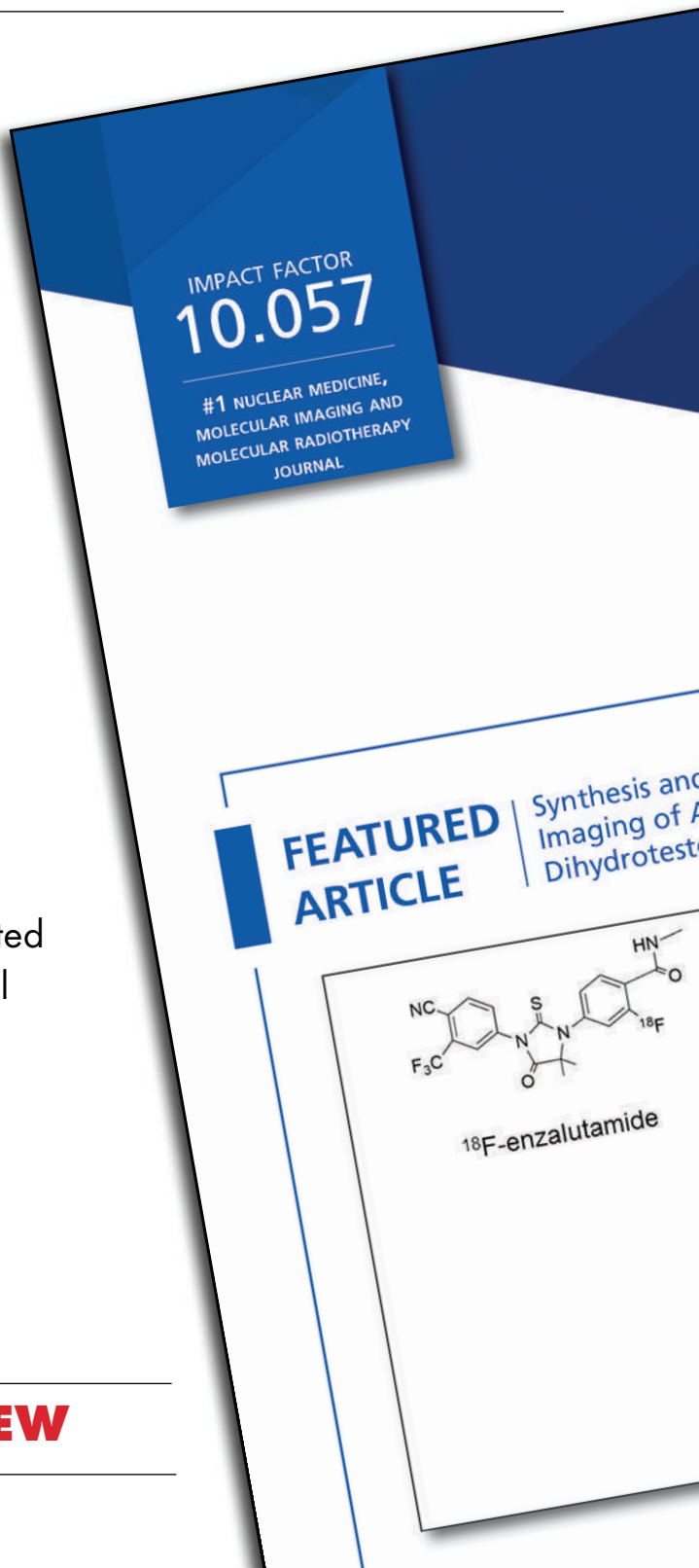

SNMMI Value Initiative
SOCIETY OF NUCLEAR MEDICINE & MOLECULAR IMAGING

www.snmmi.org/RENEW

JNM

Volume 62 • Number 10 • October 2021

SNMMI NEWSLINE

9N 2021 SNMMI Highlights Lecture: Oncology and Therapy, Part 1
Heiko Schöder

15N SNMMI and ACGME Equity Matters Initiative

16N In memoriam: Amnon (Amy) Piepsz, MD (1938–2021)
Alain Prigent, M. Donald Blaufox, Andrew Taylor, and Naomi Alazraki

17N SNMMI Leadership Update: State of the Society: SNMMI Thrives Despite COVID-19 Challenges
Virginia Pappas

18N Newsbriefs

THE STATE OF THE ART

1323 Somatostatin Receptor Imaging and Theranostics: Current Practice and Future Prospects
Sonya Park, Ashwin Singh Parihar, Lisa Bodei, Thomas A. Hope, Nadine Mallak, Corina Millo, Kalpna Prasad, Don Wilson, Katherine Zukotynski, and Erik Mittra

HOT TOPICS

1330 Artificial Intelligence for PET Image Reconstruction
Andrew J. Reader and Georg Schramm

CONTINUING EDUCATION

1334 PET/MRI Improves Management of Children with Cancer
Lucia Baratto, K. Elizabeth Hawk, Lisa States, Jing Qi, Sergios Gatidis, Louise Kiru, and Heike E. Daldrup-Link

FOCUS ON MOLECULAR IMAGING

1341 The Latest Advances in Imaging Crosstalk Between the Immune System and Fibrosis in Cardiovascular Disease
Gyu Seong Heo, Lanlan Lou, Deborah Sultan, and Yongjian Liu

EDITORIAL

1347 Imaging of Small Intestine Neuroendocrine Neoplasms: Is SSTR PET the Holy Grail?
Alessio Imperiale, Leah Meuter, Karel Pacak, and David Taïeb

ONCOLOGY

Clinical

1349 Simultaneous Mapping of Vasculature, Hypoxia, and Proliferation Using Dynamic Susceptibility Contrast MRI, ^{18}F-FMISO PET, and ^{18}F-FLT PET in Relation to Contrast Enhancement in Newly Diagnosed Glioblastoma
Solène Collet, Jean-Sébastien Guillamo, David Hassanein Berro, Ararat Chakhoyan, Jean-Marc Constans, Emmanuèle Lechapt-Zalcman, Jean-Michel Derlon, Mathieu Hatt, Dimitris Visvikis, Stéphane Guillouet, et al.

1357 Technologic (R)Evolution Leads to Detection of More Sentinel Nodes in Patients with Melanoma in the Head and Neck Region
Danique M.S. Berger, Nynke S. van den Berg, Vincent van der Noort, Bernies van der Hiel, Renato A. Valdés Olmos, Tessa A. Buckle, Gijs H. KleinJan, Oscar R. Brouwer, Lenka Vermeeren, Baris Karakullukçu, et al.

1363 Diagnostic Value, Oncologic Outcomes, and Safety Profile of Image-Guided Surgery Technologies During Robot-Assisted Lymph Node Dissection with Sentinel Node Biopsy for Prostate Cancer
Elio Mazzone, Paolo Dell'Oglio, Nikos Grivas, Esther Wit, Maarten Donswijk, Alberto Briganti, Fijs Van Leeuwen, and Henk van der Poel

1372 Diagnostic Contribution of Contrast-Enhanced CT as Compared with Unenhanced Low-Dose CT in PET/CT Staging and Treatment Response Assessment of ^{18}F-FDG–Avid Lymphomas: A Prospective Study
Lara Marchetti, Luca Perrucci, Fabio Pellegrino, Luca Baroni, Annalisa Merlo, Massimo Tilli, Ilaria Rambaldi, Elisa Maietti, Aldo Carnevale, Mirco Bartolomei, et al.

1380 ■ BRIEF COMMUNICATION. Prognostic Value of Bone Marrow Metabolism on Pretreatment ^{18}F-FDG PET/CT in Patients with Metastatic Melanoma Treated with Anti-PD-1 Therapy
Ryusuke Nakamoto, Lisa C. Zaba, Tie Liang, Sunil Arani Reddy, Guido Davidzon, Carina Mari Aparici, Judy Nguyen, Farshad Moradi, Andrei Iagaru, and Benjamin Lewis Franc

Basic

1384 Exploiting the MUC5AC Antigen for Noninvasive Identification of Pancreatic Cancer
Kelly E. Henry, Travis M. Shaffer, Kyeara N. Mack, Janine Ring, Anuja Ogirala, Susanne Klein-Scory, Christina Eilert-Micus, Wolff Schmiegel, Thilo Bracht, Barbara Sitek, et al.

THERANOSTICS

Clinical

1391 ■ BRIEF COMMUNICATION. First-in-Humans Application of ^{161}Tb: A Feasibility Study Using ^{161}Tb-DOTATOC
Richard P. Baum, Aviral Singh, Harshad R. Kulkarni, Peter Bernhardt, Tobias Rydén, Christiane Schuchardt, Nadezda Gracheva, Pascal V. Grundler, Ulli Köster, Dirk Müller, et al.

1398 ■ FEATURED ARTICLE OF THE MONTH. A Prospective, Randomized, Double-Blind Study to Evaluate the Safety, Biodistribution, and Dosimetry of ^{68}Ga-NODAGA-LM3 and ^{68}Ga-DOTA-LM3 in Patients with Well-Differentiated Neuroendocrine Tumors
Wenjia Zhu, Yuejuan Cheng, Ru Jia, Hong Zhao, Chunmei Bai, Jianming Xu, Shaobo Yao, and Li Huo

1406 Quantitative ^{68}Ga-DOTATATE PET/CT Parameters for the Prediction of Therapy Response in Patients with Progressive Metastatic Neuroendocrine Tumors Treated with ^{177}Lu-DOTATATE
Claudia Ortega, Rebecca K.S. Wong, Josh Schaefferkoetter, Patrick Veit-Haibach, Sten Myrehaug, Rosalyn Juergens, David Laidley, Reut Anconina, Amy Liu, and Ur Metser

1415 Improved Primary Staging of Marginal-Zone Lymphoma by Addition of CXCR4-Directed PET/CT
Johannes Duell, Franziska Krummenast, Andreas Schirbel, Philipp Klassen, Samuel Samnick, Hilka Rauert-Wunderlich, Leo Rasche, Andreas K. Buck, Hans-Jürgen Wester, Andreas Rosenwald, et al.

1422 **Matched-Pair Comparison of ^{18}F-DCFPyL PET/CT and ^{18}F-PSMA-1007 PET/CT in 240 Prostate Cancer Patients: Interreader Agreement and Lesion Detection Rate of Suspected Lesions**
Maurits Wondergem, Friso M. van der Zant, Wouter A.M. Broos, and Remco J.J. Knol

1430 **Prospective, Single-Arm Trial Evaluating Changes in Uptake Patterns on Prostate-Specific Membrane Antigen–Targeted ^{18}F-DCFPyL PET/CT in Patients with Castration-Resistant Prostate Cancer Starting Abiraterone or Enzalutamide**
Katherine A. Zukotynski, Urban Emmenegger, Sebastien Hotte, Anil Kapoor, Wei Fu, Amanda L. Blackford, John Valliant, François Bénard, Chun K. Kim, Mark C. Markowski, et al.

1438 ■ **INVITED PERSPECTIVE. RESIST-PC: U.S. Academic Foray into PSMA Theranostic Trials**
Amir Iravani and Thomas A. Hope

1440 **Prospective phase 2 trial of PSMA-targeted molecular RadiothErapy with ^{177}Lu-PSMA-617 for metastatic castration-reSISTant Prostate Cancer (RESIST-PC): efficacy results of the UCLA cohort**
Jeremie Calais, Andrei Gafita, Matthias Eiber, Wesley R. Armstrong, Jeannine Gartmann, Pan Thin, Kathleen Nguyen, Vincent Lok, Laura Gosa, Tristan Grogan, et al.

1447 **Safety of PSMA-Targeted Molecular Radioligand Therapy with ^{177}Lu-PSMA-617: Results from the Prospective Multicenter Phase 2 Trial RESIST-PC (NCT03042312)**
Jeremie Calais, Johannes Czernin, Pan Thin, Jeannine Gartmann, Kathleen Nguyen, Wesley R. Armstrong, Martin Allen-Auerbach, Andrew Quon, Shadfar Bahri, Pawan Gupta, et al.

1457 ■ **BRIEF COMMUNICATION. Head-to-Head Comparison of ^{68}Ga-NOTA (^{68}Ga-NGUL) and ^{68}Ga-PSMA-11 in Patients with Metastatic Prostate Cancer: A Prospective Study**
Minseok Suh, Hyung-Jun Im, Hyun Gee Ryoo, Keon Wook Kang, Jae Min Jeong, Sneha Prakash, Sanjana Ballal, Madhav P. Yadav, Chandrasekhar Bal, Chang Wook Jeong, et al.

Basic

1461 ■ **FEATURED BASIC SCIENCE ARTICLE. Rational Linker Design to Accelerate Excretion and Reduce Background Uptake of Peptidomimetic PSMA-Targeting Hybrid Molecules**
Ann-Christin Eder, Martin Schäfer, Jana Schmidt, Ulrike Bauder-Wüst, Mareike Roscher, Karin Leotta, Uwe Haberkorn, Klaus Kopka, and Matthias Eder

1468 **Utility of ^{211}At-Trastuzumab for the Treatment of Metastatic Gastric Cancer in the Liver: Evaluation of a Preclinical α-Radioimmunotherapy Approach in a Clinically Relevant Mouse Model**
Huizi Keiko Li, Yukie Morokoshi, Satoshi Kodaira, Tamon Kusumoto, Katsuyuki Minegishi, Hiroaki Kanda, Kotaro Nagatsu, and Sumitaka Hasegawa

1475 **Identification of a PET Radiotracer for Imaging of the Folate Receptor-α: A Potential Tool to Select Patients for Targeted Tumor Therapy**
Patrycja Guzik, Hsin-Yu Fang, Luisa M. Deberle, Martina Benešová, Susan Cohrs, Silvan D. Boss, Simon M. Ametamey, Roger Schibli, and Cristina Müller

LETTERS TO THE EDITOR

1482 **PSMA-Targeted Therapeutics: A Tale About Law and Economics**
Johannes Notni

1483 **Reply: PSMA-Targeted Therapeutics: A Tale About Law and Economics**
Johannes Czernin

1483 **^{18}F-FDG–Avid Axillary Lymph Nodes After COVID-19 Vaccination**
B. Jake Johnson, Kathryn M. Van Abel, Daniel J. Ma, Derek R. Johnson

1484 **Specific and Nonspecific Uptake in Quantitative ^{89}Zr-Immuno-PET**
Eric Laffon and Roger Marthan

DEPARTMENTS

8A **This Month in JNM**

JNM The Journal of NUCLEAR MEDICINE

The Official Publication of **SNMMI**

MISSION STATEMENT: *The Journal of Nuclear Medicine* advances the knowledge and practice of molecular imaging and therapy and nuclear medicine to improve patient care through publication of original basic science and clinical research.

JNM (ISSN 0161-5505 [print]; ISSN 2159-662X [online]) is published monthly by SNMMI, 1850 Samuel Morse Drive, Reston, VA 20190-5316. Periodicals postage is paid at Herndon, VA, and additional mailing offices. Postmaster, send address changes to *The Journal of Nuclear Medicine,* 1850 Samuel Morse Drive, Reston, VA 20190-5316. The costs of publication of all nonsolicited articles in *JNM* were defrayed in part by the payment of page charges. Therefore, and solely to indicate this fact, these articles are hereby designated "advertisements" in accordance with 18 USC section 1734.

DISCLOSURE OF COMMERCIAL INTEREST: Johannes Czernin, MD, editor-in-chief of *The Journal of Nuclear Medicine,* has indicated that he is a founder of Sofie Biosciences and holds equity in the company and in intellectual property invented by him, patented by the University of California, and licensed to Sofie Biosciences. He is also a founder and board member of Trethera Therapeutics and holds equity in the company and in intellectual property invented by him, patented by the University of California, and licensed to Triangle. He also serves on the medical advisory board of Actinium Pharmaceuticals and on the scientific advisory boards of POINT Biopharma, RayzeBio, and Jubilant Pharma and is a consultant for Amgen. No other potential conflicts of interest were reported. Manuscripts submitted to *JNM* with potential conflicts are handled by a guest editor.

EDITORIAL COMMUNICATIONS should be sent to: Editor-in-Chief, Johannes Czernin, MD, *JNM* Office, SNMMI, 1850 Samuel Morse Drive, Reston, VA 20190-5316. Phone: (703) 326-1185; Fax: (703) 708-9018. To submit a manuscript, go to https://submit-jnm.snmjournals.org.

BUSINESS COMMUNICATIONS concerning permission requests should be sent to the publisher, SNMMI, 1850 Samuel Morse Drive, Reston, VA 20190-5316; (703) 708-9000; home page address: jnm.snmjournals.org. Subscription requests and address changes should be sent to Membership Department, SNMMI at the address above. Notify the Society of change of address and telephone number at least 30 days before date of issue by sending both the old and new addresses. Claims for copies lost in the mail are allowed within 90 days of the date of issue. Claims are not allowed for issues lost as a result of insufficient notice of change of address. For information on advertising, contact Team SNMMI (Kevin Dunn, Rich Devanna, and Charlie Meitner; (201) 767-4170; fax: (201) 767-8065; TeamSNMMI@cunnasso.com). Advertisements are subject to editorial approval and are restricted to products or services pertinent to nuclear medicine. Closing date is the first of the month preceding the date of issue.

INDIVIDUAL SUBSCRIPTION RATES for the 2021 calendar year are $574 within the United States and Canada; $617 elsewhere. Make checks payable to the SNMMI. CPC IPM Sales Agreement No. 1415158. Sales of individual back copies from 1999 through the current issue are available for $60 at http://www.snmmi.org/subscribe (subscriptions@snmmi.org; fax: (703) 667-5134). Individual articles are available for sale online at http://jnm.snmjournals.org.

JNM The Journal of NUCLEAR MEDICINE

Somatostatin receptor theranostics: Park and colleagues provide an overview of the current role of SSTR PET in neuroendocrine neoplasms, including selection of patients for peptide-receptor radionuclide therapy, PET-based response assessment, and standardized reporting. . . . . ***Page 1323***

AI in PET image reconstruction: Reader and Schramm consider the methodologies, benefits, and challenges of artificial intelligence applications in PET imaging reconstruction, with a focus on deep learning. . . . ***Page 1330***

PET/MRI in children with cancer: Baratto and colleagues offer an educational review of clinical applications of integrated ^{18}F-FDG PET/MRI in pediatric oncology, including benefits in patient management and future research potential. . . . . ***Page 1334***

Imaging immune-fibrosis crosstalk: Heo and colleagues discuss key biomarkers upregulated in the immune-fibrosis axis in cardiovascular disease and describe molecular imaging agents with promise in elucidating this pathologic process. . . . . ***Page 1341***

^{18}F-FDOPA PET/CT in small intestine NENs: Imperiale and colleagues look at recent comparative studies on PET/CT tracers in small intestine neuroendocrine neoplasms and argue for a continued role for ^{18}F-FDOPA in this context. . . . . ***Page 1347***

Multimodal glioblastoma imaging: Collet and colleagues look at proliferation, hypervascularization, and hypoxia using multiparametric MRI and PET with ^{18}F-FLT and ^{18}F-FMISO to optimize management and treatment of patients with glioblastoma. . . . . ***Page 1349***

Evolution of sentinel node biopsy: Berger and colleagues review the 30-y technologic development of sentinel lymph node biopsy through a retrospective database of patients with cutaneous melanoma in the head and neck region. . . . . ***Page 1358***

SNB in prostate cancer: Mazzone and colleagues describe the added diagnostic value of sentinel node biopsy for identification of nodal metastases in extended pelvic lymph node dissection, including rates of complications and oncologic outcomes. . . . ***Page 1363***

PET/CECT in ^{18}F-FDG–avid lymphomas: Marchetti and colleagues assess the added diagnostic contribution of contrast-enhanced CT as compared with unenhanced CT in PET/CT staging and treatment response assessment of ^{18}F-FDG–avid lymphomas. . . . . ***Page 1372***

PET before anti-PD-1 in melanoma: Nakamoto and colleagues determine the prognostic value of ^{18}F-FDG PET/CT parameters in melanoma patients before beginning therapy with antibodies to the programmed cell death–1 receptor. . . . . ***Page 1380***

MUC5AC-targeted PET in pancreatic cancer: Henry and colleagues describe development of RA96, an anti-MUC5AC antibody, and assess its utility in pancreatic cancer diagnosis through immunohistochemical analysis and whole-body PET. . . . . ***Page 1384***

First-in-humans application of ^{161}Tb: Baum and colleagues report on the use of ^{161}Tb-DOTATOC in 2 patients to investigate γ-scintigraphy and SPECT/CT visualization of physiologic and tumor biodistributions to support future development of terbium-based targeted radionuclide therapy. . . . . ***Page 1391***

^{68}Ga-NODAGA-LM3 and ^{68}Ga-DOTA-LM3 in NETs: Zhu and colleagues evaluate the safety, biodistribution, and dosimetry of these somatostatin receptor–specific antagonists for PET/CT imaging in patients with well-differentiated neuroendocrine tumors. . . . . ***Page 1398***

^{68}Ga-DOTATATE PET for NET therapy response: Ortega and colleagues report on the utility of quantitative parameters from baseline ^{68}Ga-DOTATATE PET/CT and PET performed before the second cycle of peptide receptor radionuclide therapy in predicting response and progression-free survival. . . . . ***Page 1406***

CXCR4 imaging in marginal-zone lymphoma: Duell and colleagues investigate the value of adding CXCR4-directed ^{68}Ga-pentixafor PET/CT to conventional staging in patients with marginal-zone lymphoma. . . . . ***Page 1415***

^{18}F-DCFPyL versus ^{18}F-PSMA-1007: Wondergem and colleagues analyze differences in interreader agreement and detection rates for these regularly used ^{18}F-labeled prostate-specific membrane antigen receptor–targeting radiopharmaceuticals. . . ***Page 1422***

PSMA PET after antiandrogen therapy: Zukotynski and colleagues assess changes in uptake on prostate-specific membrane antigen–targeted PET in men with metastatic castration-resistant prostate cancer starting abiraterone or enzalutamide. . . . . ***Page 1430***

RESIST-PC trial: Iravani and Hope offer background and context on the results of a U.S. trial on the efficacy and safety of ^{177}Lu-prostate-specific membrane antigen-617, as presented in 2 articles in this month's issue of *JNM*. . . . . ***Page 1438***

RESIST-PC efficacy results: Calais and colleagues report on a prospective multicenter phase 2 study intended to determine the efficacy profiles of 2 activity regimens of ^{177}Lu-prostate-specific membrane antigen therapy in patients with progressive metastatic castrate-resistant prostate cancer. . . . . ***Page 1440***

RESIST-PC safety results: Calais and colleagues detail the safety evaluation of ^{177}Lu-PSMA-617 as derived from a cohort of 64 patients with progressive metastatic castrate-resistant prostate cancer exposed to ^{177}Lu-PSMA-617 in the RESIST-PC trial. . . . . ***Page 1447***

^{68}Ga-NGUL versus ^{68}Ga-PSMA-11: Suh and colleagues compare performances in biodistribution and detection of primary and metastatic lesions for these 2 prostate-specific membrane antigen–targeting tracers in a group of patients with prostate cancer. . . ***Page 1457***

Linker design for PSMA hybrid molecules: Eder and colleagues describe a rational linker design aimed at development of a second generation of prostate-specific membrane antigen-11–based hybrid molecules with enhanced pharmacokinetic profiles and improved imaging contrast. . . . . ***Page 1461***

α-RIT for HER2-positive LMGC: Li and colleagues explore in a mouse model whether an α-particle radioimmunotherapy approach with ^{211}At-labeled trastuzumab has efficacy against liver metastasis from primary gastric cancer that is positive for human epidermal growth factor receptor 2. . . . . ***Page 1468***

FRα-selective PET imaging: Guzik and colleagues introduce a folate receptor-α–selective PET agent potentially suitable for identification of patients who might benefit from FRα-targeted therapies. . . . . ***Page 1475***

2021 SNMMI Highlights Lecture: Oncology and Therapy, Part 1

Heiko Schöder, MD, MBA, Memorial Sloan Kettering Cancer Center, New York, NY

From the Newsline Editor: The Highlights Lecture, presented at the closing session of each SNMMI Annual Meeting, was originated and presented for more than 30 years by Henry N. Wagner, Jr., MD. Beginning in 2010, the duties of summarizing selected significant presentations at the meeting were divided annually among 4 distinguished nuclear and molecular medicine subject matter experts. Each year Newsline publishes these lectures and selected images. The 2021 Highlights Lectures were delivered on June 15 as part of the SNMMI Virtual Annual Meeting. In this issue we feature the first part of the lecture by Heiko Schöder, MD, MBA, chief of the Molecular Imaging and Therapy Service at Memorial Sloan Kettering Cancer Center (New York, NY) and a professor of radiology at the Weill Medical College of Cornell University (New York, NY), who spoke on oncology and therapy highlights from the meeting. The second part of the lecture will appear in the November issue of Newsline. Note that in the following presentation summary, numerals in brackets represent abstract numbers as published in The Journal of Nuclear Medicine *(2021;62[suppl 1]).*

First I would like to thank the organizers for inviting me to give this year's highlights lecture on oncology and therapy. It is a pleasure to present these findings. We will begin with a brief statistical characterization of the oncology-related abstracts presented at the 2021 SNMMI Annual Meeting. The majority (51%) came from North America, with a second large percentage of contributions from Asia (41%), and others from Europe (6%), Africa (1%), and South America (1%). Among international countries contributing, a large number of abstracts came from China (166), followed by Korea (61), Japan (57), India (34), Canada (34), and Australia (20). As in past years, the majority (80%) of these abstracts focused on diagnostics, with only about 20% on therapeutic applications.

Among the highest rated abstracts in the clinical area, many were focused on fibroblast activation protein inhibitor (FAPI) and prostate-specific membrane antigen (PSMA) imaging in one form or another, and these will be discussed in detail in this lecture. In the area of basic research, no clear topic emerged as dominant. A number of new probes were presented at the meeting, and we will look at several of these. In the area of therapy, the large majority of abstracts focused on prostate cancer and neuroendocrine tumors.

Clinical Diagnostics

FAPI

Many of us remember the 2019 SNMMI Image of the Year (Fig. 1) from multiple researchers at the University Hospital Heidelberg (Germany), which showed FAPI uptake across a wide range of malignancies (*1*). In the intervening 2 years, numerous case reports and small clinical studies have shown the utility of FAPI-based imaging in diagnosis, staging, radiation therapy planning, and changes in patient management across a range of malignant diseases and sites, including (among others) the lung, pancreas, lower gastrointestinal tract, and head and neck and in sarcoma and peritoneal carcinomatosis. Results from these and other studies, however, have also shown that FAPI is not a cancer-specific agent. Uptake has been shown in a range of inflammatory conditions, including thyroiditis, benign pancreatic lesions, pulmonary fibrosis, solitary fibrous tumor, and others, as well as in the postmyocardial infarction setting.

Heiko Schöder, MD

As background, the tumor microenvironment includes blood vessels, extracellular matrix, and a number of different types of cells, including cancer-associated fibroblasts (CAFs). CAFs are relevant in cancer progression, resistance to therapy, and also in regulating the immune environment. They can be targeted by a number of therapies. FAP is a transmembrane glycoprotein and prognostic marker in cancer expressed only on activated fibroblasts, including activated CAFs. FAP can be targeted in a variety of ways, including by FAPIs, which we use for imaging. As noted, a number of smaller studies have been published, and the field is ready to move on to larger and more quantitative analyses to study the role of FAPI in selected malignancies.

Kessler et al. from the University of Duisberg-Essen, the German Cancer Consortium (DKTK, Essen; DKFZ, Heidelberg), and University Hospital Essen (all in Germany) reported on "^{68}Ga-FAPI for sarcoma imaging: Data from the FAPI-PET prospective observational trial" [126]. The study included 47 patients with bone and soft tissue sarcoma who underwent clinical ^{68}LGa-FAPI PET imaging, 46 of whom also underwent ^{18}F-FDG PET. The study's primary endpoint was association of ^{68}Ga-FAPI PET uptake intensity and histopathologic FAP expression. Secondary endpoints were detection rate, positive predictive value (PPV), interrater reproducibility, and change in management. The ^{68}Ga-FAPI tracer showed high sensitivity and PPV on a per patient and per region basis. In a comparison of detected rates, ^{68}Ga-FAPI PET results were similar to those with ^{18}F-FDG PET, although in some instances ^{18}F-FDG provided additional

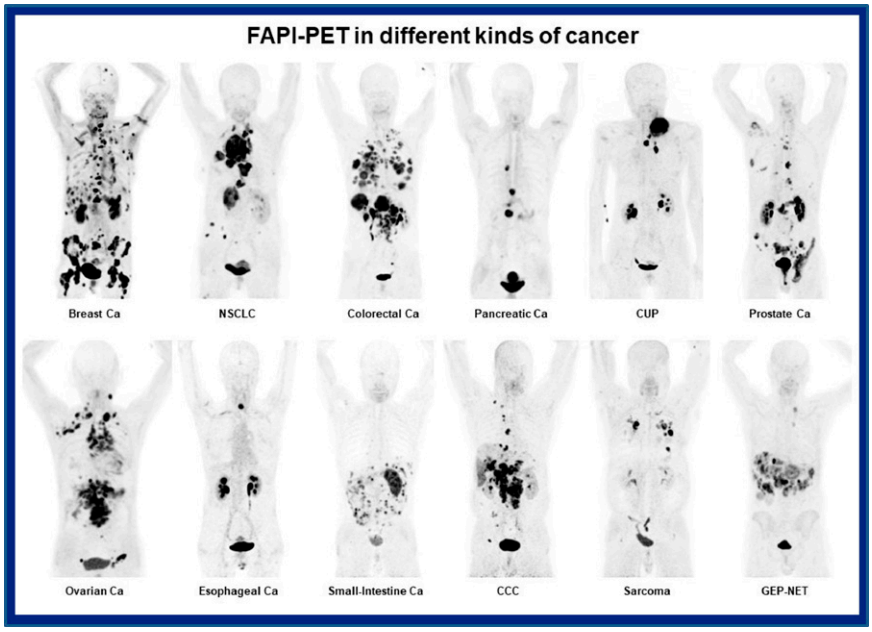

FIGURE 1. SNMMI 2019 Image of the Year: ^{68}Ga-FAPI PET/CT in patients reflecting 12 different tumor entities. Ca = cancer; NSCLC = non–small cell lung cancer; CUP = carcinoma of unknown primary; CCC = cholangiocarcinoma; GEP-NET = gastroenteropancreatic neuroendocrine tumor. Image was created with contributions from Clemens Kratochwil, Paul Flechsig, Thomas Lindner, Labidi Abderrahim, Annette Altmann, Walter Mier, Sebastian Adeberg, Hendrik Rathke, Manuel Rohrich, Hauke Winter, Peter Plinkert, Frederik Marme, Matthias Lang, Hans Ulrich Kauczor, Dirk Jaeger, Juergen Debus, Uwe Haberkorn, and Frederik L. Giesel, each of whom was affiliated with University Hospital Heidelberg (Germany).

information. It is possible that in the future, at least in some patients, complete workups may require both radiotracers. The authors found that the ^{68}Ga-FAPI tracer uptake correlated with immunohistochemistry (IHC)-assessed FAP expression in sarcoma: the higher the FAP expression on IHC, the higher the SUV. Figure 2 is an example from 2 patients, 1 with negative IHC FAP and no uptake on imaging, 1 with positive IHC FAP and high uptake on imaging.

Mona et al. from the University of California Los Angeles/University of California Los Angeles Medical Center reported on "Validation of FAPi PET biodistribution by immunohistochemistry in patients with solid cancers: A prospective exploratory imaging study" [1000]. This study included 15 patients and a variety of tumors and looked at similar correlations, using tissue microarrays to explore whether ^{68}Ga-FAPi-46 PET image biodistribution accurately reflects FAP expression from resected tumor and nontumor specimens. Figure 3 is an interesting patient example, showing strong uptake in a pancreatic tail ductal adenocarcinoma with the corresponding IHC stain. FAP IHC in representative histologic sections demonstrated variable negative-to-weak FAP expression in normal pancreatic parenchyma, except for a subpopulation of cells in normal islets consistently showing strong FAP expression. Again, we see a direct relationship between IHC in tissue and SUV on FAPI PET. The researchers concluded that this and associated translational validation "pave the way for large-scale prospective trials on the use of ^{68}Ga-FAPi-46 PET/CT as a biomarker and stratification tool for FAP-targeted therapies."

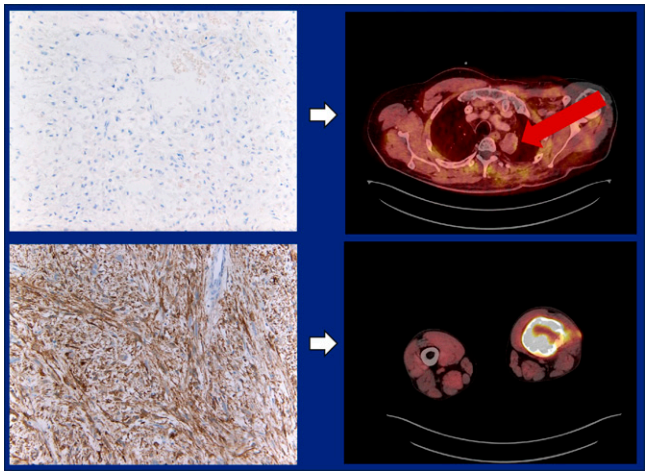

FIGURE 2. ^{68}Ga-FAPI for sarcoma imaging. Data from the FAPI-PET prospective observational trial [126]. Immunochemistry (IHC)-assessed FAP expression in sarcoma correlated well with ^{68}Ga-FAPI tracer uptake. Top: IHC (left) and FAPI PET/CT (right) images in a patient with FAP– disease. Bottom: corresponding images in a patient with FAP+ disease.

Other abstracts on FAPI imaging were presented at this meeting, and time does not allow me to detail each of these, but several have already been published in major journals. Chen et al. from First Affiliated Hospital of Xiamen University/Xiamen University (China) reported on the "Role of ^{68}Ga-FAPI PET/CT in the evaluation of peritoneal carcinomatosis and comparison with ^{18}F-FDG PET/CT" [20] (*2*). This is a challenging indication in PET and PET/CT imaging. The retrospective study included 46 patients (16 with diffuse-type peritoneal carcinomatosis, 27 with nodular-type peritoneal carcinomatosis, and 3 true-negative patients). The researchers presented encouraging data indicating that FAPI uptake was higher than that of ^{18}F-FDG, that FAPI PET allowed detection of smaller lesions, and that a particular

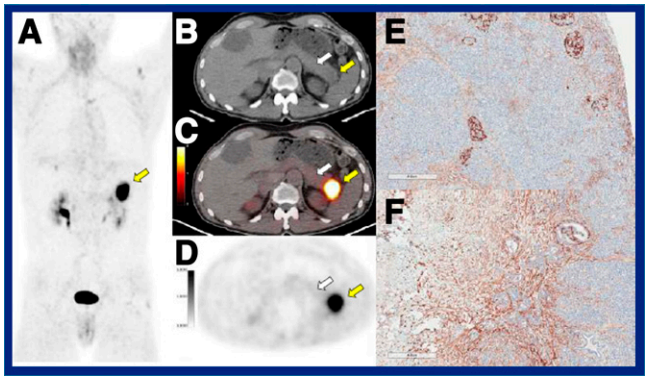

FIGURE 3. Validation of FAPi PET biodistribution by immunohistochemistry (IHC) in patients with solid cancers. Example: 65-year-old man with pancreatic ductal adenocarcinoma (yellow arrows: pancreatic tail ductal adenocarcinoma lesion; white arrows: resected normal pancreas region). (A) Whole-body PET; (B) transaxial CT; (C) transaxial PET/CT (SUV_{max} 15.69); (D) transaxial PET (SUV_{mean} 12.51). (E) FAP IHC on representative histologic sections demonstrated variable negative-to-weak FAP expression in normal pancreatic parenchyma with a subpopulation of cells in normal islets consistently showing strong FAP expression; and (F) moderate-to-strong FAP expression was noted for tumor tissue.

advantage for FAPI PET was evident in gastric and colon cancers.

Pang et al. from Xiamen University/First Affiliated Hospital of Xiamen (China) reported on "Comparison of ^{68}Ga-FAPI and ^{18}F-FDG uptake in gastric, duodenal, and colorectal cancers" [125] (*3*). They reported that ^{68}Ga-FAPI PET/CT was superior to ^{18}F-FDG PET/CT in detection of primary and metastatic lesions, with higher tracer uptake in most primary and metastatic lesions.

Other related abstracts looked at nasopharyngeal cancer, where FAPI imaging provided additional advantages in evaluating skull base invasion, suggesting that FAPI PET/MR may become routine in future evaluations in this setting. Qin et al. from Union Hospital, Tongji Medical College, and Huazhong University of Science and Technology (Wuhan, China) reported on "A head-to-head comparison of ^{68}Ga-DOTA-FAPI-04 and ^{18}F-FDG PET/MR in patients with nasopharyngeal carcinoma: A prospective study" [124] (*4*). They found that ^{68}Ga-FAPI outperformed ^{18}F-FDG in delineating primary tumors and detecting distant metastases, particularly in the evaluation of skull-base and intracranial invasion, concluding that "^{68}Ga-FAPI hybrid PET/MR has the potential to serve as a single-step staging modality" for patients with nasopharyngeal cancer. Zhao et al. from the First Affiliated Hospital of Xiamen University (China) reported on the "Clinical utility of ^{68}Ga-FAPI PET/CT for primary staging and recurrence detection in nasopharyngeal carcinoma" [1086] (*5*) in a study with 45 participants. Their data also indicated higher uptake of ^{68}Ga-FAPI than ^{18}F-FDG.

Prostate Cancer

Prostate cancer remains a significant burden across the globe, including the Americas, large portions of Africa and Europe, and Australia. On May 12, a new Lancet Commission was announced to study prostate cancer in greater detail, to create recommendations for prostate cancer diagnosis and treatment, and to address disparities in prostate cancer management. The announcement noted that "genomic tools and imaging, particularly PSMA PET-CT, are likely to be increasingly important in treatment decisions in the future" (*6*).

Two large and influential recent studies have focused on prostate cancer, 1 on ^{68}Ga-PSMA-11 and the other on ^{18}F-DCFPyL. Fendler from the University of California at Los Angeles and an international consortium of research centers reported in *JAMA Oncology* on an "Assessment of ^{68}Ga-PSMA-11 PET accuracy in localizing recurrent prostate cancer: A prospective single-arm clinical trial" (*7*). The study included 635 men with biochemically recurrent prostate cancer after treatment and identified high PPV, high detection rate, and high interreader agreement for localization with ^{68}Ga-PSMA-11 PET. Morris et al. from Memorial Sloan Kettering Cancer Center (New York, NY) and an international consortium of research centers reported in *Clinical Cancer Research* on "Diagnostic performance of ^{18}F-DCFPyL-PET/CT in men with biochemically recurrent prostate cancer: Results from the CONDOR phase III, multicenter study" (*8*). The study included 208 men with rising prostate-specific antigen (PSA) ≥0.2 ng/mL after prostatectomy or ≥2 ng/mL above nadir after radiotherapy. Of note, patients were included in the ^{68}Ga-PSMA-11 study irrespective of prior imaging findings, whereas in the ^{18}F-DCFPyL study, the median PSA was lower and only patients with negative or equivocal prior imaging were enrolled. Nevertheless, we can identify common themes in their findings: higher overall detection rates (75% for ^{68}Ga-PSMA-11; 59%–66% with ^{18}F-DCFPyL) correlated with increasing PSA levels and very respectable numbers in terms of PPV and sensitivity (sensitivity here referring to cases with histologic verification). Reader agreement results were also good with both tracers.

Rowe from Johns Hopkins Medicine (Baltimore, MD) and the CONDOR consortium provided additional data from their study at this meeting in "A phase 3 study of ^{18}F-DCFPyL PET/CT in patients with biochemically recurrent prostate cancer (CONDOR): An analysis of disease detection rate and PPV by anatomic region" [123]. They found that ^{18}F-DCFPyL PET/CT detected and localized metastatic lesions with high PPV regardless of anatomic region (prostate/prostate bed, pelvic lymph nodes, or extrapelvic regions, including lymph nodes, bone, and viscera/soft tissue) (Fig. 4). Higher PPVs were observed in extrapelvic lymph nodes and bone compared to viscera/soft tissue. This is, of course, important, because an imaging agent may not be very useful if it addresses disease only in the pelvis but not outside (or vice versa). I should point out that the number of visceral lesions in this study was quite small, so related data probably should not be overinterpreted.

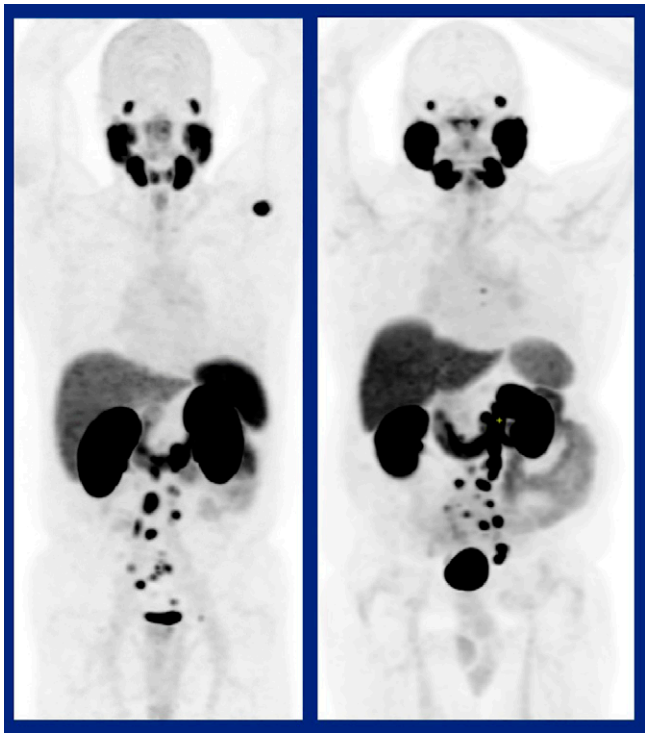

FIGURE 4. Left: Representative imaging from the ^{68}Ga-PSMA-11 PET/CT trial from UCLA and an international consortium. Right: Representative imaging from the CONDOR phase III ^{18}F-DCFPyL PET/CT trial. Despite difference in enrollment criteria and procedures, common findings included higher overall detection rates that correlated with increasing prostate-specific antigen levels, good positive-predictive values, and improved sensitivity. Reader agreement results were also high with both tracers.

Other abstracts were presented on these and other PSMA compounds. Although I cannot detail each one, I want to highlight 4 as illustrative of current research and findings. Lin et al. from the University of California at San Francisco reported on "The increased prevalence of low and heterogeneous PSMA uptake in the setting of metastatic castration-resistant prostate cancer" [1349]. In this retrospective study, low PSMA uptake (≥1 lesion with no-to-low PSMA uptake) was seen on >50% of scans, and heterogeneous uptake (defined as both low and high PSMA uptake lesions on the same scan) was seen on >40% of scans. The authors concluded that this high degree of heterogeneity within patients and in low PSMA-expressing tumors may complicate treatment, particularly with PSMA-targeted radioligand therapy.

Maliha et al. from McGill University Health Center, the University of Montreal, and the Jewish General Hospital (all in Montreal, Canada) reported on "Physiological DCFPyL PSMA-targeted tracer uptake in the epididymis head newly appreciated on digital PET/CT" [1321]. This was an interesting incidental finding, and the authors noted that it is both common and more frequent in patients with higher serum testosterone levels. They emphasized that this physiologic finding should not be misinterpreted as pathologic.

Lindenberg et al. from the National Cancer Institute (NCI), the University of California San Francisco, Johns Hopkins University School of Medicine (Baltimore, MD), Yale University (New Haven, CT), and Novartis Pharmaceuticals (East Hanover, NJ; Turin, Italy; and Geneva, Switzerland) reported on "Safety and tolerability of ^{68}Ga-PSMA-R2 as an imaging agent in patients with biochemical recurrence or metastatic prostate cancer" [1319]. In this safety and tolerability study, the PSMA agent was well tolerated with no significant adverse events. The authors concluded that the lesion detectability and low radiation dose absorbed by salivary and lacrimal glands compared with other PSMA PET agents are promising for future therapeutic applications.

Miksch et al. from University Hospital Ulm, the Technical University Munich (Garching), and the German Armed Forces Hospital Ulm (all in Germany) reported that "Novel ^{18}F-siPSMA-14 shows favorable kinetics and high interobserver agreement in staging of prostate cancer patients" [1328]. The study analyzed biodistribution, detection rates, and interobserver agreement in 134 patients with either primary prostate cancer or recurrent disease. On a 5-point grading system, good agreement was noted (94% in primary and 86% in recurrent disease). As in previous abstracts, higher detection rates were found with higher PSA levels. No forced diuresis was used in the study. Target-to-nontarget ratios were notably high in PET/CT-positive tumors (9.3 in prostate, 11.6 in lymphatic, 14.3 in bone, and 14.6 in visceral lesions), enabling excellent contrast imaging. This contrast is evident in Figure 5 in a patient assessed for primary disease after chemotherapy. On the left, excreted activity in

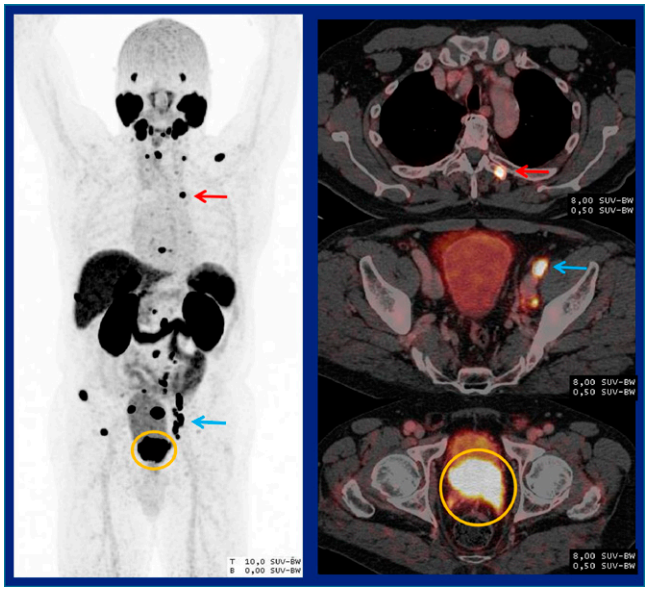

FIGURE 5. ^{18}F-siPSMA-14 in staging prostate cancer patients. Images acquired in a 64-year-old man with progressive disease after chemotherapy (prostate-specific antigen = 100 ng/mL). Left: excreted activity on PET in the urinary bladder obscures the primary tumor. Right: contrast is high on ^{18}F-siPSMA-14 PET/CT for bone (top), lymph node metastases (middle), and (although some excreted activity is seen in the bladder) much higher uptake is apparent in the primary tumor (bottom).

the urinary bladder obscures the primary tumor; on the right, contrast is high for bone and lymph node metastases and, although some excreted activity is seen in the bladder, much higher uptake is apparent in the tumor. This tracer is especially promising, then, for detecting locoregional recurrence.

Other Applications

Naghavi-Behzad et al. from the University of Southern Demark (Odense), Odense University Hospital (Odense, Denmark), the Basel Academy for Quality and Research in Medicine (Switzerland), and the Technical University of Munich (Germany) reported on "Response monitoring in metastatic breast cancer: A comparison of survival times between FDG PET/CT and contrast-enhanced CT" [129]. This study is relevant to a challenge with which many of us deal on a day-to-day basis in our practices: arguing with insurance companies about whether a scan should be preapproved for reimbursement. Patients in the study underwent conventional imaging with contrast-enhanced CT (144 patients), FDG PET/CT (83 patients), or both (72 patients) as part of response monitoring to treatment. Their results indicated that overall, 5-year survival rates for patients with metastatic breast cancer were significantly higher with PET/CT alone (41.9%) or in combination with contrast-enhanced-CT (43.3%) than with contrast-enhanced CT alone (15.8%). Why would patients with PET imaging have better survival? The answer, of course, is that the improved survival is not related to the modality per se but to the fact that PET enables earlier detection of recurrence and more timely and appropriate management decisions. This study is clear evidence of the utility of PET/CT in response assessment in patients with breast cancer and provides the kind of quantitative data that may prove persuasive to third-party payers.

Clinical Therapies

Great advances are being reported in clinical therapies in our field, highlighted this year by 2 recent clinical trials in patients with advanced prostate cancer. Results from the VISION trial were reviewed on June 6 at the American Society of Clinical Oncology (ASCO) meeting by Michael Morris, MD, from Memorial Sloan Kettering Cancer Center (New York, NY). The study has primary endpoints comparing radiographic progression-free survival and overall survival in patients with progressive PSMA-positive metastatic castrate-resistant prostate cancer who receive ^{177}Lu-PSMA-617 in addition to best supportive/best standard of care versus patients treated with best supportive/best standard of care alone. The study enrolled patients who had positive PSMA signals on PET imaging and who had previously received taxane therapy and novel androgen axis therapy and were now deemed eligible only for best supportive care. It is important to point out that no PSMA-only arm was included in the study. Both the ASCO presentation and recently published results show that the treatment arm in the VISION trial had better overall survival and better radiographic progression-free survival with improved quality of life. We look forward to more analyses and results from this trial.

The next trial was the TheraP trial, which had some important differences from the VISION trial. Hofman et al. from the Peter MacCallum Cancer Centre/University of Melbourne, St. Vincent's Hospital and Garvan Institute of Medical Research (Sydney), Royal Brisbane and Women's Hospital (Brisbane), Royal Adelaide Hospital, Sir Charles Gairdner Hospital Western Australia (Nedlands), Calvary Mater Newcastle, Austin Health Melbourne, Monash Health (Melbourne), and Fiona Stanley Hospital (Murdoch; all in Australia) reported at the SNMMI meeting on "^{177}Lu-PSMA-617 versus cabazitaxel in metastatic castration-resistant prostate cancer: A randomized, open-label, phase 2 trial (TheraP)" [1703] (*9*). Patients with progressive disease after docetaxel therapy at 11 sites in Australia were first imaged with both ^{68}Ga-PSMA and ^{18}F-FDG PET/CT. Only those with positive PSMA uptake that was concordant with FDG uptake were included in the trial. A resulting total of 200 men were then randomized to ^{177}Lu-PSMA-617 or cabazitaxel. Figure 6 includes examples from the study illustrating the concordant and discordant imaging findings used in patient selection. The patient on the top left, for example, showed low PSMA uptake and high FDG uptake, and so was ineligible for the trial. Next is a patient who had positive uptake of both tracers but with additional metastases seen only on FDG, a discordance that made the patient ineligible. This is in contrast to the eligible patients (bottom row) with concordant uptake on both scans and with PSMA-dominant findings. Imaging, then, was used to maximize the inclusion of patients most likely to benefit from ^{177}Lu-PSMA-617 treatment. ^{177}Lu-PSMA-617 led to significantly greater PSA reductions (66% experienced ≥50% reduction in PSA from baseline, compared with only 37% with cabazitaxel), higher objective response rates (49% vs. 24%; RECIST 1.1), longer progression-free survival at 1 year (19% vs. 3%), and significant improvements in several patient-reported outcome domains. Of note, the investigators also reported on comparative side effects. Patients in the ^{177}Lu-PSMA-617 arm experienced fewer grade 3 or 4 adverse events (53% vs 33%) and overall reported fewer side effects. We look forward to seeing immediate benefits with this life-saving and quality-of-life-improving treatment for our patients with prostate cancer. [*Author's note:* On the same day this lecture was given, the U.S. Food and Drug Administration announced that it had granted Breakthrough Therapy designation for ^{177}Lu-PSMA-617 in metastatic castration-resistant prostate cancer.]

In the context of radionuclide therapies, dosimetry is very important for both normal organs/tissues and target lesions. The process, however, can be quite time-consuming, requiring multiple scans on several subsequent days. Investigators across the globe are looking for solutions, particularly at whether advanced computational modeling can be used to derive dosimetry data with reasonable accuracy from a single time-point scan. Chicheportiche

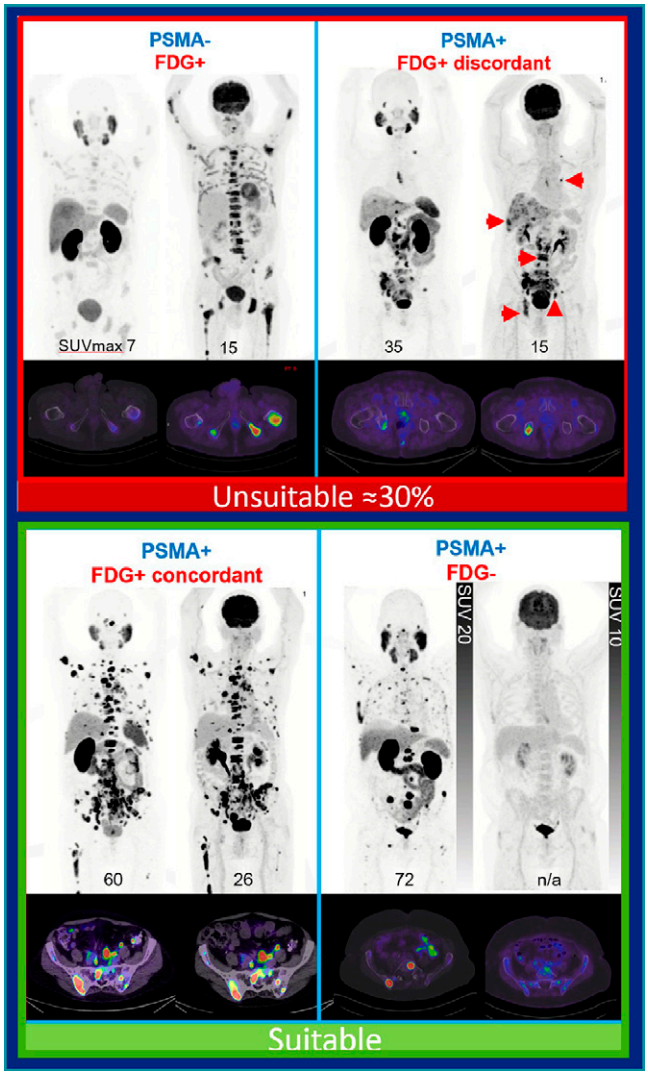

FIGURE 6. ^{177}Lu-PSMA-617 vs cabazitaxel in metastatic castration-resistant prostate cancer: TheraP trial. Patients with progressive disease after docetaxel therapy were first imaged with both ^{68}Ga-PSMA and ^{18}F-FDG PET/CT, and only those with positive PSMA uptake that was concordant with FDG uptake were included in the trial. Images show PET (top) and PET/CT (bottom row) illustrating concordant and discordant findings used in patient selection. Top box: A patient with low PSMA uptake and high FDG uptake (left, ineligible for the trial); patient with positive uptake of both tracers but additional metastases seen only on FDG (right, discordant, ineligible). Bottom row: patient with concordant uptake on both scans (left, eligible); and patient with PSMA-dominant findings (right, eligible). Imaging was used to maximize inclusion of patients most likely to benefit from ^{177}Lu-PSMA-617 treatment.

et al. from Hadassah–Hebrew University Medical Center (Jerusalem, Israel), Hebrew University of Jerusalem (Israel), and University College London/UCL Hospitals NHS Trust (London, UK) asked "Can absorbed radiation doses by organs and tumors after peptide-receptor radionuclide therapy (PRRT) be estimated from a single SPECT/CT study?" [18]. The aim was to assess the feasibility of using a single quantitative SPECT/CT study after each PRRT cycle combined with a trained multiple linear regression model for absorbed dose calculation. The researchers found that in

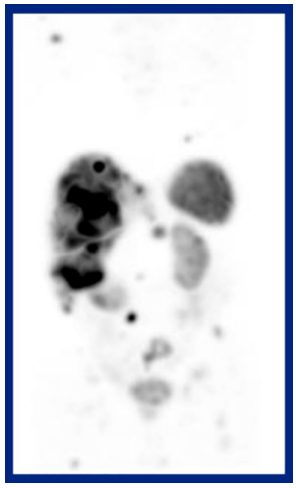

FIGURE 7. Single-timepoint imaging for dosimetry in peptide-receptor radionuclide therapy (PRRT). Researchers used a trained model for dose calculation with a single quantitative SPECT/CT study after each PRRT cycle for absorbed dose calculation (example image shown). The method was in good agreement with the standard multi-timepoint imaging protocol, with no associated changes in management decisions.

a test set with data from 40 patients, their dosimetry calculation method was in good agreement with the standard multi-timepoint imaging protocol, with no associated changes in management decisions (Fig. 7). The conclusion was that if this can be confirmed in a larger series it may very well be possible to perform a single scan to derive accurate dosimetry for PRRT and potentially other applications. This would result not only in simplification of the dosimetry process but also improved patient comfort and reduced scanner and staff time.

Interest continues in using nonimaging tools to improve our ability to predict and measure response to therapies. Blood-based molecular gene signatures are being incorporated into noninvasive tools to provide clinical guidance and facilitate management during PRRT, which may prove especially useful, because radiographic pseudoprogression is a known confounding factor during PRRT. Bodei et al. from Memorial Sloan Kettering Cancer Center (New York, NY), Wren Laboratories (Branford, CT), and Yale University School of Medicine (New Haven, CT) reported on "Blood-based genomic assessment of the clinical efficacy and toxicity of PRRT" [78]. These researchers used 3 independent blood-based gene expression assays: a 51-marker gene NETest (liquid biopsy) to monitor therapeutic efficacy, PRRT Predictor Quotient (a molecular marker used to predict PRRT responsiveness), and a 16-gene radiation toxicity assay to assess PRRT-related toxicity. In a cohort of ^{177}Lu-PRRT–treated patients with gastroenteropancreatic neuroendocrine and lung tumors, these assays were explored for their suitability in predicting treatment response, monitoring response, or use as safety biomarkers to monitor renal function and predict toxicity. Each of the assays showed quite positive results. This is a work in progress, and series with larger numbers are forthcoming. If validated, this will be a helpful tool in predicting and monitoring patient response to DOTATATE therapy in neuroendocrine tumors.

Morgan et al. from the University of Colorado Medical Center (Aurora) reported on "Utilization and cost of

^{223}Ra-dichloride (Xofigo) for treatment of metastatic castration-resistant prostate cancer in the U.S. Medicare population" [1309]. This is an interesting study because the authors looked not only at utilization patterns from 2015 to 2017 (a period during which they noted a significant increase) but at which physicians/disciplines were actually administering the therapy. More than 57% of treatments were administered by radiation oncologists. This seems to be a clear call to action for the nuclear medicine community. Two years ago, Czernin et al. published an article in *The Journal of Nuclear Medicine* highlighting potential weaknesses and challenges for nuclear medicine, including insufficient training, loss of ownership, and lack of desire to perform theranostic applications or to perform therapy (*10*). There is a reason that the word "medicine" is in the name of our discipline—we encompass both diagnosis and therapy. We can continue to administer therapy and expand the range of these activities only if we as a community have the collective desire to do so, as well as the skills, infrastructure, and training programs. This is an appeal to all nuclear medicine professionals to work together to remain as owners of our therapy and theranostic applications.

Part 2 of the 2021 Oncology and Therapy Highlights, in the November issue of Newsline, will focus on new targets for radionuclide therapy and other novel therapy approaches, as well as new techniques and methods for data analysis.

REFERENCES

1. SNMMI. SNMMI Annual Meeting spotlights new innovations and expanding horizons. *J Nucl Med*. 2019;60[8]:2N.
2. Zhao L, Pang Y, Luo Z, et al. Role of [^{68}Ga]Ga-DOTA-FAPI-04 PET/CT in the evaluation of peritoneal carcinomatosis and comparison with [^{18}F]-FDG PET/CT. *Eur J Nucl Med Mol Imaging*. 20201;48(6):1944–1955.
3. Pang Y, Zhao L, Luo Z, et al. Comparison of ^{68}Ga-FAPI and ^{18}F-FDG uptake in gastric, duodenal, and colorectal cancers. *Radiology*. 2021;298(2):393–402.
4. Qin C, Liu F, Huang J, et al. A head-to-head comparison of ^{68}Ga-DOTA-FAPI-04 and ^{18}F-FDG PET/MR in patients with nasopharyngeal carcinoma: A prospective study. *Eur J Nucl Med Mol Imaging*. 2021 Feb 20. Online ahead of print.
5. Zhao L, Pang Y, Zheng H, et al. Clinical utility of [^{68}Ga]-labeled activation protein inhibitor (FAPI) positron emission tomography/computed tomography for primary staging and recurrence detection in nasopharyngeal carcinoma. *Eur J Nucl Med Mol Imaging*. 2021 Apr 1. Online ahead of print.
6. James N, Lee N, Horton R. Announcing the Lancet Commission on Prostate Cancer. *Lancet*. 2021; 397(10288):1865–1966.
7. Fendler WP, Calais J, Eiber M, et al. Assessment of ^{68}Ga-PSMA-11 PET accuracy in localizing recurrent prostate cancer: A prospective single-arm clinical trial. *JAMA Oncol*. 2019;5[6]:856–863.
8. Morris MJ, Rowe SP, Gorin, et al. Diagnostic performance of ^{18}F-DCFPyL-PET/CT in men with biochemically recurrent prostate cancer: Results from the CONDOR phase III, multicenter study. *Clin Cancer Res*. 2021;27(13):3674–3682.
9. Hofman MS, Emmett L, Sandhu S, et al. [^{177}Lu]Lu-PSMA-617 versus cabazitaxel in patients with metastatic castration-resistant prostate cancer (TheraP): A randomised, open-label, phase 2 trial. *Lancet*. 2021;397(10276):797–804.
10. Czernin J, Sonni I, Rasmaria A, Calais J. The future of nuclear medicine as an independent specialty. *J Nucl Med*. 2019;60(suppl 2):3S–12S.

SNMMI and ACGME Equity Matters Initiative

SNMMI announced on August 4 its partnership with the Accreditation Council for Graduate Medical Education (ACGME) in ACGME Equity Matters, a new initiative that introduces a framework for continuous learning and process improvement in diversity, equity, inclusion, and antiracism practices. The initiative aims to drive change within graduate medical education by increasing physician workforce diversity and building safe and inclusive learning environments, while promoting health equity by addressing racial disparities in health care and overall population health.

The ACGME Equity Matters framework includes 2 key components: (1) educational resources that will be available to all involved in GME; and (2) collaborative Learning Communities drawn from national stakeholder groups made up of GME Sponsoring Institutions and programs, including faculty members and individual residents/fellows, as well as specialty societies and other health care partners. The Council of Medical Specialty Societies (CMSS), of which SNMMI is a member, and the Organization of Program Director Associations (OPDA) launched their participation in the program with the convening of 2 Learning Communities that will initiate an 18-mo engagement cycle. This partnership will support diversity, equity, inclusion, and antiracist practices and policies across the full continuum from physician training to physicians in practice. Core teams from CMSS and OPDA members will include an elected leader to champion the initiative and senior executive leaders who will be accountable for implementing policy and practice changes.

The ACGME program will offer a phased curriculum to enable participants to move through progressively more complex concepts within 4 domains: acknowledgment, acceptance and accountability, action, and assessment and adaptation. Also included will be tools and skills training to drive implementation of innovative interventions, practices, policies, and data strategies. Forty-two organizations, including 31 CMSS Member Specialty Societies and 11 PDAs, will be participating in the inaugural 18-mo cohort of the learning communities. More information is available at: https://acgme.org/What-We-Do/Diversity-Equity-and-Inclusion/ACGME-Equity-Matters/.

SNMMI
ACGME

Amnon (Amy) Piepsz, MD (1938–2021)

Amnon Piepsz was born in 1938 in Antwerp (Belgium) and died in Brussels (Belgium) on July 26, 2021, after a 2-year illness. He completed his studies in pediatrics in 1967 at the Vrije Universiteit Brussel (VUB) and became interested in nuclear medicine methodologies very early in his career, attracted by its physiologic and noninvasive approach. He completed his studies in nuclear medicine in 1969 at the VUB and advanced there rapidly to become a full professor of both pediatrics and nuclear medicine. His PhD thesis in 1988 was on a "Methodology of separate clearance measurement by means of ^{99m}Tc-DTPA and the gamma camera."

Dr. Piepsz radiated enthusiasm for nuclear medicine throughout his career and was a major contributor to the "Consensus report on quality control of quantitative measurements of renal function obtained from the renogram" (*Semin Nucl Med.* 1999; 29:146–159), published by the International Scientific Committee of Radionuclides in Nephrourology (ISCORN). His main areas of interests are reflected in more than 250 peer-reviewed publications and were directed toward development of clearance methodologies in children and adults and both experimental and clinical studies related to pediatric nephrourologic problems.

He worked as a pediatrician in a general outpatient clinic with special interests in urinary tract infections, the mother–child relationship, and psychosomatic diseases. Most of his career was spent at the Centre Hospitalier Universitaire Saint-Pierre (Brussels, Belgium) and in the Academic Hospital of the VUB. After his official retirement, he continued to work as a volunteer at Ghent University Hospital, where he pursued his research and the education of trainees.

Dr. Piepsz became a genuine world citizen, giving lectures and courses in such diverse locales as Bombay, Cape Town, Djakarta, and Paris. He also lectured under the sponsorship of the International Atomic Energy Agency, the European School of Nuclear Medicine (European Association of Nuclear Medicine [EANM]), and the Université Paris-Sud. In addition, he was active in supporting the development of nuclear medicine in many less developed countries and in South America, especially Chile. He was fluent in multiple languages, including French, Flemish, German, English, Italian, and Spanish and loved to visit cities to become familiar with their inhabitants and cultures.

He was an active member of the Societies of Nuclear Medicine and of Pediatrics of Belgium and of the EANM. He was the beloved chair of the Paediatric Task Group of the EANM, on which he served for more than 20 years. He served as an editor of the *European Journal of Nuclear Medicine* and a scientific reviewer for *The Journal of Nuclear Medicine* and many other journals. He also coedited *Functional Imaging in Nephro-Urology* (London, UK: Taylor and Francis; 2006) under the auspices of ISCORN.

His life outside of medicine was rich. As a 15-year-old, he earned First Prize in piano at the Conservatoire Royal de Musique of Brussels. An extraordinary pianist, he played a wide range of music with expertise and feeling. He gave private concerts in duet with a violinist and also sang bass in the European Union Choir (of which he was president from 1999–2004). He was a lover of art and liked to swim, play tennis, and hike in the mountains with colleagues.

His nickname, Amy, perfectly characterized his generous personality ("ami" being French for "friend"). He had qualities rarely seen in a single person and was an inspirational figure for all in nuclear medicine. He was especially attentive to trainees and eager to share his scientific knowledge and clinical hands-on techniques. He was far more than an imaging specialist; he was an attentive clinician and sympathetic physician who was devoted to his pediatric patients, their parents, members of his department, and his collaborators. He always shared his enthusiasm and joy with others. We will miss him and remember him fondly.

Alain Prigent, MD, PhD
Paris, France
M. Donald Blaufox, MD, PhD
New York, NY
Andrew Taylor, MD
Atlanta, GA
Naomi Alazraki, MD
Atlanta, GA

State of the Society: SNMMI Thrives Despite COVID-19 Challenges

Virginia Pappas, CAE, SNMMI CEO

Over the past year, SNMMI has navigated the most difficult operating environment we have experienced in our history. Throughout the year, SNMMI's board of directors and management team collaborated closely to enable the organization to deliver services to our members and meet the health and safety needs of our employees, then move above and beyond to conceive and implement new, exciting programs and ideas.

From the start of the pandemic, SNMMI took precautions to ensure the safety of members and staff, changing meetings to virtual formats and creating a new, effective work environment for staff and society operations. With SNMMI's already extensive experience in the virtual environment, these functions not only proved engaging and effective but also expanded our presence in the nuclear medicine space worldwide.

At the same time, the society worked closely with federal organizations and other groups on COVID-related issues, including vaccination priority for members and the availability of essential isotopes and amino acid solution. SNMMI also created an online COVID-19 Resource Center to ensure that members had the news, information, and advice they needed to support them in their practice.

Despite the challenges of the pandemic, SNMMI has advanced not only our existing projects but also a wide range of new initiatives. To promote advances in radiopharmaceutical therapy, a Radiopharmaceutical Therapy Centers of Excellence program and a Radiopharmaceutical Therapy Registry have been created. A therapy toolkit for sites beginning implementation has been developed, as well as practice resources, education, and information regarding dosimetry. New research fellowships, awards, and a technologist therapy badging program are now available or in progress. Much of this information can be found on the new RPT website portal at www.snmmi.org/therapy.

SNMMI has launched a new initiative to increase awareness of nuclear medicine among referring physicians and the general public, utilizing broad-based consumer media outreach. The society has also promoted cutting-edge research via *The Journal of Nuclear Medicine*, which dramatically increased its impact and influence among 133 medical journals in the medical imaging category.

In the health policy and regulatory affairs area, the FIND Act of 2021 was introduced in both the House of Representatives and the Senate. If passed, this legislation would significantly expand patient access to a wide range of diagnostic radiopharmaceuticals that can better detect conditions such as heart disease, Alzheimer and Parkinson disease, breast and prostate cancer, and neuroendocrine tumors. This legislation would also help providers better manage costs while delivering more targeted and cost-efficient care.

Years of work from SNMMI and its partners also paid off this summer as the Centers for Medicare and Medicaid Services (CMS) and Humana allowed coverage for noncologic PET imaging. In addition, with the retirement of the National Coverage Determination for ^{18}F-FDG PET infection and inflammation, coding barriers have been removed and coverage determinations are now made by local Medicare Administrative Contractors. CMS is also considering new coverage for beta-amyloid imaging, which is supported by SNMMI.

Understanding that artificial intelligence will greatly impact the future of medicine, SNMMI has created several related initiatives. An Artificial Intelligence Taskforce, formed earlier this year, launched a challenge in conjunction with the Michael J. Fox Foundation to collect clinical data from DaTScan images. The task force has also been drafting manuscripts for submission to *JNM* and planning for an Artificial Intelligence Summit to be held in early 2022.

During the pandemic, fantastic progress has been made in the development of new agents and therapies, setting up the profession for increasing growth. Looking forward, we hope to hold events in-person to support this growth, including the Therapeutics Conference, November 11–14, 2021, in New Orleans, LA, and the Mid-Winter Meeting, January 28–31, 2022, in Orlando, FL.

I am proud to share with you that the decisions we made have put SNMMI on track to end fiscal year 2021 with very healthy positions of operating cash and investments. We are extremely grateful for our leadership, members, volunteers, corporate partners, and employees who have come together during this challenging time to enable SNMMI to continue to promote the value of nuclear medicine, molecular imaging, and radionuclide therapy. The innovative programs and services developed were extraordinarily successful and have allowed the society to remain healthy and strong.

HHS Inspector General to Review FDA Accelerated Approval Pathway

The Office of Inspector General (OIG) of the U.S. Health and Human Services announced on August 4 that it would launch a review process of the recent U.S. Food and Drug Administration (FDA) approval of Aduhelm (aducanumab) to treat patients with Alzheimer disease under the accelerated approval pathway. The pathway allows the FDA to approve drugs that treat serious conditions and that fill an unmet medical need based on a surrogate endpoint. According to an OIG press release, this approval "raised concerns due to alleged scientific disputes within the FDA, the advisory committee's vote against approval, allegations of an inappropriately close relationship between the FDA and the industry, and the FDA's use of the accelerated approval pathway." In the review, the OIG will assess how the FDA implements the accelerated approval pathway and manages interactions with outside parties, as well as other aspects of the process, such as deciding how scientific disputes are resolved. FDA's relevant policies and procedures, along with compliance, will be included in the review, based on a sample of drugs approved using the accelerated pathway. The OIG will not assess the scientific appropriateness of the FDA approval of any drugs under review. This work may result in multiple reports, expected to be issued in 2023.

Office of Inspector General
U.S. Health and Human Services

FIND Bills in House and Senate

On July 16, Congresspersons Scott Peters (D-CA), Bobby Rush (D-IL), Neal Dunn (R-FL), and Greg Murphy (R-NC) introduced the Facilitating Innovative Nuclear Diagnostics (FIND) Act of 2021 (HR 4479), intended to significantly expand patient access to advanced nuclear diagnostic imaging technologies. The bill (previously HR 3772) targets creation of a legislative fix to the Center for Medicare and Medicaid Services (CMS) bundling of diagnostic radiopharmaceuticals in the hospital outpatient space after a 3-year pass-through period postapproval by the U.S. Food and Drug Administration.

SNMMI and its coalition partners, the Medical Imaging & Technology Alliance and the Council on Radionuclides and Radiopharmaceuticals, in addition to dozens of patient advocacy organizations, praised the proposed legislation. "Innovative radiopharmaceuticals are revolutionizing the diagnosis and treatment of a wide variety of diseases, but under current CMS payment policies, these remarkable agents often are not available to Medicare beneficiaries, resulting in inequities in health care. The FIND Act addresses this current important problem and will improve access to these life-saving imaging agents," said Richard Wahl, MD, president of SNMMI.

"America leads the world in medical research and innovation—but far too often, patients are unable to access the benefits of innovative medical technologies because of outdated Medicare reimbursement policy," added Representative Dunn at the act's introduction. "The FIND Act is a common-sense, bipartisan proposal to address these current reimbursement problems, giving patients access to the diagnostic tools they need, when they need them. Early detection saves lives and we must do what we can to expand access to these life-saving tools."

On August 4, Senators Marsha Blackburn (R-TN) and Tammy Baldwin (D-WI) introduced a companion bill in the U.S. Senate (S. 2609). "Innovative technology like diagnostic radiopharmaceuticals are important tools in detecting and treating diseases such as cancer and Alzheimer's," said Senator Blackburn. "The FIND Act would increase patient access to more cost-effective treatment options while promoting further research and development opportunities for medical manufacturers."

The FIND Act addresses structural issues in the packaging methodology used in the Medicare outpatient setting by directing the Department of Health and Human Services to pay separately for all diagnostic radiopharmaceuticals with a cost threshold per day of $500. If passed, this bill would give patients greater access to a wide range of diagnostic radiopharmaceuticals that can better detect conditions such as heart disease, Alzheimer and Parkinson disease, breast and prostate cancer, and neuroendocrine tumors. This legislation would also help providers better manage costs while delivering more targeted and cost-efficient care.

For more information on the FIND Act, including avenues for advocacy, please see: https://www.snmmi.org/IssuesAdvocacy/content.aspx?ItemNumber=34002&navItemNumber=34003.

SNMMI

New NIA Alzheimer Trial Recruitment Tool

The National Institute on Aging (NIA) announced on July 30 at the annual meeting of the Alzheimer's Association International Conference a new online research tool to help increase participation by traditionally underrepresented populations in clinical trials focusing on Alzheimer disease (AD) and related dementias. Called Outreach Pro, the tool will enable researchers to create and customize participant recruitment communications, such as websites, handouts, videos, and social media posts.

"We are facing a critical and growing need for people living with Alzheimer's and related dementia, as well as those at higher risk, and healthy people, to participate in clinical trials," said NIA Director Richard J. Hodes, MD. "That need is especially acute for frequently underrepresented groups such as Black and Hispanic Americans, which is why Outreach Pro includes an emphasis on helping clinical trial

researchers connect with these and other important communities."

Outreach Pro is one of a suite of NIA efforts to implement the National Strategy for Recruitment and Participation in Alzheimer's and Related Dementias Clinical Research (2018). To use Outreach Pro, researchers and clinicians first select desired templates with 1 of 3 communication goals: (1) to educate about AD, related dementias, and/or brain health; (2) to increase awareness and interest in AD and related dementias clinical trials; or (3) to provide information about a specific AD or related dementia clinical trial currently enrolling participants. Each template can be customized using a central library of messages, headlines, photos, and text that have been tested in individuals representing diverse and underserved populations. The materials will be available initially in English and Spanish, with plans for adding Asian American and Pacific Islander resources and languages later in 2021. Materials for American Indian and Alaska Native communities will be developed and added in 2022. NIA developed Outreach Pro and its content systematically by using literature reviews, environmental scans, listening sessions with stakeholders, focus groups, national surveys, and user testing. NIA plans to add content and scale up the tool's capabilities based on feedback and performance measurement.

In total, NIA is currently supporting 270 AD and related dementia clinical trials. Additional information on Outreach Pro is available at: https://outreachpro.nia.nih.gov/.

National Institute on Aging

NIH Expands Biomedical Research in the Cloud

The National Institutes of Health (NIH) announced on July 10 that Microsoft Azure had joined the NIH Science and Technology Research Infrastructure for Discovery, Experimentation, and Sustainability (STRIDES) Initiative as the newest cloud service provider to support biomedical research. Google Cloud and Amazon Web Services joined the initiative in 2018. The STRIDES Initiative aims to accelerate biomedical research in the cloud by reducing economic and process barriers as well as providing cost-effective access to cloud platforms, training, cloud experts, and best practices for optimizing research.

The initiative has already expanded access to critical infrastructure and cutting-edge cloud resources for NIH researchers, as well as NIH-funded investigators at more than 2,500 academic institutions across the United States. To date, NIH has helped more than 425 research programs and projects leverage cloud resources through the STRIDES initiative. Researchers have collectively used more than 83 million h of computational resources to access and analyze more than 115 petabytes of high-value biomedical data in the cloud. By leveraging the initiative, the National Library of Medicine's Sequence Read Archive (among the world's largest publicly available genome sequence repositories) migrated more than 43 petabytes of next-generation sequencing data to the cloud, easing access for millions of researchers. Researchers can now search the entire catalog of genomic data and take advantage of the computational tools for analysis.

A central tenet of the STRIDES Initiative is that data made available through these partnerships will incorporate standards endorsed by the biomedical research community to make data findable, accessible, interoperable, and reusable (FAIR). "NIH has an ambitious vision of a modernized, FAIR biomedical data landscape," said Susan K. Gregurick, PhD, associate director for Data Science and director of the Office of Data Science Strategy at NIH. "By partnering with Microsoft Azure, which has over 3 decades of experience in the cloud space, we can strengthen NIH's data ecosystem and accelerate data-driven research and discovery." Additional information is available at: https://datascience.nih.gov/strides/.

National Institutes of Health

Medical Imaging Radiation Limits

On August 11 the American Association of Physicists in Medicine (AAPM), the American College of Radiology, and the Health Physics Society issued a joint statement in opposition to cumulative radiation dose limits for patient imaging, citing potential adverse effects on patient care. The statement comes in response to an opposing position by several organizations and recently published papers on the high-profile topic. According to the statement "the decision to perform a medical imaging exam should be based on clinical grounds, including the information available from prior imaging results, and not on the dose from prior imaging-related radiation exposures." In a related press release, AAPM stated its recommendation "against using dose values, including effective dose, from a patient's prior imaging exams for the purposes of medical decision-making. Using quantities such as cumulative effective dose may, unintentionally or by institutional or regulatory policy, negatively impact medical decisions and patient care." In addition, the position statement applied to "the use of metrics to longitudinally track a patient's dose from medical radiation exposures and infer potential stochastic risk from them." It does not apply to the use of organ-specific doses for purposes of evaluating the onset of deterministic effects (e.g., absorbed dose to the eye lens or skin) or performing epidemiologic research. The joint statement, a list of answers to frequently asked questions on the topic of medical radiation safety, and a list of references to research papers supporting the signatories' position is available at: https://www.aapm.org/org/policies/details.asp?id=1533.

American Association of Physicists in Medicine

FDA and Collaborative Communities

The U.S. Food and Drug Administration (FDA) announced on August 4 participation in several new "collaborative communities" designed to address challenges in patient health care. Collaborative communities are continuing forums in which private and public sector representatives work together on medical device challenges to achieve common objectives and outcomes. "We're pleased to announce the progress we've made with participation in collaborative communities. These collaborations with diverse stakeholders are not only a strategic priority for the FDA's Center for Devices and Radiological Health, they also provide much needed forums for deep discussion and solution-driven initiatives to tackle important issues within the medical device ecosystem," said Jeff Shuren, MD, JD, director of the Center for Devices and Radiological Health. "The insights and outcomes developed by these groups will have long-standing impacts on public health."

The FDA currently participates in 12 collaborative communities, which are established, managed, and controlled by external stakeholders. These communities are collectively charting paths to accelerate and address regulatory science and other knowledge gaps to aid in medical device review and oversight. They may also impact the delivery of health care and change clinical care paradigms. The most recent collaborations focus on topics such as: medical device development and product quality; understanding of valvular heart disease; innovations in digital pathology; reducing rates of intended self-injury and suicidal acts by individuals with diabetes; and strategies to increase the awareness, understanding, and participation of racial and ethnic minorities in the medical technology industry.

Collaborative communities are convened by interested stakeholders and may exist indefinitely, produce deliverables as needed, and tackle challenges with broad impacts. The FDA does not establish, lead, or operate the communities, nor are they intended to advise the FDA. Instead, the FDA may participate in the community to contribute its knowledge and perspective to discussions of public health challenges and solutions. For more about the FDA and collaborative communities, see: https://www.fda.gov/about-fda/cdrh-strategic-priorities-and-updates/collaborative-communities-addressing-health-care-challenges-together.

U.S. Food and Drug Administration

Breast Cancer Risk in Health Professionals

In a study published on August 9 ahead of print in the *American Journal of Preventive Medicine*, Shen et al. from the Kaohsiung Municipal Ta-Tung Hospital, Kaohsiung Medical University Chung-Ho Memorial Hospital, and Kaohsiung Medical University (Kaohsiung City, Taiwan) and the Ministry of Labor (Taipei, Taiwan) reported on a 35-year longitudinal study of breast cancer risk among health professionals. The study included data from 4 country-wide population-based databases in Taiwan, including matched cohorts of 277,543 health professionals and 555,086 non–health professionals. The researchers found that health professionals had a significantly higher risk of breast cancer and that this elevated risk was associated with birth age, job tenure, rotating day/night work, and several specific health professional license types, including physician, pharmacist, registered nurse, midwife, medical technologist, and psychologist. The authors suggested that regular ultrasound for younger women health care professionals and mammography for those older than 45 y should be considered.

American Journal of Preventive Medicine

Somatostatin Receptor Imaging and Theranostics: Current Practice and Future Prospects

Sonya Park[1], Ashwin Singh Parihar[2,3], Lisa Bodei[4], Thomas A. Hope[5], Nadine Mallak[6], Corina Millo[7], Kalpna Prasad[8], Don Wilson[9,10], Katherine Zukotynski[11–13], and Erik Mittra[6]

[1]Department of Nuclear Medicine, Seoul St. Mary's Hospital, Seoul, Korea; [2]Department of Nuclear Medicine, Postgraduate Institute of Medical Education and Research, Chandigarh, India; [3]Mallinckrodt Institute of Radiology, Washington University School of Medicine, St. Louis, Missouri; [4]Molecular Imaging and Therapy Service, Memorial Sloan Kettering Cancer Center, New York, New York; [5]Department of Radiology and Biomedical Imaging, University of California San Francisco, San Francisco, California; [6]Department of Diagnostic Radiology, Oregon Health & Science University, Portland, Oregon; [7]Department of Nuclear Medicine, RAD&IS, Clinical Center, National Institutes of Health, Bethesda, Maryland; [8]Department of Nuclear Medicine, Walter Reed National Military Medical Center, Bethesda, Maryland; [9]BC Cancer, Vancouver, British Columbia, Canada; [10]Department of Radiology, University of British Columbia, Vancouver, British Columbia, Canada; [11]Departments of Radiology and Medicine, McMaster University, Hamilton, Ontario, Canada; [12]Department of Medical Imaging, Schulich School of Medicine & Dentistry, Western University, London, Ontario, Canada; and [13]Department of Radiology, University of British Columbia, Vancouver, British Columbia, Canada

A new era of precision diagnostics and therapy for patients with neuroendocrine neoplasms began with the approval of somatostatin receptor (SSTR) radiopharmaceuticals for PET imaging followed by peptide receptor radionuclide therapy (PRRT). With the transition from SSTR-based γ-scintigraphy to PET, the higher sensitivity of the latter raised questions regarding the direct application of the planar scintigraphy–based Krenning score for PRRT eligibility. Also, to date, the role of SSTR PET in response assessment and predicting outcome remains under evaluation. In this comprehensive review article, we discuss the current role of SSTR PET in all aspects of neuroendocrine neoplasms, including its relation to conventional imaging, selection of patients for PRRT, and the current understanding of SSTR PET–based response assessment. We also provide a standardized reporting template for SSTR PET with a brief discussion.

Key Words: somatostatin; SSTR; peptide receptor radionuclide therapy; neuroendocrine neoplasms; ^{68}Ga-DOTATATE; ^{68}Ga-DOTANOC

J Nucl Med 2021; 62:1323–1329
DOI: 10.2967/jnumed.120.251512

Neuroendocrine neoplasms (NENs) are rare, heterogeneous, and typically slow-growing, accounting for about 0.5% of all diagnosed malignancies. Originating from the secretory cells of the neuroendocrine system at almost any anatomic site, their site of origin is often linked to disease biology. For example, tumors of the ileum typically have a high malignant potential, although metastatic lesions tend to have an indolent course. Gastric and rectal tumors have a low metastatic potential but can grow aggressively once metastatic (*1*). Gastroenteropancreatic, pulmonary, and thymic NENs are among the most commonly diagnosed (*2*). The term NENs encompasses both well-differentiated neuroendocrine tumors (NETs) and poorly differentiated neuroendocrine carcinomas. Whereas neuroendocrine carcinomas are of high grade by default, NETs are classified further according to histologic grade and degree of differentiation, with site-specific parameters (cutoffs). Grading for gastroenteropancreatic NETs, for example, is based on proliferation using either the Ki-67 index or mitotic count per 10 high-power fields. Grade 1 (G1 or low-grade) refers to a Ki-67 of less than 3% and fewer than 2 mitoses per 10 high-power fields, G2 refers to a Ki-67 of 3%–20% or 2–20 mitoses per 10 high-power fields, and G3 refers to a Ki-67 of more than 20% or more than 20 mitoses per 10 high-power fields (*3*). On the basis of the degree of differentiation, they are categorized as either well-differentiated or poorly differentiated tumors. Most NENs are sporadic, although some arise in the setting of inherited syndromes such as multiple endocrine neoplasia, tuberous sclerosis, Von Hippel–Lindau disease, or neurofibromatosis (*1*).

NENs typically have increased expression of somatostatin receptors (SSTRs), which are G-protein–coupled receptors modulating cellular proliferative and secretory activity. This expression forms the basis of functional imaging with SSTR-targeting radiopharmaceuticals and treatment with somatostatin analogs (SSAs), including octreotide and octreotate. There are 5 subtypes of SSTRs, with subtypes 2, 3, and 5 most commonly expressed (*4*). ^{111}In-diethylenetriamine pentaacetate–conjugated octreotide (^{111}In-pentetreotide/OctreoScan; Mallinckrodt Nuclear Medicine) was the first agent to receive U.S. Food and Drugs Administration approval (in 1994) for functional imaging of NENs with planar scintigraphy or SPECT (*5*). ^{99m}Tc-labeled SSAs, including the commercially available ^{99m}Tc-ethylenediaminediacetic acid hydrazinonicotinamide-[D-Phe^1, Tyr^3-octreotide], were also developed to improve image quality with lower absorbed radiation dose (*6*). Newer ^{68}Ga- or ^{64}Cu-tetraxetan (DOTA)–conjugated SSAs for PET have shown diagnostic performance superior to that of ^{111}In-pentetreotide and are the current modality of choice for functional imaging (*5*,*7*). Different DOTA peptides exist and have varying affinity for the SSTR subtypes (Table 1).

Management of NENs is based on the grade, subtype, distribution, and extent of disease. Anatomic imaging with CT and MRI is standard practice to assess disease location and extent, although

Received Feb. 5, 2021; revision accepted Jun. 29, 2021.
For correspondence or reprints, contact Erik Mittra (mittra@ohsu.edu).
Published online July 22, 2021.

TABLE 1
In Vitro Affinity of DOTA Peptides for Common SSTR Subtypes (*5*)

Radiopeptide	SSTR-2	SSTR-3	SSTR-5
^{111}In-DOTANOC	2.9	8	11.2
^{111}In-DOTATATE	1.5	>1,000	547
^{111}In-DOTATOC	4.6	120	130
^{68}Ga-DOTANOC	1.9	40	7.2
^{68}Ga-DOTATATE	0.2	>1,000	377
^{68}Ga-DOTATOC	2.5	613	73

Data are half-maximal inhibitory concentration in nanomoles (lower values represent higher affinity).

radiopharmaceutical development has led to improvements in imaging and therapy (together termed theranostics). Initially, high-dose ^{111}In-pentetreotide was used for therapy (*8*), via Auger electrons, although the efficacy was limited (*9*). The use of ^{177}Lu or ^{90}Y (β-emitters) conjugated to SSAs with DOTA has been more effective (*10*). Specifically, ^{177}Lu-DOTATATE–based peptide receptor radionuclide therapy (PRRT), studied in a phase 3, multicenter, randomized controlled trial (NETTER-1) in patients with inoperable or advanced and progressive midgut NENs, showed superior outcomes to standard-of-care therapy (*10*).

This paper reviews the current status and advances in imaging of NENs, with a focus on the use of SSTR PET with respect to PRRT.

THE ROLE OF CONVENTIONAL IMAGING

CT is commonly the initial imaging modality for evaluation of a suspected NEN. The detection rate of primary small-bowel NENs is about 50% (*11*,*12*). Metastatic mesenteric nodes are typically larger than the primary itself and are often calcified. When a small-bowel NEN is known or suspected, a negative oral contrast medium (methylcellulose, polyethylene glycol, or water) is preferred over a conventional radiopaque contrast medium, to avoid masking the primary enhancing lesion on the bowel wall (*13*,*14*). Primary pancreatic NENs have a detection rate of about 80%–100% on CT (*15*). It is important to obtain an abdominal multiphase CT scan with intravenous contrast medium, since most pancreatic NENs and their hepatic metastases are arterially enhancing and occult on a single portal venous phase (Fig. 1) (*11*,*14*,*16*). Around 22% of pancreatic NENs are arterially hypoenhancing, and in these cases the portal venous and delayed phases can help in detection (*11*,*17*).

NOTEWORTHY

- SSTR PET can be used to reliably assess SSTR expression both visually and semiquantitatively.
- SSTR PET is essential for the proper assessment of eligibility for PRRT.
- SSTR expression is both a prognostic (correlates with outcome regardless of the therapy) and predictive (correlates specifically with response to PRRT) parameter for NENs.

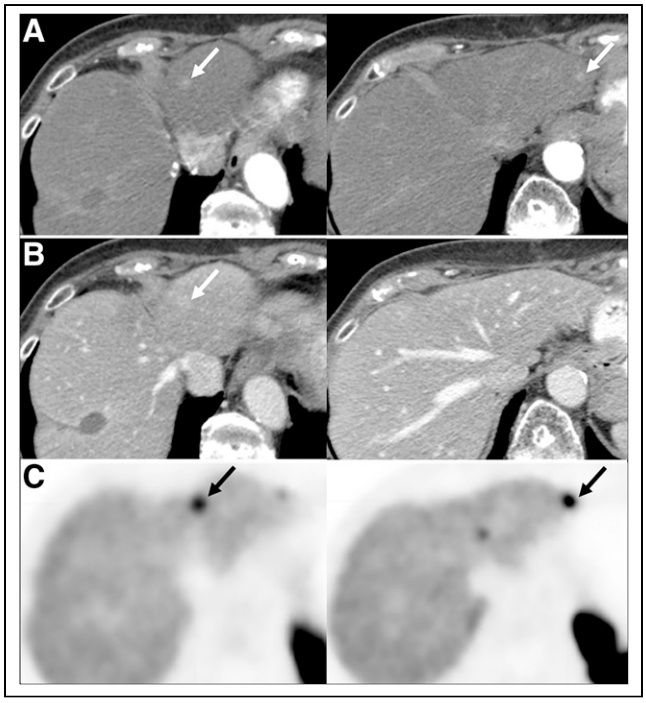

FIGURE 1. Pancreatic NEN with hepatic metastases (arrows). (A) Abdominal contrast-enhanced CT showing 2 small arterially enhancing left hepatic lesions. (B) Corresponding portal venous phase, where lesions are less conspicuous. (C) Transaxial PET images showing ^{68}Ga-DOTATATE avidity in same lesions.

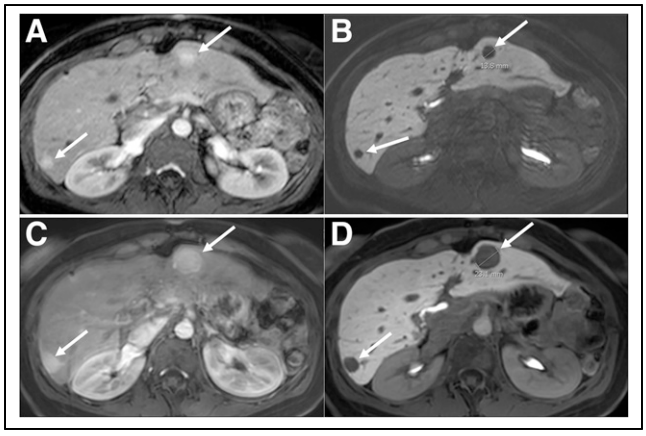

FIGURE 2. Abdominal contrast-enhanced MRI (with gadoxetate disodium) in patient with pancreatic NEN with hepatic metastases. (A and B) On arterial phase (A) and 20-min delayed-phase (B) images, 2 metastatic lesions (arrows) show arterial enhancement and contrast washout during delayed phase. (C and D) On arterial phase (C) and delayed-phase (D) images, size of previous lesions on 18-mo follow-up MRI has increased. Lesions are better delineated during delayed phase, facilitating accurate size measurements.

MRI is superior to CT for detecting hepatic metastases (*18*,*19*). As with CT, multiphase MRI with intravenous contrast medium is recommended since most primary and metastatic NENs show arterial enhancement. Additionally, diffusion-weighted imaging and the delayed postcontrast phase using gadoxetic acid (hepato-specific paramagnetic contrast agent) are useful for detection of hepatic

metastases. Hepatic metastases typically show a high signal on diffusion-weighted imaging (combination of T2 shine-through and true diffusion restriction), making them more conspicuous; this tool is especially helpful in patients with severe renal failure, for whom intravenous gadolinium is contraindicated (*19*,*20*). The most sensitive tool for detection of hepatic metastases is the 20-min postcontrast delayed phase after intravenous administration of gadoxetic acid (Fig. 2), which is retained in hepatocytes but not in metastases, creating a high lesion-to-background contrast on the delayed image. In addition to having high sensitivity for lesion detection, the 20-min delayed phase allows for more accurate and reproducible measurement of baseline and follow-up lesion dimensions on imaging (*20–23*).

Findings on anatomic imaging associated with higher-grade tumors, which apply to both CT and MRI, include large tumor size (≥2 cm), ill-defined margins, low or moderate arterial hyperenhancement, dilatation of the main pancreatic duct, vascular invasion, and presence of nodal or distant metastases; findings specific to MRI include nonintense T2 signal and, most importantly, high diffusion restriction (*24*,*25*). Several studies show that apparent diffusion coefficients inversely correlate with mitotic count and Ki-67 index. A significant difference in apparent diffusion coefficients has been observed between G1 and G2 tumors and between G1/G2 and G3 tumors, with suggested apparent diffusion coefficient cutoffs of below 0.95×10^{-3} to 1.19×10^{-3} mm^2/s for G3 tumors (*18*,*19*).

PET RADIOPHARMACEUTICALS

Introduced in 2001, ^{68}Ga-DOTATOC was the first PET-SSA ligand (*26*). As opposed to the SSTR-2–selective DOTATATE, DOTATOC retains an octreotide-like affinity profile (Table 1)

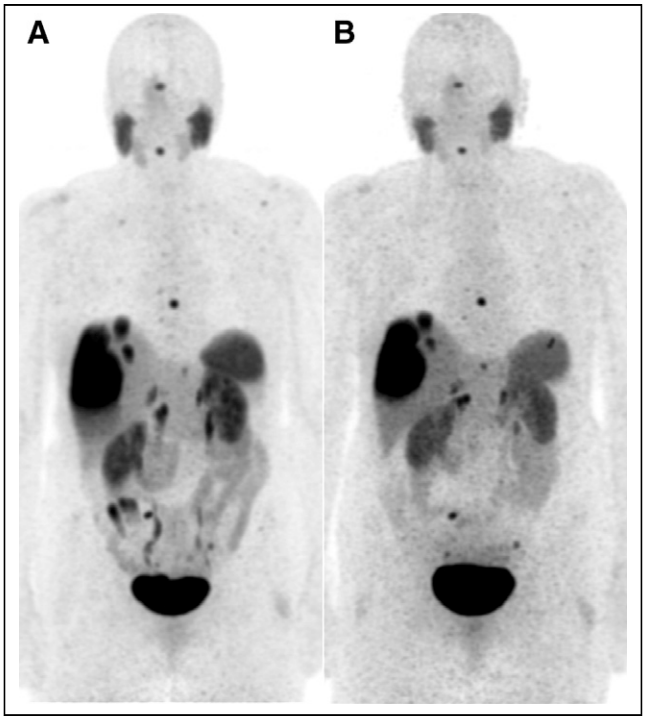

FIGURE 3. ^{68}Ga-DOTATATE (A) and ^{64}Cu-DOTATATE (B) maximum-intensity-projection PET images of metastatic NEN showing similar findings. Both studies were performed as part of PET/MRI, with uptake times for ^{68}Ga-DOTATATE and ^{64}Cu-DOTATATE being 113 and 118 min, respectively (3 min/bed position for both).

(*27*). A comparison of ^{68}Ga-DOTATOC to ^{68}Ga-DOTATATE PET/CT in the same patients showed a similar diagnostic accuracy, despite potential advantages for ^{68}Ga-DOTATOC in the total number of detected lesions and a higher SUV_{max} (*28*). Today, ^{68}Ga-DOTATOC and ^{68}Ga-DOTATATE are the most commonly used radiopharmaceuticals for imaging NENs, with no clear superiority of either one of these compounds.

One of the main disadvantages of ^{68}Ga-SSA–based imaging is the high liver background and short radiopharmaceutical half-life. For the latter, newer SSTR radiopharmaceuticals, such as ^{64}Cu-labeled SSA (Food and Drug Administration–approved in September 2020) may provide an advantage. Figure 3 shows the same patient imaged with the 2 different radioisotopes. Potential advantages of ^{64}Cu include its longer half-life (12.7 h vs. 68 min for ^{68}Ga) and resultant higher target-to-background ratios on delayed imaging, as well as a shorter positron range in tissue (mean, 0.6 mm, vs. 3.5 mm for ^{68}Ga). These factors may result in better imaging characteristics, especially at later times (3–24 h after injection) (*29*). Conversely, ^{64}Cu has a significantly lower positron branching ratio (0.17) than ^{68}Ga (0.89), which may degrade image quality or at least require a longer acquisition time. A prospective head-to-head comparison of ^{64}Cu-DOTATATE and ^{68}Ga-DOTATOC PET/CT in 59 subjects with NENs showed ^{64}Cu-DOTATATE to be advantageous, detecting 83% of the true-positive lesions that were discordant between the radiopharmaceuticals (*30*). However, dual-time-point imaging with ^{64}Cu-DOTATATE in 35 patients showed similar accuracy for 1-h and 3-h imaging (*31*), suggesting that the improved detection rate seen in the previous study was due to factors other than the target-to-background ratio. Notably, ^{64}Cu-DOTA is prone to demetallation and transchelation in vivo, and better results may be expected with new sarcophagine-based chelators (*32*).

The SSAs discussed thus far are SSTR agonists, resulting in activation and internalization of the receptor on binding. Radiolabeled SSTR antagonists, such as ^{68}Ga-DOTA-JR11, are characterized by a lack of internalization, rapid blood-pool clearance, and greater tumor uptake, aiding detection of metastases (*33*). A prospective head-to-head comparison between ^{68}Ga-NODAGA-JR11, a SSTR antagonist, and ^{68}Ga-DOTATOC PET/CT in 12 patients with NENs demonstrated that the favorable biodistribution of the antagonist resulted in a higher detection rate of hepatic metastases and a significantly greater lesion-based overall sensitivity (94% vs. 59%) (*34*).

When SSTR imaging is suboptimal, other PET agents have been developed to target different receptors overexpressed by the NENs, including the glucagon-like peptide 1 receptor ligand ^{68}Ga-DOTA-exendin-4, which may facilitate the detection of benign insulinomas (frequently SSTR-negative) (*35*,*36*). The CXCR-4 ligand ^{68}Ga-pentixafor seems superior to conventional SSTR imaging for G3 NETs, but its role relative to ^{18}F-FDG PET remains to be determined (*37*). SSTR PET typically shows high uptake in well-differentiated or low-grade lesions and lower uptake in poorly differentiated or high-grade lesions. In the latter scenario, ^{18}F-FDG PET is complementary in that it detects aggressive, poorly differentiated disease with higher grade and worse prognosis (Fig. 4; Supplemental Figs. 1 and 2; supplemental materials are available at http://jnm.snmjournals.org). No more than around 40% of patients with G1 disease are thought to have ^{18}F-FDG uptake, whereas almost all patients with G3 disease have ^{18}F-FDG uptake (*38–41*). Since NENs are vastly heterogeneous and it would be impossible to sample all lesions in

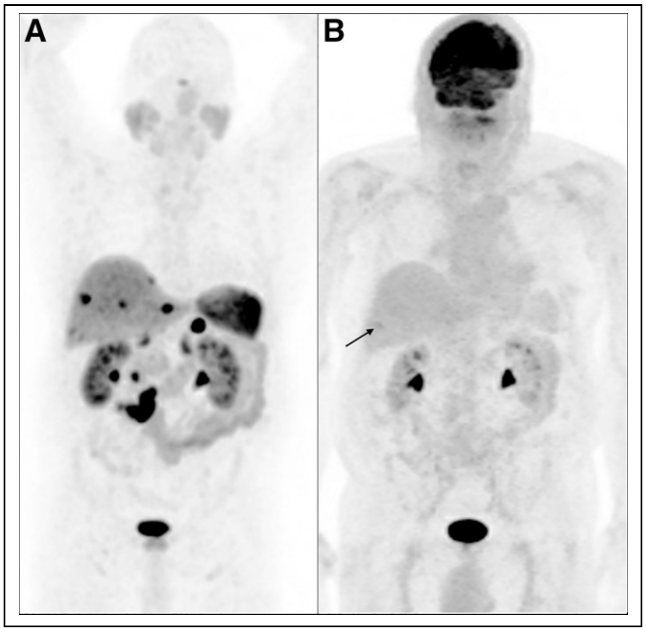

FIGURE 4. Maximum-intensity projection images of patient with metastatic grade 1 (Ki-67 < 2%) NEN from small-bowel primary. (A) ^{68}Ga-DOTATATE PET shows prominent uptake in primary tumor, lymphadenopathy, and liver metastases. (B) ^{18}F-FDG PET shows no abnormal uptake (arrow points out incidentally noted fractured rib).

the body, the combination of SSTR and ^{18}F-FDG PET provides a noninvasive understanding of disease heterogeneity and likelihood of PRRT response (*42*).

Currently, ^{18}F-FDG PET is used for staging G3 disease and can be used to complement SSTR PET when Ki-67 is 10% or more (*41*). Also, a positive ^{18}F-FDG PET result may be used to reconsider PRRT for a patient. Specifically, the combination of high SSTR and low ^{18}F-FDG avidity increases the likelihood of benefit from PRRT; however, the ratio of differentiated to dedifferentiated disease at which PRRT ceases to be useful remains to be determined. In fact, it seems possible that in the event of marked uptake on SSTR PET with limited sites of ^{18}F-FDG–avid disease, a combination of PRRT and targeted external radiation to the ^{18}F-FDG–avid lesions may prolong survival. Ultimately, a combination of SSTR and ^{18}F-FDG PET will likely provide a synergistic pictorial road map of disease for determining when to use PRRT, combination PRRT, and targeted external radiotherapy versus an alternative therapy (*43–45*).

TUMOR QUANTIFICATION, CURRENT GUIDELINES, AND THE KRENNING SCALE

SSTR PET can be used to assess SSTR expression visually and semiquantitatively. Cell membrane–based SSTR-2 expression on immunohistochemistry in NENs correlates with the SUVs on ^{68}Ga-DOTATOC PET/CT (*46*). Some cases considered negative on immunohistochemistry demonstrated mild uptake on SSTR PET, possibly because of SSTR-5 binding or tumor heterogeneity. Campana et al. (*47*) suggested that the SUV_{max} correlated with clinicopathologic features of NENs and could serve as a prognostic index, alongside anatomic location, primary tumor grade, and Ki-67 status. Velikyan et al. (*48*) reported that kinetic modeling parameters, rather than SUV, reflected receptor density more accurately based on absence of a linear correlation between SUV and net uptake rate in tumors with high SSTR expression. Specifically, SUVs correlated with receptor density at low values, with a nonlinear relationship thereafter leading to underestimation of receptor expression. Although this finding might reflect plasma peptide availability as a limiting factor for tracer uptake in patients with high SSTR expression and high tumor burden, an alternative explanation could be related to receptor saturation.

More recently, volumetric parameters have been evaluated in well-differentiated NENs (*49*). Specifically, the concept of SSTR-expressing tumor volume, representing the volume of tumor with more than 50% SUV_{max}, and total-lesion SSTR expression, calculated as SSTR-expressing tumor volume × SUV_{mean} in the volume of interest, have been defined. A sum of each of these volumetric parameters can be calculated; the literature suggests there may be a significant correlation between whole-body cumulative SSTR-expressing tumor volume and progression-free survival after PRRT. Nevertheless, estimation of tumor volume based on uptake will likely remain problematic given the intrinsic heterogeneity in tumoral SSTR expression.

Recent guidelines formulated under the auspices of the European Association of Nuclear Medicine recommend the use of ^{68}Ga-labeled SSAs in combination with CT or MRI for diagnosis, for staging, for restaging after surgery, for following progression, and for known or suspected NETs (*50*). The National Comprehensive Cancer Network guidelines recommend SSTR PET before PRRT for advanced NENs (*51*). Although a few studies using ^{68}Ga-DOTATOC have suggested that SUV_{max} thresholds be used to determine eligibility for PRRT—for example, SUV_{max} cutoffs of 17.9 (*52*) and 16.5 (*53*)—differences between scanners and imaging techniques may produce slight variations, which make SUV_{max} problematic to use. An alternative is to use a tumor-to-liver ratio of 2.2 (*53*). The American College of Radiology practice parameters suggest visually assessed tumor uptake equal to or more than liver uptake as an eligibility criterion for PRRT (*54*).

The Krenning score was developed using ^{111}In-pentetreotide scintigraphy (*8*) and has been extrapolated to SSTR PET (modified Krenning score). A 5-point scale has been proposed on the basis of a qualitative assessment of lesion uptake relative to blood pool and hepatic activity, where 0 is no uptake, 1 is very low uptake, 2 is uptake no more than in the liver, 3 is uptake greater than in the liver, and 4 is uptake greater than in the spleen (*55*). However, the relationship between the Krenning score from ^{111}In-pentetreotide scintigraphy and the modified Krenning score from SSTR PET is limited (*56*). Disease has a bias toward higher scores on SSTR PET than on ^{111}In-pentetreotide scintigraphy (Supplemental Fig. 3). Part of this bias is due to differences in equipment (higher sensitivity of PET vs. planar scintigraphy or SPECT) and imaging time points (^{111}In-pentetreotide scintigraphy at 24 h after injection vs. SSTR PET at 1 h after injection).

Although there are few formal data to support the use of SSTR PET over ^{111}In-pentetreotide scintigraphy, SSTR PET has become the standard for pre-PRRT patient selection because of its higher sensitivity, faster imaging times, and lower radiation dose. For lesions larger than 2 cm, it is appropriate to use the modified Krenning score, and PRRT should be considered with a score of 3 or 4. Caution should be used before treating patients with lesions smaller than 2 cm with a modified Krenning score of 3 or 4, as these patients are unlikely to have fulfilled criteria if imaged with ^{111}In-pentetreotide. This is to emphasize that the current data do not provide

sufficient evidence for the use of SSTR PET in this setting. PRRT should not be considered when lesions show no or low uptake on SSTR PET.

REPORTING SSTR PET

There is a need for standardized interpretation of SSTR PET given that findings on baseline imaging partly determine treatment success with radioligand therapies (*57*). The report (Supplemental Fig. 4) should include a concise clinical history, including NEN subtype, tumor grade and differentiation, and prior treatments (medical or surgical). The imaging parameters, in terms of the specific radiopeptide and its administered activity, uptake time, duration of imaging (time per bed position), and area imaged, should be documented. Comparison and correlation with any prior SSTR imaging, ^{18}F-FDG PET, and other anatomic imaging should be performed. Findings should detail the site and size of the lesions (the latter if seen on corresponding CT/MRI) and uptake intensity, which can be expressed semiquantitatively (commonly as SUV_{max}). The pattern of tracer uptake (intralesional heterogeneity) and assessment of lesion resectability (i.e., relation with vascular and major structures) may be helpful to further guide management. The conclusion should provide the modified Krenning score, and additional diagnostic examinations or follow-up can be suggested.

The NETPET score is a grading system that combines findings on SSTR and ^{18}F-FDG PET with a single parameter (*58*). This scoring system has been developed as a prognostic biomarker. Although rarely included in reports since SSTR and ^{18}F-FDG PET are not routinely performed together, its rate of inclusion may change in the future.

The SSTR reporting and data systems (RADS) has also been introduced as part of the umbrella molecular imaging RADS, a 5-point scale (from 1 [no evidence of disease and definitely benign] to 5 [high certainty of NEN]) indicating both disease site and radiotracer avidity (*55*). SSTR RADS entails a 3-point qualitative scoring of uptake level, where up to 5 target (largest, most avid) lesions can be identified, with overall score defined as the highest scored lesion. A summed RADS score, including all 5 target lesions, has also been suggested (*59*). Future validation of this framework is warranted, including inter- and intraobserver agreement studies and histopathology correlation.

Disease Burden, Outcome Prediction, and Response Assessment

SSTR expression is both a prognostic (correlates with outcome regardless of therapy) and predictive (correlates specifically with response to PRRT) parameter for NENs. (*60*). The current literature suggests that higher baseline SUVs on SSTR PET predict better post-PRRT outcomes. Öksüz et al. (*52*) reported that high pretherapy primary tumor uptake suggested a good response to PRRT; Kratochwil et al. (*53*) reported that high pretherapy uptake in liver metastases suggested a good response; and Ambrosini et al. (*60*) reported better outcomes in patients with high baseline SUVs. To avoid scanner-related variations, parameters such as tumor-to-liver and tumor-to spleen ratios may be used. It has been reported that a tumor-to-liver ratio of more than 2.2 is predictive of a favorable response. It has, however, been demonstrated that a high uptake (e.g., Krenning grade 4) is associated with response to PRRT in only 60% of patients (*61*).

The literature on response evaluation is more variable, and we are only beginning to understand how post-therapy SSTR PET correlates with endpoints such as time to progression, progression-free, and overall survival. Haug et al. (*62*) studied SUV_{max} and tumor-to-spleen ratio for prediction of time to progression and clinical outcome after a first PRRT cycle in well-differentiated NENs. The authors found that reduced uptake after therapy predicted time to progression and correlated with clinical improvement. Further, interval change in tumor-to-spleen ratio was superior to interval change in SUV_{max}. Meanwhile, Gabriel et al. (*6*) reported essentially random SUV fluctuations after PRRT. The question remains: Does diminishing tumoral radiotracer uptake reflect true disease improvement or is there a higher degree of tumor dedifferentiation with loss of SSTR expression? Accordingly, the recently updated appropriate-use criteria (*63*) for SSTR PET notes that response should be assessed by the disappearance of known lesions or development of new lesions, rather than changes in SUVs.

Monitoring response to PRRT with SSTR PET and attempting to interpret the biologic significance of tumor uptake change are challenging. One study evaluated 46 patients with advanced NENs treated with 2–7 cycles of PRRT and compared the results from the post-therapy ^{68}Ga-DOTATATE PET to CT/MRI with RECIST. The authors found little advantage to SSTR PET over conventional imaging for response assessment (*6*). In another study, of 66 patients, ^{68}Ga-DOTATOC and ^{18}F-FDG PET was done at baseline, at 3 mo, and again at 6–9 mo after completion of PRRT. The authors concluded that uptake on ^{18}F-FDG PET at baseline and follow-up had a stronger correlation with the outcome than did SSTR PET and that combination imaging with both radiopharmaceuticals might be advisable across all tumor grades (*43*).

Also, a high overall tumor burden and tumor heterogeneity on SSTR PET is likely to be associated with worse prognosis. SSTR PET helps in assessing the heterogeneity of NENs that exist at the interpatient, intrapatient, interlesional level at a specific time point or longitudinally at different time points. This heterogeneity implies a variety of cells displaying variable characteristics in terms of metabolism, proliferation, metastatic potential, and therapy response. Distinct metastases may harbor different cellular clones with varying SSTR expression. The primary tumor and its metastases may also differ. Indeed, this may impact the chance of PRRT success and explains why cure is rarely possible with systemic metastatic disease. In a study by Graf et al. (*64*), only patients with at least 90% of metastases positive for SSTR were treated with PRRT. Positive lesions were viewed in 3 dimensions,

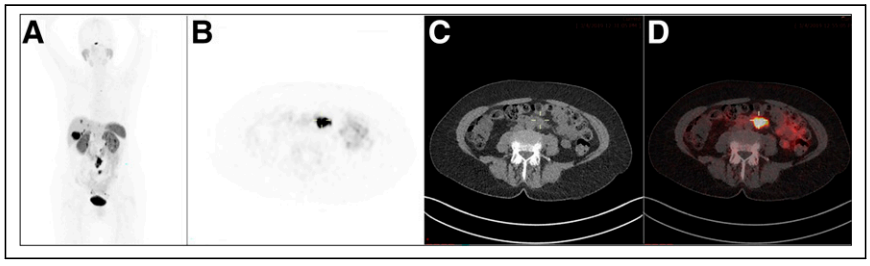

FIGURE 5. A 60-y-old woman with small-bowel NET on octreotide therapy. ^{68}Ga-DOTATATE PET/CT (maximum-intensity projection [A], transaxial PET [B], CT [C], PET/CT [D]) shows prominent uptake at tumor sites. This finding would make patient eligible for PRRT, but overall limited extent of disease in liver and retroperitoneum favors surgical resection over PRRT.

and a lesion that had a change in score from 3 or 4 to 2, or from 2 to 1, that persisted over more than 5 mm in any plane was defined as heterogeneous. Only the solid portion of a necrotic lesion was assessed. If more than 50% of lesions were deemed heterogeneous, the patient was labeled as heterogeneous. This study confirmed that heterogeneity had a negative impact on overall survival and time to progression after PRRT. Indeed, heterogeneity surpassed Ki-67 as a prognostic marker, especially related to PRRT, reinforcing the suspicion that PRRT may target the less aggressive, SSTR-positive cells, sparing the rest. Thus, even when decreased tumor size suggests response by RECIST, the more aggressive cells might remain viable. These observations highlight an intrinsic flaw of using quantitative parameters such as SUV_{max} alone, which do not account for the intralesional variation in SSTR expression. Interestingly, some authors have observed that, after PRRT, heterogeneous lesions may become more homogeneous. In the future, use of textural characteristics such as entropy and skewness may prove superior to our current methodology for lesion analysis.

Recently, a prospective study on 158 patients divided into 3 independent ^{177}Lu-PRRT cohorts demonstrated that specific circulating tumor transcripts (messenger RNA) specifically predict the outcome of PRRT and therefore represent a marker of radiosensitivity (*65*), whereas the circulating transcript signature NETest allows accurate monitoring of the course of disease during treatment and integrates with imaging (*66*).

The primary site of the tumor, which can often be elucidated with SSTR PET, is a prognostic factor and should be incorporated in the decision algorithm for PRRT. Midgut and pancreatic NENs are included in the Food and Drug Administration–approved indications for PRRT. Bronchial NENs represent a special category, with typical tumors considered more appropriate for PRRT because of higher SSTR expression. In the case of a pheochromocytoma or paraganglioma, the current recommendation reserves PRRT for metaiodobenzylguanidine-negative tumors only, for which ^{131}I-metaiodobenzylguanidine treatment is precluded. The distribution and extent of disease, ideally evaluated with SSTR PET, also affects management. In general, caution is needed in tumors with extensive mesenteric and peritoneal involvement, since PRRT may increase the risk of complications from a desmoplastic reaction. As the tumors metastasize, the total tumor burden may play a role, depending on the primary site of disease. For example, pancreatic NENs with more than 25% liver involvement and bone metastases have worse prognosis, whereas gastric NENs show no significant difference in outcome based on distribution (*67*). In general, tumor burden is termed limited if fewer than 5 lesions are detected at 1 site, moderate if more than 5 lesions at 2 sites, and extensive if more than 2 sites are involved, and this affects the treatment approach (Fig. 5). Most gastroenteropancreatic NENs present with hepatic metastases at diagnosis despite low Ki-67, and the presence of hepatic metastases profoundly decreases overall survival. PRRT may be helpful for nonresectable hepatic metastases and indeed may render the lesions resectable. In liver-dominant disease, intraarterial PRRT is being investigated.

CONCLUSION

SSTR PET is the preferred imaging modality at initial diagnosis of low- and intermediate-grade NENs, especially for localization of the primary tumor and determining disease extent. SSTR PET is essential for selecting patients for PRRT, whereas its role in response monitoring is still being evaluated. Although SSTR expression can be assessed visually and semiquantitatively, with various suggested thresholds, a modified Krenning score is used in current clinical practice.

DISCLOSURE

No potential conflict of interest relevant to this article was reported.

REFERENCES

1. Cives M, Strosberg JR. Gastroenteropancreatic neuroendocrine tumors. *CA Cancer J Clin.* 2018;68:471–487.
2. Rindi G, Klimstra DS, Abedi-Ardekani B, et al. A common classification framework for neuroendocrine neoplasms: an International Agency for Research on Cancer (IARC) and World Health Organization (WHO) expert consensus proposal. *Mod Pathol.* 2018;31:1770–1786.
3. Nagtegaal ID, Odze RD, Klimstra D, et al. The 2019 WHO classification of tumours of the digestive system. *Histopathology.* 2020;76:182–188.
4. Krenning EP, Kwekkeboom DJ, Bakker WH, et al. Somatostatin receptor scintigraphy with [^{111}In-DTPA-D-Phe^{1}]- and [^{123}I-Tyr^{3}]-octreotide: the Rotterdam experience with more than 1000 patients. *Eur J Nucl Med.* 1993;20:716–731.
5. Rufini V, Calcagni ML, Baum RP. Imaging of neuroendocrine tumors. *Semin Nucl Med.* 2006;36:228–247.
6. Gabriel M, Oberauer A, Dobrozemsky G, et al. ^{68}Ga-DOTA-Tyr^{3}-octreotide PET for assessing response to somatostatin-receptor-mediated radionuclide therapy. *J Nucl Med.* 2009;50:1427–1434.
7. Buchmann I, Henze M, Engelbrecht S, et al. Comparison of ^{68}Ga-DOTATOC PET and ^{111}In-DTPAOC (Octreoscan) SPECT in patients with neuroendocrine tumours. *Eur J Nucl Med Mol Imaging.* 2007;34:1617–1626.
8. Krenning EP, Valkema R, Kooij PP, et al. Scintigraphy and radionuclide therapy with [indium-111-labelled-diethyl triamine penta-acetic acid-D-Phe1]-octreotide. *Ital J Gastroenterol Hepatol.* 1999;31(suppl 2):S219–S223.
9. Kwekkeboom D, Krenning EP, de Jong M. Peptide receptor imaging and therapy. *J Nucl Med.* 2000;41:1704–1713.
10. Kunikowska J, Królicki L, Hubalewska-Dydejczyk A, Mikołajczak R, Sowa-Staszczak A, Pawlak D. Clinical results of radionuclide therapy of neuroendocrine tumours with ^{90}Y-DOTATATE and tandem ^{90}Y/^{177}Lu-DOTATATE: which is a better therapy option? *Eur J Nucl Med Mol Imaging.* 2011;38:1788–1797.
11. Maxwell JE, O'Dorisio TM, Howe JR. Biochemical diagnosis and preoperative imaging of gastroenteropancreatic neuroendocrine tumors. *Surg Oncol Clin N Am.* 2016;25:171–194.
12. Dahdaleh FS, Lorenzen A, Rajput M, et al. The value of preoperative imaging in small bowel neuroendocrine tumors. *Ann Surg Oncol.* 2013;20:1912–1917.
13. Woodbridge LR, Murtagh BM, Yu DF, Planche KL. Midgut neuroendocrine tumors: imaging assessment for surgical resection. *Radiographics.* 2014;34:413–426.
14. Sahani DV, Bonaffini PA, Fernández-Del Castillo C, Blake MA. Gastroenteropancreatic neuroendocrine tumors: role of imaging in diagnosis and management. *Radiology.* 2013;266:38–61.
15. Kuo JH, Lee JA, Chabot JA. Nonfunctional pancreatic neuroendocrine tumors. *Surg Clin North Am.* 2014;94:689–708.
16. Bushnell DL, Baum RP. Standard imaging techniques for neuroendocrine tumors. *Endocrinol Metab Clin North Am.* 2011;40:153–162.
17. Worhunsky DJ, Krampitz GW, Poullos PD, et al. Pancreatic neuroendocrine tumours: hypoenhancement on arterial phase computed tomography predicts biological aggressiveness. *HPB (Oxford).* 2014;16:304–311.
18. Dromain C, de Baere T, Lumbroso J, et al. Detection of liver metastases from endocrine tumors: a prospective comparison of somatostatin receptor scintigraphy, computed tomography, and magnetic resonance imaging. *J Clin Oncol.* 2005;23:70–78.
19. Yu R, Wachsman A. Imaging of neuroendocrine tumors: indications, interpretations, limits, and pitfalls. *Endocrinol Metab Clin North Am.* 2017;46:795–814.
20. Shimada K, Isoda H, Hirokawa Y, Arizono S, Shibata T, Togashi K. Comparison of gadolinium-EOB-DTPA-enhanced and diffusion-weighted liver MRI for detection of small hepatic metastases. *Eur Radiol.* 2010;20:2690–2698.
21. Ba-Ssalamah A, Uffmann M, Saini S, Bastati N, Herold C, Schima W. Clinical value of MRI liver-specific contrast agents: a tailored examination for a confident noninvasive diagnosis of focal liver lesions. *Eur Radiol.* 2009;19:342–357.
22. Qian HF, Zhu YM, Wu X, Li FQ, Xuan HB, Shen J. Comparison of enhanced magnetic resonance and diffusion-weighted imaging for detection of hepatic metastases [in Chinese]. *Chung Kuo I Hsueh Ko Hsueh Yuan Hsueh Pao.* 2012;34:621–624.
23. Giesel FL, Kratochwil C, Mehndiratta A, et al. Comparison of neuroendocrine tumor detection and characterization using DOTATOC-PET in correlation with contrast enhanced CT and delayed contrast enhanced MRI. *Eur J Radiol.* 2012;81:2820–2825.

24. Besa C, Ward S, Cui Y, Jajamovich G, Kim M, Taouli B. Neuroendocrine liver metastases: value of apparent diffusion coefficient and enhancement ratios for characterization of histopathologic grade. *J Magn Reson Imaging.* 2016;44:1432–1441.
25. Kim M, Kang TW, Kim YK, et al. Pancreatic neuroendocrine tumour: correlation of apparent diffusion coefficient or WHO classification with recurrence-free survival. *Eur J Radiol.* 2016;85:680–687.
26. Hofmann M, Maecke H, Börner R, et al. Biokinetics and imaging with the somatostatin receptor PET radioligand ^{68}Ga-DOTATOC: preliminary data. *Eur J Nucl Med.* 2001;28:1751–1757.
27. Reubi JCSJ, Waser B, Wenger S, Heppeler A, Schmitt JS, Mäcke HR. Affinity profiles for human somatostatin receptor subtypes SST1-SST5 of somatostatin radiotracers selected for scintigraphic and radiotherapeutic use. *Eur J Nucl Med.* 2000; 27:273–282.
28. Poeppel TD, Binse I, Petersenn S, et al. ^{68}Ga-DOTATOC versus ^{68}Ga-DOTATATE PET/CT in functional imaging of neuroendocrine tumors. *J Nucl Med.* 2011;52: 1864–1870.
29. Pfeifer A, Knigge U, Binderup T, et al. ^{64}Cu-DOTATATE PET for neuroendocrine tumors: a prospective head-to-head comparison with ^{111}In-DTPA-octreotide in 112 patients. *J Nucl Med.* 2015;56:847–854.
30. Johnbeck CB, Knigge U, Loft A, et al. Head-to-head comparison of ^{64}Cu-DOTATATE and ^{68}Ga-DOTATOC PET/CT: a prospective study of 59 patients with neuroendocrine tumors. *J Nucl Med.* 2017;58:451–457.
31. Loft M, Carlsen EA, Johnbeck CB, et al. Cu-DOTATATE PET in patients with neuroendocrine neoplasms: prospective, head-to-head comparison of imaging at 1 hour and 3 hours after injection. *J Nucl Med.* 2021;62:73–80.
32. Hicks RJ, Jackson P, Kong G, et al. Cu-SARTATE PET imaging of patients with neuroendocrine tumors demonstrates high tumor uptake and retention, potentially allowing prospective dosimetry for peptide receptor radionuclide therapy. *J Nucl Med.* 2019;60:777–785.
33. Krebs S, Pandit-Taskar N, Reidy D, et al. Biodistribution and radiation dose estimates for ^{68}Ga-DOTA-JR11 in patients with metastatic neuroendocrine tumors. *Eur J Nucl Med Mol Imaging.* 2019;46:677–685.
34. Nicolas GP, Schreiter N, Kaul F, et al. Sensitivity comparison of ^{68}Ga-OPS202 and ^{68}Ga-DOTATOC PET/CT in patients with gastroenteropancreatic neuroendocrine tumors: a prospective phase II imaging study. *J Nucl Med.* 2018;59:915–921.
35. Antwi K, Fani M, Heye T, et al. Comparison of glucagon-like peptide-1 receptor (GLP-1R) PET/CT, SPECT/CT and 3T MRI for the localisation of occult insulinomas: evaluation of diagnostic accuracy in a prospective crossover imaging study. *Eur J Nucl Med Mol Imaging.* 2018;45:2318–2327.
36. Parihar AS, Vadi SK, Kumar R, et al. ^{68}Ga DOTA-exendin PET/CT for detection of insulinoma in a patient with persistent hyperinsulinemic hypoglycemia. *Clin Nucl Med.* 2018;43:e285–e286.
37. Werner RA, Weich A, Higuchi T, et al. Imaging of chemokine receptor 4 expression in neuroendocrine tumors: a triple tracer comparative approach. *Theranostics.* 2017; 7:1489–1498.
38. Garin E, Le Jeune F, Devillers A, et al. Predictive value of ^{18}F-FDG PET and somatostatin receptor scintigraphy in patients with metastatic endocrine tumors. *J Nucl Med.* 2009;50:858–864.
39. Binderup T, Knigge U, Loft A, Federspiel B, Kjaer A. ^{18}F-fluorodeoxyglucose positron emission tomography predicts survival of patients with neuroendocrine tumors. *Clin Cancer Res.* 2010;16:978–985.
40. Johnbeck CB, Knigge U, Langer SW, et al. Prognostic value of ^{18}F-FLT PET in patients with neuroendocrine neoplasms: a prospective head-to-head comparison with ^{18}F-FDG PET and Ki-67 in 100 patients. *J Nucl Med.* 2016;57:1851–1857.
41. Ezziddin S, Adler L, Sabet A, et al. Prognostic stratification of metastatic gastroenteropancreatic neuroendocrine neoplasms by ^{18}F-FDG PET: feasibility of a metabolic grading system. *J Nucl Med.* 2014;55:1260–1266.
42. Bahri H, Laurence L, Edeline J, et al. High prognostic value of ^{18}F-FDG PET for metastatic gastroenteropancreatic neuroendocrine tumors: a long-term evaluation. *J Nucl Med.* 2014;55:1786–1790.
43. Nilica B, Waitz D, Stevanovic V, et al. Direct comparison of ^{68}Ga-DOTA-TOC and ^{18}F-FDG PET/CT in the follow-up of patients with neuroendocrine tumour treated with the first full peptide receptor radionuclide therapy cycle. *Eur J Nucl Med Mol Imaging.* 2016;43:1585–1592.
44. Sansovini M, Severi S, Ianniello A, et al. Long-term follow-up and role of FDG PET in advanced pancreatic neuroendocrine patients treated with ^{177}Lu-D OTATATE. *Eur J Nucl Med Mol Imaging.* 2017;44:490–499.
45. Hofman MS, Michael M, Kashyap R, Hicks RJ. Modifying the poor prognosis associated with ^{18}F-FDG-avid NET with peptide receptor chemo-radionuclide therapy (PRCRT). *J Nucl Med.* 2015;56:968–969.
46. Miederer M, Seidl S, Buck A, et al. Correlation of immunohistopathological expression of somatostatin receptor 2 with standardised uptake values in ^{68}Ga-DOTATOC PET/CT. *Eur J Nucl Med Mol Imaging.* 2009;36:48–52.
47. Campana D, Ambrosini V, Pezzilli R, et al. Standardized uptake values of ^{68}Ga-DOTANOC PET: a promising prognostic tool in neuroendocrine tumors. *J Nucl Med.* 2010;51:353–359.
48. Velikyan I, Sundin A, Sörensen J, et al. Quantitative and qualitative intrapatient comparison of ^{68}Ga-DOTATOC and ^{68}Ga-DOTATATE: net uptake rate for accurate quantification. *J Nucl Med.* 2014;55:204–210.
49. Toriihara A, Baratto L, Nobashi T, et al. Prognostic value of somatostatin receptor expressing tumor volume calculated from ^{68}Ga-DOTATATE PET/CT in patients with well-differentiated neuroendocrine tumors. *Eur J Nucl Med Mol Imaging.* 2019;46:2244–2251.
50. Ambrosini V, Kunikowska J, Baudin E, et al. Consensus on molecular imaging and theranostics in neuroendocrine neoplasms. *Eur J Cancer.* 2021;146:56–73.
51. Shah MH, Goldner WS, Halfdanarson TR, et al. NCCN guidelines insights: neuroendocrine and adrenal tumors, version 2.2018. *J Natl Compr Canc Netw.* 2018;16:693–702.
52. Öksüz MÖ, Winter L, Pfannenberg C, et al. Peptide receptor radionuclide therapy of neuroendocrine tumors with ^{90}Y-DOTATOC: is treatment response predictable by pre-therapeutic uptake of ^{68}Ga-DOTATOC? *Diagn Interv Imaging.* 2014;95:289–300.
53. Kratochwil C, Stefanova M, Mavriopoulou E, et al. SUV of [^{68}Ga]DOTATOC-PET/CT predicts response probability of PRRT in neuroendocrine tumors. *Mol Imaging Biol.* 2015;17:313–318.
54. Subramaniam RM, Bradshaw ML, Lewis K, Pinho D, Shah C, Walker RC. ACR practice parameter for the performance of gallium-68 DOTATATE PET/CT for neuroendocrine tumors. *Clin Nucl Med.* 2018;43:899–908.
55. Werner RA, Solnes LB, Javadi MS, et al. SSTR-RADS version 1.0 as a reporting system for SSTR PET imaging and selection of potential PRRT candidates: a proposed standardization framework. *J Nucl Med.* 2018;59:1085–1091.
56. Hope TA, Calais J, Zhang L, Dieckmann W, Millo C. ^{111}In-pentetreotide scintigraphy versus 68 Ga-DOTATATE PET: impact on Krenning scores and effect of tumor burden. *J Nucl Med.* 2019;60:1266–1269.
57. Werner RA, Bundschuh RA, Bundschuh L, et al. Novel structured reporting systems for theranostic radiotracers. *J Nucl Med.* 2019;60:577–584.
58. Chan DL, Pavlakis N, Schembri GP, et al. Dual somatostatin receptor/FDG PET/CT imaging in metastatic neuroendocrine tumours: proposal for a novel grading scheme with prognostic significance. *Theranostics.* 2017;7:1149–1158.
59. Werner RA, Thackeray JT, Pomper MG, et al. Recent updates on Molecular Imaging Reporting and Data Systems (MI-RADS) for theranostic radiotracers-navigating pitfalls of SSTR- and PSMA-targeted PET/CT. *J Clin Med.* 2019;8:1060.
60. Ambrosini V, Campana D, Polverari G, et al. Prognostic value of ^{68}Ga-DOTANOC PET/CT SUVmax in patients with neuroendocrine tumors of the pancreas. *J Nucl Med.* 2015;56:1843–1848.
61. Kwekkeboom DJ, Kam BL, van Essen M, et al. Somatostatin-receptor-based imaging and therapy of gastroenteropancreatic neuroendocrine tumors. *Endocr Relat Cancer.* 2010;17:R53–R73.
62. Haug AR, Auernhammer CJ, Wängler B, et al. ^{68}Ga-DOTATATE PET/CT for the early prediction of response to somatostatin receptor-mediated radionuclide therapy in patients with well-differentiated neuroendocrine tumors. *J Nucl Med.* 2010;51: 1349–1356.
63. Hope TA, Bergsland EK, Bozkurt MF, et al. Appropriate use criteria for somatostatin receptor PET imaging in neuroendocrine tumors. *J Nucl Med.* 2018;59:66–74.
64. Graf J, Pape UF, Jann H, et al. Prognostic significance of somatostatin receptor heterogeneity in progressive neuroendocrine tumor treated with Lu-177 DOTATOC or Lu-177 DOTATATE. *Eur J Nucl Med Mol Imaging.* 2020;47:881–894.
65. Bodei L, Kidd MS, Singh A, et al. PRRT genomic signature in blood for prediction of ^{177}Lu-octreotate efficacy. *Eur J Nucl Med Mol Imaging.* 2018;45:1155–1169.
66. Bodei L, Kidd MS, Singh A, et al. PRRT neuroendocrine tumor response monitored using circulating transcript analysis: the NETest. *Eur J Nucl Med Mol Imaging.* 2020; 47:895–906.
67. Pu N, Habib JR, Bejjani M, et al. The effect of primary site, functional status and treatment modality on survival in gastroenteropancreatic neuroendocrine neoplasms with synchronous liver metastasis: a US population-based study. *Ann Transl Med.* 2021;9:329.

Artificial Intelligence for PET Image Reconstruction

Andrew J. Reader[1] and Georg Schramm[2]

[1]*School of Biomedical Engineering and Imaging Sciences, King's College, London, United Kingdom; and* [2]*Division of Nuclear Medicine, Department of Imaging and Pathology, KU/UZ, Leuven, Belgium*

Artificial intelligence (AI) continues to deliver a remarkable impact on numerous and highly diverse fields, such as physics, natural language processing, finance, human resources, image processing, protein folding (*1*), and prediction of viral mutations (*2*). In broad terms, AI is any technology that can learn how to perform tasks from example data or experiences. This technology contrasts with the conventional paradigm of a human programmer or engineer providing extensive and exhaustive instructions in order for a task to be performed.

The power of AI is beyond question, but its adoption, as with other groundbreaking technologies, can initially lead to concerns, skepticism, and even ethical questions. In particular, use of AI in medical imaging has demonstrated immense potential (*3*), but a key question is how much we can trust AI in the formation of images that inform clinical decisions, when lives of patients are often at stake.

This brief article will consider the methodologies, benefits, and concerns regarding AI for the case of the formation, or reconstruction, of PET images (*4*) and will focus on a subdiscipline of AI, namely deep learning (*5*). We will define deep learning and then use this term interchangeably with AI.

UNDERSTANDING AI AND DEEP LEARNING

So what is deep learning exactly? Deep learning can be considered as a sequence of steps that operate on input data to perform a desired task, with the steps being learned from example inputs and desired outputs (training data). These sequences of operations are comparable to conventional computer code, which similarly executes a sequence of operations designed (without training data) to specifically accomplish tasks. Therefore, deep learning can be more generally regarded as a data-informed, trainable version of our existing, well-established algorithms.

Taking the example task of PET image reconstruction, algorithms that have been developed by the PET reconstruction community over many decades (drawing on knowledge from imaging physics, mathematics and statistics), can now also be integrated into the learning AI paradigm. Better still, state-of-the-art image reconstruction methods can likely be made even more reliable with AI-informed refinement.

However, AI has been frequently misunderstood, either because of the notion of AI being a black box, or as a result of conventional low–dimensional mathematical perspectives on fitting models to limited data. The black box misconception originates partly from the highly successful use of deep learning in computer vision tasks, in which its performance has launched deep learning to its deserved level of current recognition. Early successes via the automated hierarchical feature-learning of convolutional neural networks have resulted in large uptake of these networks to other tasks, in which there has been a temptation to use these large architectures without careful design considerations, relying instead on large numbers of trainable parameters. Use of poorly justified and highly parameterized architectures has made it easy to dismiss any chance of understanding (let alone designing) these sophisticated nonlinear mappings, fueling AI skepticism. As for conventional mathematical perspectives on the feasibility of optimization and fitting to limited data in high dimensions, these have proven not to be the showstoppers that they were expected to be. On the contrary, deep learning's success has revealed a need to revise our thinking on optimization, regularization, and generalization.

Hence, the rapid progress of AI methods, sometimes with loss of principled design choices and often to the surprise of conventional mathematical thinking, has resulted in concern over the interpretability and trustworthiness of AI. This situation has not been helped by reduced levels of rigor arising from the surge of innovation and exciting successes. But black box concerns (Fig. 1) and conventional mathematical views on optimization are becoming dated perspectives, particularly in the context of deep learning for signal and image processing. In these fields, increasingly meaningful design choices are being made by embedding the AI paradigm into conventional and well-understood algorithmic processing (such as the discrete Fourier and Radon transforms).

WHY USE AI FOR PET IMAGE RECONSTRUCTION?

In applying AI to image reconstruction for PET, we are recognizing that PET image reconstruction actually needs help. First, improving spatial resolution and lowering noise in PET images will very likely assist in the clinical utility of PET. Second, even if current image quality is deemed acceptable, the desire for shorter acquisition times or reduced radiation doses will require more advanced techniques to try and retain standard image quality from lower-count (noisier) data. Similarly, achieving higher temporal resolution, such as for improved motion correction, will likewise demand improved reconstruction.

Let us now recall what reconstruction actually is: it is the use of raw list-mode or projection data acquired from a PET scan to form an image representing a radiotracer's spatiotemporal distribution within the human body. For conventional PET, the spatial resolution of such images is of the order of a few millimeters, and the temporal

Received May 31, 2021; revision accepted Jun. 14, 2021.

For correspondence or reprints, contact Georg Schramm (georg.schramm@kuleuven.be).

Published online July 8, 2021

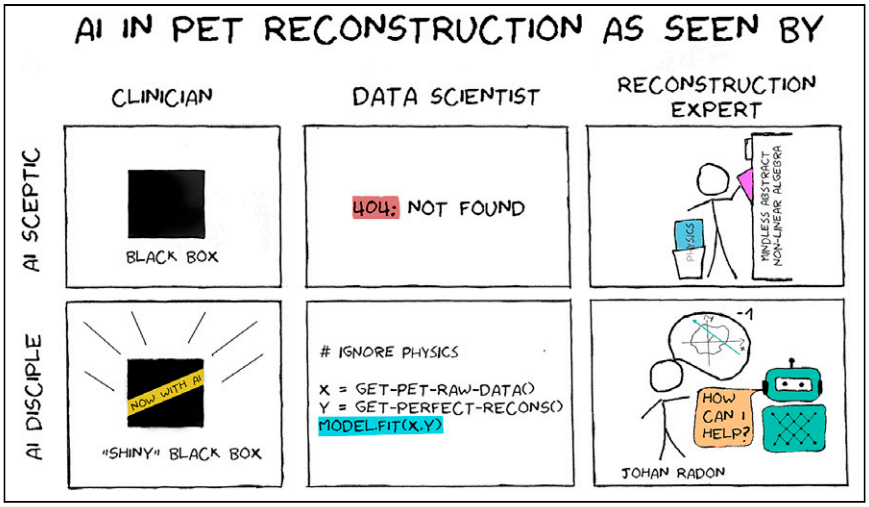

FIGURE 1. AI in PET reconstruction as seen from various perspectives (*15*).

resolution is of the order of many seconds. These limitations are due to limited photon counts, scanner design, and physics. Nonetheless, advances in statistical image reconstruction methods for PET have made greater use of the acquired data, lowering image noise and improving spatial and temporal resolution, through accurate modeling of the imaging physics and statistics and through use of prior information (including from CT or MRI). Even with such progress, the limited counts and resolution still place a performance ceiling on the potential of PET for clinical imaging, and as mentioned, the desire to reduce the dose and to shorten scan times means that limited data pose ongoing challenges to PET image reconstruction.

This is where AI can make a huge difference, in 2 main ways. First, with sufficient example data, AI can learn the vast (but nonetheless highly restricted) set of PET images that can realistically ever be expected from a PET scan (this set is often referred to as the manifold). For example, we know a PET scan can never deliver a CT or MR image, let alone a natural photographic image. Yet the mathematics of current image reconstruction methods do not exploit any of this obviously robust prior information but instead can readily accommodate wrong images. This is because current state-of-the-art image reconstruction uses simple, mathematically convenient priors for PET images, which are excessively general (e.g., requiring only that the images be smooth, to suppress noise but at the cost of resolution and details). This process discards considerable amounts of a priori information. In contrast, AI's learning of the manifold of all feasible PET images can be applied to make better use of each and every acquired count in a PET scan. Acquired PET data can therefore be projected, or encoded, into this realistic manifold.

Second, since this learned manifold of all feasible PET images can in fact be represented in infinitely many ways, AI can learn how to encode the acquired PET scan data into latent feature representations that best serve our desired goals. These representations include reduced-dimension representations (bottlenecks) to assist in noise reduction and can also involve projection to higher dimensions to assist in classification tasks. The point is that AI can learn how best to capture and encode key explanatory information, salient to our task, from a given scan.

Therefore, the power of AI is not only its ability to learn how to encode into useful latent representations or feature maps, and learn transforms between them, but also its ability to learn how to decode from these latent representations, to generate outputs for various desired tasks. This could be generation of low-noise reconstructed PET images with high resolution, generation of radiological reports, or indeed diagnostic and prognostic predictions. Learning encodings of acquired PET scan data into contextually rich feature spaces consistent with the PET manifold, and decoding into task-specific forms, is the sublimely powerful ability of AI, which PET would do well to exploit more fully.

HOW CAN WE USE AI IN PET IMAGE RECONSTRUCTION?

There are currently 3 main approaches to using AI in PET reconstruction. The first group of approaches, direct AI (e.g., AUTOMAP (*6*) or DeepPET (*7*)), learns an encoding from the raw data, via a latent feature space, to decode to the desired image. The key point here is that the overall mapping is trained by supervised learning, in order to take noisy raw PET data and deliver inferences of the ground-truth object or high-quality reference image, according to the pairings of datasets used in the training phase. Direct AI can easily be understood by comparison to conventional curve-fitting and regression tasks, except that in the case of deep learning of PET reconstruction we are performing regressions with extremely high-dimensional vectors. The input raw PET data are fully 3-dimensional sets of measured (time-of-flight) sinograms (with $\sim 10^8$–10^9 bins), for mapping to output 3-dimensional images (with $\sim 10^7$ voxels). At present, these direct deep learning methods look to be impractical, having been demonstrated only for small 2-dimensional reconstructions (e.g., 128 × 128 images), as they have colossal demands for computational memory and training set sizes ($>10^5$ datasets). Furthermore, they may not generalize well for unseen data (e.g., for data that are too different from the example training data). Early tests of direct methods for real-data 2-dimensional PET reconstructions have delivered images that have yet to convince some experts.

By far the more promising methods, sometimes called physics-informed AI, take the learning paradigm from AI and integrate this into our existing state-of-the-art statistical iterative image reconstruction methods. Here, the standard iterative loop of an image reconstruction algorithm (such as ordered-subsets expectation maximization) is unrolled, or unfolded (*8*), into a deep network—the word *deep* meaning that there are many successive steps, as indeed in any piece of computer code. Iterative reconstruction is thus nothing more than a deep cascade of successive operations, each operation taking the raw PET data and progressively transforming it (by a series of operations, primarily forward and back projections) into a reconstruction of the PET radiotracer distribution. Deep learning is then integrated into the unfolded reconstruction to provide rich, data-informed, prior information to the iterative process, which makes repeated use of the actual raw data throughout. Thus, the benefits of

decades of reconstruction research are combined with the power of the AI paradigm (i.e., learning from high-quality reference datasets), allowing the manifold of feasible PET images to be used as a powerful, yet relatively safe (data-consistent), prior in the image reconstruction process. Compared with direct AI methods, the need for training data in these unrolled methods is reduced by orders of magnitude, as the physics and statistics of PET data acquisition do not need to be learned from scratch. Furthermore, their scope for generalization to unseen data is better than that of direct methods, as has been demonstrated in other imaging inverse problems (*9*).

The third main category of AI for PET reconstruction acts on existing standard reconstructed PET images. Such postprocessing is much simpler to implement, and this is where advances are being quickly made, with commercial options already available (such as subtlePET [https://www.subtlemedical.com], which seeks to map low-count [25% dose] PET images to their full-dose equivalents). Research in this area is burgeoning, with a myriad of differing deep network mappings being proposed, to denoise, upgrade, and even mimic state-of-the-art PET reconstructions from higher-count data (*10*).

At present, nearly all AI methods for PET reconstruction have leaned heavily on convolutional neural network (*11*) mappings. However, the surge of more advanced data-mixing architectures, such as the immense success of transformers (*12*), with their powerful self-attention mechanism for rapid learning of long-range contexts in data, has yet to reach the PET reconstruction community, but it is sure to come. These highly successful architectures should deliver still more powerful ways of harnessing all acquired PET data to generate feature-rich manifold embeddings, benefiting clinical imaging tasks and even ultimately aiding management of the patient pathway.

PROBLEMS TO TACKLE AND OUTLOOK

There have, however, been ongoing expressions of concern regarding AI. For example, in the context of MRI the risk of hallucinations, artificial features, and instability has been studied (*13*). Such problems, even evidenced in physics-informed approaches (unrolled iterative methods), will need comprehensive investigation, research, and resolution for PET image reconstruction in order to deliver the robustness required for clinical imaging.

A crucial part of such research will be the need for benchmark datasets through which new AI algorithms for PET image reconstruction can be assessed. Such datasets ideally need international collaboration and contributions from clinicians and researchers in reconstructions from multiple institutions. Such datasets have already existed for decades in the image processing community and have been established more recently in the deep learning, computer vision, and MRI communities (e.g., CIFAR, MNIST, ImageNet, and fastMRI (*14*)). Ideally, benchmark datasets for PET image reconstruction should be provided and linked with particular clinical tasks (e.g., neurological disorder diagnosis or tumor detection).

Furthermore, to have confidence in the high image quality that can be delivered by AI approaches to image reconstruction, the arrival of evidential deep learning is timely. Also known as Bayesian deep learning, these approaches not only would provide high-quality reconstructed PET images but also deliver unequivocal indications of the AI's uncertainty (known as epistemic uncertainty) in various regions and details of the image—information that would be crucial during clinical reading.

Although supervised learning remains central to current developments in PET reconstruction, the field will need to exploit larger datasets for which the costly ground truth labels or targets are not known. Unsupervised pretraining of networks has shown great potential in computer vision, and image reconstruction models could very likely benefit from pretraining with unlabeled data, followed by fine tuning with the labor-intensive supervised labels. Better still, self-supervised learning paradigms should prove useful. In essence, instead of providing explicit, labor-intensive example inputs and outputs, only example data are provided, along with instructions on how to create the set of inputs and targets from the data for supervised learning. Self-supervised approaches have enabled training of huge-scale language models, including powerful transformer-based architectures such as GPT-3.

CONCLUSION

AI is here to stay, and validated PET reconstruction that makes use of its power will deliver images of enhanced clinical benefit, compared with methods that ignore its capabilities. Yet to arrive at this point it will be necessary to build confidence, and 2 approaches may help. First, adoption may need to be in a gentle, progressive fashion. At the very simplest level, deep learning can provide optimization of merely the degree of standard image smoothing, which has low risk but also a reduced degree of benefit. This small step up from our existing regularized reconstruction methods could allow use of AI to decide how much anatomical (CT or MRI) guidance information can reliably be applied for PET reconstruction.

Second, to ensure safe adoption of more sophisticated AI methods, it may prove necessary to use routes such as evidential deep learning, in which, for example, epistemic uncertainty is clearly expressed alongside the images. The AI output would thus be twofold: "this is the best estimate of the image for the patient" and "this is my confidence level for each detail and region in the image."

The methods that are set to flourish will harness all our knowledge of physics, math, and statistics for PET reconstruction and synergistically combine these with the learning power of AI, with feasible demands for training data. Simply put: there is no reason to learn from scratch that which we know well already, and conversely there is no reason to insist on simple mathematical expressions for complex images. For example, we cannot analytically derive or program what a feasible PET image should look like, but deep learning can do this with ease.

Finally, the endpoint assessment of the impact of AI reconstruction on clinical tasks, preferably with well-understood benchmark datasets, will of course be essential. Without question, in the development and validation of AI for reconstruction, critical feedback from clinicians will be needed more than ever.

DISCLOSURE

No potential conflict of interest relevant to this article was reported.

REFERENCES

1. Senior AW, Evans R, Jumper J, et al. Improved protein structure prediction using potentials from deep learning. *Nature.* 2020;577:706–710.
2. Salama MA, Hassanien AE, Mostafa A. The prediction of virus mutation using neural networks and rough set techniques. *EURASIP J Bioinform Syst Biol.* 2016; 2016:10.

3. Kermany DS, Goldbaum M, Cai W, et al. Identifying medical diagnoses and treatable diseases by image-based deep learning. *Cell.* 2018;172:1122–1131.e9.
4. Mehranian A, Reader AJ. Deep learning for PET image reconstruction. *IEEE Trans Radiat Plasma Med Sci.* 2020;5:54–64.
5. Reader AJ, Corda G, Mehranian A, Costa-Luis Cd, Ellis S, Schnabel JA. Deep learning for PET image reconstruction. *IEEE Trans Radiat Plasma Med Sci.* 2021;5:1–25.
6. Zhu B, Liu JZ, Cauley SF, Rosen BR, Rosen MS. Image reconstruction by domain-transform manifold learning. *Nature.* 2018;555:487–492.
7. Häggström I, Schmidtlein CR, Campanella G, Fuchs TJ. DeepPET: a deep encoder-decoder network for directly solving the PET image reconstruction inverse problem. *Med Image Anal.* 2019;54:253–262.
8. Gregor K, LeCun Y. Learning fast approximations of sparse coding. In: *Proceedings of the 27th International Conference on International Conference on Machine Learning.* Omnipress; 2010:399–406.
9. Gilton D, Ongie G, Willett R. Neumann networks for linear inverse problems in imaging. *IEEE Trans Comput Imaging.* 2020;6:328–343.
10. Schramm G, Rigie D, Vahle T, et al. Approximating anatomically-guided PET reconstruction in image space using a convolutional neural network. *Neuroimage.* 2021;224:117399.
11. LeCun Y, Bottou L, Bengio Y, Haffner P. Gradient-based learning applied to document recognition. *Proc IEEE.* 1998;86:2278–2323.
12. Vaswani A, Shazeer N, Parmar N, et al. Attention is all you need. arXiv website. https://arxiv.org/abs/1706.03762. Published June 12, 2017. Revised December 6, 2017. Accessed July 27, 2021.
13. Antun V, Renna F, Poon C, Adcock B, Hansen AC. On instabilities of deep learning in image reconstruction and the potential costs of AI. *Proc Natl Acad Sci U S A.* 2020; 117:30088–30095.
14. Knoll F, Murrell T, Sriram A, et al. Advancing machine learning for MR image reconstruction with an open competition: overview of the 2019 fastMRI challenge. *Magn Reson Med.* 2020;84:3054–3070.
15. AI in PET image reconstruction v1.2. figshare website. https://figshare.com/articles/figure/AI_in_PET_image_reconstruction_v1_0/14685915. Published May 27, 2021. Accessed July 27, 2021.

PET/MRI Improves Management of Children with Cancer

Lucia Baratto[1], K. Elizabeth Hawk[1], Lisa States[2], Jing Qi[3], Sergios Gatidis[4], Louise Kiru[1], and Heike E. Daldrup-Link[1,5]

[1]Department of Radiology, Stanford University, Stanford, California; [2]Department of Radiology, Children's Hospital of Philadelphia, Philadelphia, Pennsylvania; [3]Department of Radiology, Children's Wisconsin, Milwaukee, Wisconsin; [4]Department of Diagnostic and Interventional Radiology, University Hospital Tübingen, Tübingen, Germany; and [5]Department of Pediatrics, Stanford University, Stanford, California

Learning Objectives: On successful completion of this activity, participants should be able to describe (1) why integrated ^{18}F-FDG PET/MR can be a time-efficient, convenient, and safe approach for the management of children with cancer; (2) the advantages of integrated ^{18}F-FDG PET/MR in the evaluation of children with cancer and predisposition syndromes such as lymphoma, sarcoma, and neurofibromatosis 1; and (3) future research directions for the use of integrated ^{18}F-FDG PET/MR in children with cancer.

Financial Disclosure: This study was supported by a grant from the National Institute of Child Health and Human Development (NICHD, R01HD081123) and the Sarcoma Foundation. The authors of this article have indicated no other relevant relationships that could be perceived as a real or apparent conflict of interest.

CME Credit: SNMMI is accredited by the Accreditation Council for Continuing Medical Education (ACCME) to sponsor continuing education for physicians. SNMMI designates each *JNM* continuing education article for a maximum of 2.0 AMA PRA Category 1 Credits. Physicians should claim only credit commensurate with the extent of their participation in the activity. For CE credit, SAM, and other credit types, participants can access this activity through the SNMMI website (http://www.snmmilearningcenter.org) through October 2024.

Integrated PET/MRI has shown significant clinical value for staging and restaging of children with cancer by providing functional and anatomic tumor evaluation with a 1-stop imaging test and with up to 80% reduced radiation exposure compared with ^{18}F-FDG PET/CT. This article reviews clinical applications of ^{18}F-FDG PET/MRI that are relevant for pediatric oncology, with particular attention to the value of PET/MRI for patient management. Early adopters from 4 different institutions share their insights about specific advantages of PET/MRI technology for the assessment of young children with cancer. We discuss how whole-body PET/MRI can be of value in the evaluation of certain anatomic regions, such as soft tissues and bone marrow, as well as specific PET/MRI interpretation hallmarks in pediatric patients. We highlight how whole-body PET/MRI can improve the clinical management of children with lymphoma, sarcoma, and neurofibromatosis, by reducing the number of radiologic examinations needed (and consequently the radiation exposure), without losing diagnostic accuracy. We examine how PET/MRI can help in differentiating malignant tumors versus infectious or inflammatory diseases. Future research directions toward the use of PET/MRI for treatment evaluation of patients undergoing immunotherapy and assessment of different theranostic agents are also briefly explored. Lessons learned from applications in children might also be extended to evaluations of adult patients.

Key Words: oncology; pediatrics; PET/MRI; cancer; pediatric oncology

J Nucl Med 2021; 62:1334–1340
DOI: 10.2967/jnumed.120.259747

Traditional 1-stop imaging tests, such as CT and PET/CT, are associated with considerable radiation exposure and risk of secondary cancer development later in life (*1*,*2*). This is particularly concerning for children, as they are more sensitive to radiation effects than adults are. Because advances in cancer therapy have significantly improved survival in pediatric cancer patients, these patients now live long enough to encounter secondary cancers (*3*–*5*). Integrated PET/MRI provides cancer staging and restaging with up to 80% reduced radiation exposure compared with PET/CT by replacing CT with MRI for anatomic colocalization of radiotracer data (*6*). Although many studies have addressed the technical aspects of a PET/MRI examination, few studies have discussed how PET/MRI can improve patient management compared with standard imaging modalities. For this review article, we have assembled a team of early adopters of pediatric PET/MRI from different backgrounds (radiologists, nuclear medicine physicians, and researchers), different hospitals, and different states or countries who summarize important clinical–translational PET/MRI applications for children with cancer and predisposition syndromes. This article focuses on new developments in the field of PET/MRI, with particular attention to patient management.

CLINICAL APPLICATIONS OF PET/MRI IN CHILDREN WITH CANCER AND NEUROFIBROMATOSIS TYPE 1

Special Considerations for PET/MRI of Children

PET/MRI of children under the age of 6 y usually requires sedation or anesthesia to minimize patient motion. A significant benefit of integrated PET/MRI compared with 2 separate examinations for young children is a reduction in the number of sedations, which reduces the risk of related complications, such as aspiration, and adverse neurocognitive effects (*7*). In addition, the high soft-tissue contrast provided by MRI can help in the differentiation of age-dependent normal from abnormal findings.

One of the most common physiologic findings in the pediatric age group is increased ^{18}F-FDG uptake in the Waldeyer ring and cervical lymph nodes. In patients with intrinsic high ^{18}F-FDG activity in the Waldeyer tonsillar ring, MRI can help to characterize normal tonsils. Preserved tonsil morphology with homogeneous signal intensity and symmetric ^{18}F-FDG uptake is likely benign, whereas globular tonsil

Received Nov. 5, 2020; revision accepted May 21, 2021.
For correspondence or reprints, contact Heike E. Daldrup-Link (heiked@stanford.edu).

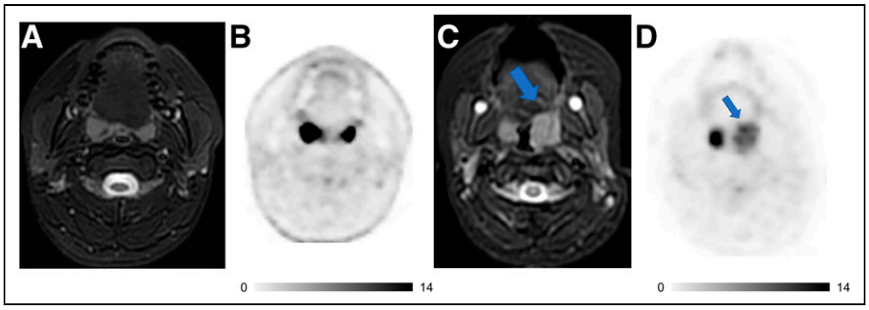

FIGURE 1. ^{18}F-FDG PET/MRI helps to characterize activity in tonsils and stage patients with lymphoma. (A and B) Axial T2-weighted fat-saturated fast-spin-echo (FSE) image (A) and ^{18}F-FDG PET image (B) of 15-y-old boy with follicular lymphoma show symmetric morphology and marked ^{18}F-FDG uptake of both tonsils with reactive hyperplasia. (C and D) Axial T2-weighted FSE image (C) and ^{18}F-FDG PET image (D) of 4-y-old girl with large B-cell lymphoma demonstrate asymmetric globular enlargement and relatively less intensive ^{18}F-FDG uptake of left tonsil (arrows). Tonsillectomy revealed large B-cell lymphoma in left tonsil and reactive tissue in right tonsil. Intrinsic uptake in tonsil is more avid than lymphomatous involvement on second patient. Radiologists must be cognizant of this caveat and integrate metabolic and morphologic information to increase diagnostic accuracy.

enlargement or asymmetric ^{18}F-FDG activity is concerning for malignancy (Fig. 1).

Prominent benign cervical lymph nodes are common in children. In children, the short-axis diameter is less than 15 mm for normal level II lymph nodes and less than 10 mm for all other cervical levels (*8*). Vali et al. found increased ^{18}F-FDG lymph node uptake in 29% of patients who underwent PET/CT for non–head and neck tumors (*9*). Benign lymph nodes had a lower SUV_{max} than malignant lesions, with a mean SUV_{max} of 2.1 and 4.2, respectively. A suggested SUV_{max} cutoff for benign lymph nodes was less than 3.2. Diffusion-weighted imaging is helpful for identification of lymph nodes, although it does not outperform size criteria for characterization of malignant nodes (*10–12*).

The thymus has a variable appearance depending on age, physiology, and treatment status. The normal thymus can be large in young children and will have a homogeneous signal intensity and convex borders in the youngest patients. The borders become straight in older children and concave in adolescents (*13*). The normal thymus usually has an SUV_{max} of less than 4 (*14*). During chemotherapy, the thymus shrinks because of physiologic stress. Within approximately 12 mo after treatment, there is a recovery phase in which the thymus can enlarge up to 1.5 times the original size and demonstrate increased ^{18}F-FDG uptake. This thymic rebound is often accompanied by bone marrow reconversion. MRI can confirm that the thymus has a homogeneous signal and lacks restricted diffusion (*13*).

Age-related changes are also seen in the pediatric bone marrow. At birth, red marrow is seen throughout the skeleton. An orderly conversion to yellow marrow follows a predicted course and is most easily detected on non–fat-saturated T1-weighted images. During the first year of life, the initial site of conversion to yellow, fatty marrow is the epiphyses of the long bones, followed by the diaphyses in young children and metaphyses in older children. The last change is in the proximal metaphyses of the proximal long bones, with residual red marrow often seen in teens and young adults. The axial skeleton, including the spine and pelvis, converts to red marrow over a slower course. The fluid-sensitive, fat-suppressed sequences such as T2-weighted fast spin echo and short-inversion-time inversion recovery, provide high sensitivity for detecting metastatic lesions because of increased water content and increased vascularity; however, sensitivity may be decreased in children with red marrow. The detection of metastases is improved with the addition of ^{18}F-FDG PET, which increases the sensitivity from 82% to 96% (*15*). When compared with normal marrow, bone marrow metastases demonstrate increased ^{18}F-FDG uptake, low T1 signal (less than muscle or intervertebral disk as internal standards), increased T2 signal, restricted diffusion, increased water content, and increased contrast enhancement on gadolinium-enhanced MRI. Although one of these characteristics might be masked, the rich information from MRI allows for the detection of bone marrow metastases with higher accuracy than is possible with bone marrow biopsies (*16*).

An example of how information from PET/MRI helped in staging a patient is shown in Figure 2.

PET/MRI evaluation of pulmonary lesions is challenging; in fact, diagnostic MRI of the lungs is difficult to perform because of the inherent low proton density in the lungs, resulting in a low signal-to-noise ratio, cardiac and respiratory motion artifacts, and susceptibility artifacts at the tissue–air interface. Hence, for characterization of small pulmonary nodules, additional chest CT may be useful (*17*).

PET/MRI of Children with Lymphoma

^{18}F-FDG PET is preferred for evaluation of lymphoma (*18*). Most children with lymphoma have excellent long-term survival (*19*), and minimizing ionizing radiation exposure is particularly important in these patients. ^{18}F-FDG PET/MRI and PET/CT demonstrated equivalent diagnostic performance for detection, classification, Ann Arbor staging, and treatment response assessment of pediatric lymphoma (*6*,*20*,*21*).

There is a strong correlation between PET/MRI- and PET/CT-derived SUV. SUVs on PET/MRI based on segmented attenuation maps are lower than those on PET/CT using transmission-based attenuation correction (*6*,*20*,*22*,*23*). Only a few studies reported higher SUVs on PET/MRI than on PET/CT, and that was attributed to ^{18}F-FDG trapping in the tumor due to an extended uptake time (*21*). Since differences in SUV occurred in a systematic fashion, they are not clinically relevant as long as the same modality is used for a given patient.

^{18}F-FDG PET is superior to core biopsy in the detection of bone marrow involvement (*16*). Heacock et al. suggested that PET/MRI had an advantage in the detection of bone marrow disease and enhances diagnostic confidence (*22*). The detection of bone marrow involvement can facilitate earlier aggressive treatment. At some institutions, bone marrow core biopsy can be avoided if PET/MRI is negative for marrow involvement (*24*).

Sensitivity is lower for ^{18}F-FDG PET/MRI than for PET/CT in detecting subcentimeter lung nodules (*17*); however, lung involvement by lymphoma could be successfully depicted on PET/MRI, because these nodules are typically larger and ^{18}F-FDG–avid (*21*).

PET/MRI of Children with Sarcoma

For many children with solid malignancies, including pediatric patients with osteogenic and soft-tissue sarcomas, MRI is already

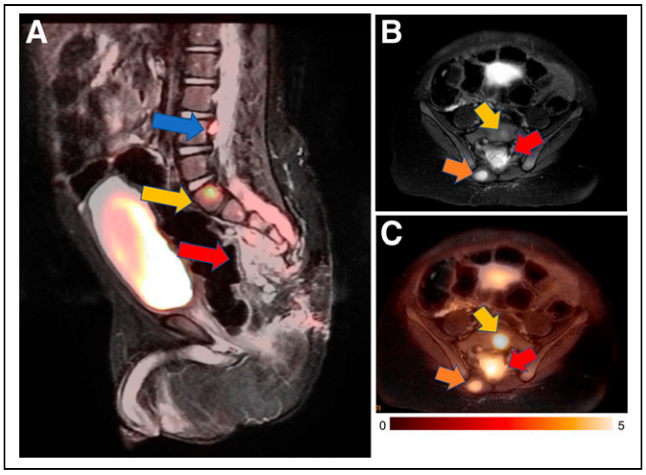

FIGURE 2. ^{18}F-FDG PET/MRI detects tumor invasion into spinal canal in 18-mo-old boy with metastasized germ cell tumor. (A) Sagittal short-inversion-time inversion recovery image, fused with simultaneously acquired ^{18}F-FDG PET image, demonstrates presacral mass (red arrow), which extends into spinal canal. Also noted is ^{18}F-FDG–avid lesion in S1 vertebra (yellow arrow) and extradural focus posterior to L4 vertebra (blue arrow). (B) Axial T2-weighted fast-recovery fast-spin-echo fat-saturated image shows soft-tissue mass entering spinal canal (red arrow). Also noted are metastatic lesions in S1 (yellow arrow) and right paraspinal muscle (orange arrow). (C) Fast-recovery fast-spin-echo fat-saturated image fused with ^{18}F-FDG PET image shows hypermetabolism of all lesions. Information from PET/MRI helped in staging by showing metastatic disease and extent of disease in spinal canal, hence impacting patient management. Patient started chemotherapy right after PET/MRI.

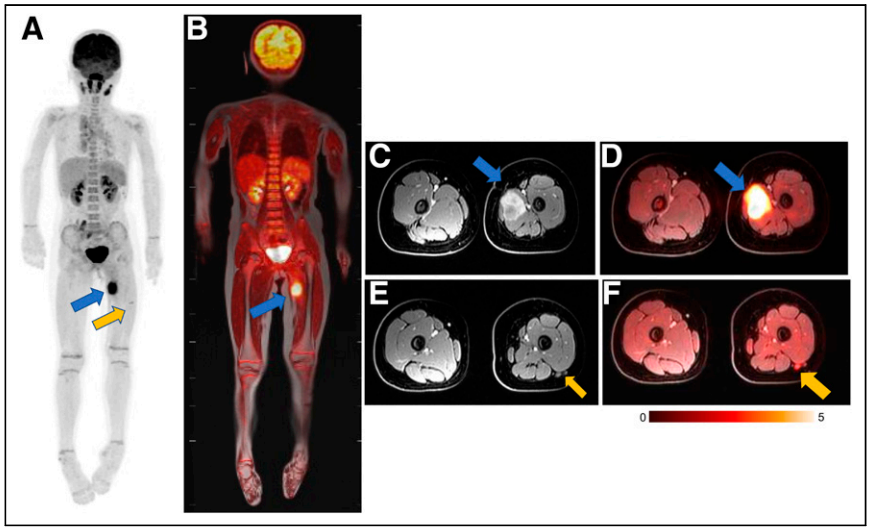

FIGURE 3. ^{18}F-FDG PET/MRI accurately stages rhabdomyosarcoma in 9-y-old girl. (A and B) Maximum-intensity projection of ^{18}F-FDG PET scan (A) and ^{18}F-FDG PET/MRI scan (B) show avid ^{18}F-FDG uptake in lesion in thigh adductor muscles (blue arrow) and tiny additional ^{18}F-FDG–avid lymph node in lateral thigh (yellow arrow). MRI helps to exclude any bone marrow disease or cortical invasion. (C and D) Axial contrast-enhanced fat-saturated T1-weighted MRI scan (C) and ^{18}F-FDG PET/MRI scan (D) demonstrate relation between primary tumor (arrow) and superficial and deep femoral artery and vein. (E and F) Axial contrast-enhanced fat-saturated T1-weighted MRI scan (E) and ^{18}F-FDG PET/MRI scan (F) demonstrate small lymph node (arrow) posterior to vastus lateralis muscle. Primary tumor and lymph node were resected and positive for sarcoma.

the clinical standard for local staging. In these patients, integrated ^{18}F-FDG PET/MRI can provide local and whole-body staging in one session (Fig. 3). Diffusion-weighted MRI can predict tumor therapy response better than changes in tumor size or MR contrast enhancement (*25*,*26*). Patients with sarcomas who responded to chemotherapy demonstrated increasing tumor apparent diffusion coefficient (ADC) values, while nonresponders demonstrated stable or decreasing ADC values (*26*,*27*). We discovered that chemotherapy first decreases glucose metabolism and then increases hydrogen proton diffusion in solid tumors (*28*). At 8–12 wk after the start of therapy, most sarcomas demonstrate an excellent agreement between changes in SUV and apparent diffusion coefficients (*29*). It is not known if patients with a metabolic response on ^{18}F-FDG PET, but a delayed response on diffusion-weighted imaging, have worse outcomes than patients with a concordant response on both imaging modalities.

PET/MRI can also improve monitoring of pediatric tumors after immunotherapy (*29*). Cotreatment with drugs that stimulate marrow reconversion (e.g., granulocyte colony-stimulating factor) can mask metastases. Intravenously administered ferumoxytol nanoparticles are taken up by normal bone marrow and not tumor in the early (0–1 h) postcontrast phase and, thereby, can improve tumor detection (*30*,*31*).

In the future, earlier identification of nonresponders might help prevent side effects from ineffective therapies. Osteosarcomas contain high quantities of tumor-associated macrophages (TAM) and have shown an impressive response to TAM-targeted immunotherapies in mouse models (*32*,*33*). CD47 monoclonal antibodies activate TAM to phagocytose cancer cells (*34*–*38*). Treatment with CD47 monoclonal antibodies significantly inhibited tumor growth and increased survival in mice with bone and soft-tissue sarcomas (*36*,*39*,*40*). We showed that ferumoxytol MRI can detect TAM in osteosarcomas in mouse models (*40*) and patients (*41*) and can monitor TAM response to CD47 monoclonal antibodies (*42*).

PET/MRI of Children with Neurofibromatosis Type 1

In patients with neurofibromatosis type 1, which is a cancer predisposition syndrome, MRI provides a detailed depiction of peripheral neurofibromata and central nervous system lesions (*43*). However, MRI provides limited accuracy in detecting lesion transformation into malignant peripheral nerve sheath tumors (MPNSTs) (*44*). ^{18}F-FDG PET can add information about increased glucose metabolism in MPNSTs (Fig. 4) (*43*,*45*,*46*). Higher ^{18}F-FDG uptake has been shown in MPNSTs than in benign neurofibromatosis type 1 lesions, with suggested SUV cutoffs ranging between approximately 2.5 and 6 (*43*,*45*–*48*).

With respect to MRI, different parameters such as rapid growth, ill-defined margins, and large size have been suggested as potentially discriminative between benign lesions and MPNSTs. (*49*). Lesion apparent diffusion coefficient can reflect increased cellularity in MPNSTs, with overall inconclusive results regarding its added benefit (*43*,*44*,*50*). Recent studies have also assessed the

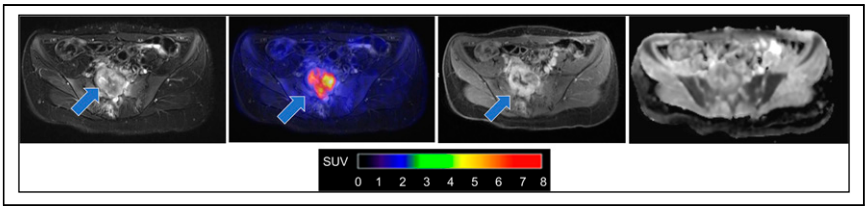

FIGURE 4. ^{18}F-FDG PET/MRI enabled image-informed surgical planning in 21-y-old patient with neurofibromatosis type 1. From left to right: axial fat-saturated T2-weighted image through pelvis reveals heterogeneous lesion infiltrating sacrum (arrow); ^{18}F-FDG PET fused with T2-weighted MRI scan shows increased glucose metabolism of sacral lesion (SUV_{max} = 6; arrow); axial contrast-enhanced fat-saturated T1-weighted MRI scan shows heterogeneous tumor enhancement (arrow); apparent diffusion coefficient map demonstrates restricted diffusion of lesion with mean apparent diffusion coefficient of $0.85 \cdot 10^{-3}$ mm^2 s, which is suggestive of MPNST. Curative treatment of MPNST is critically dependent on early detection. Combined information from ^{18}F-FDG PET and diffusion-weighted MRI led to tumor resection and histologic confirmation of MPNST.

potential role of radiomic analyses on PET and MR images for the detection of MPNST (*46*,*51*).

First studies investigating the value of integrated ^{18}F-FDG PET/MRI in neurofibromatosis type 1 confirmed the diagnostic roles of ^{18}F-FDG PET/MRI for lesion characterization and treatment planning (*43*,*45*). In addition, these studies emphasize further advantages of PET/MRI over sequential PET/CT and MRI, including optimal alignment of MRI and PET in cases of multiple neurofibromas that are closely related, comprehensive examination of the central nervous system and peripheral lesions in a single examination, and significantly reduced diagnostic radiation exposure for patients who need multiple scans during their lifetime.

Table 1 summarizes PET/MRI basic protocols for pediatric oncology in 4 different medical centers, and Table 2 describes the advantages of PET/MRI over PET/CT in the management of pediatric cancer and predisposition syndromes.

Infection or Inflammatory Diseases in Pediatric Cancer Evaluation

Both infectious and inflammatory etiologies can coexist in children with cancer and complicate assessment of PET/MRI images. It is critical to be able to recognize entities that are most likely attributed to nonneoplastic causes.

In the head and neck region, a sinusitis, otitis, or odontogenic infection can demonstrate hypermetabolic activity; MRI provides structural and functional contrast in soft tissues, helping in the differential diagnosis with neoplastic lesions.

Intrathoracic infection and inflammation are commonly encountered in pediatric PET/MRI oncologic evaluations; pneumonia can often present as a masslike region and can be recognized on the basis of the segmental distribution of hypermetabolic activity as shown in

TABLE 1
^{18}F-FDG PET/MRI Basic Protocols for Pediatric Oncology at 4 Different Medical Centers

Institution, scanner model, and FOV	Basic protocol for children	PET/MRI acquisition time and injected dose	Chest CT
Children's Hospital of Philadelphia; GE Healthcare Signa (TOF); FOV, WB	WB MRAC axial 3D T1 spoiled gradient echo (LAVA Flex); axial FRFSE Flex WB diffusion-weighted imaging (b = 50, 400, 800) (no intravenous contrast); local imaging if required	Varies with patient height; WB scan; 30–60 min; PET, 3 min/bed ≥ 5 y or 4 min/bed < 5 y; injected dose, 3.7 MBq/kg	Required
Children's Wisconsin; GE Healthcare Signa (TOF); FOV, WB	WB MRAC; axial 3D T1 spoiled gradient echo (LAVA Flex) (sagittal and coronal reformats); axial FRFSE Flex (no intravenous contrast); local imaging if required	Varies with patient height; WB scan < 30 min; PET, 3 min/bed; injected dose: 2.96 MBq/kg	Only for small lung lesions
University of Tübingen; Siemens Biograph mMR; FOV, WB	WB MRAC; contrast-enhanced axial 3D T1 Dixon spoiled gradient echo (VIBE); WB STIR coronal; WB DWI (b = 50,800); local imaging if required	Varies with patient height; WB scan, 45–90 min; PET, 6 min/bed; injected dose, 3.7 MBq/kg	Only if therapeutic consequence is possible (e.g., resection of lung metastases in sarcoma)
Stanford University; GE Healthcare Signa (TOF); FOV, WB	WB MRAC; contrast-enhanced axial 3D T1 spoiled gradient echo (LAVA Flex); axial FRFSE Flex; WB DWI (b = 50, 600 or 800); local imaging if required	Varies with patient height; WB scan, 60 − 90 min; PET, 4 min/bed; injected dose, 3.7 MBq/kg	Only if therapeutic consequence is possible

Typical WB PET/CT acquisition time for protocols mentioned in table is less than 30 min.

TOF = time of flight; FOV = field of view; WB = whole body; MRAC = MRI attenuation correction; 3D = 3-dimensional; T1 = T1-weighted; LAVA = Dixon liver acquisition with volume acquisition; Flex = fat/water separation; FRFSE = fast relaxation fast spin echo; bed = bed position; VIBE = volumetric interpolated breath-hold examination; DWI = diffusion-weighted imaging; STIR = short-inversion-time inversion recovery.

TABLE 2
Advantages of PET/MRI over PET/CT

Tumor type	Advantage
Overall	Simultaneous PET and MRI acquisition (precise registration of MRI and PET)
	One-stop local and whole-body staging
	Decreased ionizing radiation
	Reduced number of total examinations
	Better characterization of incidental findings
	More accurate measurement of lesions than with unenhanced CT
Lymphoma	Increased sensitivity to detect bone marrow involvement
	Avoidance of core biopsy if PET/MRI results are negative
	Reduced dose of ionizing radiation (particularly important for patients with therapy-refractory disease who need multiple scans to closely monitor treatment efficacy)
Neurofibromatosis 1 and MPNST	Detailed depiction of peripheral neurofibromata and central nervous system
	Optimal alignment of MRI and PET in cases of multiple neurofibromas
	Comprehensive examination of central nervous system and peripheral lesions in single examination
Sarcoma	Better characterization of bones and soft tissues
	Higher sensitivity for bone marrow metastases
	Improved monitoring of pediatric tumors after immunotherapy

Supplemental Figure 1 (supplemental materials are available at http://jnm.snmjournals.org) (*52*). Radiation pneumonitis is another acute inflammatory process that needs to be recognized and usually occurs about 3–6 mo after completion of radiotherapy.

In the gastrointestinal system, gastritis, enteritis, appendicitis, and colitis can present as diffuse segmental hypermetabolic activity (*53*). MRI can help in differentiating ^{18}F-FDG activity in the abdomen, by the assessment of mural signal intensity and enhancement specific to both active and chronic inflammatory changes (*54*).

There are a wide range of infectious and inflammatory conditions that can present with hypermetabolic activity on ^{18}F-FDG PET/MRI pediatric evaluations. Differentiating infectious findings from neoplasms is critical to avoid mischaracterization and to expedite symptom management.

RESEARCH APPLICATIONS OF PET/MRI IN CHILDREN WITH CANCER

Identifying Responders to New Immunotherapies Can Improve Outcomes

Integration of molecular and cellular immunotherapies in oncologic practice has transformed cancer treatment. Immunotherapeutic antibodies that include anti–programmed death-ligand 1 (*55*) and cell-based agents, such as chimeric antigen receptors T cells (*56*), aim to redirect the immune system to eradicate tumors. Molecular imaging methods can classify responders and nonresponders, monitor on/off target effects, and elucidate the mechanism of action and distribution of cellular therapeutics.

Radiotracer-based techniques have been used for many years to label white blood cells and detect inflammation (*57*,*58*). Therapeutic immune cells can be directly radiolabeled for PET imaging (*59*) or labeled with iron oxide nanoparticles for MRI (*60*). These rapid and relatively simple methods do not require genetic manipulation. However, dilution or efflux of the label can result in signal dissipation, thereby limiting the imaging time course. By contrast, reporter gene imaging enables long-term measurements of the biologic fate of the therapeutic cells (*61*,*62*). The most commonly used PET reporter gene for visualizing T cells is the herpes simplex virus type 1 thymidine kinase (*63*). Although genetic modification of immune cells with reporter genes ensures the propagation of the gene to daughter cells during cellular division, immunogenicity in patients has been observed (*64*).

Assessments of responses to cancer immunotherapy incorporate existing RECIST (*65*) and immune-related RECIST used in immunotherapy trials (*66*). Immunotherapy can lead to immune cell activation in the tumor, transient tumor swelling, increased MRI contrast enhancement, and increased ^{18}F-FDG metabolic activity in solid tumors, referred to as pseudoprogression (*67*,*68*). Advanced PET/MRI approaches might help to differentiate tumor progression from pseudoprogession (*69*).

The use of clinical PET/MRI to image immunotherapy response is described in Supplemental Figure 2 (*70*).

Theranostics for Children

Classic chemotherapy affects both tumors and normal tissues, leading to significant side effects. New receptor-targeted therapeutics, including small chemical molecules and peptides, antibodies, and nanoparticles, have recently gained a lot of attention (*71*) because they provide higher molecular-target specificity, increased tumor accumulation, and fewer side effects. Theranostic agents, which comprise a diagnostic and a therapeutic drug, can be used for patient stratification and image-guided therapy. Both PET and MRI theranostic agents have been studied in children with cancer (*72*–*74*). From the PET side, DOTATATE compounds have recently been evaluated in children with refractory neuroblastoma (*72*). A high correlation between ^{68}Ga-DOTATATE PET findings and somatostatin receptor type 2 expression in the tumor was reported, and the subsequent peptide receptor radionuclide therapy showed promising results (*72*). An example of ^{68}Ga-DOTATATE PET/MRI is shown in Supplemental Figure 3.

From the MRI side, superparamagnetic iron oxide nanoparticles can be used to carry therapeutic drugs or genes into tumors (*73*), and both radiolabeled and iron-labeled nanoparticles have been used for imaging of TAM (*74*). Integration of these TAM imaging approaches into whole-body PET/MRI restaging protocols would allow monitoring of both metabolic and TAM responses to immunotherapy in a single examination.

Novel hybrid PET/MRI contrast agents (created by adding a radioisotope to an MRI contrast agent) are under development in preclinical settings (*75*). So far, they have been tested mostly for stem cell monitoring, Wilms tumor, and tumor angiogenesis (*75*) and might be used in the future as theranostic agents.

CONCLUSION

PET/MRI is a safe, sensitive, and efficient imaging technology for cancer evaluation in children, combining metabolic information with high spatial resolution and high soft-tissue contrast while reducing radiation exposure compared with PET/CT. Performing PET/MRI as a 1-stop imaging technique reduces the need for repetitive anesthesia or sedation and decreases the overall scan time as compared with performing the 2 imaging studies separately.

Integrated PET/MRI is useful for staging and restaging of solid tumors in children and may be helpful for assessing response to novel immunotherapies. Novel developments include personalized treatments with theranostic nanoparticles and radiolabeled peptides. Future directions should focus on improving the detection of small pulmonary nodules, the time- and cost-effectiveness of combined whole-body and local scans, and accessibility to them.

REFERENCES

1. Pearce MS, Salotti JA, Little MP, et al. Radiation exposure from CT scans in childhood and subsequent risk of leukaemia and brain tumours: a retrospective cohort study. *Lancet.* 2012;380:499–505.
2. Mathews JD, Forsythe AV, Brady Z, et al. Cancer risk in 680,000 people exposed to computed tomography scans in childhood or adolescence: data linkage study of 11 million Australians. *BMJ.* 2013;346:f2360.
3. Brenner DJ, Doll R, Goodhead DT, et al. Cancer risks attributable to low doses of ionizing radiation: assessing what we really know. *Proc Natl Acad Sci USA.* 2003;100:13761–13766.
4. Hall EJ, Brenner DJ. Cancer risks from diagnostic radiology. *Br J Radiol.* 2008;81:362–378.
5. Robbins E. Radiation risks from imaging studies in children with cancer. *Pediatr Blood Cancer.* 2008;51:453–457.
6. Schäfer JF, Gatidis S, Schmidt H, et al. Simultaneous whole-body PET/MR imaging in comparison to PET/CT in pediatric oncology: initial results. *Radiology.* 2014;273:220–231.
7. Vanderby SA, Babyn PS, Carter MW, Jewell SM, McKeever PD. Effect of anesthesia and sedation on pediatric MR imaging patient flow. *Radiology.* 2010;256:229–237.
8. Spijkers S, Littooij AS, Nievelstein RAJ. Measurements of cervical lymph nodes in children on computed tomography. *Pediatr Radiol.* 2020;50:534–542.
9. Vali R, Bakkari A, Marie E, Kousha M, Charron M, Shammas A. FDG uptake in cervical lymph nodes in children without head and neck cancer. *Pediatr Radiol.* 2017;47:860–867.
10. Latifoltojar A, Humphries PD, Menezes LJ, et al. Whole-body magnetic resonance imaging in paediatric Hodgkin lymphoma: evaluation of quantitative magnetic resonance metrics for nodal staging. *Pediatr Radiol.* 2019;49:1285–1298.
11. Muehe AM, Siedek F, Theruvath AJ, et al. Differentiation of benign and malignant lymph nodes in pediatric patients on ferumoxytol-enhanced PET/MRI. *Theranostics.* 2020;10:3612–3621.
12. Bartlett ES, Walters TD, Yu E. Can axial-based nodal size criteria be used in other imaging planes to accurately determine "enlarged" head and neck lymph nodes? *ISRN Otolaryngol.* 2013;2013:232968.
13. Gawande RS, Khurana A, Messing S, et al. Differentiation of normal thymus from anterior mediastinal lymphoma and lymphoma recurrence at pediatric PET/CT. *Radiology.* 2012;262:613–622.
14. Jerushalmi J, Frenkel A, Bar-Shalom R, Khoury J, Israel O. Physiologic thymic uptake of ^{18}F-FDG in children and young adults: a PET/CT evaluation of incidence, patterns, and relationship to treatment. *J Nucl Med.* 2009;50:849–853.
15. Daldrup-Link HE, Franzius C, Link TM, et al. Whole-body MR imaging for detection of bone metastases in children and young adults: comparison with skeletal scintigraphy and FDG PET. *AJR.* 2001;177:229–236.
16. Voltin CA, Goergen H, Baues C, et al. Value of bone marrow biopsy in Hodgkin lymphoma patients staged by FDG PET: results from the German Hodgkin Study Group trials HD16, HD17, and HD18. *Ann Oncol.* 2018;29:1926–1931.
17. Dahlsgaard-Wallenius SE, Hildebrandt MG, Johansen A, et al. Hybrid PET/MRI in non-small cell lung cancer (NSCLC) and lung nodules: a literature review. *Eur J Nucl Med Mol Imaging.* 2021;48:584–591.
18. Barrington SF, Mikhaeel NG, Kostakoglu L, et al. Role of imaging in the staging and response assessment of lymphoma: consensus of the International Conference on Malignant Lymphomas Imaging Working Group. *J Clin Oncol.* 2014;32:3048–3058.
19. Ward E, DeSantis C, Robbins A, Kohler B, Jemal A. Childhood and adolescent cancer statistics, 2014. *CA Cancer J Clin.* 2014;64:83–103.
20. Sher AC, Seghers V, Paldino MJ, et al. Assessment of sequential PET/MRI in comparison with PET/CT of pediatric lymphoma: a prospective study. *AJR.* 2016;206:623–631.
21. Ponisio MR, McConathy J, Laforest R, Khanna G. Evaluation of diagnostic performance of whole-body simultaneous PET/MRI in pediatric lymphoma. *Pediatr Radiol.* 2016;46:1258–1268.
22. Heacock L, Weissbrot J, Raad R, et al. PET/MRI for the evaluation of patients with lymphoma: initial observations. *AJR.* 2015;204:842–848.
23. Lyons K, Seghers V, Sorensen JI, et al. Comparison of standardized uptake values in normal structures between PET/CT and PET/MRI in a tertiary pediatric hospital: a prospective study. *AJR.* 2015;205:1094–1101.
24. Badr S, Kotb M, Elahmadawy MA, Moustafa H. Predictive value of FDG PET/CT versus bone marrow biopsy in pediatric lymphoma. *Clin Nucl Med.* 2018;43:e428–e438.
25. Subhawong TK, Jacobs MA, Fayad LM. Diffusion-weighted MR imaging for characterizing musculoskeletal lesions. *Radiographics.* 2014;34:1163–1177.
26. Hayashida Y, Yakushiji T, Awai K, et al. Monitoring therapeutic responses of primary bone tumors by diffusion-weighted image: initial results. *Eur Radiol.* 2006;16:2637–2643.
27. Oka K, Yakushiji T, Sato H, Hirai T, Yamashita Y, Mizuta H. The value of diffusion-weighted imaging for monitoring the chemotherapeutic response of osteosarcoma: a comparison between average apparent diffusion coefficient and minimum apparent diffusion coefficient. *Skeletal Radiol.* 2010;39:141–146.
28. Theruvath AJ, Siedek F, Muehe AM, et al. Therapy response assessment of pediatric tumors with whole-body diffusion-weighted MRI and FDG PET/MRI. *Radiology.* 2020;296:143–151.
29. Byun BH, Kong CB, Lim I, et al. Combination of ^{18}F-FDG PET/CT and diffusion-weighted MR imaging as a predictor of histologic response to neoadjuvant chemotherapy: preliminary results in osteosarcoma. *J Nucl Med.* 2013;54:1053–1059.
30. Daldrup-Link HE. 10 things you might not know about iron oxide nanoparticles. *Radiology.* 2017;284:616–629.
31. Daldrup-Link HE, Rummeny EJ, Ihssen B, Kienast J, Link TM. Iron-oxide-enhanced MR imaging of bone marrow in patients with non-Hodgkin's lymphoma: differentiation between tumor infiltration and hypercellular bone marrow. *Eur Radiol.* 2002;12:1557–1566.
32. Mohanty S, Yerneni K, Graef CM, et al. Imaging therapy response of osteosarcoma to anti-CD47 therapy. *Cell Death Dis.* 2019;10:36–49.
33. Mohanty S, Aghighi M, Yerneni K, Theruvath JL, Daldrup-Link HE. Improving the efficacy of osteosarcoma therapy: combining drugs that turn cancer cell 'don't eat me' signals off and 'eat me' signals on. *Mol Oncol.* 2019;13:2049–2061.
34. Majeti R, Chao MP, Alizadeh AA, et al. CD47 is an adverse prognostic factor and therapeutic antibody target on human acute myeloid leukemia stem cells. *Cell.* 2009;138:286–299.
35. Chao MP, Alizadeh AA, Tang C, et al. Anti-CD47 antibody synergizes with rituximab to promote phagocytosis and eradicate non-Hodgkin lymphoma. *Cell.* 2010;142:699–713.
36. Edris B, Weiskopf K, Volkmer AK, et al. Antibody therapy targeting the CD47 protein is effective in a model of aggressive metastatic leiomyosarcoma. *Proc Natl Acad Sci USA.* 2012;109:6656–6661.
37. Chao MP, Jaiswal S, Weissman-Tsukamoto R, et al. Calreticulin is the dominant pro-phagocytic signal on multiple human cancers and is counterbalanced by CD47. *Sci Transl Med.* 2010;2:63ra94.
38. Chao MP, Alizadeh AA, Tang C, et al. Therapeutic antibody targeting of CD47 eliminates human acute lymphoblastic leukemia. *Cancer Res.* 2011;71:1374–1384.
39. Herrmann D, Seitz G, Fuchs J, Armeanu-Ebinger S. Susceptibility of rhabdomyosarcoma cells to macrophage-mediated cytotoxicity. *OncoImmunology.* 2012;1:279–286.

40. Mohanty S, Yerneni K, Theruvath JL, et al. Nanoparticle enhanced MRI can monitor macrophage response to CD47 mAb immunotherapy in osteosarcoma. *Cell Death Dis.* 2019;10:36.
41. Aghighi M, Theruvath AJ, Pareek A, et al. Magnetic resonance imaging of tumor-associated macrophages: clinical translation. *Clin Cancer Res.* 2018;24:4110–4118.
42. Daldrup-Link HE, Golovko D, Ruffell B, et al. MRI of tumor-associated macrophages with clinically applicable iron oxide nanoparticles. *Clin Cancer Res.* 2011; 17:5695–5704.
43. Reinert CP, Schuhmann MU, Bender B, et al. Comprehensive anatomical and functional imaging in patients with type I neurofibromatosis using simultaneous FDG-PET/MRI. *Eur J Nucl Med Mol Imaging.* 2019;46:776–787.
44. Well L, Salamon J, Kaul MG, et al. Differentiation of peripheral nerve sheath tumors in patients with neurofibromatosis type 1 using diffusion-weighted magnetic resonance imaging. *Neuro Oncol.* 2019;21:508–516.
45. Raad RA, Lala S, Allen JC, et al. Comparison of hybrid ^{18}F-fluorodeoxyglucose positron emission tomography/magnetic resonance imaging and positron emission tomography/computed tomography for evaluation of peripheral nerve sheath tumors in patients with neurofibromatosis type 1. *World J Nucl Med.* 2018;17:241–248.
46. Cook GJR, Lovat E, Siddique M, Goh V, Ferner R, Warbey VS. Characterisation of malignant peripheral nerve sheath tumours in neurofibromatosis-1 using heterogeneity analysis of ^{18}F-FDG PET. *Eur J Nucl Med Mol Imaging.* 2017;44:1845–1852.
47. Salamon J, Derlin T, Bannas P, et al. Evaluation of intratumoural heterogeneity on ^{18}F-FDG PET/CT for characterization of peripheral nerve sheath tumours in neurofibromatosis type 1. *Eur J Nucl Med Mol Imaging.* 2013;40:685–692.
48. Ferner RE, Golding JF, Smith M, et al. [^{18}F]2-fluoro-2-deoxy-D-glucose positron emission tomography (FDG PET) as a diagnostic tool for neurofibromatosis 1 (NF1) associated malignant peripheral nerve sheath tumours (MPNSTs): a long-term clinical study. *Ann Oncol.* 2008;19:390–394.
49. Yu YH, Wu JT, Ye J, Chen MX. Radiological findings of malignant peripheral nerve sheath tumor: reports of six cases and review of literature. *World J Surg Oncol.* 2016; 14:142.
50. Ahlawat S, Fayad LM. Imaging cellularity in benign and malignant peripheral nerve sheath tumors: utility of the "target sign" by diffusion weighted imaging. *Eur J Radiol.* 2018;102:195–201.
51. Uthoff J, De Stefano FA, Panzer K, et al. Radiomic biomarkers informative of cancerous transformation in neurofibromatosis-1 plexiform tumors. *J Neuroradiol.* 2019;46:179–185.
52. Giraudo C, Evangelista L, Fraia AS, et al. Molecular imaging of pulmonary inflammation and infection. *Int J Mol Sci.* 2020;21:894.
53. Frickenstein AN, Jones MA, Behkam B, McNally LR. Imaging inflammation and infection in the gastrointestinal tract. *Int J Mol Sci.* 2019;21:243.
54. Sollini M, Berchiolli R, Kirienko M, et al. PET/MRI in infection and inflammation. *Semin Nucl Med.* 2018;48:225–241.
55. Hoos A. Development of immuno-oncology drugs: from CTLA4 to PD1 to the next generations. *Nat Rev Drug Discov.* 2016;15:235–247.
56. Maldini CR, Ellis GI, Riley JL. CAR T cells for infection, autoimmunity and allotransplantation. *Nat Rev Immunol.* 2018;18:605–616.
57. Thakur ML. Immunoscintigraphic imaging of inflammatory lesions: preliminary findings and future possibilities. *Semin Nucl Med.* 1990;20:92–98.
58. Williams LE. Anniversary paper: nuclear medicine: fifty years and still counting. *Med Phys.* 2008;35:3020–3029.
59. Weist MR, Starr R, Aguilar B, et al. PET of adoptively transferred chimeric antigen receptor T cells with ^{89}Zr-oxine. *J Nucl Med.* 2018;59:1531–1537.
60. Kircher MF, Allport JR, Graves EE, et al. In vivo high resolution three-dimensional imaging of antigen-specific cytotoxic T-lymphocyte trafficking to tumors. *Cancer Res.* 2003;63:6838–6846.
61. Larimer BM. Reporter genes for PET imaging of CAR T cells offers insight into adoptive cell transfer. *J Nucl Med.* 2018;59:1892–1893.
62. Krebs S, Ahad A, Carter LM, et al. Antibody with infinite affinity for in vivo tracking of genetically engineered lymphocytes. *J Nucl Med.* 2018;59:1894–1900.
63. Keu KV, Witney TH, Yaghoubi S, et al. Reporter gene imaging of targeted T cell immunotherapy in recurrent glioma. *Sci Transl Med.* 2017;9:eaag2196.
64. Riddell SR, Elliott M, Lewinsohn DA, et al. T-cell mediated rejection of gene-modified HIV-specific cytotoxic T lymphocytes in HIV-infected patients. *Nat Med.* 1996;2:216–223.
65. Eisenhauer EA, Therasse P, Bogaerts J, et al. New response evaluation criteria in solid tumours: revised RECIST guideline (version 1.1). *Eur J Cancer.* 2009;45:228–247.
66. Seymour L, Bogaerts J, Perrone A, et al. iRECIST: guidelines for response criteria for use in trials testing immunotherapeutics. *Lancet Oncol.* 2017;18:e143–e152.
67. Brandsma D, Stalpers L, Taal W, Sminia P, van den Bent MJ. Clinical features, mechanisms, and management of pseudoprogression in malignant gliomas. *Lancet Oncol.* 2008;9:453–461.
68. Hygino da Cruz LC Jr, Rodriguez I, Domingues RC, Gasparetto EL, Sorensen AG. Pseudoprogression and pseudoresponse: imaging challenges in the assessment of posttreatment glioma. *AJNR.* 2011;32:1978–1985.
69. Kasten BB, Udayakumar N, Leavenworth JW, et al. Current and future imaging methods for evaluating response to immunotherapy in neuro-oncology. *Theranostics.* 2019;9:5085–5104.
70. Yaghoubi SS, Jensen MC, Satyamurthy N, et al. Noninvasive detection of therapeutic cytolytic T cells with ^{18}F-FHBG PET in a patient with glioma. *Nat Clin Pract Oncol.* 2009;6:53–58.
71. Pruis IJ, van Dongen G, Veldhuijzen van Zanten SEM. The added value of diagnostic and theranostic PET imaging for the treatment of CNS tumors. *Int J Mol Sci.* 2020; 21:1029.
72. Kong G, Hofman MS, Murray WK, et al. Initial experience with gallium-68 DOTA-octreotate PET/CT and peptide receptor radionuclide therapy for pediatric patients with refractory metastatic neuroblastoma. *J Pediatr Hematol Oncol.* 2016;38:87–96.
73. Li K, Nejadnik H, Daldrup-Link HE. Next-generation superparamagnetic iron oxide nanoparticles for cancer theranostics. *Drug Discov Today.* 2017;22:1421–1429.
74. Mukherjee S, Sonanini D, Maurer A, Daldrup-Link HE. The yin and yang of imaging tumor associated macrophages with PET and MRI. *Theranostics.* 2019;9:7730–7748.
75. Kiani A, Esquevin A, Lepareur N, Bourguet P, Le Jeune F, Gauvrit J. Main applications of hybrid PET-MRI contrast agents: a review. *Contrast Media Mol Imaging.* 2016;11:92–98.

The Latest Advances in Imaging Crosstalk Between the Immune System and Fibrosis in Cardiovascular Disease

Gyu Seong Heo*, Lanlan Lou*, Deborah Sultan, and Yongjian Liu

Mallinckrodt Institute of Radiology, Washington University, St. Louis, Missouri

Inflammation and fibrosis are hallmarks of tissue repair processes and organ failure progression in cardiovascular diseases. Paradigm-shifting research on diverse immune cell populations within the cardiovascular system have enabled discovery of new biomarkers fostering development of diagnostic and therapeutic agents at the molecular level to better manage cardiovascular diseases. To date, a variety of molecular imaging agents have been developed to visualize the biomarkers expressed on immune cells and fibroblasts within their crosstalk network, which drives the pathogenesis of fibrosis triggered by both innate and adaptive immunity. Herein, key biomarkers upregulated in the immune-fibrosis axis are discussed. The promising molecular imaging agents to reveal this critical pathologic process are summarized.

Key Words: immune system; inflammation; fibrosis; cardiovascular diseases; molecular imaging

J Nucl Med 2021; 62:1341–1346
DOI: 10.2967/jnumed.120.255539

Fibrosis, a scarring process, is defined as an uncontrolled accumulation of extracellular matrix (ECM) molecules on injured tissues and ultimately leads to adverse tissue remodeling, organ damage, and failure. Inflammatory and immunologic reactions involving both innate and adaptive immune systems are the underlying players driving fibrosis (*1*,*2*). In cardiovascular diseases (CVDs), vascular remodeling triggered by inflammatory stimuli is significantly associated with atherogenesis, deposition of ECM proteins on the arterial wall, and eventually vascular fibrosis. It is known that cardiac fibrosis is a major contributor to many CVDs, including myocardial infarction (MI) (*3*). Clinical diagnostics mostly provide an anatomic characterization of fibrotic scars at the stage when disease is irreversible and irreparable. The limited options of antifibrotic medications in the clinic compel an urgent search for novel diagnostic methods using molecular imaging to identify new biomarkers overexpressed during immune response and tissue repair within the immune-fibrosis network at an early stage for potential intervention and theranostics (*4*,*5*).

Many molecular probes have been developed for inflammation and fibrosis imaging in CVDs (*6*,*7*). However, the mechanism of crosstalk between immune cells and fibroblasts is not fully understood. Detection of the early onset of immune response and wound healing process, such as activation of immune cells and subsequent fibrotic response, is underexplored. Herein, we briefly discuss current imaging research on targets upregulated in the molecular and cellular pathways of the immune-fibrosis crosstalk network. We focus on PET and SPECT radiotracers because of their high sensitivity, quantitative measurement, and well-established translational strategies (*4*,*8*,*9*).

IMMUNE CELLS INVOLVED IN INFLAMMATION, TISSUE REPAIR, AND FIBROGENESIS

CVDs arise from various types of injurious stimuli on heart or blood vessels, either acute (e.g., ischemia/reperfusion [I/R] injury in MI) or chronic (e.g., cholesterol deposition for atherosclerosis). After injury, the immune system is activated and initiates a wound healing process to minimize damage and restore function to injured tissues (Fig. 1) (*1–3*,*10–12*). Within minutes of injury, damaged, stressed, and dying cells release damage-associated molecular patterns, which bind to pattern recognition receptors, including toll-like receptors and receptors for advanced glycation end products, which are expressed on surviving adjacent cells and leukocytes. Stimulation of these pattern recognition receptors activates complementary signaling pathways for not only proinflammatory cytokines and chemokines but also cell adhesion molecules. These inflammatory mediators promote the recruitment of leukocytes, including neutrophils and proinflammatory monocytes expressing high levels of Ly6C ($Ly6C^{high}$ monocytes in mice), to remove damaged cells by efferocytosis and release enzymes (proteases and oxidases) for tissue digestion. After the clearance of neutrophils, monocytes expressing low levels of Ly6C (Ly6Clow monocytes in mice) are recruited to the lesion and differentiate into reparative macrophages, which secrete antiinflammatory mediators such as transforming growth factor (TGF)-β and interleukin-10 to promote myofibroblast and vascular cell infiltration for tissue repair and regeneration. Macrophages interact with fibroblasts via secreting cytokines, chemokines, and other factors such as high levels of MMPs, which cause extensive matrix breakdown, altering the mechanical properties of the tissues to increase the expression of tumor necrosis factor-α, TGF-α, and TGF-β (*13*). Additionally, the loss of interleukin-1β and interleukin-10 expression during the proliferative phase allows fibroblasts to transdifferentiate into myofibroblasts, which produce ECM proteins to help maintain the structural integrity of injured tissues (*14*). During this dynamic and phasic process, crosstalk between the immune system and fibrosis plays a crucial role in regulating the secretion of proinflammatory and antiinflammatory mediators, fibrogenesis, remodeling, and tissue repair. Therefore, the real-time detection of biomarkers overexpressed by immune cells and fibroblasts and targets elevated during their interactions may facilitate comprehension of the

Received December 1, 2020; revision accepted April 13, 2021.
For correspondence or reprints, contact Yongjian Liu (yongjianliu@wustl.edu).
*Contributed equally to this work.
Published online April 16, 2021.

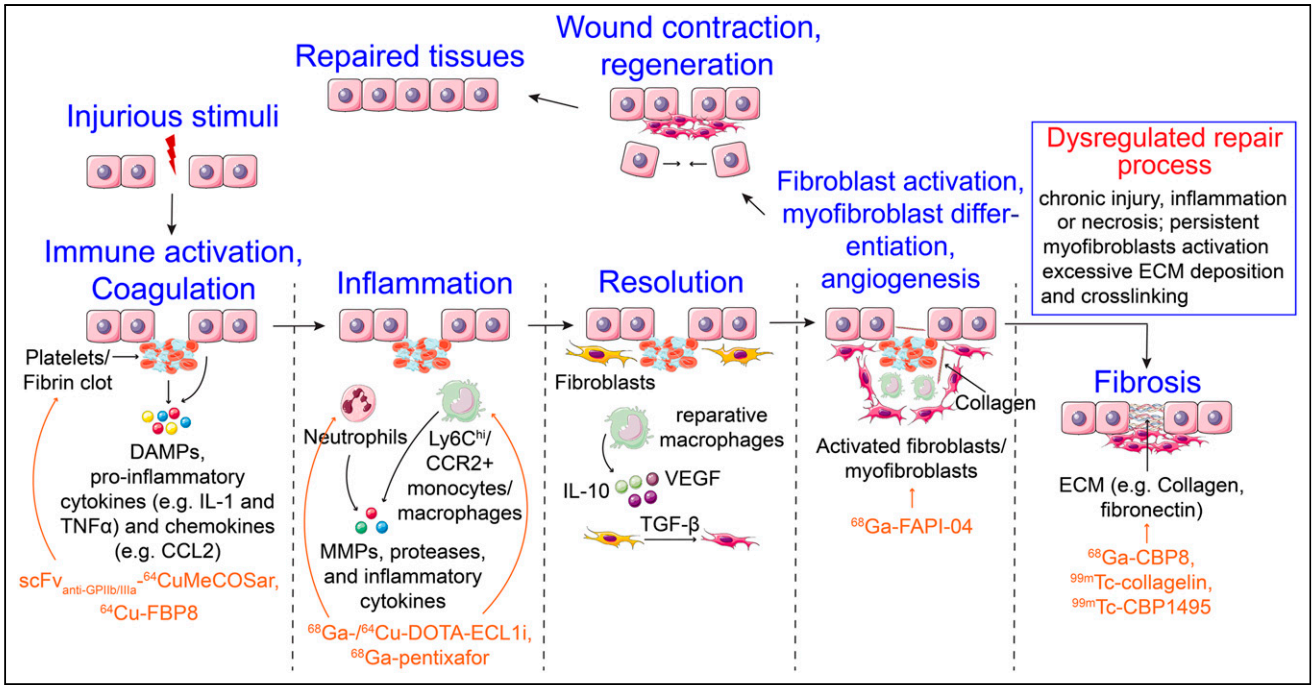

FIGURE 1. Molecular and cellular processes of immune cells involved in inflammation, tissue repair, and fibrosis. (Adapted with permission of (*4*).) DAMPs = damage-associated molecular patterns; IL-10 = interleukin 10; TNF = tumor necrosis factor; VEGF = vascular endothelial growth factor.

underlying mechanism of the crosstalk and illuminate the discovery of targeted treatment for timely intervention to improve patient outcome (*3*).

MOLECULAR IMAGING OF CROSSTALK BETWEEN IMMUNE SYSTEM AND FIBROSIS IN CVDS

Immune Cell Imaging

Because of the elevated expression of CXCR4 on multiple leukocytes after cardiovascular/cardiac injury, much effort has been devoted to the development of CXCR4-targeting radiotracers. At day 3 after I/R injury in mice, ^{68}Ga-pentixafor uptake was determined at the site of infarct, with signal proportional to leukocyte infiltration (*6*). In humans, ^{68}Ga-pentixafor demonstrated heterogeneous PET signals in hearts between days 4 and 6 after MI, suggesting alternative regulation of chemokine signaling and inflammatory response (*15*). Through the combination with plerixafor for targeted intervention, improved treatment efficacy was observed in MI mice when treatment was administrated at high ^{68}Ga-pentixafor uptake compared with those at low PET signals. This was illustrated with improved left ventricular (LV) remodeling and cardiac function measured at 6 wk after MI, as well as fewer neutrophils and Ly6C^{high} monocytes in LV (*16*), which highlighted the importance of CXCR4 PET measuring the spatiotemporal distribution of CXCR4-positive (+) cells to optimize the treatment outcome.

Monocytes and macrophages are indispensable effector cells involved in tissue repair and remodeling. The remarkable heterogeneity of macrophage populations in CVDs is well documented and encompasses their distinct functions in promotion of inflammation, tissue repair and regeneration, and inflammation resolution (*1*). Because of the dynamic variation of macrophage lineage populations, spatiotemporal detection of macrophage subtypes could facilitate the understanding of their identities, origins, and functions along the initiation and progression of the inflammation–fibrosis axis.

After MI in mice, the composition and ontogeny of macrophages are dramatically shifted. Ly6C^{high}, CCR2+ monocytes infiltrate the heart, replace resident cardiac macrophages (CCR2-negative [−]), and differentiate into CCR2+ macrophages to stimulate proinflammatory responses and collateral tissue damage and ultimately contribute to heart failure pathogenesis (*17*). In mice with acute autoimmune myocarditis, siRNA silencing of CCR2 significantly decreased the number of Ly6C^{high} monocytes in hearts and led to a reduction of LV fibrosis (*18*). These findings implicate the role of infiltrating CCR2+ monocytes and macrophages as important mediators of heart failure pathogenesis and the potential of CCR2-targeted therapies to improve outcomes of MI patients. In mouse models of sterile cardiac injury, ^{68}Ga-DOTA-extracellular loop 1 inverso (ECL1i) specifically detected infiltrating CCR2+ monocytes and macrophages into the injured heart (Fig. 2) with a loss of signal in CCR2$^{-/-}$ mice. Tracer uptake in the injured myocardium at day 4 showed a linear correlation with LV function and infarct size measured on day 28 after I/R injury, demonstrating its potential predictive value for adverse effects governed by CCR2+ leukocyte subsets (*19*). Moreover, ^{64}Cu-DOTA-ECL1i not only showed comparable imaging efficiency to ^{68}Ga-DOTA-ECL1i in mouse heart injury models (*20*) but also has been used to track CCR2+ monocytes and macrophages in atherosclerosis and other fibrotic diseases (*21*,*22*). Ongoing clinical studies will further evaluate the performance of ^{64}Cu-DOTA-ECL1i for tracking CCR2+ cells in humans (*23*). Recently, an ^{18}F-radiolabeled small molecule was also developed for CCR2 preclinical imaging (*24*).

Matrix metalloproteinases (MMPs) are a multigene family of endopeptidases that selectively digest individual components of

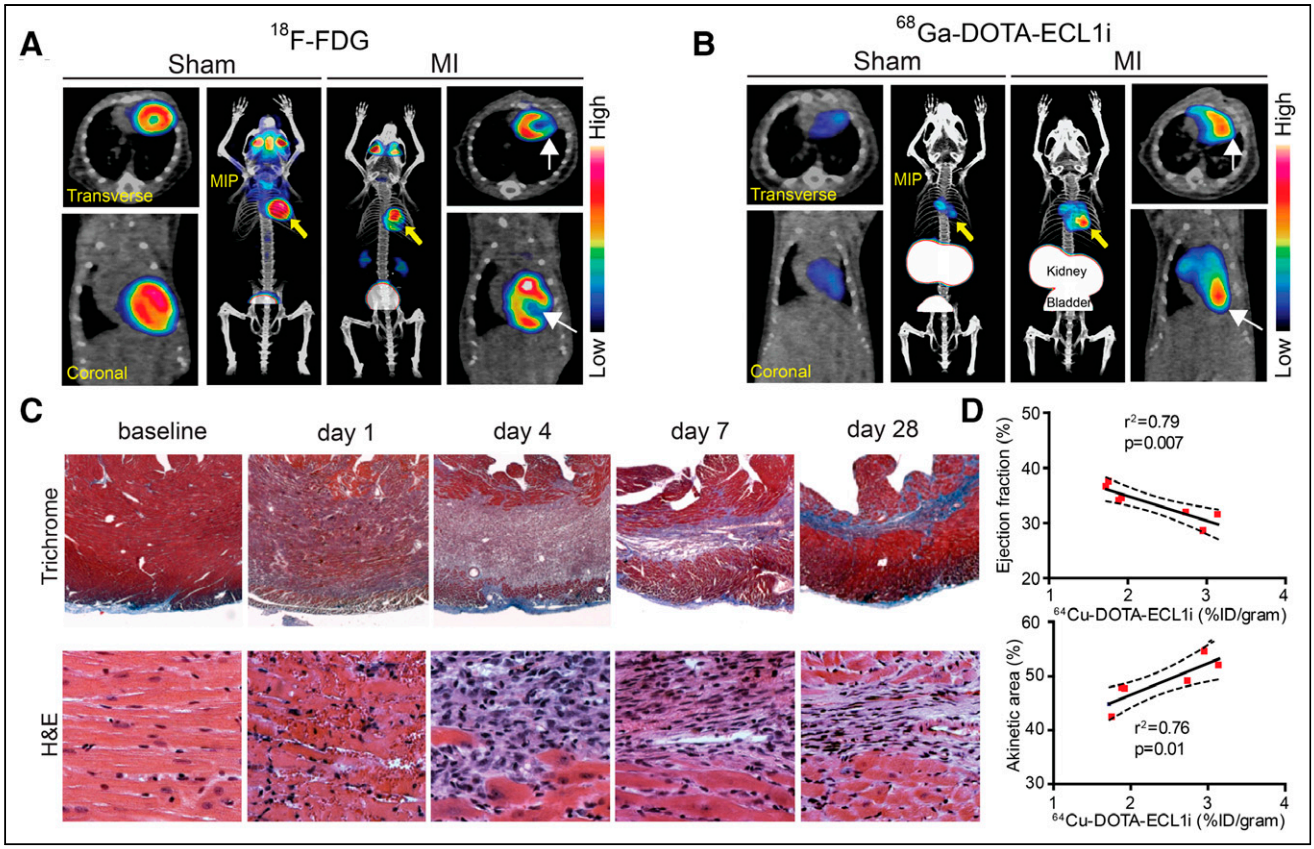

FIGURE 2. PET of ^{68}Ga-DOTA-ECL1i in mouse model of closed-chest I/R injury. (A) Representative ^{18}F-FDG PET/CT images obtained 5 d after 90 min of I/R injury identifying infarct region in mice that underwent I/R compared with sham controls. Transverse, coronal, and maximal-intensity-projection views are shown, and white arrows denote infarct area. (B) ^{68}Ga-DOTA-ECL1i PET/CT images showing regional accumulation of ^{68}Ga-DOTA-ECL1i signal in infarct and border zone 4 d after I/R injury. Yellow arrows identify tracer uptake in hearts that underwent I/R injury compared with sham controls. White arrows denote infarct area as determined by ^{18}F-FDG imaging. (C) Trichrome and hematoxylin and eosin (H&E) staining show evolution of fibrosis (trichrome-blue, ×40) and cell infiltration (H&E, ×200) over time in closed-chest I/R injury model. Dense accumulation of cells is seen within infarct 4 d after I/R injury. (D) Linear regression analyses showing relationship between ^{68}Ga-DOTA-ECL1i heart uptake measured on day 4 and echocardiographic assessment of LV ejection fraction and akinetic area measured on day 28 after I/R injury. %ID = percentage injected dose. (Reprinted with permission of (*19*).)

ECM. Their activities are associated with tissue remodeling, including recruitment and migration of immune cells and promotion of angiogenesis and apoptosis, making them attractive targets for inflammation and fibrosis imaging (*25*). An MMP-2 inhibitor, RP805, and a pan-MMP inhibitor, RYM1, were both radiolabeled with ^{99m}Tc for CVD imaging in preclinical models using SPECT (*5*,*26*). In contrast to ^{99m}Tc-RP805, ^{99m}Tc-RYM1 had desirable pharmacokinetics and low blood retention. In a mouse abdominal aortic aneurysm model, ^{99m}Tc-RYM1 uptake at aneurysm correlated with CD68 macrophage and activated MMP activity, indicating its potential for inflammation and fibrosis imaging.

Besides CCR2 and MMP, a variety of radiotracers have been developed for macrophages by targeting other chemokine receptors, somatostatin receptors, translocator proteins, and mannose receptors (*6*,*27*). Further studies are warranted using these radiotracers to image the subtypes of macrophages, shedding light on their varied roles in the inflammation–fibrosis axis.

Fibroblast and Myofibroblast Imaging

Fibroblasts not only modulate the recruitment of immune cells but also regulate their behavior, retention, and survival in damaged tissue. Cardiac fibroblasts contribute to myocardial homeostasis by synthesizing and maintaining the ECM network critical for structural and functional integrity. When activated, fibroblasts express cytoplasmic actin and adhesion complexes, permitting migration to the injury site. On differentiation, fibroblasts become a phenotypically distinct cell referred to as a myofibroblast, which is the key cellular effector for tissue repair and fibrogenesis (*28*). Myofibroblasts produce and deposit structural ECM proteins, including collagen, fibronectin, and elastin, in injured tissues. They release proteases such as MMPs and their inhibitors regulating matrix remodeling. Therefore, activated fibroblasts and myofibroblasts are undisputable target cell populations for molecular imaging to predict outcomes of tissue repair and remodeling process in CVDs.

Fibroblast activation protein (FAP) exhibits a specific expression on activated fibroblasts, making it a promising cell surface biomarker for targeted imaging of fibrotic diseases. Because of its upregulation on cancer-associated fibroblasts, various radiolabeled FAP inhibitors have been developed for tumor imaging (*29*). In a mouse model of hypertensive cardiac injury and fibrosis, depletion of FAP+ fibroblasts reduced myocardial fibrosis and restored cardiac function, indicating the potential of FAP for CVD imaging and therapy (*29*,*30*). Through ^{68}Ga radiolabeling of a FAP inhibitor, ^{68}Ga-FAPI-04 specifically determined the activated fibroblasts in

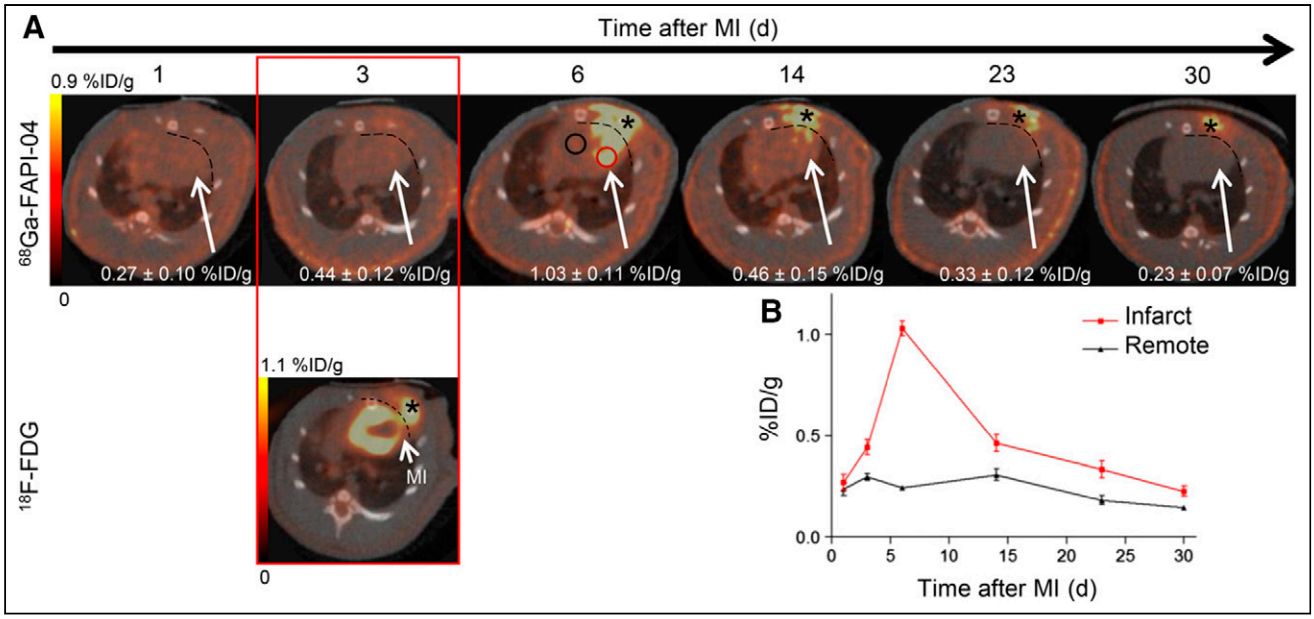

FIGURE 3. ^{68}Ga-FAPI-04 PET/CT in rat MI model. (A) Static PET/CT matched axial slices in same rat subjected to coronary ligation and scanned 1 h after injection of ^{68}Ga-FAPI-04 (1, 3, 6, 14, 23, and 30 d after MI) and ^{18}F-FDG (3 d after MI). Dashed lines separate tracer uptake in myocardium from uptake in surgical wounds. At day 6, representative regions of interest drawn over infarct border zone and remote myocardium are illustrated as red and black circles, respectively. (B) Corresponding time–activity curves for infarcted and noninfarcted heart tissue (mean ± SD, n = 3). ^{68}Ga-FAPI-04 and ^{18}F-FDG exhibited elevated uptake in scars from operation (asterisk). %ID = percentage injected dose. (Reprinted from (*31*).)

injured heart in a rat MI model (Fig. 3) (*31*). In humans, a retrospective analysis of ^{68}Ga-FAPI-04 imaging in cancer patients revealed an association between tracer uptake by the heart and LV ejection fraction, indicating its potential for risk stratification regarding early detection or progression of LV remodeling (*7*,*32*). Therefore, molecular imaging of activated fibroblasts and myofibroblasts has great potential for assessing the probability and complications of fibrosis in CVDs, providing information to optimize treatment, and monitoring treatment response for better management.

Because of the pivotal role of angiotensin-converting enzyme inhibitors in the treatment of CVDs, angiotensin-converting enzyme inhibitor–based tracers are of interest for monitoring disease progression and the effectiveness of therapeutic interventions. Many angiotensin-converting enzyme inhibitors, such as ^{18}F-captopril, have been used to image ventricular remodeling after MI in animal models (*9*). Moreover, the expression of angiotensin II receptor type 1 on fibroblasts and myofibroblasts triggered the radiolabeling of angiotensin II receptor type 1 antagonists such as ^{11}C-KR31173 for post-MI remodeling and fibrosis imaging (*9*). Because of the upregulation of $\alpha_v\beta_3$ integrin on activated fibroblasts, several radiotracers have been developed (*4*,*11*). However, its expression on other cells, including macrophages and endothelial cells, warrants further investigation to ascertain its value for imaging activated fibroblasts.

Activated Platelets

Besides their role in hemostasis, additional functions of platelets have been uncovered in regeneration and remodeling of injured tissue, including immune cell recruitment, apoptosis, angiogenesis, and ECM formation (*33*). Activated platelets are involved in immune responses through expression of a variety of membrane receptors (e.g., CD40 ligand) and the release of soluble inflammatory mediators (e.g., TGF-β1, CCL5, and CXCL12), which further promote the production of ECM from myofibroblasts. In ST-elevation MI patients, platelet activities were associated with adverse LV remodeling and fibrosis, indicating their potential not only as an imaging biomarker for the early assessment of tissue repair process but also as therapeutic targets (*34*). Moreover, on activation, the major platelet integrin glycoprotein GPIIb/IIIa (α_{IIb}/β_{IIIa}; CD41/CD61) undergoes a conformation change, making the altered conformation a unique targeting epitope for the detection of activated platelets. Through ^{64}Cu radiolabeling, the single-chain antibody tracer (scFv$_{anti\text{-}GPIIb/IIIa}$-^{64}CuMeCOSar) revealed significantly higher uptake in the ischemic myocardium compared with the nonischemic region in an I/R injury mouse model, suggesting its further evaluation to predict outcomes of subsequent tissue repair processes (*35*).

Targets Expressed on Thrombus

Thrombosis is a common pathology underlying ischemic heart disease, ischemic stroke, and venous thromboembolism triggered by either a mechanical injury or the rupture of an atherosclerotic plaque. Molecular imaging of the components involved in thrombus formation may afford accurate and early detection of thrombosis to minimize the risk of complications for improved treatment (*36*). Blood coagulation factor (FXIII) is an enzyme (tissue transglutaminase) that modulates fibrin crosslinking to form stable blood clots, making it a potential biomarker for cross-linked thrombi. Through ^{99m}Tc radiolabeling, the peptide-based tracer ^{99m}Tc-NC100668 revealed specific detection of active factor (FXIII) signals in the lesions of a coronary microvascular disease mouse model. The relative retention of ^{99m}Tc-NC100668 (microvascular disease–to–septal region ratio) determined at 2 h was approximately 3- to 12-fold higher than those acquired from 3 to 14 d after microvascular disease, suggesting its potential for the early detection

of coronary microvascular disease associated with thrombus (*37*). Fibrin is typically upregulated in fresh thrombi and gradually replaced by collagen and other fibrotic protein, making the detection of fibrin an attractive strategy for identification of thrombosis and fibrosis. A ^{64}Cu-radiolabeled fibrin binding probe 8 demonstrated favorable thrombus uptake, background clearance, and imaging efficacy in preclinical models and has been translated for human imaging (*36*).

UNDEREXPLORED MOLECULAR IMAGING OF ADAPTIVE IMMUNE SYSTEM IN CVDS

In addition to the innate immune system, the adaptive immune system also plays critical roles in tissue repair processes and fibrosis (*2*,*38*). The pivotal role of T cells modulating cardiac fibroblasts and of MMP activity has been demonstrated in CVDs including heart failure, myocardial fibrosis, ischemia, and MI (*39*). The recent popularity of cancer immunotherapy has prompted the development of a range of T-cell imaging probes (*40*), which could be used to image subset T cells to investigate the underlying mechanisms of tissue repair and fibrosis.

CONCLUSIONS AND FUTURE DIRECTIONS

Tissue repair and fibrosis are governed by the immune system. Balance between inflammatory and preparative immune responses guides the optimal tissue repair process. Thus, the immune–fibrosis axis is an unquestionable target for molecular imaging and immunomodulatory therapy. PET and SPECT imaging have shown great promise for visualizing signatures of the immune system, allowing insight into whether injured tissue will be properly repaired or subject to subsequent pathologic fibrosis. To date, a variety of radiotracers have been developed to detect the immune response and fibrosis in CVDs. Additional research needs to focus on the sensitivity and specificity of these radiotracers detecting the subtype of immune cells and fibroblasts. Moreover, longitudinal studies are required to uncover the connection between measured immune system activity and resulting fibrosis. Through the combination of multiple imaging agents targeting a range of biomarkers upregulated during the immune–fibrosis network, these studies will provide quantitative measurement of early-onset immune response, fibroblast activity, and subsequent pathologic fibrosis to elucidate the mechanism of crosstalk between the 2 systems and highlight the predictive value of molecular imaging. The early, sensitive, and specific detection of malfunctioning pathways causing pathologic fibrosis within the crosstalk network will enable the identification of potential therapeutic targets and provide real-time guidance to antifibrotic or targeted immunomodulatory therapy. The multimodality imaging using PET/MRI has great potential to differentiate subtypes of fibrosis (e.g., replacement vs. reactive fibrosis) and provide information on cellular and molecular profiles in those fibrotic lesions for better management. After establishment of a pathway for radiotracer translation for a first-in-humans study (*22*), these imaging strategies may hold the potential to decipher the heterogeneity of fibrotic diseases in patients for individualized treatment.

Taking together all these considerations, we envision a critical role for molecular imaging within the immune–fibrosis network to delineate the functions and interaction of immune cells and fibroblasts along the pathogenesis of fibrotic processes and to better elucidate the mechanisms of CVDs. The information we gather from ongoing clinical studies or future translational research will not only facilitate the development of diagnostic agents to phenotype and risk-stratify patients but also promote the discovery of novel therapeutic agents for targeted treatment.

DISCLOSURE

This work is supported by 1R35HL145212-01 from NHLBI. No other potential conflict of interest relevant to this article was reported.

REFERENCES

1. Wynn TA, Vannella KM. Macrophages in tissue repair, regeneration, and fibrosis. *Immunity.* 2016;44:450–462.
2. Gieseck RL III, Wilson MS, Wynn TA. Type 2 immunity in tissue repair and fibrosis. *Nat Rev Immunol.* 2018;18:62–76.
3. Frangogiannis NG. Cardiac fibrosis: cell biological mechanisms, molecular pathways and therapeutic opportunities. *Mol Aspects Med.* 2019;65:70–99.
4. Desogere P, Montesi SB, Caravan P. Molecular probes for imaging fibrosis and fibrogenesis. *Chemistry.* 2019;25:1128–1141.
5. Montesi SB, Desogere P, Fuchs BC, Caravan P. Molecular imaging of fibrosis: recent advances and future directions. *J Clin Invest.* 2019;129:24–33.
6. Heo GS, Sultan D, Liu Y. Current and novel radiopharmaceuticals for imaging cardiovascular inflammation. *Q J Nucl Med Mol Imaging.* 2020;64:4–20.
7. Siebermair J, Kohler MI, Kupusovic J, et al. Cardiac fibroblast activation detected by Ga-68 FAPI PET imaging as a potential novel biomarker of cardiac injury/remodeling. *J Nucl Cardiol.* 2021;28:812–821.
8. Hess A, Thackeray JT, Wollert KC, Bengel FM. Radionuclide image-guided repair of the heart. *JACC Cardiovasc Imaging.* 2020;13:2415–2429.
9. Curley D, Lavin Plaza B, Shah AM, Botnar RM. Molecular imaging of cardiac remodelling after myocardial infarction. *Basic Res Cardiol.* 2018;113:10.
10. Eming SA, Wynn TA, Martin P. Inflammation and metabolism in tissue repair and regeneration. *Science.* 2017;356:1026–1030.
11. de Haas HJ, Arbustini E, Fuster V, Kramer CM, Narula J. Molecular imaging of the cardiac extracellular matrix. *Circ Res.* 2014;114:903–915.
12. Swirski FK, Nahrendorf M. Cardioimmunology: the immune system in cardiac homeostasis and disease. *Nat Rev Immunol.* 2018;18:733–744.
13. Hitscherich P, Lee EJ. Crosstalk between cardiac cells and macrophages postmyocardial infarction: insights from in vitro studies. *Tissue Eng Part B Rev.* December 3, 2020 [Epub ahead of print].
14. Sager HB, Kessler T, Schunkert H. Monocytes and macrophages in cardiac injury and repair. *J Thorac Dis.* 2017;9(suppl):S30–S35.
15. Thackeray JT, Bengel FM. Molecular imaging of myocardial inflammation with positron emission tomography post-ischemia: a determinant of subsequent remodeling or recovery. *JACC Cardiovasc Imaging.* 2018;11:1340–1355.
16. Hess A, Derlin T, Koenig T, et al. Molecular imaging-guided repair after acute myocardial infarction by targeting the chemokine receptor CXCR4. *Eur Heart J.* 2020;41:3564–3575.
17. Bajpai G, Bredemeyer A, Li W, et al. Tissue resident CCR2− and CCR2+ cardiac macrophages differentially orchestrate monocyte recruitment and fate specification following myocardial injury. *Circ Res.* 2019;124:263–278.
18. Leuschner F, Courties G, Dutta P, et al. Silencing of CCR2 in myocarditis. *Eur Heart J.* 2015;36:1478–1488.
19. Heo GS, Kopecky B, Sultan D, et al. Molecular imaging visualizes recruitment of inflammatory monocytes and macrophages to the injured heart. *Circ Res.* 2019;124:881–890.
20. Heo GS, Bajpai G, Li W, et al. Targeted PET imaging of chemokine receptor 2-positive monocytes and macrophages in the injured heart. *J Nucl Med.* 2021;62:111–114.
21. Li W, Luehmann HP, Hsiao HM, et al. Visualization of monocytic cells in regressing atherosclerotic plaques by intravital two-photon and positron emission tomography-based imaging. *Arterioscler Thromb Vasc Biol.* 2018;38:1030–1036.
22. Brody SL, Gunsten SP, Luehmann HP, et al. Chemokine receptor 2-targeted molecular imaging in pulmonary fibrosis: a clinical trial. *Am J Respir Crit Care Med.* 2021;203:78–89.
23. 7 Studies found for: CCR2 PET. ClinicalTrials.gov website. https://www.clinicaltrials.gov/ct2/results?cond=&term=CCR2+PET&cntry=&state=&city=&dist=. Accessed August 9, 2021.
24. Wagner S, de Moura Gatti F, Silva DG, et al. Development of the first potential nonpeptidic positron emission tomography tracer for the imaging of CCR2 receptors. *ChemMedChem.* 2021;16:640–645.

25. DeLeon-Pennell KY, Meschiari CA, Jung M, Lindsey ML. Chapter two: matrix metalloproteinases in myocardial infarction and heart failure. In: Khalil RA, ed. *Progress in Molecular Biology and Translational Science.* Vol 147: Academic Press; 2017:75–100.
26. Toczek J, Ye Y, Gona K, et al. Preclinical evaluation of RYM1, a matrix metalloproteinase-targeted tracer for imaging aneurysm. *J Nucl Med.* 2017;58:1318–1323.
27. Li X, Rosenkrans ZT, Wang J, Cai W. PET imaging of macrophages in cardiovascular diseases. *Am J Transl Res.* 2020;12:1491–1514.
28. Gibb AA, Lazaropoulos MP, Elrod JW. Myofibroblasts and fibrosis: mitochondrial and metabolic control of cellular differentiation. *Circ Res.* 2020;127:427–447.
29. Altmann A, Haberkorn U, Siveke J. The latest developments in imaging of fibroblast activation protein. *J Nucl Med.* 2021;62:160–167.
30. Aghajanian H, Kimura T, Rurik JG, et al. Targeting cardiac fibrosis with engineered T cells. *Nature.* 2019;573:430–433.
31. Varasteh Z, Mohanta S, Robu S, et al. Molecular imaging of fibroblast activity after myocardial infarction using a ^{68}Ga-labeled fibroblast activation protein inhibitor, FAPI-04. *J Nucl Med.* 2019;60:1743–1749.
32. Heckmann MB, Reinhardt F, Finke D, et al. Relationship between cardiac fibroblast activation protein activity by positron emission tomography and cardiovascular disease. *Circ Cardiovasc Imaging.* 2020;13:e010628.
33. Eisinger F, Patzelt J, Langer HF. The platelet response to tissue injury. *Front Med (Lausanne).* 2018;5:317.
34. Ziegler M, Wang X, Peter K. Platelets in cardiac ischaemia/reperfusion injury: a promising therapeutic target. *Cardiovasc Res.* 2019;115:1178–1188.
35. Ziegler M, Alt K, Paterson BM, et al. Highly sensitive detection of minimal cardiac ischemia using positron emission tomography imaging of activated platelets. *Sci Rep.* 2016;6:38161.
36. Oliveira BL, Caravan P. Peptide-based fibrin-targeting probes for thrombus imaging. *Dalton Trans.* 2017;46:14488–14508.
37. Zhuang ZW, Huang Y, Ju R, et al. Molecular imaging of factor XIII activity for the early detection of mouse coronary microvascular disease. *Theranostics.* 2019;9:1474–1489.
38. Sánchez-Trujillo L, Vazquez-Garza E, Castillo EC, Garcia-Rivas G, Torre-Amione G. Role of adaptive immunity in the development and progression of heart failure: new evidence. *Arch Med Res.* 2017;48:1–11.
39. Zhang M, Zhang S. T cells in fibrosis and fibrotic diseases. *Front Immunol.* 2020;11:1142.
40. Wei W, Jiang D, Ehlerding EB, Luo Q, Cai W. Noninvasive PET imaging of T cells. *Trends Cancer.* 2018;4:359–373.

Imaging of Small Intestine Neuroendocrine Neoplasms: Is SSTR PET the Holy Grail?

Alessio Imperiale[1], Leah Meuter[2], Karel Pacak[2], David Taïeb[2,3]

[1]*Department of Nuclear Medicine and Molecular Imaging – Institut de Cancérologie de Strasbourg Europe (ICANS), IPHC, UMR 7178, CNRS/University of Strasbourg, Strasbourg, France;* [2]*Section on Medical Neuroendocrinology, Eunice Kennedy Shriver National Institute of Child Health and Human Development, National Institutes of Health, Bethesda, Maryland; and* [3]*Department of Nuclear Medicine, La Timone University Hospital, CERIMED, Aix-Marseille University, Marseille, France*

Management of patients with neuroendocrine neoplasms (NENs) is a complex task and warrants referral of these patients to high volume centers with appropriate expertise in order to ensure favorable outcomes and appropriate follow-up. PET/CT becomes increasingly important in almost every step of patient management and outcomes. In the recent years, somatostatin receptor (SSTR) PET/CT using ^{68}Ga-labeled somatostatin analogs ([^{68}Ga]Ga-SSAs) has proven to be successful in the evaluation of well-differentiated gastroenteropancreatic NENs, and it is also tightly connected to the use of targeted radiotherapy (peptide receptor radionuclide therapy [PRRT]) in inoperable and progressive metastatic cases. Therefore, it has been deemed as a first "grab" tracer in many consensus and position statements made by expert panels (*1,2*). There has been global enthusiasm and excitement surrounding [^{68}Ga]Ga-SSA, including its added value compared with previously used ^{99m}Tc- or ^{111}In-based somatostatin receptor scintigraphy, its worldwide availability, and on-site production. This, however, has thrown the baby out with the bathwater in regard to ^{18}F-FDOPA PET. SSTR PET is clearly superior to ^{18}F-FDOPA PET for certain NENs and should be positioned at the forefront of pancreatic NENs (except for insulinomas, for which data are still scarce and GLP1-receptor imaging appears to be more promising). However, is this also the case for small intestine NENs (SI-NENs)?

The selection of a specific radiopharmaceutical is important in distinguishing between diagnostic and theranostic settings. In a theranostic setting (a time and cost-effective approach), SSTR PET is used as an evidence-based companion diagnostic for selecting candidates who will likely benefit from PRRT, regardless of tumor origin. ^{18}F-FDG also has great potential for predicting outcomes to PRRT. What is the role ^{18}F-FDOPA in the evaluation of NENs if it cannot be used in a theranostic setting and has the potential to be more costly? Are the data, usage, and popularity of [^{68}Ga]Ga-SSAs enough to disqualify or abandon ^{18}F-FDOPA in countries where it is approved, available, and previously used? Can we truly abandon ^{18}F-FDOPA when we have seen it be more specific, have higher resolution, and have less small intestine activity compared with [^{68}Ga]Ga-SSA? Are both tracers similar in terms of sensitivity? Until recently, no study has specifically addressed this issue. Three historical studies have compared ^{18}F-FDOPA PET/CT and SSTR PET/CT in a small case series (*3–5*). Although interesting, each study is hampered by mixing NENs of various origins with a very small number of pathologically proven SI-NETs, which may have decreased the performance of ^{18}F-FDOPA.

More recently, 3 studies have compared ^{18}F-FDOPA PET/CT and SSTR PET/CT in gastroenteropancreatic NENs, focusing on SI-NENs (*6–8*). Although retrospective, these studies provide novel insights and analysis on optimal evaluation of patients with rare diseases. Our group retrospectively evaluated [^{68}Ga]Ga-DOTATOC and carbidopa-assisted ^{18}F-FDOPA PET/CT in 41 patients with well differentiated ileal NETs (*7*). All patients' primary tumors were previously resected and all were investigated by PET for restaging. ^{18}F-FDOPA PET/CT had a better detection rate than [^{68}Ga]Ga-DOTATOC (96% vs. 80%, $P < 0.001$). In a total of 605 lesions, 458 (76%) were positive on both modalities, 25 (4%) by [^{68}Ga]Ga-DOTATOC only, and 122 (20%) by ^{18}F-FDOPA PET/

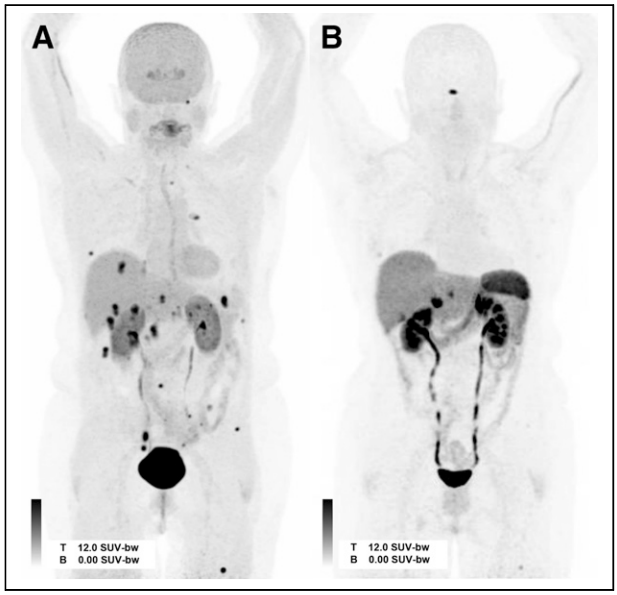

FIGURE 1. Illustrative image showing superiority of ^{18}F-FDOPA (A) over [^{68}Ga]Ga-DOTATOC (B) in patient with SI-NET. SUV-bw = body weight–normalized SUV; T = top; B = bottom.

Received Feb. 14, 2021; revision accepted Mar. 19, 2021.
For correspondence or reprints, contact David Taïeb (david.taieb@ap-hm.fr).
Published online March 26, 2021.

DOI: 10.2967/jnumed.121.262140

CT only, corresponding to liver, peritoneal, or lymph node metastases. Because of the recruitment of patients with extensive metastases, both examinations yielded a similar management plan. Ansquer et al. have compared ^{18}F-FDOPA PET/CT (without carbidopa premedication) and [^{68}Ga]Ga-DOTANOC in a series of 30 patients with SI-NENs (*6*). PET/CT studies were performed for initial staging in 9 cases and restaging in the remaining cases. ^{18}F-FDOPA PET/CT detected significantly more lesions than [^{68}Ga]Ga-DOTANOC, with sensitivities of 95.5% and 88.2%, respectively. ^{18}F-FDOPA PET/CT detected more lesions in 9 cases with 22 additional lesions from variable locations. [^{68}Ga]Ga-DOTANOC was superior to ^{18}F-FDOPA PET/CT in only 3 cases with a limited number of additional lesions. In concordant liver metastases, the tumor-to-liver uptake ratio was superior in ^{18}F-FDOPA compared with [^{68}Ga]Ga-DOTANOC in 63% of cases. A more favorable uptake ratio in ^{18}F-FDOPA could potentially explain the higher detection rate of liver metastases. It is expected that SSTR antagonists could perform better than agonists in this setting. Lastly, Veenstra et al. have compared ^{18}F-FDOPA (under carbidopa) and [^{68}Ga]Ga-DOTATOC PET/CT in 45 NEN patients, including 23 (51%) SI-NENs, followed by pancreatic, large intestine, lung, ovarium, and NENs of unknown origin. Considering the subgroup of SI-NENs, ^{18}F-FDOPA detected more lesions than [^{68}Ga]Ga-DOTATOC in 16 of 23 patients (70%) whereas [^{68}Ga]Ga-DOTATOC detected more lesions than ^{18}F-FDOPA in only 4 of 23 patients.

Taken collectively, these results show that both SSTR PET/CT and ^{18}F-FDOPA PET/CT are excellent for disease staging and restaging, although ^{18}F-FDOPA PET/CT is frequently the most sensitive tracer (Fig. 1). Therefore, there is no reason to disqualify its use in the face of simplifying paradigms. This conclusion aligns with the 2017 European Association of Nuclear Medicine guidelines for PET/CT imaging of NENs (*9*). Additionally, ^{18}F-FDOPA PET/CT provides a specific molecular signature linked to serotonin secretion and potential underlying biologic characteristics. This has been illustrated in pheochromocytoma and paraganglioma, where imaging phenotype is tightly linked to tumor location (sympathetic versus parasympathetic paraganglia; adrenal versus extra-adrenal), genetic status, biochemical phenotype, and size, with all being intimately interconnected (*10*). In conclusion, ^{18}F-FDOPA PET/CT can perform better than SSTR PET in SI-NETs. These findings could be important in a diagnostic setting before major operations such as hepatic cytoreductive surgery or liver transplantation.

DISCLOSURE

No potential conflict of interest relevant to this article was reported.

REFERENCES

1. Niederle B, Pape UF, Costa F, et al. ENETS consensus guidelines update for neuroendocrine neoplasms of the jejunum and ileum. *Neuroendocrinology.* 2016;103:125–138.
2. Sundin A, Arnold R, Baudin E, et al. ENETS Consensus guidelines for the standards of care in neuroendocrine tumors: radiological, nuclear medicine & hybrid imaging. *Neuroendocrinology.* 2017;105:212–244.
3. Ambrosini V, Tomassetti P, Castellucci P, et al. Comparison between ^{68}Ga-DOTA-NOC and ^{18}F-DOPA PET for the detection of gastro-entero-pancreatic and lung neuro-endocrine tumours. *Eur J Nucl Med Mol Imaging.* 2008;35:1431–1438.
4. Haug A, Auernhammer CJ, Wangler B, et al. Intraindividual comparison of ^{68}Ga-DOTA-TATE and ^{18}F-DOPA PET in patients with well-differentiated metastatic neuroendocrine tumours. *Eur J Nucl Med Mol Imaging.* 2009;36:765–770.
5. Putzer D, Gabriel M, Kendler D, et al. Comparison of ^{68}Ga-DOTA-Tyr(3)-octreotide and ^{18}F-fluoro-L-dihydroxyphenylalanine positron emission tomography in neuroendocrine tumor patients. *Q J Nucl Med Mol Imaging.* 2010;54:68–75.
6. Ansquer C, Touchefeu Y, Faivre-Chauvet A, et al. Head-to-head comparison of ^{18}F-DOPA PET/CT and ^{68}Ga-DOTANOC PET/CT in patients with midgut neuroendocrine tumors. *Clin Nucl Med.* 2021;46:181–186.
7. Ouvrard E, Chevalier E, Addeo P, et al. Intraindividual comparison of ^{18}F-FDOPA and ^{68}Ga-DOTATOC PET/CT detection rate for metastatic assessment in patients with ileal neuroendocrine tumours. *Clin Endocrinol (Oxf).* 2021;94:66–73.
8. Veenstra EB, de Groot DJA, Brouwers AH, Walenkamp AME, Noordzij W. Comparison of ^{18}F-DOPA versus ^{68}Ga-DOTATOC as preferred PET imaging tracer in well-differentiated neuroendocrine neoplasms. *Clin Nucl Med.* 2021;46:195–200.
9. Bozkurt MF, Virgolini I, Balogova S, et al. Guideline for PET/CT imaging of neuroendocrine neoplasms with ^{68}Ga-DOTA-conjugated somatostatin receptor targeting peptides and ^{18}F-DOPA. *Eur J Nucl Med Mol Imaging.* 2017;44:1588–1601.
10. Taïeb D, Hicks RJ, Hindie E, et al. European Association of Nuclear Medicine practice guideline/Society of Nuclear Medicine and Molecular Imaging procedure standard 2019 for radionuclide imaging of phaeochromocytoma and paraganglioma. *Eur J Nucl Med Mol Imaging.* 2019;46:2112–2137.

Simultaneous Mapping of Vasculature, Hypoxia, and Proliferation Using Dynamic Susceptibility Contrast MRI, ^{18}F-FMISO PET, and ^{18}F-FLT PET in Relation to Contrast Enhancement in Newly Diagnosed Glioblastoma

Solène Collet[1,2], Jean-Sébastien Guillamo*[1,3,4], David Hassanein Berro*[1,5], Ararat Chakhoyan[1], Jean-Marc Constans[1,6], Emmanuèle Lechapt-Zalcman[1,7,8], Jean-Michel Derlon[1], Mathieu Hatt[9], Dimitris Visvikis[9], Stéphane Guillouet[10], Cécile Perrio[10], Myriam Bernaudin[1], and Samuel Valable[1]

[1]*Normandie University, UNICAEN, CEA, CNRS, ISTCT/CERVOxy Group, GIP Cyceron, Caen, France;* [2]*Radiophysics Department, Centre François Baclesse, Caen, France;* [3]*Department of Neurology, CHU de Caen, Caen, France;* [4]*Department of Neurology, CHU de Nimes, Nimes, France;* [5]*Department of Neurosurgery, CHU de Caen, Caen, France;* [6]*Department of Neuroradiology, CHU de Caen, Caen, France;* [7]*Department of Pathology, CHU de Caen, Caen, France;* [8]*Department of Neuropathology, GHU Paris Psychiatry and Neuroscience, Paris, France;* [9]*LaTIM, INSERM, UMR 1101, University of Brest, Brest, France; and* [10]*Normandie University, UNICAEN, CEA, CNRS, ISTCT/LDM-TEP Group, GIP Cyceron, Caen, France*

Conventional MRI plays a key role in the management of patients with high-grade glioma, but multiparametric MRI and PET tracers could provide further information to better characterize tumor metabolism and heterogeneity by identifying regions having a high risk of recurrence. In this study, we focused on proliferation, hypervascularization, and hypoxia, all factors considered indicative of poor prognosis. They were assessed by measuring uptake of ^{18}F-3'-deoxy-3'-^{18}F-fluorothymidine (^{18}F-FLT), relative cerebral blood volume (rCBV) maps, and uptake of ^{18}F-fluoromisonidazole (^{18}F-FMISO), respectively. For each modality, the volumes and high-uptake subvolumes (hot spots) were semiautomatically segmented and compared with the contrast enhancement (CE) volume on T1-weighted gadolinium-enhanced (T1w-Gd) images, commonly used in the management of patients with glioblastoma. **Methods:** Dynamic susceptibility contrast-enhanced MRI (31 patients), ^{18}F-FLT PET (20 patients), or ^{18}F-FMISO PET (20 patients), for a total of 31 patients, was performed on preoperative glioblastoma patients. Volumes and hot spots were segmented on SUV maps for ^{18}F-FLT PET (using the fuzzy locally adaptive bayesian algorithm) and ^{18}F-FMISO PET (using a mean contralateral image + 3.3 SDs) and on rCBV maps (using a mean contralateral image + 1.96 SDs) for dynamic susceptibility contrast-enhanced MRI and overlaid on T1w-Gd images. For each modality, the percentages of the peripheral volumes and the peripheral hot spots outside the CE volume were calculated. **Results:** All tumors showed highly proliferated, hypervascularized, and hypoxic regions. The images also showed pronounced heterogeneity of both tracers regarding their uptake and rCBV maps, within each individual patient. Overlaid volumes on T1w-Gd images showed that some proliferative, hypervascularized, and hypoxic regions extended beyond the CE volume but with marked differences between patients. The ranges of peripheral volume outside the CE volume were 1.6%–155.5%, 1.5%–89.5%, and 3.1%–78.0% for ^{18}F-FLT, rCBV, and ^{18}F-FMISO, respectively. All patients had hyperproliferative hot spots outside the CE volume, whereas hypervascularized and hypoxic hot spots were detected mainly within the enhancing region. **Conclusion:** Spatial analysis of multiparametric maps with segmented volumes and hot spots provides valuable information to optimize the management and treatment of patients with glioblastoma.

Key Words: proliferation; vasculature; hypoxia; MRI; PET; glioblastoma

J Nucl Med 2021; 62:1349–1356
DOI: 10.2967/jnumed.120.249524

Despite the use of aggressive treatments (*1*), glioblastoma remains one of the deadliest human cancers, being characterized by a 5-y survival of 6.8% (*2*). Glioblastomas are highly heterogeneous tumors characterized by a strong interpatient heterogeneity at both the molecular (*3*,*4*) and the macroscopic levels. More importantly, glioblastomas are also characterized by a pronounced intratumoral heterogeneity (*5*), which is macroscopically visible on conventional MRI as regions of necrosis and contrast enhancement (CE) (*6*) and has been associated with a large range of response to therapies (*7*).

Among the various pathophysiologic parameters that may influence patient survival, proliferation and invasion are 2 key parameters considered to be predictive of patient survival (*8*). Interestingly, the dynamic interactions among tumor cells, the vasculature, and hypoxia are also considered a key feature that affects tumor growth (*9*–*11*).

Although various work has addressed the spatial relationship between pairs of parameters (*10*,*12*–*17*), the concomitant and quantitative measurement of these 3 parameters remains challenging and has been performed only on histologic specimens (*9*), which do not allow for an overall view of the entire 3-dimensional (3D) tumor volume.

Until now, conventional MRI with the so-called CE area remains the most used imaging modality to characterize glioblastoma and guide treatment. However, multiparametric imaging is most

Received May 12, 2020; revision accepted Jan. 14, 2021.
For correspondence or reprints, contact Samuel Valable (samuel.valable@cnrs.fr).
*Contributed equally to this work.
Published online May 20, 2021.

appropriate to assess biologic tumor heterogeneity and, more specifically, to quantitatively analyze these 3 compartments together.

Specific imaging markers of tumor activity have emerged recently, providing additional information to further characterize the tumor and its environment (*18*,*19*). In the field of neurooncology, these markers include those derived from multiparametric MRI, such as perfusion, diffusion, and MR spectroscopy. For PET imaging, the radiotracers that have emerged as most pertinent for this tumor type are those reflecting cell proliferation, such as ^{18}F-3′-deoxy-3′-^{18}F-fluorothymidine (^{18}F-FLT) (*13*,*20*,*21*); those that trace amino acids, such as ^{11}C-methionine, *O*-(2-^{18}F-fluoroethyl)-L-tyrosine or 3,4-dihydroxy-6-^{18}F-fluoro-L-phenylalanine (*22*); and those that can specifically differentiate true tumor boundaries from equivocal lesions on the basis of the degree of hypoxia, such as ^{18}F-fluoromisonidazole (^{18}F-FMISO) (*10*,*12*,*23*).

However, to the best of our knowledge, a spatial analysis of these 3 parameters—that is, proliferation, hypervascularization, and hypoxia—has never been reported using noninvasive imaging for newly diagnosed glioblastoma, and only a few studies have performed such a characterization in other tumor locations (*24*,*25*). Interestingly, the most proliferative, vascularized, and hypoxic subvolumes (i.e., hot spots) could also represent regions at high risk of relapse, and consequently, their identification is of real interest to overcome resistance to therapies such as surgery or radiation therapy.

Therefore, in this study, we aimed to spatially evaluate the volumes and hot-spot subvolumes of proliferation, hypervascularization, and hypoxia by using ^{18}F-FLT PET, relative cerebral blood volume (rCBV) MRI, and ^{18}F-FMISO PET, respectively, relative to CE volume in preoperative glioblastoma patients.

MATERIALS AND METHODS

Patients

Patients with de novo glioblastoma were included from 2 prospective clinical trials ("FLT" study and "HypOnco" study) funded by Institut National du Cancer and approved by the local ethics committee and Agence Française de Sécurité Sanitaire des Produits de Santé (French Agency for the Safety of Health Products) agreement (ClinicalTrials.gov identifiers NCT00850278 and NCT01200134). Thirty-one patients were included at the Caen University Hospital on the basis of the inclusion criteria: presenting with histopathologically proven grade IV gliomas based on World Health Organization criteria, being eligible in the final analysis with MR and PET imaging modalities, having an age of at least 18 y, having a Karnofsky Performance Status of at least 50%, having a normal blood cell count and normal biologic hepatic function, and providing written informed consent to voluntary participation in research. The patients underwent ^{18}F-FLT PET (n = 20) or ^{18}F-FMISO PET (n = 20) and multiparametric MRI (n = 31) (Table 1) within the same week and before surgery. Thereafter, the patients underwent surgery, resection, or biopsy depending on the location of the tumor. The specimens were histopathologically evaluated by an experienced neuropathologist, and only patients with an established diagnosis of glioblastoma were analyzed.

TABLE 1
Flowchart of Study

	FLT study	HypOnco study	
Patient no.	^{18}F-FLT PET	rCBV MRI	^{18}F-FMISO PET
1	✓	✓	
2	✓	✓	
3	✓	✓	
4	✓	✓	
5	✓	✓	
6	✓	✓	
7	✓	✓	
8	✓	✓	
9	✓	✓	
10	✓	✓	✓
11	✓	✓	✓
12	✓	✓	
13	✓	✓	
14	✓	✓	✓
15		✓	✓
16	✓	✓	✓
17	✓	✓	✓
18	✓	✓	✓
19	✓	✓	✓
20	✓	✓	✓
21	✓	✓	✓
22		✓	✓
23		✓	✓
24		✓	✓
25		✓	✓
26		✓	✓
27		✓	✓
28		✓	✓
29		✓	✓
30		✓	✓
31		✓	✓

HypOnco = Hypoxia in Brain Tumors; ✓ = patients were followed in the "FLT study" by ^{18}F-FLT PET along with MRI or in the "HypOnco study" by ^{18}F-FMISO along with MRI. Some patients were followed in the 2 studies.

Image Acquisition

MRI was performed on a 1.5-T GE Healthcare Signa HDXt, version 15.0. After scout-view and coronal T2-weighted imaging, an axial fluid-attenuated inversion recovery (FLAIR) sequence was performed (24 slices; slice spacing, 5.5 mm; pixel resolution, 0.47 × 0.47 mm; repetition time/echo time, 9,602/150 ms). For dynamic susceptibility contrast-enhanced MRI, a dynamic gradient-echo T2*-weighted echo-planar imaging sequence was used (14 slices; 35 repetitions; slice spacing, 7 mm; pixel resolution, 2.19 × 2.19 mm; repetition time/echo time, 2,280/60 ms) to track a 0.1 mmol/kg bolus of gadolinium-DOTA (Dotarem; Guerbet). An injection delay of 20 s was applied to obtain an accurate estimate of the baseline signal intensity before arrival of the contrast agent, and the acquisition lasted 1 min 20 s.

Immediately thereafter, a 3D T1-weighted gadolinium-enhanced (T1w-Gd) sequence (124 slices; slice spacing, 1.5 mm; pixel resolution, 1.01 × 1.01 mm; repetition time/echo time, 17/3 ms) was performed to evaluate the CE.

^{18}F-FLT and ^{18}F-FMISO were both produced by the LDM-TEP (Laboratoire de Développement Méthodologique en TEP) group of ISTCT (Imaging and Therapeutical Strategies in Cerebral and Tumoral Pathologies) and GIP Cyceron (a biomedical imaging platform facility) and synthesized as previously described (*12*,*13*,*26*). Data within a brain-focused field of view were acquired on 2 consecutive days 40 min (^{18}F-FLT) and 2 h (^{18}F-FMISO) after the intravenous injection of 5 MBq/kg (both tracers) and lasted 10 min (^{18}F-FLT, to match a clinically feasible approach) and 20 min (^{18}F-FMISO). Acquisitions were performed on a GE Healthcare Discovery VCT 64 PET/CT scanner (Cyceron platform). The CT-based attenuation-corrected PET images were reconstructed with an ordered-subsets expectation maximization 2-dimensional algorithm (9 subsets and 2 iterations) and filtered in 3 dimensions with a Butterworth filter on a 1.95 × 1.95 × 3.27 mm voxel size. SUVs (g/mL) were calculated using the measured concentration in tissue (counts, kBq/mL) divided by the injected activity (kBq/g of body weight).

Image Analysis

MR image analysis was performed with in-house macros based on ImageJ software (*27*). PET analyses were performed with PMOD software, version 3.1.

rCBV maps were computed using dynamic susceptibility contrast-enhanced MRI. Variations of the T2* signal in the tissue were calculated with in-house macros based on ImageJ software as follows: $\Delta R_2^*(t) = -1 \cdot \ln(S(t)/S_0)/\text{echo time}$, where R_2 is the transverse relaxation rate (corresponding to 1/T2), expressed in msec-1 and t is time, ln = natural logarithm, S(t) is signal intensity over time, and S_0 is signal intensity before contrast agent injection. Then, cerebral blood volume (CBV) maps were generated by integrating the area under the γ-variate–fitted curves to avoid an effect of recirculation (*28*). Images were then normalized by dividing CBV maps by the mean value of the normal-appearing contralateral side to obtain rCBV maps.

Coregistration. rCBV maps, FLAIR, 3D T1w-Gd, and ^{18}F-FMISO PET images were coregistered with trilinear interpolation, rigid matching, and normalized mutual information on ^{18}F-FLT PET images (PMOD software, version 3.1).

Volume Segmentation. In the present study, we had to tune the segmentation for each imaging modality since none of the various methods we used was considered pertinent enough for the 3 imaging modalities, which differed in term of contrast-to-tumor ratio and signal intensity. Also, we paid attention to the accuracy of the segmentation modality for all patients in 1 imaging modality. When 2 methods were almost the same, we retained the most restrictive one to avoid any overinterpretation of our results.

Volume Segmentation for ^{18}F-FLT PET. The visual inspection easily enabled us to eliminate 40% of SUV_{max}, which underestimates volume, whereas a mean contralateral image (Mean Contra) + 3.3 SDs overestimates volume (Supplemental Fig. 1; supplemental materials are available at http://jnm.snmjournals.org). A semiautomated fuzzy locally adaptive bayesian (FLAB) algorithm previously validated for ^{18}F-FLT PET images was exploited, using 2 or 3 classes (*29*–*33*).

Volume Segmentation for ^{18}F-FMISO PET. We considered FLAB, a standard 1.2 tissue-to-blood segmentation, 40% of SUV_{max}, and Mean Contra + 3.3 SDs, and compared them with each other quantitatively and visually.

As exemplified in Supplemental Fig. 2, the standard 1-to-2 tissue-to-blood segmentation failed for some patients. For 40% of SUV_{max}, it was visually striking that an overestimation of hypoxic volumes occurred. We then performed either FLAB segmentation or a semiautomated segmentation using a statistical approached based on the Mean Contra + 3.3 SDs (*34*). As compared with the tissue-to-blood segmentation approach, we believe this segmentation could be very well suited in the routine situation because it does not require drawing and processing of radioactive blood. Thus, with the exception of a few pixels removed by hiding with FLAIR hypersignal, no further manual intervention was necessary, making this technique particularly well suited. This statistical approach, Mean Contra + 3.3 SDs, seems suitable for a tracer such as ^{18}F-FMISO with an average uptake and a large SD in the healthy brain parenchyma and a poor tumor–to–contralateral-tissue contrast.

FLAB and Mean Contra + 3.3 SDs led to very similar results (Supplemental Fig. 2). In some cases, FLAB provided slightly larger hypoxic volumes than Mean Contra + 3.3 SDs; we retained the less permissive strategy.

Volume Segmentation for CBV. The CBV segmentation relates to the ^{18}F-FMISO situation. Because a volume of blood is present in healthy brain tissue, the statistical approach resulted in accurate segmentation compared with the visual approach using the naked eye. We used an already-published methodology (*35*) assuming a threshold of 2 or 3 times the signal of the normal-appearing white matter. We also compared this first methodology with a contralateral region of interest (ROI) composed of both gray and white matter and using a threshold of Mean Contra + 1.96 SDs. For both methods, only the region included in the FLAIR region was retained. The 2 methods provided very similar results, but Mean Contra + 1.96 SDs was less permissive (Supplemental Fig. 3).

Hot-Spot Segmentation. For each modality, the hot-spot area was defined as the 95th percentile of histogram distribution in the 3D ROI defined by the FLAIR hypersignal. This definition was designed to include all voxels that may extend to the CE ROI. All segmented areas were then used as 3D ROIs for further studies.

Peripheral Volume and Hot-Spot Calculation. After the segmentation process, for each modality and each patient we defined a peripheral volume and a peripheral hot-spot subvolume as the percentage of the ROI of the modality of interest that is outside the volume of CE. This volume was calculated using a Boolean operation in the following equations.

$$\textit{Peripheral volume}\ (\%) = \frac{\textit{ROI of the volume of the modality NOT ROI of CE}}{\textit{ROI of CE}} \times 100$$

$$\textit{Peripheral hot spot}\ (\%) = \frac{\textit{ROI of the hot spot of the modality NOT ROI of CE}}{\textit{ROI of CE}} \times 100$$

RESULTS

All tumors were confirmed to be a glioblastoma by the pathologist and exhibited a marked CE on 3D T1w-Gd images, elevated rCBV, and pronounced ^{18}F-FLT and ^{18}F-FMISO uptake. Figure 1 shows representative examples of multimodal imaging of 2 glioblastoma patients, including 3D T1w-Gd MR images, ^{18}F-FLT PET images, rCBV maps, and ^{18}F-FMISO PET images. On the basis of visual inspection by an expert in PET imaging, a marked intratumoral heterogeneity of tracer uptake on both PET images was observed. Since the CE is the main target of treatments (surgery or radiation therapy), we then paid attention to the spatial relationship between each modality and the CE region.

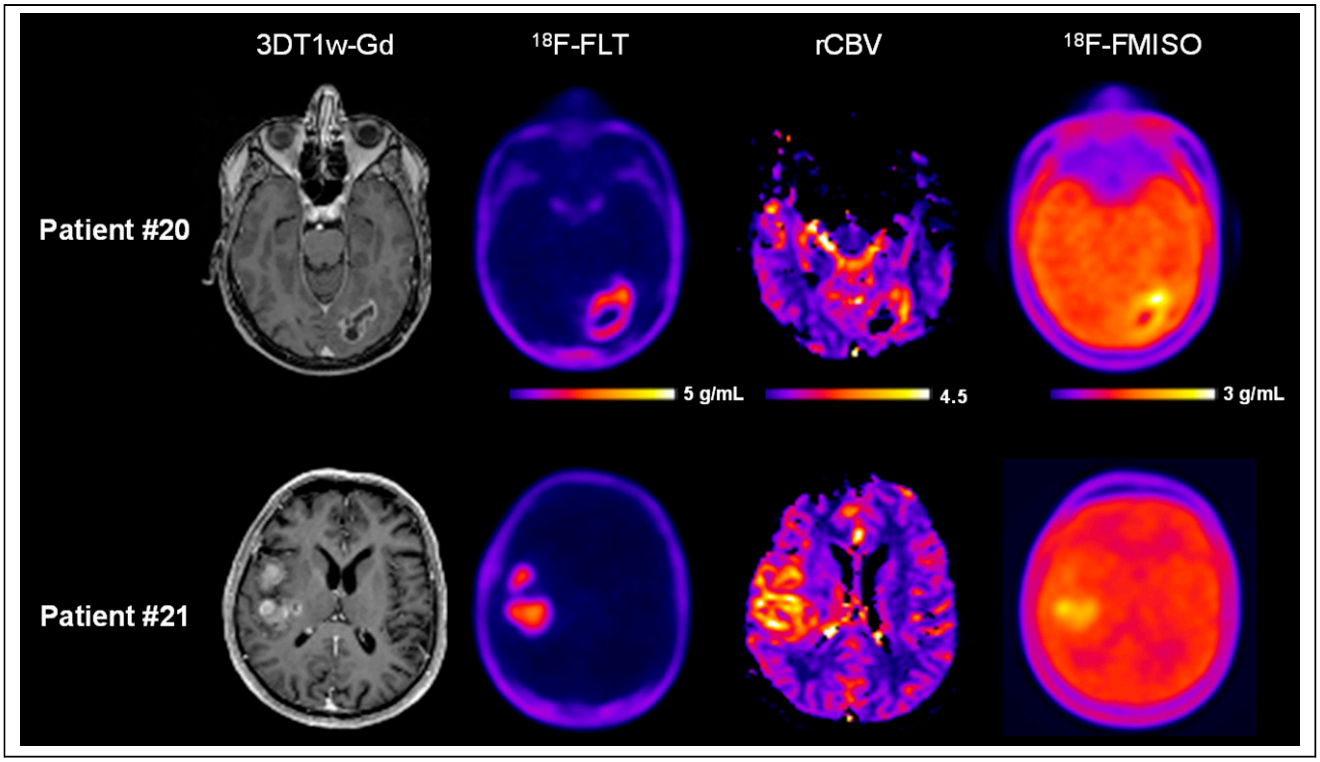

FIGURE 1. Multimodal imaging of 2 glioblastoma patients with 3D T1w-Gd, ^{18}F-FLT PET, rCBV MRI, and ^{18}F-FMISO PET.

Analyses of the Peripheral Volume Outside the CE Region

Thresholded regions of proliferation with ^{18}F-FLT, of hypervascularization with rCBV, and of hypoxia with ^{18}F-FMISO (Fig. 2, top) were overlaid on the T1w-Gd images (Fig. 2, bottom). Figure 2 and the calculated peripheral volume (Fig. 3, patient 20) illustrated that the volume of ^{18}F-FLT uptake extended far from the CE area (139%). A similar situation also occurred for ^{18}F-FMISO uptake but was less pronounced, with the peripheral volume being 43% whereas for CBV only 11% of the segmented area extended into the nonenhancing area. A representative example of the 3 modalities' segmentation overlayed on the T1w-Gd image is provided (Supplemental Fig. 4).

The calculated peripheral volume outside the CE volume for each patient (Fig. 3) clearly demonstrated that extension of metabolic areas beyond the CE volume was highly variable. The ranges of peripheral volumes for ^{18}F-FLT, rCBV, and ^{18}F-FMISO were, respectively, 1.6%–155.5%, 1.5%–89.5%, and 3.1%–78.0%. More precisely, over the 20 patients investigated with ^{18}F-FLT, 9 had a peripheral volume range of 0%–20%, 5 had a peripheral volume range of 20%–40%, and 6 had a peripheral volume greater than 40%. For CBV, 17 of 31 patients had a peripheral volume range of 0%–20%, 10 had a peripheral volume range of 20%–40%, and 4 had a peripheral volume greater than 40%. For ^{18}F-FMISO, 10 of 20 had a peripheral volume range of 0%–20%; 7 had a peripheral volume range of 20%–40%, and 3 had a peripheral volume greater than 40%.

Analyses of the Peripheral Hot Spots Outside the CE Region

Considering the strong intratumor heterogeneity observed on multiparametric imaging, we were interested in further identifying subvolumes in the tumor that were likely associated with resistance and early recurrence. Hyperproliferative, hypervascularized, and severely hypoxic hot spots were thresholded (Fig. 4, top) and overlaid on the T1w-Gd images (Fig. 4, bottom). In this example, a percentage of the hyperproliferative region (18%), the hypervascular region (11%), and the most hypoxic region (3%) were located outside the CE region.

The peripheral hot spots outside the CE volume were calculated for each patient (Fig. 5) and showed that all patients had a hyperproliferative volume outside the CE volume (8.8%–32.5%). More precisely, 1 of 20 had less than 10%, 15 had 10%–20%, and 4 had 20%–40%. Concerning hypervascularized hot spots (0%–25.2%), in 23 of 31 patients the hot-spot fraction was less than 5%, in 7 it was 5%–20%, and in 1 it was 25%. Last, most hypoxic areas were detected mainly in the CE region (0%–5.7%); 14 of 20 patients had less than 1% of the ^{18}F-FMISO hot spot outside the CE volume, and the others had around 5% outside the CE volume.

DISCUSSION

In the context of glioblastoma, intertumoral and intratumoral heterogeneity has been attributed to the failure of standardized treatments. Among the factors influencing tumor growth, the in vivo relationship between proliferation, angiogenesis, and hypoxia remains of great interest relative to the conventionally aggressive region defined on CE MRI. In the context of glioblastoma, the present study is the first one, to our knowledge, to show the spatial distribution of each modality together and relative to CE.

The literature and multivariate analyses have shown that each parameter is independently associated with tumor volume (*17*,*26*,*36*). In gliomas, elevated ^{18}F-FLT uptake has been shown to correlate with Ki-67 immunostaining expression and to reflect proliferation (*37*–*39*). Also in gliomas, high hypoxia has been shown to be a factor in a poor prognosis (*40*).

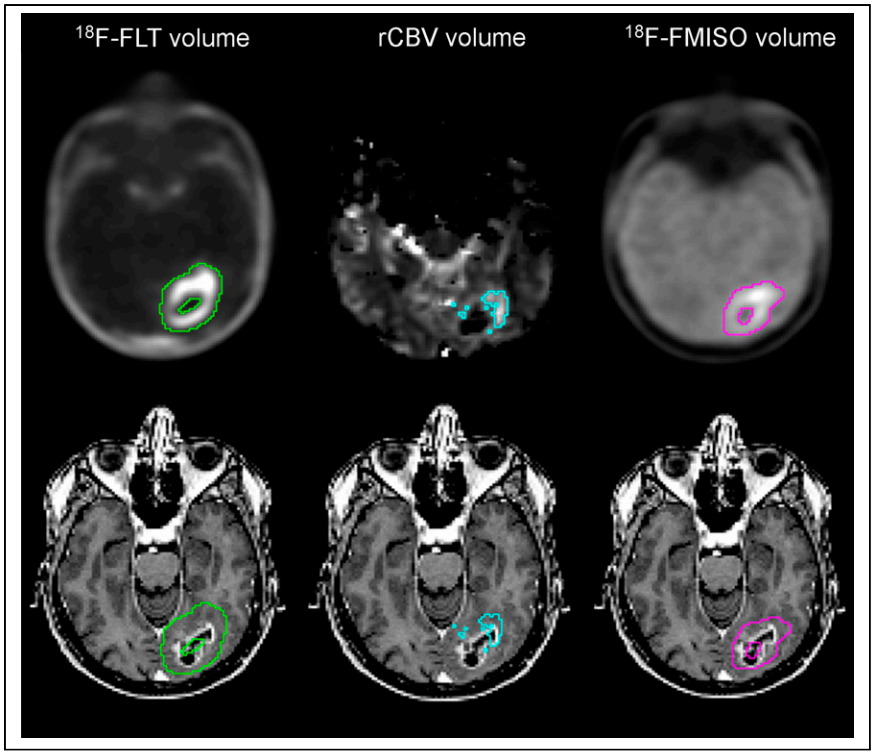

FIGURE 2. Example of proliferative volume in green, hypervascularized volume in blue, and hypoxic volume in pink on segmented (top) and overlaid (bottom) 3D T1w-Gd MR images.

As exemplified in Figure 1, our results confirm that all 3 analyzed parameters are interlinked and that an increase in each parameter occurs concomitantly (*9*,*11*). Increased rCBV along with hypoxia might indicate tumor-induced angiogenesis to counteract changes in oxygenation that occur along with the metabolic demand of proliferating cells.

After a visual inspection, each modality in Figure 1 clearly showed a variable uptake distribution that would need to be exploited. Our findings confirm previous publications (*9*,*10*,*17*) indicating that the heterogeneity can be mapped using multimodal imaging.

However, our results on peripheral volume also showed that active tumor tissues were already present in areas that could be considered nonpathologic according to CE on MRI and that therefore might not be targeted by the treatment. This possibility is especially true for ^{18}F-FLT PET, which clearly showed that proliferating cells extended outside the CE region on T1w-Gd images, as demonstrated in earlier publications (*36*).

One of our main results is that the ^{18}F-FLT PET volume was greater than the other volumes. The spatial analysis

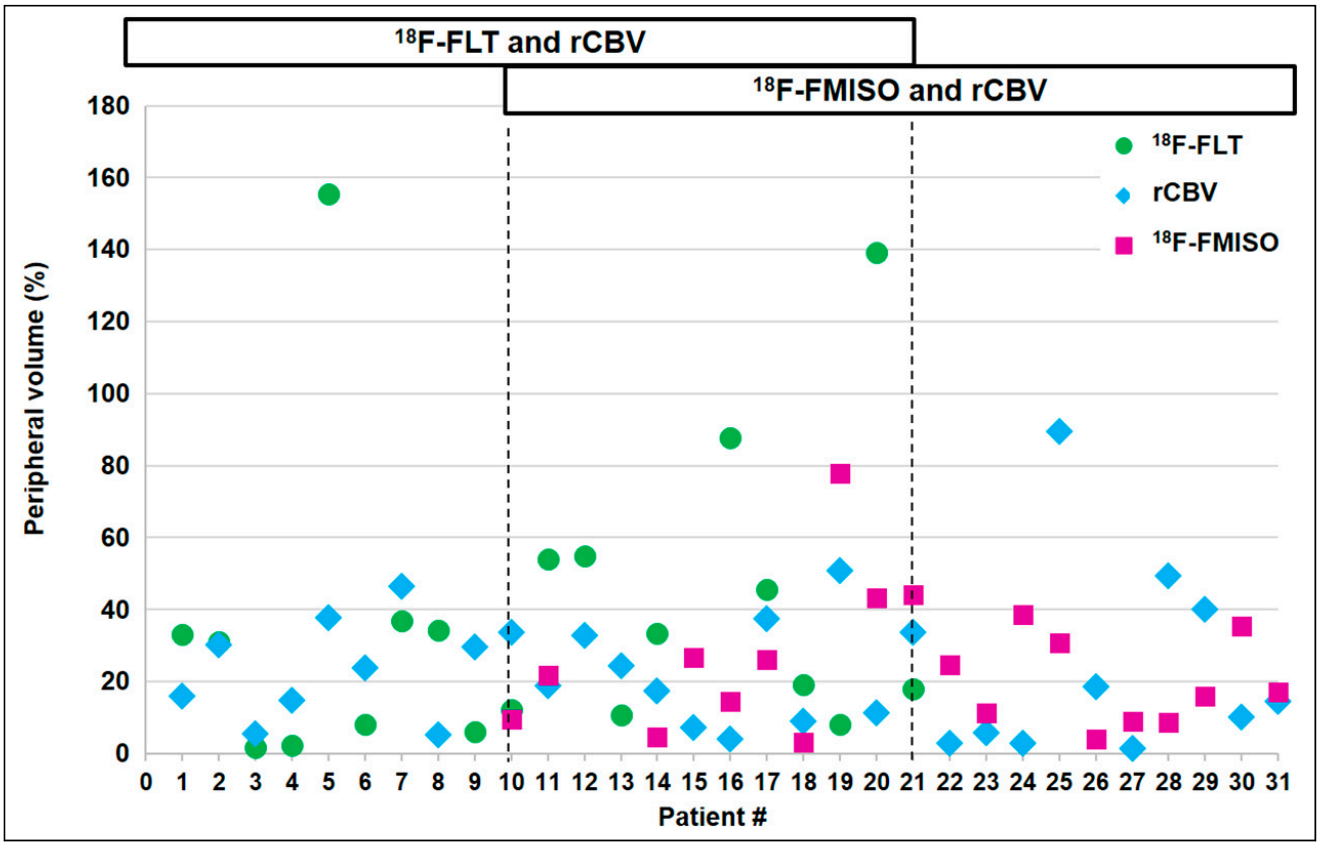

FIGURE 3. Percentage of peripheral volume of ^{18}F-FLT, rCBV, and ^{18}F-FMISO outside CE volume.

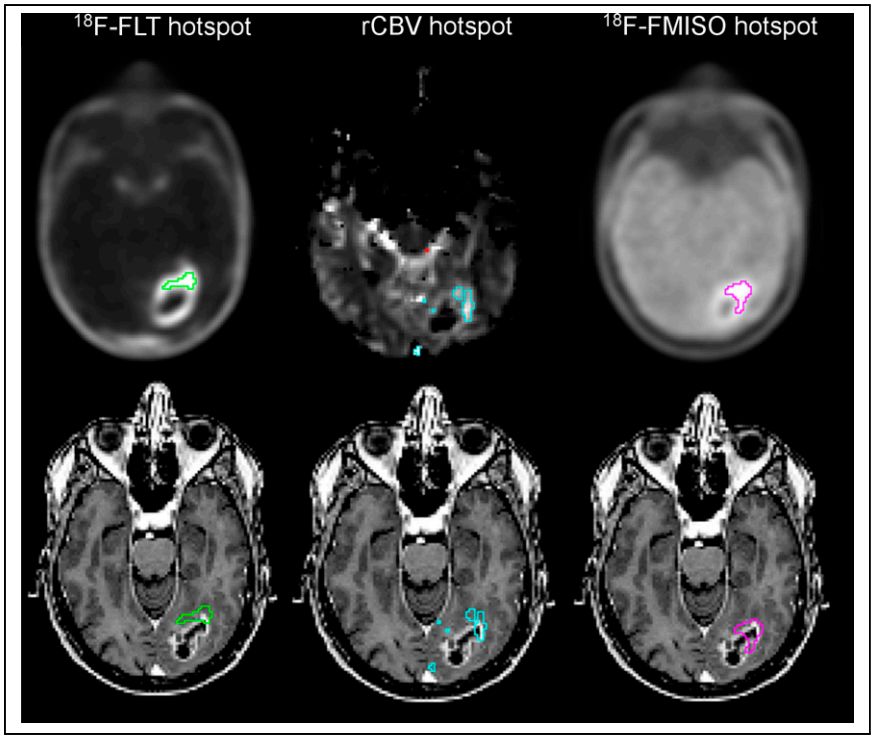

FIGURE 4. Example of proliferative hot spot in green, hypervascularized hot spot in blue, and hypoxic hot spot in pink on segmented (top) and overlaid (bottom) T1w-Gd MR images.

showed that the ^{18}F-FLT volume encompasses the rCBV, the CE volume, and the ^{18}F-FMISO volume for most patients. This result is in line with previously published results, which also demonstrated that in most cases, the volume of ^{18}F-FLT uptake was larger than the tumor volume assessed by anatomic MRI. In glioma, elevated ^{18}F-FLT uptake correlates with Ki-67 and reflects proliferation (*37*,*38*). This result strengthens the hypothesis that tumoral proliferation is the driving force of the other parameters analyzed in this study, namely angiogenesis and hypoxia.

Various papers have discussed the dependency of ^{18}F-FLT uptake on the integrity of the BBB (*41*). It is recognized that a major limiting factor in ^{18}F-FLT uptake is the transport mechanism, and leakage via the disrupted blood–tumor barrier could result in increased uptake. A paper from Watkins et al. (*42*) suggests that the presence of only a small number of glioma cells could be sufficient to damage the integrity of the BBB, potentially explaining the ability of ^{18}F-FLT to detect proliferating cells in nonenhancing regions of the tumor.

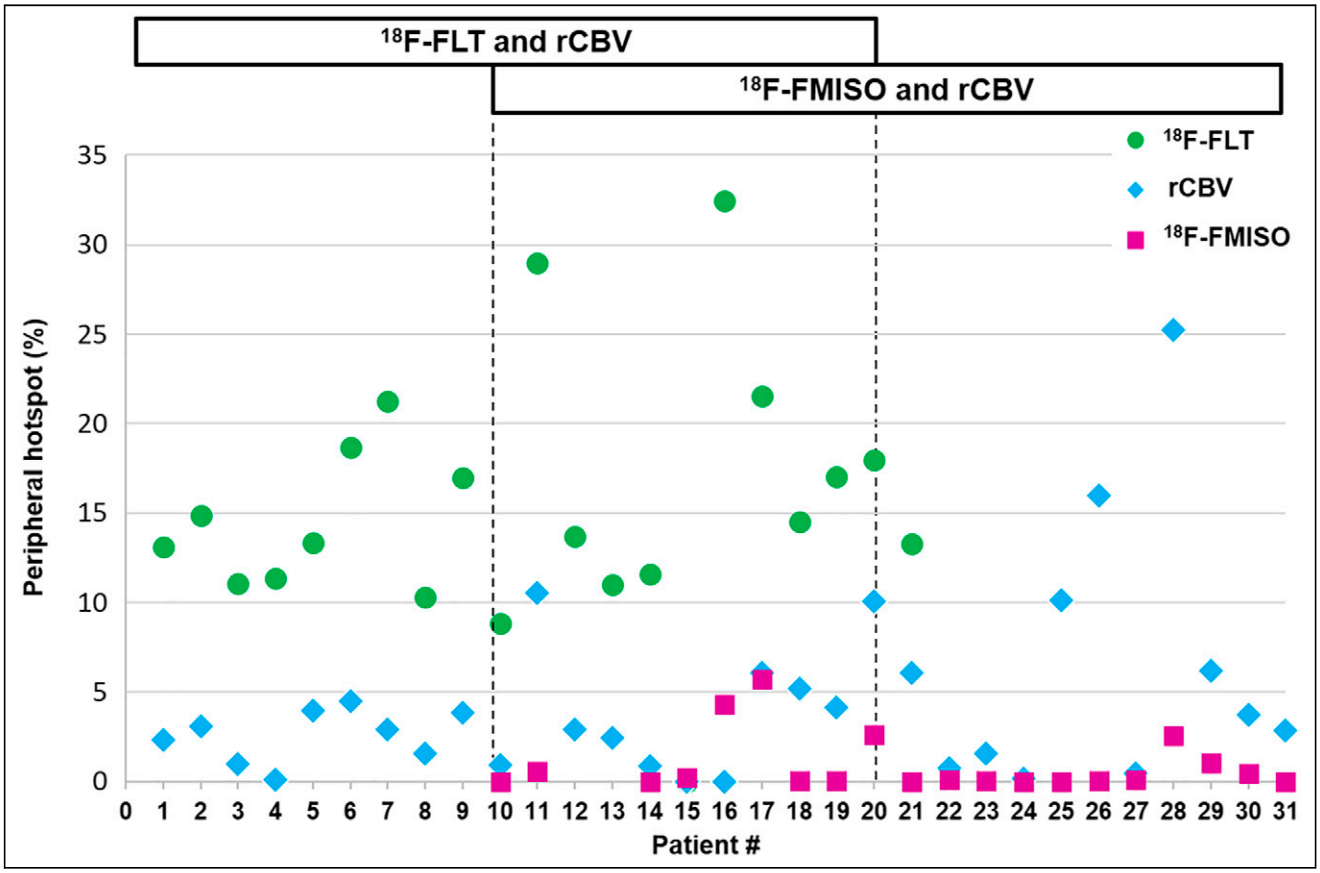

FIGURE 5. Percentage of peripheral hot-spot volume of ^{18}F-FLT, rCBV, and ^{18}F-FMISO outside CE volume.

The hot-spot analysis showed that all tumors had a hyperproliferative area that extended outside the CE volume, whereas hypervascularized or severely hypoxic areas were mostly included within the CE volume. This result concurs with a recent publication using ^{11}C-methionine and demonstrating the presence of metabolic tumor volume after gross tumor resection (*43*).

These results strengthen the fact that tumor cells have already infiltrated the nonenhancing tissue and ought to be included in the surgical treatment or in the definition of the biologic target volume for radiotherapy (*43*).

The current standard surgical treatment for glioblastoma is removal of the CE area (*44*). Because our study showed that metabolically active areas are visible outside the CE volume, removal of only the CE volume could contribute to explaining a rapid recurrence of glioblastoma. We suggest that glioblastoma be resected beyond the CE volume up to the functional limit required to preserve the quality of life (*45*). The presence of metabolically active areas outside the CE volume may also be used as a parameter for improving the accuracy of the biopsy analysis, and if biopsy and imaging concur, it could be used to improve the quality of resection.

The presence of metabolically active areas outside the CE volume contributes to the definition of gross target volumes for radiotherapy, integrating these findings in the concept of biologic target volume (*46*). The integration of the metabolically active areas could lead to better tumor control, as it is known that most relapses occur within the irradiation field (*47*,*48*) because of radiation resistance in some areas within the irradiated volume. It is assumed that the current radiotherapy regimen does not guarantee the curative doses necessary to counteract radioresistance in some areas of the tumor identified as hot spots in this paper and that this problem may contribute to failure of conventional treatments (*49*). Radiotherapy is likely to be optimized by specifically targeting these unfavorable biologic characteristics (*49*,*50*).

This study had some limitations. We studied each modality only with respect to T1 CE, and we did not perform voxelwise analyses between the various modalities. However, the main goal of the present analysis was to make the study as simple as possible relative to T1 CE in order to provide information the physician will find useful in adapting or tuning therapeutic strategies at the individual level. The use of other types of PET tracer, such as amino acid tracers (^{11}C-methionine, *O*-(2-^{18}F-fluoroethyl)-L-tyrosine, and 3,4-dihydroxy-6-^{18}F-fluoro-L-phenylalanine), might also provide accurate information in mapping regions potentially involved in tumor recurrence. For the hot-spot study, given the method of calculation for each patient, a potential overinterpretation of low activity could occur. As a consequence, comparison of our results to include the peripheral volumes or the hot-spot subvolumes in therapeutic strategies or in stereotactic biopsies would also be of great importance. We are now incorporating this strategy in ongoing clinical trials.

CONCLUSION

Even if it is difficult to draw a general overview for each individual patient, this study underlines the complementary value of using different multiparametric imaging methods to assess tumor heterogeneity and to define tumor volumes and subvolumes that are likely to be resistant to conventional therapies.

DISCLOSURE

Funding was received from Conseil Régional de Normandie, Elen Fund, Institut National du Cancer (grant RECF1475), and Agence Nationale de la Recherche-Labex IRON (ANR-11-LABX-0018-01). No other potential conflict of interest relevant to this article was reported.

ACKNOWLEDGMENT

We are grateful to Dr. Aurélien Corroyer-Dulmont for his helpful comments.

KEY POINTS

QUESTION: What is the spatial relationship between proliferation, vascularization, and hypoxia in preoperative glioblastoma patients, with respect to the CE area on T1w-Gd images?

PERTINENT FINDINGS: Clinical trials demonstrated the heterogeneity of the 3 parameters measured—namely proliferation, vasculature, and hypoxia—over the classically used CE volume.

IMPLICATIONS FOR PATIENT CARE: Incorporating more functional parameters for patient management will improve the delineation of aggressive areas for tumor resection and will help in designing biologic target volume for radiotherapy.

REFERENCES

1. Stupp R, Hegi ME, Mason WP, et al. Effects of radiotherapy with concomitant and adjuvant temozolomide versus radiotherapy alone on survival in glioblastoma in a randomised phase III study: 5-year analysis of the EORTC-NCIC trial. *Lancet Oncol.* 2009;10:459–466.
2. Wen PY, Weller M, Lee EQ, et al. Glioblastoma in adults: a Society for Neuro-Oncology (SNO) and European Society of Neuro-Oncology (EANO) consensus review on current management and future directions. *Neuro Oncol.* 2020;22:1073–1113.
3. Louis DN, Perry A, Reifenberger G, et al. The 2016 World Health Organization classification of tumors of the central nervous system: a summary. *Acta Neuropathol (Berl).* 2016;131:803–820.
4. Verhaak RGW, Hoadley KA, Purdom E, et al. Integrated genomic analysis identifies clinically relevant subtypes of glioblastoma characterized by abnormalities in PDGFRA, IDH1, EGFR, and NF1. *Cancer Cell.* 2010;17:98–110.
5. Bergmann N, Delbridge C, Gempt J, et al. The intratumoral heterogeneity reflects the intertumoral subtypes of glioblastoma multiforme: a regional immunohistochemistry analysis. *Front Oncol.* 2020;10:494.
6. Li C, Wang S, Yan J-L, et al. Intratumoral heterogeneity of glioblastoma infiltration revealed by joint histogram analysis of diffusion tensor imaging. *Neurosurgery.* 2019;85:524–534.
7. Chinot OL, Wick W, Mason W, et al. Bevacizumab plus radiotherapy-temozolomide for newly diagnosed glioblastoma. *N Engl J Med.* 2014;370:709–722.
8. Swanson KR, Bridge C, Murray JD, Alvord EC. Virtual and real brain tumors: using mathematical modeling to quantify glioma growth and invasion. *J Neurol Sci.* 2003;216:1–10.
9. Evans SM, Jenkins KW, Chen HI, et al. The relationship among hypoxia, proliferation, and outcome in patients with de novo glioblastoma: a pilot study. *Transl Oncol.* 2010;3:160–169.
10. Gerstner ER, Zhang Z, Fink J, et al. ACRIN 6684: assessment of tumor hypoxia in newly diagnosed GBM using ^{18}F-FMISO PET and MRI. *Clin Cancer Res.* 2016;22:5079–5086.
11. Swanson KR, Rockne RC, Claridge J, Chaplain MA, Alvord EC, Anderson ARA. Quantifying the role of angiogenesis in malignant progression of gliomas: in silico modeling integrates imaging and histology. *Cancer Res.* 2011;71:7366–7375.
12. Bekaert L, Valable S, Lechapt-Zalcman E, et al. [^{18}F]-FMISO PET study of hypoxia in gliomas before surgery: correlation with molecular markers of hypoxia and angiogenesis. *Eur J Nucl Med Mol Imaging.* 2017;44:1383–1392.
13. Collet S, Valable S, Constans JM, et al. [^{18}F]-fluoro-L-thymidine PET and advanced MRI for preoperative grading of gliomas. *Neuroimage Clin.* 2015;8:448–454.
14. Fernandez P, Zanotti-Fregonara P, Eimer S, et al. Combining 3'-deoxy-3'-[^{18}F] fluorothymidine and MRI increases the sensitivity of glioma volume detection. *Nucl Med Commun.* 2019;40:1066–1071.
15. Leimgruber A, Hickson K, Lee ST, et al. Spatial and quantitative mapping of glycolysis and hypoxia in glioblastoma as a predictor of radiotherapy response and sites of relapse. *Eur J Nucl Med Mol Imaging.* 2020;47:1476–1485.

16. Ponte KF, Berro DH, Collet S, et al. In vivo relationship between hypoxia and angiogenesis in human glioblastoma: a multimodal imaging study. *J Nucl Med.* 2017;58:1574–1579.
17. Szeto MD, Chakraborty G, Hadley J, et al. Quantitative metrics of net proliferation and invasion link biological aggressiveness assessed by MRI with hypoxia assessed by FMISO-PET in newly diagnosed glioblastomas. *Cancer Res.* 2009;69:4502–4509.
18. Kickingereder P, Radbruch A, Burth S, et al. MR perfusion-derived hemodynamic parametric response mapping of bevacizumab efficacy in recurrent glioblastoma. *Radiology.* 2016;279:542–552.
19. Miyake K, Shinomiya A, Okada M, Hatakeyama T, Kawai N, Tamiya T. Usefulness of FDG, MET and FLT-PET studies for the management of human gliomas. *J Biomed Biotechnol.* 2012;2012:205818.
20. Berro DH, Collet S, Constans J-M, et al. Comparison between MRI-derived ADC maps and ^{18}FLT-PET in pre-operative glioblastoma. *J Neuroradiol.* 2019;46:359–366.
21. Brahm CG, den Hollander MW, Enting RH, et al. Serial FLT PET imaging to discriminate between true progression and pseudoprogression in patients with newly diagnosed glioblastoma: a long-term follow-up study. *Eur J Nucl Med Mol Imaging.* 2018;45:2404–2412.
22. Najjar AM, Johnson JM, Schellingerhout D. The emerging role of amino acid PET in neuro-oncology. Bioeng Basel Switz. 2018;5:104.
23. Chakhoyan A, Guillamo J-S, Collet S, et al. FMISO-PET-derived brain oxygen tension maps: application to glioblastoma and less aggressive gliomas. *Sci Rep.* 2017;7:10210.
24. van Elmpt W, Zegers CML, Reymen B, et al. Multiparametric imaging of patient and tumour heterogeneity in non-small-cell lung cancer: quantification of tumour hypoxia, metabolism and perfusion. *Eur J Nucl Med Mol Imaging.* 2016;43:240–248.
25. Vera P, Bohn P, Edet-Sanson A, et al. Simultaneous positron emission tomography (PET) assessment of metabolism with ^{18}F-fluoro-2-deoxy-D-glucose (FDG), proliferation with ^{18}F-fluoro-thymidine (FLT), and hypoxia with ^{18}fluoro-misonidazole (F-miso) before and during radiotherapy in patients with non-small-cell lung cancer (NSCLC): a pilot study. *Radiother Oncol.* 2011;98:109–116.
26. Jacobs AH, Thomas A, Kracht LW, et al. ^{18}F-fluoro-L-thymidine and ^{11}C-methylmethionine as markers of increased transport and proliferation in brain tumors. *J Nucl Med.* 2005;46:1948–1958.
27. Schneider CA, Rasband WS, Eliceiri KW. NIH image to imageJ: 25 years of image analysis. *Nat Methods.* 2012;9:671–675.
28. Boxerman JL, Schmainda KM, Weisskoff RM. Relative cerebral blood volume maps corrected for contrast agent extravasation significantly correlate with glioma tumor grade, whereas uncorrected maps do not. *AJNR.* 2006;27:859–867.
29. Hatt M, Cheze le Rest C, Turzo A, Roux C, Visvikis D. A fuzzy locally adaptive bayesian segmentation approach for volume determination in PET. *IEEE Trans Med Imaging.* 2009;28:881–893.
30. Hatt M, Cheze le Rest C, Descourt P, et al. Accurate automatic delineation of heterogeneous functional volumes in positron emission tomography for oncology applications. *Int J Radiat Oncol Biol Phys.* 2010;77:301–308.
31. Arens AIJ, Troost EGC, Hoeben BAW, et al. Semiautomatic methods for segmentation of the proliferative tumour volume on sequential FLT PET/CT images in head and neck carcinomas and their relation to clinical outcome. *Eur J Nucl Med Mol Imaging.* 2014;41:915–924.
32. Hatt M, Laurent B, Ouahabi A, et al. The first MICCAI challenge on PET tumor segmentation. *Med Image Anal.* 2018;44:177–195.
33. Hatt M, Lee JA, Schmidtlein CR, et al. Classification and evaluation strategies of auto-segmentation approaches for PET: Report of AAPM task group no. 211. *Med Phys.* 2017;44:e1–e42.
34. Henriques de Figueiredo B, Zacharatou C, Galland-Girodet S, et al. Hypoxia imaging with [^{18}F]-FMISO-PET for guided dose escalation with intensity-modulated radiotherapy in head-and-neck cancers. *Strahlenther Onkol.* 2015;191:217–224.
35. Crawford FW, Khayal IS, McGue C, et al. Relationship of pre-surgery metabolic and physiological MR imaging parameters to survival for patients with untreated GBM. *J Neurooncol.* 2009;91:337–351.
36. Kawai N, Maeda Y, Kudomi N, et al. Correlation of biological aggressiveness assessed by ^{11}C-methionine PET and hypoxic burden assessed by ^{18}F-fluoromisonidazole PET in newly diagnosed glioblastoma. *Eur J Nucl Med Mol Imaging.* 2011;38:441–450.
37. Corroyer-Dulmont A, Pérès EA, Petit E, et al. Detection of glioblastoma response to temozolomide combined with bevacizumab based on μMRI and μPET imaging reveals [^{18}F]-fluoro-L-thymidine as an early and robust predictive marker for treatment efficacy. *Neuro-oncol.* 2013;15:41–56.
38. Ullrich R, Backes H, Li H, et al. Glioma proliferation as assessed by 3'-fluoro-3'-deoxy-L-thymidine positron emission tomography in patients with newly diagnosed high-grade glioma. *Clin Cancer Res.* 2008;14:2049–2055.
39. Viel T, Talasila KM, Monfared P, et al. Analysis of the growth dynamics of angiogenesis-dependent and -independent experimental glioblastomas by multimodal small-animal PET and MRI. *J Nucl Med.* 2012;53:1135–1145.
40. Spence AM, Muzi M, Swanson KR, et al. Regional hypoxia in glioblastoma multiforme quantified with [^{18}F]fluoromisonidazole positron emission tomography before radiotherapy: correlation with time to progression and survival. *Clin Cancer Res.* 2008;14:2623–2630.
41. Nikaki A, Angelidis G, Efthimiadou R, et al. ^{18}F-fluorothymidine PET imaging in gliomas: an update. *Ann Nucl Med.* 2017;31:495–505.
42. Watkins S, Robel S, Kimbrough IF, Robert SM, Ellis-Davies G, Sontheimer H. Disruption of astrocyte-vascular coupling and the blood-brain barrier by invading glioma cells. *Nat Commun.* 2014;5:4196.
43. Miller S, Li P, Schipper M, et al. Metabolic tumor volume response assessment using ^{11}C-methionine positron emission tomography identifies glioblastoma tumor subregions that predict progression better than baseline or anatomic magnetic resonance imaging alone. *Adv Radiat Oncol.* 2019;5:53–61.
44. D'Amico RS, Englander ZK, Canoll P, Bruce JN. Extent of resection in glioma: a review of the cutting edge. *World Neurosurg.* 2017;103:538–549.
45. Duffau H. Surgery for malignant brain gliomas: fluorescence-guided resection or functional-based resection? *Front Surg.* 2019;6:21.
46. Ling CC, Humm J, Larson S, et al. Towards multidimensional radiotherapy (MD-CRT): biological imaging and biological conformality. *Int J Radiat Oncol Biol Phys.* 2000;47:551–560.
47. Ghose A, Lim G, Husain S. Treatment for glioblastoma multiforme: current guidelines and canadian practice. *Curr Oncol.* 2010;17:52–58.
48. Milano MT, Okunieff P, Donatello RS, et al. Patterns and timing of recurrence after temozolomide-based chemoradiation for glioblastoma. *Int J Radiat Oncol Biol Phys.* 2010;78:1147–1155.
49. Gérard M, Corroyer-Dulmont A, Lesueur P, et al. Hypoxia imaging and adaptive radiotherapy: a state-of-the-art approach in the management of glioma. *Front Med (Lausanne).* 2019;6:117.
50. Piroth MD, Pinkawa M, Holy R, et al. Integrated boost IMRT with FET-PET-adapted local dose escalation in glioblastomas: results of a prospective phase II study. *Strahlenther Onkol.* 2012;188:334–339.

Technologic (R)Evolution Leads to Detection of More Sentinel Nodes in Patients with Melanoma in the Head and Neck Region

Danique M.S. Berger[1], Nynke S. van den Berg[2], Vincent van der Noort[3], Bernies van der Hiel[4], Renato A. Valdés Olmos[4], Tessa A. Buckle[5], Gijs H. KleinJan[6], Oscar R. Brouwer[7], Lenka Vermeeren[8], Baris Karakullukçu[1], Michiel W.M. van den Brekel[1], Bart A. van de Wiel[9], Omgo E. Nieweg[10], Alfons J.M. Balm[1], Fijs W.B. van Leeuwen[5], and W. Martin C. Klop[1]

[1]Department of Head and Neck Surgery and Oncology, The Netherlands Cancer Institute–Antoni van Leeuwenhoek, Amsterdam, The Netherlands; [2]Department of Otolaryngology–Head and Neck Surgery, Stanford University School of Medicine, Stanford, California; [3]Department of Biometrics, The Netherlands Cancer Institute–Antoni van Leeuwenhoek, Amsterdam, The Netherlands; [4]Department of Nuclear Medicine, The Netherlands Cancer Institute–Antoni van Leeuwenhoek, Amsterdam, The Netherlands; [5]Interventional Molecular Imaging Laboratory, Department of Radiology, Leiden University Medical Center, Leiden, The Netherlands; [6]Department of Urology, Leiden University Medical Center, Leiden, The Netherlands; [7]Department of Urology, The Netherlands Cancer Institute–Antoni van Leeuwenhoek, Amsterdam, The Netherlands; [8]Department of Otorhinolaryngology, Onze Lieve Vrouwe Gasthuis, Amsterdam, The Netherlands; [9]Department of Pathology, The Netherlands Cancer Institute–Antoni van Leeuwenhoek, Amsterdam, The Netherlands; and [10]Melanoma Institute Australia and Central Medical School, University of Sydney, Sydney, Australia

Sentinel lymph node (SN) biopsy (SNB) has proven to be a valuable tool for staging melanoma patients. Since its introduction in the early 1990s, this procedure has undergone several technologic refinements, including the introduction of SPECT/CT, as well as radioguidance and fluorescence guidance. The purpose of the current study was to evaluate the effect of this technologic evolution on SNB in the head and neck region. The primary endpoint was the false-negative (FN) rate. Secondary endpoints were number of harvested SNs, overall operation time, operation time per harvested SN, and postoperative complications. **Methods:** A retrospective database was queried for cutaneous head and neck melanoma patients who underwent SNB at The Netherlands Cancer Institute between 1993 and 2016. The implementation of new detection techniques was divided into 4 groups: 1993–2005, with preoperative lymphoscintigraphy and intraoperative use of both a γ-ray detection probe and patent blue (n = 30); 2006–2007, with addition of preoperative road maps based on SPECT/CT (n = 15); 2008–2009, with intraoperative use of a portable γ-camera (n = 40); and 2010–2016, with addition of near-infrared fluorescence guidance (n = 192). **Results:** In total, 277 patients were included. At least 1 SN was identified in all patients. A tumor-positive SN was found in 59 patients (21.3%): 10 in group 1 (33.3%), 3 in group 2 (20.0%), 6 in group 3 (15.0%), and 40 in group 4 (20.8%). Regional recurrences in patients with tumor-negative SNs resulted in an overall FN rate of 11.9% (group 1, 16.7%; group 2, 0%; group 3, 14.3%; group 4, 11.1%). The number of harvested nodes increased with advancing technologies (P = 0.003), whereas Breslow thickness and operation time per harvested SN decreased (P = 0.003 and P = 0.017, respectively). There was no significant difference in percentage of tumor-positive SNs, overall operation time, and complication rate between the different groups. **Conclusion:** The use of advanced detection technologies led to a higher number of identified SNs without an increase in overall operation time, possibly indicating an improved surgical efficiency. Operation time per harvested SN decreased; the average FN rate remained 11.9% and was unchanged over 23 y. There was no significant change in postoperative complication rate.

Key Words: melanoma; head and neck; sentinel lymph node biopsy; false-negative

J Nucl Med 2021; 62:1357–1362
DOI: 10.2967/jnumed.120.246819

One fifth of all cutaneous melanomas occur in the head and neck region (*1*). Sentinel lymph node (SN) biopsy (SNB) for head and neck melanoma was introduced at our institute in the early 1990s for patients with clinically localized disease (*2,3*). SNB improves survival in node-positive patients, and the tumor status of the SN is the strongest prognostic factor (*4*). The more accurate staging facilitates selection of patients for adjuvant therapy and for trials (*5*).

Detection of SNs in the head and neck is often challenging because of the complex anatomy, and interlacing lymph vessels can yield unexpected drainage patterns to multiple and bilateral sites (*6*). Moreover, nodes in the head and neck region, especially in the parotid gland, are easily overlooked on lymphoscintigraphy because they are near the injection site, where most of the radioactive tracer remains. These factors are responsible for a median false-negative (FN) rate of 20.4% in the reviewed reports, with a range of 3.3%–44% (*6–9*).

In recent years, various complementing SNB technologies have facilitated the procedure for lymphatic mapping. First, ^{99m}Tc-nanocolloid was used for dynamic and static lymphoscintigraphy to map the lymphatic drainage and for intraoperative γ-ray detection probe tracing in combination with patent blue to visualize the afferent lymph vessels and the SNs (*10,11*). Because of disadvantages such as allergic reactions, coloring of the skin, and fast shiftingof the dye to lymph nodes and pathways, patent blue is now omitted in the head and neck (*12–15*). The addition of preoperative SPECT/CT visualized SNs in their anatomic context (*16*). With the introduction of intraoperative use of a portable γ-camera, a better overview of the SNs in the surgical field was provided (*17*). Lastly, a complex of indocyanine green (ICG) with ^{99m}Tc-nanocolloid was implemented to integrate near-infrared fluorescence imaging into the procedure (*18–20*). This facilitated detection of superficial (<1 cm

Received Sep. 21, 2020; revision accepted Jan. 28, 2021.
For correspondence or reprints, contact Danique M.S. Berger (d.berger@nki.nl/m.klop@nki.nl).
Published online February 26, 2021.

deep) lymphatic vessels and SNs, using a dedicated fluorescence camera. So, the currently used technologies enable preoperative visualization of the lymphatic drainage pattern, imaging of the SNs within the surrounding anatomy, intraoperative tracing of radioactive SNs, and visualization of the afferent lymphatic ducts and lymph nodes.

The purpose of this study was to determine the impact of the sequential technical advances, over a period of 23 y, on SNB outcomes in patients with melanoma in the head and neck region. The primary endpoint was the FN rate. Secondary endpoints were number of harvested SNs, duration of the procedure, operation time per harvested SN, and postoperative complication rate.

MATERIALS AND METHODS

This retrospective analysis concerned 277 patients with primary cutaneous head and neck melanoma who underwent reexcision and SNB at The Netherlands Cancer Institute between December 1993 and January 2016. SNB was performed for at least pT1b head and neck melanoma without clinical lymph node involvement as determined by palpation, ultrasound, and ultrasound-guided fine-needle aspiration cytology of suggestive lymph nodes according to the guidelines of the Dutch Head and Neck Society based on the eight edition of the American Joint Committee on Cancer–Union for International Cancer Control TNM classification (*21*). Patients who had a history of previous melanoma in the head and neck region or had already undergone wide excision or radiotherapy of the melanoma site were not eligible.

The medical charts were reviewed for tumor characteristics, overall operation time (from start of surgery to closure of incision), operation time per harvested SN (overall operation time divided by number of SNs), and SNB characteristics, as well as other clinicopathologic features. The institutional review board approved this retrospective study, and the requirement to obtain informed consent was waived. All procedures involving patients were in accordance with the ethical standards of the Medical Ethical Committee of The Netherlands Cancer Institute, and conformed with the Declaration of Helsinki (1964) and later amendments.

Imaging and SNB

An SN was defined as any lymph node receiving direct lymphatic drainage from the primary tumor (*22*). Depending on the patient admission date, different lymph node mapping techniques were used for 4 different groups. Group 1 ($n = 30$) covered the period 1993–2005, when preoperative lymphoscintigraphy as well as an intraoperative γ-ray detection probe (Neoprobe; Johnson and Johnson Medical) and patent blue (Laboratoire Guerbet) were used. Group 2 covered 2006–2007, when preoperative SPECT/CT (Symbia; Siemens) was added to visualize SNs in their anatomic habitat. Patent blue was omitted after 2007. Group 3 ($n = 40$) reflected 2008 and 2009 and included the addition of intraoperative use of a portable γ-camera (Sentinella; OncoVision). Group 4 ($n = 192$) covered 2010–2016 and included the addition of near-infrared fluorescence guidance in lieu of patent blue using the hybrid tracer ICG-^{99m}Tc-nanocolloid and a fluorescence camera (Photo Dynamic Eye, Photo Dynamic Eye-Modality, or Fluorescence Imaging System-00; Hamamatsu Photonics K.K.).

For lymphoscintigraphy, the radiopharmaceutical (^{99m}Tc-nanocolloid or ICG-^{99m}Tc-nanocolloid, 80 MBq for 1-d procedure and 120 MBq for 2-d procedure) was injected intradermally around the tumor or biopsy wound in 4 deposits of 0.1 mL (*23*). Immediately after injection, anterior and lateral dynamic planar imaging was performed for 10 min to identify first-echelon SNs and distinguish these from higher-echelon nodes. This was followed by acquisition of 5-min static images roughly 10 min and 2 h after injection to identify SNs in other (aberrant) regions. SPECT/CT imaging was performed directly after the 2-h static imaging. SN locations were marked on the skin and indicated on SPECT/CT key images (so-called surgical road maps), which were transferred to a picture archiving and communication system. The imaging results were discussed with the head and neck surgeon before the operation.

When used in the operation (before 2007), 1 mL of patent blue was injected intradermally around the melanoma site and the area was massaged for 5 min. Subsequently, the SNs were traced using a combination of the probe and the patent blue. To maintain visibility of the lymphatic ducts, patent blue injection was repeated every 90 min. With the introduction of a portable γ-camera, pre- and intraoperative images were acquired.

With the advent of the hybrid tracer, a dedicated near-infrared fluorescence camera was also incorporated. When a presumed SN was roughly located using the γ-ray detection probe and portable γ-camera, the lights in the operating room were dimmed and its precise location was determined using fluorescence imaging.

To verify completion of SNB, the wound was inspected and palpated and intraoperative imaging (fluorescence or portable γ-camera) was repeated. When a residual signal was observed at the location of the original SN, this node was considered a missed SN or part of a cluster of multiple adjacent SNs and also removed.

Histopathologic Examination

Following the recommendations of the European Organization for Research and Treatment of Cancer, multiple levels of the SN were analyzed using hematoxylin and eosin staining and immunohistochemistry for melanocytic differentiation antigens S-100 and glycoprotein 100/human melanoma black 45 (1993–2003) or melanocyte-antigen/melanoma antigen recognized by T cell 1 (2004 onward). Since February 2014, our protocol changed from examining 3 levels to examining 6 levels 50–150 μm each with hematoxylin and eosin staining and immunohistochemistry (*24*).

Follow-up

SN-negative patients were followed every 3 mo in year 1, every 6 mo in years 2–5, and annually thereafter. SN-positive patients were followed every 3 mo in years 1–2 and every 6 mo in years 3–10.

Statistical Analysis

The procedure was considered to be FN if a recurrence developed in the nodal region from which a tumor-free SN had been removed without any signs of local, other regional, or distant tumor activity. The FN rate was calculated by dividing the number of patients who presented with nodal recurrence after a tumor-negative SNB by the sum of those with a true-positive SN (TP) and those with nodal recurrence (FN/(TP + FN)), which is 1 − sensitivity (*25–27*).

Descriptive statistics are presented with means or medians and with 95% CIs or interquartile ranges or, in the case of nominal data, with numbers. In cases of continuous or ordinal variables, 1-way ANOVA or χ^2 tests, respectively, were performed to assess the difference between the different imaging techniques. Significance was defined as a P level of less than 0.05. All statistical analyses were performed using SPSS, version 22.0, or STATA, version 13.

RESULTS

Clinicopathologic Features and Follow-up

Clinicopathologic features for the entire cohort are described in Table 1. Age differed among the 4 groups (Table 2). The Breslow thickness decreased over the years ($P = 0.003$). Follow-up details are presented in Table 2.

Operative and Postoperative Findings

Between 1993 and 2016, 14 head and neck surgeons performed SNB our institute. In all 277 patients, all preoperatively visualized

TABLE 1
Baseline Characteristics

Characteristic	Data
Sex	
Female	100 (36.1%)
Male	177 (63.9%)
Age at SNB (y)	59 (46–68)
Location of primary tumor	
Scalp	77 (27.8%)
Face	103 (37.2%)
Ear	55 (19.9%)
Nose	14 (5.1%)
Neck	28 (10.1%)
Breslow (mm)	2.2 (1.5–3.6)
T*	
T1b	21 (SNB+, 7.7 [4.8%])
T2	94 (SNB+, 34.3 [13.8%])
T3	93 (SNB+, 34.1 [30.1%])
T4	65 (SNB+, 23.8 [26.2%])
Ulceration	
Absent	195 (70.9%)
Present	69 (25.1%)
Unknown	11 (4.0%)

*According to eighth edition of American Joint Committee on Cancer–Union for International Cancer Control TNM classification.

Qualitative data are number and percentage; continuous data are median and interquartile range. Percentages may not equal 100 because of rounding.

SNs were identified during surgery. A mean of 3.8 (95% CI, 3.5–4.1) SNs per patient was excised in a median operation time of 115 min (interquartile range, 87–153 min) (Table 2). The overall operation time remained stable over the years ($P = 0.74$). The number of harvested SNs increased over time ($P = 0.003$), whereas the number of tumor-positive SNs remained equal. The operation time per SN decreased with the advancing technology ($P = 0.017$).

Twelve patients (4.3%) developed postoperative complications that were related to SNB. The complication rate was similar among the groups. Hemorrhage required treatment in 7 patients: 1 in group 1 (3.3%), 1 in group 2 (6.7%), 1 in group 3 (2.5%), and 4 in group 4 (2.1%). Wound infection developed in 1 patient in group 3 (2.5%) and 2 in group 4 (1.0%). One patient in group 1 (3.3%) developed transient facial nerve palsy, and a case of transient spinal accessory nerve dysfunction was seen in group 3.

SNB Outcomes

A tumor-positive SN was found in 59 patients (21.3%) (Table 3). In group 1, 33.3% of the patients had a tumor-positive SN; in group 2, 20.0%; in group 3, 15.0%; and in group 4, 20.8%. There was no significant difference among the groups. Eight patients with tumor-negative SNs and no disease elsewhere had recurrence in their nodal region, resulting in an overall sensitivity of 88.1% and a FN percentage of 11.9. Two patients had an FN procedure in group 1 (16.7%), none in group 2, 1 in group 3 (14.3%), and 5 in group 4 (11.1%). FN nodes were located infraauricularly and retroauricularly in the parotid gland at levels II and V. With the exception of the level II recurrence, all were located near the primary melanoma, where most of the injected radioactivity remained. Follow-up details and recurrences are visualized in Table 4.

DISCUSSION

This study assessed the sequential impact of SPECT/CT, intraoperative use of a portable γ-camera, and intraoperative fluorescence guidance using a hybrid tracer on SNB in patients with melanoma in the head and neck region. With the introduction of these sophisticated techniques, more SNs were harvested per patient whereas the duration of the operations remained the same. So, SNs were identified more quickly, improving the surgical workflow. In this respect, the increasing experience of the individual surgeons in SN identification should also be considered. The greater number of SNs could also imply an increase in postoperative morbidity, but this was not the case. The observed downward trend in FN rate over time from 16.7 to 11.1 could suggest that some—tumor positive—SNs were missed in the early days.

Several large series of patients with head and neck melanomas report the removal of an average of 2.0–2.5 SNs per patient, which is less than the 3.8 in our entire population (*8,28,29*). Although the current data suggest that this higher yield is due to the portable γ-camera and the fluorescence imaging, depiction of extra sentinel nodes by SPECT/CT in the preoperative work-up cannot be neglected (*30*). The high tissue penetration of radioactive γ-rays in combination with the high spatial resolution of the fluorescence signal increased the identification of SNs within clusters of lymph nodes (*23*). If the SN could not be identified separately, the entire cluster was harvested and all nodes were classified as SNs. Since not all of these were necessarily on a direct drainage pathway from the tumor, the lack of intraoperative visualization of afferent lymph vessels may thus inadvertently have increased the number of "SNs."

Our tumor-positive SNB rate of 21.3% is higher than for melanomas elsewhere in the body (*31,32*). In a systematic review of 12 studies on head and neck melanoma, de Rosa et al. demonstrated an average tumor-positive rate of 15.1% (*9*). The high number of thick melanomas in our first cohort may well explain our relatively high rate of tumor-positive SNs.

The current overall FN rate of 11.9% concurs with other studies, which included a wide spectrum of melanoma sites (mean, 14.0%; range, 2.8%–32.1%) (*25,27,32–34*). Although one would intuitively expect innovative detection methods to improve FN rates, we could not establish a significant difference among the groups. Results to improve melanoma staging by ICG vary in the literature. In a large prospective cohort of melanoma patients, ICG and lymphoscintigraphy resulted in higher SN positive rates than the predicted true-positive SNB rate based on the literature and their cohort (*35*). However, another recent prospective study of 121 melanoma patients demonstrated that the combination of lymphoscintigraphy, probe, and ICG fluorescence improved the SN detection rate only marginally (*36*).

In addition to the introduction of new detection techniques and advancing surgical skills, the more elaborate histopathologic examination plays an important role in the sensitivity of SNB. After the number of levels of examination of SNs was increased from 3 to 6 in 2014, the number of FN procedures dropped from 8 in 193 patients to none in the subsequent 84.

TABLE 2
Patient and Tumor Characteristics

Characteristic	Overall, 1993–2016 (n = 277)	Group 1, lymphoscintigraphy, 1993–2005 (n = 30)	Group 2, SPECT/CT, 2006–2007 (n = 15)	Group 3, portable γ-camera, 2008–2009 (n = 40)	Group 4, hybrid tracer, 2010–2016 (n = 192)	P
Median age	59 (IQR, 46–68)	49 (IQR, 39–62)	53 (IQR, 45–66)	54 (IQR, 45–68)	60 (IQR, 50–70)	0.007*
Breslow thickness	2.2 (IQR, 1.5–3.6)	3.0 (IQR, 1.8–4.9)	2.9 (IQR, 1.9–6.0)	2.2 (IQR, 1.5–3.4)	2.0 (IQR, 1.4–3.5)	0.003*
Mean excised SNs (n)	3.8 (CI, 3.5–4.1)	2.8 (CI, 2.0–3.5)	2.5 (CI, 1.9–3.2)	3.3 (CI, 2.7–3.8)	4.2 (CI, 3.8–4.6)	0.003*
Mean tumor-positive SNs (n)	1.5 (CI, 1.3–1.7)	1.8 (CI, 0.9–2.7)	1.3 (CI, 0–2.0)	1.2 (CI, 0.7–1.6)	1.5 (CI, 1.2–1.7)	0.90*
Median operation time (min)	115 (IQR, 87–153)	118 (IQR, 96–149)	149 (IQR, 90–164)	98 (IQR, 77–142)	115 (89–154)	0.74*
Median time per SN (min)	38 (IQR, 25–54)	51 (IQR, 33–71)	54 (IQR, 39–66)	40 (IQR, 30–51)	34 (IQR, 22–51)	0.017*
Complications (n)	12 (4.3%)	2 (7.1%)	1 (7.1%)	3 (8.1%)	6 (3.1%)	0.49†
Surgeons (n)	14	6	5	7	10	NA
Median follow-up (mo)	41 (IQR, 25–65)	85 (IQR, 31–138)	106 (IQR, 65–125)	69 (IQR, 53–88)	35 (IQR, 22–53)	NA

*One-way ANOVA.
†χ^2 (exact) test.
NA = not applicable.
Percentages may not equal 100 because of rounding.

The variety in definitions of an SN and of an FN SNB hampers meaningful comparison of results of different studies. Some investigators consider the procedure to be FN in cases of a nodal recurrence anywhere after a tumor-negative SNB, whereas in most studies only in-field nodal recurrences count (*25,37*). Instead of using the formula FN/(TP + FN) (*27*), some other investigators calculate the rate of FN over the entire group of patients or over the group of tumor-negative SNBs (*1,29,38*). The differences in follow-up duration are a further limiting factor, as the number of FN cases goes up as more recurrences develop with longer follow-up (*9*).

There is great geographic variability in the type of radiotracer used. Human serum albumin–based radiocolloids (particle range, 15–100 nm) are generally used in Europe, whereas sulfur colloids (particle range, 20–1000 nm) are commonly used in the United States and antimony sulfide colloids (particle range, 10–15 nm) in Australia (*39,40*). The more recently approved ^{99m}Tc-tilmanocept is now also being studied in the head and neck region (*41*). No randomized studies have been performed to establish superiority of one radiotracer over another.

The retrospective design, single institution, and relatively small sample size in the time span of the first 2 modalities (Table 3) can also be considered limitations of this study. Although all participating surgeons involved were dedicated head and neck specialists, their substantial number and varying experience might possibly be a limiting factor for the secondary endpoints of the study. Furthermore, the consecutive addition of new technologies without associated randomized studies makes it difficult to discern the independent contribution of each of these.

CONCLUSION

Using advanced image guidance technologies, we found more SNs without increasing the overall operation time or the postoperative complication rate, possibly indicating an improvement of surgical

TABLE 3
SNB Outcomes

Outcome	Overall, 1993–2016 (n = 277)	Group 1, lymphoscintigraphy, 1993–2005 (n = 30)	Group 2, SPECT/CT, 2006–2007 (n = 15)	Group 3, portable γ-camera, 2008–2009 (n = 40)	Group 4, hybrid tracer, 2010–2016 (n = 192)
SNB-negative (n)	210 (75.8%)	18 (60%)	12 (80%)	33 (82.5%)	147 (76.6%)
SNB-positive (n)	59 (21.3%)	10 (33.3%)	3 (20%)	6 (15%)	40 (20.8%)
FN rate (n)	8 (11.9%)	2 (16.7%)	0 (0%)	1 (14.3%)	5 (11.1%)
Sensitivity	88.1%	83.3%	100%	85.7%	88.9%
Specificity	100%	100%	100%	100%	100%

TABLE 4
Follow-up (in Months) and Recurrences

Parameter	Overall (n = 277)	SNB-negative (n = 218)	SNB-positive (n = 59)
Follow-up	41 (25–65)	44 (24–67)	37 (23–60)
Follow-up recurrence	33 (18–60)	35 (19–61)	26 (10–52)
Recurrence	81 (29%)	50 (23%)	31 (53%)
Local	21	11	10
Regional	17	12*	5
Distant	43	27	16

*Consisted of 8 FN nodes, 3 locoregional recurrences, and 1 contralateral node recurrence with simultaneous distant metastasis.
Qualitative data are number and percentage; continuous data are median and interquartile range.

efficiency. Operation time per harvested SN decreased, and the average FN rate remained 11.9% and was unchanged over 23 y.

DISCLOSURE

This work was, in part, supported by the Netherlands Organization for Scientific Research (Rubicon grant [019.171LW.022], VIDI grant [STW BGT11272], and VICI grant [AES BGT 16141]) and by a European Research Council starting grant (ERC-2012-StG-306890). Fijs van Leeuwen acts as a consultant for Hamamatsu Photonics and is chief innovation officer at ORSI Academy. Bart van de Wiel has an advisory role with BMS. No other potential conflict of interest relevant to this article was reported.

KEY POINTS

QUESTION: Does the technologic evolution of SNB in the head and neck region have an impact on the FN rate?

PERTINENT FINDINGS: This retrospective study found that, over time, there was a higher number of identified SNs with an unchanged FN rate.

IMPLICATIONS FOR PATIENT CARE: The improved outcome of the SNB procedure will make the patient's prognosis more accurate.

REFERENCES

1. Gomez-Rivera F, Santillan A, McMurphey AB, et al. Sentinel node biopsy in patients with cutaneous melanoma of the head and neck: recurrence and survival study. *Head Neck.* 2008;30:1284–1294.
2. Morton DL, Wen D-R, Wong JH, et al. Technical details of intraoperative lymphatic mapping for early stage melanoma. *Arch Surg.* 1992;127:392–399.
3. Morton DL, Cochran AJ, Thompson JF, et al. Sentinel node biopsy for early-stage melanoma: accuracy and morbidity in MSLT-I, an international multicenter trial. *Ann Surg.* 2005;242:302–311.
4. Morton DL, Thompson JF, Cochran AJ, et al. Final trial report of sentinel-node biopsy versus nodal observation in melanoma. *N Engl J Med.* 2014;370:599–609.
5. Faries MB, Thompson JF, Cochran AJ, et al. Completion dissection or observation for sentinel-node metastasis in melanoma. *N Engl J Med.* 2017;376:2211–2222.
6. O'Brien CJ, Uren RF, Thompson JF, et al. Prediction of potential metastatic sites in cutaneous head and neck melanoma using lymphoscintigraphy. *Am J Surg.* 1995;170:461–466.
7. Wells KE, Rapaport DP, Cruse CW, et al. Sentinel lymph node biopsy in melanoma of the head and neck. *Plast Reconstr Surg.* 1997;100:591–594.
8. Shpitzer T, Segal K, Schachter J, et al. Sentinel node guided surgery for melanoma in the head and neck region. *Melanoma Res.* 2004;14:283–287.
9. de Rosa N, Lyman GH, Silbermins D, et al. Sentinel node biopsy for head and neck melanoma: a systematic review. *Otolaryngol Head Neck Surg.* 2011;145:375–382.
10. Alazraki N, Glass EC, Castronovo F, et al. Society of Nuclear Medicine. Procedure guideline for lymphoscintigraphy and the use of intraoperative gamma probe for sentinel lymph node localization in melanoma of intermediate thickness 1.0. *J Nucl Med.* 2002;43:1414–1418.
11. Brouwer OR, Valdés Olmos RA, Vermeeren L, et al. SPECT/CT and a portable γ-camera for image-guided laparoscopic sentinel node biopsy in testicular cancer. *J Nucl Med.* 2011;52:551–554.
12. van der Ploeg IMC, Madu MF, van der Hage JA, et al. Blue dye can be safely omitted in most sentinel node procedures for melanoma. *Melanoma Res.* 2016;26:464–468.
13. Haque RA, Wagner A, Whisken JA, et al. Anaphylaxis to patent blue V: a case series and proposed diagnostic protocol. *Allergy.* 2010;65:396–400.
14. Howard JD, Moo V, Sivalingam P. Anaphylaxis and other adverse reactions to blue dyes: a case series. *Anaesth Intensive Care.* 2011;39:287–292.
15. Bézu C, Coutant C, Salengro A, et al. Anaphylactic response to blue dye during sentinel lymph node biopsy. *Surg Oncol.* 2011;20:e55–e59.
16. van der Ploeg IMC, Valdés Olmos RA, Nieweg OE, et al. The additional value of SPECT/CT in lymphatic mapping in breast cancer and melanoma. *J Nucl Med.* 2007;48:1756–1760.
17. Vermeeren L, Valdés Olmos RA, Klop WMC, et al. A portable γ-camera for intraoperative detection of sentinel nodes in the head and neck region. *J Nucl Med.* 2010;51:700–703.
18. van den Berg NS, Miwa M, KleinJan GH, et al. (Near-infrared) fluorescence-guided surgery under ambient light conditions: a next step to embedment of the technology in clinical routine. *Ann Surg Oncol.* 2016;23:2586–2595.
19. van den Berg NS, Brouwer OR, Schaafsma BE, et al. Multimodal surgical guidance during sentinel node biopsy for melanoma: combined gamma tracing and fluorescence imaging of the sentinel node through use of the hybrid tracer indocyanine green-^{99m}Tc-nanocolloid1. *Radiology.* 2015;275:521–529.
20. Brouwer OR, Klop WMC, Buckle T, et al. Feasibility of sentinel node biopsy in head and neck melanoma using a hybrid radioactive and fluorescent tracer. *Ann Surg Oncol.* 2012;19:1988–1994.
21. Richtlijnen hoofd-hals tumoren. Nederlandse Werkgroep Hoofd-Hals Tumoren website. http://www.nwhht.nl/richtlijnen. Accessed May 27, 2021.
22. Nieweg OE, Tanis PJ, Kroon BBR. The definition of a sentinel node. *Ann Surg Oncol.* 2001;8:538–541.
23. KleinJan GH, van Werkhoven E, van den Berg NS, et al. The best of both worlds: a hybrid approach for optimal pre- and intraoperative identification of sentinel lymph nodes. *Eur J Nucl Med Mol Imaging.* 2018;45:1915–1925.
24. Chakera AH, Hesse B, Burak Z, et al. EANM-EORTC general recommendations for sentinel node diagnostics in melanoma. *Eur J Nucl Med Mol Imaging.* 2009;36:1713–1742.
25. Nieweg OE. What is a sentinel node and what is a false-negative sentinel node? *Ann Surg Oncol.* 2004;11(suppl):169S–173S.
26. Testori A, De Salvo GL, Montesco MC, et al. Clinical considerations on sentinel node biopsy in melanoma from an Italian multicentric study on 1,313 patients (SOLISM-IMI). *Ann Surg Oncol.* 2009;16:2018–2027.
27. Nieweg OE. False-negative sentinel node biopsy. *Ann Surg Oncol.* 2009;16:2089–2091.
28. de Wilt JHW, Thompson JF, Uren RF, et al. Correlation between preoperative lymphoscintigraphy and metastatic nodal disease sites in 362 patients with cutaneous melanomas of the head and neck. *Ann Surg.* 2004;239:544–552.

29. Carlson GW, Murray DR, Lyles RH, et al. Sentinel lymph node biopsy in the management of cutaneous head and neck melanoma. *Plast Reconstr Surg.* 2005;115:721–728.
30. Vermeeren L, van der Ploeg IMC, Valdés Olmos RA, et al. SPECT/CT for preoperative sentinel node localization. *J Surg Oncol.* 2010;101:184–190.
31. Callender GG, Egger ME, Burton AL, et al. Prognostic implications of anatomic location of primary cutaneous melanoma of 1 mm or thicker. *Am J Surg.* 2011;202:659–664.
32. Hodges M, Jones E, Jones T, et al. Analysis of melanoma recurrence following a negative sentinel lymph node biopsy. *Melanoma Manag.* 2015;2:285–294.
33. Veenstra HJ, Wouters MWJM, Kroon BBR, et al. Less false-negative sentinel node procedures in melanoma patients with experience and proper collaboration. *J Surg Oncol.* 2011;104:454–457.
34. Nieweg OE, Veenstra HJ. False-negative sentinel node biopsy in melanoma. *J Surg Oncol.* 2011;104:709–710.
35. Knackstedt R, Couto RA, Gastman B. Indocyanine green fluorescence imaging with lymphoscintigraphy for sentinel node biopsy in head and neck melanoma. *Ann Surg Oncol.* 2019;26:3550–3560.
36. de Carvalho CEB, Capuzzo R, Crovador C, et al. Near infrared (NIR) fluorescence is not a substitute for lymphoscintigraphy and gamma probe for melanoma sentinel node detection: results from a prospective trial. *Ann Surg Oncol.* 2020; 27:2906–2912.
37. Saltman BE, Ganly I, Patel SG, et al. Prognostic implication of sentinel lymph node biopsy in cutaneous head and neck melanoma. *Head Neck.* 2010;32:1686–1692.
38. Chao C, Wong SL, Edwards MJ, et al. Sentinel lymph node biopsy for head and neck melanomas. *Ann Surg Oncol.* 2003;10:21–26.
39. Vidal-Sicart S, Vera DR, Valdés Olmos RA. Next generation of radiotracers for sentinel lymph node biopsy: what is still necessary to establish new imaging paradigms? *Rev Esp Med Nucl Imagen Mol.* 2018;37:373–379.
40. Scolyer RA, Thompson JF, Li LX, et al. Failure to remove true sentinel nodes can cause failure of the sentinel node biopsy technique: evidence from antimony concentrations in false-negative sentinel nodes from melanoma patients. *Ann Surg Oncol.* 2004;11(suppl):174S–178S.
41. den Toom IJ, Mahieu R, van Rooij R, et al. Sentinel lymph node detection in oral cancer: a within-patient comparison between [^{99m}Tc]Tc-tilmanocept and [^{99m}Tc]Tc-nanocolloid. *Eur J Nucl Med Mol Imaging.* 2021;48:851–858.

Diagnostic Value, Oncologic Outcomes, and Safety Profile of Image-Guided Surgery Technologies During Robot-Assisted Lymph Node Dissection with Sentinel Node Biopsy for Prostate Cancer

Elio Mazzone*[1], Paolo Dell'Oglio*[2,3,5], Nikos Grivas[3], Esther Wit[3], Maarten Donswijk[4], Alberto Briganti[1], Fijs Van Leeuwen[3,5], and Henk van der Poel[3]

[1]*Department of Urology and Division of Experimental Oncology, Urological Research Institute, IRCCS San Raffaele Scientific Institute, Milan, Italy;* [2]*Department of Urology, ASST Grande Ospedale Metropolitano Niguarda, Milan, Italy;* [3]*Department of Urology, Antoni van Leeuwenhoek Hospital, The Netherlands Cancer Institute, Amsterdam, The Netherlands;* [4]*Department of Nuclear Medicine, Antoni van Leeuwenhoek Hospital, The Netherlands Cancer Institute, Amsterdam, The Netherlands; and* [5]*Interventional Molecular Imaging laboratory, Department of Radiology, Leiden University Medical Centre, Leiden, The Netherlands*

Despite good sensitivity and a good negative predictive value, the implementation of sentinel node biopsy (SNB) in robot-assisted radical prostatectomy with extended pelvic lymph node dissection (ePLND) for prostate cancer is still controversial. For this reason, we aimed to define the added value of SNB (with different tracer modalities) to ePLND in the identification of nodal metastases. Complication rates and oncologic outcomes were also assessed. **Methods:** From January 2006 to December 2019, prospectively collected data were retrospectively analyzed from a single-institution database regarding prostate cancer patients treated with robot-assisted radical prostatectomy and ePLND with or without additional use of SNB, either with the hybrid tracer indocyanine green (ICG)–^{99m}Tc-nanocolloid or with free ICG. Multivariable logistic and Cox regression models tested the impact of adding SNB (either with the hybrid tracer or with free ICG) on lymph nodal invasion detection, complications, and oncologic outcomes. **Results:** Overall, 1,680 patients were included in the final analysis: 1,168 (69.5%) in the non-SNB group, 161 (9.6%) in the ICG-SNB group, and 351 (20.9%) in the hybrid-SNB group. The hybrid-SNB group (odds ratio, 1.61; 95%CI, 1.18–2.20; $P = 0.002$) was an independent predictor of nodal involvement, whereas the ICG-SNB group did not reach independent predictor status when compared with the non-SNB group (odds ratio, 1.35; 95%CI, 0.89–2.03; $P = 0.1$). SNB techniques were not associated with higher rates of complications. Lastly, use of hybrid SNB was associated with lower rates of biochemical recurrence (0.79; 95%CI, 0.63–0.98) and of clinical recurrence (hazard ratio, 0.76, $P = 0.035$) than were seen in the non-SNB group. **Conclusion:** The implementation of hybrid-SNB technique with ICG–^{99m}Tc-nanocolloid in prostate cancer improves detection of positive nodes and potentially lowers recurrence rates with subsequent optimization of patient management, without harming patient safety.

Key Words: image-guided surgery; indocyanine green; fluorescence; lymph node dissection; sentinel node biopsy; prostate cancer

J Nucl Med 2021; 62:1363–1371
DOI: 10.2967/jnumed.120.259788

Received Nov. 11, 2020; revision accepted Jan. 13, 2021.
For correspondence or reprints, contact Elio Mazzone (mazzone.elio@hsr.it).
*Contributed equally to this work.
Published online February 5, 2021.

During the last decade, there has been increasing interest in identifying and implementing new staging modalities for lymphatic metastatic dissemination in prostate cancer patients. An extended pelvic lymph node dissection (ePLND) represents the best available staging tool for prostate cancer patients with a risk of lymph node invasion (LNI) higher than 5% (*1*, *2*). Although this approach is invasive, it can still miss aberrant dissemination pathways to approximately 30% of lymph nodes—those that are outside the ePLND template (*2*). Tailored staging modalities that help predict the routes of lymphatic spread, such as sentinel node biopsy (SNB), have been proposed to improve the accuracy of ePLND in identifying nodal metastases (*3*, *4*). Despite the good sensitivity and good negative predictive value of SNB (*2*), its added value relative to ePLND in detecting LNI remains a subject of discussion. As a consequence, SNB in prostate cancer is still considered experimental (*2*). One concern is that the safety profile of adding SNB to ePLND, in terms of complications, has never been tested. Finally, evidence supporting the oncologic benefit of SNB and ePLND in prostate cancer is still limited and often controversial (*1*, *5*–*7*).

On this basis and to overcome these limitations, we used the largest available case series of patients who underwent robot-assisted radical prostatectomy and ePLND with or without SNB to define the effect of SNB and different SNB tracer modalities on LNI staging accuracy, complication rates, and midterm oncologic outcomes.

MATERIALS AND METHODS

Data Source and Patient Selection

From January 2006 to December 2019, prospectively collected data were retrospectively analyzed from a single-institution database (Antoni van Leeuwenhoek Hospital, The Netherlands Cancer Institute, Amsterdam) regarding prostate cancer patients treated with robot-assisted radical prostatectomy and standard ePLND with or without additional use of SNB. SNB was performed using either the hybrid fluorescent and radioactive tracer indocyanine green (ICG)–^{99m}Tc-nanocolloid or free ICG (*8*–*10*). We focused on patients with more than a 5% risk of LNI according to the nomogram of Briganti et al. (*11*), which has been found to be one of the most accurate predictive

models for LNI in external validation studies (*12*), particularly for the time span of our analysis. All surgeries were performed by the robotic approach, and all patients with complete follow-up pathologic data and recurrence data were included. Overall, 1,680 patients were included in the final analysis: 1,168 (69.5%) who were offered ePLND only (non-SNB group), 161 (9.6%) who received ePLND complemented by SNB using free ICG (ICG-SNB group), and 351 (20.9%) who received ePLND complemented by SNB using ICG–^{99m}Tc-nanocolloid (hybrid-SNB group). Patients receiving ePLND without SNB were treated between 2006 and 2019, those receiving ePLND and hybrid tracer were treated between 2010 and 2019, and those receiving ICG SNB were treated between 2016 and 2019.

The study protocol was approved by the institutions' medical ethics committees (approvals NL28143.031.09, NL41285.031.12, and NL46580.031.13). An approval from the institutional review board was received for the data collection and analysis.

SNB and ePLND Technique

The ePLND, SNB technique, and pathologic examination were previously described (*13*). Patients first underwent SNB, followed by ePLND and robot-assisted radical prostatectomy. Sentinel nodes (SNs) were identified via lymphatic mapping with ICG–^{99m}Tc-nanocolloid (0.5 mg of albumin, 0.25 mg of ICG, and 240 MBq of ^{99m}Tc in 2 mL of saline) or free ICG (5 mg in 2 mL of sterile water).

On the morning of the surgery, ICG–^{99m}Tc-nanocolloid (2 mL) was transrectally injected under ultrasound guidance into the peripheral zone of each quadrant of the prostate, as previously described (*14*, *15*). Early and late dynamic lymphoscintigraphy was performed at, respectively, 15 min and 2 h after injection. In the hybrid-SNB group, preoperative SN mapping was performed with lymphoscintigraphy and SPECT supplemented with low-dose CT (SPECT/CT). The nuclear medicine physician assessed all acquired images and reported the anatomic localization of the individual SNs. Surgery was planned to start 4 h after the ICG–^{99m}Tc-nanocolloid injection. All SNs were pursued with radioguidance and fluorescence guidance. The radioguidance was provided by the Europrobe laparoscopic 0° γ-probe (Eurorad S.A.) used in combination with a sterile cover. The fluorescence guidance was provided by the integrated FireFly camera of the DaVinci Si robotic system (Intuitive Surgical).

In the ICG-SNB group, 2 mL of ICG were transrectally injected in the operating room under ultrasound guidance before the surgery began. All SNs were pursued with FireFly fluorescence guidance (*15*) followed by an ePLND template, which was defined as the region encompassed by the ureteric crossing and including the bifurcation of the common iliac artery, along the external iliac (the distal limit being the deep circumflex vein and femoral canal), the internal iliac vessels, and the obturator fossa. The lateral border was the genitofemoral nerve, and the medial border was the perivesical fat. Thirteen surgeons were included in the current large cohort of individuals who performed robot-assisted radical prostatectomy, but the SNB procedures were performed exclusively by 3 surgeons.

Outcomes

The primary endpoint of our study was to assess the added value of SNB to ePLND in the identification of nodal metastases. Additionally, we tested the lymph node detection rate according to the preoperative LNI risk, based on the 2012 version of the nomogram of Briganti et al. (*11*). Secondary endpoints were the safety profile of SNB by reporting rates of postoperative complications and midterm oncologic outcomes, namely biochemical recurrence (BCR) and clinical recurrence (CR). BCR was defined as 2 consecutive prostate-specific antigen measures of at least 0.2 ng/mL (*2*). CR consisted of any radiologically confirmed locoregional or distant tumor recurrence. Postoperative complications were graded according to the Clavien–Dindo classification (*16*).

Variable Definition

The clinical covariates were age at surgery, use of neoadjuvant androgen deprivation therapy, clinical T stage (T1c, T2, T3), clinical N stage (Nx, N0, N1), biopsy Gleason score, and preoperative initial level of prostate-specific antigen. Pathologic and postoperative covariates consisted of pathologic T stage (≤pT2, pT3a, ≥pT3b), pathologic N stage (pN0, pN1), pathologic Gleason score (*6–10*), number of lymph nodes removed, presence of positive surgical margins, and use of salvage radiation therapy.

Statistical Analysis

Statistical analyses, as well as reporting and interpretation of the results, were conducted according to established guidelines (*17*) and consisted of 4 steps. First, medians and interquartile ranges were reported for continuous variables, and frequencies and proportions were reported for categoric variables. The Mann–Whitney and χ^2 tests were applied to compare the statistical significance of differences in the distribution of continuous or categoric variables, respectively.

Second, multivariable logistic regression models were fitted to assess the impact of SNB (non-SNB group vs. hybrid-SNB group vs. ICG-SNB group) on LNI rate at the final pathologic examination, after adjusting for several clinical confounders. Models were adjusted using prespecified clinical covariates. Thereafter, the multivariable-derived probability of LNI detection according to different SNB methods was plotted against preoperative score according to the nomogram of Briganti et al. (*11*) using a locally weighted scatterplot smoother function (*18*, *19*), after accounting for the confounders.

Third, 2 sets of logistic regression models were fitted to test the impact of SNB use and type on postoperative complications, after adjusting for age at surgery, neoadjuvant androgen deprivation therapy, cT stage, cN stage, preoperative prostate-specific antigen level, and biopsy Gleason score. Logistic regression models were repeated for a Clavien–Dindo grade of at least II and at least III. Additionally, to test the hypothesis that refinements in SN technique may have impacted the complication rate, an interaction term between type of SN (non-SNB group vs. hybrid-SNB group vs. ICG-SNB group) and year of surgery was used.

Fourth, Kaplan–Meier plots were used to depict BCR- and CR-free survival after stratification according to non-SNB group versus hybrid-SNB group versus ICG-SNB group. Finally, multivariable Cox regression models tested for predictors of BCR and CR. Previously defined pathologic covariates were included as predictors in Cox regression models. Moreover, models predicting CR were further adjusted for the use of salvage radiation therapy. Analyses were performed using R software, version 3.6.3, and all tests were 2-sided with the significance level set at a P value of less than 0.05.

RESULTS

Patient Characteristics

Table 1 and Figure 1 depict the clinical characteristics of our cohort. Compared with the non-SNB group, the patients of the ICG-SNB group were older (67 vs. 65 y old, $P < 0.001$), and more had a Gleason score of 8–10 at biopsy (41.6% vs. 29.4%, $P < 0.001$) or cN1 at preoperative imaging (15.5% vs. 5.7%, < 0.001). No statistically significant differences in cT stage or prostate-specific antigen at surgery were recorded between the ICG-SNB and non-SNB groups. On the other hand, more of the patients in the hybrid-SNB group than in the non-SNB group had a Gleason score of 7 at biopsy (65.2% vs. 54%, $P < 0.001$), and fewer had cN1 at preoperative imaging (0.9% vs. 5.7%, < 0.001). When compared with the ICG-SNB group, fewer of the patients in the hybrid-SNB group had cN1 at preoperative imaging (0.9% vs. 15.5%, $P < 0.001$), and the hybrid-SNB group had a lower

TABLE 1
Patient Characteristics

Characteristic	Parameter	Overall	Non-SNB, n = 1,168 (69.5%)	ICG SNB, n = 161 (9.6%)	P, non-SNB vs. ICG SNB	Hybrid SNB, n = 351 (20.9%)	P, non-SNB vs. hybrid SNB	P, ICG SNB vs. hybrid SNB
PSA before treatment (ng/mL)	Median	9.5	9.7	9.4	0.6	9	0.002	0.1
	IQR	6.8–16	6.9–16	6.7–18		6.4–14		
Age (y)	Median	65	65	67	<0.001	65	0.1	<0.001
	IQR	60–69	60–68	64–71		60.5–69		
Briganti LNI risk*	Median	12.6	11.9	20.5	<0.001	12.4	0.4	<0.001
	IQR	6.1–30.5	5.6–29.1	10.9–41.7		6.2–29.2		
Biopsy GS	6	212 (12.6)	187 (16)	7 (4.3)	<0.001	18 (5.1)	<0.001	0.03
	7	954 (56.8)	638 (54.6)	87 (54)		229 (65.2)		
	8–10	514 (30.6)	343 (29.4)	67 (41.6)		104 (29.6)		
cT	cT1c	250 (14.9)	180 (15.4)	18 (11.2)	0.3	52 (14.8)	0.8	0.5
	cT2	941 (56)	655 (56.1)	94 (58.4)		192 (54.7)		
	≥cT3	489 (29.1)	333 (28.5)	49 (30.4)		107 (30.5)		
Percentage of positive cores	<33%	454 (27)	319 (27.3)	23 (14.3)	<0.001	112 (31.9)	0.2	<0.001
	33%–66%	711 (42.3)	504 (43.2)	67 (41.6)		140 (39.9)		
	>66%	515 (30.7)	345 (29.5)	71 (44.1)		99 (28.2)		
cN	cNx	387 (23)	323 (27.7)	3 (1.9)	<0.001	61 (17.4)	<0.001	<0.001
	cN0	1198 (71.3)	778 (66.6)	133 (82.6)		287 (81.8)		
	cN1	95 (5.7)	67 (5.7)	25 (15.5)		3 (0.9)		
Follow-up (mo)	Median	38	46.5	15	<0.001	35	<0.001	<0.001
	IQR	14–66	17–70	7–25		14–58		
Operative time (min)	Median	119	115	111	0.01	121	<0.001	<0.001
	IQR	100–126	99–128	97–121		113.5–131		
LNs removed	Median	12	11	20	<0.001	17	<0.001	<0.001
	IQR	8–18	6–15	17–25		11–21		
pN stage	pN0	1 302 (77.5)	947 (81.1)	103 (64)	<0.001	252 (71.8)	<0.001	<0.001
	pN1	378 (22.5)	221 (18.9)	58 (36)		99 (28.2)		
Pathologic GS	6	158 (9.4)	129 (11)	3 (1.9)	<0.001	26 (7.4)	0.1	<0.001
	7	1 116 (66.4)	754 (64.6)	131 (81.4)		231 (65.8)		
	8–10	406 (24.2)	285 (24.4)	27 (16.8)		94 (26.8)		
pT stage	≤pT2c	851 (50.7)	593 (50.8)	55 (34.2)	<0.001	203 (57.8)	0.005	<0.001
	pT3a	411 (24.5)	260 (22.3)	68 (42.2)		83 (23.6)		
	≥pT3b	418 (24.9)	315 (27)	38 (23.6)		65 (18.5)		
Positive nodes	>2	121 (7.2)	68 (5.8)	19 (11.8)	<0.001	34 (9.7)	<0.001	0.1
	0	1 302 (77.5)	948 (81.2)	102 (63.4)		252 (71.8)		
	1–2	257 (15.3)	152 (13)	40 (24.8)		65 (18.5)		
Surgical margins	Negative	1 054 (62.7)	712 (61)	102 (63.4)	0.6	240 (68.4)	0.01	0.3
	Positive	626 (37.3)	456 (39)	59 (36.6)		111 (31.6)		
Salvage radiotherapy	No	1 232 (73.3)	843 (72.2)	133 (82.6)	0.006	256 (72.9)	0.8	0.02
	Yes	448 (26.7)	325 (27.8)	28 (17.4)		95 (27.1)		

*According to nomogram of Briganti et al. (11).
PSA = prostate-specific antigen; IQR = interquartile range; GS = Gleason score; LN = lymph nodes.
Qualitative data are number followed by percentage in parentheses.

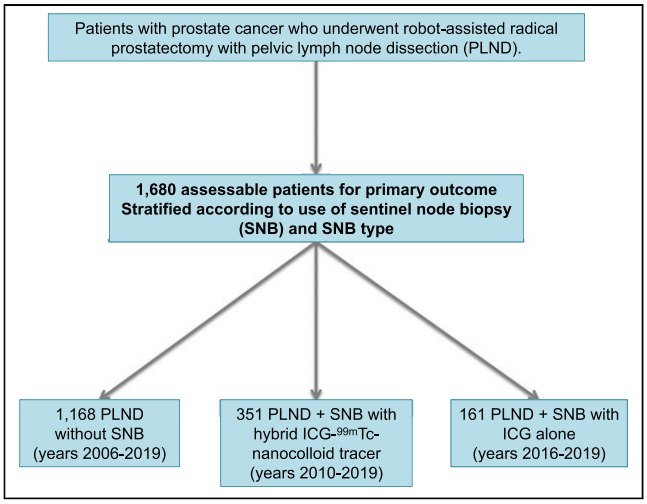

FIGURE 1. Flowchart describing final patient population included in study and implementation of different tracers for SNB over time.

median preoperative LNI risk score (12.4 vs. 20.5, $P < 0.001$). Regarding operative time, the ICG-SNB group had a shorter surgical median duration (111 min) than either the hybrid-SNB group (121 min) or the non-SNB group (115 min) ($P = 0.001$ and 0.01, respectively). Lastly, the rate of administration of salvage radiation therapy did not differ between the hybrid-SNB group (27.1%) and the non-SNB group (27.8%) ($P = 0.8$), whereas it was lower in ICG-SNB group (17.4%) than in either the hybrid-SNB group ($P = 0.02$) or the non-SNB group ($P = 0.006$).

Pathologic Report and Nodal Staging

Pathologic findings are reported in Table 1. Overall, in patients from the ICG-SNB group, disease was less frequently organ-confined (≤pT2c: 34% vs. 50.8%, $P < 0.001$) than in the non-SNB group, and fewer had a Gleason score of 8–10 (16.8% vs. 24.4%, $P < 0.001$). Notably, the rate of pN1 in the ICG-SNB group was double that in the non-SNB group (36% vs. 18.9%, $P < 0.001$). Along the same line, the nodal yield increased for the ICG-SNB group (median, 20 vs. 11; $P < 0.001$), yielding a higher rate of patients with more than 2 positive nodes at pathology (11.8% vs. 5.8%, $P < 0.001$). Similarly, the pN1 rate (28.2% vs. 18.9%, $P < 0.001$), the number of removed LNs (median, 17 vs. 11; $P < 0.001$), and the rate of patients with more than 2 positive nodes (9.7 vs. 5.8, $P < 0.001$) were remarkably higher in patients from the hybrid-SNB than in patients from the non-SNB group. Compared with the ICG-SNB group, patients in the hybrid-SNB group had a lower pN1 rate (28% vs. 36%, $P < 0.001$) and a lower number of lymph nodes removed (median, 17 vs. 20; $P < 0.001$).

In multivariable models predicting pN1, being in the hybrid-SNB group (odds ratio [OR], 1.61; 95%CI, 1.18–2.20; $P = 0.002$) was an independent predictor of LNI detection at final pathology, compared with being in the non-SNB group, after accounting for all preoperative covariates including number of removed nodes. On the other hand, being in the ICG-SNB group did not reach independent predictor status when compared with being in the non-SNB group (OR, 1.35; 95%CI, 0.89–2.03; $P = 0.1$; Table 2)[ID]TBL2[/ID]. Compared with being in the ICG-SNB group, being in the hybrid-SNB group (OR, 1.19; 95%CI, 0.76–1.86; $P = 0.4$) was not associated with a significant increase in LNI detection at final pathology.

Subsequently, we graphically represented the variation in pN1 detection rate for the hybrid-SNB technique versus the non-SNB technique across different preoperative LNI risk levels calculated according to the nomogram of Briganti et al. (Fig. 2) (*11*). Use of the hybrid-SNB approach was associated with a higher pN1 detection rate across all predicted levels of preoperative LNI risk.

Postoperative Complications

Overall, 572 (34%) patients experienced postoperative complications (Table 3). According to the Clavien–Dindo classification, 78 patients (4.6%) experienced grade I complications; 237 (14.1%), grade II; 128 (7.6%), grade IIIa; 72 (4.3%), grade IIIB; and 3 (0.2%), grade IV. The overall rate of complications that were at least grade II was 25.1%, 25.5%, and 30.2% in the non-SNB, ICG-SNB, and hybrid-SNB groups, respectively. Similarly, complications of at least grade IIIa were found in 11.8%, 11.2%, and 13.4% of patients in the respective groups.

In multivariable models, the ICG-SNB group was not associated with a higher rate of experiencing at least a grade II complication (OR 1.22, 95%CI 0.80–1.85, $P = 0.3$; Table 4) or at least a grade IIIa complication (OR, 1.02; 95%CI, 0.56–1.77; $P = 0.9$; Table 4), whereas the hybrid-SNB group tended to have a higher risk of at least a grade II complication (OR, 1.30; 95%CI, 0.98–1.70; $P = 0.059$; Table 4) but not of at least a grade III complication (OR, 1.16; 95%CI, 0.79–1.67; $P = 0.4$; Table 4). Of note, the year of surgery was associated with a reduced risk of complications that were at least grade II (OR, 0.927; 95%CI, 0.889–0.967; $P < 0.001$) or at least grade IIIa (OR, 0.922; 95%CI, 0.872–0.974; $P = 0.004$), demonstrating a reduction of complication rates over time (Table 4). Particularly, the interaction test for the hypothesis that refinements in SNB technique in more recent years reduced postoperative complication of grade II or higher was statistically significant for the hybrid-SNB group (OR, 0.90; 95%CI, 0.81–0.99; $P = 0.041$). Specifically, the risk of experiencing at least a grade II complication decreased approximately 10% every year when compared with the risk of experiencing at least a grade II complication with standard lymph node dissection. On the other hand, no significant interaction with year of surgery was recorded for the ICG-SNB group (Table 4).

Finally, no statistically significant interaction was found between the year of surgery and complications that were grade IIIa or higher; therefore, technical refinement of the SNB procedure over time did not affect the rate of severe complications (all $P > 0.05$).

Oncologic Outcomes

At 5 y of follow-up, unadjusted Kaplan–Meier plots depicted BCR-free survival rates of 54.9% for the non-SNB group, 38.4% for the ICG-SNB group, and 57.7% for the hybrid-SNB group ($P = 0.39$; Supplemental Fig. 1A; supplemental materials are available at http://jnm.snmjournals.org). Similarly, 5-y CR-free survival rates were 67%, 73%, and 67.4% ($P = 0.9$) for the respective groups (Supplemental Fig. 1B). In multivariable Cox models, being in the ICG-SNB group was not an independent predictor of BCR (hazard ratio [HR], 0.84; 95%CI, 0.61–1.15; $P = 0.2$) or CR (HR, 0.73; 95%CI, 0.49–1.15; $P = 0.1$), compared with being in the non-SNB group. Conversely, being in the hybrid-SNB

TABLE 2
Multivariable Logistic Regression Model Predicting Detection of Positive Nodes at Final Pathology

Variable	Parameter	OR	95%CI	*P*
cT stage	cT1c	Ref		
	cT2	1.14	0.74–1.79	0.4
	≥cT3	3.25	2.11–5.14	<0.001
Biopsy GS	6	Ref		
	7	1.99	1.20–3.46	0.009
	8–10	3.00	1.79–5.27	<0.001
cN stage	cNx	Ref		
	cN0	0.85	0.58–1.23	0.4
	cN1	3.02	1.84–4.98	<0.001
Percentage of positive cores		1.633	1.371–1.94	<0.001
PSA at RP		1.010	1.002–1.018	0.01
Number of removed nodes		1.032	1.015–1.049	<0.001
SNB use	Non-SNB	Ref		
	ICG SNB	1.35	0.89–2.03	0.1
	Hybrid SNB	1.61	1.18–2.20	0.002

Ref = reference; GS = Gleason score; PSA = prostate-specific antigen; RP = radical prostatectomy.

group was associated with a lower risk of BCR (HR, 0.79; 95%CI, 0.63–0.98; $P = 0.037$) and of CR (HR, 0.76; 95%CI, 0.58–0.98; $P = 0.035$) than was being in the non-SNB group (Table 5). As further confirmation of these results, when the hybrid-SNB group was considered a reference, the ICG-SNB group did not differ from it in BCR (HR, 1.06; 95%CI, 0.75–1.50; $P = 0.7$) or CR (HR, 0.97; 95%CI, 0.63–1.49; $P = 0.9$), whereas the non-SNB group had a higher risk of BCR (HR, 1.26; 95%CI, 1.01–1.57; $P = 0.037$) and CR (HR, 1.32; 95%CI, 1.02–1.71; $P = 0.035$). Graphical representations of the multivariable adjusted Cox-derived BCR- and CR-free survival using Kaplan–Meier plots are shown in Figures 3A and 3B.

DISCUSSION

In this largest (to our knowledge) retrospective series of prostate cancer patients treated with robot-assisted radical prostatectomy and ePLND with or without SNB, we tested the impact of SNB on different outcomes, namely LNI staging accuracy, complication rates, and midterm oncologic outcomes. These aims were based on recent literature suggesting a potential benefit from using SNB to detect nodal metastases outside the standard ePLND template (*20*). Additionally, other evidence suggested that the addition of SNB, compared with standard ePLND, is associated with a potential decrease in the BCR rate (*5*). Our analyses highlighted several important findings.

First, the findings in the non-SNB group underlined that meticulous ePLND does not ensure complete accuracy with regard to nodal status. Adding SNB to standard ePLND improved the LNI detection rate in univariable analysis. Specifically, ICG–^{99m}Tc-nanocolloid allowed detection of 10% more LNI than did ePLND without SNB. Similarly, ICG was associated with an 18% absolute increase in the LNI detection rate, relative to standard ePLND (Table 1). Our results reinforce recent findings in a systematic review of the diagnostic accuracy of the SNB procedure in prostate cancer (*4*). In that review, the SN or SNs were the only metastatic site or sites in 73% of LN-positive patients, and positive LNs would have been missed without SNB in 1 of 20 patients who underwent ePLND (*4*). Our findings confirm that SNB should always be combined with ePLND, as supported by a recent SN consensus panel (*21*). Despite being in line with previous series based on tertiary-care referral centers (*6*, *22*) or population-based data repositories (*23*), it may be argued that the lower lymph nodal yield in the non-SNB group (median, 11 nodes) than in the hybrid-SNB or ICG-SNB group might have affected the reported differences in LNI. However, we demonstrated for the first time (to our knowledge) that in a multivariable model accounting for multiple confounders including the number of nodes removed, there was diagnostic added value for the hybrid-SNB group (OR, 1.65) but not for the ICG-SNB group (OR, 1.35). This finding suggests that ICG extends the ePLND template without providing specific guidance on aberrant lymphatic drainage pathways, whereas the hybrid tracer highlights aberrant drainage profiles, impacting the ePLND template. The fact that these aberrant profiles are seen at preoperative imaging impacts the ePLND template used during surgery. Additionally, when we graphically explored the variation in the actual LNI rate for the hybrid-SNB group versus the non-SNB group across different levels of preoperative LNI risk, we

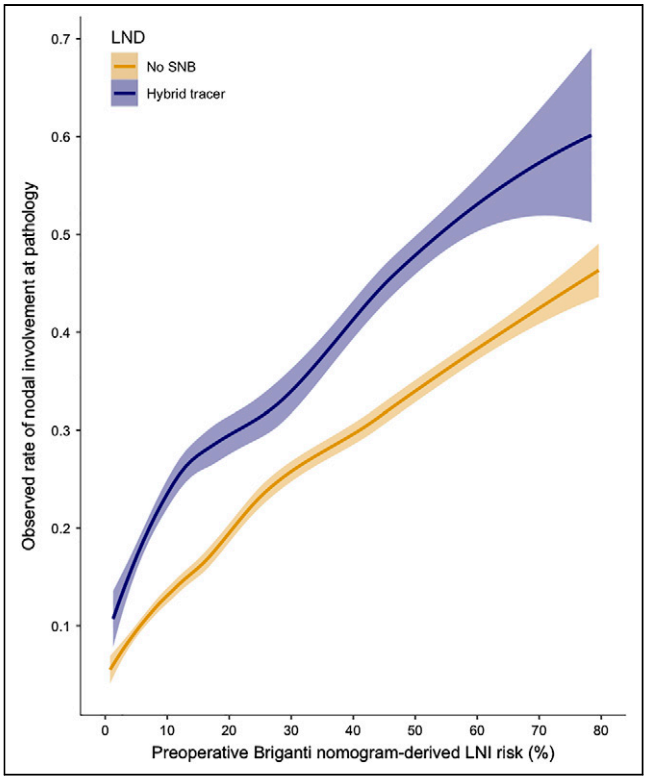

FIGURE 2. Locally weighted scatterplot smoothing plot representing observed LNI rate at final pathology plotted against preoperative predicted risk of nodal involvement calculated according to nomogram of Briganti et al. (11), stratified according to use of hybrid SNB or no SNB. LND = lymph node dissection.

confirmed that the hybrid-SNB approach was associated with a higher pN1 detection rate across all predicted levels of preoperative LNI risk, corroborating the accuracy of SNB in detecting pN1 both in low-risk and in high-risk patients. For instance, for a preoperative predicted risk of LNI of 20%, the intraoperative guidance of the hybrid tracer can reduce the risk of false-negative findings by approximately 10%, meaning that in 1 of 10 patients who underwent lymph node dissection, a lymph nodal invasion would have been missed without using SNB with the hybrid tracer.

Second, when we assessed the safety profile of the SNB procedure, we observed that neither ICG SNB nor hybrid SNB was associated with an increased risk of postoperative complications that were at least Clavien–Dindo grade II. Thus, SNB appears to be safe and can be implemented in routine clinical practice without exposing patients to a higher risk of complications. Also, the interaction term between year of surgery and SNB showed a significant reduction of these grade II or higher complications over time for the hybrid tracer, which historically was also the first to be applied (non-SNB, 2006–2019; ICG SNB, 2016–2019; hybrid SNB, 2010–2019). This finding suggests that the time during which the hybrid tracer was used allowed for refinement of the surgical skill with which the SNB procedure was performed. This learning curve seems to have benefited the ICG-SNB group, which was the last to be initiated. Regarding high-grade complications (Clavien–Dindo grade $\geq$ III), we failed to observe any effect of year of surgery on SNB, suggesting that severe complications are not related to the SNB procedure. Lastly, the addition of SNB with a hybrid tracer was associated with a longer operative time than was needed for ePLND alone or for SNB with free ICG, probably because of the time needed to introduce and guide the laparoscopic γ-probe toward the target tissue. However, such differences were small (median, +6 min and +10 min, respectively; Table 1) and, in consequence, had a very limited clinical impact.

Third, when we explored the effect of SNB on oncologic outcomes, we found that the risk of BCR was significantly lower for the hybrid-SNB group than for the non-SNB group; there was a 20% lower risk of harboring BCR. We failed to observe this benefit for the ICG-SNB group. Our findings corroborated previous evidence that adding SNB to ePLND improves BCR-free survival (*5*), when we added a subanalysis according to type of SNB tracer used. This protective effect of

TABLE 3
Complication Rates and Grading

Variable	Parameter	Overall	Non-SNB, *n* = 1,168 (69.5%)	ICG SNB, *n* = 161 (9.6%)	Hybrid SNB, *n* = 351 (20.9%)
Any postoperative complication	No	1,108 (66)	777 (66.5)	115 (71.4)	216 (61.5)
	Yes	572 (34)	391 (33.5)	46 (28.6)	135 (38.5)
Clavien–Dindo grade*	I	78 (4.6)	58 (5)	4 (2.5)	16 (4.6)
	II	237 (14.1)	155 (13.3)	23 (14.3)	59 (16.8)
	IIIa	128 (7.6)	80 (6.8)	16 (9.9)	32 (9.1)
	IIIb	72 (4.3)	56 (4.8)	2 (1.2)	14 (4)
	IV	3 (0.2)	2 (0.2)	0 (0)	1 (0.3)
	Unknown	54 (3.2)	40 (3.4)	1 (0.6)	13 (3.7)

*Patients may have experienced more than one complication.
Data are number followed by percentage in parentheses.

TABLE 4
Multivariable Logistic Regression Models Predicting Clavien–Dindo Grade ≥ 2 and ≥ 3 Before and After Testing for Interaction Between Type of SNB and Year of Surgery

		Grade ≥ 2				Grade ≥ 3			
Variable	Parameter	OR	2.5%	97.5%	*P*	OR	2.5%	97.5%	*P*
Age		1.008	0.990	1.027	0.3	1.025	1.000	1.052	0.046
Year of surgery		0.927	0.889	0.967	<0.001	0.922	0.872	0.974	0.004
SNB type	No SNB								
	ICG only	1.22	0.80	1.85	0.3	1.02	0.56	1.77	0.9
	ICG + ^{99m}Tc	1.30	0.98	1.70	0.059	1.16	0.79	1.67	0.4
cT stage	cT1c								
	cT2	0.87	0.64	1.20	0.4	1.01	0.66	1.56	0.9
	≥cT3	0.71	0.50	1.02	0.06	0.63	0.39	1.05	0.07
Biopsy GS	≤6								
	7	1.39	0.96	2.06	0.08	1.95	1.14	3.50	0.01
	8–10	1.62	1.09	2.44	0.01	1.66	0.94	3.07	0.08
cN stage	cN0								
	cNx	0.65	0.47	0.89	0.009	0.50	0.32	0.78	0.002
	cN1	0.90	0.52	1.49	0.7	1.35	0.68	2.46	0.3
PSA at surgery		0.989	0.978	0.998	0.038	0.998	0.986	1.008	0.8
Neo-ADT	No								
	Yes	1.14	0.79	1.62	0.4	1.34	0.84	2.09	0.1
SNB–year interaction	No SNB	Ref							
	SNB and ICG	1.41	0.97	2.12	0.08	1.21	0.75	2.11	0.4
	SNB and ICG + ^{99m}Tc	0.90	0.81	0.99	0.041	1.06	0.93	1.21	0.3

GS = Gleason score; PSA = prostate-specific antigen; ADT = androgen deprivation therapy; Ref = reference.

the hybrid tracer on BCR may be explained by the identification of aberrant lymphatic drainage pathways that are not usually included in standard lymph-node-dissection templates, thus optimizing nodal staging and improving patient management. Moreover, after adjusting for use of salvage radiation therapy, we confirmed the added value of the hybrid tracer when CR was assessed. Specifically, the hybrid tracer was associated with a significant, 24%, reduction in the risk of experiencing CR. These findings are noteworthy, and to the best of our knowledge, we are the first to demonstrate that adding SNB with a hybrid tracer to ePLND potentially reduces the risk of locoregional or distant recurrence. However, considering the relatively short follow-up and the limited number of events in our cohort, further studies are needed to confirm our results.

Recently, a new γ-probe for image-guided robotic surgery was developed (i.e., a drop-in probe) and implanted into clinical practice (*24–27*). Its increased maneuverability yielded a higher in vivo SN detection rate than that of a laparoscopic rigid γ-probe (*25*), suggesting that the impact of hybrid SNB might be further improved in future studies that rely on the drop-in probe as radioguidance in the robotic setting. It is also interesting that the FireFly fluorescence guidance realized within the hybrid-SNB group was achieved while injecting a 20-times-lower amount of ICG than in the ICG-SNB group. Lastly, even though we did not specifically assess the cost of the SNB procedures in the current analysis, the SNB correlated with additional technologic resources (e.g., γ-probe, drop-in probes, and SPECT/CT), extra scanning time (fees vary across the health-care systems of different countries), and longer operative time, in turn increasing the overall costs of the procedure. Therefore, this point should be considered when SNB is implemented in a routine surgical practice. However, the prices of γ-probes are expected to decrease soon because of their expanding use and novel (hybrid) camera systems (*28*).

Despite its strengths, our study was not devoid of limitations. First, our report is based on a retrospective analysis, with all of its inherent limitations, and bias in selecting patients for specific methods of ePLND cannot be excluded. Second, our data reflect a single tertiary-care referral center with a high volume of SN procedures and trained surgeons for radioguided SN procedures. On the basis of the impact that nuclear medicine imaging had on the success of the hybrid-SNB group, the generalizability of our findings may be limited to centers with a nuclear medicine department. Third, the median follow-up was relatively short. Future randomized controlled trials are needed to confirm the findings reported here. Fourth, the fact that the ICG-SNB group was considerably smaller than the hybrid-SNB group might have influenced

TABLE 5
Multivariable Cox Regression Models Predicting BCR and CR in Patients Undergoing ePLND With or Without SNB

		BCR			BCR		
Variable	Parameter	HR	95%CI	*P*	HR	95%CI	*P*
SNB technique	Non-SNB	Ref					
	ICG SNB	0.84	0.61–1.15	0.2	0.73	0.49–1.11	0.1
	Hybrid SNB	0.79	0.63–0.98	0.037	0.76	0.58–0.98	0.035
pN stage	pN0						
	pN1	3.11	2.59–3.72	<0.001	3.40	2.74–4.23	<0.001
PSA at surgery		1.009	1.006–1.01	<0.001	1.010	1.006–1.014	<0.001
Pathologic GS	6						
	7	1.91	1.17–3.10	0.009	3.77	1.53–9.26	0.003
	8–10	3.50	2.13–5.74	<0.001	8.84	3.59–21.7	<0.001
pT stage	≤pT2c						
	pT3a	1.63	1.30–2.06	<0.001	1.99	1.50–2.64	<0.001
	≥pT3b	2.17	1.74–2.71	<0.001	2.17	1.66–2.85	<0.001
PSM	No						
	Yes	1.23	1.04–1.46	0.01	0.93	0.76–1.14	0.5
Number of removed nodes		1.005	0.994–1.018	0.3	1.00	0.985–1.015	0.9
Salvage radiation therapy	No	–			Ref		
	Yes	–			1.29	0.92–1.58	0.1

Ref = reference; PSA = prostate-specific antigen; GS = Gleason score; PSM = positive surgical margins.

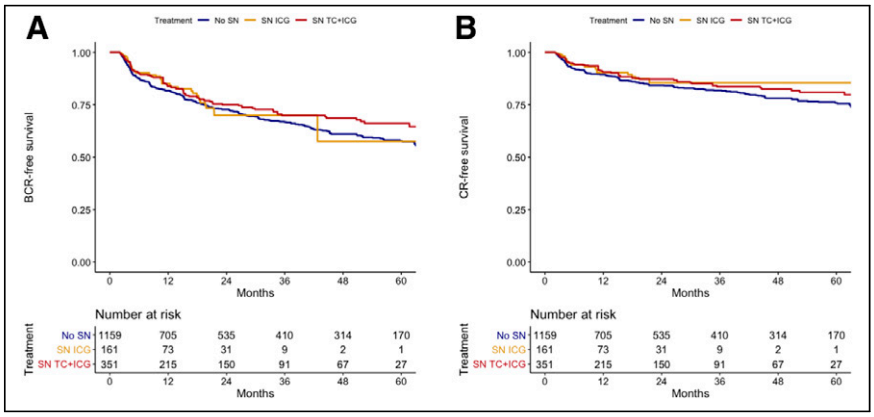

FIGURE 3. Kaplan–Meier plots depicting multivariable Cox-derived BCR-free (A) and CR-free (B) survival after robot-assisted radical prostatectomy and ePLND with or without use of additional SNB (either hybrid tracer or free ICG). TC = ^{99m}Tc.

our findings; this possibility needs further validation in a bigger sample size. Lastly, the current study did not involve the use of hybrid tracers relying on prostate cancer–specific biomarkers such as ^{99m}Tc-based prostate-specific membrane antigen (^{99m}Tc-PSMA). However, despite having a lower specificity for prostatic tissue than ^{99m}Tc-PSMA does, the ICG–^{99m}Tc-nanocolloid tracer has important advantages. It allows intraoperative delineation of the lymphatic drainage profile of the prostate—something not possible with PSMA-based tracers, which, conversely, allow identification of metastatic lesions, when present, but not definition of the lymphatic drainage profile. Moreover, the intraoperative use of PSMA-based tracers was tested mainly in the context of recurrent prostate cancer in patients with a positive lesion on preoperative PET/CT (*29*); therefore, its utility and staging accuracy in the primary treatment of intermediate- or high-risk patients is still under evaluation.

CONCLUSION

SNB with the hybrid tracer ICG–^{99m}Tc-nanocolloid improves the LNI detection rate in prostate cancer patients, reducing the risk of false-negative findings at final pathology without increasing postoperative complications. Moreover, we find that this method may have a potential benefit in terms of BCR and CR.

DISCLOSURE

This research was in part supported by an NWO-TTW-VICI grant (TTW 16141). No other potential conflict of interest relevant to this article was reported.

KEY POINTS

QUESTION: Is the implementation of SNB for prostate cancer able to improve nodal staging and, consequently, oncologic outcomes in patients receiving radical prostatectomy and lymph node dissection?

PERTINENT FINDINGS: The use of ICG–^{99m}Tc-nanocolloid tracer was an independent predictor of nodal involvement and lower BCR and CR rates, whereas the use of free ICG did not reach independent predictor status, when compared with the use of no SNB.

IMPLICATIONS FOR PATIENT CARE: The implementation of hybrid-SNB technique in prostate cancer improves detection of positive nodes and allows subsequent optimization of patient management without harming patient safety.

REFERENCES

1. Fossati N, Willemse PPM, Van den Broeck T, et al. The benefits and harms of different extents of lymph node dissection during radical prostatectomy for prostate cancer: a systematic review. *Eur Urol.* 2017;72:84–109.
2. Mottet N, van den Bergh RCN, Briers E, et al. EAU-EANM-ESTRO-ESUR-SIOG guidelines on prostate cancer—2020 update. Part 1: screening, diagnosis, and local treatment with curative intent. *Eur Urol.* 2021;79:243–262.
3. Harke NN, Godes M, Wagner C, et al. Fluorescence-supported lymphography and extended pelvic lymph node dissection in robot-assisted radical prostatectomy: a prospective, randomized trial. *World J Urol.* 2018;36:1817–1823.
4. Wit EMK, Acar C, Grivas N, et al. Sentinel node procedure in prostate cancer: a systematic review to assess diagnostic accuracy. *Eur Urol.* 2017;71:596–605.
5. Grivas N, Wit EMK, Kuusk T, et al. The impact of adding sentinel node biopsy to extended pelvic lymph node dissection on biochemical recurrence in prostate cancer patients treated with robot-assisted radical prostatectomy. *J Nucl Med.* 2018;59:204–209.
6. Mazzone E, Preisser F, Nazzani S, et al. The effect of lymph node dissection in metastatic prostate cancer patients treated with radical prostatectomy: a contemporary analysis of survival and early postoperative outcomes. *Eur Urol Oncol.* 2019;2:541–548.
7. Ventimiglia E, Seisen T, Abdollah F, et al. A systematic review of the role of definitive local treatment in patients with clinically lymph node-positive prostate cancer. *Eur Urol Oncol.* 2019;2:294–301.
8. van Leeuwen AC, Buckle T, Bendle G, et al. Tracer-cocktail injections for combined pre- and intraoperative multimodal imaging of lymph nodes in a spontaneous mouse prostate tumor model. *J Biomed Opt.* 2011;16:016004.
9. Schaafsma BE, Verbeek FPR, Rietbergen DDD, et al. Clinical trial of combined radio- and fluorescence-guided sentinel lymph node biopsy in breast cancer. *Br J Surg.* 2013;100:1037–1044.
10. Cacciamani GE, Shakir A, Tafuri A, et al. Best practices in near-infrared fluorescence imaging with indocyanine green (NIRF/ICG)-guided robotic urologic surgery: a systematic review-based expert consensus. *World J Urol.* 2020;38:883–896.
11. Briganti A, Larcher A, Abdollah F, et al. Updated nomogram predicting lymph node invasion in patients with prostate cancer undergoing extended pelvic lymph node dissection: the essential importance of percentage of positive cores. *Eur Urol.* 2012;61:480–487.
12. Hueting TA, Cornel EB, Somford DM, et al. External validation of models predicting the probability of lymph node involvement in prostate cancer patients. *Eur Urol Oncol.* 2018;1:411–417.
13. KleinJan GH, van den Berg NS, Brouwer OR, et al. Optimisation of fluorescence guidance during robot-assisted laparoscopic sentinel node biopsy for prostate cancer. *Eur Urol.* 2014;66:991–998.
14. van der Poel HG, Buckle T, Brouwer OR, Valdés Olmos RA, van Leeuwen FWB. Intraoperative laparoscopic fluorescence guidance to the sentinel lymph node in prostate cancer patients: clinical proof of concept of an integrated functional imaging approach using a multimodal tracer. *Eur Urol.* 2011;60:826–833.
15. KleinJan GH, van den Berg NS, de Jong J, et al. Multimodal hybrid imaging agents for sentinel node mapping as a means to (re)connect nuclear medicine to advances made in robot-assisted surgery. *Eur J Nucl Med Mol Imaging.* 2016;43:1278–1287.
16. Dindo D, Demartines N, Clavien PA. Classification of surgical complications: a new proposal with evaluation in a cohort of 6336 patients and results of a survey. *Ann Surg.* 2004;240:205–213.
17. Assel M, Sjoberg D, Elders A, et al. Guidelines for reporting of statistics for clinical research in urology. *Eur Urol.* 2019;75:358–367.
18. Dell'Oglio P, Mazzone E, Lambert E, et al. The effect of surgical experience on perioperative and oncological outcomes after robot-assisted radical cystectomy with intracorporeal urinary diversion: evidence from a high-volume center. *Eur Urol Suppl.* 2019;18:e2637–e2639.
19. Cleveland WS. Robust locally weighted regression and smoothing scatterplots. *J Am Stat Assoc.* 1979;74:829–836.
20. Preisser F, Bandini M, Marchioni M, et al. Extent of lymph node dissection improves survival in prostate cancer patients treated with radical prostatectomy without lymph node invasion. *Prostate.* 2018;78:469–475.
21. van der Poel HG, Wit EM, Acar C, et al. Sentinel node biopsy for prostate cancer: report from a consensus panel meeting. *BJU Int.* 2017;120:204–211.
22. Poelaert F, Joniau S, Roumeguère T, et al. Current management of pT3b prostate cancer after robot-assisted laparoscopic prostatectomy. *Eur Urol Oncol.* 2019;2:110–117.
23. Mazzone E, Dell'Oglio P, Rosiello G, et al. Technical refinements in superextended robot-assisted radical prostatectomy for locally advanced prostate cancer patients at multiparametric magnetic resonance imaging. *Eur Urol.* September 14, 2020 [Epub ahead of print].
24. Collamati F, van Oosterom MN, De Simoni M, et al. A DROP-IN beta probe for robot-assisted ^{68}Ga-PSMA radioguided surgery: first ex vivo technology evaluation using prostate cancer specimens. *EJNMMI Res.* 2020;10:92.
25. Dell'Oglio P, Meershoek P, Maurer T, et al. A DROP-IN gamma probe for robot-assisted radioguided surgery of lymph nodes during radical prostatectomy. *Eur Urol.* 2021;79:124–132.
26. Meershoek P, van Oosterom MN, Simon H, et al. Robot-assisted laparoscopic surgery using DROP-IN radioguidance: first-in-human translation. *Eur J Nucl Med Mol Imaging.* 2019;46:49–53.
27. van Oosterom MN, Simon H, et al. Revolutionizing (robot-assisted) laparoscopic gamma tracing using a drop-in gamma probe technology. *Am J Nucl Med Mol Imaging.* 2016;6:1–17.
28. Dell'Oglio P, de Vries HM, Mazzone E, et al. Hybrid indocyanine green–^{99m}Tc-nanocolloid for single-photon emission computed tomography and combined radio- and fluorescence-guided sentinel node biopsy in penile cancer: results of 740 inguinal basins assessed at a single institution. *Eur Urol.* 2020;78:865–872.
29. Maurer T, Robu S, Schottelius M, et al. ^{99m}Technetium-based prostate-specific membrane antigen-radioguided surgery in recurrent prostate cancer. *Eur Urol.* 2019;75:659–666.

Diagnostic Contribution of Contrast-Enhanced CT as Compared with Unenhanced Low-Dose CT in PET/CT Staging and Treatment Response Assessment of ^{18}F-FDG–Avid Lymphomas: A Prospective Study

Lara Marchetti[1], Luca Perrucci[2], Fabio Pellegrino[2], Luca Baroni[2], Annalisa Merlo[2], Massimo Tilli[3], Ilaria Rambaldi[4], Elisa Maietti[5], Aldo Carnevale[1], Mirco Bartolomei[4], and Melchiore Giganti[2]

[1]*Department of Interventional and Diagnostic Radiology, Azienda Ospedaliero–Universitaria Sant'Anna, Ferrara, Italy;* [2]*Section of Diagnostic Imaging, Department of Morphology, Surgery, and Experimental Medicine, University of Ferrara, Ferrara, Italy;* [3]*Ferrara Department of Interventional and Diagnostic Radiology, Ospedale di Lagosanto, Azienda AUSL, Ferrara, Italy;* [4]*Department of Nuclear Medicine, Azienda Ospedaliero–Universitaria Sant'Anna, Ferrara, Italy; and* [5]*Medical and Surgical Sciences Department, University of Bologna, Bologna, Italy*

The aim of this study was to assess the added diagnostic value of contrast-enhanced CT (CECT) as compared with unenhanced CT (UECT) in PET/CT staging and treatment response assessment of ^{18}F-FDG–avid lymphomas. **Methods:** 170 PET/UECT scans followed by CECT scans were prospectively performed for staging (n = 85) and for treatment response assessment (n = 85) of ^{18}F-FDG–avid lymphomas, during a single session using an integrated 64-slice PET/CT scanner. CECT and UECT images were evaluated separately by 2 radiologists, whereas PET images were evaluated by 2 nuclear physicians. Nodal and extranodal UECT and CECT findings were classified according to the Lugano criteria and were successively compared with PET/CT results, considered the gold standard. In the analyzed groups, the agreement rate with the disease status determined via PET was calculated separately for UECT and CECT using the McNemar test on paired data. The added value of the contrast medium was shown by the agreement between the PET and CECT results and the lack of agreement between UECT and PET. **Results:** CECT enabled the identification of additional extranodal lesions (hepatic, muscular, and gastric) in only 3 staging group cases (3.5%), indicating different stages as compared with UECT, whereas there was absolute agreement between CECT and UECT in terms of treatment response assessment. The added diagnostic value of CECT was lower than the established threshold for clinical relevance (15%). The McNemar test indicated no statistical significance in either group. The incidental findings detected by CECT but not UECT were important for clinical management but not sufficient to alter lymphoma treatment strategy. **Conclusion:** According to our results, it might be possible to exclude CECT examination of ^{18}F-FDG–avid lymphoma from staging and treatment response assessment, with the consequent advantages of reducing radiation exposure and potential contrast-related risks.

Key Words: PET; CECT; ^{18}F-FDG–avid lymphoma; staging; treatment response

J Nucl Med 2021; 62:1372–1379
DOI: 10.2967/jnumed.120.259242

Received Oct. 29, 2020; revision accepted Jan. 29, 2021.
For correspondence or reprints, contact Fabio Pellegrino (fabiopellegrino07@gmail.com).
Published online March 12, 2021.

In the Western world, lymphoma represents the fifth most prevalent tumor, with an incidence of 19–20 cases/100,000 inhabitants, with Caucasian males being at greater risk (*1*,*2*).

A major distinction can be made between Hodgkin lymphoma (HL) and non-Hodgkin lymphoma (NHL), with the most frequent histotypes being diffuse large B-cell lymphoma, follicular lymphoma, and HL (*3*).

In patients with lymphoma, the diagnostic pathway involves multiple radiologic and nuclear imaging examinations and a histotype-dependent follow-up (*4*). Since lymphomas are frequently ^{18}F-FDG–avid, ^{18}F-FDG PET/CT is considered the gold standard for staging and treatment response assessment (*5*), providing absolutely essential functional and metabolic information regarding lymphomatous lesions, whether morphologically altered or normal (*6*). Moreover, treatment guided by PET/CT staging results in better survival of aggressive NHL than does therapy based on contrast-enhanced CT (CECT) (*7*). Intravenous iodine contrast medium in PET/CT protocols improves identification of anatomic structures, detection of pathologic lesions, and their characterization (*8*). The advantages of contrast medium are more evident in several anatomic sites where delineation of disease from muscles, vascular structures, or the bowel is critical (*8*).

Lymphoma Staging and Treatment Response Assessment

According to the International Conference on Malignant Lymphoma (2011) (*4*), staging and treatment response assessment of ^{18}F-FDG–avid lymphomas requires PET/CT examination and baseline CECT, which should be performed during the same session (*9*). These imaging modalities are also helpful for radiation therapy planning and prognostic evaluation (*10*); further imaging is performed during therapy for interim evaluation (*11*).

PET/CT includes first the PET scan and then a low-dose unenhanced CT (UECT) acquisition, aimed to correct the attenuation of PET data and to enable anatomic correlation through image fusion. PET/UECT is then followed by a full-dose diagnostic CECT acquisition (*5*).

PET/CT imaging is interpreted according to the revised Lugano criteria, which combine information about the metabolic activity of the disease furnished by PET with the morphologic data from

CT (*4*). The Lugano criteria recommend the Ann Arbor classification for staging, whereas for the purposes of treatment response assessment they recommend the Deauville criteria for PET and the Cheson criteria for CECT (*4*,*5*,*9*).

This routine diagnostic pathway may generate several disadvantages, primarily a high cumulative radiation dose, with the potential risk of radiation-induced carcinogenesis (*12*) over the course of serial CT (staging, interim, end-of-treatment, follow-up); moreover, the repeated administration of iodinated contrast agents may lead to allergic reactions (*13*), contrast-induced nephropathy (*14*), and transient thyroid dysfunction, with potentially dangerous complications such as atrial fibrillation in hyperthyroidism and myxedema coma in hypothyroidism (*15*).

In this context, there have been very few studies on the added diagnostic value that iodine contrast injection may bring to staging or treatment response assessment in ^{18}F-FDG–avid lymphomas (*16*–*22*).

The aim of this study was to evaluate the added diagnostic value of contrast injection in staging and treatment response assessment of ^{18}F-FDG–avid lymphomas, comparing CECT with UECT and considering PET as the gold standard. Indeed, if the added diagnostic value of CECT is not clinically and statistically significant, it may be possible to leave it out of the diagnostic pathway without affecting treatment or outcomes, thereby reducing the potential contrast-related risks and superfluous radiation exposure.

MATERIALS AND METHODS

This study was conducted according to the Declaration of Helsinki; Ethics Committee approval for data collection was obtained (protocol 631/2018/Oss/AOUFe), and all subjects gave written informed consent.

The study prospectively enrolled 170 patients referred to our Oncohematology Department with a histologically confirmed diagnosis of ^{18}F-FDG–avid lymphoma over a 2-y period (between December 2017 and August 2019). All patients underwent PET/CT followed by CECT, both performed at a single session using an integrated 64-slice PET/CT scanner (mCT Biograph FlowMotion; Siemens) at our nuclear medicine department in collaboration with the hospital and university radiology unit. The exclusion criteria were an age of less than 18 y, confirmed or suspected pregnancy, breastfeeding, diabetes mellitus, an absolute contraindication for iodized contrast administration, lymphoma not ^{18}F-FDG–avid, and immunotherapy. The enrolled patients were assigned to 1 of 2 groups: a staging group for those with a first diagnosis or relapse of lymphoma, and a treatment response group, in whom the outcome ad interim or at the end of therapy was compared with a baseline examination.

PET/CT Protocol

The patients were invited to drink 500 mL of water and to rest before the scan, fasting for at least 6 h, and blood glucose levels were checked before the examination to ensure glycemia control and to limit bias caused by anomalous uptake of ^{18}F-FDG. The PET acquisition was started 60 ± 5 min after intravenous ^{18}F-FDG injection (an average of 370 MBq, with a range of 200–450 MBq), with a scan area from skull base to proximal thigh. The patients were scanned with an empty bladder and while supine with their arms raised over their head if possible. First, low-dose CT was performed (100–120 kV; 30–100 mAs with automatic tube current modulation; tube rotation time, 0.5 s; pitch, 0.8 s; slice thickness, 3 mm; reconstruction matrix, 512 × 512 at 3 mm for UECT and 5 mm for images fused with PET). Subsequently a 3-dimensional PET scan was acquired via the FlowMotion technique, requiring a total time of 12–15 min with a speed 1.10 mm/s (range, 0.8–1.7 mm/s, depending on body region and administered activity). *syngo*.via software (Siemens) was used to fuse and display PET, PET/CT, and CT scans with a 3-dimensional maximum-intensity-projection PET view. For semiquantitative analysis, a volume of interest was selected, and the contextual SUV was calculated.

CECT Protocol

After the PET/CT scan, a diagnostic CECT scan of the neck, thorax, and abdomen was acquired after a preliminary anteroposterior scout view (100–120 kV; 60–200 mAs with automatic tube current modulation; tube rotation time, 0.5 s; pitch, 0.65 s; slice thickness, 2 mm; reconstruction matrix, 512 × 512; reconstruction thickness, 2 mm) and intravenous administration of iodinated contrast agent (Omnipaque, 350 mg I/mL; GE Healthcare), modulated according to the weight of the patient, with an average flow of 3 mL/s and bolus-tracking mode. Contrast phases were established by the radiologist according to the clinical scenario, always including a whole-body portal venous phase and, when deemed necessary, also arterial or delayed phases.

Image Analysis

Two nuclear physicians evaluated the PET scans independently without knowing the CECT findings, whereas 2 independent radiologists evaluated the CECT and UECT scans without access to the PET/CT data. The operators were, however, informed of the lymphoma diagnosis. They were asked to assess staging group patients on the basis of the revised Ann Arbor/Cotswolds criteria (*4*).

Subsequently, for the treatment response group scans, the Lugano criteria were applied in a masked manner to each imaging modality, comparing the findings with a baseline acquired via the same imaging technique (corresponding to the staging examination). Higher ^{18}F-FDG uptake than background in nonphysiologic locations was considered consistent with lymphomatous tissue, according to the Deauville criteria. Nodal and extranodal findings in UECT and CECT were separately compared with PET/CT results (gold standard) for each study to assess the agreement between methods.

Statistical Analysis

In both staging and treatment response groups, the agreement rate with the disease status determined via PET was calculated separately for UECT and CECT. The Cohen κ-coefficient was applied to assess interrater reliability. The relative frequencies of agreement between PET and both UECT and CECT were compared using the McNemar test on paired data. The added value of contrast medium was considered proven when PET and CECT findings agreed but UECT and PET did not. Data were analyzed using the statistical software Stata, version 13 (StataCorp), and a P value of less than 0.05 was considered statistically significant.

RESULTS

Study Population

The study comprised 170 PET/CT and CECT scans, of which 85 were assigned to the staging group and 85 to the treatment response group. In the treatment response group, of the total of 85 patients, 50 were evaluable for interim treatment response analysis and 35 for end-of-treatment assessment. The participants in the study comprised 97 men and 73 women with a mean age of 53 y (range, 20–82 y): 41 diagnosed with HL and 129 with NHL. A deeper analysis of the population characteristics and histotypes is reported in Table 1.

Staging Group

Agreement with PET was 80% for CECT and 76.5% for UECT ($P < 0.001$ in both cases). In 82 of 85 patients (96.5%), CECT provided the same Ann Arbor stage as assigned by low-dose

TABLE 1
Characteristics of Staging and Treatment Response Groups

Characteristic	Staging (n = 85)	Treatment response (n = 85)
Mean age (y)	57.6 (range, 24–82)	48.2 (range, 20–81)
Sex		
Male	50 (59%)	47 (55%)
Female	35 (41%)	38 (45%)
HL	15 (18%)	26 (31%)
NHL	70 (82%)	59 (69%)
Diffuse large B-cell lymphoma	30 (35%)	28 (33%)
Follicular	17 (20%)	9 (11%)
Mantle cells	8 (9%)	7 (8%)
Marginal zone	2 (2%)	5 (6%)
Burkitt lymphoma	2 (2%)	7 (8%)
Others*	11 (13%)	3 (3%)
Performance status (ECOG)		
0	73 (86%)	79 (93%)
1	8 (10%)	4 (5%)
2	2 (2%)	1 (1%)
Missing	2 (2%)	1 (1%)
International Prognostic Index		
0	10 (12%)	5 (6%)
1	8 (9%)	8 (9%)
2	9 (11%)	9 (11%)
3	7 (8%)	13 (15%)
4	1 (1%)	4 (5%)
Missing	50 (59%)	46 (54%)
Lactate dehydrogenase		
Less than or equal to ULN	53 (63%)	54 (64%)
Greater than ULN	25 (29%)	29 (34%)
Missing	7 (8%)	2 (2%)
Bulky mass	13 (15%)	7 (8%)

*Peripheral T-cell lymphoma, gastric lymphoma, nasal natural-killer/T-cell lymphoma, anaplastic large cell lymphoma, indolent B-cell lymphomas, angioimmunoblastic lymphoma, high-grade B-cell lymphoma, nonspecific high-grade lymphoma.

ECOG = Eastern Cooperative Oncology Group; ULN = upper limit of normal.

UECT, and nodal findings were detected equally by CECT and UECT. In only 3 patients (3.5%) did CECT identify further extranodal lesions (hepatic, muscular, and gastric), assigning a different Ann Arbor stage to low-dose UECT. The first of these patients had HL, and CECT revealed a paravertebral, intramuscular hypodense nodular area, indicating stage IV, whereas the same area was not visible under UECT, which indicated stage III. On the PET scan, that lesion was hypermetabolic and therefore indicative of stage IV (Fig. 1). The second patient also had HL and showed several intrahepatic, hypodense nodular areas on CECT (indicating stage IV) that were not visible on UECT (which indicated stage III). At PET examination, those hepatic nodules appeared as hypermetabolic foci, indicating stage IV and thus confirming the CECT results (Fig. 2). In the last patient, who had NHL (diffuse large B-cell lymphoma), CECT revealed heterogeneous thickening of the gastric wall, indicating stage I, which was confirmed by radiotracer uptake in PET images. Conversely, since gastric wall thickening was not evident without iodine contrast medium, this patient was classified as without any abnormality on the UECT examination (Fig. 3). In all 3 patients, PET and CECT staging were concordant whereas UECT slightly underestimated the disease stage (Table 2; Fig. 4). The main reason for the discordance between CT imaging and the gold standard, PET, was that PET showed ^{18}F-FDG uptake in bone lesions that were not visible under either UECT or CECT.

Our results indicate that the added diagnostic value of CECT was very small because there was a 3.5% lack of agreement (95% CI, 0%–7.5%) between CECT and UECT staging (Table 3). This value is under the threshold considered clinically relevant (15%), and furthermore, the McNemar test showed no statistical significance ($P = 0.083$).

Examining the cases of HL (15 cases) and NHL (70 cases) separately, the respective agreement of CECT and UECT with PET was 93% and 80% in HL and 77% and 76% in NHL; for both CECT and UECT, the agreement with PET was statistically significant ($P < 0.001$). Analysis of the HL and NHL subgroups showed no difference in results (Table 4). In fact, 2 of the 3 cases of discordance between CECT and UECT staging were HL, and the use of contrast medium in these patients would not have modified the treatment strategy. Conversely, in the case of gastric NHL, CECT showing an additional lesion led to a change in treatment. In the HL group, on the other hand, the additional diagnostic value of contrast administration (13.3%; 95% CI, 0%–30.5%) was just under the threshold considered clinically relevant (15%), although the McNemar test indicated a lack of statistical significance ($P = 0.157$).

Treatment Response

In the 85 patients evaluated according to the Lugano criteria ad interim and at the end of treatment, there was absolute agreement (100%) between CECT and low-dose UECT (32 cases with complete response, 49 with partial response, and 4 with stable disease), with both being equally comparable to PET, even in the 2 different HL and NHL histotypes (Table 5). Consequently, CECT did not contribute to the therapy response assessment and may therefore be considered superfluous for this purpose. However, as expected, agreement with PET was low for both CECT and UECT (38.8%), but the difference was not statistically significant in either case ($P = 0.104$). Bone lesions were the main reason for discordance between PET and UECT/CECT, since they were not visible on CT but were revealed by ^{18}F-FDG uptake, and the enlarged lymph nodes were devoid of ^{18}F-FDG uptake. Therefore, there is no added value of CECT over UECT in terms of directing the lymphoma treatment strategy, regardless of histotype.

Incidental Findings

Finally, CECT detected some incidental findings that were not recognizable at UECT alone. These included portal vein

FIGURE 1. In patient with HL, UECT did not detect lesion in right paravertebral muscles (A), revealed as hypovascular nodular area (circle) by CECT (B), thereby indicating Ann Arbor stage III instead of stage IV as suggested by CECT (C) and evident as hypermetabolic focus on ^{18}F-FDG PET (C).

FIGURE 2. In patient with HL, UECT did not detect hepatic lesion in right lobe (A), revealed as hypodense nodular area (circle) by CECT (B), thereby indicating Ann Arbor stage III instead of stage IV as suggested by CECT and evident as hypermetabolic focus on ^{18}F-FDG PET (C).

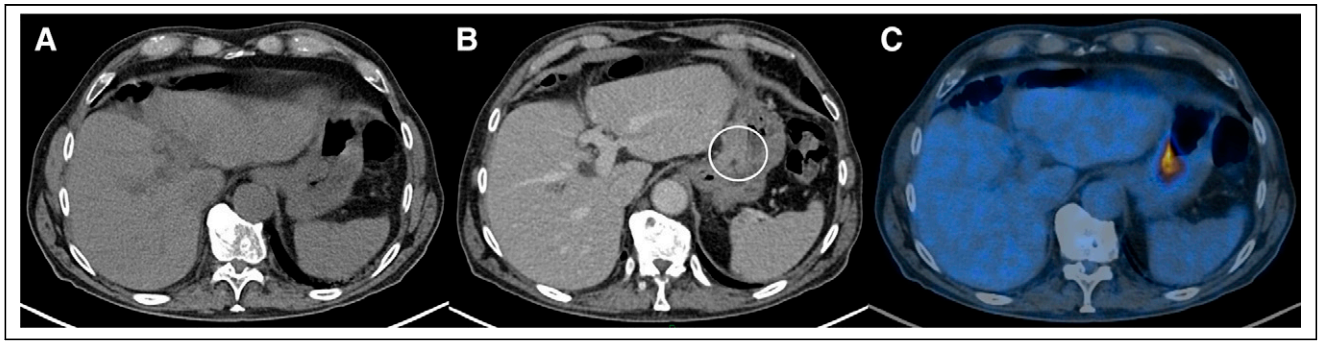

FIGURE 3. In patient with NHL, UECT did not show gastric lesion (A), revealed as thickened gastric wall (circle) by CECT (B), thereby indicating no detected abnormality instead of stage I as suggested by CECT and evident as hypermetabolic focus on ^{18}F-FDG PET (C).

thrombosis (Fig. 5), pulmonary thromboembolism (Supplemental Fig. 1; supplemental materials are available at http://jnm.snmjournals.org), and spleen infarction (Supplemental Fig. 2). None of these influenced lymphoma staging or treatment response assessment, but for obvious reasons, they did influence the overall clinical management of the affected patients.

DISCUSSION

This study investigated the additional value of CECT in comparison to UECT for both staging and treatment response assessment purposes in a group of 170 patients with ^{18}F-FDG–avid lymphoma, considering PET as the gold standard. In the staging group, CECT and UECT displayed 80% and 76.5% agreement with PET, respectively, and agreement was statistically significant in both cases. Lack of agreement was ascribable to the higher sensitivity of PET for some types of lymphomatous bone lesions as compared with UECT and CECT (*17*,*23*). Muscular, hepatic, and gastric lesions, on the other hand, were detected by both PET and CECT but were not recognizable via UECT in the patients assessed for staging. In discrimination between HL and NHL, the agreement with PET was always significantly greater than 75% for both CECT and UECT.

On closer analysis of the 3 cases (3.5%) of lack of agreement between CECT and UECT in the staging group, in the 2 HL patients the correct staging provided by CECT would not have changed the treatment strategy, whereas in the third case (i.e., NHL) the correct CECT staging led to a change in clinical management with respect to what would have been prescribed on the basis of UECT findings alone. In this light, in the HL subgroup the added diagnostic value of CECT for staging purposes was 13.5%, close to the clinically relevant threshold (15%), but this

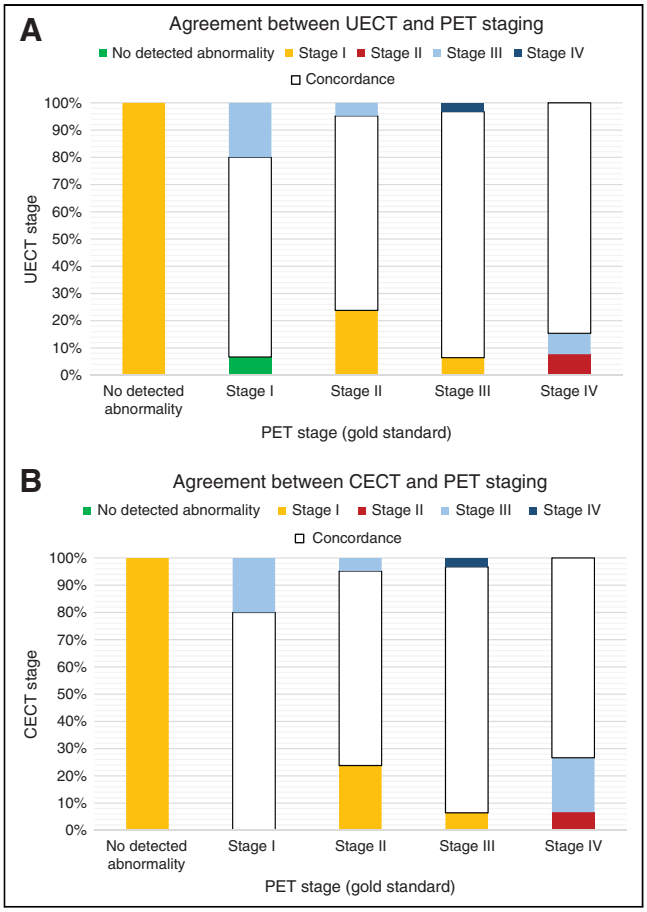

FIGURE 4. White bars representing agreement between Ann Arbor stages assigned on basis of PET as compared with 2 CT techniques: UECT (A) and CECT (B).

TABLE 2
Agreement Between CT and PET Staging According to Ann Arbor Classification

	PET					
CT	NA	I	II	III	IV	Total
UECT						
NA	0*	1	0	0	0	1
I	1	11*	5	2	0	19
II	0	0	15*	0	1	16
III	0	3	1	28*	5	37
IV	0	0	0	1	11*	12
Total	1	15	21	31	17	85
CECT						
NA	0*	0	0	0	0	0
I	1	12*	5	2	0	20
II	0	0	15*	0	1	16
III	0	3	1	28*	3	35
IV	0	0	0	1	13*	14
Total	1	15	21	31	17	85

*Case of agreement.
NA = no abnormality detected.
In 65 of 85 cases, UECT agreed with PET (76.5% agreement; 95% CI, 66.0%–85.0%; $P < 0.001$ and k = 0.676). In 20 of 85 cases, UECT disagreed with PET: in 6 patients (7%), UECT overstaged; in 14 patients (16.5%), UECT understaged. These data are plotted in Figure 4A. In 68 of 85 cases, CECT agreed with PET (80% agreement; 95% CI, 69.9%–87.9%; $P < 0.001$ and k = 0.726). In 17 of 85 cases, CECT disagreed with PET: in 6 patients (7%), CECT overstaged; in 11 patients (13%), CECT understaged. These data are plotted in Figure 4B.

value was influenced by the limited number of patients (n = 15),whereas in the larger subgroup, NHL (n = 70), this value was clearly lower than the threshold (1.4%). Therefore, a potential increased diagnostic value of CECT in HL compared with NHL should be demonstrated in a larger sample group.

On the basis of our findings, however, PET/UECT should be suggested as the imaging modality of choice for staging of ^{18}F-FDG–avid lymphomas. This conclusion is in line with that by van Hamersvelt et al. (*16*), who recommended ^{18}F-FDG PET/UECT as the primary imaging modality for staging ^{18}F-FDG–avid lymphomas after a similar study, comparing the staging findings of ^{18}F-FDG PET/UECT and CECT in a group of 29 patients newly diagnosed with ^{18}F-FDG–avid lymphoma. In that study, the stage indicated by CECT differed from that indicated by UECT on the basis of the Ann Arbor classification in 7% of patients, but without changes in therapeutic approach, thus supporting the hypothesis that iodinated contrast medium is unnecessary for staging purposes.

Indeed, another prospective study, by Rodríguez-Vigil et al. (*24*), found no difference between unenhanced low-dose ^{18}F-FDG PET/CT and contrast-enhanced full-dose ^{18}F-FDG PET/CT in 47 patients newly diagnosed with lymphoma, except that the latter technique showed fewer indeterminate findings and a higher number of extranodal lesions. UECT and CECT correlated well in terms of nodal and extranodal lesion detection, and the authors therefore concluded that unenhanced low-dose PET/CT could be used for initial imaging in lymphomas, reserving CECT for only selected cases. However, similarly to our results, they found that contrast-enhanced full-dose ^{18}F-FDG PET/CT detected important incidental findings in 2 patients (4.3%)—findings that were not observed via unenhanced low-dose ^{18}F-FDG PET/CT (*24*).

In this regard, another study, by Pinilla et al. (*25*), found comparable results regarding nodal involvement and parenchymal evaluation, bone marrow included. In unenhanced low-dose and contrast-enhanced full-dose ^{18}F-FDG PET/CT obtained for 101 patients with newly diagnosed lymphoma, the authors showed that CECT revealed important incidental findings in 6 patients (5.9%). They also concluded that there were no significant differences between the modalities in terms of initial lymphoma staging accuracy but that CECT enabled the detection of incidental findings not revealed using UECT.

However, Sabaté-Llobera et al. (*19*), who studied 28 patients with diffuse large B-cell lymphoma assessed for staging purposes via ^{18}F-FDG PET/UECT and CECT, found disagreement between the 2 techniques in 21% of cases, in half of which the treatment strategy would have been impacted. In particular, they concluded that PET/UECT is more sensitive than CECT in detecting nodal and extranodal lesions and therefore suggested that contrast administration might be avoidable. Alnouby et al. (*23*), analyzing a group of 144 patients with various lymphoma histotypes

TABLE 3
Agreement Between CECT and UECT Staging According to Ann Arbor Classification

	UECT					
CECT	NA	I	II	III	IV	Total
NA	0*	0	0	0	0	0
I	1	19*	0	0	0	20
II	0	0	16*	0	0	16
III	0	0	0	35*	0	35
IV	0	0	0	2	12*	14
Total	1	19	16	37	12	85

*Case of agreement.
NA = no abnormality detected.

TABLE 4
Agreement Between PET and UECT or CECT Staging According to Ann Arbor Classification in NHL and HL

	PET					
CT	NA	I	II	III	IV	Total
UECT						
NHL						
NA	0*	1	0	0	0	1
I	1	9*	5	2	0	17
II	0	0	10*	0	1	11
III	0	3	1	25*	2	31
IV	0	0	0	1	9*	10
Total	1	13	16	28	12	70
HL						
NA	0*	0	0	0	0	0
I	0	2*	0	0	0	2
II	0	0	5*	0	0	5
III	0	0	0	3*	3	6
IV	0	0	0	0	2*	2
Total	0	2	5	3	5	15
CECT						
NHL						
NA	0*	0	0	0	0	0
I	1	10*	5	2	0	18
II	0	0	10*	0	1	11
III	0	3	1	25*	2	31
IV	0	0	0	1	9*	10
Total	1	13	16	28	12	70
HL						
NA	0*	0	0	0	0	0
I	0	2*	0	0	0	2
II	0	0	5*	0	0	5
III	0	0	0	3*	1	4
IV	0	0	0	0	4*	4
Total	0	2	5	3	5	15

*Case of agreement.
NA = no abnormality detected.
Overstaging of 4 NHL patients on CECT and UECT compared with PET, with consequent therapeutic planning change, was due to enlarged nodes (longest diameter in axial plane > 1.5 cm) localized on both sides of diaphragm without significant PET uptake.

including those weakly avid for ^{18}F-FDG, also reported results indicating that PET/UECT assessment is more sensitive for extranodal involvement than CECT (respective sensitivity of 97% and 89.6% and respective accuracy of 91.7% and 87.5%), especially in the spleen, bone, and bone marrow, since ^{18}F-FDG highlights metabolically active areas in structures of normal morphology. Similarly, Panebianco et al. (*17*), in their study of 62 cases of newly diagnosed HL, found that CECT was less sensitive than ^{18}F-FDG PET/CT in the detection of some bone marrow lesions but more reliable in assessing hepatic tumors, whereas no difference emerged between the 2 imaging modalities in terms of detecting lung involvement; they confirmed that PET/CT allows better staging in HL through the detection of nodal lesions. Furthermore, Paone et al. (*18*) investigated the advantage of using contrast medium in end-of-treatment low-dose PET/CT to detect sites of disease in 30 patients with follicular lymphoma (agreement rate between CECT and UECT, 87%) and concluded that the clinical impact of CECT was limited to cases with suspected residual disease in mesenteric and iliac nodal stations.

Similarly, in our study the additional diagnostic value of contrast medium in staging and treatment response assessment in ^{18}F-FDG–avid lymphomas was limited to very few cases, in which CECT would have assigned a less advanced Ann Arbor stage than the gold standard low-dose ^{18}F-FDG PET/CT, and in only 1 case would it have affected the treatment pathway. The added diagnostic value, 3.5%, that we found for CECT is not statistically significant, suggesting that it may be possible to omit CECT from the process of staging ^{18}F-FDG–avid lymphomas, irrespective of their histotype. Nonetheless, should our results be confirmed in a larger sample, CECT could still have a role in HL staging, because the added value of contrast medium was close to the threshold of clinical significance.

In assessing treatment response, on the other hand, CECT did not demonstrate any advantage over UECT in ^{18}F-FDG–avid lymphomas, confirming that UECT should be the first-choice low-dose ^{18}F-FDG PET/CT imaging mode in this type of disease. The main additional information provided by contrast enhancement was the detection of extranodal involvement, which was, however, always revealed by the gold standard, PET. Although CECT allowed the detection of additional incidental findings unrelated to the lymphoma, these were clinically significant in only a few cases and did not affect lymphoma staging or treatment response assessment. Consequently, these findings did not increase the diagnostic value of CECT in the assessment of ^{18}F-FDG–avid lymphomas, with the addition of a consistent increase in radiation exposure (*26*). An advantage of our study is the use of a standardized protocol in which CECT was performed after PET/CT, preventing inaccuracies in SUV quantification due to the artifacts of iodine contrast attenuation (*26*). Both exams were executed in a single session, allowing a better overlapping of the acquired images. Some limitations of the study should be also acknowledged. First,

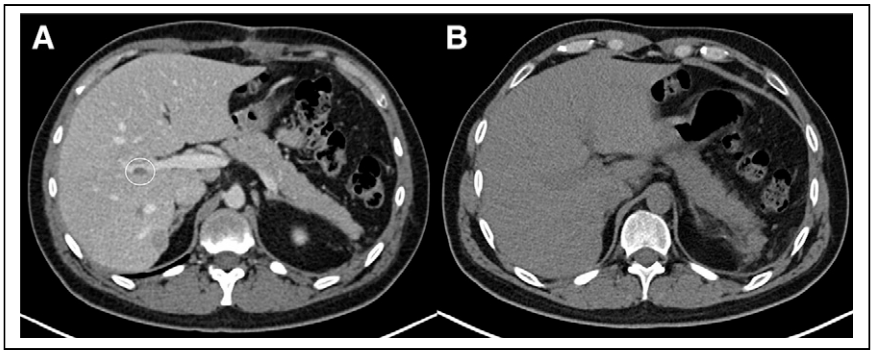

FIGURE 5. NHL patient presenting with portal vein thrombosis (circle) detected by venous-phase CECT (A) but not recognizable on UECT (B).

it was a single-center study. Second, the protocol did not estimate the effective dose delivered by PET/CT and CECT for each acquisition. Finally, the different numbers of patients in the HL and NHL subgroups make the diagnostic added value of CECT difficult to compare based on the different histotypes: in particular, in the HL population, the diagnostic added value of CECT should be calculated on a more representative sample size to confirm our data.

TABLE 5
Agreement Between PET and UECT or CECT Response Classes According to Lugano Criteria in Treatment Response Group and in HL and NHL Groups

	PET				
UECT/CECT	CR	PR	SD	PD	Total
Treatment response					
CR	31*	0	0	1	32
PR	44	2*	1	2	49
SD	4	0	0*	0	4
PD	0	0	0	0*	0
Total	79	2	1	3	85
HL					
CR	22*	0	0	1	23
PR	32	1*	1	0	34
SD	2	0	0*	0	2
PD	0	0	0	0*	0
Total	56	1	1	1	59
NHL					
CR	9*	12	2	0	23
PR	0	1*	0	0	1
SD	0	0	0*	0	0
PD	0	2	0	0*	2
Total	9	15	2	0	26

*Case of agreement.

CR = complete response; PR = partial response; SD = stable disease; PD = progressive disease.

In 33 of 85 cases, UECT and CECT agreed with PET (38.8% agreement; 95% CI, 28.4%–50.0%), a value that is not statistically significant ($P = 0.104$ and $k = 0.038$).

CONCLUSION

According to our data, it is conceivable that, in the ^{18}F-FDG–avid lymphoma examination, CECT should be justifiable only in patients with negative PET findings and equivocal UECT findings and in patients with PET findings suspected of being nonlymphomatous lesions.

Since the most important benefit of CECT data as part of the combined PET/CT examination relates to more precise anatomic localization of disease by differentiation of the lesion from its surrounding structures, CECT might be useful for planning radiotherapy, interventional procedures, and surgery.

Limiting the field of application of CECT to the aforementioned cases could prevent undue exposure of patients, both young and elderly, to the drawbacks of repeated irradiation and iodinated contrast medium. Furthermore, this approach could also lessen the financial burden, allowing better management and more efficient distribution of resources. However, further studies are required to confirm these results in a larger cohort, in order to better select those patients who really need CECT examination, especially in cases of suspected extranodal disease.

DISCLOSURE

No potential conflict of interest relevant to this article was reported.

KEY POINTS

QUESTION: Does CECT have an added value over UECT in PET/CT staging and in assessment of response to treatment of ^{18}F-FDG–avid lymphomas?

PERTINENT FINDINGS: In this prospective study of 85 patients who underwent PET/UECT followed by CECT for staging, and 85 patients who underwent treatment response assessment of ^{18}F-FDG–avid lymphomas, in only 3.5% of patients did CECT indicate a stage different from that indicated by UECT, whereas there was absolute agreement between CECT and UECT in the assessment of treatment response.

IMPLICATIONS FOR PATIENT CARE: CECT examination in PET/CT staging and in treatment response assessment of ^{18}F-FDG–avid lymphoma may be useless.

REFERENCES

1. Morton LM, Wang SS, Devesa SS, Hartge P, Weisenburger DD, Linet MS. Lymphoma incidence patterns by WHO subtype in the United States, 1992-2001. *Blood.* 2006;107:265–276.
2. Luminari S, Cesaretti M, Rashid I, et al. Incidence, clinical characteristics and survival of malignant lymphomas: a population-based study from a cancer registry in northern Italy. *Hematol Oncol.* 2007;25:189–197.
3. Smith A, Crouch S, Lax S, et al. Lymphoma incidence, survival and prevalence 2004–2014: sub-type analyses from the UK's Haematological Malignancy Research Network. *Br J Cancer.* 2015;112:1575–1584.
4. Cheson BD, Fisher RI, Barrington SF, et al. Recommendations for initial evaluation, staging, and response assessment of Hodgkin and non-Hodgkin lymphoma: the Lugano classification. *J Clin Oncol.* 2014;32:3059–3068.

5. Barrington SF, Mikhaeel NG, Kostakoglu L, et al. Role of imaging in the staging and response assessment of lymphoma: consensus of the International Conference on Malignant Lymphomas Imaging Working Group. *J Clin Oncol.* 2014;32:3048–3058.
6. Floridi C, Carnevale A, Fumarola EM, et al. Percutaneous lung tumor biopsy under CBCT guidance with PET-CT fusion imaging: preliminary experience. *Cardiovasc Intervent Radiol.* 2019;42:1644–1648.
7. Metser U, Prica A, Hodgson DC, et al. Effect of PET/CT on the management and outcomes of participants with Hodgkin and aggressive non-Hodgkin lymphoma: a multicenter registry. *Radiology.* 2019;290:488–495.
8. Antoch G, Freudenberg LS, Beyer T, Bockisch A, Debatin JF. To enhance or not to enhance? ^{18}F-FDG and CT contrast agents in dual-modality ^{18}F-FDG PET/CT. *J Nucl Med.* 2004;45(suppl 1):56S–65S.
9. Cheson BD, Pfistner B, Juweid ME, et al. Revised response criteria for malignant lymphoma. *J Clin Oncol.* 2007;25:579–586.
10. Boellaard R, Delgado-Bolton R, Oyen WJG, et al. FDG PET/CT: EANM procedure guidelines for tumour imaging—version 2.0. *Eur J Nucl Med Mol Imaging.* 2015;42:328–354.
11. Meignan M, Hutchings M, Schwartz LH. Imaging in lymphoma: the key role of fluorodeoxyglucose-positron emission tomography. *Oncologist.* 2015;20:890–895.
12. Lowry KP, Turan EA, Eisenberg J, Kong CY, Barnes JA, Pandharipande PV. Projected effects of radiation-induced cancers on life expectancy in patients undergoing CT surveillance for limited-stage Hodgkin lymphoma: a Markov model. *AJR.* 2015;204:1228–1233.
13. Cha MJ, Kang DY, Lee W, et al. Hypersensitivity reactions to iodinated contrast media: a multicenter study of 196 081 patients. *Radiology.* 2019;293:117–124.
14. Eng J, Wilson RF, Subramaniam RM, et al. Comparative effect of contrast media type on the incidence of contrast-induced nephropathy: a systematic review and meta-analysis. *Ann Intern Med.* 2016;164:417–424.
15. Lee SY, Rhee CM, Leung AM, Braverman LE, Brent GA, Pearce ENA. Review: radiographic iodinated contrast media-induced thyroid dysfunction. *J Clin Endocrinol Metab.* 2015;100:376–383.
16. van Hamersvelt HP, Kwee TC, Fijnheer R, Beek FJA, de Klerk JMH, Nievelstein RAJ. Can full-dose contrast-enhanced CT be omitted from an FDG-PET/CT staging examination in newly diagnosed FDG-avid lymphoma? *J Comput Assist Tomogr.* 2014;38:620–625.
17. Panebianco M, Bagni O, Cenfra N, et al. Comparison of ^{18}F FDG PET-CT AND CECT in pretreatment staging of adults with Hodgkin's lymphoma. *Leuk Res.* 2019;76:48–52.
18. Paone G, Raditchkova-Sarnelli M, Stathis A, Giovanella L, Zucca E, Ceriani L. Limited benefit of additional contrast-enhanced CT to end-of-treatment PET-CT evaluation in patients with follicular lymphoma. *Blood.* 2016;128:5925.
19. Sabaté-Llobera A, Cortés-Romera M, Mercadal S, et al. Low-dose PET/CT and full-dose contrast-enhanced CT at the initial staging of localized diffuse large B-cell lymphomas. *Clin Med Insights Blood Disord.* 2016;9:29–32.
20. Raanani P, Shasha Y, Perry C, et al. Is CT scan still necessary for staging in Hodgkin and non-Hodgkin lymphoma patients in the PET/CT era? *Ann Oncol.* 2006;17:117–122.
21. Elstrom RL, Leonard JP, Coleman M, Brown RKJ. Combined PET and low-dose, noncontrast CT scanning obviates the need for additional diagnostic contrast-enhanced CT scans in patients undergoing staging or restaging for lymphoma. *Ann Oncol.* 2008;19:1770–1773.
22. Schaefer NG, Hany TF, Taverna C, et al. Non-Hodgkin lymphoma and Hodgkin disease: coregistered FDG PET and CT at staging and restaging—do we need contrast-enhanced CT? *Radiology.* 2004;232:823–829.
23. Alnouby A, Ibraheem Nasr I, Ali I, Rezk M. F-18 FDG PET-CT versus contrast enhanced CT in detection of extra nodal involvement in patients with lymphoma. *Indian J Nucl Med.* 2018;33:183–189.
24. Rodríguez-Vigil B, Gómez-León N, Pinilla I, et al. PET/CT in lymphoma: prospective study of enhanced full-dose PET/CT versus unenhanced low-dose PET/CT. *J Nucl Med.* 2006;47:1643–1648.
25. Pinilla I, Gómez-León N, Del Campo-Del Val L, et al. Diagnostic value of CT, PET and combined PET/CT performed with low-dose unenhanced CT and full-dose enhanced CT in the initial staging of lymphoma. *Q J Nucl Med Mol Imaging.* 2011;55:567–575.
26. Chalaye J, Luciani A, Enache C, et al. Clinical impact of contrast-enhanced computed tomography combined with low-dose ^{18}F-fluorodeoxyglucose positron emission tomography/computed tomography on routine lymphoma patient management. *Leuk Lymphoma.* 2014;55:2887–2892.

Prognostic Value of Bone Marrow Metabolism on Pretreatment ^{18}F-FDG PET/CT in Patients with Metastatic Melanoma Treated with Anti-PD-1 Therapy

Ryusuke Nakamoto[1], Lisa C. Zaba[2], Tie Liang[1], Sunil Arani Reddy[3], Guido Davidzon[1], Carina Mari Aparici[1], Judy Nguyen[1], Farshad Moradi[1], Andrei Iagaru[1], and Benjamin Lewis Franc[1]

[1]*Department of Radiology, Stanford University, Stanford, California;* [2]*Department of Dermatology, Stanford University, Stanford, California; and* [3]*Department of Oncology, Stanford University, Stanford, California*

Our purpose was to investigate the prognostic value of ^{18}F-FDG PET/CT parameters in melanoma patients before beginning therapy with antibodies to the programmed cell death 1 receptor (anti-PD-1). **Methods:** Imaging parameters including SUV_{max}, metabolic tumor volume, and the ratio of bone marrow to liver SUV_{mean} (BLR) were measured from baseline PET/CT in 92 patients before the start of anti-PD-1 therapy. The association with survival and imaging parameters combined with clinical factors was evaluated. Clinical and laboratory data were compared between the high-BLR group (>median) and the low-BLR group (≤median). **Results:** Multivariate analyses demonstrated that BLR was an independent prognostic factor for progression-free and overall survival ($P = 0.017$ and $P = 0.011$, respectively). The high-BLR group had higher white blood cell counts and neutrophil counts and a higher level of C-reactive protein than the low-BLR group ($P < 0.05$). **Conclusion:** Patients with a high BLR were associated with poor progression-free and overall survival, potentially explained by evidence of systemic inflammation known to be associated with immunosuppression.

Key Words: ^{18}F-FDG; PET/CT; bone marrow uptake; immunotherapy; melanoma

J Nucl Med 2021; 62:1380–1383
DOI: 10.2967/jnumed.120.254482

Metabolic tumor volume (MTV) and the glucose metabolism of normal tissues associated with immunity on ^{18}F-FDG PET/CT before and during immune checkpoint inhibitor therapy have been explored as predictors of therapeutic efficacy (*1–4*). The link between ^{18}F-FDG uptake by immune-mediating tissues, such as the bone marrow (BM) and spleen, and poor cancer outcomes is hypothesized to be explained by generalized inflammation (*5*,*6*).

We hypothesized that imaging parameters, including physiologic uptake in hematopoietic tissues on baseline PET/CT, combined with known clinical prognostic factors for melanoma may be more accurate than clinical factors alone in predicting the therapeutic efficacy and prognosis of melanoma patients treated with antibodies to the programmed cell death 1 receptor (anti-PD-1).

Received Aug. 6, 2020; revision accepted Jan. 14, 2021.
For correspondence or reprints, contact Ryusuke Nakamoto (inabook@stanford.edu).
Published online February 5, 2021.

MATERIALS AND METHODS

Patients

Ninety-two melanoma patients who received anti-PD-1 therapy (pembrolizumab or nivolumab) as first-line immunotherapy between April 2012 and June 2019 were enrolled in this retrospective study. The Institutional Review Board approved this study and waived the requirement for obtaining written informed consent.

^{18}F-FDG PET/CT Protocol and Data Analysis

Approximately 1 h after intravenous injection of ^{18}F-FDG, PET/CT images from the vertex to the toes were acquired per the standard-of-care protocol at our institution using a Discovery 600, 690, 710, or MI scanner (GE Healthcare). SUV_{max}, SUV_{mean}, MTV, and total lesion glycolysis with an SUV of at least 2.5 were measured for all ^{18}F-FDG–avid lesions.

Liver and spleen SUV_{mean} were measured by drawing a spheric volume of interest in the center of an area of nondiseased right hepatic lobe (3 cm; Fig. 1A) and spleen (2 cm; Fig. 1C), respectively. For the BM, spheric 1.5-cm volumes of interest were placed within the center of nondiseased L1–L4 vertebral bodies (Fig. 1B), and an average SUV_{mean} was calculated for the lumbar vertebral bodies. Then, the BM-to-liver ratio (BLR) and spleen-to-liver ratio were calculated by dividing the BM SUV_{mean} by the liver SUV_{mean} and the spleen SUV_{mean} by the liver SUV_{mean}, respectively (*1*,*7*,*8*).

Comparison of Clinical Characteristics and Imaging Parameters of Patients with High and Low BLR

To clarify the clinical characteristics of patients with increased BM uptake, patients were classified into a high-BLR group (>median) and a low-BLR group (≤median), and physical data, laboratory data, and imaging parameters were compared between the 2 groups.

Statistical Analysis

Values were compared between groups using the Mann–Whitney *U* test. Progression-free survival (PFS) was assessed from the start date of immunotherapy to disease progression based on immune-related RECIST (*9*). Overall survival (OS) was assessed from the start date of immunotherapy to death or last follow-up. Cutoffs for age and imaging parameters were set on median values. The patients' cohort was divided into separate groups based on the following parameters: age, sex, primary site, BRAF mutation status, presence of brain metastasis, serum lactate dehydrogenase (LDH) level, and imaging parameters. Factors identified as being significant in the log-rank test ($P < 0.05$) were entered into a multivariate Cox proportional-hazards model. Kaplan–Meier curves were generated for subgroups. The method of Holm was used to adjust the *P* values for multiple comparisons. Spearman rank correlation coefficients were calculated to assess the

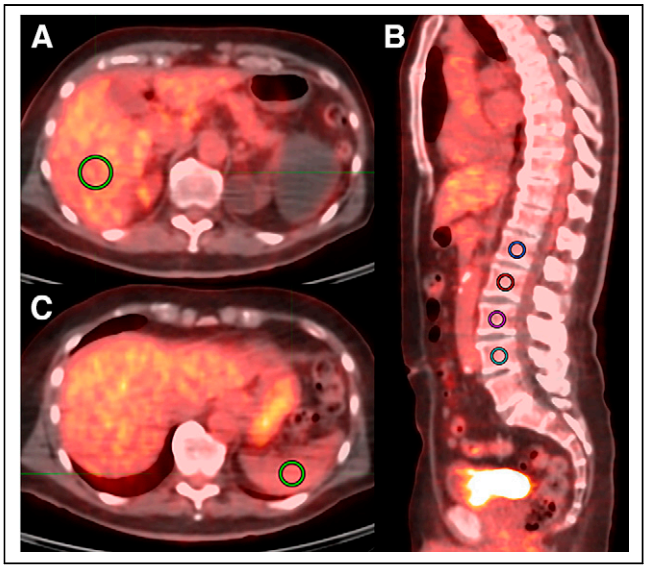

FIGURE 1. Illustration of placement of volume of interest in liver (A), L1–L4 vertebral bodies (B), and spleen (C).

relationships between continuous variables. *P* values of less than 0.05 were considered statistically significant.

RESULTS

Relationship of ^{18}F-FDG PET Parameters to PFS and OS

Patient characteristics are summarized in Table 1. After the median follow-up of 18.2 mo, 53 patients had disease progression, and 32 of them died. Median PFS and OS were 11.6 mo (95% CI, 7.1–28.3 mo) and more than 60 mo, respectively. Multivariate analysis based on the results of univariate analysis (Supplemental Table 1; supplemental materials are available at http://jnm.snmjournals.org) demonstrated that BLR and BRAF mutation were independent prognostic factors for PFS ($P = 0.017$ and 0.018, respectively), and BLR, BRAF mutation, and LDH elevation were independent prognostic factors for OS ($P = 0.011$, 0.0078, and 0.013, respectively) (Table 2). Figure 2 shows Kaplan–Meier curves generated for subgroups based on variables significant in multivariate analysis for PFS and OS. The median PFS of the high-BLR (>0.78) group was 8.6 mo (95% CI, 3.0–42.5 mo), significantly shorter than that of the low-BLR group (28.3 mo; 95% CI, 7.7–54.9 mo) ($P = 0.027$). Similarly, the median OS of the high-BLR group was 28.0 mo (95% CI, 17.2–28.7 mo), significantly shorter than that of the low-BLR group (>60 mo) ($P = 0.019$).

Combining BLR and Clinical Factors

Combining BLR and independent clinical factors (BRAF mutation and LDH elevation) provided further patient stratification. The population was stratified into 3 risk categories: low risk (low BLR and favorable clinical risk factors), intermediate risk (low BLR and unfavorable clinical risk factors or high BLR and favorable clinical risk factors), and high risk (high BLR and unfavorable clinical risk factors). The OS of the high-risk group was significantly worse than that of any other risk group (Fig. 3), and this combined approach to risk stratification differentiated patients according to survival better than BLR or the set of clinical parameters alone. The median OS of patients with a high BLR was 28.0 mo, whereas in patients with a

TABLE 1
Patient Characteristics

Characteristic	Data
Patients	92
Race	
White	79 (85.9%)
Hispanic	8 (8.7%)
Asian	3 (3.3%)
Other	2 (2.2%)
Age (y)	69 (55–76)
Male	55 (59.8%)
Primary site	
Skin	74 (80.4%)
Other or unknown	18 (19.6%)
BRAF V600 mutation	24/91 (26.4%)
Brain metastasis	26/91 (28.6%)
LDH level > normal	15/92 (16.3%)
Immune checkpoint inhibitors	
Pembrolizumab (anti-PD-1 therapy)	72
Nivolumab (anti-PD-1 therapy)	9
Nivolumab and ipilimumab (anti-CTLA-4 therapy)	10
Nivolumab and relatlimab (anti-LAG-3 therapy)	1
Intervals (d)	
Baseline PET to therapy initiation	33.5 (18–50)
Baseline PET and laboratory test	22 (9–34.3)

Qualitative data are number and percentage; continuous data are median and interquartile range.

TABLE 2
Results of Multivariate Analyses for Predicting PFS and OS

	PFS			OS		
Variable	Hazard ratio	95% CI	*P*	Hazard ratio	95% CI	*P*
High BLR (>0.78)	2.07	1.14–3.77	0.017	2.85	1.28–6.39	0.011
BRAF mutation	2.06	1.13–3.75	0.018	2.71	1.30–5.65	0.0078
Brain metastasis	1.85	0.99–3.45	0.053	2.09	0.99–4.43	0.054
Elevated LDH	2.00	0.90–4.42	0.085	3.31	1.29–8.46	0.013

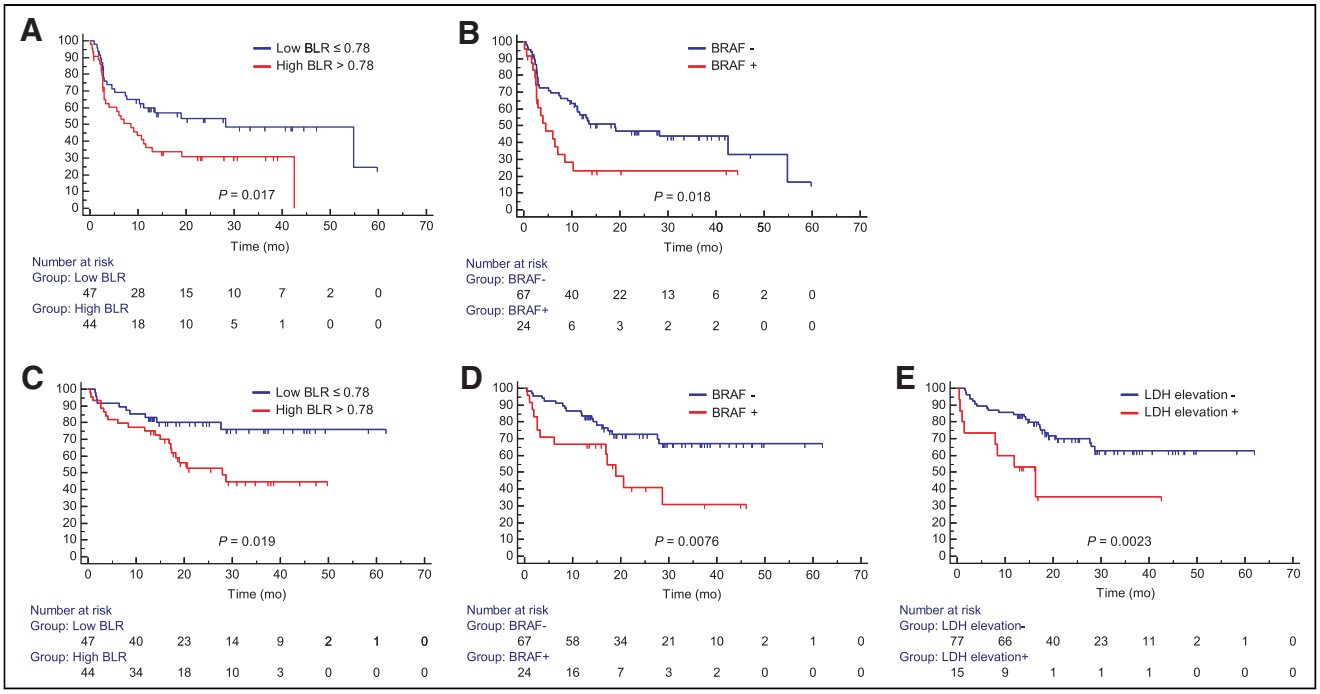

FIGURE 2. Kaplan–Meier curves for PFS (A and B) and OS (C–E) divided into 2 groups based on factors identified as being significant in multivariate analysis.

high BLR together with BRAF mutation or LDH elevation, OS was 16.9 and 1.0 mo, respectively.

Comparison of Clinical Characteristics and Imaging Parameters of Patients with High and Low BLR

The high-BLR group had higher white blood cell, neutrophil, and red blood cell counts; a higher CRP level; a higher MTV; and lower levels of hemoglobin and albumin than the low-BLR group ($P < 0.05$) (Supplemental Table 2). Neutrophil count had the strongest correlation with BLR ($\rho = 0.40$, $P = 0.0002$) among laboratory data, and MTV correlated weakly with BLR ($\rho = 0.34$, $P = 0.0011$) (Supplemental Table 3).

DISCUSSION

BLR on baseline ^{18}F-FDG PET showed a significant inverse correlation with PFS and OS in melanoma patients treated with anti-PD-1 therapy. Like previously published studies showing a relationship between laboratory markers of inflammation and BM metabolism (*7*,*10*), we found a significantly positive correlation between ^{18}F-FDG uptake in the BM and neutrophil count ($\rho = 0.40$) (*11*). This correlation could potentially be explained by the predominance of neutrophils in the BM, the high rates of granulopoiesis required to maintain the neutrophil population, and the preference of neutrophils to use glycolysis for energy production (*11*,*12*). A weak positive correlation between BLR and tumor burden (MTV, $\rho = 0.34$) was also found. An accumulation of inflammatory factors leads to immunosuppression, which is associated with cancer progression and poor outcomes (*5*). In melanoma, BM-derived cells play a key role in tumor progression, neovascularization, and priming of metastasis (*13*,*14*), potentially explaining the negative relationship between BM hypermetabolism and clinical outcomes observed in our study.

By combining information on BRAF and LDH elevation with BLR, we could extract a very poorly prognostic high-risk group with a median OS of 16.9 and 1.0 mo, respectively. We believe that this combination of predictive factors could allow the

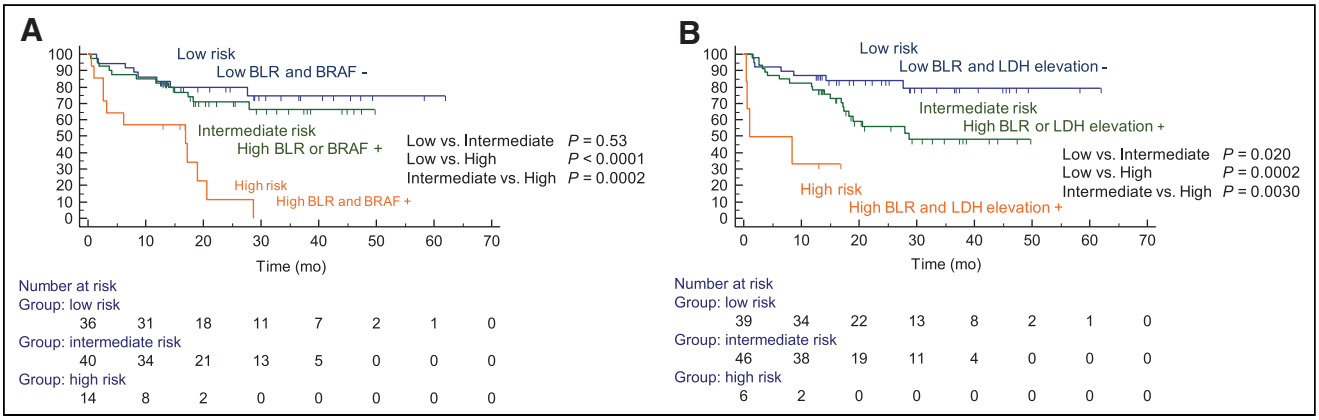

FIGURE 3. Kaplan–Meier curves for OS in 3 risk groups stratified according to BLR combined with BRAF mutation (A) or LDH elevation (B).

identification of high-risk patients who are not expected to benefit from anti-PD-1 therapy before treatment, allowing rapid selection of a potentially more efficacious treatment, such as novel therapies targeting cancer-related inflammation (*15*).

A recent retrospective study of 55 melanoma patients before treatment with anti-PD-1 reported the utility of BLR for predicting outcomes (*3*). The difference between the current study and this previous one is that we analyzed a larger number of patients (n = 92) and included patients with brain metastasis. Brain metastasis is not less frequent in patients with advanced melanoma who receive immunotherapy (*16*); in fact, 28.6% of our patients had brain metastasis before immunotherapy. Therefore, we determined that patients with brain metastasis should be included in the search for imaging biomarkers useful for predicting the response to, and the prognosis after, immunotherapy based on real-world clinical scenarios. However, there was a recent report contradicting our finding that melanoma patients who responded to immunotherapy had significantly higher ^{18}F-FDG uptake in the BM (BM SUV_{mean} normalized by blood-pool activity) than did nonresponders (*17*).

Our study had several limitations. First, it was retrospective. In addition, the use of different PET scanners could have resulted in variability in SUV measurements of the MTV. However, the estimation of BM metabolism was assessed by standardizing values with liver background, allowing for harmonization of the PET features and potential generalizability of our model.

CONCLUSION

Increased metabolism in the BM was associated with poor PFS and OS, potentially explained by evidence of systemic inflammation known to be associated with immunosuppression.

DISCLOSURE

No potential conflict of interest relevant to this article was reported.

KEY POINTS

QUESTION: Is pretreatment ^{18}F-FDG uptake in the BM useful in the prognostic evaluation of advanced melanoma patients treated with anti-PD-1 therapy?

PERTINENT FINDINGS: Univariate and multivariate analyses revealed that BLR was an independent prognostic factor for PFS and OS (P = 0.017 and 0.011, respectively). Patients with high BLR uptake (>median) tended to have systemic inflammation, known to be associated with immunosuppression.

IMPLICATIONS FOR PATIENT CARE: BLR may be a helpful imaging biomarker to select patients with advanced melanoma for immune-modulating therapies

REFERENCES

1. Wong A, Callahan J, Keyaerts M, et al. ^{18}F-FDG PET/CT based spleen to liver ratio associates with clinical outcome to ipilimumab in patients with metastatic melanoma. *Cancer Imaging.* 2020;20:36.
2. Nakamoto R, Zaba LC, Rosenberg J, et al. Prognostic value of volumetric PET parameters at early response evaluation in melanoma patients treated with immunotherapy. *Eur J Nucl Med Mol Imaging.* 2020;47:2787–2795.
3. Seban R-D, Nemer JS, Marabelle A, et al. Prognostic and theranostic ^{18}F-FDG PET-biomarkers for anti-PD1 immunotherapy in metastatic melanoma: association with outcome and transcriptomics. *Eur J Nucl Med Mol Imaging.* 2019;46:2298–2310.
4. Ito K, Schoder H, Teng R, et al. Prognostic value of baseline metabolic tumor volume measured on ^{18}F-fluorodeoxyglucose positron emission tomography/computed tomography in melanoma patients treated with ipilimumab therapy. *Eur J Nucl Med Mol Imaging.* 2019;46:930–939.
5. Diakos CI, Charles KA, McMillan DC, Clarke SJ. Cancer-related inflammation and treatment effectiveness. *Lancet Oncol.* 2014;15:e493–e503.
6. Seban R-D, Robert C, Dercle L, et al. Increased bone marrow SUVmax on ^{18}F-FDG PET is associated with higher pelvic treatment failure in patients with cervical cancer treated by chemoradiotherapy and brachytherapy. *OncoImmunology.* 2019;8:e1574197.
7. Lee JW, Ban MJ, Park JH, Lee SM. Effect of F-18 fluorodeoxyglucose uptake by bone marrow on the prognosis of head and neck squamous cell carcinoma. *J Clin Med.* 2019;8:1169.
8. Prévost S, Boucher L, Larivée P, Boileau R, Bénard F. Bone marrow hypermetabolism on ^{18}F-FDG PET as a survival prognostic factor in non–small cell lung cancer. *J Nucl Med.* 2006;47:559–565.
9. Bohnsack O, Hoos A, Ludajic K. Adaptation of the immune related response criteria: irRECIST [abstract]. *Ann Oncol.* 2014;25(suppl 4):iv369.
10. Lee JW, Seo KH, Kim ES, Lee SM. The role of ^{18}F-fluorodeoxyglucose uptake of bone marrow on PET/CT in predicting clinical outcomes in non-small cell lung cancer patients treated with chemoradiotherapy. *Eur Radiol.* 2017;27:1912–1921.
11. Murata Y, Kubota K, Yukihiro M, Ito K, Watanabe H, Shibuya H. Correlations between ^{18}F-FDG uptake by bone marrow and hematological parameters: measurements by PET/CT. *Nucl Med Biol.* 2006;33:999–1004.
12. Yagi M, Froelich J, Arentsen L, et al. Longitudinal FDG-PET revealed regional functional heterogeneity of bone marrow, site-dependent response to treatment and correlation with hematological parameters. *J Cancer.* 2015;6:531–537.
13. Kaplan RN, Riba RD, Zacharoulis S, et al. VEGFR1-positive haematopoietic bone marrow progenitors initiate the pre-metastatic niche. *Nature.* 2005;438:820–827.
14. Hiratsuka S, Nakamura K, Iwai S, et al. MMP9 induction by vascular endothelial growth factor receptor-1 is involved in lung-specific metastasis. *Cancer Cell.* 2002;2:289–300.
15. Urbanska AM, Zhang X, Prakash S. Bioengineered colorectal cancer drugs: orally delivered anti-inflammatory agents. *Cell Biochem Biophys.* 2015;72:757–769.
16. Zhang D, Wang Z, Shang D, Yu J, Yuan S. Incidence and prognosis of brain metastases in cutaneous melanoma patients: a population-based study. *Melanoma Res.* 2019;29:77–84.
17. Schwenck J, Schörg B, Fiz F, et al. Cancer immunotherapy is accompanied by distinct metabolic patterns in primary and secondary lymphoid organs observed by non-invasive in vivo ^{18}F-FDG-PET. *Theranostics.* 2020;10:925–937.

Exploiting the MUC5AC Antigen for Noninvasive Identification of Pancreatic Cancer

Kelly E. Henry[*1], Travis M. Shaffer[*1,2], Kyeara N. Mack[1,3], Janine Ring[1], Anuja Ogirala[1], Susanne Klein-Scory[4], Christina Eilert-Micus[4], Wolff Schmiegel[4], Thilo Bracht[5], Barbara Sitek[5], Marguerite Clyne[6], Colm J. Reid[6], Bence Sipos[7], Jason S. Lewis[1,3,8,9], Holger Kalthoff[10], and Jan Grimm[1,3,8]

[1]Department of Radiology, Memorial Sloan Kettering Cancer Center, New York, New York; [2]Department of Radiology, Stanford University, Stanford, California; [3]Molecular Pharmacology Program, Memorial Sloan Kettering Cancer Center, New York, New York; [4]Department of Medicine, Ruhr University Bochum, Bochum, Germany; [5]Medical Proteome Center, Ruhr University Bochum, Bochum, Germany; [6]School of Medicine, Health Sciences Centre, University College Dublin, Dublin, Ireland; [7]Department of Medical Oncology and Pneumology, University Hospital Tübingen, Tübingen, Germany; [8]Departments of Pharmacology and Radiology, Weill Cornell Medical College, New York, New York; [9]Radiochemistry and Molecular Imaging Probes Core, Memorial Sloan Kettering Cancer Center, New York, New York; and [10]Institute for Experimental Cancer Research, Christian-Albrechts University, Kiel, Germany

Pancreatic cancer (PC) remains the fourth leading cause of cancer death; therefore, there is a clinically unmet need for novel therapeutics and diagnostic markers to treat this devastating disease. Physicians often rely on biopsy or CT for diagnosis, but more specific protein biomarkers are highly desired to assess the stage and severity of PC in a noninvasive manner. Serum biomarkers such as carbohydrate antigen 19-9 are of particular interest as they are commonly elevated in PC but have exhibited suboptimal performance in the clinic. MUC5AC has emerged as a useful serum biomarker that is specific for PC versus inflammation. We developed RA96, an anti-MUC5AC antibody, to gauge its utility in PC diagnosis through immunohistochemical analysis and whole-body PET in PC. **Methods:** In this study, extensive biochemical characterization determined MUC5AC as the antigen for RA96. We then determined the utility of RA96 for MUC5AC immunohistochemistry on clinical PC and preclinical PC. Finally, we radiolabeled RA96 with ^{89}Zr to assess its application as a whole-body PET radiotracer for MUC5AC quantification in PC. **Results:** Immunohistochemical staining with RA96 distinguished chronic pancreatitis, pancreatic intraepithelial neoplasia, and varying grades of pancreatic ductal adenocarcinoma in clinical samples. ^{89}Zr-desferrioxamine-RA96 was able to detect MUC5AC with high specificity in mice bearing capan-2 xenografts. **Conclusion:** Our study demonstrated that RA96 can differentiate between inflammation and PC, improving the fidelity of PC diagnosis. Our immuno-PET tracer ^{89}Zr-desferrioxamine-RA96 shows specific detection of MUC5AC-positive tumors in vivo, highlighting the utility of MUC5AC targeting for diagnosis of PC.

Key Words: pancreatic cancer; RA96; immuno-PET; 89Zr; MUC5AC

J Nucl Med 2021; 62:1384–1390
DOI: 10.2967/jnumed.120.256776

Pancreatic cancer (PC) is a devastating disease with a 5-y survival rate of only 9% (*1*). Poor survival for PC patients is most often associated with a late-stage diagnosis, when the disease has already spread and continues to exhibit rapid metastatic progression. PC has few reliable biomarkers that are able to properly diagnose and guide treatment, especially within the window of early detection. As PC is inevitably more difficult to treat at this stage, biomarkers that can diagnose PC in asymptomatic patients may allow more patients to undergo potential curative tumor resection and greatly improve their prognosis.

Serum biomarkers as an indicator for disease are incredibly useful and can be tested routinely from blood work in patients (*2*). Elevated levels of carbohydrate antigen 19-9 (CA19-9) in the blood of patients with PC are typically a red flag in the clinical follow-up (*3*). If CA19-9 levels are abnormal, recurrence has to be assumed and patients are guided to have additional work-up, including abdominal CT scans or MRI (*4*). However, CA19-9 is elevated in approximately only 65% of PC, is not always elevated early in the disease, and can also be elevated in nonmalignant conditions such as chronic pancreatitis (CP) and other inflammatory disorders (*2*). As such, CA19-9 remains suboptimal for PC detection.

Recent evidence has shown that other serum biomarkers, such as mucins, may be more specific and detectable, particularly for differentiating inflammation from oncogenic lesions (*5,6*). Comprehensive genomic analyses of normal pancreas versus CP and PC tissue identified MUC5AC as the most differentially expressed mucin gene compared with benign pancreatic pathologies (*5,7,8*). MUC5AC belongs to a group of high-molecular-weight *O*-glycoproteins that are either secreted or membrane-bound (*5*). MUC5AC was further validated as a useful biomarker both in tandem with CA19-9 and independently when it comes to PC diagnosis (*8–10*) but has never been targeted for imaging.

In this study, we developed an antibody against MUC5AC and applied it for both immunohistochemical analysis and immuno-PET for PC diagnosis. Uptake of radiolabeled MUC5AC showed successful tumor delineation in a PC xenograft out to 144 h after injection of the radiotracer. The uptake of our radiotracer in vivo was blockable, as was demonstrated by a coinjection of excess unlabeled antibody, and also was significantly increased compared with the IgG control ($P < 0.001$), marking its specificity for the

Received Sep. 11, 2020; revision accepted Jan. 13, 2021.
For correspondence or reprints, contact Jan Grimm (grimmj@mskcc.org).
*Contributed equally to this work.
Published online March 12, 2021.

MUC5AC target. We postulate that our anti-MUC5AC antibody has the potential to improve diagnosis of PC both in vivo and ex vivo and change the paradigm for PC serum biomarkers.

MATERIALS AND METHODS

Cell Culture

All tissue culturing was performed using sterile techniques, and all cells were grown at 37°C and 5% CO_2 in a humidified atmosphere according to ATCC instructions. All cell lines discussed in this article were thawed from the same original stocks and routinely tested for *Mycoplasma* contamination.

RA96 Antibody, Protein Extraction, and RA96 Antigen Preparation

RA96 antibody was developed against intra- and intercellular tumor-associated antigens. Secretomes were obtained from supernatants of cells cultured for 48 h in serum-free media and prepared as previously described by us (*11*). Aliquots of lysates (50 μg) or aliquots of secretomes (15 μg) were separated in horizontal 1% agarose gels less than 5 mm thick (high-electroendosmosis, ultra-quality; CarlRoth) with running buffer (40 mM Tris-acetate, 1 mM ethylenediaminetetraacetic acid, and 0.1% sodium dodecyl sulfate, pH 8.0) according to previously published procedures (*12*).

Immunoprecipitation

As antigen sources, the secretomes (40 μg) or the lysates (200 μg) from RA96-reactive and nonreactive cells were used for immunoprecipitation. For comparative analyses, an alternative antibody against MUC5AC—2-11M1—was used in parallel to the RA96 hybridoma supernatant. The antibody 2-11M1 detects the globular D1/D2 domain located in the N terminus of MUC5AC (*13*).

Mass Spectrometry (MS) and Data Mining

Gel pieces containing the antibody-reactive or corresponding nonreactive signals were excised from the nonblotted gel part corresponding to the RA96-reactive region and subjected to the tryptic digestion procedure. The peptides were analyzed by liquid chromatography–tandem MS on a Q Exactive HF instrument (Thermo Fisher Scientific) coupled to an Ultimate 3000 RSLCnano high-performance liquid chromatography system (Dionex) as described previously (*14*). The lists of identified proteins from positive and corresponding negative samples were compared, and accession numbers found exclusively in positive control gel pieces were defined (Supplemental Table 1). A compilation of annotated tandem MS spectra can be found in the supplemental materials. Further criteria for the antigen identification were that the putative RA96 antigen had to be a high-molecular-mass protein of more than 300 kDa and could be associated with or belong to the mucin family (*15*).

Knockdown of MUC5AC and Recombinant Expression of MUC5AC Fragments

To further demonstrate that MUC5AC is the antigen for RA96 antibody, we performed small interfering RNA (siRNA) knockdown experiments and expression experiments on recombinant MUC5AC fragments in negative cell lines. For siRNA experiments, cells were grown to a confluency of approximately 30% and incubated with 100 μM Dharmacon ON-TARGETplus MUC5AC siRNA (D-001810-02-05; GE Healthcare) or Dharmacon ON-TARGETplus nontargeting siRNA (no. 2, lot 1876332; GE Healthcare) as a control using Dharmacon Dharmafect (GE Healthcare) for 2 d followed by incubation in serum-free medium for another 2 d. The protein samples were analyzed by immune blots with RA96. For expression of recombinant MUC5AC fragments, Cos7 cells and Paca44 cells were transfected with the MUC5AC sequences bearing the pcDNA3.1 expression system as previously described (*12*). N-terminal, C-terminal, and N + 2TR + C-terminal MUC5AC coding sequences and green fluorescent protein–pcDNA3.1 control DNA were transferred to cells using the Effectene transfection procedure (Qiagen). Three days after transfection, the proteins were prepared, separated by NuPAGE 7% gels (Pierce/ThermoFisher Scientific), transferred to an Immobilon-FL (Merck) polyvinylidene fluoride membrane, and probed by RA96 and anti-MUC5AC 2-11M1.

Immunohistochemistry with RA96

The tissue microarray was constructed as described previously (*16*). Briefly, 6 tissue microarrays containing 300 cores of normal ducts and pancreatic intraepithelial neoplasias (PanINs), originating from 21 disease-free pancreata and 81 resected pancreata (because of other neoplasms), 30 alcoholic chronic pancreatitis (CP) and 10 autoimmune pancreatitis specimens, and 48 pancreatic ductal adenocarcinomas (G1–G3) were evaluated. Immunohistochemical staining was performed with RA96, including deparaffinization of the formalin-fixed paraffin-embedded tissue sections and heat-induced antigen retrieval. The intensity of the reactions was scored as mild, moderate, or strong (score 1, 2, or 3, respectively) by an experienced pathologist.

Preparation and Radiolabeling of ^{89}Zr-Desferrioxamine (DFO) Antibodies

RA96 and isotype-matched IgG (~150 kDa) were functionalized with *p*-isothiocyanatobenzyl-DFO (DFO-Bn-NCS; Macrocyclics, Inc.) as described previously (*17*). DFO–antibody conjugates were analyzed via matrix-assisted laser desorption ionization time-of-flight MS and found to have 3–4 chelates per antibody. ^{89}Zr was produced through proton beam bombardment of yttrium foil and isolated in high purity as ^{89}Zr-oxalate at Memorial Sloan Kettering Cancer Center (MSKCC) according to published procedures (*18*). DFO-RA96 and DFO-IgG were incubated with neutralized ^{89}Zr-oxalate in Chelex (Bio-Rad) phosphate-buffered saline at pH 7.0 and 37°C for 1 h. Radioconjugates were purified using disposable size-exclusion (PD-10) columns with phosphate-buffered saline buffer exchange and characterized via instant thin-layer chromatography.

Small-Animal Models

All animal studies were conducted in accordance with the guidelines set by the Institutional Animal Care and Use Committee at MSK. Capan-2 cells (5×10^6/mouse) in 200 μL of 1:1 medium:Matrigel (BD Biosciences) were implanted subcutaneously in the lower right flank of female athymic nude (NU/NU) mice (6–8 wk old and weighing 20–22 g; Charles River Laboratories) and grown to a tumor volume of approximately 100–150 mm^3 (4–5 wk) before imaging studies. Mia PaCa-2, Capan-2, and Capan-1 cells were implanted orthotopically into the head of the pancreas of female athymic nude mice (40,000 cells, 1:1 Matrigel, 20 μL). The tumors were palpated weekly and grown to a volume of approximately 150–200 mm^3 (4–5 wk).

Enzyme-Linked Immunosorbent Assay on Serum Samples

Serum samples were collected from animals 1 wk before imaging studies. MUC5AC levels were detected with a human MUC5AC enzyme-linked immunosorbent assay kit (Aviva Systems Biology) according to the manufacturer's instructions.

In Vivo Imaging

The mice were anesthetized with 1.5%–2% isoflurane (Baxter Healthcare) supplemented with medical air and were injected with ^{89}Zr-DFO-RA96 or ^{89}Zr-DFO-IgG (10–11 MBq, 30–40 μg) in 130–150 μL of phosphate-buffered saline via the lateral tail vein. PET whole-body acquisitions were recorded at 24, 48, 72, 96, 120, and 144 h after injection using a dual small-animal PET/CT scanner (Inveon; Siemens). Images were collected at no less than 50 million coincidence events per animal and reconstructed using standard 2-dimensional ordered-subsets expectation maximization.

Biodistribution Studies

Ex vivo γ-counting of tissues was performed to measure the uptake of the radioconjugate in tissues at 144 h after radiotracer administration. Radioactivity within each organ was counted using a PerkinElmer γ-counter with isotope-dependent calibrated protocols. Tracer uptake expressed as percentage injected dose per gram (%ID/g) was calculated as the radioactivity associated with each tissue divided by the organ mass, using the mass of the decay-corrected injected dose at the time of counting.

Statistical Considerations

All data were analyzed by the unpaired, 2-tailed Student *t* test, and differences at the 95% confidence level ($P < 0.05$) were considered statistically significant. Positive and negative controls were included whenever possible to ensure rigor and reproducibility throughout the experimental design.

RESULTS

MS Analysis Identifies MUC5AC Target

To characterize the Ra96 antigen, we performed secretome analyses. By immune detection of secretomes and lysates of the cell lines and by immune fluorescence analyses of PC cell lines, we selected the RA96-reactive and nonreactive cells. The cell line Capan-1 secreted the highest amounts of RA96 antigen, followed by A818, BxPC3, and Panc1. MiaPaCa2, Panctu II, Paca44, and the human pancreatic duct epithelial cells show no detectable reactivity for RA96 antibodies (Supplemental Fig. 1). The RA96 antigen is a high-molecular-weight protein that is sensitive against reducing conditions and disappeared after treatment of the samples with dithiothreitol. For MS analysis, we chose Panctu II as the negative cells and A818 cells as the positive cells because of the more focused region in Western blots than for Capan-1. MS results were compiled in an additional file (Supplemental Fig. 2). Only MUC5AC was exclusively found with maximally 5 unique peptides in the secretome samples from RA96-reactive cell lines with or without immunoprecipitation (the supplemental materials include tables of the MS results).

Immunoprecipitation Confirms MUC5AC at RA96 Target

To confirm the conclusion of the MS results, we performed immunoprecipitation with RA96 and in parallel with MUC5AC monoclonal antibody 2-11M1 (Biomol) in the same experiments (Supplemental Fig. 3) and tested the immune complexes with the antibodies and vice versa. The immune-precipitated proteins isolated by 2-11M1 antibodies were recognized by RA96 antibodies, and the proteins immune-precipitated by RA96 were also recognized by anti MUC5AC clone 2-11M1. A MUC5AC N-terminal peptide (Sigma-Aldrich) was used for competition of the RA96 immune signals in Western blots. The signal intensity of the 2-11M1 antibody could be reduced to 50% by treatment with a 10 μg/mL concentration of N-terminal peptide, whereas this treatment was not sufficient to significantly diminish the RA96 signals (data not shown).

MUC5AC siRNA Experiments and Reexpression Confirms RA96 Specificity

We used siRNA on-target, as well as for knockdown of Muc5AC expression in positive cells (Supplemental Figs. 4A and 4B). In Western blots, the RA96 signal intensity dropped to 20% of the untreated sample. To characterize the epitope of RA96 in more detail, we performed MUC5AC reexpression experiments. The constructs were described by Ryan et al. (kindly provided to us by Marguerite Clyne and Colm Reid), and coding for MUC5AC (N-terminal, C-terminal, and N + 2TR + C-terminal fragments) was used in Cos7 control cells (*12*). RA96 and anti-MUC5AC 2-11M1 recognized the lysates of MUC5AC-transfected cells with the N + 2TR + C-terminal construct and with the N-terminal (Supplementary Fig. 4C). Neither RA96 nor 2-11M1 detected the C-terminal fragment. The expression of the C-terminal part in transfected Cos7 cells was checked with the help of the flag tags on the C-terminal construct (data not shown).

Immunohistochemistry with RA96 Highlights Specificity for PC Lesions over CP

RA96 shows positive staining and a specific progression of severity in clinical samples. Positive staining begins at the PanIN level and increases in different grades of pancreatic ductal adenocarcinoma, including staining in capan-2 xenografts (Fig. 1). There is little to no staining in the CP samples, highlighting specificity for PC over other inflammatory conditions that are often conflated by serum biomarkers. Clinical immunohistochemistry is tabulated and quantified in Supplemental Figure 5 (*19*).

^{89}Zr-DFO-RA96 Shows Significant Tumor Delineation in Capan-2 Xenografts

Multiple stoichiometric ratios (×10, ×20, and ×40) of chelator (DFO) to antibody (RA96 or IgG) were characterized via matrix-

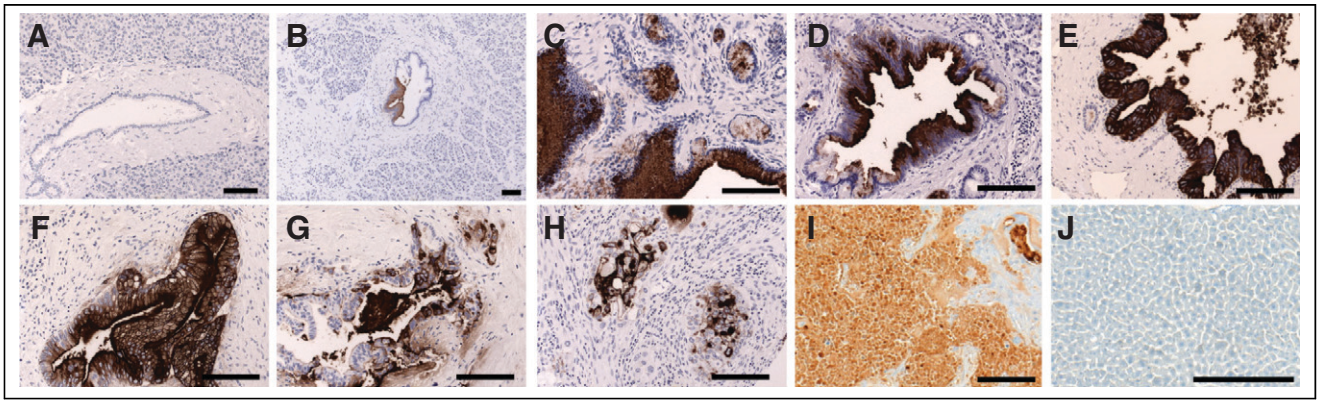

FIGURE 1. Immunohistochemistry of MUC5AC with RA96. (A) No expression of RA96 in normal human pancreas. (B) No or weak expression in chronic pancreatitis. (C–E) Strong staining with RA96 in PanINs 1–3. (F–H) Moderate to strong expression in pancreatic ductal adenocarcinoma of different grades. More detail is provided in supplemental materials with regard to grade and scoring. (I) Capan-2 xenografts also staining positively with RA96. (J) Control tissue showing no background staining in liver. Each line indicates 50 μm.

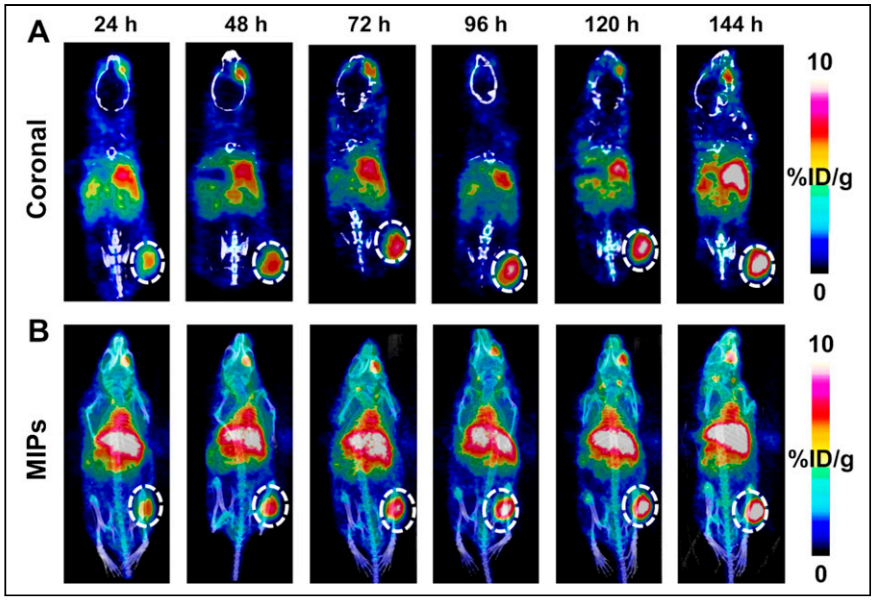

FIGURE 2. Serial PET/CT imaging of ^{89}Zr-DFO-RA96 over course of 144 h. Images are represented as coronal slices (A) and maximum-intensity projections (MIPs) (B). Tumors are on right flank and encircled by dotted line. Mice were retroorbitally bled from right eye 1 wk previously, resulting in nonspecific uptake of radiotracer in eye region. Increasing uptake of radiotracer in tumor is shown over time, with maximum at 144 h.

assisted light desorption ionization time-of-flight MS. Reaction conditions that resulted in DFO-RA96 and DFO-IgG with an average of 3–4 chelators per antibody were used in further radiolabeling procedures. All radiotracers were examined for their stability in serum; each showed more than 95% stability out to 1 wk for RA96 and more than 90% stability for IgG radiolabeled constructs (Supplemental Fig. 6). The radiochemical yield for each reaction ranged from 90% to 95%, and all tracers used in vivo were processed to a radiochemical purity of more than 99%. The specific activity and molar activity for both ^{89}Zr-DFO-RA96 and ^{89}Zr-DFO-IgG were 0.3–0.4 MBq/μg and 45–55 GBq/μmol, respectively. Serial PET imaging with ^{89}Zr-DFO-RA96 shows significant uptake (14.6 ± 1.5 %ID/g) compared with the blocking group (6.6 ± 1.5 %ID/g) and ^{89}Zr-DFO-IgG (8.8 ± 0.3 %ID/g), with a P value of less than 0.001 for both. In capan-2 tumors, increased accumulation of antibody was observed over the course of 144 h (Fig. 2), as expected for antibody-based radiotracers. To mitigate liver uptake for a shed serum biomarker, we tried the preinjection strategy as previously described by Houghton et al. with anti-CA19-9 radiotracer (*20*). To mimic these studies, we preinjected a ×3 cold dose (unlabeled RA96) 4 h before ^{89}Zr-DFO-RA96 administration. Interestingly, we observed a partial block of the system, with no statistical difference between ^{89}Zr-DFO-RA96 tumor uptake via a ×3 preinjection or a ×30 cold blocking dose coinjection (6.2 ± 0.8 %ID/g for the ×3 preinjection vs. 6.6 ± 1.5 %ID/g for the ×30 coinjection). The ×30 dose was specifically administered for blocking purposes to confirm the specificity of the RA96 tracer. The block and partial-block groups, along with the ^{89}Zr-DFO-IgG arm, have a P value of less than 0.001 when compared with the specific uptake of ^{89}Zr-DFO-RA96 in the tumor (Fig. 3). This can also be observed as early as 24 h and is consistent at 72 h as well (Supplemental Figs. 7 and 8). We performed an enzyme-linked immunosorbent assay experiment on serum samples collected from capan-2 mice 1 wk before PET imaging experiments to assess the degree of MUC5AC antigen shedding in this model. We could not find any detectable MUC5AC in serum samples of these animals, despite the successful calibration curve and quality controls for the kit (Supplemental Fig. 9). These results are consistent with our partial block of our target from the preinjection of unlabeled antibody.

^{89}Zr-DFO-RA96 Shows Significant Tumor Delineation in Orthotopic Xenografts of Varying MUC5AC Expression

To further expand on the utility of this tracer, we inoculated animals orthotopically with tumors of varying MUC5AC expression and RA96 immunogenicity. We found that the uptake did indeed correlate with low, medium, and high MUC5AC expression in orthotopic models of MIA PaCA-2, Capan-2, and Capan-1, respectively (Fig. 4). Additional imaging of this cohort at 72 h can be found in Supplemental Figure 10.

DISCUSSION

With all these data taken together, we were able to confirm that RA96 can demarcate MUC5AC expression in PC tumors. Our immuno-PET tracer ^{89}Zr-DFO-RA96 shows excellent and specific tumor delineation in MUC5AC-positive tumors that can be blocked with both a partial and excess administration of unlabeled RA96. Although the capan-2 tumor model has been characterized as a shed antigen model for serum biomarker CA19-9 (*20*), we did not observe significant shedding of MUC5AC, despite clinical data showing a similar effect of this secreted biomarker (*9*). Moreover, we also indicate that ^{89}Zr-DFO-RA96 is able to detect orthotopic lesions in multiple models of PC of varying MUC5AC expression. Finally, RA96 is multipurposed in its ability to serve as an antibody for immunohistochemistry, successfully delineating CP from PC through staining of MUC5AC in PanINs and increasing grades of pancreatic ductal adenocarcinoma. We show strong evidence that this biomarker, antibody, and radiotracer have great potential for the field of PC diagnostics through multiple modalities.

Repeat biopsies are invasive and often lack reproducibility because of sampling issues, particularly in heterogeneous tumors such as PC. More importantly, biopsies may not be particularly useful for patients with widespread metastasis, which is often the case for PC. A whole-body imaging agent that is specific for PC over CP could serve as an early diagnostic for PanINs and would be a game-changing biomarker that serves to fulfill a diagnostic niche that the field of PC is desperately missing. Currently, the standard for diagnostic imaging of PC in the clinic is typically CT or MRI. Although these techniques can be sufficient for diagnostic purposes, CT and MRI do not offer all the advantages that PET does in terms of quantitative measurement of a specific biomarker.

Establishing biomarkers in PC is a critically unmet need to improve the prognosis of this challenging disease. Although several diagnostic biomarkers for PC have been investigated, most have yielded suboptimal results (*21–23*). CA19-9, a blood-based biomarker for follow-up, is useful for disease prognosis but has limited utility as an early detection marker due to its variable sensitivity (60%–90%), specificity (68%–91%), and positive predictive value (0.9%–2.4%) (*24,25*). Additionally, CA19-9 can be elevated

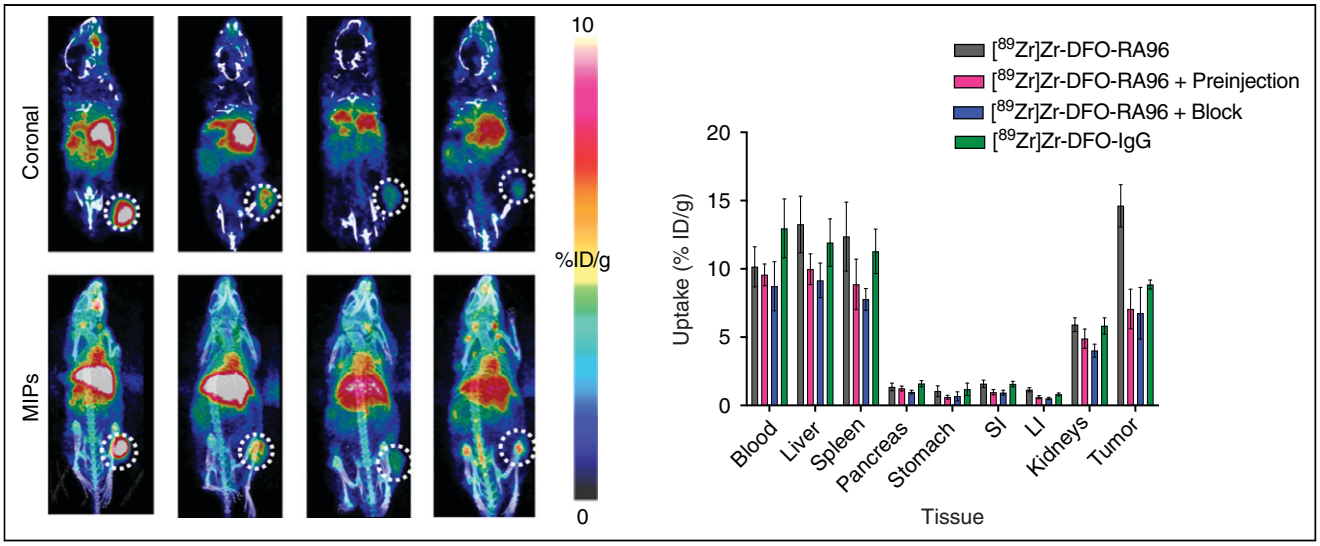

FIGURE 3. Serial PET/CT imaging of ^{89}Zr-DFO-RA96 and ^{89}Zr-DFO-IgG, with corresponding ex vivo biodistribution at 144 h. Images are represented as coronal slices (A) and maximum-intensity projections (MIPs) (B). Tumors are on right flank and encircled by dotted line. Significant differences are noted when comparing ^{89}Zr-DFO-RA96 with all control groups ($P < 0.001$). "Preinjection" indicates partial block, with ×3 amount of unlabeled antibody injected 4 h before injection with ^{89}Zr-DFO-RA96. "Block" indicates full block with ×30 amount of unlabeled antibody coinjected with ^{89}Zr-DFO-RA96. "IgG" indicates injection of isotype-matched control ^{89}Zr-DFO-IgG. Mice were retroorbitally bled from right eye 1 wk previously, resulting in nonspecific uptake of radiotracer in eye region. LI = large intestine; SI = small intestine.

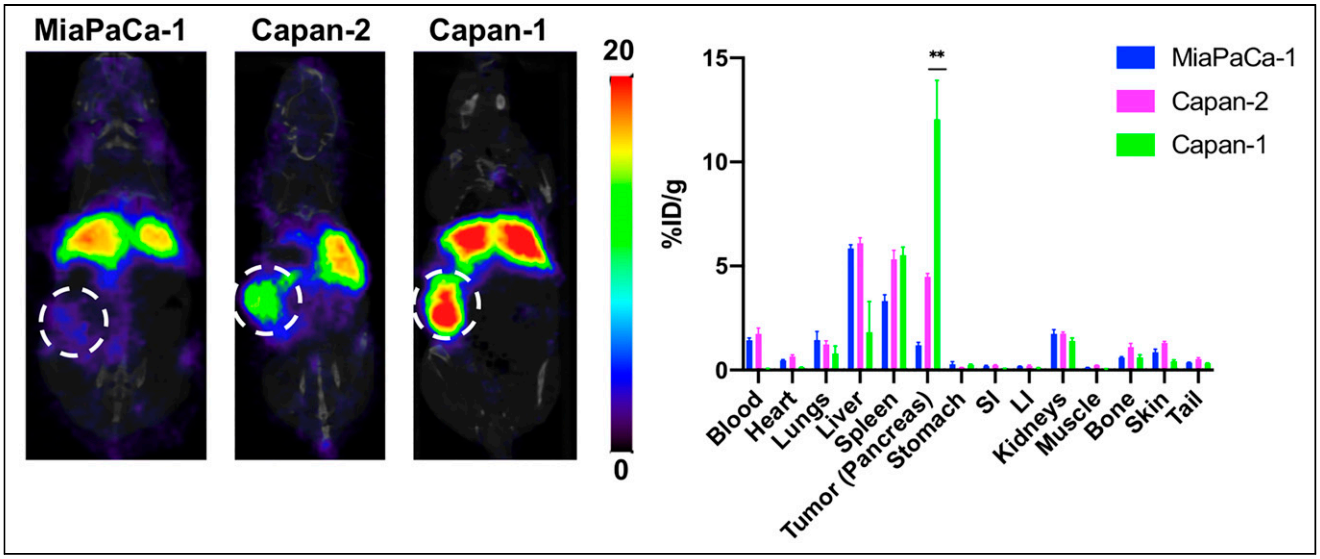

FIGURE 4. PET/CT imaging of ^{89}Zr-DFO-RA96, with corresponding ex vivo biodistribution at 144 h in multiple orthotopic tumor models. Images are represented as coronal slices, and tumors are encircled by dotted line. From left to right: MiaPaCa-1 tumors (low MUC5AC expression), Capan-2 tumors (medium MUC5AC expression), and Capan-1 tumors (high MUC5AC expression). LI = large intestine; SI = small intestine.

in benign conditions such as CP, jaundice, and cirrhosis. Furthermore, approximately 5%–10% of Caucasians are unable to synthesize CA19-9 (*25–27*), which makes it challenging for widespread reliability as a biomarker in the clinic. Approximately 65% of resectable PC cases have elevated levels of CA19-9 in the blood (*21*). In light of the sporadic nature of PC and asymptomatic early disease stages, identification and characterization of serum markers that can either complement or outperform CA19-9 are highly desirable.

Previous studies have shown that CA19-9 levels can predict stage and survival in resectable PC (*28*) and in locally unresectable PC (*29*). Multiple recent studies have also revealed the nonspecific nature of CA19-9 as a diagnostic marker (*2–4,30*). Several promising studies focus on CA19-9 for both imaging and radioimmunotherapy (*31,32*) and are ongoing at MSK. We aim to apply our expertise in order to evaluate novel biomarkers for both early and specific detection of PC and to drive the improvement of clinical outcomes for this devastating disease. Clinical gold standard

metabolic radiotracers such as ^{18}F-FDG are often nonspecific for malignancy (*33*). Our MUC5AC-targeted radiotracer could fill the gap that exists for serum biomarkers and serve to fulfill an unmet need for early diagnosis in PC.

CONCLUSION

Current biomarkers for PC are unreliable when it comes to differentiating between inflammation and malignancy. The RA96 antibody has been well characterized to be a MUC5AC conformation–dependent antigen. RA96 has the ability to achieve early detection of PC as it can detect lesions from PanINs all the way to fully developed pancreatic ductal adenocarcinoma via immunohistochemistry, as well as specifically demarcate PC from CP in patient samples. We have successfully developed an immuno-PET tracer with RA96 and shown that it can noninvasively and specifically demarcate MUC5AC expression in PC. We expect that immuno-PET targeting MUC5AC has high potential to be clinically useful for early detection of PC.

DISCLOSURE

Assistance was received from the Antibody & Bioresource, Small Animal Imaging, and Radiochemistry and Molecular Imaging Probe Core Facilities at MSK, which are supported in part by NIH grant P30 CA08748. Financial support was received from Mr. William H. Goodwin and Mrs. Alice Goodwin and the Commonwealth Foundation for Cancer Research and the Experimental Therapeutics Center of MSK (Jan Grimm) and from NIH grant R35 CA232130-01A1 (Jason Lewis) and the MSK Center for Molecular Imaging and Nanotechnology Tow Fellowship (Kelly Henry). A part of this study was funded by P.U.R.E. (Protein Research Unit Ruhr within Europe), Ministry of Innovation, Science, and Research of North-Rhine Westphalia, Germany. Jan Grimm and Jason S. Lewis are both associate editors of *The Journal of Nuclear Medicine*. No other potential conflict of interest relevant to this article was reported.

ACKNOWLEDGMENTS

We acknowledge BioRender for preparing the graphical abstract. This work is dedicated to the late Prof. Siegfried Matzku, DKFZ, Heidelberg, Germany, who initiated in vivo targeting strategies decades ago. We also sincerely appreciate the long-standing support of Prof. Günter Klöppel, now Pathology Munich, who helped to select the best candidates from an overwhelming number of hybridoma cultures during the common projects in Hamburg.

KEY POINTS

QUESTION: The central hypothesis of this study is that our MUC5AC-targeted antibody RA96 could detect PC lesions that are specific from other instances of inflammation such as CP.

PERTINENT FINDINGS: We demonstrate that our immuno-PET strategy can be used to noninvasively detect MUC5AC expression in PC, a key serum biomarker that is able to not only detect PanINs but also specifically demarcate PC from CP.

IMPLICATIONS FOR PATIENT CARE: There is a critical need for developing better biomarkers to improve early detection of PC. Current biomarkers for PC are unreliable when it comes to differentiating between inflammation and malignancy. ^{89}Zr-DFO-RA96 could be a valuable tool to specifically demarcate PC from CP and detect early-onset PanINs.

REFERENCES

1. McGuigan A, Kelly P, Turkington RC, Jones C, Coleman HG, McCain RS. Pancreatic cancer: a review of clinical diagnosis, epidemiology, treatment and outcomes. *World J Gastroenterol.* 2018;24:4846–4861.
2. Song J, Sokoll LJ, Pasay JJ, et al. Identification of serum biomarker panels for the early detection of pancreatic cancer. *Cancer Epidemiol Biomarkers Prev.* 2019;28:174–182.
3. Ballehaninna UK, Chamberlain RS. Serum CA 19-9 as a biomarker for pancreatic cancer: a comprehensive review. *Indian J Surg Oncol.* 2011;2:88–100.
4. Ballehaninna UK, Chamberlain RS. The clinical utility of serum CA 19-9 in the diagnosis, prognosis and management of pancreatic adenocarcinoma: an evidence based appraisal. *J Gastrointest Oncol.* 2012;3:105–119.
5. Kato S, Hokari R, Crawley S, et al. MUC5AC mucin gene regulation in pancreatic cancer cells. *Int J Oncol.* 2006;29:33–40.
6. Rachagani S, Torres MP, Kumar S, et al. Mucin (Muc) expression during pancreatic cancer progression in spontaneous mouse model: potential implications for diagnosis and therapy. *J Hematol Oncol.* 2012;5:68.
7. Iacobuzio-Donahue CA, Velculescu VE, Wolfgang CL, Hruban RH. Genetic basis of pancreas cancer development and progression: insights from whole-exome and whole-genome sequencing. *Clin Cancer Res.* 2012;18:4257–4265.
8. Matull WR, Andreola F, Loh A, et al. MUC4 and MUC5AC are highly specific tumour-associated mucins in biliary tract cancer. *Br J Cancer.* 2008;98:1675–1681.
9. Kaur S, Smith LM, Patel A, et al. A Combination of MUC5AC and CA19-9 improves the diagnosis of pancreatic cancer: a multicenter study. *Am J Gastroenterol.* 2017;112:172–183.
10. Kim GE, Bae HI, Park HU, et al. Aberrant expression of MUC5AC and MUC6 gastric mucins and sialyl Tn antigen in intraepithelial neoplasms of the pancreas. *Gastroenterology.* 2002;123:1052–1060.
11. Adamczyk KA, Klein-Scory S, Tehrani MM, et al. Characterization of soluble and exosomal forms of the EGFR released from pancreatic cancer cells. *Life Sci.* 2011;89:304–312.
12. Ryan A, Smith A, Moore P, et al. Expression and characterization of a novel recombinant version of the secreted human mucin MUC5AC in airway cell lines. *Biochemistry.* 2015;54:1089–1099.
13. Nollet S, Escande F, Buisine MP, et al. Mapping of SOMU1 and M1 epitopes on the apomucin encoded by the 5′ end of the MUC5AC gene. *Hybrid Hybridomics.* 2004;23:93–99.
14. Witzke KE, Rosowski K, Müller C, et al. Quantitative secretome analysis of activated Jurkat cells using click chemistry-based enrichment of secreted glycoproteins. *J Proteome Res.* 2017;16:137–146.
15. Kalthoff H, Schmiegel W-H, Auerswald U, et al. Monoclonal antibody RA-96 defines a new mucin antigen in pancreatic cancer. *Digestion.* 1988;40:90.
16. Neesse A, Hahnenkamp A, Griesmann H, et al. Claudin-4-targeted optical imaging detects pancreatic cancer and its precursor lesions. *Gut.* 2013;62:1034–1043.
17. Henry KE, Dacek MM, Dilling TR, et al. A PET imaging strategy for interrogating target engagement and oncogene status in pancreatic cancer. *Clin Cancer Res.* 2019;25:166–176.
18. Holland JP, Sheh Y, Lewis JS. Standardized methods for the production of high specific-activity zirconium-89. *Nucl Med Biol.* 2009;36:729–739.
19. Juhl H, Stritzel M, Wroblewski A, et al. Immunocytological detection of micrometastatic cells: comparative evaluation of findings in the peritoneal cavity and the bone marrow of gastric, colorectal and pancreatic cancer patients. *Int J Cancer.* 1994;57:330–335.
20. Houghton JL, Abdel-Atti D, Scholz WW, Lewis JS. Preloading with unlabeled CA19.9 targeted human monoclonal antibody leads to improved PET imaging with ^{89}Zr-5B1. *Mol Pharm.* 2017;14:908–915.
21. Goggins M. Molecular markers of early pancreatic cancer. *J Clin Oncol.* 2005;23:4524–4531.
22. Kaur S, Baine MJ, Jain M, Sasson AR, Batra SK. Early diagnosis of pancreatic cancer: challenges and new developments. *Biomark Med.* 2012;6:597–612.
23. Koopmann J, Rosenzweig CNW, Zhang Z, et al. Serum markers in patients with resectable pancreatic adenocarcinoma: macrophage inhibitory cytokine 1 versus CA19-9. *Clin Cancer Res.* 2006;12:442–446.
24. Locker GY, Hamilton S, Harris J, et al. ASCO 2006 update of recommendations for the use of tumor markers in gastrointestinal cancer. *J Clin Oncol.* 2006;24:5313–5327.
25. Duffy MJ, Sturgeon C, Lamerz R, et al. Tumor markers in pancreatic cancer: a European Group on Tumor Markers (EGTM) status report. *Ann Oncol.* 2010;21:441–447.
26. Brody JR, Witkiewicz AK, Yeo CJ. The past, present, and future of biomarkers: a need for molecular beacons for the clinical management of pancreatic cancer. *Adv Surg.* 2011;45:301–321.
27. Ghaneh P, Costello E, Neoptolemos JP. Biology and management of pancreatic cancer. *Postgrad Med J.* 2008;84:478–497.

28. Ferrone CR, Finkelstein DM, Thayer SP, Muzikansky A, Fernandez-delCastillo C, Warshaw AL. Perioperative CA19-9 levels can predict stage and survival in patients with resectable pancreatic adenocarcinoma. *J Clin Oncol.* 2006;24:2897–2902.
29. Yang GY, Malik NK, Chandrasekhar R, et al. Change in CA 19-9 levels after chemoradiotherapy predicts survival in patients with locally advanced unresectable pancreatic cancer. *J Gastrointest Oncol.* 2013;4:361–369.
30. Wong S-J, Hong C-M, Wang H-P, Cheng T-Y. High serum level of CA 19-9 not always related to the pancreas: an asymptomatic case of highly elevated CA 19-9 related to lung adenocarcinoma. *J Pancreas.* 2016;17:653–655.
31. Lohrmann C, O'Reilly EM, O'Donoghue JA, et al. Retooling a blood-based biomarker: phase I assessment of the high-affinity CA19-9 antibody HuMab-5B1 for immuno-PET imaging of pancreatic cancer. *Clin Cancer Res.* 2019;25:7014–7023.
32. Poty S, Carter LM, Mandleywala K, et al. Leveraging bioorthogonal click chemistry to improve ^{225}Ac-radioimmunotherapy of pancreatic ductal adenocarcinoma. *Clin Cancer Res.* 2019;25:868–880.
33. Ibrahim N, Cho S, Hall L, Perlman S. Is it cancer? Potential pitfalls of FDG PET/CT imaging [abstract]. *J Nucl Med.* 2016;57(suppl 2):1315.

First-in-Humans Application of ^{161}Tb: A Feasibility Study Using ^{161}Tb-DOTATOC

Richard P. Baum*[1], Aviral Singh*[1,2], Harshad R. Kulkarni[1], Peter Bernhardt[3,4], Tobias Rydén[3,4], Christiane Schuchardt[1], Nadezda Gracheva[5], Pascal V. Grundler[5], Ulli Köster[6], Dirk Müller[7], Michael Pröhl[7], Jan Rijn Zeevaart[8], Roger Schibli[5,9], Nicholas P. van der Meulen[5,10], and Cristina Müller[5]

[1]Theranostics Center for Molecular Radiotherapy and Precision Oncology, ENETS Center of Excellence, Zentralklinik Bad Berka, Bad Berka, Germany; [2]GROW–School for Oncology and Developmental Biology, Maastricht University Medical Center, Maastricht, The Netherlands; [3]Department of Radiation Physics, The Sahlgrenska Academy, University of Gothenburg, Gothenburg, Sweden; [4]Department of Medical Physics and Medical Bioengineering, Sahlgrenska University Hospital, Gothenburg, Gothenburg, Sweden; [5]Center for Radiopharmaceutical Sciences ETH-PSI-USZ, Paul Scherrer Institute, Villigen-PSI, Switzerland; [6]Institut Laue Langevin, Grenoble, France; [7]Department of Radiopharmacy, Zentralklinik Bad Berka, Bad Berka, Germany; [8]Radiochemistry, South African Nuclear Energy Corporation (Necsa), Pelindaba, South Africa; [9]Department of Chemistry and Applied Biosciences, ETH Zurich, Zurich, Switzerland; and [10]Laboratory of Radiochemistry, Paul Scherrer Institute, Villigen-PSI, Switzerland

^{161}Tb has decay properties similar to those of ^{177}Lu but, additionally, emits a substantial number of conversion and Auger electrons. The aim of this study was to apply ^{161}Tb in a clinical setting and to investigate the feasibility of visualizing the physiologic and tumor biodistributions of ^{161}Tb-DOTATOC. **Methods:** ^{161}Tb was shipped from Paul Scherrer Institute, Villigen-PSI, Switzerland, to Zentralklinik Bad Berka, Bad Berka, Germany, where it was used for the radiolabeling of DOTATOC. In 2 separate studies, 596 and 1,300 MBq of ^{161}Tb-DOTATOC were administered to a 35-y-old male patient with a metastatic, well-differentiated, nonfunctional malignant paraganglioma and a 70-y-old male patient with a metastatic, functional neuroendocrine neoplasm of the pancreatic tail, respectively. Whole-body planar γ-scintigraphy images were acquired over a period of several days for dosimetry calculations. SPECT/CT images were reconstructed using a recently established protocol and visually analyzed. Patients were observed for adverse events after the application of ^{161}Tb-DOTATOC. **Results:** The radiolabeling of DOTATOC with ^{161}Tb was readily achieved with a high radiochemical purity suitable for patient application. Planar images and dosimetry provided the expected time-dependent biodistribution of ^{161}Tb-DOTATOC in the liver, kidneys, spleen, and urinary bladder. SPECT/CT images were of high quality and visualized even small metastases in bones and liver. The application of ^{161}Tb-DOTATOC was well tolerated, and no related adverse events were reported. **Conclusion:** This study demonstrated the feasibility of imaging even small metastases after the injection of relatively low activities of ^{161}Tb-DOTATOC using γ-scintigraphy and SPECT/CT. On the basis of this essential first step in translating ^{161}Tb to clinics, further efforts will be directed toward the application of ^{161}Tb for therapeutic purposes.

Key Words: ^{161}Tb; SPECT/CT imaging; DOTATOC; Auger electrons; first-in-humans

J Nucl Med 2021; 62:1391–1397
DOI: 10.2967/jnumed.120.258376

Terbium comprises 4 medically interesting radioisotopes (^{149}Tb, ^{152}Tb, ^{155}Tb, ^{161}Tb) that are potentially useful for various applications in nuclear medicine using chemically identical radiopharmaceuticals (*1*). Several years ago, the production and a preliminary preclinical application of all 4 Tb radioisotopes were demonstrated at Paul Scherrer Institute in Villigen, Switzerland (*2*). Since then, additional studies have been performed with the aims of improving production methods (*3*) and investigating the potential of these radioisotopes for nuclear imaging (^{152}Tb, ^{155}Tb) (*4*,*5*) and targeted radionuclide therapy (^{149}Tb, ^{161}Tb) (*6*–*10*) in more detail. In terms of clinical translation, ^{152}Tb was the only terbium radioisotope that was applied to patients in 2 independent proof-of-concept studies (*11*,*12*). ^{152}Tb-DOTATOC, a somatostatin receptor agonist, was administered to a patient with a metastatic neuroendocrine neoplasm (NEN) of the ileum at Zentralklinik Bad Berka, Bad Berka, Germany (*11*). The PET images were convincing and, because of the relatively long half-life of ^{152}Tb (17.5 h), image acquisition over an extended time period was feasible and enabled the visualization of the metastases (*11*).

^{161}Tb is, nevertheless, at the most advanced stage of all Tb radioisotopes in terms of production and preclinical investigations. This radionuclide is of particular interest for targeted radionuclide therapy because its decay properties are similar to those of ^{177}Lu (half-life of ^{161}Tb: 6.95 d (*13*); half-life of ^{177}Lu: 6.65 d) and because of the emission of medium-energy β$^-$-particles (154 keV for ^{161}Tb; 134 keV for ^{177}Lu). Importantly, ^{161}Tb emits a substantial number of conversion and Auger electrons, which are believed to make ^{161}Tb therapeutically more effective than ^{177}Lu (*14*). Several theoretic dosimetry studies consistently predicted the high potential of this radionuclide for nuclear oncology purposes (*15*–*20*). Preclinically, it was consistently shown that ^{161}Tb-labeled tumor-targeting agents delayed tumor growth in mice more effectively than their ^{177}Lu-labeled counterparts (*7*,*9*,*21*). It was also demonstrated in preclinical studies as well as in clinical phantom studies that ^{161}Tb can be visualized using SPECT because of the emission of γ-radiation and, thus, potentially can be used for dosimetry purposes and monitoring of the activity distribution in patients (*7*,*9*,*22*).

Received Oct. 16, 2020; revision accepted Jan. 19, 2021.
For correspondence or reprints, contact Richard P. Baum (baum@curanosticum.de) and Cristina Müller (cristina.mueller@psi.ch).
*Contributed equally to this work.
Published online February 5, 2021.

Lehenberger et al. demonstrated the concept of ^{161}Tb production using the ^{160}Gd(n,γ)^{161}Gd → ^{161}Tb nuclear reaction in analogy to the production of no-carrier-added ^{177}Lu (*14*). More recently, this production route was stepwise optimized at Paul Scherrer Institute, enabling the preparation of ^{161}Tb at a high activity and in a quality comparable to that of commercially available ^{177}Lu (*3*).

In the present study, we aimed to demonstrate first-in-humans application of ^{161}Tb-DOTATOC. After irradiation of gadolinium targets at a high-flux reactor to obtain ^{161}Tb, the ampoules were shipped to Paul Scherrer Institute, where ^{161}Tb was chemically separated from its target material. The product was transported to Zentralklinik Bad Berka, where it was directly used for the radiolabeling of DOTATOC. ^{161}Tb-DOTATOC was administered to 2 patients with NENs for whole-body planar γ-scintigraphy as well as for SPECT/CT imaging.

MATERIALS AND METHODS

Production of ^{161}Tb

^{161}Tb was produced using the ^{160}Gd(n,γ)^{161}Gd → ^{161}Tb nuclear reaction as previously reported (*3*,*14*). In brief, enriched ^{160}Gd targets were irradiated at the high-flux reactor at Institut Laue Langevin, Grenoble, France, or at the SAFARI-1 reactor at the South African Nuclear Energy Corp., Pelindaba, South Africa. ^{161}Tb was chemically separated from the gadolinium target material and other impurities as previously reported (*3*).

Radiosynthesis of ^{161}Tb-DOTATOC for Patient Application

The ^{161}Tb product was used to radiolabel DOTATOC (JPT Peptide Technologies GmbH) at Zentralklinik Bad Berka. In brief, a solution of DOTATOC (60 μg and 250 μg, for Patient 1 and Patient 2, respectively) in sodium acetate buffer (500 μL, 1 M, pH 5.5) was added to a solution of $^{161}TbCl_3$ in 0.05 M HCl (629 and 1,740 MBq for Patient 1 and Patient 2, respectively; 100 μL). The reaction mixture was incubated at 95°C for 30 min. Quality control was performed using an analytic high-pressure liquid chromatography system (Jasco PU-1580 system) equipped with a radiometric detector and a reversed-phase column (Jupiter Proteo; Phenomenex). The reaction solution was diluted with 5 mL of sterile saline and filtered using a 0.2-μm sterile filter. Samples were taken for sterility and endotoxin testing using an Endosafe-PTS cartridge (Charles River Endosafe MS, Germany). The pH of the final product was approximately 5.

Ethical and Regulatory Issues for Patient Application

^{161}Tb-DOTATOC was applied to patients in compliance with the German Medicinal Products Act (section 13, subsection 2b) and the 1964 Declaration of Helsinki (including subsequent amendments). The study was approved by an institutional review board, and the patients signed written informed consent forms before the investigation, which was performed in accordance with the regulations of the German Federal Agency for Radiation Protection (*23*). Written informed consent was obtained from the patients for collection and storage of their data in the institutional electronic data bank and for publication of the data.

Patient Selection and Characteristics

Patient 1. A 35-y-old male patient with a well-differentiated, nonfunctional malignant right glomus caroticum tumor (paraganglioma; Ki-67, 5%) and lymph node, pulmonary, hepatic, and osseous metastases was selected for this study (Table 1; Supplemental Table 1 [supplemental materials are available at http://jnm.snmjournals.org]). On diagnosis in 2011, he underwent right neck dissection, with partial excision of the primary tumor and locoregional lymphadenectomy followed by radiochemotherapy. Further partial excision of the residual tumor with lymphadenectomy was performed in early 2017. From April to July 2017, the patient received 2 cycles of intravenously

TABLE 1
Characteristics of Patients in This Study

Characteristic	Patient 1	Patient 2
Age (y)	35	70
Sex	Male	Male
Height (cm)	183	193
Body weight (kg)	94	85
Oncologic diagnosis	Metastatic, well-differentiated, nonfunctional malignant paraganglioma (initial presentation as right glomus caroticum tumor)	Metastatic, functional NEN of pancreatic tail
Metastases	Lymph node, pulmonary, hepatic, osseous	Lymph node, hepatic, pulmonary, osseous, peritoneal
Proliferation rate (Ki-67)	5%	4%
Initial diagnosis	September 2011	September 1996
Genetic predisposition	c.301G > T (p.Gly101Trp) heterozygous CDKN2A	N/A
Karnofsky Performance Score (at time of this study)	90%	80%
Previous treatments*	Surgery (2011)	Surgery (1996/2017)
	Radiochemotherapy (2011)	Chemotherapy (everolimus; 2016)
	Radionuclide therapy (2017)	Radionuclide therapy (2017)

*Detailed descriptions of previous treatments are provided in Supplemental Table 1.
N/A = not available.

applied peptide receptor radionuclide therapy using ^{177}Lu-DOTATOC. However, ^{68}Ga-DOTATOC PET/CT demonstrated progressive disease in July 2017. At the time of ^{161}Tb-DOTATOC application, the patient's Karnofsky Performance Score was 90%.

Patient 2. A 70-y-old male patient with a functional NEN of the pancreatic tail (G2) and lymph node, hepatic, pulmonary, osseous, and peritoneal metastases was selected for the (Supplemental Table 1). After initial diagnosis in 1996, partial left pancreatectomy and splenectomy followed. In 2016, he was treated with everolimus; however, this treatment was stopped because of severe stomatitis. In early 2017, the patient underwent surgical debulking of the tumor, including right hemihepatectomy, excision of hepatic segment 3, extirpation of lymph nodes in the hepatoduodenal ligament area, and tumor excision from teres as well as falciform ligaments, peritoneal adhesiolysis, and cholecystectomy. From 2005 to 2017, the patient received a total of 9 cycles of peptide receptor radionuclide therapy using either an intraarterial injection of ^{90}Y-DOTATATE or an intravenous injection of ^{177}Lu-DOTATATE or ^{177}Lu-DOTA-LM3, a somatostatin receptor antagonist. Despite these extensive treatments, the patient experienced disease progression, as demonstrated by somatostatin receptor antagonist (^{68}Ga-NODAGA-LM3)–based PET/CT. At the time of ^{161}Tb-DOTATOC application, the patient's Karnofsky Performance Score was 80%.

SPECT/CT Imaging of ^{161}Tb

SPECT/CT imaging was performed using a Siemens Symbia T camera system (Siemens Healthcare GmbH) with the following settings: low-energy high-resolution collimator, peak at 75 keV (energy window: 67.1–89.5 keV; 6% upper and lower scatter windows), 128 × 128 matrix, projections acquired with 30 s per step, step and shoot, and body contour. The numbers of projections for patients 1 and 2 were 64 and 120, respectively. The following γ-camera settings were used for planar whole-body imaging: MEDISO spirit DH-V dual-head γ-camera (Medical Imaging Systems), low-energy high-resolution collimator, peak at 49 keV (20% energy window) and peak at 77 keV (15% energy window), and scan speed of 15 cm/min. SPECT images were reconstructed with a Monte Carlo–based ordered-subset expectation maximization model using the Sahlgrenska Academy reconstruction code (*22*,*24*). The Sahlgrenska Academy reconstruction code simulates photon attenuation, scattering, and the collimator–detector resolution in the forward projection. The backprojection applies narrow-beam attenuation (without scattering). Six iterations and 4 subsets were used for all reconstructions.

Imaging of Patients After Application of ^{161}Tb-DOTATOC

Patient 1. ^{161}Tb-DOTATOC (596 MBq) was administered via a dedicated radionuclide therapy application system into a peripheral arm vein (Table 2). Ondansetron and dexamethasone were administered intravenously as premedication to prevent possible adverse effects. For nephroprotection, an amino acid solution (consisting of 1,100 mL of 5% lysine HCl, 250 mL of 10% L-arginine HCl, and 250 mL of 0.9% NaCl; pH 7.4; 400 mOsm/L) was infused intravenously over a period of 4 h, along with forced diuresis using furosemide as an intravenous bolus. After the application of ^{161}Tb-DOTATOC, 5 sets of whole-body planar (anterior and posterior) images were acquired at early time points (30 min and 3.0 h after injection), at the standard acquisition time point (24 h after injection), and at late time points (49.5 and 71 h after injection). SPECT/CT images of the thorax and of the abdomen and pelvis were acquired at 46 and 46.5 h after injection, respectively.

Patient 2. ^{161}Tb-DOTATOC (1,300 MBq) was administered using the same premedication as that described for patient 1 (Table 2). As a nephroprotective measure, diuresis was forced by the administration of furosemide, followed by adequate hydration with a balanced electrolyte solution Deltajonin (Deltamedica GmbH, Germany; 1,000 mL). After the application of ^{161}Tb-DOTATOC, 5 sets of whole-body planar (anterior and posterior) images were acquired at early time points (30 min and 2.5 h after injection), at the standard acquisition time point after 1 d (20 h after injection), and at late time points (93 and 113 h after injection). SPECT/CT of the liver and upper abdomen was performed at 19 h after injection.

The ^{161}Tb-DOTATOC SPECT/CT images were interpreted independently by 2 experienced physicians (2 board-certified nuclear medicine physicians, each with over 10 y of experience).

Dosimetry Estimation

Dosimetry was performed using planar image data from patients 1 and 2 in accordance with a previously described protocol (*25*). Time-dependent activity in the whole body and kidneys and, for patient 1,

TABLE 2
Application of ^{161}Tb-DOTATOC, Premedication, and Scan Times

Characteristic	Patient 1	Patient 2
Premedication to prevent adverse effects	Ondansetron (8 mg), intravenously	Ondansetron (8 mg), intravenously
	Dexamethasone (8 mg), intravenously	Dexamethasone (8 mg), intravenously
Measures for nephroprotection	Amino acid solution (Lys/Arg) (1,600 mL) intravenously	Electrolyte solution (1,000 mL) intravenously
	Furosemide (20 mg), intravenously	Furosemide (20 mg), intravenously
Application of ^{161}Tb-DOTATOC	596 MBq, intravenously (July 2018)	1,300 MBq, intravenously (November 2018)
Planar scans (whole body)	0.5 h after injection	0.5 h after injection
	3 h after injection	2.5 h after injection
	24 h after injection	20 h after injection
	49.5 h after injection	93 h after injection
	71 h after injection	113 h after injection
SPECT/CT scan	22.5 h after injection (thorax)	19 h after injection (liver and abdomen)
	46 h after injection (thorax)	
	46.5 h after injection (abdomen and pelvis)	

also in the liver and spleen was determined by drawing regions of interest on serial whole-body scans after the administration of ^{161}Tb-DOTATOC. The time–activity curves of source regions were fitted to exponential functions of the first or second order to determine the time-integrated activity coefficient. The mean absorbed doses were estimated with OLINDA 2.0 software.

Clinical Safety of ^{161}Tb-DOTATOC

The patients were monitored for adverse events, such as nausea, emesis, rash, erythema, pruritus, or fever, and potential changes in vital parameters, including blood pressure, pulse rate, and temperature, immediately after the ^{161}Tb-DOTATOC administration and at the follow-up review. Laboratory values, such as blood cell and relevant blood plasma parameters, were measured. The estimated glomerular filtration rate, the C-reactive protein level, and relevant tumor markers were also assessed (Supplemental Table 2).

RESULTS

Production of ^{161}Tb and Preparation of ^{161}Tb-DOTATOC

^{161}Tb was produced with product data specifications as previously defined by Gracheva et al. (*3*). The radiolabeling of DOTATOC with ^{161}Tb was performed for patient application at Zentralklinik Bad Berka to obtain ^{161}Tb-DOTATOC at a molar activity of 9.9–14.9 GBq/μmol. After incubation of the reaction mixture for 30 min at 95°C, ^{161}Tb was coordinated, and no "free" (uncoordinated) ^{161}Tb was detected by high-pressure liquid chromatography–based quality control. No microbial growth was detected in the final product when tested for sterility. The content of bacterial endotoxins in the final product was determined to be less than 10 endotoxin units/mL, in accordance with the *European Pharmacopoeia* (*26*).

First-in-Humans Application

Physiologic Biodistribution in Patient 1. Whole-body images acquired at early time points demonstrated the biodistribution of ^{161}Tb-DOTATOC within the background soft tissue, liver, spleen, and both kidneys (Figs. 1A and 1B). Accumulation of activity in the urinary bladder was due to renal excretion of ^{161}Tb-DOTATOC. At the standard image acquisition time point (24 h after injection), a moderate intensity of physiologically accumulated ^{161}Tb-DOTATOC was observed in the liver, spleen, intestines, and both kidneys, with residual activity in the bladder (Fig. 1C). Delayed images acquired 3 d after application (71 h after injection) demonstrated that ^{161}Tb-DOTATOC was continuously cleared from the normal organs and tissues (Fig. 1D). At this late time point, the spleen visually demonstrated a comparatively high accumulation of ^{161}Tb-DOTATOC (Fig. 1D). The SPECT/CT images of the thorax, abdomen, and pelvis acquired 2 d after injection demonstrated physiologic uptake of ^{161}Tb-DOTATOC in the liver, spleen, and both kidneys (Fig. 2).

Pathologic Uptake in Patient 1. Images acquired at different time points after the injection of ^{161}Tb-DOTATOC demonstrated uptake of the radiopeptide within some of the known skeletal lesions, such as the sternum and the left frontal bone, as well as in some liver lesions. The comparatively larger sternal metastasis was evident from the images obtained 3 h after injection and onward and was persistently visualized on delayed images up to 71 h after injection. The whole-body planar images acquired at 24 h after injection demonstrated distinct uptake of ^{161}Tb-DOTATOC in the relatively smaller lesion in the left orbital part of the frontal bone (Fig. 1C).

Fused SPECT/CT images of the thorax (46 h after injection) and of the abdomen and pelvis acquired 2 d after application demonstrated uptake of ^{161}Tb-DOTATOC in the osseous sternal manubrium metastasis as well as heterogeneously distributed physiologic uptake in the liver and spleen (Fig. 2).

Physiologic Biodistribution in Patient 2. Images obtained at early time points (0.5 and 2.5 h) after the injection of ^{161}Tb-DOTATOC demonstrated normal blood-pool activity, including

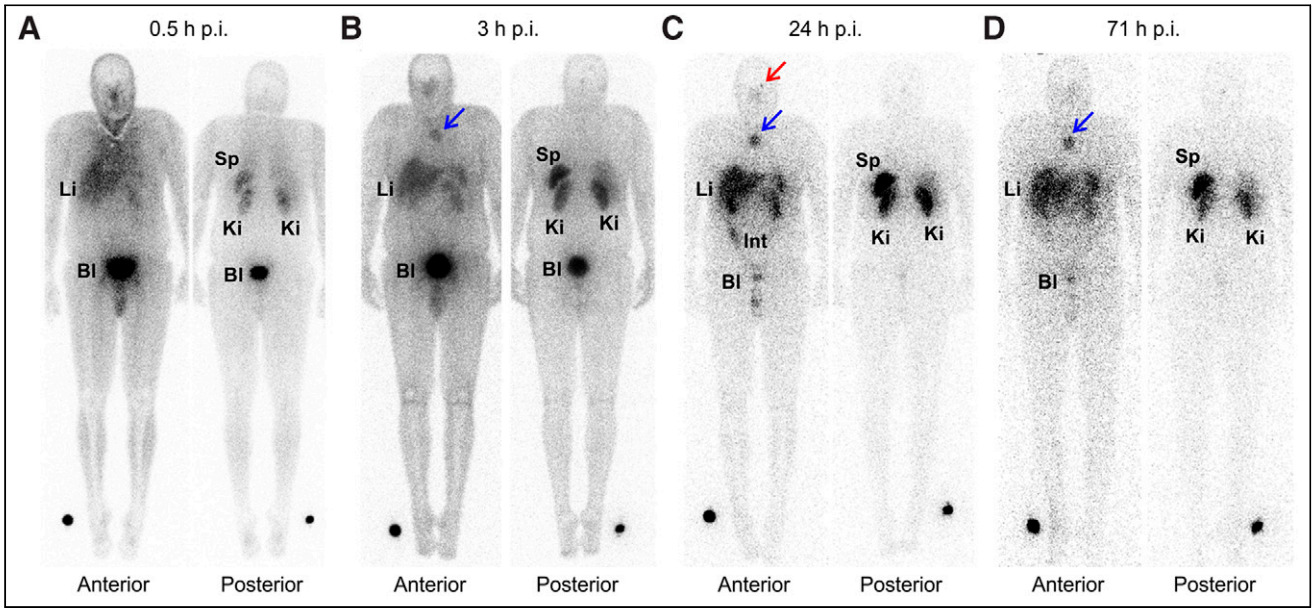

FIGURE 1. Whole-body images of patient 1 at 0.5 h after injection (A), 3 h after injection (B), 24 h after injection (C), and 3 d (71 h) (D) after injection of ^{161}Tb-DOTATOC. Images demonstrated physiologic biodistribution of ^{161}Tb-DOTATOC in liver (Li), spleen (Sp), intestines (Int), and kidneys (Ki) and excretion into urinary bladder (Bl). In addition, accumulation in known osseous metastases (sternal manubrium [blue arrows] and orbital part of frontal bone on left [red arrow]) was visualized. p.i. = after injection.

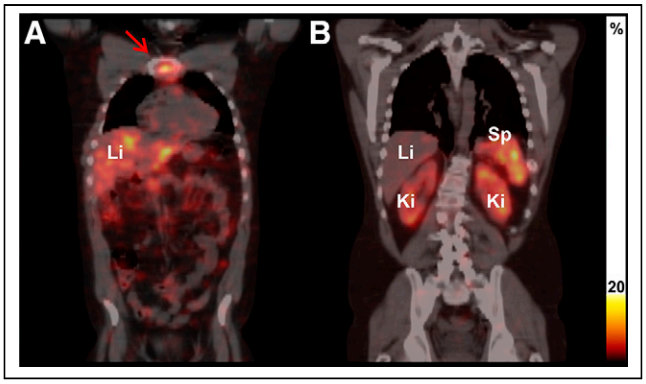

FIGURE 2. Fused coronal SPECT/CT images of patient 1 obtained on the second day after injection of ^{161}Tb-DOTATOC. Images showed pathologic uptake of ^{161}Tb-DOTATOC in osseous metastasis (sternal manubrium [red arrow]) (A) and physiologic uptake of ^{161}Tb-DOTATOC in kidneys (Ki), liver (Li), and spleen (Sp) (B).

the heart and blood vessels. Distribution of the radiopeptide was also seen in the soft tissues, liver, both kidneys, and urinary bladder (Figs. 3A and 3B). The accumulation of ^{161}Tb-DOTATOC in the kidneys and intestinal tract was observed on images obtained at 20 h after injection (Fig. 3C). The uptake of activity in the kidneys and urinary bladder was ascribed to renal excretion of ^{161}Tb-DOTATOC, as is commonly also the case for ^{177}Lu-DOTATOC. ^{161}Tb-DOTATOC was effectively cleared from normal tissues over time, as demonstrated by the reduced activity seen on images acquired at delayed time points (Fig. 3D). SPECT/CT images acquired at 19 h after injection demonstrated physiologic distribution of ^{161}Tb-DOTATOC in both kidneys as well as normal liver tissue (Fig. 4).

Pathologic Uptake in Patient 2. Whole-body planar images obtained at multiple time points demonstrated that the accumulation of ^{161}Tb-DOTATOC in bilobar hepatic metastases as early as 0.5 h after injection was still seen on images acquired at late time points (113 h after injection). Multiple skeletal metastases demonstrated faint uptake of the radiopeptide on (early) images at 2.5 h after injection of ^{161}Tb-DOTATOC, with further significant accumulation visible on images acquired at 113 h after injection (Fig. 3). SPECT/CT of the liver and upper abdomen acquired at 19 h after injection demonstrated significant accumulation of ^{161}Tb-DOTATOC in the hepatic metastases as well as moderate uptake in the multiple osseous lesions of the thoracolumbar vertebrae and the pelvis (Fig. 4).

Dosimetry Estimation

Dosimetry data from patient 1 were in a range similar to that expected when using ^{177}Lu-DOTATOC (Supplemental Table 3). Patient 2 showed slower renal clearance of ^{161}Tb-DOTATOC and, hence, higher absorbed kidney and whole-body doses (1.5 and 0.07 Gy/GBq, respectively) than patient 1 (0.8 and 0.04 Gy/GBq, respectively).

Clinical Safety of ^{161}Tb-DOTATOC

The administration of ^{161}Tb-DOTATOC and postapplication imaging procedures were well tolerated by both patients. No adverse events were reported by the patients and no significant changes in vital parameters were observed or reported by the patients during, immediately after, or at follow-up review after the administration of ^{161}Tb-DOTATOC. According to the Common Terminology Criteria for Adverse Events (CTCAE v5.0) (*27*), there were no clinically significant changes in relevant laboratory values (hematologic, renal, and hepatic panels) at the subsequent follow-up of the patients after the administration of ^{161}Tb-DOTATOC (Supplemental Table 2).

DISCUSSION

^{161}Tb was suggested for clinical translation because of its favorable physical decay properties (*16*,*18*–*20*). Importantly, ^{161}Tb can

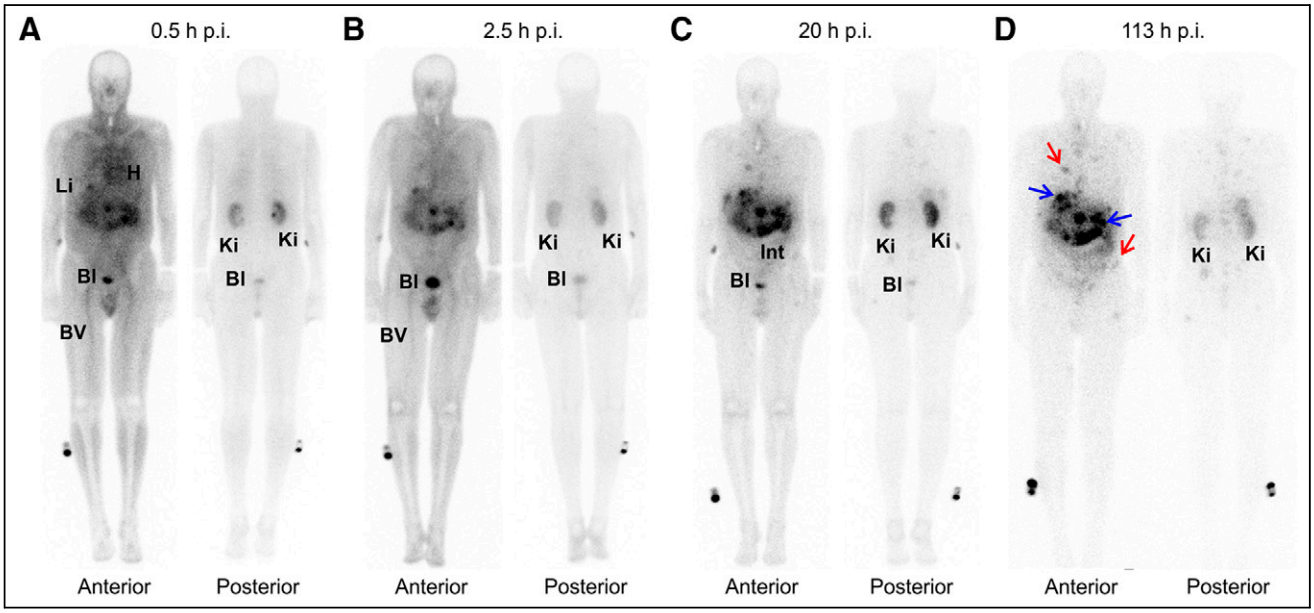

FIGURE 3. Whole-body images of patient 2 at 0.5 h after injection (A), 2.5 h after injection (B), 20 h after injection (C), and 113 h after injection (D) of ^{161}Tb-DOTATOC. Early blood-pool activity was noted in heart (H) and blood vessels (BV) up to 2.5 h after injection. Physiologic uptake of radiopeptide was observed in soft tissues, liver (Li), kidneys (Ki), intestines (Int) and urinary bladder (Bl). Pathologic accumulation of ^{161}Tb-DOTATOC was demonstrated in bilobar liver (blue arrows) and multifocal osseous metastases (red arrows). p.i. = after injection.

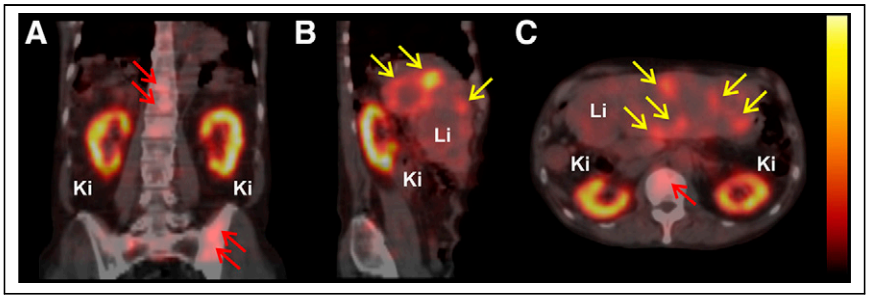

FIGURE 4. SPECT/CT images of patient 2 at 19 h after injection of ^{161}Tb-DOTATOC. (A) Coronal section. (B) Sagittal section. (C) Transverse section. Images showed uptake of ^{161}Tb-DOTATOC in bilobar hepatic metastases (yellow arrows) as well as multiple osteoblastic skeletal metastases in vertebral column and pelvis (red arrows). Physiologic uptake of ^{161}Tb-DOTATOC was seen in both kidneys (Ki) as well as in liver (Li).

be stably coordinated with a DOTA chelator because of its chemical similarity to ^{177}Lu. Therefore, it can be applied with, potentially, any tumor-targeting agent that comprises a DOTA chelator, as demonstrated in several preclinical studies (*5*,*7*,*9*,*11*).

The feasibility of using the emitted γ-radiation of ^{161}Tb for clinical SPECT was recently demonstrated with human phantoms (*22*). Low-energy high-resolution collimators were revealed to be most suited to obtaining high-resolution images, and SPECT/CT-based dosimetry was predicted to be feasible for ^{161}Tb-labeled radiopharmaceuticals (*22*). To our knowledge, the data presented in this article are the first results for ^{161}Tb clinical imaging in patients.

FIGURE 5. PET/CT sagittal section of patient 1 at 60 min after injection of ^{68}Ga-DOTATOC. Pathologic uptake was seen in multiple skeletal metastases (sternal manubrium, left orbital part of frontal bone, occipital bone, and multiple vertebrae [red arrows]). Comparatively higher physiologic uptake of ^{68}Ga-DOTATOC was observed in spleen (Sp). Accumulation of activity in urinary bladder (Bl) was seen because of renal excretion of radiopeptide.

Two patients with somatostatin receptor–expressing malignancies received ^{161}Tb-DOTATOC to analyze the distribution of the radiopeptide visualized on postapplication whole-body planar and SPECT/CT imaging. The resultant images showed a distribution profile for ^{161}Tb-DOTATOC similar to that expected for ^{177}Lu-DOTATOC. Considering that high interpatient as well as high intrapatient variations in dosimetry data are expected (*25*), the dosimetry results for the 2 patients who received ^{161}Tb-DOTATOC are of minor informative value. They confirmed, however, the expected tissue distribution of ^{161}Tb-DOTATOC. The comparatively higher absorbed kidney and whole-body doses in patient 2 can be ascribed to the slower renal clearance of ^{161}Tb-DOTATOC in this patient; the slower clearance was due to the reduced renal function demonstrated by elevated renal plasma parameters (Supplemental Table 2) (*28*).

In patient 1, despite the low administered activity of ^{161}Tb-DOTATOC, the resultant images visualized previously known osseous metastases, in agreement with visualization of the lesions on the PET/CT scan performed the previous week using ^{68}Ga-DOTATOC (Fig. 5). It is not surprising that not all of the pathologic lesions observed on ^{68}Ga-DOTATOC PET/CT images were visualized on SPECT images, which generally have lower sensitivity than high-resolution, state-of-the-art diagnostic PET/CT images. In agreement with diagnostic PET/CT images, high accumulation of ^{161}Tb-DOTATOC was found in the spleen; this was a peptide-specific feature (*29*). Patient 2 had undergone a splenectomy; consequently, the accumulation of activity in the spleen was not observed in this patient and, therefore, dosimetry data were not available.

Images acquired after the application of ^{161}Tb-DOTATOC in patient 2 demonstrated significant radiopeptide uptake in bilobar hepatic as well as multifocal osseous metastases, with visually excellent target-to-background ratios (Fig. 4). The somewhat better image quality and detection of more pathologic lesions for patient 2 were ascribed to the fact that about twice as much activity was applied in this case. Because of multiple heterogeneously distributed and difficult to delineate liver metastases in this patient, dosimetry data for the liver could not be determined.

In both patients, ^{161}Tb-DOTATOC was well tolerated, without any signs of adverse events during or after the procedure, indicating that the application of ^{161}Tb-DOTATOC is safe.

There is no doubt that ^{161}Tb holds promise as an alternative to ^{177}Lu for peptide receptor radionuclide therapy; however, it may be important to use a targeting agent that will fully exploit the short-range electron emission.

CONCLUSION

The patient images obtained with ^{161}Tb in the present study confirmed that the emitted γ-radiation of ^{161}Tb can be used for whole-body planar as well as SPECT/CT imaging of even low activities of injected ^{161}Tb. The results of the present study will serve as a basis for further investigations in patients with ^{161}Tb-based radiopharmaceuticals and a stepwise escalation of the ^{161}Tb activity applied, thereby achieving therapeutic efficacy.

DISCLOSURE

Roger Schibli, Nicholas P. van der Meulen, Cristina Müller, and Richard P. Baum received the Neuroendocrine Tumor Research Foundation (NETRF) Peterson Investigator Award 2018 (United States), which was a major contribution to the funding of this project. Peter Bernhardt and Tobias Rydén were supported by the Swedish Cancer Society, Swedish Radiation Safety Authority, King Gustav V. Jubilee Clinic Cancer Research Foundation, Swedish Research Council, and Swedish State under an agreement between the Swedish government and the county councils (the ALF agreement). No other potential conflict of interest relevant to this article was reported.

KEY POINTS

QUESTION: Is it feasible to visualize metastases in patients with NENs after injection of ^{161}Tb-DOTATOC?

PERTINENT FINDINGS: This first-in-humans application of ^{161}Tb demonstrated the feasibility of imaging metastases of NENs after the injection of relatively low activities of ^{161}Tb-DOTATOC using γ-scintigraphy and SPECT.

IMPLICATIONS FOR PATIENT CARE: The feasibility of imaging ^{161}Tb in patients is an essential finding in view of ^{161}Tb-based radionuclide therapy in future clinical trials.

ACKNOWLEDGMENTS

We thank Lebogang Sepini at Necsa for arrangements with the shipment of irradiated targets from South Africa to Switzerland. We also thank the people responsible for radiation safety, transport of radioactive materials, and technical assistance at Paul Scherrer Institute. Furthermore, we thank the nursing staff as well as the nuclear medicine technologists for patient management at Zentralklinik Bad Berka.

REFERENCES

1. Müller C, Domnanich KA, Umbricht CA, van der Meulen NP. Scandium and terbium radionuclides for radiotheranostics: current state of development towards clinical application. *Br J Radiol.* 2018;91:20180074.
2. Müller C, Zhernosekov K, Köster U, et al. A unique matched quadruplet of terbium radioisotopes for PET and SPECT and for α- and β^--radionuclide therapy: an in vivo proof-of-concept study with a new receptor-targeted folate derivative. *J Nucl Med.* 2012;53:1951–1959.
3. Gracheva N, Müller C, Talip Z, et al. Production and characterization of no-carrier-added ^{161}Tb as an alternative to the clinically-applied ^{177}Lu for radionuclide therapy. *EJNMMI Radiopharm Chem.* 2019;4:12.
4. Müller C, Fischer E, Behe M, et al. Future prospects for SPECT imaging using the radiolanthanide terbium-155: production and preclinical evaluation in tumor-bearing mice. *Nucl Med Biol.* 2014;41(suppl):e58–e65.
5. Müller C, Vermeulen C, Johnston K, et al. Preclinical in vivo application of ^{152}Tb-DOTANOC: a radiolanthanide for PET imaging. *EJNMMI Res.* 2016;6:35.
6. Müller C, Reber J, Haller S, et al. Folate receptor targeted alpha-therapy using terbium-149. *Pharmaceuticals (Basel).* 2014;7:353–365.
7. Müller C, Reber J, Haller S, et al. Direct in vitro and in vivo comparison of ^{161}Tb and ^{177}Lu using a tumour-targeting folate conjugate. *Eur J Nucl Med Mol Imaging.* 2014;41:476–485.
8. Müller C, Vermeulen C, Köster U, et al. Alpha-PET with terbium-149: evidence and perspectives for radiotheragnostics. *EJNMMI Radiopharm Chem.* 2017;1:5.
9. Müller C, Umbricht CA, Gracheva N, et al. Terbium-161 for PSMA-targeted radionuclide therapy of prostate cancer. *Eur J Nucl Med Mol Imaging.* 2019;46:1919–1930.
10. Umbricht CA, Köster U, Bernhardt P, et al. Alpha-PET for prostate cancer: preclinical investigation using ^{149}Tb-PSMA-617. *Sci Rep.* 2019;9:17800.
11. Baum RP, Singh A, Benesova M, et al. Clinical evaluation of the radiolanthanide terbium-152: first-in-human PET/CT with ^{152}Tb-DOTATOC. *Dalton Trans.* 2017;46:14638–14646.
12. Müller C, Singh A, Umbricht CA, et al. Preclinical investigations and first-in-human application of ^{152}Tb-PSMA-617 for PET/CT imaging of prostate cancer. *EJNMMI Res.* 2019;9:68.
13. Durán MT, Juget F, Nedjadi Y, et al. Determination of ^{161}Tb half-life by three measurement methods. *Appl Radiat Isot.* 2020;159:109085.
14. Lehenberger S, Barkhausen C, Cohrs S, et al. The low-energy beta$^-$ and electron emitter ^{161}Tb as an alternative to ^{177}Lu for targeted radionuclide therapy. *Nucl Med Biol.* 2011;38:917–924.
15. Bernhardt P, Benjegard SA, Kolby L, et al. Dosimetric comparison of radionuclides for therapy of somatostatin receptor-expressing tumors. *Int J Radiat Oncol Biol Phys.* 2001;51:514–524.
16. Bernhardt P, Forssell-Aronsson E, Jacobsson L, Skarnemark G. Low-energy electronemitters for targeted radiotherapy of small tumours. *Acta Oncol.* 2001;40:602–608.
17. Uusijärvi H, Bernhardt P, Rösch F, Mäcke HR, Forssell-Aronsson E. Electron- and positron-emitting radiolanthanides for therapy: aspects of dosimetry and production. *J Nucl Med.* 2006;47:807–814.
18. Hindié E, Zanotti-Fregonara P, Quinto MA, Morgat C, Champion C. Dose deposits from ^{90}Y, ^{177}Lu, ^{111}In, and ^{161}Tb in micrometastases of various sizes: implications for radiopharmaceutical therapy. *J Nucl Med.* 2016;57:759–764.
19. Champion C, Quinto MA, Morgat C, Zanotti-Fregonara P, Hindié E. Comparison between three promising β^--emitting radionuclides, ^{67}Cu, ^{47}Sc and ^{161}Tb, with emphasis on doses delivered to minimal residual disease. *Theranostics.* 2016;6:1611–1618.
20. Alcocer-Ávila ME, Ferreira A, Quinto MA, Morgat C, Hindie E, Champion C. Radiation doses from ^{161}Tb and ^{177}Lu in single tumour cells and micrometastases. *EJNMMI Phys.* 2020;7:33.
21. Haller S, Pellegrini G, Vermeulen C, et al. Contribution of Auger/conversion electrons to renal side effects after radionuclide therapy: preclinical comparison of ^{161}Tb-folate and ^{177}Lu-folate. *EJNMMI Res.* 2016;6:13.
22. Marin I, Ryden T, Van Essen M, et al. Establishment of a clinical SPECT/CT protocol for imaging of ^{161}Tb. *EJNMMI Phys.* 2020;7:45.
23. Ministry GF. Laws and regulations of radiation protection. *The Radiation Protection Act, Germany.* 2017:78.
24. Rydén T, Heydorn Lagerlof J, Hemmingsson J, et al. Fast GPU-based Monte Carlo code for SPECT/CT reconstructions generates improved ^{177}Lu images. *EJNMMI Phys.* 2018;5:1.
25. Schuchardt C, Kulkarni HR, Prasad V, Zachert C, Müller D, Baum RP. The Bad-Berka dose protocol: comparative results of dosimetry in peptide receptor radionuclide therapy using ^{177}Lu-DOTATATE, ^{177}Lu-DOTANOC, and ^{177}Lu-DOTATOC. *Recent Results Cancer Res.* 2013;194:519–536.
26. European Directorate for the Quality of Medicines & HealthCare. Bacterial endotoxins. Council of Europe. 2019. European pharmacopoeia. Strasbourg: Council of Europe, Ph. Eur. 9.0 (German ed.), 277.
27. National Cancer Institute. *Common Terminology Criteria for Adverse Events (CTCAE).* Washington, DC: U.S. Department of Health and Human Services; 2017.
28. Svensson J, Berg G, Wangberg B, Larsson M, Forssell-Aronsson E, Bernhardt P. Renal function affects absorbed dose to the kidneys and haematological toxicityduring ^{177}Lu-DOTATATE treatment. *Eur J Nucl Med Mol Imaging.* 2015;42:947–955.
29. Melis M, Kaemmerer D, de Swart J, et al. Localization of radiolabeled somatostatin analogs in the spleen. *Clin Nucl Med.* 2016;41:e111–e114.

A Prospective, Randomized, Double-Blind Study to Evaluate the Safety, Biodistribution, and Dosimetry of ^{68}Ga-NODAGA-LM3 and ^{68}Ga-DOTA-LM3 in Patients with Well-Differentiated Neuroendocrine Tumors

Wenjia Zhu[1], Yuejuan Cheng[2], Ru Jia[3], Hong Zhao[4], Chunmei Bai[2], Jianming Xu[3], Shaobo Yao[5], and Li Huo[1]

[1]Department of Nuclear Medicine, Beijing Key Laboratory of Molecular Targeted Diagnosis and Therapy in Nuclear Medicine, Peking Union Medical College Hospital, CAMS and PUMC, Beijing, China; [2]Department of Oncology, Peking Union Medical College Hospital, Beijing, China; [3]Department of Gastrointestinal Oncology, Fifth Medical Center, General Hospital of PLA, Beijing, China; [4]Department of Hepatobiliary Surgery, National Cancer Center/National Clinical Research Center for Cancer/Cancer Hospital, Chinese Academy of Medical Sciences and Peking Union Medical College, Beijing, China; and [5]Department Nuclear Medicine, First Affiliated Hospital of Fujian Medical University, Fuzhou, Fujian, China

^{68}Ga-NODAGA-LM3 (where LM3 is *p*-Cl-Phe-cyclo(D-Cys-Tyr-D-4-amino-Phe(carbamoyl)-Lys-Thr-Cys)D-Tyr-NH_2) and ^{68}Ga-DOTA-LM3 are somatostatin receptor subtype 2 (SSTR2)–specific antagonists used for PET/CT imaging. The purpose of this study was to evaluate the safety, biodistribution, and dosimetry of ^{68}Ga-NODAGA-LM3 and ^{68}Ga-DOTA-LM3 in patients with well-differentiated neuroendocrine tumors. **Methods:** Patients were equally randomized into 2 arms, with arm A receiving ^{68}Ga-NODAGA-LM3 and arm B receiving ^{68}Ga-DOTA-LM3. Serial PET scans were acquired at 5, 15, 30, 45, 60, and 120 min after ^{68}Ga-NODAGA-LM3 (200 MBq ± 11 MBq/40 μg of total peptide mass) or ^{68}Ga-DOTA-LM3 (172 MBq ± 21 MBq/40 μg of total peptide mass) injection. The biodistribution in normal organs, tumor uptake, and safety were assessed. Radiation dosimetry was calculated using OLINDA/EXM (version 1.0). **Results:** Sixteen patients, 8 in each arm, were recruited in the study. Both tracers were well tolerated in most patients. Two patients in arm B had nausea (grade 2), and one of them had vomiting (grade 1). The PET images of the other 14 patients were further analyzed. Significantly lower organ uptake was observed in the pituitary, parotids, liver, spleen, pancreas, adrenal, stomach, small intestine, and kidneys with ^{68}Ga-DOTA-LM3 than with ^{68}Ga-NODAGA-LM3. In total, 38 lesions were analyzed, including 18 with ^{68}Ga-NODAGA-LM3 and 20 with ^{68}Ga-DOTA-LM3. Both tracers showed good tumor uptake and retention. With ^{68}Ga-NODAGA-LM3, the tracer accumulation in tumor lesions increased by 138%, from an average SUV_{max} of 31.3 ± 19.7 at 5 min to 74.6 ± 56.3 at 2 h. With ^{68}Ga-DOTA-LM3, the tumor uptake rapidly reached a high level at 5 min after injection, with an average SUV_{max} of 36.6 ± 23.6, and continued to increase to 45.3 ± 29.3 until 30 min after injection. The urinary bladder wall was the organ receiving the highest absorbed dose in both arms. The mean effective dose was 0.026 ± 0.003 mSv/MBq for ^{68}Ga-NODAGA-LM3 and 0.025 ± 0.002 mSv/MBq for ^{68}Ga-DOTA-LM3. **Conclusion:** Both ^{68}Ga-NODAGA-LM3 and ^{68}Ga-DOTA-LM3 show favorable biodistribution, high tumor uptake, and good tumor retention, resulting in high image contrast. The dosimetric data are comparable to those for other ^{68}Ga-labeled SSTR2 antagonists. Further studies are required to look into the potential antagonistic effects of ^{68}Ga-NODAGA-LM3 and ^{68}Ga-DOTA-LM3.

Key Words: somatostatin receptor antagonist; 68Ga-NODAGA-LM3; 68Ga-DOTA-LM3; neuroendocrine tumor; PET/CT

J Nucl Med 2021; 62:1398–1405
DOI: 10.2967/jnumed.120.253096

Neuroendocrine tumors (NETs) are a family of heterogeneous tumors featured by overexpression of somatostatin receptor (SSTR), especially SSTR subtype 2 (SSTR2), which could be a target for molecular imaging and radionuclide therapy. The role of radiolabeled somatostatin analogs such as TOC, TATE, and NOC in staging and restaging of NETs has been widely discussed (*1*). All these agents are SSTR agonists, which will be internalized into tumor cells after ligand–receptor interaction (*2*).

SSTR antagonists have emerged as another type of somatostatin analog, characterized by a low internalization rate and high tumor affinity (*3*–*7*). They bind to significantly more receptor sites than do agonists (*4*). Previous clinical studies have demonstrated higher sensitivity and better image contrast for ^{68}Ga-NODAGA-JR11 than for ^{68}Ga-DOTATOC (*8*). Data from our group suggested that ^{68}Ga-DOTA-JR11 has better performance than ^{68}Ga-DOTATATE in the detection of liver metastases (*9*). Nevertheless, ^{68}Ga-DOTA-JR11 showed an overall lower tumor uptake than ^{68}Ga-DOTATATE.

p-Cl-Phe-cyclo(D-Cys-Tyr-D-4-amino-Phe(carbamoyl)-Lys-Thr-Cys)D-Tyr-NH_2 (LM3) is a novel SSTR antagonist developed by Fani et al. (*10*). It was coupled with different chelators (NODAGA, DOTA, and 1,4,8,11-tetraazabicyclo[6.6.2]hexadecane-4,11-diacetic acid) and radiometals (^{68}Ga, ^{64}Cu, and ^{177}Lu). In vitro studies have shown ^{68}Ga-NODAGA-LM3 and ^{68}Ga-DOTA-LM3 to have high SSTR2 affinities, with a 50% inhibitory concentration of 1.3 and 12.5 nmol/L, respectively (*10*). In animal models, both tracers showed good image contrast at 1 h after injection, and this contrast can be blocked by cold peptides. Zhang et al. reported a case with ^{68}Ga-DOTATOC–negative high-grade liver metastases (*11*, *12*). The patient was successfully imaged with ^{68}Ga-NODAGA-LM3 PET/CT and subsequently treated with ^{177}Lu-DOTA-LM3. Nearly complete remission was achieved after 3 cycles of intraarterial peptide receptor radionuclide therapy.

Received Jul. 6, 2020; revision accepted Jan. 27, 2021.
For correspondence or reprints, contact Li Huo (huoli@pumch.cn).
Published online February 12, 2021.

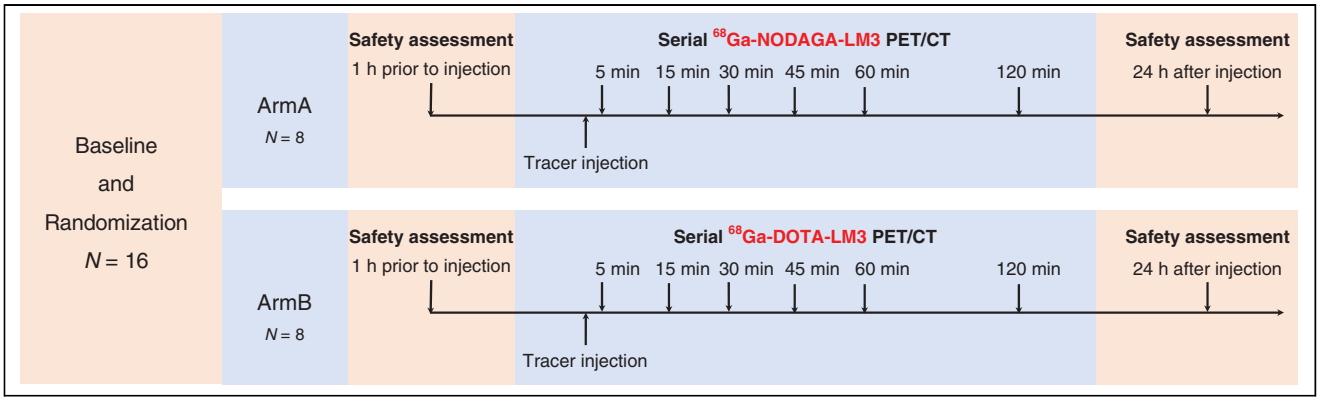

FIGURE 1. Diagram of study design. Sixteen patients were prospectively recruited in this study and equally randomized into 2 arms. In arm A, 8 patients underwent serial PET/CT scans at 5, 15, 30, 45, 60, and 120 min after ^{68}Ga-NODAGA-LM3 injection. In arm B, 8 patients (anticipated) underwent serial PET/CT scans at 5, 15, 30, 45, 60, and 120 min after ^{68}Ga-DOTA-LM3 injection. Two patients from arm B withdrew from study because of AEs.

Given the promising preclinical results and preliminary clinical data, we designed this prospective, randomized, double-blind study to evaluate the safety, biodistribution, dosimetry (phase I), and diagnostic efficacy (phase II) of ^{68}Ga-labeled LM3 in patients with well-differentiated NETs. Both ^{68}Ga-NODAGA-LM3 and ^{68}Ga-DOTA-LM3 were investigated in this study, which was designed to have 2 parallel arms (arm A receiving ^{68}Ga-NODAGA-LM3 and arm B receiving ^{68}Ga-DOTA-LM3). The results of phase I are presented and discussed in this paper.

MATERIALS AND METHODS

Study Design

This study had a prospective, 2-armed, randomized, double-blind, phase I/II, single-center design (ClinicalTrials.gov identifier NCT04318561). It was approved by the institutional review board of Peking Union Medical College Hospital, and all patients gave written informed consent before study participation. The inclusion and exclusion criteria can be found in Supplemental Table 1 (supplemental materials are available at http://jnm.snmjournals.org). The primary objectives of the phase I study were to determine the safety, biodistribution, and dosimetry of ^{68}Ga-NODAGA-LM3 and ^{68}Ga-DOTA-LM3. Sixteen patients with well-differentiated NETs were prospectively and consecutively recruited in this study (Fig. 1). The patients were equally randomized into 2 arms, and they were unaware of their arm.

Synthesis and Radiolabeling

Good-manufacturing-process–grade precursors, NODAGA-LM3 and DOTA-LM3, were supplied by CS Bio Co. The radiolabeling procedure was performed manually in a hot cell. Briefly, ^{68}Ga was eluted from a ^{68}Ge/^{68}Ga generator (Eckert & Ziegler) using 5 mL of 0.1 M hydrochloric acid directly into a reaction vial containing 40 μg of precursor

TABLE 1
Demographic and Clinical Characteristics of Patients

Patient no.*	Arm	Age (y)	Sex	Grade	Ki-67	Primary tumor	Tumor function
1	A	39	Female	2	5	Unknown	Yes (gastrinoma)
2	B	64	Male	2	20	Pancreas	No
3	B	69	Male	1	2	Pancreas	Yes (insulinoma)
4	B	58	Male	1	1	Lung	No
5	A	69	Male	2	3	Pancreas	No
6	A	58	Male	2	10	Pancreas	No
7	B	37	Female	2	3	Pancreas	No
8	B	33	Female	3	30	Pancreas	Yes (insulinoma)
9	A	33	Male	2	3	Stomach	No
10	A	18	Female	3	30	Pancreas	Yes (gastrinoma)
11	A	58	Female	2	5	Rectus	No
12	B	38	Female	1	1	Pancreas	No
13	A	54	Female	3	40	Pancreas	No
14	A	57	Female	2	10	Small intestine	No
15	B	40	Male	3	25	Pancreas	No
16	B	48	Male	2	5	Rectus	No

*Patients were numbered according to recruiting sequence.

dissolved in sodium acetate buffer, for a final reaction mixture pH of 4. The mixture was heated to 100°C for 10 min to allow for radionuclide incorporation. After cooling to room temperature, the reaction mixture was diluted with 5 mL of water and then loaded onto an Oasis HLB light cartridge (preconditioned with 5 mL of ethanol and 5 mL of water) and washed with normal saline to remove unincorporated radionuclide. Finally, the product was eluted off the cartridge with 0.5 mL of 75% ethanol solution followed by 5 mL of normal saline through a Millipore filter (0.22 μm, 25 mm) into a sterile product vial. The radiochemical purity was more than 95%. The final product comprised 150–200 MBq of radiopharmaceutical, approximately 0.38 mL of ethanol, and approximately 40 μg of total peptide mass.

PET/CT Imaging

The study was performed on a time-of-flight PET/CT scanner (Polestar m660; SinoUnion Health Care Inc.). The patients received ^{68}Ga-NODAGA-LM3 (200 MBq ± 11 MBq) or ^{68}Ga-DOTA-LM3 (172 MBq ± 21 MBq) intravenously by a quick bolus injection (5 mL over 15 s). A low-dose CT scan (120 keV; 100 mAs; pitch, 1.3; 2.5-mm slice thickness; 0.5-s rotation time) from head to proximate thigh was obtained for anatomic localization and attenuation correction. Serial PET scans were acquired at 5, 15, 30, 45, 60, and 120 min after injection. The patients were required to lie still on the exam table during the first hour. Images were reconstructed using an ordered-subsets expectation maximization algorithm (2 iterations, 10 subsets, 192 × 192 matrix) and corrected for CT-based attenuation, dead time, random events, and scatter.

Safety Assessment

Heart rate, blood pressure, pulse oximetry, and 3-lead electrocardiography were recorded within 1 h before and at 24 h after LM3 injection. Clinical symptoms were monitored and graded according to the Common Terminology Criteria for Adverse Events (version 4.03).

Image Analysis

The ^{68}Ga-NODAGA-LM3 and ^{68}Ga-DOTA-LM3 PET/CT images were anonymized and reviewed by an experienced nuclear medicine expert, masked to the medical history of the patients, on MIM software (MIM Software Inc.).

The physiologic uptake was evaluated in the following organs at all time points: pituitary gland, parotids, thyroids, lungs, blood pool, liver, spleen, pancreas (uncinate process), stomach, small intestine, kidneys, and adrenal glands. Regions of interest were drawn over these organs to exclude focal lesions, and the SUV_{max} (normalized to patients' body weight) was recorded. In the case of bilateral organs such as the parotids, thyroids, lungs, and kidneys, the average SUV_{max} was calculated. For the adrenal glands, only the left adrenal gland was measured because uptake by the right adrenal gland could easily be influenced by adjacent liver uptake.

Any focal accumulations not explained by physiologic uptake were interpreted as focal lesions. Up to 4 lesions were chosen in each patient, including 2 hepatic lesions and 2 extrahepatic lesions. The lesion uptake was measured using SUV_{max}. Tumor-to-background ratio was quantified using blood pool, kidney, and liver as reference tissues.

Radiation Dosimetry

Whole-organ volumes of interest were manually drawn over the source organs, including spleen, liver, kidneys, pituitary glands, vertebral bodies L1–L5, and urinary bladder, at each time point. The non–decay-corrected activities at different time points were documented as percentage injected dosage and fitted with monoexponential curves. The area under the time–activity curve between time 0 and the first time point was calculated assuming a linear increase from 0 to the first measured activity. The area under the time–activity curve after the first time point was calculated by trapezoidal integration from the first time point to the last time point and extrapolation from the last data point using the fitted monoexponential function. For bone marrow, the residence time was derived using an image-based integration of the L1–L5 vertebrae, assuming L1–L5 have 12.3% of the whole-body bone marrow (*13*). Urinary bladder residence time was determined using the voiding bladder model implemented in OLINDA/EXM software, setting a 2-h bladder-voiding interval. The residence time in the remainder of the body was calculated as the maximum possible residence time (based on physical decay only) minus the sum of the residence time of all source organs. Absorbed dose for target organs and whole-body effective dose were determined with OLINDA/EXM software (version 1.0) using adult male models.

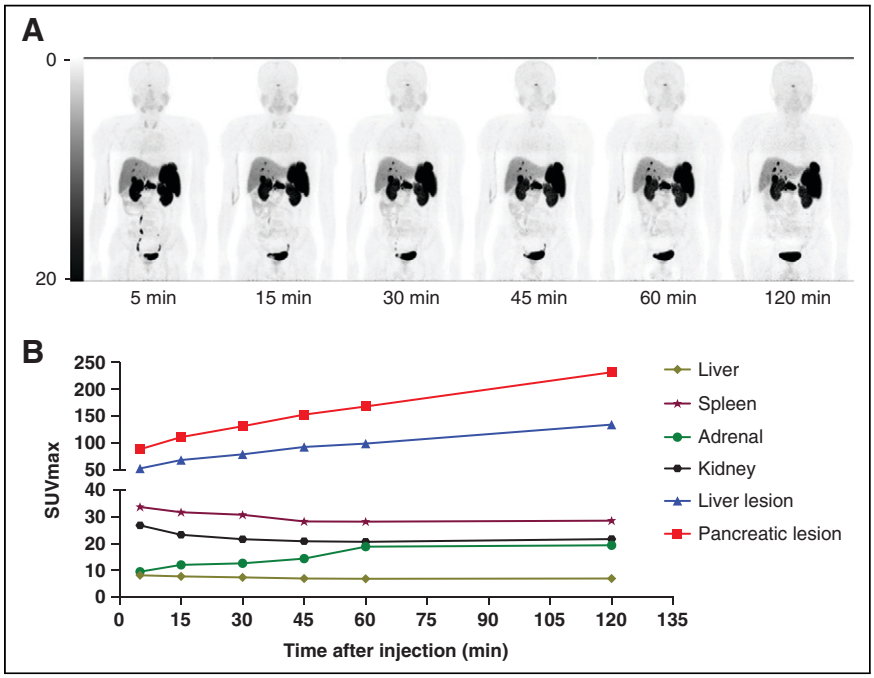

FIGURE 2. Patient 6 with grade 2 pancreatic NET as well as multiple hepatic and lymph node metastases. (A) Biodistribution of ^{68}Ga-NODAGA-LM3 at 5, 15, 30, 45, 60, and 120 min after injection. Physiologic uptake could be visualized in SSTR-positive organs such as pituitary, adrenals, and spleen. Liver demonstrated moderate accumulation of ^{68}Ga-NODAGA-LM3. (B) SUV_{max}–time curves showed excellent tumor retention in both pancreatic tumor and hepatic metastases.

Statistical Analysis

Data were expressed as mean ± SD. The differences between ^{68}Ga-NODAGA-LM3 and ^{68}Ga-DOTA-LM3 were evaluated using the Student *t* test (SPSS, version 22). Because of 2 dropouts in arm B, PET analyses were done for only 14 patients, whereas safety evaluations were done for all 16 patients. A *P* value of less than 0.05 was considered to indicate statistical significance.

RESULTS

Patients and Safety

Sixteen patients, 8 in each arm, were recruited in this phase. There were 2

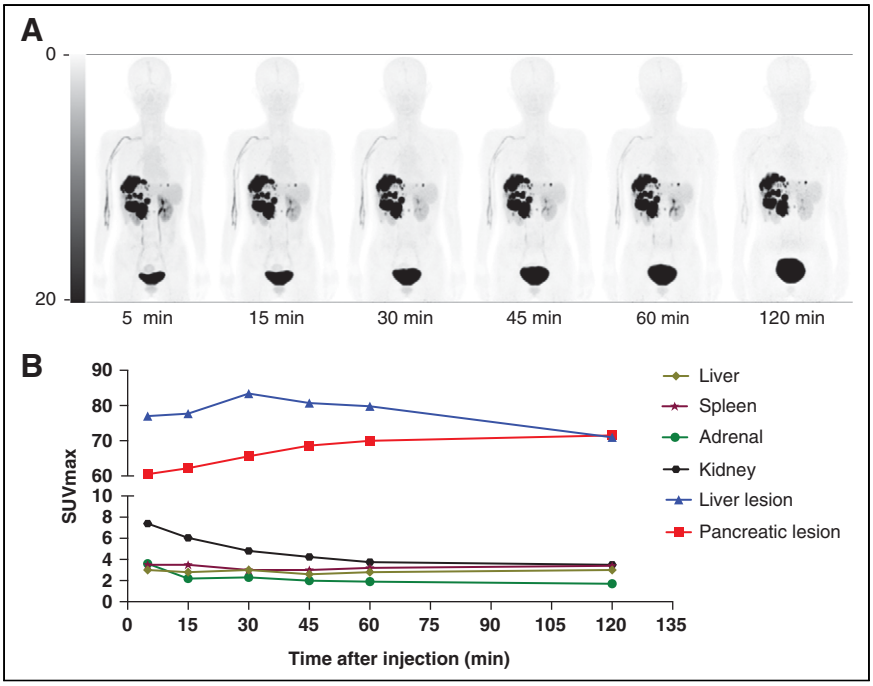

FIGURE 3. Patient 12 with grade 1 pancreatic NET as well as multiple hepatic and lymph node metastases. (A) Biodistribution of ^{68}Ga-DOTA-LM3 at 5, 15, 30, 45, 60, and 120 min after injection. No significant uptake is noted in any normal organs except for urinary tract. Spleen demonstrated only mild ^{68}Ga-DOTA-LM3 accumulation. (B) SUV_{max}–time curves. SUV_{max} of normal organs remained at low level after ^{68}Ga-DOTA-LM3 administration. Both primary and metastatic lesions showed good tracer accumulation, leading to high image contrast.

dropouts due to adverse events (AEs) at 10–15 min after injection. The demographic and clinical characteristics are summarized in Table 1 (including the 2 dropouts).

There was a mild decrease in blood pressure at 24 h after injection, compared with baseline (127.5/82.4 mm Hg vs. 133.6/86.3 mmHg, $P < 0.05$). No patients had symptoms related to hypotension after LM3 injection. No significant change in other vital signs or 3-lead electrocardiography was recorded.

There were 2 AEs (patients 3 and 8). Patient 3 was a 69-y-old man with functional pancreatic NET (grade 1 insulinoma; Ki-67 index, 2%; primary tumor resected) and multiple hepatic metastases. He had grade 2 nausea 10 min after tracer injection. Patient 8 was a 33-y-old woman also with functional pancreatic NET (grade 3 insulinoma; Ki-67 index, 30%) as well as multiple hepatic and lymph node metastases and a solitary bone metastasis. She had grade 2 nausea and grade 1 vomiting 15 min after tracer injection. The scans were discontinued after the AEs, and both patients withdrew from the study. The symptoms abated after a few hours without any intervention. Vital signs were stable during that period and also at 24 h after injection. Both patients were from arm B. No other AEs were reported.

Biodistribution in Normal Organs

Figure 2 shows the biodistribution of ^{68}Ga-NODAGA-LM3 at 5, 15, 30, 45, 60, and 120 min after injection in a patient with pancreatic NET. Figure 3 shows the biodistribution of ^{68}Ga-DOTA-LM3 in another patient with pancreatic NET. Significantly lower organ uptake was observed in the pituitary, parotids, liver, spleen, pancreas, adrenal, stomach, small intestine, and kidneys with ^{68}Ga-DOTA-LM3 than with ^{68}Ga-NODAGA-LM3. The biodistribution in normal organs is summarized in Figure 4. The SUV_{max} at 1 h after injection is compared in Table 2.

Tumor Uptake

In total, 38 lesions were analyzed in 14 patients, including 18 lesions (13 hepatic, 2 pancreatic, 1 lymph node, 1 bone, and 1 stomach) with ^{68}Ga-NODAGA-LM3 and 20 lesions (12 hepatic, 4 pancreatic, 2 lymph node, 1 bone, and 1 brain) with ^{68}Ga-DOTA-LM3. With ^{68}Ga-NODAGA-LM3, the tracer accumulation in tumor lesions increased by 138%, from an average SUV_{max} of 31.3 ± 19.7 at 5 min to 74.6 ± 56.3 at 2 h. With ^{68}Ga-DOTA-LM3, the tumor uptake rapidly reached a high level at 5 min after injection, with an average SUV_{max} of 36.6 ± 23.6, and continued to increase to 45.3 ± 29.3 until 30 min after injection, remaining at a plateau thereafter. The SUV_{max} and tumor-to-background ratios are summarized in Figure 5 (data available in Supplemental Table 2). Because of the relatively lower kidney and liver background for ^{68}Ga-DOTA-LM3, it showed a significantly higher tumor-to-kidney and tumor-to-liver ratios than did ^{68}Ga-NODAGA-LM3 at all time points. There were no significant differences in SUV_{max} or tumor-to-background ratios between hepatic and extrahepatic lesions in either arm ($P > 0.05$).

Radiation Dosimetry

The residence time of source organs and the absorbed dose of target organs are summarized in Tables 3 and 4, respectively. The urinary bladder wall received the highest radiation dose, 0.162 mGy/MBq for ^{68}Ga-NODAGA-LM3 and 0.202 mGy/MBq for ^{68}Ga-DOTA-LM3. Liver residence time and absorbed doses were higher in patients with than in patients without fulminant liver diseases (Supplemental Table 3). The effective dose was 0.026 ± 0.003 mSv/MBq for ^{68}Ga-NODAGA-LM3 and 0.025 ± 0.002 mSv/MBq for ^{68}Ga-DOTA-LM3.

DISCUSSION

The antagonists ^{68}Ga-NODAGA-LM3 and ^{68}Ga-DOTA-LM3 show high SSTR2 affinities in both in vitro and in vivo preclinical studies. To our knowledge, this was the first clinical study to evaluate these 2 tracers in patients with NETs. The results show favorable biodistribution and dosimetry features, and both tracers were well tolerated in most patients.

One important finding of our study was the high tumor accumulation of ^{68}Ga-NODAGA-LM3 and ^{68}Ga-DOTA-LM3. Both tracers showed high tumor uptake; the highest SUV_{max} was up to 231.9 for ^{68}Ga-NODAGA-LM3 and 126.9 for ^{68}Ga-DOTA-LM3. The average SUV_{max} at 1 h after injection was 57.5 ± 39.4 for ^{68}Ga-NODAGA-LM3 and 47.2 ± 32.6 for ^{68}Ga-DOTA-LM3—values that are certainly comparable to those for SSTR agonists and other SSTR2 antagonists (*8*, *14–18*). Furthermore, both tracers showed excellent tumor retention. Our data agree with the previous finding

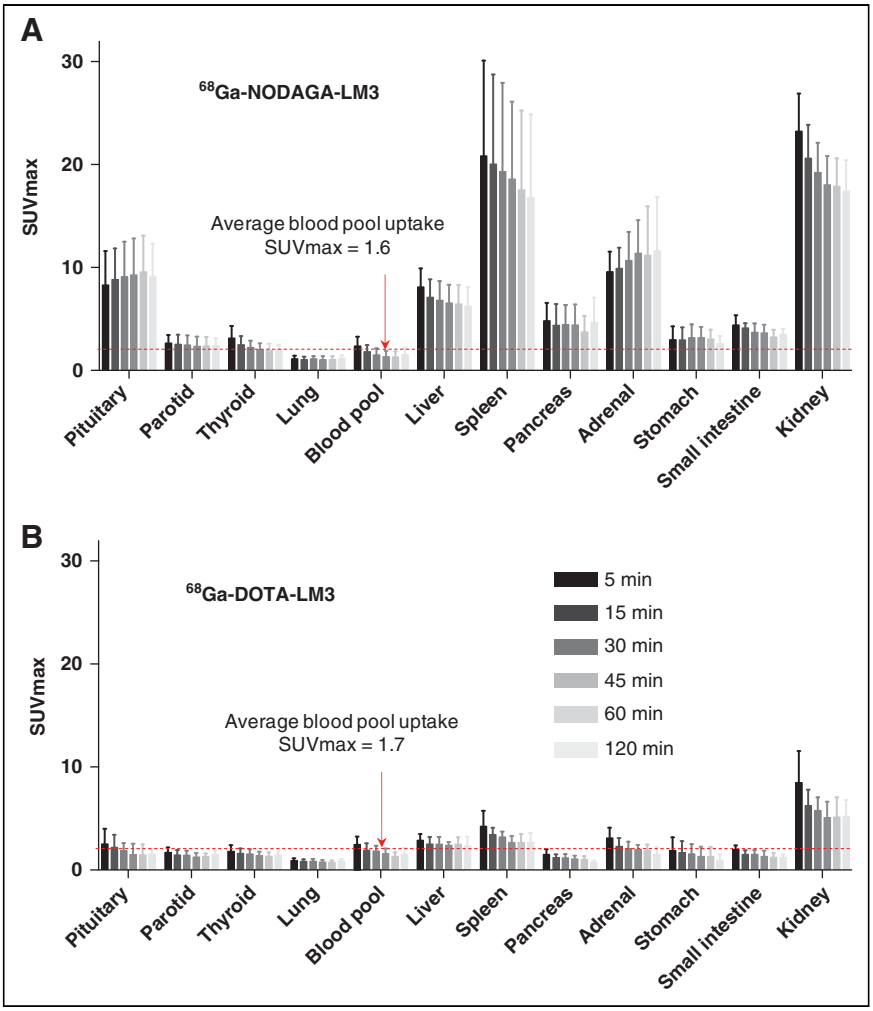

FIGURE 4. Biodistribution of ^{68}Ga-NODAGA-LM3 (A) and ^{68}Ga-DOTA-LM3 (B) in normal organs at 5, 15, 30, 45, 60, and 120 min after injection.

that radioantagonists show long tumor retention despite little internalization (*6*, *10*). High tumor retention is a key feature for peptide receptor radionuclide therapy. Zhang et al. provided preliminary evidence of efficacy using ^{177}Lu-DOTA-LM3 treatment in a patient with ^{68}Ga-DOTATOC–negative liver metastases (*11*, *12*). The patient was in nearly complete remission after 3 cycles of intraarterial peptide receptor radionuclide therapy, with a total of 20.4 GBq of ^{177}Lu-DOTA-LM3. Our finding suggests that the antagonist LM3 may be another available peptide for peptide receptor radionuclide therapy in the future and that both ^{68}Ga-NODAGA-LM3 and ^{68}Ga-DOTA-LM3 may be promising diagnostic companions.

The biodistribution of ^{68}Ga-NODAGA-LM3 was similar to that of SSTR2 agonists, which show moderate or high uptake in SSTR2-positive organs (*19*). The highest organ SUV_{max} (except for the kidneys and urinary bladder) was observed in the spleen, followed by the adrenal and pituitary glands. ^{68}Ga-DOTA-LM3, on the other hand, showed minimal uptake in almost all organs apart from the urinary tract. Only the liver and spleen showed slightly higher ^{68}Ga-DOTA-LM3 accumulation than the blood pool, whereas all other organs showed either comparable or lower uptake. Interestingly, the differences in organ uptake between these 2 tracers were observed not only in SSTR2-positive organs, such as the pituitary, spleen, and adrenals, but

TABLE 2
Uptake of Normal Organs at 1 Hour After Injection

Organ	SUV_{max}		*P*
	^{68}Ga-NODAGA-LM3	^{68}Ga-DOTA-LM3	
Pituitary	9.6 ± 3.5	1.5 ± 1.0	< 0.001
Parotids	2.4 ± 0.9	1.3 ± 0.3	0.012
Thyroids	1.9 ± 0.6	1.3 ± 0.4	0.072
Lungs	1.0 ± 0.3	0.8 ± 0.2	0.062
Blood pool	1.3 ± 0.5	1.3 ± 0.4	0.973
Liver	6.4 ± 1.8	2.5 ± 0.7	< 0.001
Spleen	17.5 ± 7.7	2.6 ± 0.8	0.012
Pancreas	3.7 ± 1.6	0.8 ± 0.5	0.005
Adrenal	11.2 ± 4.8	1.9 ± 0.6	0.001
Stomach	3.0 ± 0.9	1.3 ± 0.9	0.005
Small intestine	3.2 ± 0.7	1.2 ± 0.4	< 0.001
Kidneys	17.9 ± 2.7	5.1 ± 1.9	< 0.001

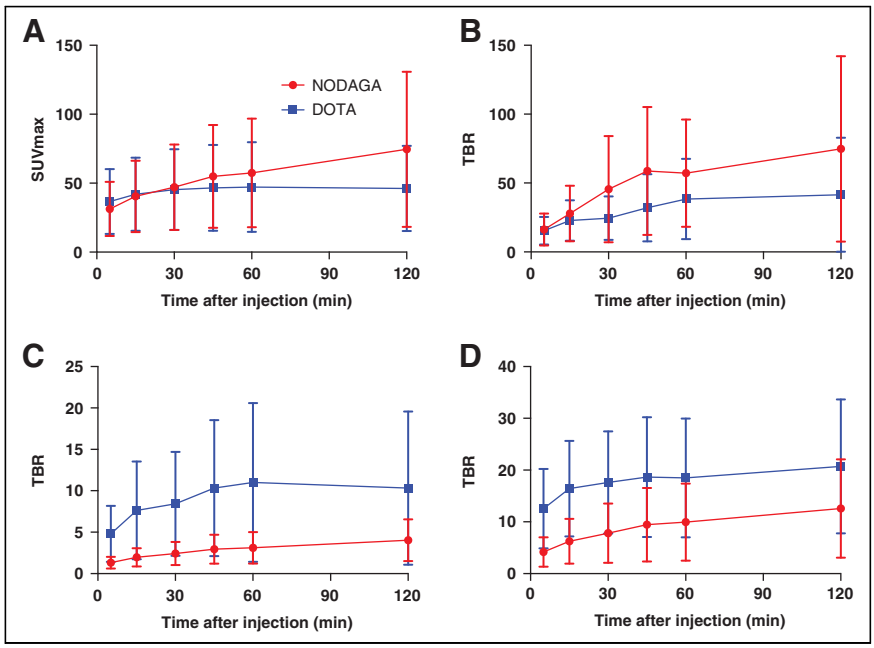

FIGURE 5. SUV_{max} (A), tumor–to–blood-pool ratio (B), tumor-to-kidney ratio (C), and tumor-to-liver ratio (D) of 38 reference lesions, including 18 lesions with ^{68}Ga-NODAGA-LM3 PET and 20 lesions with ^{68}Ga-DOTA-LM3 PET. TBR = tumor-to-background ratio.

also in the liver, reputed to be an SSTR2-negative organ. The lower background of ^{68}Ga-DOTA-LM3 was further translated into significantly higher tumor-to-kidney and tumor-to-liver ratios. The reason for the differences in organ uptake is currently not well understood and requires further study. SSTR2 antagonists are sensitive to the chelator appended. With different chelators attached, a previous study has shown ^{68}Ga-NODAGA-LM3 to have an SSTR2 affinity (1.3 nmol/L) 10-fold higher than that of ^{68}Ga-DOTA-LM3 (12.5 nmol/L) (*10*). Our study suggests that the chelators not only affect tumor uptake and retention but also biodistribution in normal organs. It should be noted, however, that our data are partially in contrast to those published by Fani et al. (*10*). They found kidney uptake to be 65% higher for ^{68}Ga-DOTA-LM3 than for ^{68}Ga-NODAGA-LM3 (percentage injected dose per gram, 32.50 vs. 19.68) in animal models, whereas our study showed kidney uptake to be 72% lower for ^{68}Ga-DOTA-LM3 than for ^{68}Ga-NODAGA-LM3 (SUV_{max}, 5.1 vs. 17.9). The differences may result from different species and peptide amounts used.

The dosimetry data for ^{68}Ga-NODAGA-LM3 and ^{68}Ga-DOTA-LM3 showed an effective dose slightly higher than, yet comparable to, that of other SSTR2 antagonists (0.024 mSv/MBq for ^{68}Ga-NODAGA-JR11 and 0.022 mSv/MBq for ^{68}Ga-DOTA-JR11) (*18*, *20*). We also observed a higher liver dose for ^{68}Ga-DOTA-LM3 despite a lower liver background. This finding is attributed mainly to dosimetry methodology. We used whole-organ volumes of interest to calculate the whole-organ activity (including disease activity). In our study, several patients (patient 1 in arm A, and patients 2, 7, and 16 in arm B) had fulminant hepatic metastases (Supplemental Fig. 1), which led to a much longer liver residence time and a much higher absorbed dose than in the other patients (Supplemental Table 3). These metastases explain the higher liver dose seen for ^{68}Ga-DOTA-LM3 despite the lower liver background and are also responsible for the comparable effective dose between these 2 tracers despite faster washout of ^{68}Ga-DOTA-LM3.

The administration of ^{68}Ga-NODAGA-LM3 was well tolerated in all patients in arm A. However, 2 patients with functional pancreatic NET (insulinoma) in arm B reported AEs at 10–15 min after ^{68}Ga-DOTA-LM3 injection. Both patients experienced nausea (grade 2), and one of them had vomiting (grade 1). These 2 AEs were considered to be related to the ^{68}Ga-DOTA-LM3 injection. In a previous study investigating the safety of another antagonist, ^{68}Ga-NODAGA-JR11 (^{68}Ga-OPS202), no pharmacologic response to the radiopharmaceutical was reported (*20*). However, Krebs et al. reported potential SSTR2 antagonistic properties for ^{68}Ga-DOTA-JR11 (*18*). In their study, 2 patients with functional NETs (the type of tumor was not specified) experienced symptoms such as flushing, hypotension (grade 3), nausea, and lightheadedness. Our study suggests that administration of an SSTR2 antagonist might trigger side effects such as nausea and vomiting. However, because so few patients were recruited, it is too early to tell whether these side effects were related to tumor functional status, antagonist peptides, or chelating agents. In fact, nausea and vomiting are common side effects of injecting somatostatin analogs. Patients with NETs, functional or nonfunctional, could have nausea and vomiting after administration of a therapeutic dose of octreotide acetate (Sandostatin; Novartis Pharmaceuticals Corp.). The AEs observed in our study may be related to the quick bolus administration. A slow bolus injection or infusion might help to relieve the symptom. Though the 2 patients with AEs in our study discontinued the scan because they were not able to lie still on the exam table for the first hour, the AEs were usually mild and would not affect an image acquisition at 60 min after injection.

Blood pressure was significantly lower at 24 h after injection than at baseline (127.5/82.4 mm Hg vs. 133.6/86.3 mm Hg, $P < 0.05$). However, this finding was not translated into any clinically

TABLE 3
Residence Time in Source Organs

Source organ	Residence time (h)	
	^{68}Ga-NODAGA-LM3	^{68}Ga-DOTA-LM3
Kidneys	0.097 ± 0.025	0.025 ± 0.008
Red marrow	0.041 ± 0.013	0.029 ± 0.017
Liver	0.194 ± 0.105	0.357 ± 0.278
Spleen	0.079 ± 0.059*	0.011 ± 0.008
Urinary bladder	0.132 ± 0.038	0.168 ± 0.062
Remainder body	1.105 ± 0.089	1.004 ± 0.196
Whole body	1.63	1.63

*n = 5 (splenectomy in 3 patients).

TABLE 4
Absorbed Doses to Target Organs and Effective Dose

Target organ	Organ doses (mGy/MBq)	
	^{68}Ga-NODAGA-LM3	^{68}Ga-DOTA-LM3
Adrenals	0.014 ± 0.001	0.014 ± 0.001
Brain	0.009 ± 0.001	0.008 ± 0.002
Breasts	0.009 ± 0.000	0.009 ± 0.001
Gallbladder wall	0.015 ± 0.001	0.017 ± 0.004
Lower large intestine wall	0.012 ± 0.001	0.012 ± 0.002
Small intestine	0.012 ± 0.001	0.013 ± 0.003
Stomach wall	0.012 ± 0.000	0.011 ± 0.001
Upper large intestine wall	0.012 ± 0.000	0.012 ± 0.001
Heart wall	0.011 ± 0.000	0.011 ± 0.001
Kidneys	0.136 ± 0.061	0.064 ± 0.052
Liver	0.056 ± 0.028	0.098 ± 0.075
Lungs	0.011 ± 0.000	0.010 ± 0.001
Muscle	0.010 ± 0.000	0.010 ± 0.001
Ovaries	0.013 ± 0.001	0.012 ± 0.002
Pancreas	0.015 ± 0.002	0.013 ± 0.000
Red marrow	0.016 ± 0.003	0.013 ± 0.003
Osteogenic cells	0.019 ± 0.002	0.016 ± 0.003
Skin	0.009 ± 0.000	0.008 ± 0.001
Testes	0.010 ± 0.001	0.010 ± 0.002
Spleen	0.132 ± 0.151	0.034 ± 0.022
Thymus	0.010 ± 0.001	0.010 ± 0.001
Thyroid	0.010 ± 0.001	0.009 ± 0.001
Urinary bladder wall	0.162 ± 0.045	0.202 ± 0.073
Uterus	0.015 ± 0.002	0.015 ± 0.003
Total body	0.013 ± 0.000	0.013 ± 0.000
Effective dose (mSv/MBq)	0.026 ± 0.002	0.025 ± 0.002

relevant events. A blood pressure change is not a specific finding and may be influenced by many conditions, such as the patient's emotional status, body temperature, exercise status, and caffeine consumption (*21*). Given the low peptide dose (40 μg) used in our study and the fast clearance of the radiopharmaceuticals (median biologic half-life of 5.18 h), the change in blood pressure at 24 h after injection was probably not related to antagonist injection.

Our study was limited by the small number of patients, which is typical for dosimetry evaluation of radiopharmaceuticals. Besides, neither blood nor urine samples were collected in our study. Blood and urine samples could allow us to search for metabolites. Lastly, the ideal comparison between ^{68}Ga-NODAGA-LM3 and ^{68}Ga-DOTA-LM3 would be one conducted on the same group of patients. A further head-to-head comparison study is required.

CONCLUSION

Both ^{68}Ga-NODAGA-LM3 and ^{68}Ga-DOTA-LM3 show a favorable biodistribution, high tumor uptake, and good tumor retention, resulting in high image contrast. The dosimetry data are comparable to those for other ^{68}Ga-labeled SSTR2 antagonists. Further studies are required to look into the potential antagonistic effects of ^{68}Ga-NODAGA-LM3 and ^{68}Ga-DOTA-LM3.

DISCLOSURE

This work was sponsored in part by the CAMS Initiative for Innovative Medicine (2017-I2M-4-002 and 2018-I2M-3-001) and by the Nonprofit Central Research Institute Fund of the Chinese Academy of Medical Sciences (2019PT310026). No other potential conflict of interest relevant to this article was reported.

ACKNOWLEDGMENTS

We thank Prof. Richard P. Baum for inspiring us on the LM3 project. We also thank all the patients who participated in this study, Yue Zhang (SinoUnion Healthcare Inc., China) for image acquisition, and Dr. Chengyan Dong (GE Healthcare, China) for critical proofreading and figure suggestions.

KEY POINTS

QUESTION: Do ^{68}Ga-NODAGA-LM3 and ^{68}Ga-DOTA-LM3 show suitable biodistribution and dosimetry data in NET, and are they safe?

PERTINENT FINDINGS: Both ^{68}Ga-NODAGA-LM3 and ^{68}Ga-DOTA-LM3 show a favorable biodistribution, high tumor uptake, and good tumor retention. Few AEs were reported using ^{68}Ga-DOTA-LM3.

IMPLICATIONS FOR PATIENT CARE: Both ^{68}Ga-NODAGA-LM3 and ^{68}Ga-DOTA-LM3 are promising in NET imaging.

REFERENCES

1. Virgolini I, Ambrosini V, Bomanji JB, et al. Procedure guidelines for PET/CT tumour imaging with ^{68}Ga-DOTA-conjugated peptides: ^{68}Ga-DOTA-TOC, ^{68}Ga-DOTA-NOC, ^{68}Ga-DOTA-TATE. *Eur J Nucl Med Mol Imaging*. 2010;37:2004–2010.
2. Reubi JC, Waser B, Cescato R, Gloor B, Stettler C, Christ E. Internalized somatostatin receptor subtype 2 in neuroendocrine tumors of octreotide-treated patients. *J Clin Endocrinol Metab.* 2010;95:2343–2350.
3. Fani M, Nicolas GP, Wild D. Somatostatin receptor antagonists for imaging and therapy. *J Nucl Med.* 2017;58(suppl):61S–66S.
4. Ginj M, Zhang H, Waser B, et al. Radiolabeled somatostatin receptor antagonists are preferable to agonists for in vivo peptide receptor targeting of tumors. *Proc Natl Acad Sci USA*. 2006;103:16436–16441.
5. Wild D, Fani M, Behe M, et al. First clinical evidence that imaging with somatostatin receptor antagonists is feasible. *J Nucl Med.* 2011;52:1412–1417.
6. Nicolas GP, Mansi R, McDougall L, et al. Biodistribution, pharmacokinetics, and dosimetry of ^{177}Lu-, ^{90}Y-, and ^{111}In-labeled somatostatin receptor antagonist OPS201 in comparison to the agonist ^{177}Lu-DOTATATE: the mass effect. *J Nucl Med.* 2017;58:1435–1441.
7. Dalm SU, Nonnekens J, Doeswijk GN, et al. Comparison of the therapeutic response to treatment with a ^{177}Lu-labeled somatostatin receptor agonist and antagonist in preclinical models. *J Nucl Med.* 2016;57:260–265.
8. Nicolas GP, Schreiter N, Kaul F, et al. Sensitivity comparison of ^{68}Ga-OPS202 and ^{68}Ga-DOTATOC PET/CT in patients with gastroenteropancreatic neuroendocrine tumors: a prospective phase II imaging study. *J Nucl Med.* 2018;59:915–921.
9. Zhu W, Cheng Y, Wang X, et al. Head-to-head comparison of ^{68}Ga-DOTA-JR11 and ^{68}Ga-DOTATATE PET/CT in patients with metastatic, well-differentiated neuroendocrine tumors: a prospective study. *J Nucl Med.* 2020;61:897–903.
10. Fani M, Del Pozzo L, Abiraj K, et al. PET of somatostatin receptor-positive tumors using ^{64}Cu- and ^{68}Ga-somatostatin antagonists: the chelate makes the difference. *J Nucl Med.* 2011;52:1110–1118.
11. Zhang J, Kulkarni HR, Singh A, Baum RP. Successful intra-arterial peptide receptor radionuclide therapy of DOTATOC-negative high-grade liver metastases of a pancreatic neuroendocrine neoplasm using ^{177}Lu-DOTA-LM3. *Clin Nucl Med.* 2020;45:e165–e168.
12. Zhang J, Singh A, Kulkarni HR, et al. From bench to bedside: the Bad Berka experience with first-in-human studies. *Semin Nucl Med.* 2019;49:422–437.
13. Basic anatomical and physiological data for use in radiological protection: reference values—a report of age- and gender-related differences in the anatomical and physiological characteristics of reference individuals. ICRP Publication 89. *Ann ICRP*. 2002;32:5–265.
14. Aalbersberg EA, de Wit-van der Veen BJ, Versleijen MWJ, et al. Influence of lanreotide on uptake of ^{68}Ga-DOTATATE in patients with neuroendocrine tumours: a prospective intra-patient evaluation. *Eur J Nucl Med Mol Imaging*. 2019;46:696–703.
15. Wild D, Bomanji JB, Benkert P, et al. Comparison of ^{68}Ga-DOTANOC and ^{68}Ga-DOTATATE PET/CT within patients with gastroenteropancreatic neuroendocrine tumors. *J Nucl Med.* 2013;54:364–372.
16. Brogsitter C, Zophel K, Hartmann H, Schottelius M, Wester HJ, Kotzerke J. Twins in spirit part II: DOTATATE and high-affinity DOTATATE—the clinical experience. *Eur J Nucl Med Mol Imaging*. 2014;41:1158–1165.
17. Velikyan I, Sundin A, Sorensen J, et al. Quantitative and qualitative intrapatient comparison of ^{68}Ga-DOTATOC and ^{68}Ga-DOTATATE: net uptake rate for accurate quantification. *J Nucl Med.* 2014;55:204–210.
18. Krebs S, Pandit-Taskar N, Reidy D, et al. Biodistribution and radiation dose estimates for ^{68}Ga-DOTA-JR11 in patients with metastatic neuroendocrine tumors. *Eur J Nucl Med Mol Imaging*. 2019;46:677–685.
19. Moradi F, Jamali M, Barkhodari A, et al. Spectrum of ^{68}Ga-DOTA TATE uptake in patients with neuroendocrine tumors. *Clin Nucl Med.* 2016;41:e281–e287.
20. Nicolas GP, Beykan S, Bouterfa H, et al. Safety, biodistribution, and radiation dosimetry of ^{68}Ga-OPS202 in patients with gastroenteropancreatic neuroendocrine tumors: a prospective phase I imaging study. *J Nucl Med.* 2018;59:909–914.
21. Jin J. Checking blood pressure at home. *JAMA*. 2017;318:310.

Quantitative ^{68}Ga-DOTATATE PET/CT Parameters for the Prediction of Therapy Response in Patients with Progressive Metastatic Neuroendocrine Tumors Treated with ^{177}Lu-DOTATATE

Claudia Ortega[1], Rebecca K.S. Wong[2], Josh Schaefferkoetter[3], Patrick Veit-Haibach[1], Sten Myrehaug[4], Rosalyn Juergens[5], David Laidley[6], Reut Anconina[1], Amy Liu[7], and Ur Metser[1]

[1]*Joint Department of Medical Imaging, University Health Network, Mount Sinai Hospital and Women's College Hospital, University of Toronto, Toronto, Ontario, Canada;* [2]*Department of Radiation Oncology, Princess Margaret Cancer Centre, University Health Network and University of Toronto, Toronto, Ontario, Canada;* [3]*Siemens Medical Solutions USA, Inc., Knoxville, Tennessee;* [4]*Division of Radiation Oncology, Odette Cancer Centre, Sunnybrook Health Sciences Centre, Toronto, Ontario, Canada;* [5]*Department of Oncology, Juravinski Cancer Centre, McMaster University, Hamilton, Ontario, Canada;* [6]*Division of Nuclear Medicine, St. Joseph's Health Care London, University of Western Ontario, London, Ontario, Canada; and* [7]*Department of Biostatistics, Princess Margaret Cancer Centre, Toronto, Ontario, Canada*

The aim of this study was to determine whether quantitative PET parameters on baseline ^{68}Ga-DOTATATE PET/CT and interim PET (iPET) performed before the second cycle of therapy are predictive of the therapy response and progression-free survival (PFS). **Methods:** Ninety-one patients with well-differentiated neuroendocrine tumors (mean Ki-67 index, 8.3%) underwent ^{68}Ga-DOTATATE PET/CT to determine suitability for peptide receptor radionuclide therapy as part of a prospective multicenter study. The mean follow-up was 12.2 mo. Of the 91 patients, 36 had iPET. The tumor metrics evaluated were marker lesion–based measures (mean SUV_{max} and ratio of the mean lesion SUV_{max} to the SUV_{max} in the liver or the SUV_{max} in the spleen), segmented ^{68}Ga-DOTATATE tumor volumes (DTTVs), SUV_{max} and SUV_{mean} obtained with the liver and spleen as thresholds, and heterogeneity parameters (coefficient of variation, kurtosis, and skewness). The Wilcoxon rank sum test was used for the association between continuous variables and the therapy response, as determined by the clinical response. Univariable and multivariable Cox proportional hazards models were used for the association with PFS. **Results:** There were 71 responders and 20 nonresponders. When marker lesions were used, higher mean SUV_{max} and ratio of the mean lesion SUV_{max} to the SUV_{max} in the liver were predictors of the therapy response ($P = 0.018$ and 0.024, respectively). For DTTV parameters, higher SUV_{max} and SUV_{mean} obtained with the liver as a threshold and lower kurtosis were predictors of a favorable response ($P = 0.025$, 0.0055, and 0.031, respectively). The latter also correlated with a longer PFS. The iPET DTTV SUV_{mean} obtained with the liver as a threshold and the ratio of mean SUV_{max} obtained from target lesions at iPET to baseline PET correlated with the therapy response ($P = 0.024$ and 0.048, respectively) but not PFS. From the multivariable analysis with adjustment for age, primary site, and Ki-67 index, the mean SUV_{max} ($P = 0.019$), ratio of the mean lesion SUV_{max} to the SUV_{max} in the liver ($P = 0.018$), ratio of the mean lesion SUV_{max} to the SUV_{max} in the spleen ($P = 0.041$), DTTV SUV_{mean} obtained with the liver ($P = 0.0052$), and skewness ($P = 0.048$) remained significant predictors of PFS. **Conclusion:** The degree of somatostatin receptor expression and tumor heterogeneity, as represented by several metrics in our analysis, were predictive of the therapy response or PFS. Changes in these parameters after the first cycle of peptide receptor radionuclide therapy did not correlate with clinical outcomes.

Key Words: ^{68}Ga-DOTATATE; PET/CT; neuroendocrine tumors; PRRT; response; survival

J Nucl Med 2021; 62:1406–1414
DOI: 10.2967/jnumed.120.256727

Neuroendocrine tumors (NETs) are uncommon malignancies with a documented population incidence of 6 or 7 per 100,000 in 2012 (*1*). The most common primary tumor sites are gastroenteropancreatic, but they may arise in the lungs, adrenal glands, and pituitary gland, among other locations (*2*). Most NETs overexpress somatostatin receptors (SSTRs) on the cell surface, allowing for SSTR-based imaging with ^{68}Ga-(DOTA)-peptide PET; in recent years, the latter technique has become the preferred imaging modality for diagnosis, staging, and selection of patients for peptide receptor radionuclide therapy (PRRT) (*3*).

Coupling β- or γ-emitting radionuclides (^{177}Lu or ^{90}Y) to somatostatin analogs allows radionuclide therapy for well-differentiated unresectable or metastatic tumors that are highly DOTA–somatostatin analog avid (*4*). Multiple studies, including a recent phase III randomized trial (NETTER-1), have shown favorable progression-free survival (PFS) and overall survival, with limited, acceptable side effects (*5–11*). In 1 of those studies, treatment of patients who had midgut NETs with ^{177}Lu-DOTATATE and octreotide long-acting release resulted in longer PFS and overall survival than treatment with octreotide long-acting release alone (*11*).

In July 2016, a prospective, multicenter trial was launched in Ontario, Canada, to assess the outcome of patients who had progressive metastatic NETs treated with individualized dosimetry-guided ^{177}Lu-DOTATATE therapy and who were provided access to PRRT with regulatory Health Canada oversight. A further aim

Received Sep. 15, 2020; revision accepted Jan. 20, 2021.
For correspondence or reprints, contact Ur Metser (ur.metser@uhn.ca).
Published online February 12, 2021.

of that trial was to evaluate the prognostic value of quantitative ^{68}Ga-DOTATATE PET/CT performed for patient selection. The purpose of the present study was to determine whether semiquantitative, volumetric, and tumor heterogeneity parameters on baseline PET (bPET) and early interim PET (iPET) performed before a second cycle of therapy are predictive of the therapy response and PFS.

MATERIALS AND METHODS

Study Design

Patients included in this analysis were enrolled in a prospective, multicenter, single-arm institutional review board–approved study (NCT02743741). All patients signed a written informed consent form. Eligibility criteria included biopsy-proven NET, with no restriction on primary site of origin; Ki-67 index of less than or equal to 30%; and progressive disease before study enrollment. All patients underwent screening with ^{68}Ga-DOTATATE PET/CT to confirm the adequate expression of SSTR type 2. In eligible patients, most tumor sites exhibited a high level of ^{68}Ga-DOTATATE uptake (defined as a Krenning score of 3 or 4) (*12*,*13*). An optional iPET scan was performed before cycle 2 of ^{177}Lu-DOTATATE therapy to explore its prognostic value for clinical outcomes. Associations between bPET or iPET parameters and the outcome measures (therapy response and PFS) were evaluated.

Study Procedure

^{68}Ga-DOTATATE PET/CT Imaging Protocol. PET was performed on a Siemens mCT40 PET/CT scanner (Siemens Healthcare). Patients were positioned supine with arms outside the region of interest. Images were obtained from the top of the skull to the upper thighs. Iodinated oral contrast material was administered for bowel opacification; no intravenous iodinated contrast material was used. Overall, 5–9 bed positions were obtained, depending on patient height, with an acquisition time of 2–3 min per bed position. A mean dose of 131.8 (SD = 29.7) MBq (range, 54.5–205 MBq) of ^{68}Ga-DOTATATE was administered, with a mean uptake time of 65.8 min (range, 50–93 min). CT parameters were 120 kV; 3.0 mm slice width, 2.0 mm collimation; 0.8 sec rotation time; 8.4 mm feed/rotation. A PET emission scan using time of flight with scatter correction was obtained covering the identical transverse field of view. PET parameters were as follows: image size: 2.6 pixels; slice: 3.27; and 5-mm full width at half maximum (FWHM) gaussian filter type. PET/CT images were reviewed on a dedicated nuclear medicine PACS system with fusion software (Mirada Medical). SUV measurements were obtained using a region of interest delineating selected tumor sites (Fig. 1).

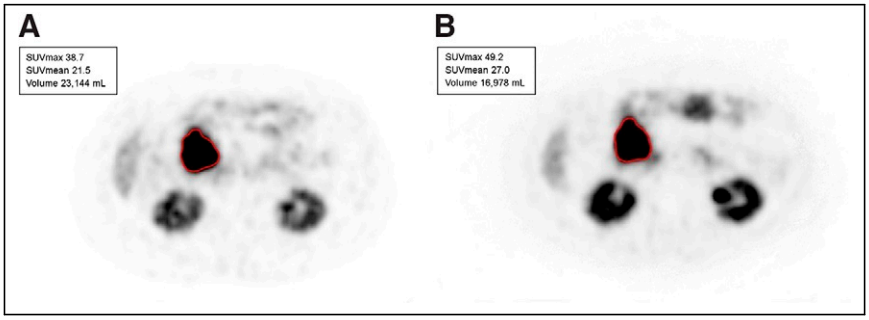

FIGURE 1. 60-y-old woman with metastases of well-differentiated small bowel NET to liver and retroperitoneal lymph nodes (G1; Ki-67 index, 6%). Lesion-based assessment was done with bPET and iPET before cycle 2 of ^{177}Lu-DOTATATE therapy. (A) Metastatic nodal mass chosen as marker lesion at bPET (SUV_{max}, 38.7) (outlined in red). (B) Same lesion before cycle 2 of therapy (SUV_{max}, 49.2) (outlined in red).

Tumor Volume Segmentation Software. A graphical user interface was developed in-house specifically to delineate whole-body tumor burden. An initial mask was defined by setting a threshold equal to the maximal value in a 3-dimensional volume of interest drawn within normal reference tissue, initially within the normal liver. From this general mask, normal physiologic tracer uptake was manually removed in a 3-dimensional maximum-intensity-projection space. The PET volume and the mask overlay were displayed at various radial angles, allowing the user to define and remove regions of normal uptake (e.g., myocardium, spleen, bladder) at any view, providing the clearest visible margins. Once the normal tissues were removed from the tumor mask, a final step allowed the user to manually add or subtract any other region to or from the mask. Correlation with morphologic imaging (contrast-enhanced CT or MRI) was performed when needed to ensure the accurate delineation of tumor sites. ^{68}Ga-DOTATATE tumor volumes (DTTVs), SUV_{max}, and SUV_{mean} were generated from the final tumor mask (Fig. 2). The same process was repeated with a threshold equal to the maximal value in a 3-dimensional volume of interest drawn within the normal spleen (a step-by-step demonstration of the segmentation process is provided in Supplemental Fig. 1 [supplemental materials are available at http://jnm.snmjournals.org]).

^{177}Lu-DOTATATE Therapy and Clinical Outcomes. Eligible patients were treated with 4 cycles of ^{177}Lu-DOTATATE or fewer if limited by toxicity or disease progression. Individualized dosimetry was used for the provision of ^{177}Lu-DOTATATE therapy. The initial administered activity of ^{177}Lu-DOTATATE was standardized at 7,400 MBq (200 mCi). Whole-body scintigraphy was performed at 4, 24, and 72 h after each cycle to estimate a recommended activity that will result in an accumulated absorbed dose to the kidneys of 23 Gy, with estimates of absorbed doses in the bone marrow and tumor. Dose escalation was capped at a maximum of 11,100 MBq (300 mCi) per dose. The final prescribed activity was determined by the treating physician on the basis of the recommended activity and patient factors, including renal and hematologic laboratory results. For the present report, the response to therapy was defined by the investigator on the basis of CT of the chest, abdomen, and pelvis performed 3 mo after the completion of therapy or earlier if disease progression was observed (*12*). Responders were defined as patients with a complete/partial response or stable disease, and nonresponders had progressive disease. Patients continued clinical and CT surveillance, and time to progression was documented for all study participants.

PET Data Abstraction

Reference Normal Tissue Values. The SUV_{max} in reference tissues, normal liver (lower threshold), and spleen (upper threshold) were recorded. In the liver, the SUV_{max} was measured in the posterior right lobe. For patients who underwent splenectomy, normal renal parenchyma was used for the upper threshold instead of the spleen (*12*,*13*). In the present report, both upper-threshold references are referred to collectively as "spleen."

Tumor Parameters. Three types of tumor parameters (marker lesion–based, whole-body DTTV, and first-order heterogeneity parameters) were assessed, for a total of 13 metrics from the baseline and before cycle 2 scans, when available.

For lesion-based parameters, reference background tracer uptake in normal liver and

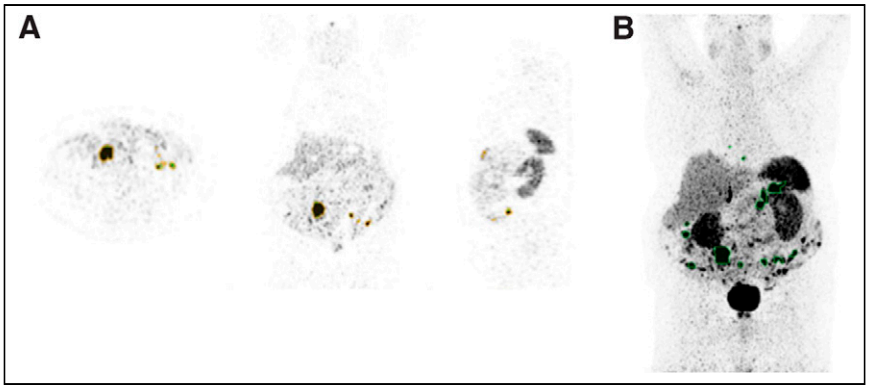

FIGURE 2. ^{68}Ga-DOTATATE tumor volume analysis using in-house automated segmentation software. (A) Multiplanar segmentation tool (to identify and confirm tumor sites). (B) Mask generated using tracer uptake in spleen as threshold (tumor lesions with SUV_{max} above that of spleen are outlined in green).

spleen tissues (or left renal cortex in the case of previous splenectomy) was measured (volumes of interest placed in the right hepatic lobe and spleen). Up to 5 well-defined, reproducible marker lesions larger than 1 cm were chosen, with no more than 2 lesions per disease site or organ, in accordance with RECIST 1.1 recommendations (*14*,*15*). The SUV_{max} of each lesion and the mean SUV_{max} of all marker lesions were recorded. In addition, the ratio of the lesion SUV_{max} to the SUV_{max} in the liver (SUV_{max} T/L) or the SUV_{max} in the spleen (SUV_{max} T/S) was calculated.

For DTTV parameters, the maximum SUV within the volume of interest drawn over the liver and spleen was used as a threshold for the measurement of DTTV in the liver and DTTV in the spleen. The total DTTV (DTTV with liver and spleen as thresholds), the SUV_{max} generated from the contoured volumes, and the SUV_{mean} generated for each threshold were documented.

TABLE 1
Patient Characteristics for Entire Cohort and Subgroup with iPET

Characteristic	Entire cohort	iPET cohort
No. of patients	91	36
Sex (M:F)	53:38	20:16
Mean age (y)	62.5 (SD = 12.9)	59.7 (SD = 14.2)
Primary site (No. of patients)		
Gastrointestinal tract	48	19
Pancreas	19	8
Unknown primary	9	2
Bronchopulmonary	6	3
Adrenal	4	2
Other	5	2
Mean tumor Ki-67 index (%)	8.3 (SD = 7.8)	10.5 (SD = 8.3)
Response status		
Nonresponders	20	6
Other	71	30
Mean follow-up (mo)	12.2 (SD = 7.2)	20.1 (SD = 9.7)

The heterogeneity of SSTR type 2 expression at the various tumor sites was assessed using the segmented 3-dimensional tumor volumes. For this purpose, 3 different first-order heterogeneity radiomics parameters were evaluated within the generated volumes: coefficient of variation, defined as the SD divided by the mean of the activity concentration in the tumor volume; skewness, the third standardized moment and measure of the asymmetry of the activity distribution at tumor sites; and kurtosis, the fourth standardized moment and measure of the "tailedness" of the probability distribution. For both skewness and kurtosis, the metrics were calculated with and without sample size bias correction, and no significant differences were observed.

Statistical Analysis

Summary statistics were used to describe patient and disease characteristics, with mean and range for continuous variables and frequency and percentage for categoric variables. Box plots were used to visualize the distribution of continuous variables between responders and nonresponders. A 2-sided Wilcoxon rank sum test was used to test for associations between continuous variables and the response. All markers for PFS, defined as survival without progression or death, were assessed using a univariable Cox proportional hazards model. Each statistically significant marker from the univariable analysis was further assessed using a multivariable Cox proportional hazards model with adjustment for patient factors, including age, primary disease site, and Ki-67 index. A P value of less than 0.05 was considered statistically significant, without adjustment for multiple comparisons.

RESULTS

Patient Demographics

At the time of data lock for the present analysis (December 2019), 96 consecutive subjects had been referred between August 2016 and January 2019 for consideration of PRRT. Five subjects who were not treated were excluded (2 withdrew from the study, and 3 had inadequate tracer uptake in tumor sites). Thus, 91 patients who fulfilled the inclusion criteria, received therapy, and had follow-up data available comprised the study cohort. Thirty-six of them underwent iPET. Patient characteristics are shown in Table 1. Patients received up to 4 cycles of PRRT (mean, 3.67: range, 1–4) with an average dose of 7,375.1 MBq (range, 972–12,659 MBq). The mean clinical follow-up was 12.2 mo (range, 1.4–38 mo). There were 71 responders (51 with stable disease; 20 with a partial response) and 20 nonresponders. The mean PFS was 18.9 mo (95% CI, 15.6–22.8 mo).

bPET Parameters

Reference Tissues. The SUV_{max} in 2 reference tissues, normal liver and spleen, were compared in responders and nonresponders. For 9 patients who underwent splenectomy, normal renal parenchyma was used instead of the spleen as the upper-threshold reference. For the lesion-based analysis, a mean of 4.7 target lesions was evaluated for each patient (median, 5; range, 2–5). Baseline reference tissue parameters (lesion-based ^{68}Ga-DOTATATE PET/CT measures, DTTV parameters, and

TABLE 2
bPET Reference Parameters, Lesion-Based Parameters, DTTV Parameters, and First-Order Heterogeneity Parameters

bPET Parameter	All Patients (n = 91)	Responders (n = 71)	Nonresponders (n = 20)	P*
Reference tissue				
SUV_{max} liver				0.49
Mean (SD)	5.7 (2.1)	5.8 (2.3)	5.3 (1.6)	
Minimum–maximum	2–13.1	3.2–8.2	2–13.1	
SUV_{max} spleen				0.30
Mean (SD)	13.8 (6.9)	14.1 (6.9)	12.6 (6.7)	
Minimum–maximum	4.4–45.8	4.4–26.7	5–45.8	
Lesion based				
Mean SUV_{max}				0.018
Mean (SD)	38.7 (25.1)	41.7 (26.8)	28.2 (14.2)	
Minimum–maximum	11–137.7	13.4–77.4	11–137.7	
Mean SUV_{max} T/L				0.024
Mean (SD)	8.3 (6.4)	9 (7)	5.8 (2.9)	
Minimum–maximum	1.4–40.5	1.4–40.5	2.9–14.6	
Mean SUV_{max} T/S				0.13
Mean (SD)	3.5 (2.7)	3.7 (2.9)	2.8 (1.8)	
Minimum–maximum	0.2–14.6	0.2–14.6	1–8.3	
DTTV				
DTTV liver†				0.12
Mean (SD)	554.1 (853.8)	611.5 (921.7)	350.4 (516.8)	
Minimum–maximum	4.7–4,891.8	4.7–4,891.8	8.1–2,200.9	
DTTV spleen†				0.06
Mean (SD)	317.1 (616.3)	363.9 (677.6)	150.9 (265.4)	
Minimum–maximum	0–3,825.3	0–3,825.3	0–1,049.6	
DTTV SUV_{max}				0.025
Mean (SD)	62.8 (46.4)	66.8 (48.4)	48.4 (36.2)	
Minimum–maximum	15.6–307)	17.1–307	15.6–186.6	
DTTV SUV_{mean} liver				0.0055
Mean (SD)	15.6 (7.3)	16.7 (7.7)	11.6 (3.6)	
Minimum–maximum	5.1–41.4	5.8–41.4	5.1–19.4	
DTTV SUV_{mean} spleen				0.06
Mean (SD)	23.5 (10.3)	24.5 (10.4)	20 (9.3)	
Minimum–maximum	0–50.4	0–50.4	7.7–45.3	
Heterogeneity				
CoV				0.17
Mean (SD)	0.6 (0.2)	0.6 (0.2)	0.6 (0.3)	
Minimum–maximum	0.2–1.6	0.3–1.5	0.2–1.6	
Skewness				0.055
Mean (SD)	1.5 (0.8)	1.4 (0.8)	1.9 (1.0)	
Minimum–maximum	0.1–4	0.1–4	0.6–4	
Kurtosis				0.031
Mean (SD)	6.4 (4.8)	5.8 (4.1)	8.6 (6.4)	
Minimum–maximum	1.7–26.7	1.7–25.8	2.8–26.7	

*P value.

†Measured in cubic centimeters.

DTTV SUV_{mean} liver = SUV_{mean} in segmented volume obtained with liver as threshold; DTTV SUV_{mean} spleen = SUV_{mean} in segmented volume obtained with spleen as threshold; DTTV liver = DTTV obtained with liver as threshold; DTTV spleen = DTTV obtained with spleen as threshold; DTTV SUV_{mean} liver = DTTV SUV_{mean} obtained with liver as threshold; DTTV SUV_{mean} spleen = DTTV SUV_{mean} obtained with spleen as threshold; CoV = coefficient of variation.

Wilcoxon rank sum test P values are shown.

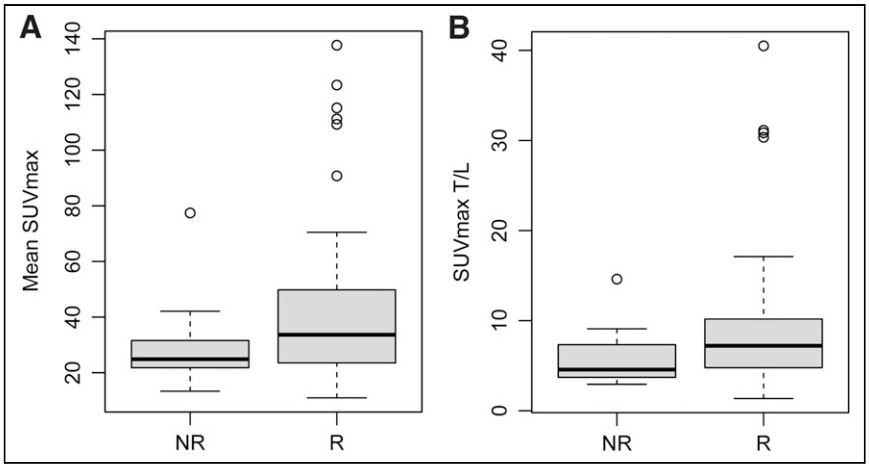

FIGURE 3. Lesion-based measures. Distributions of median SUV_{max} ($P = 0.018$) (A) and SUV_{max} T/L ($P = 0.024$) (B) are shown. Box plots represent median and upper and lower quartiles of each distribution, with whiskers showing limits of distribution (1.5 times interquartile range). NR = nonresponders; R = responders.

heterogeneity parameters) for responders and nonresponders are summarized in Table 2.

Tumor Parameters. For marker lesions, higher mean SUV_{max} and SUV_{max} T/L were predictive of the therapy response ($P = 0.018$ and 0.024, respectively) (Fig. 3). Similarly, higher SUV_{max} measured in DTTVs and SUV_{mean} of segmented tumor volumes with the liver used as a threshold were associated with the therapy response ($P = 0.025$ and 0.0055, respectively) (Fig. 4). An association of mean SUV_{max} of target lesions, SUV_{max} T/L, SUV_{max} T/S, and SUV_{mean} of segmented tumor volumes with the liver used as a threshold with progression or death was demonstrated ($P = 0.0023$. 0.028, 0.047, and 0.0053, respectively).

Of the 3 analyzed first-order heterogeneity parameters, only kurtosis emerged as a significant predictor of outcome, with higher values in nonresponders than in responders (Fig. 5). Both skewness (hazard ratio [HR], 1.49 [95% CI, 1.07–2.07]; $P = 0.017$) and kurtosis (HR, 1.06 [95% CI, 1.01–1.11]; $P = 0.022$) were associated with progression or death.

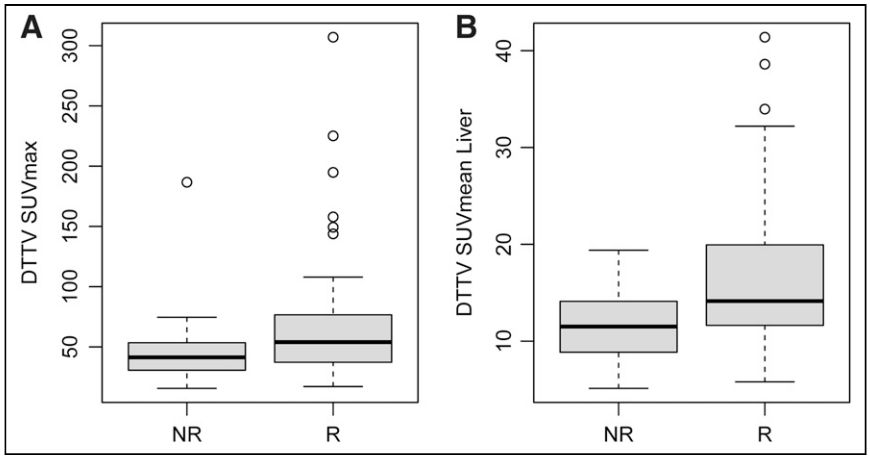

FIGURE 4. DTTV parameters. Distributions of mean DTTV SUV_{max} ($P = 0.025$) (A) and SUV_{mean} obtained with liver as threshold (SUV_{mean} Liver) ($P = 0.0055$) (B) are shown. Box plots represent median and upper and lower quartiles of each distribution, with whiskers showing limits of distribution (1.5 times interquartile range). NR = nonresponders; R = responders.

iPET Response Assessment Parameters

iPET lesion-based, DTTV, and heterogeneity parameters are shown in Table 3. Changes in the various parameters between bPET and iPET are shown in Supplemental Table 1.

PFS

There was a correlation of higher mean SUV_{max}, SUV_{max} T/L, SUV_{max} T/S, and DTTV SUV_{mean} obtained with the liver as a threshold with a longer PFS ($P = 0.023$, 0.028, 0.047, and 0.0053, respectively). Conversely, higher kurtosis and skewness were correlated with a shorter PFS ($P = 0.0022$ and 0.017, respectively).

From the multivariable analysis with adjustment for age, primary site, and Ki-67 index, the mean SUV_{max} ($P = 0.019$), SUV_{max} T/L ($P = 0.018$), SUV_{max} T/S ($P = 0.041$), DTTV SUV_{mean} obtained with the liver as a threshold ($P = 0.0052$), and skewness ($P = 0.048$) remained statistically significant predictors of PFS; however, variable kurtosis was not significant in the multivariable analysis. None of the analyzed parameters at iPET showed a statistical correlation with PFS in the univariable analysis.

Table 4 shows the results for the univariable analysis of the prediction of PFS from demographic data, the tumor Ki-67 index, lesion-based measures, DTTV parameters, and heterogeneity parameters on bPET as well as the multivariable analysis results obtained from statistically significant parameters in the univariable analysis when correlated with age, primary disease site, and Ki-67 index. The complete univariable analysis is shown in Supplemental Table 2.

DISCUSSION

The identification of biomarkers predictive of the therapy response and prognosis is essential for personalized care. PRRT is an effective mode of therapy in patients with metastatic NETs, but it is only appropriate for patients whose tumors highly overexpress somatostatin receptors (*16*). As would be expected and as previously reported, a higher tumor SUV_{max} on ^{68}Ga-DOTATATE PET/CT correlates with the treatment response (*17–20*). A few SUV-based parameters, including the mean SUV_{max} of target lesions and the SUV_{mean} generated from the DTTV with the liver as a threshold, were predictive of the response to PRRT; both the mean SUV_{max} and the DDTV SUV_{mean} obtained with the liver as a threshold also correlated with PFS (HRs, 1.04 and 1.19, respectively). A further interesting observation from the present study was that there was generally a higher SUV_{max} in reference tissues (normal liver and spleen) at iPET in patients who responded to PRRT. In the normal liver, SSTRs are predominantly found in

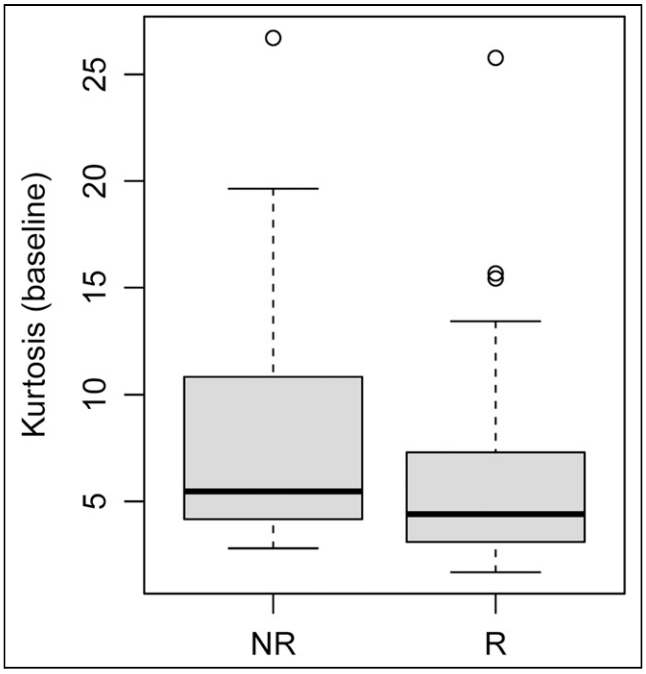

FIGURE 5. Kurtosis on baseline ^{68}Ga-DOTATATE PET/CT. Distribution of kurtosis was estimated from ^{68}Ga-DOTATATE tumor volumes (P = 0.031). Box plot represents median and upper and lower quartiles of each distribution, with whiskers showing limits of distribution (1.5 times interquartile range). NR = nonresponders; R = responders.

bile ducts, whereas in the normal spleen, autoradiography and immunohistochemistry studies have shown that they are found predominantly in red pulp (21,22). The reason for the presumed flare phenomenon in tracer uptake in normal tissues with a high level of expression of SSTRs is uncertain; however, it may reflect an inflammatory response, with an increase in activated macrophages that overexpress SSTR-1 and SSTR-2 on their cell surface (23,24). This phenomenon has also been the basis of imaging of inflammation in atherosclerosis and myocarditis with ^{68}Ga-DOTATATE PET/CT (25,26).

Early prediction of treatment failure can be a powerful clinical tool. For certain disease entities, early biomarkers have been validated and are clinically used to tailor therapy and reduce toxicity. Although generally well tolerated, PRRT can be associated with significant hematologic, renal, and hepatic toxicities (in approximately 10%, 0.4%, and 0.4% of patients, respectively) (*27*). Despite the high radiation dose delivered, disease progression is observed in 20%–30% of patients, and most patients achieve stable disease as the best response (*28*). Biomarkers that accurately predict PRRT outcomes may identify patients who are unlikely to benefit from it and limit unnecessary toxicity. Although the SUV_{mean} generated from the DTTV with the liver as a threshold on iPET was significantly higher in responders than in nonresponders (18.1 [SD = 9.1] and 11.2 [SD = 3.3], respectively), the overlap may limit the clinical utility of this observation.

NETs often exhibit intratumoral heterogeneity. Skewness and kurtosis, first-order features of heterogeneity, depict the asymmetry within the gray-level distribution observed within a

TABLE 3
iPET Reference Parameters, Lesion-Based Parameters, DTTV Parameters, and First-Order Heterogeneity Measures, Part 1

iPET	All patients (n = 36)	Responders (n = 30)	Nonresponders (n = 6)	P*
Reference tissue				
SUV_{max} liver				0.011
Mean (SD)	5.8 (1.8)	6.1 (1.8)	4.2 (1.2)	
Minimum–maximum	2.8–11.2	3.6–11.2	2.8–6.4	
SUV_{max} spleen				0.0085
Mean (SD)	19.4 (10.6)	21.2 (10.7)	10.6 (3.8)	
Minimum–maximum	4.3–49.1	7.3–49.1	4.3–14.6	
Lesion based				
Mean SUV_{max}				0.048
Mean (SD)	34.3 (19.4)	37 (20.2)	21.2 (6)	
Minimum–maximum	6.8–93.1	6.8–93.1	12.4–29.9	
Mean SUV_{max} T/L				0.57
Mean (SD)	6.1 (3.2)	6.3 (3.5)	5.2 (1.4)	
Minimum–maximum	0.9–17.4	0.9–17.4	2.9–6.8	
Mean SUV_{max} T/S				0.92
Mean (SD)	2.1 (1.2)	2.1 (1.3)	2.2 (0.9)	
Minimum–maximum	0.1–6.1	0.1–6.1	1.5–3.9	

*P value.

†Measured in cubic centimeters.

DTTV SUV_{mean} liver = SUV_{mean} in segmented volume obtained with liver as threshold; DTTV SUV_{mean} spleen = SUV_{mean} in segmented volume obtained with spleen as threshold; DTTV liver = DTTV obtained with liver as threshold; DTTV spleen = DTTV obtained with spleen as threshold; DTTV SUV_{mean} liver = DTTV SUV_{mean} obtained with liver as threshold; DTTV SUV_{mean} spleen = DTTV SUV_{mean} obtained with spleen as threshold; CoV = coefficient of variation.

Wilcoxon rank sum test P values are shown.

TABLE 3
iPET Reference Parameters, Lesion-Based Parameters, DTTV Parameters, and First-Order Heterogeneity Measures, Part 2

iPET	All patients (n = 36)	Responders (n = 30)	Nonresponders (n = 6)	P*
DTTV				
DTTV liver†				0.66
Mean (SD)	332.7 (424.6)	343.9 (438.8)	276.9 (375.1)	
Minimum–maximum	6–1,897.1	6–1,897.1	11.6–979.8	
DTTV spleen†				0.85
Mean (SD)	158.7 (256.3)	163 (270.1)	137.1 (189.9)	
Minimum–maximum	0–1,182.8	0–1,182.80	7.2–452.9	
DTTV SUV_{max}				0.11
Mean (SD)	58.8 (37.2)	63 (39.3)	38.1 (11.1)	
Minimum–maximum	16.9–197.5	16.9–197.5	25.8–55.1	
DTTV SUV_{mean} liver				0.024
Mean (SD)	16.9 (8.7)	18.1 (9.1)	11.2 (3.3)	
Minimum–maximum	5.7–50.7	5.7–50.7	6.3–16.6	
DTTV SUV_{mean} spleen				0.071
Mean (SD)	25.1 (12.6)	26.6 (13)	17.5 (7.9)	
Minimum–maximum	0–50.7	0–50.7	8–31.5	
Heterogeneity				
CoV				0.47
Mean (SD)	0.6 (0.2)	0.6 (0.2)	0.6 (0.1)	
Minimum–maximum	0.3–0.9	0.3–0.9	0.5–0.7	
Skewness				0.95
Mean (SD)	1.4 (0.8)	1.4 (0.8)	1.4 (0.8)	
Minimum–maximum	0.2–3.3	0.2–3.3	0.6–2.5	
Kurtosis				0.82
Mean (SD)	6.1 (4.1)	6.1 (4)	6.3 (5)	
Minimum–maximum	1.8–18.3	1.8–18.3	2.6–14.3	

*P value.

†Measured in cubic centimeters.

DTTV SUV_{mean} liver = SUV_{mean} in segmented volume obtained with liver as threshold; DTTV SUV_{mean} spleen = SUV_{mean} in segmented volume obtained with spleen as threshold; DTTV liver = DTTV obtained with liver as threshold; DTTV spleen = DTTV obtained with spleen as threshold; DTTV SUV_{mean} liver = DTTV SUV_{mean} obtained with liver as threshold; DTTV SUV_{mean} spleen = DTTV SUV_{mean} obtained with spleen as threshold; CoV = coefficient of variation.

Wilcoxon rank sum test P values are shown.

volume of interest and spreading of the expected gaussian curve, respectively. We have shown an inverse relationship between the baseline measurement of kurtosis and the response to PRRT. Both measured parameters correlate inversely with PFS (HRs, 0.54 and 0.9, respectively). These findings are in line with those of previous studies showing the predictive value of the subjective assessment of tumor heterogeneity and the response to PRRT (*29–31*). Graf et al. recently reported that the visual assessment of SSTR heterogeneity had both predictive value and prognostic value in progressive grade 1 or grade 2 NET patients undergoing PRRT, exceeding the prognostic value of the Ki-67 index (*31*).

There are several limitations of the present study. First, we included patients with multiple different NET sites, as the study was designed to enable broad access to PRRT for patients with metastatic NETs. However, patient selection criteria, including the Ki-67 index and SSTR type 2 expression on PET, were standardized. Second, iPET was optional and was performed only for a subset of patients. However, iPET parameters added little to patient outcomes and were not predictive of PFS. Third, DTTV and quantitative heterogeneity parameters required the use of segmentation tools, some of which are time-consuming and may not be practical for routine clinical use. However, we have shown that manual SUV_{max} measurements of target lesion can be used. Furthermore, a previous publication suggested that the subjective evaluation of heterogeneity has prognostic value, and some of our objective measures of tumor heterogeneity confirm this observation (*31*). Fourth, there was an overlap between responders and nonresponders for all of the predictive parameters, including parameters after cycle 1 of PRRT, limiting their clinical utility in isolation for guiding patient management.

TABLE 4
Univariable (UVA) and Multivariable (MVA) Analyses of Lesion-Based, Tumor Volume–Based, and Heterogeneity Parameters as Predictors of PFS

	UVA		MVA	
bPET covariate	HR (95% CI)	*P*	HR (95% CI)	*P*
Lesion based				
Mean SUV_{max}	0.98 (0.97–1)	0.023	0.98 (0.96–1)	0.019
SUV_{max} T/L	0.92 (0.85–0.99)	0.028	0.89 (0.8–0.98)	0.018
SUV_{max} T/S	0.86 (0.75–1)	0.047	0.83 (0.69–0.99)	0.041
Tumor volume				
DTTV SUV_{mean} liver	0.92 (0.87–0.98)	0.0053	0.9 (0.83–0.97)	0.0052
Heterogeneity				
Skewness	1.49 (1.07–2.07)	0.017	1.48 (1–2.18)	0.048

DTTV SUV_{mean} liver = SUV_{mean} from tumor volume obtained with liver or spleen as threshold.
Cox proportional hazards model *P* values are shown.

CONCLUSION

The degree of SSTR type 2 expression and tumor heterogeneity, as represented by several metrics in our analysis, are predictive of the therapy response or PFS. Changes in these parameters after cycle 1 of PRRT did not correlate with clinical outcomes. A model or scoring system integrating combinations of the predictive parameters identified with other clinical prognostic factors should be developed to predict the therapy response and patient outcomes more reliably.

DISCLOSURE

Funding was provided by the Ontario Health-Cancer Care Ontario Neuroendocrine Tumor Consortium to run the trial at the local sites as well as for central trial coordination. Funding was also provided by the Princess Margaret Hospital Foundation to support central trial coordination. In addition, funding was provided by the Susan Leslie Clinic for Neuroendocrine Tumors, Odette Cancer Centre, to support the implementation of the trial at Odette Cancer Center. No other potential conflict of interest relevant to this article was reported.

KEY POINTS

QUESTION: Are there quantitative ^{68}Ga-DOTATATE parameters at bPET or iPET after 1 cycle of PRRT that are predictive of the response to therapy, PFS, or both?

PERTINENT FINDINGS: Higher SUV_{max} in marker tumor sites and SUV_{mean} of segmented DTTVs obtained with the liver as a threshold at bPET and iPET correlated with the therapy response, and the baseline parameters were predictive of PFS. Skewness, a first-order feature of tumor heterogeneity, was also associated with PFS, and changes observed at iPET did not correlate with outcomes.

IMPLICATIONS FOR PATIENT CARE: Although certain quantitative ^{68}Ga-DOTATATE PET parameters are predictive of a response to PRRT and PFS, the overlap of these parameters in responders and nonresponders limits their clinical utility in isolation for guiding patient management.

REFERENCES

1. Dasari A, Shen C, Halperin D, et al. Trends in the incidence, prevalence, and survival outcomes in patients with neuroendocrine tumors in the United States. *JAMA Oncol.* 2017;3:1335–1342.
2. National Comprehensive Cancer Network. NCCN Clinical Practice Guidelines in Oncology: Neuroendocrine Tumors Version 1.2013. https://www.nccn.org/professionals/physician_gls/pdf/neuroendocrine_blocks.pdf. Accessed September 17, 2021.
3. Hope TA, Bergsland EK, Bozkurt MF, et al. Appropriate use criteria for somatostatin receptor PET imaging in neuroendocrine tumors. *J Nucl Med.* 2018;59:66–74.
4. Bodei L, Kidd M, Modlin IM, et al. Measurement of circulating transcripts and gene cluster analysis predicts and defines therapeutic efficacy of peptide receptor radionuclide therapy (PRRT) in neuroendocrine tumors. *Eur J Nucl Med Mol Imaging.* 2016;43:839–851.
5. Kwekkeboom DJ, Teunissen JJ, Bakker WH, et al. Radiolabeled somatostatin analog [^{177}Lu-DOTA0, Tyr3]octreotate in patients with endocrine gastroenteropancreatic tumors. *J Clin Oncol.* 2005;23:2754–2762.
6. Kwekkeboom DJ, de Herder WW, Kam BL, et al. Treatment with the radiolabeled somatostatin analog [^{177}Lu-DOTA0, Tyr3]octreotate: toxicity, efficacy, and survival. *J Clin Oncol.* 2008;26:2124–2130.
7. Kwekkeboom DJ, Kam BL, van Essen M, et al. Somatostatin-receptor-based imaging and therapy of gastroenteropancreatic neuroendocrine tumors. *Endocr Relat Cancer.* 2010;17:R53–R73.
8. Imhof A, Brunner P, Marincek N, et al. Response, survival, and long-term toxicity after therapy with the radiolabeled somatostatin analogue [^{90}Y-DOTA]-TOC in metastasized neuroendocrine cancers. *J Clin Oncol.* 2011;29:2416–2423.
9. Baum RP, Kulkarni HR, Singh A, et al. Results and adverse events of personalized peptide receptor radionuclide therapy with ^{90}Yttrium and ^{177}Lutetium in 1048 patients with neuroendocrine neoplasms. *Oncotarget.* 2018;9:16932–16950.
10. Hörsch D, Ezziddin S, Haug A, et al. Effectiveness and side-effects of peptide receptor radionuclide therapy for neuroendocrine neoplasms in Germany: a multi-institutional registry study with prospective follow-up. *Eur J Cancer.* 2016;58:41–51.
11. Strosberg J, El-Haddad G, Wolin E, et al. Phase 3 trial of ^{177}Lu-Dotatate for midgut neuroendocrine tumors. *N Engl J Med.* 2017;376:125–135.
12. Krenning EP, Valkema R, Kooij PP, et al. Scintigraphy and radionuclide therapy with [indium-111-labelled-diethyl triamine penta-acetic acid-D-Phe1]-octreotide. *Ital J Gastroenterol Hepatol.* 1999;31(suppl 2):S219–S223.
13. Hope TA, Calais J, Zhang L, Dieckmann W, Millo C. ^{111}In-pentetreotide scintigraphy versus ^{68}Ga-DOTATATE PET: impact on Krenning scores and effect of tumor burden. *J Nucl Med.* 2019;60:1266–1269.
14. Wahl RL, Jacene H, Kasamon Y, Lodge MA. From RECIST to PERCIST: evolving considerations for PET response criteria in solid tumors. *J Nucl Med.* 2009;50(suppl 1):122S–150S.
15. Eisenhauer EA, Therasse P, Bogaerts J, et al. New response evaluation criteria in solid tumours: revised RECIST guideline (version 1.1). *Eur J Cancer.* 2009;45:228–247.

16. de Jong M, Breeman WA, Kwekkeboom DJ, Valkema R, Krenning EP. Tumor imaging and therapy using radiolabeled somatostatin analogues. *Acc Chem Res.* 2009;42:873–880.
17. Haug AR, Auernhammer CJ, Wängler B, et al. ^{68}Ga-DOTATATE PET/CT for the early prediction of response to somatostatin receptor–mediated radionuclide therapy in patients with well-differentiated neuroendocrine tumors. *J Nucl Med.* 2010; 51:1349–1356.
18. Miederer M, Seidl S, Buck A, et al. Correlation of immunohistopathological expression of somatostatin receptor 2 with standardised uptake values in ^{68}Ga-DOTATOC PET/CT. *Eur J Nucl Med Mol Imaging.* 2009;36:48–52.
19. Campana D, Ambrosini V, Pezzilli R, et al. Standardized uptake values of ^{68}Ga-DOTANOC PET: a promising prognostic tool in neuroendocrine tumors. *J Nucl Med.* 2010;51:353–359.
20. Kratochwil C, Stefanova M, Mavriopoulou E, et al. SUV of [^{68}Ga]DOTATOC-PET/CT predicts response probability of PRRT in neuroendocrine tumors. *Mol Imaging Biol.* 2015;17:313–318.
21. Reynaert H, Rombouts K, Vandermonde A, et al. Expression of somatostatin receptors in normal and cirrhotic human liver and in hepatocellular carcinoma. *Gut.* 2004;53:1180–1189.
22. Sarikaya I, Sarikaya A, Alnafisi N, Alenezi S. Significance of splenic uptake on somatostatin receptor imaging studies. *Nucl Med Rev Cent East Eur.* 2018; 21:66–70.
23. Dalm VA, van Hagen PM, van Koetsveld PM, et al. Expression of somatostatin, cortistatin, and somatostatin receptors in human monocytes, macrophages, and dendritic cells. *Am J Physiol Endocrinol Metab.* 2003;285:E344–E353.
24. Armani C, Catalani E, Balbarini A, Bagnoli P, Cervia D. Expression, pharmacology, and functional role of somatostatin receptor subtypes 1 and 2 in human macrophages. *J Leukoc Biol.* 2007;81:845–855.
25. Li X, Bauer W, Kreissl MC, et al. Specific somatostatin receptor II expression in arterial plaque: ^{68}Ga-DOTATATE autoradiographic, immunohistochemical and flow cytometric studies in apoE-deficient mice. *Atherosclerosis.* 2013;230:33–39.
26. Lapa C, Reiter T, Li X, et al. Imaging of myocardial inflammation with somatostatin receptor based PET/CT: a comparison to cardiac MRI. *Int J Cardiol.* 2015; 194:44–49.
27. Lin E, Chen, T, Little A, et al. Safety and outcomes of ^{177} Lu-DOTATATE for neuroendocrine tumours: experience in New South Wales, Australia. *Intern Med J.* 2019;49:1268–1277.
28. Marusyk A, Polyak K. Tumor heterogeneity: causes and consequences. *Biochim Biophys Acta.* 2010;1805:105–117.
29. Werner RA, Ilhan H, Lehner S, et al. Pre-therapy somatostatin receptor-based heterogeneity predicts overall survival in pancreatic neuroendocrine tumor patients undergoing peptide receptor radionuclide therapy. *Mol Imaging Biol.* 2019;21: 582–590.
30. Wetz C, Apostolova I, Steffen IG, et al. Predictive value of asphericity in pretherapeutic [^{111}In]DTPA-octreotide SPECT/CT for response to peptide receptor radionuclide therapy with [^{177}Lu]DOTATATE. *Mol Imaging Biol.* 2017; 19:437–445.
31. Graf J, Pape U, Jann H, et al. Prognostic significance of somatostatin receptor heterogeneity in progressive neuroendocrine tumor treated with Lu-177 DOTATOC or Lu-177 DOTATATE. *Eur J Nucl Med Mol Imaging.* 2020;47:881–894.

Improved Primary Staging of Marginal-Zone Lymphoma by Addition of CXCR4-Directed PET/CT

Johannes Duell[1,2], Franziska Krummenast[1,2], Andreas Schirbel[2,3], Philipp Klassen[3], Samuel Samnick[2,3], Hilka Rauert-Wunderlich[2,4], Leo Rasche[1,2], Andreas K. Buck[2,3], Hans-Jürgen Wester[5], Andreas Rosenwald[2,4], Herrmann Einsele[1,2], Max S. Topp[1,2], Constantin Lapa[2,3,6], and Malte Kircher[2,3,6]

[1]Department of Internal Medicine II, University Hospital Würzburg, Würzburg, Germany; [2]Comprehensive Cancer Center Mainfranken, Würzburg, Germany; [3]Department of Nuclear Medicine, University Hospital Würzburg, Würzburg, Germany; [4]Institute of Pathology, University of Würzburg, Würzburg, Germany; [5]Pharmaceutical Radiochemistry, Technische Universität München, München, Germany; and [6]Nuclear Medicine, Medical Faculty, University of Augsburg, Augsburg, Germany

PET/CT with ^{18}F-FDG is an integral component in the primary staging of most lymphomas. However, its utility is limited in marginal-zone lymphoma (MZL) because of inconsistent ^{18}F-FDG avidity. One diagnostic alternative could be the targeting of C-X-C motif chemokine receptor 4 (CXCR4), shown to be expressed by MZL cells. This study investigated the value of adding CXCR4-directed ^{68}Ga-pentixafor PET/CT to conventional staging. **Methods:** Twenty-two newly diagnosed MZL patients were staged conventionally and with CXCR4 PET/CT. Lesions identified exclusively by CXCR4 PET/CT were biopsied as the standard of reference and compared with imaging results. The impact of CXCR4-directed imaging on staging results and treatment protocol was assessed. **Results:** CXCR4 PET/CT correctly identified all patients with viable MZL and was superior to conventional staging ($P < 0.001$). CXCR4-directed imaging results were validated by confirmation of MZL in 16 of 18 PET-guided biopsy samples. Inclusion of CXCR4 PET/CT in primary staging significantly impacted staging results in almost half of patients and treatment protocols in a third (upstaging, $n = 7$; downstaging, $n = 3$; treatment change, $n = 8$; $P < 0.03$). **Conclusion:** CXCR4 PET/CT is a suitable tool in primary staging of MZL and holds the potential to improve existing diagnostic algorithms.

Key Words: molecular imaging; primary diagnosis; CXCR4; PET; theranostics

J Nucl Med 2021; 62:1415–1421
DOI: 10.2967/jnumed.120.257279

Marginal-zone lymphomas (MZLs) originate from malignantly transformed lymphocytes of the B-cell lineage and belong to the family of non-Hodgkin lymphomas. Three subtypes are differentiated according to their tissue of origin. The most common subtype is extranodal MZL (EMZL), which derives from mucosa-associated lymphoid tissue and constitutes up to 70% of MZL cases. The splenic MZL (SMZL) and nodal MZL (NMZL) subtypes are less common and affect primarily spleen or lymph nodes but can also be found in peripheral blood or bone marrow (BM) (*1*).

The therapeutic approach depends on the results of staging according to the modified Ann Arbor system and includes BM biopsy, gastrointestinal endoscopy, and CT. Although limited disease (stages I and II) can often be irradiated with curative intent, either chemotherapy (with or without rituximab) is initiated or a watch-and-wait strategy is chosen in advanced stages. PET/CT with the radiolabeled glucose analog ^{18}F-FDG is well established and generally recommended as the imaging modality of choice for initial evaluation and response assessment in all ^{18}F-FDG–avid lymphomas (*2*). However, only 60%–85% of MZLs are ^{18}F-FDG–avid, and while slightly superior to conventional CT imaging, ^{18}F-FDG PET/CT tends to perform particularly poorly in EMZL (*3*, *4*).

C-X-C motif chemokine receptor 4 (CXCR4) is widely expressed throughout the human body and plays a crucial role in embryonic development, homeostasis of the adult hematopoietic system, and modulation of the immune system (*5*, *6*). In addition, CXCR4 and its cognate ligand CXCL12 have been shown to be of relevance in cancer growth and metastasis (*7*, *8*). CXCR4 not only is physiologically expressed on almost all lymphocytes but also is observed on T- and B-cell neoplasms, including MZL (*9*). The expression of human CXCR4 can be noninvasively visualized in vivo by PET/CT imaging using radiolabeled receptor ligands such as ^{68}Ga-pentixafor, which has already demonstrated applicability in imaging a variety of oncologic, hematooncologic, and inflammatory diseases (*10*–*16*). Furthermore, first proof-of-concept studies with ^{68}Ga-pentixafor PET (CXCR4 PET) have already demonstrated encouraging results in MZL patients (*17*, *18*).

In this analysis, we investigated the added value of including CXCR4 PET/CT in the primary staging algorithm for newly diagnosed, treatment-naïve MZL with respect to change of disease stage and impact on patient management. Conventional staging comprising BM biopsy, gastrointestinal endoscopy, and ^{18}F-FDG PET/CT served as the standard of reference. To validate the results of the new imaging approach, additional biopsies of exclusively CXCR4-positive ($CXCR4^+$) lesions were obtained and evaluated for the presence of MZL and CXCR4 expression.

MATERIALS AND METHODS

^{68}Ga-pentixafor was administered in compliance with §37 of the Declaration of Helsinki, the German Medicinal Products Act (AMG §13 2b), and the responsible regulatory body (Government of Upper Franconia; "Regierung von Oberfranken," Germany). All patients underwent imaging for clinical purposes and gave written informed consent to the diagnostic procedures. The local institutional review board (ethics committee

Received Sep. 20, 2020; revision accepted Jan. 27, 2021.
For correspondence or reprints, contact Constantin Lapa (constantin.lapa@uk-augsburg.de).
Published online February 12, 2021.

of the University of Würzburg, Germany) approved this retrospective study (reference number 20201123 01).

Patients and Staging

Between May 2017 and January 2019, 22 consecutive patients (15 female, 7 male; mean age, 66 ± 9 y) were referred to our institution for further diagnostic work-up of newly diagnosed MZL of any subtype (EMZL, $n = 15$; NMZL, $n = 6$; SMZL, $n = 1$). None of the patients had received treatment before imaging. Staging was done as recommended by the World Health Organization and the European Society for Medical Oncology using the modified Ann Arbor system (including ^{18}F-FDG PET/CT, which is a local standard at our institution) (*19*, *20*), further complemented by CXCR4 PET/CT imaging within a median of 4 d of each other (range, 1–7 d). In addition to biopsies obtained during conventional staging ($n = 85$), tissue samples were taken from exclusively CXCR4$^+$ lesions ($n = 18$) if lymphoma detection implied a modification of the treatment protocol. Patient characteristics and information about CXCR4-guided biopsies are shown in Table 1.

In 12 cases, follow-up imaging was available, depending on the respective tracer avidity at primary staging with either one or both tracers (^{18}F-FDG, $n = 5$; CXCR4, $n = 11$).

PET/CT Imaging

^{68}Ga-pentixafor and ^{18}F-FDG were synthesized in-house as previously described using a fully good-manufacturing-practice–compliant automated synthesizer (GRP; Scintomics) or a 16-MeV cyclotron (GE PETtrace 6; GE Healthcare), respectively (*21*). CXCR4-directed and ^{18}F-FDG PET/CT was performed on a dedicated PET/CT scanner (Biograph mCT 64; Siemens Medical Solutions)—in the case of ^{18}F-FDG, after a 6-h fasting period to ensure serum glucose levels below 130 mg/dL, and in case of ^{68}Ga-pentixafor, without any special patient preparation. The mean injected activity was 117 ± 27 MBq (range, 78–186 MBq) for ^{68}Ga-pentixafor and 298 ± 16 MBq (range, 263–334 MBq) for ^{18}F-FDG. There were no adverse or clinically detectable pharmacologic effects in any of the 22 subjects. No significant changes in vital signs or the results of laboratory studies or electrocardiograms were observed. Whole-body (top of the skull to knees) PET scans were performed 1 h after administration of the radiopharmaceutical. In CXCR4 PET, corresponding low-dose CT scans for attenuation correction and anatomic correlation were subsequently acquired (35 mAs, 120 keV, a 512 × 512 matrix, 5-mm slice thickness, increment of 30 mm/s, rotation time of 0.5 s, and pitch index of 0.8). In the case of ^{18}F-FDG PET a monophasic, contrast-enhanced CT scan (CARE Dose 4D [Siemens], 160 mAs,

TABLE 1
Patient Characteristics and Locations of CXCR4-Guided Biopsies

Patient no.	Sex	Age (y)	MZL subtype	Location/source of primary histology	Location of CXCR4-guided biopsy	Confirmation of MZL?
1	M	51	EMZL/MALT	Lung	NA	NA
2	M	50	EMZL/MALT	Lung, multifocal	Lung	Yes
3	F	70	NMZL	LN, axilla	LN, axilla	Yes
4	F	56	EMZL/MALT	Salivary gland, sublingual	Salivary gland, lower lip	Yes
5	F	76	EMZL/MALT	Orbita (no confirmation of MZL)	Orbita	Yes
6	F	69	NMZL	LN, inguinal	NA	NA
7	F	79	EMZL/MALT	Cutaneous	Subcutaneous, thigh	Yes
8	F	63	EMZL/MALT	Lacrimal gland	Conjunctiva plus LN, axilla	No (conjunctiva), yes (LN)
9	F	70	NMZL	LN, cervical (right)	LN, cervical (left)	Yes
10	F	66	NMZL	LN, cervical	LN, cervical	Yes
11	F	62	EMZL/MALT	LN, cervical (negative)	Stomach	Yes
12	M	68	EMZL/MALT	NA	Ileum	Yes
13	M	57	EMZL/MALT	LN, cervical	LN, axilla	No (not enough material)
14	M	80	EMZL/MALT	Orbita (right)	Orbita (left)	Yes
15	F	57	EMZL/MALT	Bulk, mesenterial	LN, cervical	Yes
16	F	63	NMZL	LN, axilla	LN, axilla plus BM biopsy	Yes (both)
17	F	72	SMZL	Splenectomy	LN, axilla	Yes
18	F	71	EMZL/MALT	NA	Bone, tibia	Yes
19	M	69	EMZL/MALT	Stomach	Tonsil, tonsils	Yes (all 3)
20	F	52	EMZL/MALT	LN, cervical (right)	Parotid gland	Yes
21	M	72	NMZL	LN, retroperitoneal	Soft-tissue formation, perirenal	Yes
22	F	59	EMZL/MALT	NA	Parotid gland	Yes

MALT = mucosa-associated lymphoid tissue; NA = not applicable; LN = lymph node.

120 kV, 512 × 512 matrix, 5-mm slice thickness, 64 × 0.6 mm slice collimation, pitch index of 1.4) was acquired. PET images were reconstructed using standard parameters (HD·PET [Siemens], 3 iterations, 24 subsets, 2-mm gaussian filtering, 5-mm axial resolution, 4 × 4 mm in-plane resolution), with corrections for attenuation (CT-based), dead time, random events, and scatter.

Image Analysis

PET/CT scans were separately analyzed by 2 experienced investigators masked to the respective other PET scan as well as all other staging results. ^{18}F-FDG uptake was rated according to the Lugano classification (*22*). CXCR4$^+$ lesions were visually determined as focally increased tracer retention compared with surrounding normal tissue or contralateral structures. Images were first inspected visually. Then, the SUV_{max} of all potential lesions was derived by placing volumes of interest at least 10 mm in diameter around them. To normalize uptake and account for background activity, mean blood-pool activity was measured by placing a 10-mm volume of interest in the right atrium. Then, a target-to-background ratio was calculated by dividing SUV_{max} (lesion) by SUV_{mean} (blood pool). Data were analyzed on both a per-patient and a per-lesion basis. For lesion analysis on a per-patient basis, subjects were categorized into 1 of 4 groups: no detectable focal lesion (FL), 1–5 FLs, 6–10 FLs, or more than 10 FLs. Furthermore, the lesion with the highest tracer uptake (hottest lesion) in the respective PET scans was used as a comparison parameter in the per-patient analysis.

Immunohistochemistry

In total, 103 biopsies were taken and examined for the presence of MZL and for CXCR4 expression (gastrointestinal tract, $n = 48$; bone and BM, $n = 24$; lymph nodes and tonsils, $n = 19$; salivary glands, $n = 3$; other/soft tissues, $n = 9$). Of these biopsies, 17.5% (18/103) were taken after the discovery of new lesions in CXCR4 PET, and the rest (85/103) were taken during conventional staging.

To confirm specific binding of ^{68}Ga-pentixafor, paraffin sections (1 μm) derived from PET-guided biopsies were stained using an anti-CXCR4 rabbit polyclonal antibody (ab2074; Abcam) and detected and visualized using the Dako EnVision-horseradish peroxidase rabbit labeled polymer/3,3′-diaminobenzidine. Counterstaining was performed with hematoxylin. CXCR4 positivity of the vascular epithelium served as an internal positive control, and adrenocortical tissue as an external positive control. The intensity of CXCR4 expression was visually rated using a 4-point scoring scale (0 = absent, 1 = weak, 2 = moderate, 3 = intense). To determine the proliferative activity of tumor cells, the Ki-67 labeling index after immunostaining for MIB-1 (monoclonal, clone Ki-67, 1:50; Dako) was calculated by determining the number of positive nuclei under 100 lymphoma cells per high-power field (×400) in a total of 10 high-power fields per sample. The SUV_{mean}/SUV_{max} of the respective biopsied lesion was correlated to the intensity of receptor expression and proliferation activity.

Statistical Analysis

All statistical testing was performed in SPSS Statistics, version 25 (IBM Corp.). The Kolmogorov–Smirnov test was used to verify a normal distribution of the data. Continuous parametric variables are expressed as mean ± SD. For group statistics, comparisons between MZL subtypes and gastrointestinal/BM involvement were performed using 1-way ANOVA. The significance of the observed differences between groups was confirmed with a Games–Howell post hoc test. Unpaired *t* tests were used to compare uptake ratios of both tracers in corresponding lesions. Pearson correlation coefficients (*r*) were calculated to assess the association between the uptake ratios of both tracers. *P* values of 0.05 or below were considered statistically significant.

RESULTS

Considering all available information, including follow-up, 20 patients had viable MZL manifestations at the time of imaging (EMZL, $n = 14$; NMZL, $n = 5$; SMZL, $n = 1$ [true positive, TP]), with 13.6% (3/22) of patients found to have BM infiltration and 18.2% (4/22) gastrointestinal involvement. In 2 cases with limited disease stages, initial tissue sampling led to complete removal of all suspected lesions (EMZL, $n = 1$; NMZL, $n = 1$; patients 1 and 6), and both patients remained in complete remission without treatment during follow-up (true-negative). The staging results and their impact on the treatment protocol are shown in Table 2.

Conventional Staging

Conventional staging based on ^{18}F-FDG PET/CT, endoscopy, and BM biopsy correctly identified 80.0% (16/20) of MZL patients (EMZL, 11/14; NMZL, 4/5; SMZL, 1/1); in the remaining 4 patients, no lymphoma manifestations could be delineated (EMZL, 3/14; NMZL, 1/5). One of the 2 true-negative patients was correctly rated as negative, the other one as false-positive. All patients with gastrointestinal involvement (4/4) were identified, as well as 66.7% (2/3) of subjects with BM infiltration. No lesions were found in 22.7% of patients ($n = 5$), 1–5 lesions in 40.9% ($n = 9$), 6–10 lesions in 4.5% ($n = 1$), and more than 10 lesions in 31.8% ($n = 7$). The mean SUV_{max} (^{18}F-FDG) of the hottest lesion was 10.7 ± 9.9 (median, 7.2; range, 2.3–39.6), whereas the mean target-to-background ratio was 4.4 ± 5.8 (median, 2.3; range, 0.8–25.6). Six subjects were classified as having limited disease (27.3%; Ann Arbor stage I, $n = 6$; stage II, $n = 0$) and 11 as having advanced disease (50.0%; Ann Arbor stage III, $n = 3$; stage IV, $n = 8$).

CXCR4 PET/CT

CXCR4 PET/CT correctly detected all TP (20/20) and true-negative (2/2) patients, as well as 75% (3/4) of patients with gastrointestinal involvement and all (3/3) subjects with BM infiltration. No lesions were found in 9.1% ($n = 2$) of patients, 1–5 FLs in 31.8% ($n = 7$), 6–10 FLs in 13.6% ($n = 3$), and more than 10 FLs in 45.5% ($n = 10$). The mean SUV_{max} (CXCR4) of the hottest lesion was 13.0 ± 6.4 (median, 11.7; range, 3.7–27.4), whereas the mean target-to-background ratio was 4.8 ± 2.5 (median, 4.0; range, 2.1–10.7). On the basis of CXCR4-directed imaging, 36.4% of patients were classified as having limited-stage disease ($n = 8$; Ann Arbor stage I, $n = 3$; stage II, $n = 5$), and 54.5% of patients were classified as having an advanced disease stage ($n = 12$; Ann Arbor stage III, $n = 2$; stage IV, $n = 10$).

Biopsy Results

Overall, 31.1% of tissue samples confirmed the presence of MZL (32/103; gastrointestinal tract, $n = 7$; bone/BM, $n = 5$; lymph nodes/tonsils, $n = 11$; salivary glands, $n = 3$; other/soft tissue, $n = 6$).

Of the biopsies taken during conventional staging, 18.8% (16/85) confirmed MZL, with evidence of gastrointestinal involvement in 10.9% (5/46) of specimens (patients 4, 11, 12 and 19) and of BM infiltration in 9.1% (2/22) (patients 16 and 17).

MZL was confirmed in 88.9% (16/18) of samples taken from exclusively CXCR4$^+$ lesions. Details of the biopsy locations and results are shown in Table 1 (also, maximum-intensity-projection images of all PET scans with biopsy locations are provided as Supplemental Figs. 1–22; supplemental materials are available at http://jnm.snmjournals.org).

TABLE 2
Staging Results and Impact on Patient Management

	Rated positive for MZL		BM/GI involvement		Ann Arbor classification		Changes due to CXCR4 PET/CT	
Patient no.	Conv.	CXCR4	Conv.	CXCR4	Conv.	CXCR4	Staging	Treatment protocol
1	Yes*	No			I	—	Down	Deescalation to watch and wait (RTx)
2	Yes	Yes		BM	IV	IV		
3	Yes	Yes			IV	IV		
4	Yes	Yes	GI		I	IV	Up	
5	No	Yes			—	I	Up	Escalation to RTx (none)
6	No	No			—	—		
7	Yes	Yes			IV	IV		Escalation to CTx (RTx); at f/u: $CXCR4^+$ lesion → RTx
8	Yes	Yes			I	IV	Up	Escalation to RTx of 3 lesions (RTx 1 lesion)
9	No	Yes			—	II	Up	Escalation to RTx (none)
10	Yes	Yes			III	III		
11	Yes	Yes	GI	GI, BM*	I	IV	Up	Escalation of RTx (smaller radiation field)
12	Yes	Yes	GI	GI	I	I		
13	Yes	Yes			III	II	Down	
14	Yes	Yes			IV	II	Down	
15	Yes	Yes	BM*	BM*	IV	IV		
16	Yes	Yes	BM	BM	IV	IV		
17	Yes	Yes	BM	BM	IV	IV		
18	Yes	Yes			I	I		
19	Yes	Yes	GI	GI	IV	IV		Deescalation to watch and wait (RTx)
20	No	Yes			—	II	Up	escalation to RTx (none)
21	Yes	Yes			III	III		
22	No	Yes	GI*		—	II	Up	

*False-positive.
GI = gastrointestinal; Conv. = conventional staging; RTx = radiation; CTx = chemotherapy; f/u = follow-up.
Parentheses in last column indicate initially planned therapy.

Comparison of Conventional Staging and CXCR4 PET

The difference in detection of MZL between CXCR4 PET/CT and conventional staging was significant, with correct detection of all viable MZL and true-negative cases by CXCR4 PET/CT, whereas conventional staging identified only 16 of 20 TP and 1 of 2 true-negative subjects (22/22 vs. 17/22; $P < 0.001$).

Regarding gastrointestinal involvement, CXCR4 PET/CT was not inferior to regular staging (4/4 vs. 3/4; not statistically significant). Similarly, there was no significant difference in detection of BM infiltration (3/3 vs. 2/3; not statistically significant). Of note, in 1 case BM infiltration was identified only because of CXCR4-guided biopsy, whereas the random iliac crest biopsy taken during conventional staging was false-negative. Examples of exclusively $CXCR4^+$ lesions in EMZL and gastric MZL are given in Figures 1 and 2.

No significant difference between the 2 tracers was found when comparing the respective hottest lesions (^{18}F-FDG, 10.7 ± 9.9, vs. ^{68}Ga-pentixafor, 13.0 ± 6.4; $P = 0.36$). Similarly, target-to-background ratios for ^{18}F-FDG and CXCR4 PET did not show significant differences (4.4 ± 5.8 vs. 4.8 ± 2.5; $P = 0.90$).

Results from CXCR4 PET/CT led to upstaging or downstaging and a change in treatment in a significant number of patients (total, 10/22; upstaging, $n = 7$; downstaging, $n = 3$; treatment change, $n = 8$; $P < 0.03$). The effects on patient management included both escalation (27.3%, $n = 6$) and deescalation (9.1%, $n = 2$) of therapy (Table 2).

Immunohistochemistry

Staining for CXCR4 in confirmed specimens of MZL showed a highly variable receptor expression on the surface of MZL cells, with receptor expression intensities ranging from 0 to 2. Various of the confirmed MZL lesions identified by CXCR4 PET/CT showed relatively low receptor expression on the cell surface, with a dotlike pattern. An intense staining of the residual germinal center B cells occurred particularly in NMZL manifestations (Fig. 3). The Ki-67 index ranged from 5% to 40% (mean, 14.4 ± 7.7) and correlated positively with uptake of both tracers (SUV_{mean} and SUV_{max}: ^{68}Ga-pentixafor, $r = 0.56$, $P < 0.05$; ^{18}F-FDG, $r = 0.71$, $P < 0.01$). The intensity of immunohistopathologic staining did not

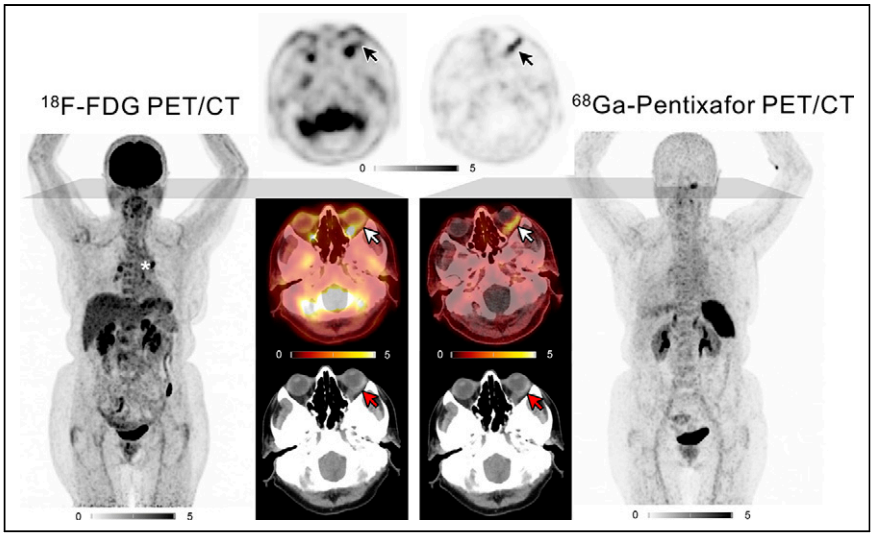

FIGURE 1. Maximum-intensity-projection ^{18}F-FDG and ^{68}Ga-pentixafor PET scans of patient 5, with EMZL. At center are shown axial sections of lymphoma manifestation in left orbita with discrepant tracer uptake (^{18}F-FDG–negative, CXCR4$^+$), as indicated by white arrows (PET/CT), black arrows (PET), and red arrows (CT). Star indicates intense focal uptake of 2 hilar lymph nodes; biopsy results revealed sarcoidosis, not MZL.

significantly relate to CXCR4-directed PET uptake (SUV_{mean}, $r = -0.20$; SUV_{max}, $r = -0.21$, not statistically significant).

DISCUSSION

This pilot study in a homogeneous cohort of patients with newly diagnosed, treatment-naïve lymphoma clearly demonstrated the capabilities of CXCR4 PET/CT for primary staging of MZL, with all patients with viable MZL being correctly identified. Whereas a recent study from Austria using CXCR4-directed PET/MRI also reported on the general feasibility of CXCR4 PET for visualizing mucosa-associated lymphoid tissue lymphoma (*18*), this was—to our knowledge—the first study to provide a systematic comparison to conventional staging, including BM biopsy, endoscopy, and ^{18}F-FDG PET/CT, and to assess the impact of CXCR4-directed imaging on patient management in all subjects.

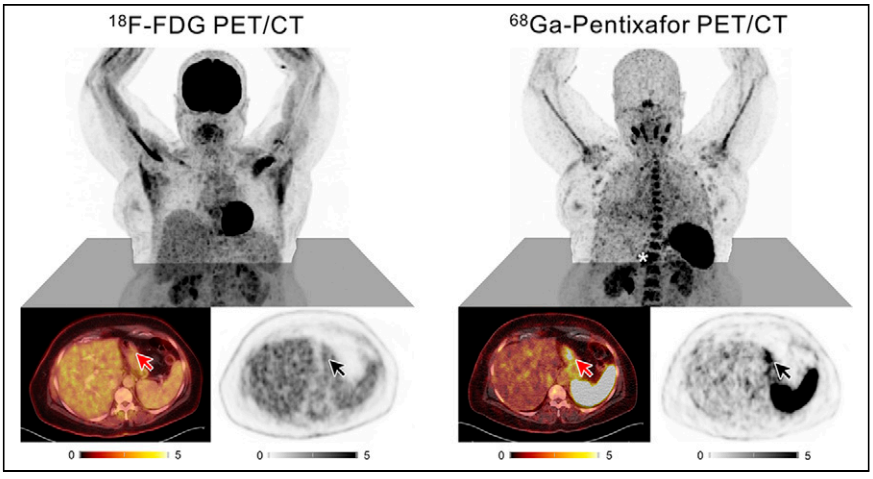

FIGURE 2. (Top) Maximum-intensity-projection ^{18}F-FDG and ^{68}Ga-pentixafor PET scans of patient 11, with gastric MZL. (Bottom) Axial sections of gastric lymphoma manifestations with discrepant tracer uptake (^{18}F-FDG–negative, CXCR4$^+$) as indicated by red arrows (PET/CT) and black arrows (PET). Star indicates gastric lymphoma in ^{68}Ga-pentixafor maximum-intensity-projection image.

Compared with conventional staging, CXCR4 PET/CT detected significantly more MZL manifestations, both on a per-patient and on a per-lesion basis ($P < 0.001$). It is noteworthy that lesions exclusively unveiled by the new imaging approach could be confirmed in locations easily missed in conventional PET or PET/CT imaging, such as subcutaneous or orbital masses. In addition, our data also indicate the noninferiority of CXCR4 PET/CT in the detection of gastrointestinal tract lesions and BM infiltration (as compared with endoscopy and BM biopsy, respectively)—sites that also pose a diagnostic challenge to imaging.

The results of imaging and biopsies are consistent with the existing literature showing robust CXCR4 expression by MZL cells in more than 90% of cases (*9*, *23*). Furthermore, prior studies have reported the relatively heterogeneous ^{18}F-FDG avidity of MZL, concordant with our data on many of the biopsy-proven, ^{18}F-FDG–negative lymphoma manifestations (*3*, *4*). Also noteworthy was a recent study on patients with lymphoplasmacytic lymphoma that reported findings similar to ours, showing superior lymphoma detection by CXCR4 PET/CT in comparison to ^{18}F-FDG PET/CT (*16*).

Thus, CXCR4-directed imaging might prove a suitable new imaging tool for comprehensive whole-body staging of MZL as well as other types of lymphoma that are not ^{18}F-FDG–avid, as it might enable a more accurate detection of lymphoma lesions and, consequently, better stage-adjusted treatment strategies.

With regard to patient management, one of the main findings of our study is that the improved detection rate of CXCR4 PET/CT had a significant impact on staging according to the modified Ann Arbor classification system, as information gained exclusively by CXCR4 PET/CT led to a reclassification in almost half of patients, with most subjects being upstaged. This in turn had a direct effect on patient management, as more than one third of patients (8/22, 36.4%) had their treatment protocol modified because of the new information; most often local treatment approaches were abandoned for the sake of systemic chemotherapy or watch-and-wait strategies due to the visualization of previously occult MZL manifestations. In an approach to provide a robust standard of reference for lesions with discrepant PET imaging results, biopsies were stringently obtained. Underlining the improved sensitivity of CXCR4-directed imaging, 88.9% (16/18) of the biopsies from CXCR4$^+$ lesions were true-positives, compared with only 18.8% (16/85) of the biopsies obtained during conventional staging being true-positive. Interestingly, very few false-positive lesions (2/18; 11.1%) were encountered—a fact that is remarkable considering the large number

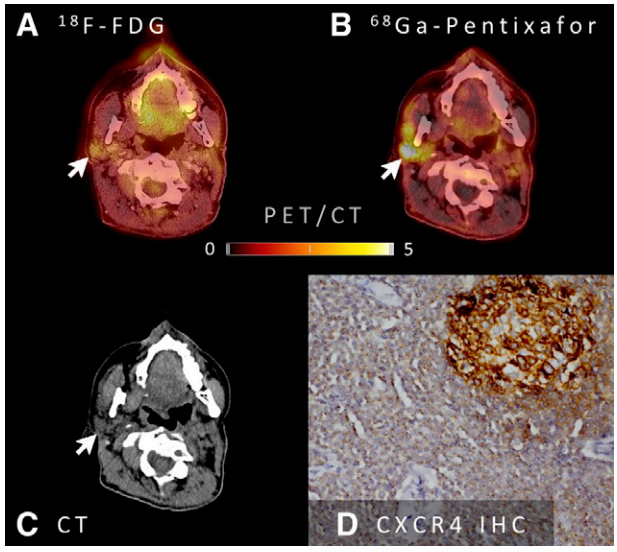

FIGURE 3. ^{18}F-FDG and CXCR4 PET/CT images (A and B), CT image (C), and immunohistochemistry (IHC) of biopsy material from MZL of right parotid gland (D) of patient 20. Arrows indicate discrepant tracer uptake (^{18}F-FDG–negative, CXCR4^{+}). IHC for CXCR4 shows strong staining in residual germinal center B cells and distinct, often dotlike, staining in neoplastic marginal-zone B-cell infiltrate.

of other cell types expressing CXCR4 on their cell surface, including inflammatory B and T cells, macrophages, and neutrophils (*6*). Therefore, it cannot be ruled out that at least part of the PET signal originates from additional, yet unknown, nonlymphoma cell types.

It is worth mentioning that the proliferation activity (as indicated by the Ki-67 index) of MZL lesions correlated positively with the intensity of the respective PET imaging signal. Although the association between tumor aggressiveness and ^{18}F-FDG uptake is well established, our findings underscore an additional potential prognostic value of CXCR4 PET in MZL and are in line with results of previous pathology studies (*9*).

The utility of CXCR4 PET/CT in restaging has not yet been demonstrated. Although the first data in a subject with EMZL of the orbital cavities (*17*) suggest that the new technique holds potential for noninvasive assessment of therapy response and patient follow-up (especially in cases with ambiguous findings in conventional imaging), the added value of CXCR4-directed PET imaging in this setting also needs to be investigated.

Given the physiologically high splenic tracer uptake and retention in CXCR4 PET/CT, SMZL is likely to pose a diagnostic challenge to this new imaging approach.

Our study had various limitations, including its retrospective nature and the small sample size, thus limiting statistical power. Furthermore, although histology could prove the presence of MZL and CXCR4 expression on cells in most biopsy specimens, receptor expression was relatively heterogeneous and did not perfectly correlate with PET imaging findings. However, histology results might be influenced by biopsy yields and by receptor kinetics and internalization, given that CXCR4 expression at the cell surface is dynamically regulated and that receptor internalization is induced by ligand binding. In contrast, strengths of our study include the stringent acquisition of histologic evidence that the PET signal originates from CXCR4^{+} MZL cells, as determined by immunohistochemical work-up of tissue samples obtained from PET-guided biopsies. In addition, all patients were newly diagnosed, were treatment-naïve, and underwent the full recommended diagnostic work-up (including ^{18}F-FDG PET/CT).

CONCLUSION

Our data show that primary staging of MZL using CXCR4 PET/CT is feasible and has a significant impact on staging results and treatment choice. Although the present data suggest that CXCR4 PET/CT has the potential to be the new imaging standard in MZL, various questions are still to be answered until its use can be unanimously recommended: Whether CXCR4 PET/CT will have an impact on progression-free-survival, overall survival, quality of life, or health-care costs has to be determined in larger, prospective studies.

DISCLOSURE

Hans-Jürgen Wester is the founder and shareholder of Scintomics, a company that entered into a joint venture with 1717 Life Science Ventures to establish PentixaPharm, the owner and distributor of the CXCR4-directed PET tracer pentixafor. No other potential conflict of interest relevant to this article was reported.

KEY POINTS

QUESTION: What impact does inclusion of CXCR4-directed PET/CT imaging into the primary staging algorithm of MZL have on staging results and treatment choice?

PERTINENT FINDINGS: This is the first study to provide a systematic comparison between conventional staging, including BM biopsy, endoscopy, and ^{18}F-FDG PET/CT, and CXCR4-directed imaging in MZL. CXCR4 PET/CT detected significantly more MZL manifestations and had a significant impact on Ann Arbor staging, with a reclassification in almost half of patients and, eventually, a change in patient management in more than one third of cases.

IMPLICATIONS FOR PATIENT CARE: Our data suggest that CXCR4 PET/CT has the potential to be the new imaging standard.

REFERENCES

1. Swerdlow S, Campo E, Harris N, et al., eds. *WHO Classification of Tumours*. 4th ed. World Health Organization; 2017:223–265.
2. Barrington SF, Kluge R. FDG PET for therapy monitoring in Hodgkin and non-Hodgkin lymphomas. *Eur J Nucl Med Mol Imaging*. 2017;44:97–110.
3. Hoffmann M, Kletter K, Becherer A, Jäger U, Chott A, Raderer M. ^{18}F-fluorodeoxyglucose positron emission tomography (^{18}F-FDG-PET) for staging and follow-up of marginal zone B-cell lymphoma. *Oncology*. 2003;64:336–340.
4. Treglia G, Zucca E, Sadeghi R, Cavalli F, Giovanella L, Ceriani L. Detection rate of fluorine-18-fluorodeoxyglucose positron emission tomography in patients with marginal zone lymphoma of MALT type: a meta-analysis. *Hematol Oncol*. 2015;33:113–124.
5. Griffith JW, Sokol CL, Luster AD. Chemokines and chemokine receptors: positioning cells for host defense and immunity. *Annu Rev Immunol*. 2014;32:659–702.
6. Hughes CE, Nibbs RJB. A guide to chemokines and their receptors. *FEBS J*. 2018;285:2944–2971.
7. Müller A, Homey B, Soto H, et al. Involvement of chemokine receptors in breast cancer metastasis. *Nature*. 2001;410:50–56.
8. Zlotnik A, Burkhardt AM, Homey B. Homeostatic chemokine receptors and organ-specific metastasis. *Nat Rev Immunol*. 2011;11:597–606.
9. Stollberg S, Kämmerer D, Neubauer E, et al. Differential somatostatin and CXCR4 chemokine receptor expression in MALT-type lymphoma of gastric and extragastric origin. *J Cancer Res Clin Oncol*. 2016;142:2239–2247.

10. Wester HJ, Keller U, Schottelius M, et al. Disclosing the CXCR4 expression in lymphoproliferative diseases by targeted molecular imaging. *Theranostics*. 2015;5:618–630.
11. Lapa C, Schreder M, Schirbel A, et al. [^{68}Ga]pentixafor-PET/CT for imaging of chemokine receptor CXCR4 expression in multiple myeloma: comparison to [^{18}F]FDG and laboratory values. *Theranostics*. 2017;7:205–212.
12. Philipp-Abbrederis K, Herrmann K, Knop S, et al. In vivo molecular imaging of chemokine receptor CXCR4 expression in patients with advanced multiple myeloma. *EMBO Mol Med.* 2015;7:477–487.
13. Kircher M, Herhaus P, Schottelius M, et al. CXCR4-directed theranostics in oncology and inflammation. *Ann Nucl Med.* 2018;32:503–511.
14. Lapa C, Lückerath K, Kleinlein I, et al. ^{68}Ga-pentixafor-PET/CT for imaging of chemokine receptor 4 expression in glioblastoma. *Theranostics*. 2016;6:428–434.
15. Kircher M, Tran-Gia J, Kemmer L, et al. Imaging inflammation in atherosclerosis with CXCR4-directed ^{68}Ga-pentixafor PET/CT: correlation with ^{18}F-FDG PET/CT. *J Nucl Med.* 2020;61:751–756.
16. Luo Y, Cao X, Pan Q, Li J, Feng J, Li F. ^{68}Ga-pentixafor PET/CT for imaging of chemokine receptor 4 expression in Waldenström macroglobulinemia/lymphoplasmacytic lymphoma: comparison to ^{18}F-FDG PET/CT. *J Nucl Med.* 2019;60:1724–1729.
17. Herhaus P, Habringer S, Vag T, et al. Response assessment with the CXCR4-directed positron emission tomography tracer [^{68}Ga]pentixafor in a patient with extranodal marginal zone lymphoma of the orbital cavities. *EJNMMI Res.* 2017;7:51.
18. Haug AR, Leisser A, Wadsak W, et al. Prospective non-invasive evaluation of CXCR4 expression for the diagnosis of MALT lymphoma using [^{68}Ga]Ga-pentixafor-PET/MRI. *Theranostics*. 2019;9:3653–3658.
19. Lister TA, Crowther D, Sutcliffe SB, et al. Report of a committee convened to discuss the evaluation and staging of patients with Hodgkin's disease: Cotswolds meeting. *J Clin Oncol.* 1989;7:1630–1636.
20. Zucca E, Arcaini L, Buske C, et al. Marginal zone lymphomas: ESMO Clinical Practice Guidelines for diagnosis, treatment and follow-up. *Ann Oncol.* 2020;31:17–29.
21. Martin R, Juttler S, Muller M, Wester HJ. Cationic eluate pretreatment for automated synthesis of [^{68}Ga]CPCR4.2. *Nucl Med Biol.* 2014;41:84–89.
22. Cheson BD, Fisher RI, Barrington SF, et al. Recommendations for initial evaluation, staging, and response assessment of Hodgkin and non-Hodgkin lymphoma: the Lugano classification. *J Clin Oncol.* 2014;32:3059–3068.
23. Trentin L, Cabrelle A, Facco M, et al. Homeostatic chemokines drive migration of malignant B cells in patients with non-Hodgkin lymphomas. *Blood*. 2004;104:502–508.

Matched-Pair Comparison of ^{18}F-DCFPyL PET/CT and ^{18}F-PSMA-1007 PET/CT in 240 Prostate Cancer Patients: Interreader Agreement and Lesion Detection Rate of Suspected Lesions

Maurits Wondergem, Friso M. van der Zant, Wouter A.M. Broos, Remco J.J. Knol

Department of Nuclear Medicine, Noordwest Ziekenhuisgroep, Alkmaar, The Netherlands

Over 20 different prostate-specific membrane antigen (PSMA)–targeting radiopharmaceuticals for both imaging and therapy have been synthesized. Although variability in biodistribution and affinity for binding to the PSMA receptor is known to exist between different PSMA-targeting radiopharmaceuticals, little is known about the clinical implications of this variability. Therefore, this study analyzed differences in interreader agreement and detection rate between 2 regularly used ^{18}F-labeled PSMA receptor–targeting radiopharmaceuticals: ^{18}F-DCFPyL and ^{18}F-PSMA-1007. **Methods:** One hundred twenty consecutive patients scanned with ^{18}F-PSMA-1007 were match-paired with 120 patients scanned with ^{18}F-DCFPyL. All 240 PET/CT scans were reviewed by 2 readers and scored according to the criteria of the PSMA Reporting and Data System. Interreader agreement and the detection rate for suspected lesions were scored for different anatomic locations such as the prostate, prostatic fossa, lymph nodes, and bone. **Results:** Great equality was found between ^{18}F-DCFPyL and ^{18}F-PSMA-1007; however, some clinically relevant and statistically significant differences were observed. ^{18}F-PSMA-1007 detected suspected prostatic or prostatic fossa lesions in a higher proportion of patients and especially in the subcohort scanned for biochemical recurrence. ^{18}F-DCFPyL and ^{18}F-PSMA-1007 showed an equal ability to detect suspected lymph nodes, although interreader agreement for ^{18}F-DCFPyL was higher. ^{18}F-DCFPyL showed fewer equivocal skeletal lesions and higher interreader agreement on skeletal lesions. Most of the equivocal lesions found with ^{18}F-PSMA-1007 at least were determined to be of nonmetastatic origin. **Conclusion:** Clinically relevant differences, which may account for diagnostic dilemmas, were observed between ^{18}F-DCFPyL and ^{18}F-PSMA-1007. Those findings encourage further studies, as they may have consequences for selection of the proper PSMA-targeting radiopharmaceutical.

Key Words: prostate cancer; PSMA; ^{18}F-DCFPyL; ^{18}F-PSMA-1007; PET/CT

J Nucl Med 2021; 62:1422–1429
DOI: 10.2967/jnumed.120.258574

In recent years, prostate-specific membrane antigen (PSMA) receptor PET/CT has rapidly evolved as a cornerstone in prostate cancer imaging. PSMA PET/CT outperforms other imaging modalities because of its superior sensitivity and specificity, although sensitivity for lymph node metastases has been found to be moderate in prospective trials (*1–5*). The better diagnostic characteristics account for better treatment selection in both primary staging and biochemical recurrence. The ability to detect small metastases, for example, may benefit patients with oligometastatic disease, offering them treatment options with a chance of cure or survival benefits (*6,7*), although scientific underpinning of the latter is needed (*8*). The additional value of PSMA PET/CT during follow-up of systemic treatment, including androgen deprivation therapy and chemotherapy, in the palliative phase of the disease also needs to be clarified.

Because of the success of PSMA PET/CT, the number of different radiopharmaceuticals targeting the PSMA receptor has increased significantly (*9*). Although most early publications on the clinical use of PSMA PET/CT reported on findings with ^{68}Ga-labeled radiopharmaceuticals, later publication also gave attention to ^{18}F-labeled radiopharmaceuticals. Positrons emitted by ^{18}F decay have lower kinetic energy than those emitted by ^{68}Ga, resulting in a higher resolution in PET images acquired using ^{18}F tracers. Furthermore, the 110-min half-life of ^{18}F, compared with 68 min for ^{68}Ga, enables imaging at later time points without significant deterioration of image quality or the need to administer higher doses. This point is of clinical importance since PSMA tracer kinetics show that the tracer accumulates in prostate cancer cells over time whereas the background activity decreases (*10–14*). Although over 20 different PSMA-targeting radiopharmaceuticals for both imaging and therapy have been synthesized, only a few are used in common clinical practice.

Variability in biodistribution and affinity for binding to the PSMA receptor is known to exist between the different PSMA-targeting radiopharmaceuticals, but little is known about the clinical implications of this variability (*15,16*). This lack is reflected in recent EAU guidelines that do not discriminate between different PSMA-targeted radiopharmaceuticals for imaging of prostate cancer (https://uroweb.org/guideline/prostate-cancer/). To investigate whether these differences are clinically important and interfere with the reproducibility of scan outcomes and lesion detection, this study analyzed—in a large matched-pair cohort of 240 patients—interreader agreement and detection rate for suspected lesions using 2 common ^{18}F-labeled PSMA receptor–targeting radiopharmaceuticals: 2-(3-(1-carboxy-5-[(6-^{18}F-fluoro-pyridine-3-carbonyl)-amino]-pentyl)-ureido)-pentanedioic acid (^{18}F-DCFPyL) and (3*S*,10*S*,14*S*)-1-(4-(((*S*)-4-carboxy-2-((*S*)-4-carboxy-2-(6-^{18}F-fluoronicotinamido)butanamido)butanamido)methyl)phenyl)-3-

Received Oct. 20, 2020; revision accepted Jan. 13, 2021.
For correspondence or reprints, contact Maurits Wondergem (m.wondergem@nki.nl).
Published online February 5, 2021.

(naphthalen-2-ylmethyl)-1,4,12-trioxo-2,5,11,13-tetraazahexadecane-10,14,16-tricarboxylic acid (^{18}F-PSMA-1007). Known differences between these 2 radiopharmaceuticals that may interfere with scan readability include differences in excretion pathways and bone marrow uptake (*15,16*). Renal excretion of ^{18}F-DCFPyL results in high activity in the urinary tract, which may interfere with detection of lesions near the ureters and urinary bladder, whereas activity in the urinary tract is usually less for ^{18}F-PSMA-1007 because biliary excretion is the most important excretion pathway. Physiologic bone marrow uptake is commonly higher for ^{18}F-PSMA-1007 and may interfere with detection of bone metastases.

MATERIALS AND METHODS

Patient Population

This study retrospectively included 120 consecutive patients imaged between April 2, 2019, and June 20, 2019, with ^{18}F-PSMA-1007 PET/CT for primary staging, biochemical recurrence, or follow-up of systemic treatment of prostate cancer. In addition, 120 patients who were imaged between November 3, 2016, and March 21, 2019, with ^{18}F-DCFPyL were extracted from a prospectively maintained database of 813 patients scanned with ^{18}F-DCFPyL. To allow for a fair comparison of these 2 cohorts, they were matched on the basis of disease stage (primary staging, biochemical recurrence, or follow-up of treatment for castration-resistant prostate cancer); prostate-specific antigen (PSA) level at the time of PET/CT (PSA difference of <10% between 2 patients); and, in cases of biochemical recurrence, previous treatment (prostatectomy, lymph node dissection, external radiation therapy, or brachytherapy).

Besides the standard PSMA PET/CT acquired for clinical indications, no additional measurements or actions affecting the patient were performed. The study was approved by the local scientific board, and the need to receive approval from the local ethical committee was waived because the study did not fall within the scope of the Dutch Medical Research Involving Human Subjects Act (section 1.b; February 26, 1998). Additionally, as a standard procedure in our department, all included patients gave written consent to use of their anonymized data for scientific purposes.

Image Acquisition

^{18}F-DCFPyL and ^{18}F-PSMA-1007 were synthesized by an on-site cyclotron facility. PET images were acquired on a Biograph-16 TruePoint PET/CT scanner (Siemens Healthcare) at 120 min after injection of ^{18}F-DCFPyL (mean of 319 MBq and range of 231–367 MBq, depending on body mass) or 90 min after injection of ^{18}F-PSMA-1007 (mean of 324 MBq and range of 239–363 MBq, depending on body mass). Images were acquired from the inguinal region to the base of the skull (5 min per bed position). Data were reconstructed using an iterative ordered-subset expectation maximization 3-dimensional algorithm using 4 iterations, 16 subsets, and a 5-mm gaussian filter. The image matrix size was 256 × 256, pixel spacing was 2.67 × 2.67 mm, and slice thickness was 4 mm. For attenuation correction, a radiocontrast-enhanced CT scan (110 mAs at 110–130 kV) was typically acquired. Collimation was 16 × 1.2 mm; pitch, 0.95; slice thickness, 4 mm; and matrix size, 512 × 512. The resulting voxel sizes were 1.37 × 1.37 mm for CT images for attenuation correction and 0.98 × 0.98 mm for diagnostic CT images.

Data Acquisition

All 240 PET/CT scans were reevaluated by 2 nuclear medicine physicians with ample experience in reading both ^{18}F-DCFPyL and ^{18}F-PSMA-1007 PET/CT (each reader had >300 readings of both ^{18}F-DCFPyL and ^{18}F-PSMA-1007). The readers had access to limited patient data, including clinical indication for PSMA PET/CT, PSA level at time of PSMA PET/CT, Gleason score, TNM stage if known before PSMA PET/CT, and previous treatments. Readers were masked to all other data, including the used radiopharmaceutical.

The scan outcome was scored for different anatomic localizations, including prostate or prostatic fossa, inguinal lymph nodes, pelvic lymph nodes (N1 nodes, according to the TNM system in the eighth edition of the *AJCC Cancer Staging System*), abdominal lymph nodes, thoracic lymph nodes, axillary lymph nodes, cervical lymph nodes, pelvic bones, vertebral bones, thoracic bones (costae, sternum, clavicula, and scapulae), bones of the extremities, and other suspected lesions. The scans were read using the criteria of the PSMA Reporting and Data System (RADS) (*17*). For each anatomic localization, scan outcomes were entered in a database. Only the lesions with the highest score or highest likelihood of malignancy according to the reading system were recorded. If one or both readers found only equivocal lesions outside the prostate or prostatic bed, the true nature of the equivocal finding was retrospectively determined using data from histopathologic biopsies, imaging at follow-up, or PSA response to therapy. Definitive proof of nonmetastasized disease included, first, histopathologic findings excluding metastasized disease and, second, complete biochemical response after local therapies including prostatectomy, lymphadenectomy, or radiation therapy without or after discontinuation of androgen deprivation therapy and without local therapy of the equivocal findings. Definitive proof of metastasized disease included concordant findings on MRI, progression of lesions on follow-up PSMA PET/CT, or PSA response to targeted therapy that was administered because of equivocal findings.

Statistical Analysis

The Mann–Whitney *U* test was used to test for differences between ^{18}F-DCFPyL and ^{18}F-PSMA-1007 outcomes. Interreader agreement was measured by calculating the weighted Cohen κ and the percentage of agreement. As conventionally done, agreement was categorized as poor, fair, moderate, good, or very good, reflecting agreement of 0%–19%, 20%–39%, 40%–59%, 60%–79%, and 80%–100%, respectively. Weighted κ is highly dependent on the proportion of positive scan results; therefore, a low weighted κ may reflect good or even very good agreement when proportions of positivity are relatively low (?<0.2) or high (?>0.8) (*18*). For calculation of differences between ^{18}F-DCFPyL and ^{18}F-PSMA-1007 and agreement between readers, some subcategories of the PSMA RADS reading system were merged since some subdivisions barely have clinical impact: 1a, 1b, and 2 (benign and likely benign); 3a, 3b, 3c, and 3d (equivocal); and 4 and 5 (likely malignant and malignant). Pie plots were constructed for outcomes that showed relevant differences. All analyses were performed using the Statistical Package for Social Sciences (SPSS Statistics, version 25.0; IBM).

RESULTS

In total, 240 ^{18}F-PSMA PET/CT scans—120 ^{18}F-DCFPyL and 120 ^{18}F-PSMA-1007—were included in the study (Table 1). Commonly found differences between ^{18}F-DCFPyL and ^{18}F-PSMA-1007 uptake are shown in Figure 1.

Prostate and Prostatic Fossa

For the prostate and prostatic fossa, interreader agreement was very good for ^{18}F-DCFPyL and good for ^{18}F-PSMA-1007 (Fig. 2). Both readers found significantly more suspected prostate lesions with ^{18}F-PSMA-1007 using the PSMA RADS criteria (Table 2; Supplemental Fig. 1; supplemental materials are available at http://jnm.snmjournals.org). Categorization of the cohort according to disease stage shows statistical differences for detection of

TABLE 1
Patient Characteristics

Characteristic	^{18}F-DCFPyL	^{18}F-PSMA-1007
All patients		
n	120	120
PSA (μg/mL)	11.6 (0.1–558)	12.0 (0.1–577)
Primary staging		
n	69	69
PSA (μg/mL)	14.8 (3.2–558)	14.7 (2.4–577)
Gleason score*		
≤7a	17	8
≥7b	51	58
Unknown	1	4
T stage†		
T1	23	15
T2	25	27
T3	16	22
T4	0	4
Unknown	5	1
Androgen deprivation therapy	0	0
Biochemical recurrence		
n	21	21
PSA (μg/mL)	2.4 (0.4–7.9)	2.4 (0.4–7.8)
Previous therapy		
Prostatectomy	7	7
Radiation therapy	12	12
Brachytherapy	2	2
Androgen deprivation therapy‡	1	2
Follow-up systemic treatment		
n	30	30
PSA (μg/mL)	24.8 (0.1–385.0)	26.3 (0.1–369.0)
Androgen deprivation therapy	30	30

*$P = 0.402$ (Mann–Whitney *U* test),
†$P = 0.009$ (Mann–Whitney *U* test).
‡Only temporarily after radiation therapy with curative intent.
Qualitative data are number; continuous data are median followed by range in parentheses.

suspected prostate lesions by both readers for patients with biochemical recurrence only (Table 3).

Lymph Nodes

Interreader agreement for lymph nodes was in general good to very good for both ^{18}F-DCFPyL and ^{18}F-PSMA-1007. However, a consistently lower agreement, for both weighted κ and percentage of agreement, was found for detection of suspected pelvic lymph nodes and lymph nodes at any localization with ^{18}F-PSMA-1007. No statistically significant differences were found between ^{18}F-DCFPyL and ^{18}F-PSMA-1007 for detection of suspected lymph nodes (Table 2). However, with ^{18}F-PSMA-1007 more lymph nodes showed low-level uptake comparable to blood-pool activity, matching score 1b or 2 (benign or likely benign) (Supplemental Fig. 2). For most anatomic regions, significantly more lymph nodes with low uptake were found with ^{18}F-PSMA-1007 than with ^{18}F-DCFPyL ($P < 0.0005$–0.037).

Bone Lesions

Regarding suspected bone lesions, almost perfect interreader agreement was found at all localizations for ^{18}F-DCFPyL. For ^{18}F-PSMA-1007, however, consistently lower agreement (both weighted κ and percentage of agreement) was found for lesions in the thoracic region and whole skeleton and to a lesser extent for suspected bone lesions in the pelvis (Fig. 2). Both readers scored a significantly greater number of equivocal bone lesions in the thoracic region with ^{18}F-PSMA-1007 (14%–33% and 3%–4% for ^{18}F-PSMA-1007 and ^{18}F-DCFPyL, respectively) at the expense of the number of scans without bone lesions (44%–62% for ^{18}F-PSMA-1007 and 76%–78% for ^{18}F-DCFPyL). The same was found for bone lesions at any localization (equivocal: 14%–33% for ^{18}F-PSMA-1007 and 3%–4% for ^{18}F-DCFPyL; no bone lesions: 30%–44% for PSMA 1007 and 64%–66% for ^{18}F-DCFPyL) (Table 2; Fig. 3). Reader 2 also scored a significantly greater number of equivocal pelvic lesions ($P = 0.027$), whereas for reader 1 no statistically significant difference was found ($P = 0.053$). Categorization according to disease stage shows that a significantly greater number of equivocal lesions were found with ^{18}F-PSMA-1007 at primary staging and biochemical recurrence ($P = 0.001$ and 0.003, respectively), also at the expense of the number of patients without bone lesions (Table 3).

Visceral Lesions

Visceral lesions were found in 3% of patients by both readers for both ^{18}F-PSMA-1007 and ^{18}F-DCFPyL, whereas equivocal lesions were found in 5%–6% of patients with ^{18}F-DCFPyL and 8% of patients with ^{18}F-PSMA-1007 (Table 2). No statistical differences were found between ^{18}F-PSMA-1007 and ^{18}F-DCFPyL for detection of other lesions. All patients who showed suspected lesions at other locations had extensive metastasized disease in lymph nodes and skeleton.

Equivocal Bone Lesions

Three patients scanned with ^{18}F-DCFPyL (1 primary staging, 1 biochemical recurrence, and 1 therapy follow-up) and 26 scanned with ^{18}F-PSMA-1007 (18 primary staging, 6 biochemical recurrence, and 2 therapy follow-up) had equivocal bone lesions as the only indication of possible metastasized disease. Clinical follow-up of these patients showed definite proof of nonmetastasized disease in 0 and 16 (62%) patients scanned with ^{18}F-DCFPyL and ^{18}F-PSMA-1007, respectively, whereas 1 (33%) and 2 (8%) showed proof of metastasized disease, and no conclusive follow-up was present in 2 (67%) and 8 (31%). Three patients had histopathologic verification of equivocal bone lesions on ^{18}F-PSMA-1007; none of these lesions were proven to be malignant (Fig. 4). Histopathology showed benign etiologies: aspecific necrosis, an aspecific lytic bone lesion with reactive changes, and normal bone tissue.

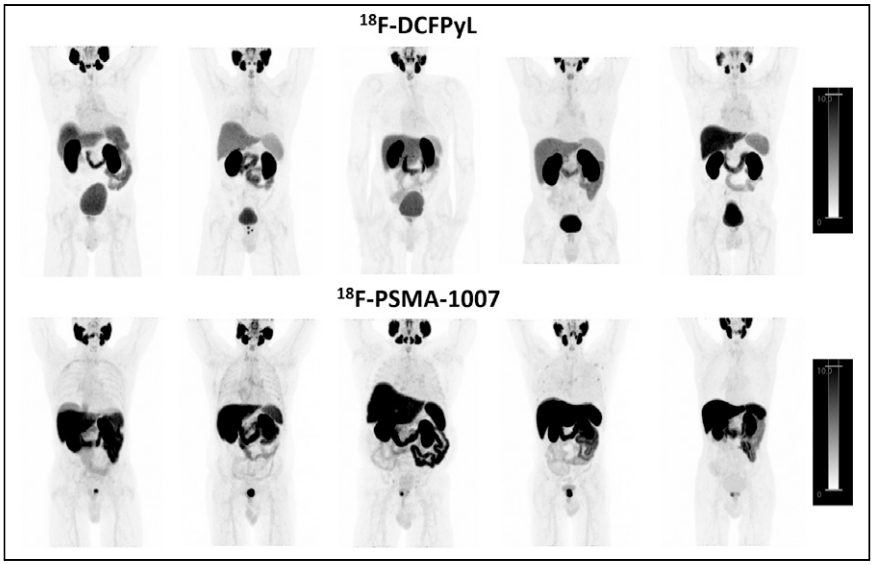

FIGURE 1. Distribution of ^{18}F-DCFPyL and ^{18}F-PSMA-1007 in patients imaged for primary screening of high-risk prostate cancer, all scored as negative for bone and lymph node metastases by 2 experienced readers. Maximum-intensity-projection images are scaled to SUV-body weight of 0.0–10.0. Lower physiologic ^{18}F-DCFPyL uptake is observed in liver, spleen, and bone marrow. Lower ^{18}F-DCFPyL uptake is observed in primary prostate tumor. Low ^{18}F-PSMA-1007 activity is seen in urinary tract and trachea. ^{18}F-PSMA-1007 uptake in skeleton is heterogeneous between patients; no uptake to diffuse uptake is observed in bone marrow, and variable patterns of irregular ^{18}F-PSMA-1007 uptake are observed in ribs of several patients. Higher ^{18}F-PSMA-1007 activity in bile ducts and gallbladder is not appreciated because of scaling.

DISCUSSION

Although great equality was found between ^{18}F-DCFPyL and ^{18}F-PSMA-1007 for interreader agreement and for detection of suspected prostate cancer lesions, there were 2 differences that may be of clinical relevance.

The first was in the prostatic region; identification of lesions in this region is of particular clinical importance for patients with biochemical recurrence. The subanalysis according to clinical stage showed that, especially in this category of patients, ^{18}F-PSMA-1007 detected significantly more suspected lesions than ^{18}F-DCFPyL, although the number of patients in this category was limited (n = 21). That finding could be the result of the lower urinary secretion of this radiopharmaceutical, allowing for better characterization of intraprostatic lesions or lesions in the prostatic fossa after prostatectomy.

Second, equivocal bone lesions were found more frequently with ^{18}F-PSMA-1007, resulting in lower interreader agreement. The greatest difference between readers was in the classification of rib uptake. Both readers acknowledged high uptake in the ribs in many patients scanned with ^{18}F-PSMA-1007. Reader 1 interpreted this uptake as probably benign (PSMA RADS 2) in a larger proportion of patients than did reader 2, who scored a larger proportion as equivocal (PSMA RADS 3a–3d). Reader 1 argued that the absence of lesions at other sites in the skeleton made bone metastases in the ribs unlikely; however, reader 2 scored these rib lesions as equivocal based purely on the increased activity in the ribs. Reader 2 argued that solitary bone metastases in the ribs are encountered in prostate cancer patients, although (as far as is known today) normally not as frequently as is observed with ^{18}F-PSMA-1007. The PSMA RADS reading criteria allow for interpretation differences, since no hard cutoffs to classify tracer uptake are given. Although allowing for differences in interpretation is scientifically less desirable, such differences continuously exist in clinical practice, and these data therefore reflect the present discussion around this topic in daily practice. Findings of equivocal PSMA-avid bone lesions may be clinically relevant and account for diagnostic dilemmas, such as when there are no other metastatic lesions or when the equivocal findings distinguish between oligo- and polymetastatic disease. In these cases, the true nature of these equivocal findings may alter patients' management and indicate the need for further diagnostic procedures.

Given that the study was retrospective, it had the drawback that histopathologic confirmation was lacking for almost all lesions. However, clinical follow-up of patients with equivocal bone lesions as the only indication of possible metastasized disease showed that in most patients (at least 16/24) with these abnormalities on ^{18}F-PSMA-1007, metastasized disease could be excluded. However, metastasized disease was proven in only 2 of 26 patients. These results indicate that equivocal bone findings with ^{18}F-PSMA-1007 PET/CT are of little clinical value and should not cause withholding of treatment options with curative intent.

As another drawback of the study, because ^{18}F-DCFPyL and ^{18}F-PSMA-1007 were compared between patients, some findings may be attributable to differences between cohorts rather than to differences between radiopharmaceuticals. However, to diminish these influences, we used 2 large cohorts comprising matched-pair

	Total cohort			
	DCFPyL		PSMA-1007	
	Weighted κ	Agreement (%)	Weighted κ	Agreement (%)
Prostate	0.925	95	0.738	90
Lymph nodes				
Inguinal	0.265	96	0.746	99
Pelvis	0.915	95	0.841	89
Abdomen	0.848	93	0.833	93
Mediastinum	0.852	96	0.673	94
Axillae	1.000	100	1.000	100
Neck	0.773	95	0.952	98
Whole body	0.916	94	0.825	88
Bone				
Pelvis	0.895	95	0.823	86
Spine	0.893	95	0.912	93
Thorax	0.925	95	0.706	74
Extremities	1.000	100	0.847	94
Whole skeleton	0.868	93	0.659	70

FIGURE 2. Interreader agreement reflected by weighted Cohen κ and by percentage for both ^{18}F-DCFPyL and ^{18}F-PSMA-1007. Dark green = very good agreement; light green = good agreement; orange = moderate agreement.

TABLE 2
Detection Rates of Suspected Lesions and Equivocal Lesions and Testing of Equality for Detection of Suspected Lesions Between ^{18}F-DCFPyL and ^{18}F-PSMA-1007 for Total Cohort

		Reader 1					Reader 2				
		^{18}F-DCFPyL		^{18}F-PSMA-1007			^{18}F-DCFPyL		^{18}F-PSMA-1007		
General site	Specific site	Suspected malignant	Equivocal	Suspected malignant	Equivocal	*P*	Suspected malignant	Equivocal	Suspected malignant	Equivocal	*P*
Prostate		86 (72)	4 (3)	98 (82)	7 (6)	0.045*	86 (72)	5 (4)	102 (85)	1 (1)	0.015*
Lymph nodes	Inguinal	4 (3)	0 (0)	2 (2)	0 (0)	0.409	4 (3)	0 (0)	1 (1)	2 (2)	0.984
	Pelvis	52 (43)	2 (2)	55 (46)	4 (3)	0.409	52 (43)	2 (2)	55 (46)	5 (4)	0.460
	Abdomen	36 (30)	0 (0)	31 (26)	0 (0)	0.473	41 (34)	2 (2)	34 (28)	2 (2)	0.331
	Mediastinum	12 (10)	0 (0)	7 (6)	4 (3)	0.760	13 (11)	4 (3)	10 (8)	1 (1)	0.332
	Axillae	6 (5)	0 (0)	1 (1)	0 (0)	0.056	6 (5)	0 (0)	1 (1)	0 (0)	0.056
	Neck	12 (10)	0 (0)	11 (9)	1 (1)	0.983	18 (15)	0 (0)	11 (9)	1 (1)	0.231
	Whole body	52 (43)	2 (2)	56 (47)	5 (4)	0.463	55 (46)	4 (3)	58 (48)	6 (5)	0.691
Bone	Pelvis	32 (27)	2 (2)	44 (37)	5 (4)	0.053	32 (27)	0 (0)	40 (33)	13 (11)	0.027*
	Spine	28 (23)	2 (2)	34 (28)	4 (3)	0.215	26 (22)	1 (1)	34 (28)	10 (8)	0.060
	Thorax	23 (19)	4 (3)	29 (24)	17 (14)	0.015*	24 (20)	5 (4)	28 (23)	40 (33)	<0.001*
	Extremities	22 (18)	0 (0)	18 (15)	4 (3)	0.929	22 (18)	0 (0)	18 (15)	4 (3)	0.929
	Whole skeleton	40 (33)	4 (3)	50 (42)	17 (14)	0.009*	36 (30)	5 (4)	44 (37)	40 (33)	<0.001*
Other	Lung	1 (1)	4 (3)	1 (1)	7 (6)	0.389	1 (1)	6 (5)	2 (2)	6 (5)	0.800
	Liver	1 (1)	0 (0)	2 (2)	1 (1)	0.312	0 (0)	1 (1)	2 (2)	1 (1)	0.318
	Funiculus	0 (0)	2 (2)	0 (0)	0 (1)	0.156	2 (2)	0 (0)	0 (0)	0 (0)	0.800
	Adrenals	1 (1)	0 (0)	1 (1)	1 (1)	0.559	0 (0)	0 (0)	0 (0)	0 (0)	1.000
	Pleural	0 (0)	0 (0)	0 (0)	1 (1)	0.317	0 (0)	0 (0)	0 (0)	1 (1)	0.317
	Thyroid	0 (0)	0 (0)	0 (0)	0 (0)	1.000	0 (0)	0 (0)	0 (0)	1 (1)	0.317
	All other	3 (3)	6 (5)	4 (3)	10 (8)	0.270	3 (3)	7 (6)	4 (3)	9 (8)	0.513

*Statistically significant ($P < 0.05$; Mann–Whitney U test).
Data are number followed by percentage in parentheses. Suspected malignant PSMA is RADS 4 and 5; equivocal PSMA is RADS 3a, 3b, 3c, and 3d.

TABLE 3

Detection Rates of Suspected Lesions and Equivocal Lesions and Testing of Equality for Detection of Suspected Lesions Between ^{18}F-DCFPyL and ^{18}F-PSMA-1007 According to Primary Staging, Biochemical Recurrence, and Follow-up of Systemic Therapies

		Primary staging (n = 69)					BCR (n = 21)					Follow-up (n = 30)				
		^{18}F-DCFPyL		^{18}F-PSMA-1007			^{18}F-DCFPyL		^{18}F-PSMA-1007			^{18}F-DCFPyL		^{18}F-PSMA-1007		
Reader	Site	SM	Eq.	SM	Eq.	P	SM	Eq.	SM	Eq.	P	SM	Eq.	SM	Eq.	P
1	Prostate	66 (96)	2 (3)	67 (97)	2 (3)	0.669	6 (29)	0 (0)	13 (62)	3 (14)	0.007*	14 (47)	2 (7)	9 (30)	2 (7)	0.186
	Lymph nodes	24 (35)	1 (1)	27 (39)	4 (6)	0.393	11 (52)	1 (5)	9 (43)	1 (5)	0.532	17 (57)	0 (0)	20 (67)	0 (0)	0.430
	Whole skeleton	17 (25)	1 (1)	20 (29)	11 (16)	0.065	2 (10)	1 (5)	6 (29)	5 (24)	0.013*	20 (67)	1 (3)	24 (80)	1 (3)	0.234
2	Prostate	67 (97)	2 (3)	68 (99)	1 (1)	0.572	6 (29)	1 (5)	13 (62)	0 (0)	0.029*	13 (43)	2 (7)	21 (70)	0 (0)	0.059
	Lymph nodes	25 (36)	4 (6)	28 (41)	4 (6)	0.595	11 (52)	0 (0)	7 (33)	1 (5)	0.285	19 (63)	0 (0)	22 (73)	1 (3)	0.356
	Whole skeleton	15 (22)	2 (3)	15 (22)	27 (39)	0.001*	3 (14)	2 (10)	7 (33)	9 (43)	0.003*	18 (60)	1 (3)	22 (73)	4 (13)	0.154

*Statistically significant ($P < 0.05$; Mann–Whitney U test).

BCR = biochemical recurrence; SM = suspected malignant; Eq. = equivocal.

Data are number followed by percentage in parentheses. Suspected malignant PSMA is RADS 4 and 5; equivocal PSMA is RADS 3a, 3b, 3c, and 3d.

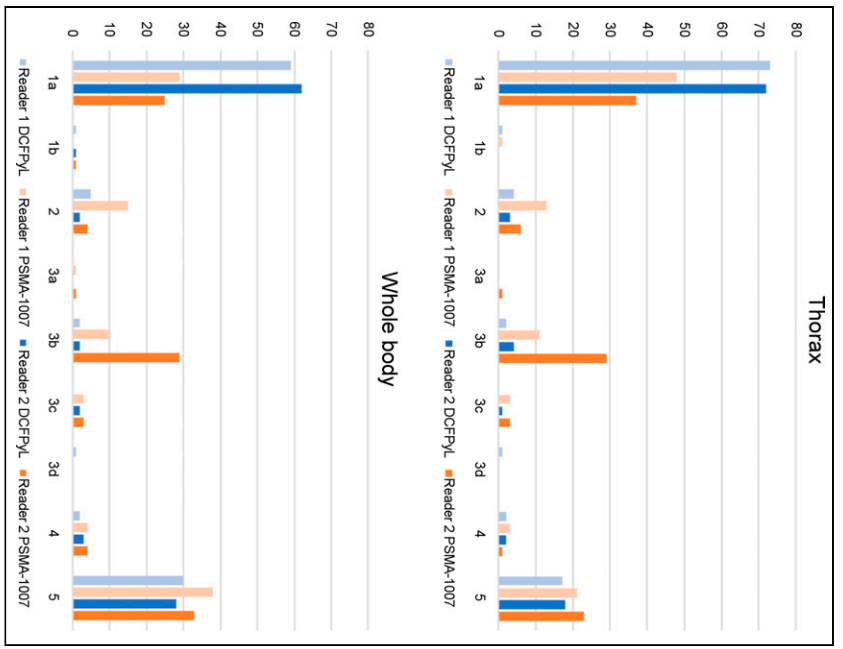

FIGURE 3. Bar graph for bone lesions in thorax and whole body. For ^{18}F-PSMA-1007, both readers scored statistically significantly greater number of equivocal lesions (3a, 3b, 3c, or 3 d) and fewer benign lesions (1a, 1b, and 2).

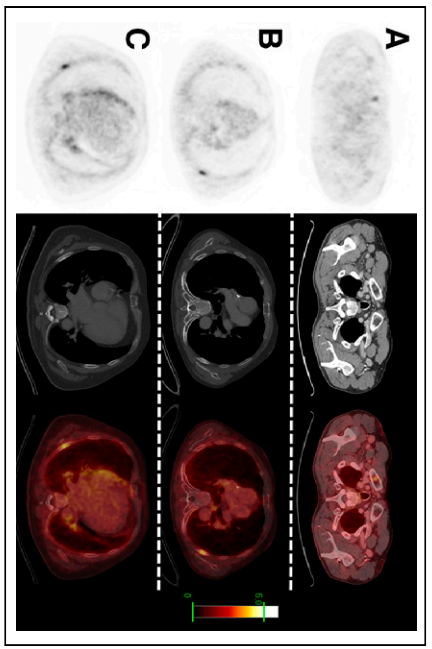

FIGURE 4. Equivocal bone lesions in right clavicula (A) and ribs (B and C) of clinical relevance for primary staging on ^{18}F-PSMA-1007 PET/CT. Tumor characteristics were cT3a, Gleason score of 7, and initial PSA of 15.2 ng/mL in A; cT2, Gleason score of 8, and initial PSA of 8.0 ng/mL in B; and cT3a, Gleason score of 6, and initial PSA of 3.7 ng/mL in C. Additional MRI could not exclude bone metastasis in A; no further imaging was performed in B and C. Histopathologic biopsy revealed no malignancy in any of these 3 patients: aspecific necrosis was found in A, aspecific lytic bone lesion with reactive changes in B, and normal bone tissue in C. Ultimately, all 3 patients were staged N0M0.

patients. Unfortunately, the databases were not large enough to enable pairing by all potentially relevant clinical characteristics that may interfere with the pretest likelihood of detecting suspected lesions. Matching of PSA was done instead of matching of Gleason score or T stage, since there are indications that ^{18}F-PSMA-PET/CT positivity for metastases is best predicted by the serum PSA value (*19*).

The findings in this study are in line with findings by Dietlein et al. in an intrapatient comparison of ^{18}F-PSMA-1007 with ^{18}F-DCFPyL, ^{68}Ga-PSMA-11, or ^{18}F-JK-PSMA-7 (*20*). In a cohort of 27 patients, an improved characterization of prostate lesions with ^{18}F-PSMA-1007 was shown ($P = 0.024$) at the expense of the interpretability of skeletal lesions. ^{18}F-PSMA-1007 showed significantly ($P = 0.0006$) more aspecific medullary focal uptake. However, in another study, which included 12 patients scanned with both ^{18}F-DCFPyL and ^{18}F-PSMA-1007, both radiopharmaceuticals identified the same lesions; the appearance of equivocal skeletal uptake was not mentioned (*15*).

Recently, Rauscher et al. performed a matched-pair analysis of ^{68}Ga-PSMA-11 and ^{18}F-PSMA-1007 and found an almost 5 times higher prevalence of PSMA-ligand–positive findings attributed to a benign origin, including among other bone lesions and lymph nodes (*21*). In this study, as in our present study, the lack of histopathologic confirmation represents a major limitation. To our knowledge, ours was the first study comprising a large cohort of patients assessing the differences between 2 widely used ^{18}F-PSMA radiopharmaceuticals.

Nonspecific skeletal ^{18}F-PSMA-1007 uptake has an unknown mechanism and shows great heterogeneity between patients (Fig. 1). It might be hypothesized that radiolysis results in free ^{18}F-fluorine; however, quality control reports from our cyclotron facility mention concentrations of free ^{18}F-fluorine below 2% at 8 h after synthesis of ^{18}F-PSMA-1007. Furthermore, the aspecific skeletal uptake was not seen in patients whose prostate cancer was scanned with ^{18}F-sodium fluoride (*22*). Therefore, it is unlikely that the uptake is explained by the presence of free ^{18}F-fluorine due to radiolysis. The literature comparing PSMA tracers with ^{68}Ga and ^{18}F has suggested that the higher number of equivocal lesions found with ^{18}F-PSMA-1007 might be explained by the lower positron energy (which improves spatial resolution), longer half-life, and generally higher injected activities of ^{18}F than of ^{68}Ga (*21*). However, since this study compared 2 different ^{18}F-labeled PSMA tracers, it can be concluded that the differences in physical properties of ^{68}Ga and ^{18}F do not offer a good explanation for the number of equivocal lesions found with ^{18}F-PSMA-1007. It is known that PSMA uptake may appear in several benign (bone) lesions (*23*); therefore, one hypothesis is that higher affinity of ^{18}F-PSMA-1007 for the PSMA receptor, as shown in preclinical studies, may result in a higher signal from these benign lesions (*24*). Another possibility is that ^{18}F-PSMA-1007 is metabolized (e.g., in the liver before excretion in the bile), resulting in radiolabeled substances that accumulate at specific sites in the skeleton, although there is no scientific underpinning for this hypothesis.

Given the findings in the present study and in the available literature, it can be concluded that there are differences between ^{18}F-DCFPyL and ^{18}F-PSMA-1007 that may have clinical consequences. Although there are clues that ^{18}F-DCFPyL may be more appropriate when information about uptake in the prostate is of no clinical value (e.g., in primary staging of prostate cancer that is already histopathologically proven), and although ^{18}F-PSMA-1007 may be more appropriate when detection of abnormalities in the prostate or prostatic fossa are most clinically relevant, there is too little evidence to support recommendations on which tracer should be used. Further studies are needed to verify the clues found in this study and in the available literature, especially studies to analyze the true nature of the equivocal bone lesions frequently found with ^{18}F-PSMA-1007 and the apparent better ability of ^{18}F-PSMA-1007 to detect lesions in the prostate and prostatic region.

CONCLUSION

Great equality was found between ^{18}F-DCFPyL and ^{18}F-PSMA-1007; however, some differences were observed that may be of clinical relevance. ^{18}F-PSMA-1007 detected prostatic lesions and prostatic fossa lesions in a higher proportion of patients, whereas ^{18}F-DCFPyL showed fewer equivocal skeletal lesions and higher interreader agreement for skeletal lesions. These differences encourage further studies to evaluate their true clinical impact, as they may have consequences for selection of the proper PSMA-targeting radiopharmaceutical.

DISCLOSURE

No potential conflict of interest relevant to this article was reported.

KEY POINTS

QUESTION: Are differences in the biologic behavior of different PSMA tracers clinically relevant to interreader agreement and to the detection rate for suspected malignant lesions?

PERTINENT FINDINGS: Interreader agreement was generally better for ^{18}F-DCFPyL than for ^{18}F-PSMA-1007, particularly regarding bone lesions. A statistically greater number of suspected lesions was found in the prostate or prostatic fossa with ^{18}F-PSMA-1007, especially in the biochemical-recurrence subcohort (P = 0.007–0.029), whereas ^{18}F-DCFPyL found a statistically lower number of equivocal bone lesions, particularly in the biochemical-recurrence (P = 0.003–0.013) and primary-staging (P = 0.001–0.065) cohorts

IMPLICATIONS FOR PATIENT CARE: Although more studies are needed to further explore the exact clinical implications of the present findings, these findings may allow for better selection of PSMA-targeted radiopharmaceuticals and therefore increase the diagnostic power of PSMA PET/CT.

REFERENCES

1. Afshar-Oromieh A, Zechmann CM, Malcher A, et al. Comparison of PET imaging with a ^{68}Ga-labelled PSMA ligand and ^{18}F-choline-based PET/CT for the diagnosis of recurrent prostate cancer. *Eur J Nucl Med Mol Imaging.* 2014;41:11–20.
2. Bluemel C, Krebs M, Polat B, et al. ^{68}Ga-PSMA-PET/CT in patients with biochemical prostate cancer recurrence and negative ^{18}F-choline-PET/CT. *Clin Nucl Med.* 2016;41:515–521.
3. Corfield J, Perera M, Bolton D, Lawrentschuk N. ^{68}Ga-prostate specific membrane antigen (PSMA) positron emission tomography (PET) for primary staging of high-risk prostate cancer: a systematic review. *World J Urol.* 2018;36:519–527.
4. van Kalmthout LWM, van Melick HHE, Lavalaye J, et al. Prospective validation of gallium-68 PSMA-PET/CT in primary staging of prostate cancer patients. *J Urol.* 2020;203:537–545.

5. Gorin MA, Rowe SP, Patel HD, et al. Prostate specific membrane antigen targeted ^{18}F-DCFPyL positron emission tomography/computerized tomography for the preoperative staging of high risk prostate cancer: results of a prospective, phase II, single center study. *J Urol.* 2018;199:126–132.
6. Roach PJ, Francis R, Emmett L, et al. The impact of ^{68}Ga-PSMA PET/CT on management intent in prostate cancer: results of an Australian prospective multicenter study. *J Nucl Med.* 2018;59:82–88.
7. Calais J, Czernin J, Cao M, et al. ^{68}Ga-PSMA-11 PET/CT mapping of prostate cancer biochemical recurrence after radical prostatectomy in 270 patients with a PSA level of less than 1.0 ng/mL: impact on salvage radiotherapy planning. *J Nucl Med.* 2018;59:230–237.
8. Ost P, Reynders D, Decaestecker K, et al. Surveillance or metastasis-directed therapy for oligometastatic prostate cancer recurrence: a prospective, randomized, multicenter phase II trial. *J Clin Oncol.* 2018;36:446–453.
9. Eiber M, Fendler WP, Rowe SP, et al. Prostate-specific membrane antigen ligands for imaging and therapy. *J Nucl Med.* 2017;58(suppl):67S–76S.
10. Szabo Z, Mena E, Rowe SP, et al. Initial evaluation of [^{18}F]DCFPyL for prostate-specific membrane antigen (PSMA)-targeted PET imaging of prostate cancer. *Mol Imaging Biol.* 2015;17:565–574.
11. Afshar-Oromieh A, Malcher A, Eder M, et al. PET imaging with a [^{68}Ga]gallium-labelled PSMA ligand for the diagnosis of prostate cancer: biodistribution in humans and first evaluation of tumour lesions. *Eur J Nucl Med Mol Imaging.* 2013;40:486–495.
12. Herrmann K, Bluemel C, Weineisen M, et al. Biodistribution and radiation dosimetry for a probe targeting prostate-specific membrane antigen for imaging and therapy. *J Nucl Med.* 2015;56:855–861.
13. Afshar-Oromieh A, Hetzheim H, Kratochwil C, et al. The theranostic PSMA ligand PSMA-617 in the diagnosis of prostate cancer by PET/CT: biodistribution in humans, radiation dosimetry, and first evaluation of tumor lesions. *J Nucl Med.* 2015;56:1697–1705.
14. Afshar-Oromieh A, Hetzheim H, Kubler W, et al. Radiation dosimetry of ^{68}Ga-PSMA-11 (HBED-CC) and preliminary evaluation of optimal imaging timing. *Eur J Nucl Med Mol Imaging.* 2016;43:1611–1620.
15. Giesel FL, Will L, Lawal I, et al. Intraindividual comparison of ^{18}F-PSMA-1007 and ^{18}F-DCFPyL PET/CT in the prospective evaluation of patients with newly diagnosed prostate carcinoma: a pilot study. *J Nucl Med.* 2018;59:1076–1080.
16. Giesel FL, Hadaschik B, Cardinale J, et al. F-18 labelled ^{18}F-PSMA-1007: biodistribution, radiation dosimetry and histopathological validation of tumor lesions in prostate cancer patients. *Eur J Nucl Med Mol Imaging.* 2017;44:678–688.
17. Rowe SP, Pienta KJ, Pomper MG, Gorin MA. PSMA-RADS version 1.0: a step towards standardizing the interpretation and reporting of PSMA-targeted PET imaging studies. *Eur Urol.* 2018;73:485–487.
18. Landis JR, Koch GG. The measurement of observer agreement for categorical data. *Biometrics.* 1977;33:159–174.
19. Wondergem M, Jansen BHE, van der Zant FM, et al. Early lesion detection with ^{18}F-DCFPyL PET/CT in 248 patients with biochemically recurrent prostate cancer. *Eur J Nucl Med Mol Imaging.* 2019;46:1911–1918.
20. Dietlein F, Kobe C, Hohberg M, et al. Intraindividual comparison of ^{18}F-PSMA-1007 with renally excreted PSMA ligands for PSMA PET imaging in patients with relapsed prostate cancer. *J Nucl Med.* 2020;61:729–734.
21. Rauscher I, Krönke M, König M, et al. Matched-pair comparison of ^{68}Ga-PSMA-11 PET/CT and ^{18}F-PSMA-1007 PET/CT: frequency of pitfalls and detection efficacy in biochemical recurrence after radical prostatectomy. *J Nucl Med.* 2020;61:51–57.
22. Wondergem M, van der Zant FM, Knol RJJ, et al. ^{99m}Tc-HDP bone scintigraphy and ^{18}F-sodiumfluoride PET/CT in primary staging of patients with prostate cancer. *World J Urol.* 2018;36:27–34.
23. Sheikhbahaei S, Afshar-Oromieh A, Eiber M, et al. Pearls and pitfalls in clinical interpretation of prostate-specific membrane antigen (PSMA)-targeted PET imaging. *Eur J Nucl Med Mol Imaging.* 2017;44:2117–2136.
24. Cardinale J, Schäfer M, Benešová M, et al. Preclinical evaluation of ^{18}F-PSMA-1007, a new prostate-specific membrane antigen ligand for prostate cancer imaging. *J Nucl Med.* 2017;58:425–431.

Prospective, Single-Arm Trial Evaluating Changes in Uptake Patterns on Prostate-Specific Membrane Antigen–Targeted ^{18}F-DCFPyL PET/CT in Patients with Castration-Resistant Prostate Cancer Starting Abiraterone or Enzalutamide

Katherine A. Zukotynski[1–3], Urban Emmenegger[4], Sebastien Hotte[5], Anil Kapoor[6], Wei Fu[7], Amanda L. Blackford[7], John Valliant[8], François Bénard[9,10], Chun K. Kim[11], Mark C. Markowski[12], Mario A. Eisenberger[12], Emmanuel S. Antonarakis[12], Kenneth J. Pienta[13], Michael A. Gorin[12–14], Matthew Lubanovic[1], Jihyun Kim[15], Martin G. Pomper[12–14], Steve Y. Cho[*15,16], and Steven P. Rowe[*12–14]

[1]Departments of Radiology and Medicine, McMaster University, Hamilton, Ontario, Canada; [2]Department of Medical Imaging, Schulich School of Medicine & Dentistry, Western University, London, Ontario, Canada; [3]Department of Radiology, University of British Columbia, Vancouver, BC; [4]Sunnybrook Odette Cancer Centre and Research Institute, University of Toronto, Toronto, Ontario, Canada; [5]Department of Oncology, McMaster University, Hamilton, Ontario, Canada; [6]Department of Urology, McMaster University, Hamilton, Ontario, Canada; [7]Division of Biostatistics, Sidney Kimmel Comprehensive Cancer Center, Johns Hopkins University School of Medicine, Baltimore, Maryland; [8]Department of Chemistry, McMaster University, Hamilton, Ontario, Canada; [9]Department of Radiology, University of British Columbia, Vancouver, British Columbia, Canada; [10]PET Functional Imaging, BC Cancer, Vancouver, British Columbia, Canada; [11]Department of Medicine, Hanyang University College of Medicine, Seoul, South Korea; [12]Sidney Kimmel Comprehensive Cancer Center, Johns Hopkins University School of Medicine, Baltimore, Maryland; [13]James Buchanan Brady Urological Institute and Department of Urology, Johns Hopkins University School of Medicine, Baltimore, Maryland; [14]Russell H. Morgan Department of Radiology and Radiological Science, Johns Hopkins University School of Medicine, Baltimore, Maryland; [15]Department of Radiology, University of Wisconsin School of Medicine and Public Health, Madison, Wisconsin; and [16]University of Wisconsin Carbone Cancer Center, Madison, Wisconsin

PET with small molecules targeting prostate-specific membrane antigen (PSMA) is being adopted as a clinical standard for prostate cancer imaging. In this study, we evaluated changes in uptake on PSMA-targeted PET in men starting abiraterone or enzalutamide. **Methods:** This prospective, single-arm, 2-center, exploratory clinical trial enrolled men with metastatic castration-resistant prostate cancer initiating abiraterone or enzalutamide. Each patient was imaged with ^{18}F-DCFPyL at baseline and within 2–4 mo after starting therapy. Patients were followed for up to 48 mo from enrollment. A central review evaluated baseline and follow-up PET scans, recording change in SUV_{max} at all disease sites and classifying the pattern of change. Two parameters were derived: the δ-percent SUV_{max} (DPSM) of all lesions and the δ-absolute SUV_{max} (DASM) of all lesions. Kaplan–Meier curves were used to estimate time to therapy change (TTTC) and overall survival (OS). **Results:** Sixteen evaluable patients were accrued to the study. Median TTTC was 9.6 mo (95% CI, 6.9–14.2), and median OS was 28.6 mo (95% CI, 18.3–not available [NA]). Patients with a mixed-but-predominantly-increased pattern of radiotracer uptake had a shorter TTTC and OS. Men with a low DPSM had a median TTTC of 12.2 mo (95% CI, 11.3–NA) and a median OS of 37.2 mo (95% CI, 28.9–NA), whereas those with a high DPSM had a median TTTC of 6.5 mo (95% CI, 4.6–NA, $P = 0.0001$) and a median OS of 17.8 mo (95% CI, 13.9–NA, $P = 0.02$). Men with a low DASM had a median TTTC of 12.2 mo (95% CI, 11.3–NA) and a median OS of NA (95% CI, 37.2 mo–NA), whereas those with a high DASM had a median TTTC of 6.9 mo (95% CI, 6.1–NA, $P = 0.003$) and a median OS of 17.8 mo (95% CI, 13.9–NA, $P = 0.002$). **Conclusion:** Findings on PSMA-targeted PET 2–4 mo after initiation of abiraterone or enzalutamide are associated with TTTC and OS. Development of new lesions or increasing intensity of radiotracer uptake at sites of baseline disease are poor prognostic findings suggesting shorter TTTC and OS.

Key Words: antiandrogen; response assessment; CRPC; radiopharmaceutical; prognosis

J Nucl Med 2021; 62:1430–1437
DOI: 10.2967/jnumed.120.259069

There is interest in the use of PET radiotracers targeting the prostate-specific membrane antigen (PSMA) to improve imaging of men with prostate cancer (PCa) (*1*). PSMA is a transmembrane type II glycoprotein that is overexpressed on most PCa cells (*2*). Over the last 5 years, PSMA-targeted imaging has been used for initial staging of men with high-risk PCa (*3*), restaging of men with biochemical failure after attempted curative local therapy (*4*), and selection of men with metastatic disease for treatment with PSMA-targeted endoradiotherapy (*5*).

There are few data on the prognostic value of PSMA-targeted PET and the use of PSMA ligands for following response to therapy in men with PCa. For first-line systemic treatment with androgen deprivation therapy, the interplay between androgen signaling and PSMA expression can lead to increased PSMA on the cell surface and a short-term flare phenomenon on PSMA-targeted PET (*6,7*). Long-term androgen deprivation therapy tends to produce decreasing lesion conspicuity (*8*). Some studies have reported a flare in

Received Oct. 21, 2020; revision accepted Jan. 27, 2021.
For correspondence or reprints, contact Steven P. Rowe (srowe8@jhmi.edu).
Published online February 19, 2021.

castration-resistant PCa after initiation of second-generation antiandrogen agents (abiraterone or enzalutamide) (*9,10*), whereas others suggest that increasing uptake on PSMA-targeted PET reflects progression and worsening disease (*11*). There is increasing interest in following patients with PCa using serial PSMA-targeted PET, and an approach to determining progression was recently introduced (*12*).

The aim of this prospective, single-arm, 2-center, exploratory clinical trial was to evaluate the ability of PSMA-targeted PET to determine progression relative to conventional imaging with bone scanning and CT. A post hoc analysis was also used to provide pilot data on the association of metrics of response and survival between baseline and short-interval follow-up PSMA-targeted PET/CT using ^{18}F-DCFPyL (*13*) in men with castration-resistant PCa starting treatment with abiraterone or enzalutamide.

MATERIALS AND METHODS

This study was registered with ClinicalTrials.gov (NCT02856100 and NCT02691169) and was performed under the auspices of a U.S. Food and Drug Administration investigational new drug application (IND121064) and a Health Canada clinical trial application (control no. 190215). The study was approved by the institutional review boards at both McMaster University and Johns Hopkins Hospital.

Patients

The inclusion criteria for the study were as follows: an age of at least 18 y; histologically or cytologically confirmed prostate adenocarcinoma without neuroendocrine differentiation or small cell features; a plan to start abiraterone or enzalutamide within 1–7 d after baseline ^{18}F-DCFPyL PET/CT; documented progressive metastatic PCa as assessed by the treating clinician, with either a rising level of serum prostate-specific antigen (PSA) on 2 determinations at least 1 wk apart or radiographic progression; ongoing androgen deprivation, with a serum testosterone level of less than 50 ng/dL; an Eastern Cooperative Oncology Group performance status of no more than 2; a hemoglobin level of at least 90 g/L; a platelet count of more than 100,000/μL; a serum albumin level of at least 30 g/L; a serum creatinine level of less than 1.5 times the upper limit of normal or a calculated creatinine clearance of at least 60 mL/min; and a serum potassium level of at least 3.5 mmol/L.

The exclusion criteria were as follows: abnormal liver function with a serum bilirubin level of at least 1.5 times the upper limit of normal or an aspartate transaminase or alanine aminotransferase level of at least 2.5 times the upper limit of normal; uncontrolled hypertension; active viral hepatitis or chronic liver disease; a history of pituitary or adrenal dysfunction; clinically significant heart disease; other malignancies, except nonmelanoma skin cancer; known brain metastases; a history of gastrointestinal disorders that would interfere with absorption of orally administered hormonal agents; unresolved acute toxicities due to prior therapy; and current enrollment in an investigational drug or device study or participation in such a study within 30 d. Figure 1 shows a Standards for Reporting Diagnostic Accuracy (STARD) diagram of this study.

Imaging Protocol

Baseline ^{18}F-DCFPyL PET/CT was performed within 7 d of initiating abiraterone or enzalutamide therapy. Follow-up PET/CT was done between 2 and 4 mo after initiation of therapy. ^{18}F-DCFPyL was synthesized according to current good manufacturing practices as previously described (*14*). Patients were asked to be *nil per os* for 4 h before radiotracer administration. ^{18}F-DCFPyL (333 MBq [9 mCi]) was administered intravenously 60 ± 10 min before imaging. PET/CT from the mid thighs through the skull vertex was performed on one of several scanners: a 128-slice Biograph mCT (Siemens Healthineers), a 16-slice Biograph (Siemens Healthineers), or a 64-slice Discovery RX

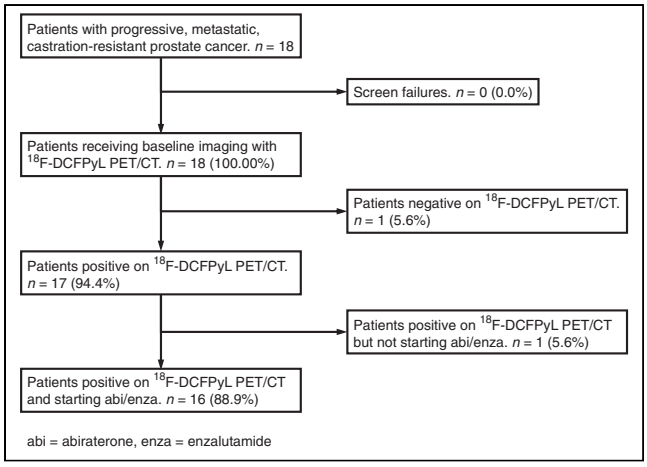

FIGURE 1. STARD diagram of study.

(GE Healthcare). The scanners were operated in 3-dimensional emission mode with CT attenuation correction. Standard ordered-subset expectation maximization reconstructions were used. All images were transferred to a central workstation for review. The baseline PET/CT is hereafter referred to as PET1 and follow-up PET/CT scan as PET2.

Within 2 wk of PET1 or PET2, respectively, baseline and follow-up conventional imaging (bone scanning and contrast-enhanced CT of the chest, abdomen, and pelvis) were performed.

Clinical Follow-up

PSA was assessed at baseline and at the time of follow-up imaging. The PSA response to therapy was considered significantly decreased (>50% PSA decrease), stable (≤50% decrease), or increased. Time to therapy change (TTTC, a surrogate for clinical progression) and overall survival (OS) were determined by review of the electronic medical record. TTTC was calculated as the number of days the patient was on a second-generation antiandrogen therapy until the primary treating oncologist determined that progression had occurred (based on standard-of-care imaging or laboratory or clinical assessment), the patient died, or the patient was lost to follow-up. OS was calculated as the number of days from initiation of second-generation antiandrogen therapy to death, loss to follow-up, or final date of censoring. Data were censored on April 20, 2020, 48 mo after the start of the study.

Image Analysis

A consensus central review was performed, with all images analyzed by 3 board-certified nuclear medicine physicians with experience in the interpretation of PSMA-targeted PET. The images were analyzed using an XD3 workstation (Mirada Medical). For each PET exam, the total number of ^{18}F-DCFPyL–positive disease sites, in addition to the location, size, and avidity (SUV_{max}) of each lesion, was recorded. The total tumor burden was defined as the total number of sites of ^{18}F-DCFPyL–positive disease. The change in avidity (SUV_{max}) for each lesion between PET1 and PET2, and the appearance of new lesions, were determined. The overall change in avidity between PET1 and PET2 was then classified into 1 of 5 categories: all-increased (all lesions increased in avidity), mixed-but-predominantly-increased (>50% of lesions increased in avidity, Fig. 2), mixed (same number of lesions increased in avidity as decreased in avidity), mixed-but-predominantly-decreased (>50% lesions decreased in avidity), and all-decreased (all lesions decreased in avidity). We defined 2 additional ^{18}F-DCFPyL PET parameters to semiquantitatively reflect change from PET1 to PET2. The first is Δ-percent SUV_{max} (DPSM), or the sum of the percentage change in SUV_{max} between PET1 and PET2 for ^{18}F-DCFPyL–positive disease sites (not including new lesions):

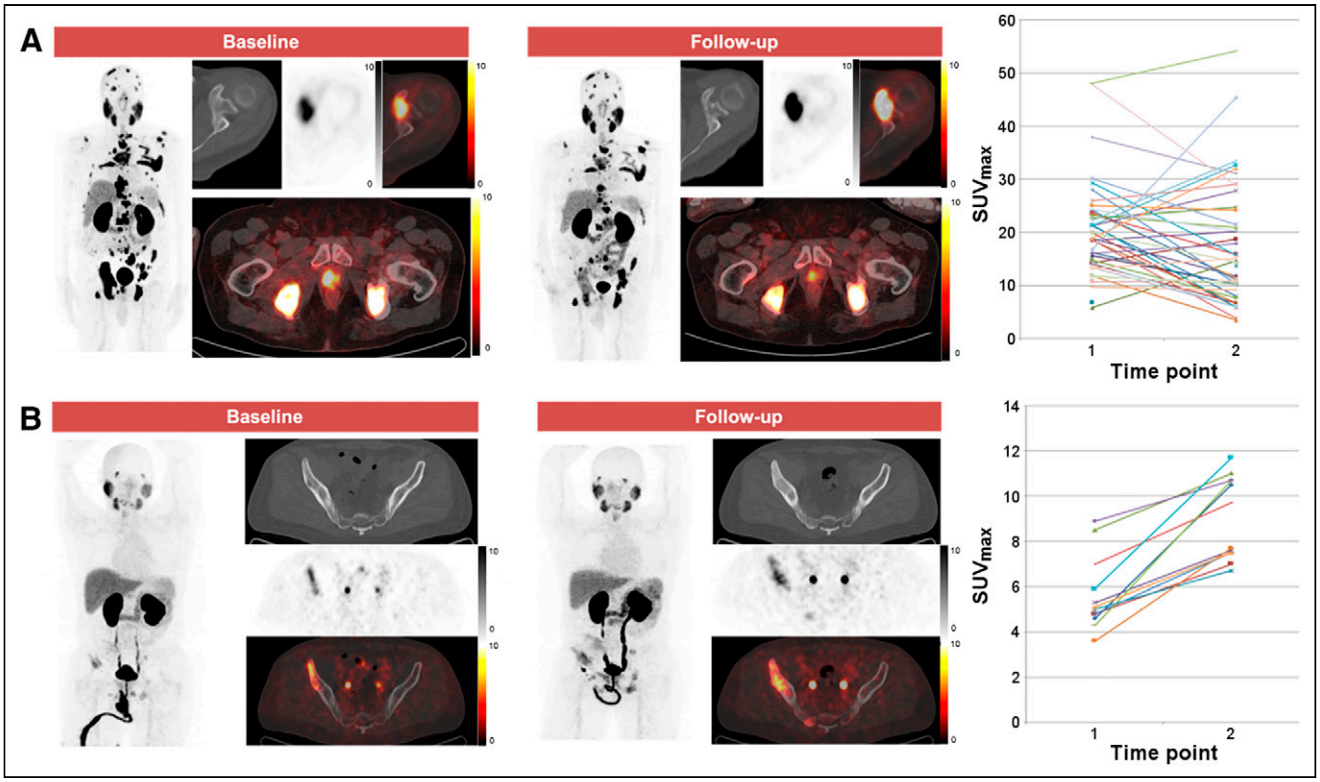

FIGURE 2. Examples of patterns of change in ^{18}F-DCFPyL uptake. (A) 72-y-old man with extensive metastatic castration-resistant PCa who developed mixed-but-predominantly-decreased pattern of uptake on PET2. This patient had TTTC of 9.3 mo and OS of 26.6 mo. (B) 52-y-old man with more limited metastatic castration-resistant PCa in whom pattern of all-increased uptake on PET2 was observed. This patient had TTTC of 7.1 mo and OS of 14.1 mo. In each subpanel, the maximum-intensity-projection image of the PET is shown followed by representative axial CT, PET, and PET/CT fused images.

$$\text{DPSM} = \sum \frac{(\text{SUV}_{\text{maxPET2}} - \text{SUV}_{\text{maxPET1}})}{\text{SUV}_{\text{maxPET1}}} \times 100.$$

The second is Δ-absolute SUV_{max} (DASM), or the sum of the absolute SUV_{max} change between PET1 and PET2 for ^{18}F-DCFPyL–positive disease sites (not including new lesions):

$$\text{DASM} = \sum \text{SUV}_{\text{maxPET2}} - \text{SUV}_{\text{maxPET1}}.$$

The conventional imaging obtained at the time of PET1 and PET2 was reviewed by the same readers. Using RECIST, version 1.1, and Prostate Cancer Clinical Trials Working Group 3 criteria all patients were classified as having response, stable disease, or progression at the PET2 time point.

Statistical Methods

Continuous variables are reported as median and interquartile range (IQR). Patients were classified into high and low groups based on median values. The cutoffs for DPSM, DASM, and number of lesions at baseline were 33, 556, and 13, respectively. To compare ^{18}F-DCFPyL PET/CT with conventional imaging, we treated DASM and DPSM above the median for this patient cohort as evidence of progression on PET. Kaplan–Meier curves were used to estimate TTTC and OS probabilities, and the univariate Cox proportional-hazards model was used to compare differences in TTTC and OS between the high and low groups. Kaplan–Meier curves were used instead of cumulative probability curves for TTTC because no deaths occurred before changes in therapy. All statistical tests were 2-sided, and statistical significance was set at a P value of less than or equal to 0.05. Analyses were performed in R, version 3.6.2 (*15*).

RESULTS

Patients

Between April 2016 and December 2016, 18 Caucasian men were enrolled (8 at Johns Hopkins and 10 through McMaster University–affiliated hospitals). One (6%) of the 18 had no visible

TABLE 1
Selected Demographic and Clinical Information for Patients Included in Analysis

Parameter	Data
Age (y)	71.5 (66.8–72.0)
Caucasian race	100%
PSA (ng/mL)	
PET1	24.0 (12.1–47.1)
PET2	11.0 (6.1–27.0)
Interval between PET1 and PET2 (d)	84 (70–91.5)
Therapy initiated	
Abiraterone	88%
Enzalutamide	13%

Qualitative data are percentages based on 16-patient sample size; continuous data are median and IQR. Mention of race is relevant in the context of prostate cancer because Black patients tend to have more aggressive underlying biology of disease and less access to health care in the United States.

TABLE 2
Selected Clinical and Imaging Data for Patients in This Study

Patient	Change in PSA (%)	DASM	DPSM	Overall change in avidity between PET1 and PET2	Conventional imaging radiologic progression	TTTC (mo)	OS (mo)
1	−71.8	+227.6	+3558.4	Mixed but predominantly increased	Yes	10.3	18.6
2	−1.6	−29.9	−462.5	All decreased	No	43.6	43.6
3	−53.3	−4.3	−38.4	Mixed	No	42.2	42.2
4	+146.5	+29.5	+1637.9	Mixed but predominantly increased	Yes	3.5	33.3
5	+63.5	+98.8	+1124.3	Mixed but predominantly increased	Yes	4.6	17.7
6	+146.9	+74.8	+2517.7	Mixed but predominantly increased	Yes	3.3	7.1
7	−57.7	+16.0	+87.2	All increased	No	12.8	37.8
8	−88.5	+40.5	+804.0	All increased	Yes	7.1	14.1
9	+87.5	+4.5	+13.2	All increased	No	11.9	47.8
10	−65.5	+13.4	+87.3	Mixed	No	14.4	45.8
11	−93.7	+3.5	+114.2	Mixed	No	11.4	29.1
12	+135.7	+171.8	+3107.9	Mixed but predominantly increased	Yes	6.2	13.4
13	−44.4	+36.6	+308.6	All Increased	No	10.4	29.4
14	−88.4	−138.4	−566.3	Mixed but predominantly decreased	Yes	9.3	26.6
15	+75.0	+275.1	+3223.7	Mixed but predominantly decreased	No	7.0	22.5
16	−68.2	+76.6	+1542.2	All increased	No	7.0	27.4

lesions on either ^{18}F-DCFPyL PET/CT scan and was excluded. Another (6%) underwent the PET1 scan but was not started on abiraterone or enzalutamide and was also excluded. For the 16 men who were analyzed, the median age was 71.5 y (IQR, 66.8–72.0 y). Serum PSA at the time of PET1 was 24.0 ng/mL (IQR, 12.1–47.1 ng/mL). Fourteen (88%) of the 16 men were started on abiraterone, and 2 (13%) were started on enzalutamide. Although not in the exclusion criteria, none of the patients had previously received either chemotherapy or a prior second-generation antiandrogen agent. Additional details are included in Table 1.

Clinical Follow-up

After therapy initiation, 10 (62.5%) of the 16 men had a serum PSA decrease, and in 8 (80%) of these 10 the decrease was more than 50%. For these 10 men, the median PSA at the first follow-up was 8.8 ng/dL (IQR, 5.5–13.4 ng/dL) and the median TTTC was 16.6 mo (IQR, 11.2–22.0 mo). Six men (38%) had a rise in PSA; for these men, the PSA at the first follow-up was 41.2 ng/mL (IQR, 17.3–54.3 ng/mL) and TTTC was 5.4 mo (IQR, 3.8–6.8 mo).

As of the final censoring date (April 20, 2020): 10 men had died, 4 remained alive, and 2 had been lost to follow-up. Of the 4 men who were still alive, 2 remained on therapy with abiraterone. The median time of follow-up was 28.2 mo (IQR, 18.4–38.9 mo).

^{18}F-DCFPyL PET/CT Image Analysis

Table 2 summarizes the clinical parameters and the corresponding PET findings.

Most of the men in our study, 12 (67%) of initial 18, had a high baseline ^{18}F-DCFPyL–avid metastatic tumor burden (5 or more ^{18}F-DCFPyL–positive lesions on PET1). Five (31%) had an all-increased pattern; 6 (38%), a mixed-but-predominantly-increased pattern; 3 (19%), a mixed pattern; 1 (6%), a mixed-but-predominantly-decreased pattern; and 1 (6%), an all-decreased pattern. A waterfall plot depicting the percentage change in PSA that occurred relative to the change in patterns of ^{18}F-DCFPyL uptake between PET1 and PET2 is shown in Figure 3.

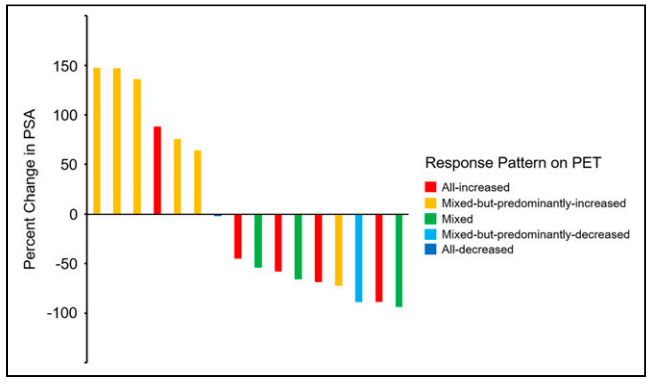

FIGURE 3. Waterfall plot demonstrating changes in PSA, color-coded according to changes in patterns of uptake on PET. Patient with smallest percentage change in PSA from baseline (seventh patient from left) is coded "all-decreased."

Nine (56%) of the 16 men who were analyzed had new sites of radiotracer uptake on PET2, and 5 (56%) had increased PSA. The median TTTC for the 9 men with new ^{18}F-DCFPyL PET–positive metastases was 7.0 mo (IQR, 4.6–9.3 mo). In comparison, of the 7 men without new ^{18}F-DCFPyL PET–positive metastases, only 1 (14%) had an increased PSA, and the median TTTC was 12.8 mo (IQR, 11.2–28.3 mo). All men (6/6, 100%) with increased PSA had either a mixed-but-predominantly-increased pattern (5/6, 83%) or an all-increased pattern (1/6, 17%) of PSMA-avid disease.

There were 6 men with mixed-but-predominantly-increased uptake on PET2, and this finding was associated with an unfavorable response to therapy, with a median TTTC of 5.4 mo (IQR, 3.8–6.8 mo). All had a high baseline tumor burden and a positive DPSM and DASM. Most subjects, 5 (83%) of 6, with a mixed-but-predominantly-increased pattern had an increased PSA and new ^{18}F-DCFPyL PET–positive sites of suspected metastases on follow-up. However, 1 man with an all-decreased pattern and a high metastatic tumor burden on baseline PET1 had a favorable therapy response with a prolonged TTTC (43.6 mo), a negative DPSM (−462.5), and a negative DASM (−29.9).

Across all men, the median TTTC was 9.6 mo (95% CI, 6.9–14.2 mo). Men with a positive and high (increasing avidity from PET1 to PET2) DPSM and DASM had an unfavorable therapy response with a shorter TTTC. As illustrated in Figure 4, there was a significant difference (P = 0.0001) in TTTC for men with an ^{18}F-DCFPyL PET–positive disease burden above the median DPSM (6.5 mo; 95% CI, 4.6 mo–NA) versus those below the median (12.2 mo; 95% CI, 11.3 mo–NA). The Cox model hazard ratio for high DPSM was 23.9 (95% CI, 2.8–203.1). In regard to DASM, for those men above the median the TTTC was 6.9 mo (95% CI, 6.1 mo–NA), versus 12.2 mo (95% CI, 11.3 mo–NA) for those below the median (P = 0.003). The Cox model hazard ratio for high DASM was 8.2 (95% CI, 1.7–40.5).

DPSM and DASM were also associated with OS (Fig. 5). Median OS across all patients was 28.6 mo (95% CI, 18.3 mo–NA). However, the median OS for men with an ^{18}F-DCFPyL PET–positive disease burden above the median DPSM was 17.8 mo (95% CI, 13.9 mo–NA), whereas the median OS for men below the median DPSM was 37.2 mo (95% CI, 28.9 mo–NA, P = 0.02; Fig. 5). The median OS for men with an ^{18}F-DCFPyL PET–positive disease burden above the median DASM was 17.8 mo (95% CI, 13.9 mo–NA), whereas for those below the median DASM it was NA (95% CI, 37.2 mo–NA), which was significant (P = 0.002). The Cox model hazard ratio for high DASM was 9.3 (95% CI, 1.8–47.9).

Stratifying patients by tumor burden suggests that the number of lesions at baseline was not associated with TTTC (Fig. 6). Although the separation of the survival curves suggests a longer OS based on a low number of lesions at baseline, this difference did not reach significance (P = 0.35).

Comparison to Conventional Imaging

Seven (44%) of 16 patients had progression by both RECIST 1.1 and the criteria of the Prostate Cancer Clinical Trials Working Group 3 on conventional imaging contemporaneous with PET2, whereas 7 (44%) had stable disease and 2 (13%) had a partial response. Of the 6 patients with rising PSA at the time of PET2, 4 (67%) had progression on conventional imaging. Of the 10 patients with decreasing PSA at the time of PET2, 3 (30%) had progression on conventional imaging.

Of the 5 patients who had an all-increased pattern of uptake on PET2, 1 (20%) demonstrated evidence of progression on conventional imaging. Of the 6 patients with mixed-but-predominantly-increased uptake on PET2, 5 (83%) had progression on conventional imaging. None of the patients with a mixed pattern of uptake had progression on conventional imaging. The 1 patient with a mixed-but-predominantly-decreased pattern of uptake on PET2 had progression on conventional imaging, and the 1 patient with an

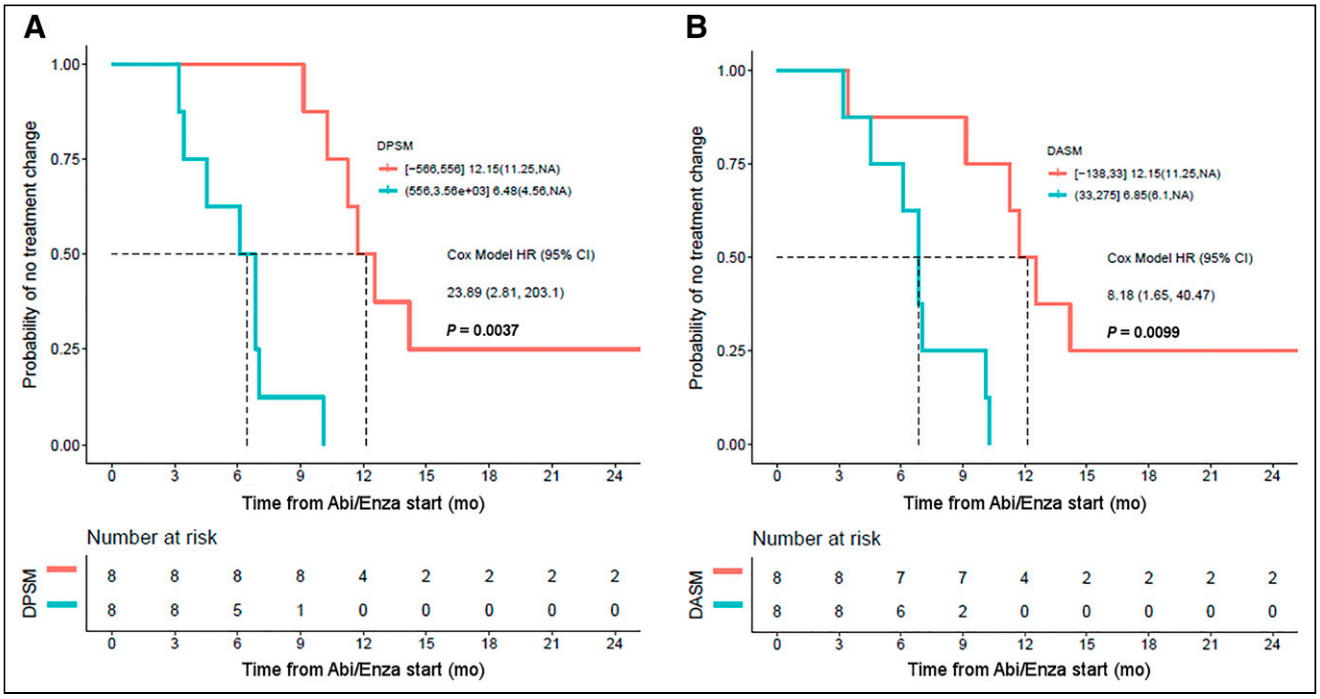

FIGURE 4. (A) Kaplan–Meier curve demonstrating that DPSM is associated with TTTC, with high DPSM corresponding to patients with shorter TTTC (blue curve) and low DPSM corresponding to patients with longer TTTC (orange curve). (B) Similar results were found with DASM. Abi/Enza = abiraterone/enzalutamide; HR = hazard ratio.

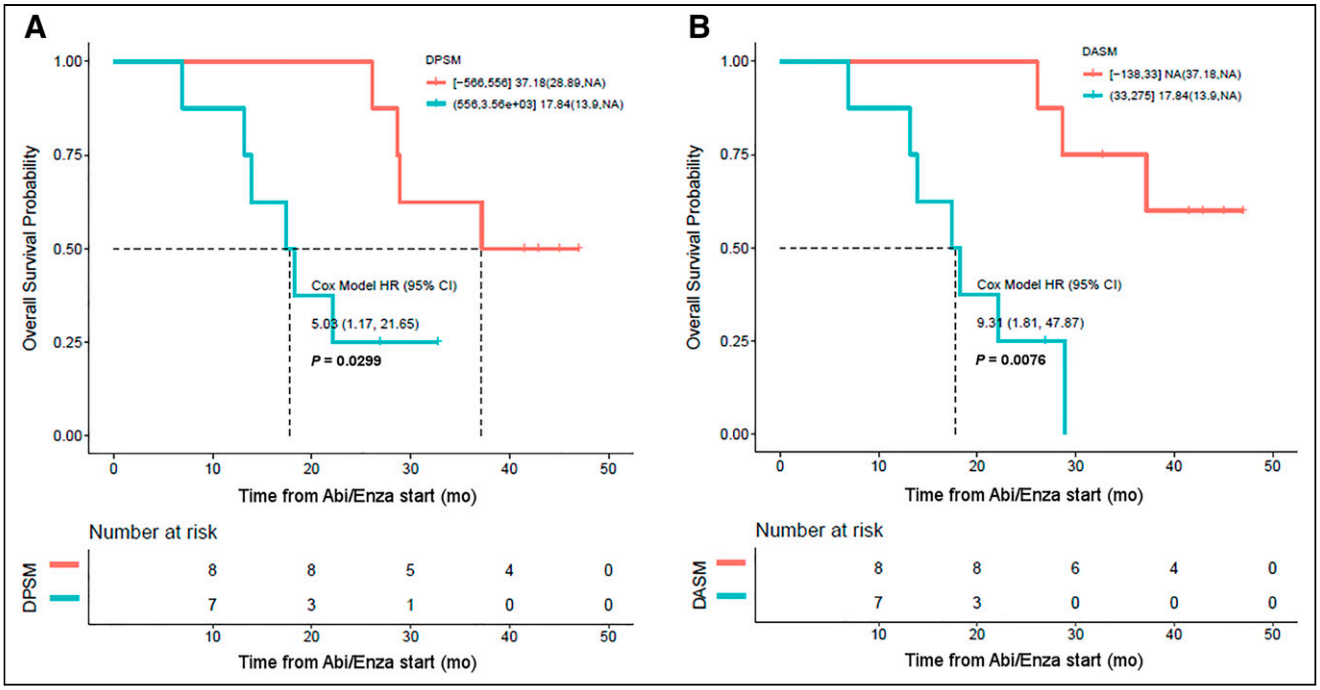

FIGURE 5. (A) Kaplan–Meier curve demonstrating that DPSM is associated with OS, with high DPSM corresponding to patients with shorter OS (blue curve) and low DPSM corresponding to patients with longer OS (orange curve). (B) Similar results were found with DASM. Abi/Enza = abiraterone/enzalutamide; HR = hazard ratio.

all-decreased pattern of uptake did not have progression on conventional imaging.

Of the 8 patients with a TTTC longer than the median, 1 (13%) had evidence of progression on conventional imaging at the time of PET2. Of the 8 patients with a TTTC shorter than the median, 6 (75%) had progression on conventional imaging. Of the 8 patients with an OS longer than the median, 1 (13%) also had progression on conventional imaging. Finally, of the 8 patients with an OS shorter than the median, 6 (75%) had progression on conventional imaging.

We considered a TTTC below the median as evidence of early progression. For detecting early progression, ^{18}F-DCFPyL PET had a sensitivity of 88%, specificity of 88%, and overall accuracy of 88%, and conventional imaging had a sensitivity of 63%, specificity of 75%, and overall accuracy of 69%.

DISCUSSION

PSMA-targeted PET is being increasingly used to evaluate PCa at the time of staging (*3*), to evaluate biochemical recurrence (*4*), and to guide therapy (*5*). However, to date, there are mixed data on the meaning of patterns of changing uptake with therapy on PSMA-targeted PET. The available data suggest there can be a complex interplay between androgen-targeted therapy, androgen receptor signaling, PSMA expression, and patient response to therapy in some imaging contexts (Table 3) (*10,11*).

Most of our subjects with castration-resistant PCa had a mixed PET response 2–4 mo after initiation of a second-generation antiandrogen agent, suggesting biologic heterogeneity between metastatic sites. We found that the imaging biomarkers associated with an unfavorable response to therapy on short-interval follow-up ^{18}F-DCFPyL

TABLE 3
Key Findings from Literature Regarding Presence or Absence of Flare Phenomenon on PSMA-Targeted PET on Initiation of Androgen-Axis Targeted Therapeutic Agents

Study	Patients (*n*)	Therapy initiated	Key results
Hope (*7*)	1	ADT	Flare on 4-wk follow-up scan
Afshar-Oromieh (*8*)	10	ADT	Long-term ADT, decreased conspicuity of lesions
Aggarwal (*10*)	8	ADT in 4 patients, enzalutamide in 4 patients	Variably observed heterogeneous flare
Emmett (*19*)	15	ADT in 8 patients, enzalutamide or abiraterone in 7 patients	Mix of flare and true progression
Plouznikoff (*11*)	26	Enzalutamide or abiraterone	No evidence of flare

ADT = androgen deprivation therapy.

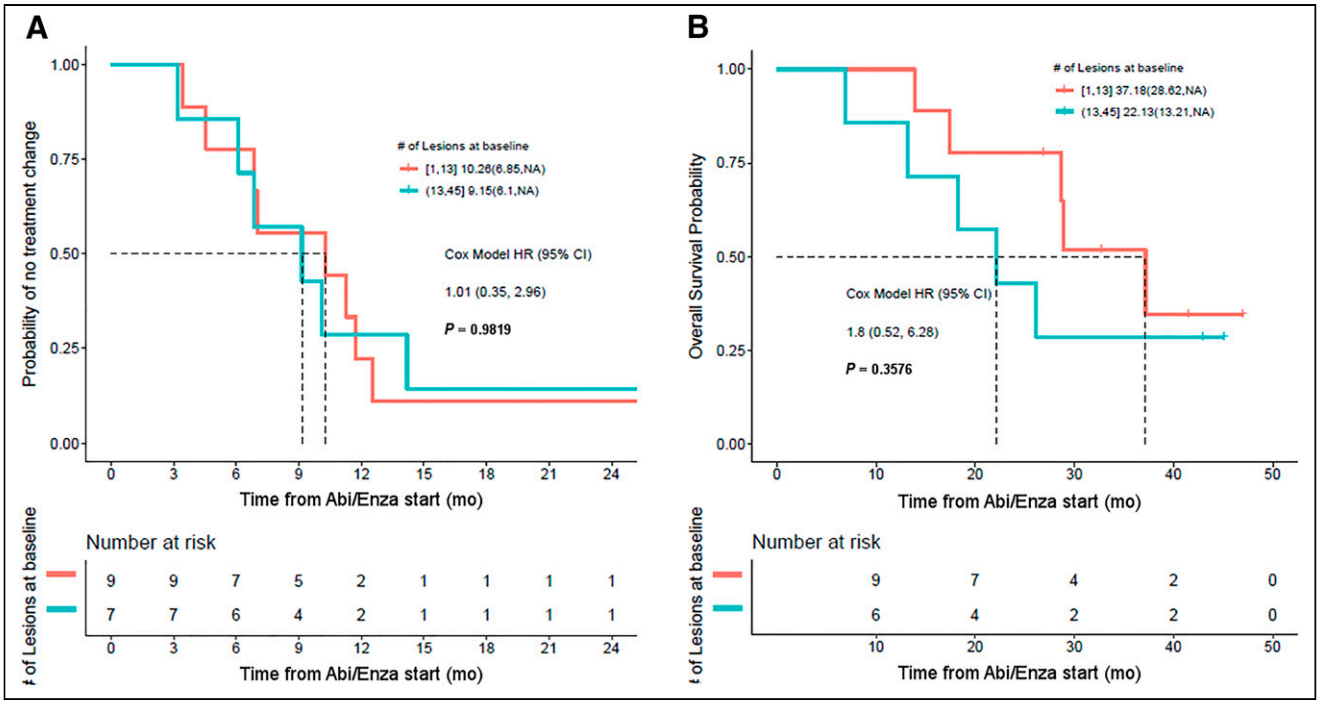

FIGURE 6. (A) Kaplan–Meier curves showing no difference in TTTC in patients with high PSMA-avid tumor burden at baseline (blue curve) and low PSMA-avid tumor burden at baseline (red curve). (B) Patients with lower baseline tumor burden also did not have significantly better OS. Abi/Enza = abiraterone/enzalutamide; HR = hazard ratio.

PET/CT included new sites of ^{18}F-DCFPyL PET–positive metastatic disease and overall increasing lesion uptake. The derived metrics DPSM and DASM were both associated with TTTC and OS: men with a net increase in ^{18}F-DCFPyL uptake across sites of disease on short-interval follow-up PET had a shorter TTTC and OS. Baseline ^{18}F-DCFPyL–avid tumor burden alone was not associated with outcomes. We also found that the sensitivity, specificity, and overall accuracy of ^{18}F-DCFPyL for detecting early progression (as defined by a short TTTC) were superior to those of conventional imaging.

The subset of 6 men with mixed but predominantly increasing ^{18}F-DCFPyL uptake at sites of disease from PET1 to PET2 had the worst outcomes. These patients all had positive DPSM and DASM parameters; most had new lesions as well as increasing PSA at follow-up. Five of the next 6 patients with the shortest TTTC had increasing uptake at all sites of disease. Most of those men presented with concurrently increased PSA at follow-up, suggesting that although some sites of disease may be increasing in avidity because of flare, increasing overall uptake suggests disease progression. Granted, there do appear to be men who have increased uptake on PSMA-targeted PET after therapy initiation, in the context of an initial decrease in PSA, who may have a flare phenomenon (*10*). However, increased uptake or more conspicuous lesions on PSMA-targeted PET after the initiation of a second-generation antiandrogen must be interpreted with caution. Lastly, patients with a mixed or mixed-but-predominantly decreasing pattern of uptake had a relatively prolonged TTTC and OS.

Interval changes in PSMA-targeted PET avidity and metastatic pattern in patients starting second-generation antiandrogen agents are likely multifactorial. The changes may be due to modulation of PSMA expression by androgen receptor signaling (*6*), tumor cell death as a result of response to therapy (*8*), loss of PSMA expression as cells differentiate toward a neuroendocrine phenotype (*16*), loss of PSMA expression in advanced adenocarcinoma (*17*), or alternative splicing variants and other aberrations that limit the interaction of androgen signaling with PSMA (*18*). Because of this inherent complexity, correlation with pathology and tissue sampling may be helpful in future studies.

The primary limitation of this study was the relatively small sample size. Additional larger, prospective studies with long-term follow-up are needed to more definitively address the causes of the uptake patterns observed with PSMA-targeted PET. Further, the endpoint of TTTC does not necessarily reflect progression, although it should be a reliable surrogate for clinical progression barring an intolerable toxicity. The use of both DPSM and DASM could be viewed as overly complex, however both of these metrics can be derived with relative ease with modern software and we were unable to statistically demonstrate that one was superior to the other. Lastly, given the exposure limitations allowed by the Food and Drug Administration for investigational radiotracers, only 2 time points could be obtained in this study. Additional PET scans at later time points would be helpful to understand the prognostic implications of changes in PSMA-targeted radiotracer uptake with time.

CONCLUSION

Short-interval follow-up PET (2–4 mo) after initiation of treatment with a second-generation antiandrogen improves detection of progression. Men with increased uptake or new lesions on early interval PET may be experiencing progression rather than flare and may require alternative therapy.

DISCLOSURE

Funding for this study was received from the Movember Foundation, the Prostate Cancer Foundation Young Investigator Award, and National Institutes of Health grants CA134675, CA184228, EB024495, and CA183031. Martin Pomper is a coinventor on a

U.S. patent covering ^{18}F-DCFPyL and as such is entitled to a portion of any licensing fees and royalties generated by this technology. This arrangement has been reviewed and approved by the Johns Hopkins University in accordance with its conflict-of-interest policies. Steven Rowe and Steve Cho are consultants for Progenics Pharmaceuticals, Inc., the licensee of ^{18}F-DCFPyL. Michael Gorin has served as a consultant for Progenics Pharmaceuticals, Inc. Martin Pomper, Michael Gorin, and Steven Rowe have received research funding from Progenics Pharmaceuticals, Inc. No other potential conflict of interest relevant to this article was reported.

KEY POINTS

QUESTION: Can PSMA-targeted PET detect early progression and provide prognostic information about men starting abiraterone or enzalutamide?

PERTINENT FINDINGS: PSMA-targeted PET improves detection of progression relative to conventional imaging. New lesions or increasing apparent tumor burden on PSMA-targeted PET are poor prognostic findings.

IMPLICATIONS FOR PATIENT CARE: Men starting treatment with abiraterone or enzalutamide who have an increasing number of lesions or increased uptake in existing lesions on PSMA-targeted PET may need alternative therapy.

REFERENCES

1. Rowe SP, Gorin MA, Allaf ME, et al. PET imaging of prostate-specific membrane antigen in prostate cancer: current state of the art and future challenges. 2016;19: 223–230.
2. Bostwick DG, Pacelli A, Blute M, et al. Prostate specific membrane antigen expression in prostatic intra-epithelial neoplasia and adenocarcinoma: a study of 184 cases. *Cancer.* 1998;82:2256–2261.
3. Gorin MA, Rowe SP, Patel HD, et al. Prostate specific membrane antigen targeted ^{18}F-DCFPyL positron emission tomography/computerized tomography for the preoperative staging of high risk prostate cancer: results of a prospective, phase II, single center study. *J Urol.* 2018;199:126–132.
4. Markowski MC, Sedhom R, Fu W, et al. PSA and PSA doubling time predict findings on ^{18}F-DCFPyL PET/CT in patients with biochemically-recurrent prostate cancer. *J Urol.* 2020;204:496–502.
5. Hofman MS, Violet J, Hicks RJ, et al. [^{177}Lu]-PSMA-617 radionuclide treatment in patients with metastatic castration-resistant prostate cancer (LuPSMA trial): a single-centre, single-arm, phase 2 study. *Lancet Oncol.* 2018;19:825–833.
6. Evans MJ, Smith-Jones PM, Wongvipat J, et al. Noninvasive measurement of androgen receptor signaling with a positron-emitting radiopharmaceutical that targets prostate-specific membrane antigen. *Proc Natl Acad Sci USA.* 2011;108: 9578–9582.
7. Hope TA, Truillet C, Ehman EC, et al. ^{68}Ga-PSMA-11 PET imaging of response to androgen receptor inhibition: first human experience. *J Nucl Med.* 2017; 58:81–84.
8. Afshar-Oromieh A, Debus N, Uhrig M, et al. Impact of long-term androgen deprivation therapy on PSMA ligand PET/CT in patients with castration-sensitive prostate cancer. *Eur J Nucl Med Mol Imaging.* 2018;45:2045–2054.
9. Zukotynski KA, Valliant J, Bénard F, et al. Flare on serial prostate-specific membrane antigen-targeted ^{18}F-DCFPyL PET/CT examinations in castration-resistant prostate cancer: first observations. *Clin Nucl Med.* 2018;43:213–216.
10. Aggarwal R, Wei X, Kim W, et al. Heterogeneous flare in prostate-specific membrane antigen positron emission tomography tracer uptake with initiation of androgen pathway blockade in metastatic prostate cancer. *Eur Urol Oncol.* 2018;1:78–82.
11. Plouznikoff N, Artigas C, Sideris S, et al. Evaluation of PSMA expression changes on PET/CT before and after initiation of novel antiandrogen drugs (enzalutamide or abiraterone) in metastatic castration-resistant prostate cancer patients. *Ann Nucl Med.* 2019;33:945–954.
12. Fanti S, Hadaschik B, Herrmann K. Proposal for systemic-therapy response-assessment criteria at the time of PSMA PET/CT imaging: the PSMA PET progression criteria. *J Nucl Med.* 2020;61:678–682.
13. Szabo Z, Mena E, Rowe SP, et al. Initial evaluation of [^{18}F]DCFPyL for prostate-specific membrane antigen (PSMA)-targeted PET imaging of prostate cancer. *Mol Imaging Biol.* 2015;17:565–574.
14. Ravert HT, Holt DP, Chen Y, et al. An improved synthesis of the radiolabeled prostate-specific membrane antigen inhibitor [^{18}F]DCFPyL. *J Labelled Comp Radiopharm.* 2016;59:439–450.
15. The R project for statistical computing. R Project website. https://www.R-project.org/. Accessed May 25, 2021.
16. Tosoian JJ, Gorin MA, Rowe SP, et al. Correlation of PSMA-targeted ^{18}F-DCFPyL PET/CT findings with immunohistochemical and genomic data in a patient with metastatic neuroendocrine prostate cancer. *Clin Genitourin Cancer.* 2017;15:e65–e68.
17. Sheikhbahaei S, Werner RA, Solnes LB, et al. Prostate-specific membrane antigen (PSMA)-targeted PET imaging of prostate cancer: an update on important pitfalls. *Semin Nucl Med.* 2019;49:255–270.
18. Antonarakis ES, Lu C, Wang H, et al. AR-V7 and resistance to enzalutamide and abiraterone in prostate cancer. *N Engl J Med.* 2014;371:1028–1038.
19. Emmett L, Yin C, Crumbaker M, et al. Rapid modulation of PSMA expression by androgen deprivation: serial ^{68}Ga-PSMA-11 PET in men with hormone-sensitive and castrate-resistant prostate cancer commencing androgen blockade. *J Nucl Med.* 2019;60:950–954.

RESIST-PC: U.S. Academic Foray into PSMA Theranostic Trials

Amir Iravani[1] and Thomas A. Hope[2]

[1]*Mallinckrodt Institute of Radiology, Washington University in St. Louis, St. Louis, Missouri; and* [2]*Department of Radiology and Biomedical Imaging, University of California San Francisco, San Francisco, California*

See the associated article on page 1440.

In this issue of *The Journal of Nuclear Medicine,* Calais et al. from UCLA present the results of their phase 2 RESIST-PC trial (*1*). This trial predated the VISION trial and enrolled patients prospectively in a 2-arm study intended to compare the efficacy and safety of ^{177}Lu-PSMA-617 dosed at either 6.0 or 7.4 GBq (*2*). The study was performed collaboratively between UCLA and Excel Diagnostics, although only the 43 patients enrolled at UCLA are presented in the article. The UCLA team must be commended for the effort in initiating and performing this study without company support. The effort required to open the first ^{177}Lu-PSMA trial in the United States cannot be understated.

The absence of support for this study required that a cost recovery mechanism be used, something that is not commonly leveraged for therapeutic trials. Unlike in the Australian phase 2 study (*3*), in which the ^{177}Lu was provided free of charge from the Australian Nuclear Science and Technology Organization, the study team had to procure ^{177}Lu at cost. Prior diagnostic cost-recovery trials led to the approval of both ^{68}Ga-DOTATOC and ^{68}Ga-PSMA-11 (*4*,*5*). It may seem odd that there was no corporate support for this study given the large interest in the field we see today, but at the time of trial design, there was limited corporate interest. Similar to cost recovery, many European studies have leveraged compassionate use in the absence of company support (*6*).

Looking at the results presented for the RESIST-PC trial, the prostate-specific antigen (PSA) response (≥50% PSA decline) was 37%, which is lower than reported in the LuPSMA (64%) and TheraP (66%) trials (*1*,*3*,*7*). Although the inclusion criterion for prostate-specific antigen (PSMA) expression was not predefined in the RESIST-PC trial, the difference in PSA response may be accounted for by a lower threshold of PSMA PET avidity. The LuPSMA trial required an SUV_{max} that was one and a half times that of the liver, whereas the TheraP trial required an SUV_{max} of 20 at one site and no measurable disease below an SUV_{max} of 10. In addition, the LuPSMA and TheraP trials used ^{18}F-FDG PET/CT to exclude patients with disease heterogeneity and sites of disease demonstrating low PSMA expression. In the LuPSMA and TheraP trials, 25%–30% of patients were excluded, whereas in the RESIST-PC trial only 2 patients (<5%) were excluded on the basis of PSMA expression. PSMA expression is critical, as shown by Violet et al., who demonstrated a positive correlation between pretreatment PSMA uptake and posttreatment dosimetry on a whole-body scale, and as further supported by Seifert et al., who showed that low average PSMA expression is a negative prognostic factor (*8*,*9*).

The VISION trial used a lower cutoff of a PSMA-positive lesion greater than liver uptake with no negative PSMA lesions, which resulted in 13% of patients being excluded, more than twice as many as in the RESIST-PC study (*2*). In the VISION trial, 46% of patients treated with ^{177}Lu-PSMA-617 had a greater than 50% reduction, a PSA response rate between the RESIST-PC trial and the TheraP/LuPSMA studies, again supporting the idea that the higher the cutoff for PSMA positivity combined with ^{18}F-FDG imaging, the better the response to treatment (*2*).

Although it appears that the higher threshold for PSMA avidity would result in a higher response rate, the threshold of PSMA avidity below which the patients may not respond to treatment remains unclear. It is also possible that patients with a limited volume of the discordant ^{18}F-FDG–avid disease may derive some benefit from ^{177}Lu-PSMA, subject to sufficient PSMA expression at other sites and as long as a more intensive therapeutic strategy is adopted. This possibility may support the combination with other oncologic treatments to tackle sites that may have been suboptimally targeted by ^{177}Lu-PSMA. Multiple phase I/II combination regimens are under way using immunotherapy (NCT03658447, NCT03805594), poly(adenosine diphosphate-ribose) polymerase inhibitor (NCT03874884), androgen receptor-targeted therapy (NCT04419402), and even tandem treatment with chemotherapy in the castration-sensitive state (NCT03828838).

A separate issue with ^{177}Lu-PSMA therapy is that the optimal treatment schedule is not well understood, including the administered activity per cycle, the interval between treatments, and the number of treatments/cumulative activity (*10*). The choice of a fixed administered activity of between 6 and 8 GBq and up to 6 cycles is based predominantly on the limits of normal-organ absorbed dose and thresholds extrapolated from external-beam radiotherapy, ignoring fundamental differences in the radiobiology of radiopharmaceutical therapies. One of the most interesting aspects of RESIST-PC was that it attempted to determine the difference in efficacy and toxicity between 2 different doses of

Received June 3, 2021; revision accepted July 21, 2021.

For correspondence or reprints, contact Thomas A. Hope (thomas.hope@ucsf.edu).

^{177}Lu-PSMA-617, although the narrow difference between the doses and the premature closure of the study prevented the team from determining which dose was superior. Determination of the appropriate number of cycles, dose per cycle, and timing between cycles still remains an art form in radioligand therapy, although it is under study; for example, Weill Cornell is studying 2 higher dose cycles (up to 11.1 GBq) given 2 wk apart (NCT03042468).

It seems self-evident that straying from the rigid treatment plans used in these trials would be beneficial. Examples to consider include continuing therapy beyond 6 cycles in a subset of patients that continues to benefit from treatment, increasing intervals beyond 6–8 wk in early responders, or rechallenging treatment at the time of progression, subject to sufficient target expression (*11*). Furthermore, incorporating posttreatment dosimetry will enhance our understanding of differences in absorbed doses in tumor and critical organs and how they impact patient outcome. Although the oversimplified approach of one size fits all would expedite the approval and increase the accessibility of this treatment, these advantages should not hinder exploiting the fundamental strengths of this treatment modality that allows individualizing the treatment on the basis of the patient's characteristics and tumor biology, as well as dynamically modifying the treatment schedule on the basis of response and posttreatment dosimetry.

It is unfortunate that completion of the RESIST-PC study was halted when the VISION trial started enrollment, as evaluating the difference between 2 different doses would have provided valuable information to the community. As we patiently await the approval of ^{177}Lu-PSMA-617 in light of the positive overall survival data from the VISION study, we would like to encourage members of the nuclear medicine community to develop and engage in multiinstitutional trials and to participate in National Cancer Institute cooperative groups, similar to what has proven successful in Australia.

DISCLOSURE

Thomas A. Hope is a consultant for Curium, and he received fees from Blue Earth Diagnostics and Ipsen outside the submitted work. No other potential conflict of interest relevant to this article was reported.

REFERENCES

1. Calais J, Gafita A, Eiber MR, et al. Prospective phase 2 trial of PSMA-targeted molecular radiotherapy with ^{177}Lu-PSMA-617 for metastatic castration-resistant prostate cancer (RESIST-PC): efficacy results of the UCLA cohort. *J Nucl Med.* 2021;62:1440–1446.
2. Sartor O, de Bono J, Chi KN, et al. Lutetium-177–PSMA-617 for metastatic castration-resistant prostate cancer. *N Engl J Med.* June 23, 2021 [Epub ahead of print].
3. Hofman MS, Sandhu S, Eu P, et al. Lutetium-177 PSMA (LuPSMA) theranostics phase II trial: efficacy, safety and QoL in patients with castrate-resistant prostate cancer treated with LuPSMA. *Ann Oncol.* 2017;28(suppl 5):v270.
4. Sartor O, Hope TA, Calais J, Fendler WP. Oliver Sartor talks with Thomas A. Hope, Jeremie Calais, and Wolfgang P. Fendler about FDA approval of PSMA. *J Nucl Med.* 2021;62:146–148.
5. Sunderland JJ. The academic NDA: justification, process, and lessons learned. *J Nucl Med.* 2020;61:480–487.
6. Rahbar K, Ahmadzadehfar H, Kratochwil C, et al. German multicenter study investigating ^{177}Lu-PSMA-617 radioligand therapy in advanced prostate cancer patients. *J Nucl Med.* 2017;58:85–90.
7. Hofman MS, Goh JC, Tan TH, et al. [^{177}Lu]Lu-PSMA-617 versus cabazitaxel in patients with metastatic castration-resistant prostate cancer (TheraP): a randomised, open-label, phase 2 trial. *Lancet.* 2021;397:797–804.
8. Seifert R, Seitzer K, Herrmann K, et al. Analysis of PSMA expression and outcome in patients with advanced prostate cancer receiving ^{177}Lu-PSMA-617 radioligand therapy. *Theranostics.* 2020;10:7812–7820.
9. Violet J, Jackson P, Ferdinandus J, et al. Dosimetry of ^{177}Lu-PSMA-617 in metastatic castration-resistant prostate cancer: correlations between pretherapeutic imaging and whole-body tumor dosimetry with treatment outcomes. *J Nucl Med.* 2019;60:517–523.
10. Iravani A, Violet J, Azad A, Hofman MS. Lutetium-177 prostate-specific membrane antigen (PSMA) theranostics: practical nuances and intricacies. *Prostate Cancer Prostatic Dis.* 2020;23:38–52.
11. Violet J, Sandhu S, Iravani A, et al. Long-term follow-up and outcomes of retreatment in an expanded 50-patient single-center phase II prospective trial of 177Lu-PSMA-617 theranostics in metastatic castration-resistant prostate cancer. *J Nucl Med.* 2020;61:857–865.

Prospective phase 2 trial of PSMA-targeted molecular RadiothErapy with ^{177}Lu-PSMA-617 for metastatic castration-reSISTant Prostate Cancer (RESIST-PC): efficacy results of the UCLA cohort

Jeremie Calais[1–4], Andrei Gafita[1], Matthias Eiber[1,5], Wesley R. Armstrong[1], Jeannine Gartmann[1], Pan Thin[1], Kathleen Nguyen[1], Vincent Lok[1], Laura Gosa[1], Tristan Grogan[6], Rouzbeh Esfandiari[7], Martin Allen-Auerbach[1,3,4], Andrew Quon[1,3,4], Shadfar Bahri[1,3,4], Pawan Gupta[1], Linda Gardner[1], David Ranganathan[8], Roger Slavik[1], Magnus Dahlbom[1,2], Ken Herrmann[1,9], Ebrahim Delpassand[7,8], Wolfgang P. Fendler[1,9], and Johannes Czernin[1,3,4]

[1]Ahmanson Translational Theranostics Division, Department of Molecular & Medical Pharmacology, University of California Los Angeles, Los Angeles, California; [2]Physics & Biology in Medicine Interdepartmental Graduate Program, David Geffen School of Medicine, University of California Los Angeles, Los Angeles, California; [3]Institute of Urologic Oncology, University of California Los Angeles, Los Angeles, California; [4]Jonsson Comprehensive Cancer Center, University of California Los Angeles, Los Angeles, California; [5]Department of Nuclear Medicine, Technical University Munich, Klinikum rechts der Isar, Munich, Germany; [6]Department of Medicine Statistics Core, David Geffen School of Medicine, University of California Los Angeles, Los Angeles, California; [7]Excel Diagnostics and Nuclear Oncology Center, Houston, Texas; [8]RadioMedix, Inc., Houston, Texas; and [9]Department of Nuclear Medicine, University of Duisburg-Essen and German Cancer Consortium (DKTK)-University Hospital Essen, Essen, Germany

See an invited perspective on this article on page 1438.

The objective of this study was to determine prospectively the efficacy profile of 2 activity regimens of ^{177}Lu-PSMA therapy in patients with progressive metastatic castrate-resistant prostate cancer (mCRPC): 6.0 vs. 7.4 GBq. **Methods:** RESIST-PC (NCT03042312) was a prospective multicenter phase 2 trial. Patients with progressive mCRPC after ≥ 1 novel androgen-axis drug, either chemotherapy naïve or postchemotherapy, with sufficient bone marrow reserve, normal kidney function, and sufficient PSMA expression by PSMA PET were eligible. Patients were randomized (1:1) into 2 activity groups (6.0 or 7.4 GBq) and received up to 4 cycles every 8 wk. The primary endpoint was the efficacy of ^{177}Lu-PSMA measured by the prostate-specific antigen (PSA) response rate (RR) after 2 cycles (≥50% decline from baseline). Secondary endpoints included the PSA RR (≥50% decline) at any time (best response), and overall survival (OS). **Results:** The study was closed at enrollment of 71/200 planned patients because of sponsorship transfer. We report here the efficacy of the University of California Los Angeles cohort results only (n = 43). The PSA RRs after 2 cycles and at any time were 11/40 (28%, 95% CI 15–44), 6/13 (46%, 95% CI 19–75), and 5/27 (19%, 95% CI 6–38), and 16/43 (37%, 95% CI 23–53), 7/14 (50%, 95% CI 23–77), and 9/29 (31%, 95% CI 15–51) in the whole cohort, the 6.0-GBq group, and the 7.4-GBq group, respectively (P = 0.12 and P = 0.31). The median OS was 14.0 mo (95% CI 10.1–17.9), 15.8 (95% CI 11.8–19.4), and 13.5 (95% CI 10.0–17.0) in the whole cohort, the 6.0-GBq group, and the 7.4 GBq group, respectively (P = 0.87). OS was longer in patients who experienced a PSA decline ≥ 50% at any time than in those who did not: median, 20.8 versus 10.8 mo (P = 0.005). **Conclusion:** In this prospective phase 2 trial of ^{177}Lu-PSMA for mCRPC, the median OS was 14 mo. Despite the heterogeneous study population and the premature study termination, the efficacy profile of ^{177}Lu-PSMA appeared to be favorable and comparable with both activity regimens (6.0 vs. 7.4 GBq). Results justify confirmation with real-world data matched-pair analysis and further clinical trials to refine and optimize the ^{177}Lu-PSMA therapy administration scheme to improve tumor radiation dose delivery and efficacy.

Key Words: metastatic castration-resistant prostate cancer; radionuclide therapy; molecular radiotherapy; prostate-specific membrane antigen; ^{177}Lu; RESIST-PC; prospective randomized phase 2 trial; theranostics

J Nucl Med 2021; 62:1440–1446
DOI: 10.2967/jnumed.121.261982

The prostate-specific membrane antigen (PSMA) is highly expressed by prostate cancer (PCa) cells and is a relevant target for PCa imaging and therapy. ^{177}Lu PSMA-617 (^{177}Lu-PSMA) therapy is an emerging therapeutic option in men with metastatic castrate-resistant PCa (mCRPC). Retrospective studies (*1–3*) and recent prospective trials from Australia (single-arm LuPSMA trial (*4*,*5*), randomized TheraP trial (*6*)) reported the efficacy and safety of ^{177}Lu-PSMA in men with mCRPC.

Here we present the first U.S. prospective results of ^{177}Lu-PSMA (RESIST-PC, NCT03042312). This multicenter prospective phase 2 study investigated the efficacy and safety of ^{177}Lu-PSMA in patients who were randomized between 2 commonly used activity regimens: 6.0 GBq and 7.4 GBq. We hypothesized that the 2 activities result in comparable antitumor effects and safety profile. This study is the first attempt to compare prospectively 2 activity regimens of ^{177}Lu-PSMA therapy.

The study was investigator-initiated and self-funded, but the development rights of PSMA-617 were acquired by Endocyte Inc.

Received Jan. 20, 2021; revision accepted May 13, 2021.
For correspondence or reprints, contact Jeremie Calais (jcalais@mednet.ucla.edu).
Guest Editor: Todd Peterson, Vanderbilt University.
Published online May 20, 2021.

during the enrollment phase and the study was closed before reaching the target population. Therefore, data acquisition and analysis as initially planned was not possible. The safety results of both study sites were used for regulatory approval and will be reported separately. We report here the efficacy results of the University of California Los Angeles (UCLA) single study-site cohort with more than 2 y of follow-up after end of therapy.

MATERIALS AND METHODS

Study Design

RESIST-PC was a prospective, randomized, open-label, multicenter phase 2 study conducted at UCLA (Los Angeles, CA, USA) and Excel Diagnostics Nuclear Oncology Center (Houston, TX, USA). We aimed at assessing the efficacy and safety of 2 ^{177}Lu-PSMA activity regimens in patients with mCRPC. The study was investigator-initiated and conducted under a physician-sponsored investigational new drug (IND#133661) application. There was no external funding for this study. Patients were charged for the drug under Title 21 of the Code of Federal Regulation Section (CFR) 312.8. The UCLA institutional review board approved the study protocol (IRB#17-000330) provided in the supplemental materials (supplemental materials are available at http://jnm.snmjournals.org). The study was registered on ClinicalTrials.gov (NCT03042312). Endocyte Inc. licensed the rights to the study drug, initiated a prospective international multicenter trial (VISION; NCT03511664), and closed RESIST-PC at a total enrollment of 71 of the 200 planned patients at both sites (see the "Statistical Analysis" section for rationale of sample size). Here we report the efficacy results of the UCLA cohort only ($n = 43$). The corresponding author had complete data access and had final responsibility to submit for publication.

Patients

Patients ≥ 18 y, who had histologically confirmed PCa, castrate levels of serum testosterone (<0.5 ng/mL), progressive disease (biochemical, radiographic, or clinical), who had received abiraterone or enzalutamide, had an Eastern Cooperative Oncology Group (ECOG) performance-status score of 0 to 2, and had the ability to understand and sign the written informed consent form were eligible. We included patients without prior chemotherapy or with any number of prior chemotherapies if at least 6 wk passed since the last treatment cycle. Patients who had received PSMA-targeted radionuclide therapy were excluded. Pretreatment PSMA PET was required to document sufficient target expression (see the "Procedures" section). Additional inclusion criteria were a sufficient bone marrow reserve (hemoglobin ≥ 9.9 g/dL, platelet count $\geq 100 \times 10^9$/L, white blood cell count $\geq 2.5 \times 10^9$/L, and absolute neutrophil count $\geq 1.5 \times 10^9$/L). Patients with diffuse bone involvement by bone scintigraphy (superscan), impaired kidney function (glomerular filtration rate < 40 mL/min, serum creatinine > 1.5×upper limit of normal [ULN], urinary tract obstruction, or marked hydronephrosis), or impaired liver function (aspartate aminotransferase [AST] and alanine aminotransferase [ALT] > 5×ULN) were excluded. Informed written and verbal consent was obtained from all patients.

Procedures

All patients underwent a screening ^{68}Ga-PSMA-11 PET/CT scan (≤3 mo before enrollment) to confirm PSMA expression assessed visually by the local investigators (tumor uptake above the liver background). Patients with PSMA-negative soft-tissue lesions seen on conventional scans (CT, MRI) were excluded (screening failure). Complete blood counts, kidney and liver function, and serum prostate-specific antigen (PSA) levels were measured within 2 wk of treatment initiation.

Patients were randomized (1:1 ratio) to receive either 6.0 or 7.4 GBq of ^{177}Lu-PSMA. Randomization (1:1 ratio) was performed in accordance with Vickers et al. (*7*) We concealed allocation by creating a list of random allocations for patients 1 to 200 and stored it at the investigator's site without modification. A clinical research coordinator who was not involved in clinical management assigned the randomized allocation. There was no masking of patients or physicians.

^{177}Lu-PSMA-617 was radiolabeled with carrier-free ^{177}Lu (RadioMedix, Inc.). The labeled product was produced, tested, released, and delivered under good-manufacturing-practice conditions as a sterile, ready-to-use solution for infusion.

^{177}Lu-PSMA was intravenously applied at 8-wk intervals (±1 wk) up to a maximum of 4 cycles (cycle 02 at wk 08; cycle 03 at wk 16; cycle 04 at wk 24). Treatment cycles continued until disease progression, severe toxicity occurred, patients withdrew consent, or investigators decided to discontinue treatment.

We performed hematologic and serum assessments at baseline and in 2-wk intervals up to the 12-wk follow-up visit after the last study drug injection. We measured serum PSA levels at baseline and every 6 wk. Subsequent assessments continued at 3-mo intervals until follow-up concluded at 24 mo or on disease progression.

Bone pain intensity was assessed at each cycle using the pain intensity score, a component of the Brief Pain Inventory–Short Form (*8*): scores ranged from 0 to 10, with lower scores representing lower levels of pain intensity; a change of 2 was required to consider a change relevant (*9*).

Because of cost considerations (no follow-up imaging was built in the study budget), imaging follow-up was performed by patient and referring oncologist preference. Because of the lack of standardization, effective conclusions could not be assured. The imaging follow-up analysis (methods, radiographic progression-free survival, disease control rate by imaging) is provided in the supplemental materials.

Outcomes

The primary endpoint measure was the PSA response rate (RR) after 2 cycles defined as the proportion of patients with a ≥ 50% decline in serum PSA levels from baseline (*10*).

Secondary endpoints included the PSA RR (≥50% decline) at any time (best response), biochemical progression-free survival (PSA PFS), pain progression-free survival (pain PFS), and pain RR. A post hoc analysis assessed overall survival (OS). These parameters were defined as the time from first treatment cycle to PSA progression, pain progression, or death from any cause, respectively. We recorded new pain development as a 2-point increase on the pain intensity score without a decrease in opiate use. Patients were included in the pain analysis if they had available baseline assessments and at least 1 follow-up data point 4–6 wk after the last treatment cycle.

All endpoints were analyzed by the local investigators.

Statistical Analysis

On the basis of previous reports (*1*), we hypothesized that the PSA RR after 2 cycles would range between 38% and 65% for both treatment activities. On the basis of the design of a single-arm phase 2 study in mCRPC (*11*), we postulated that ^{177}Lu-PSMA would be considered of value for further study if 50% or more patients met the primary endpoint and not worthy if fewer than 40% achieved the primary endpoint. A sample size of 200 patients was required to distinguish between a 40% and a 50% PSA RR with a 78% power (2-sided binomial test with α 0.05 and β 0.20).

We used descriptive statistics including median and interquartile range (IQR) for continuous variables and number and percentage for categoric variables. We present percentage changes in serum PSA levels as a waterfall plot. Kaplan–Meier analysis was used to calculate PSA PFS, pain PFS, and OS by PSA RRs. We used the log-rank test to evaluate the association between treatment arm and patient outcome. The Fisher exact test determined the association between treatment arm and PSA RRs. We tested each endpoint at a 2-sided significance level of 0.05.

In a post hoc analysis, the effect of treatment activity (6.0 vs. 7.4 GBq) on outcome data was adjusted for baseline factors (i.e., ECOG performance score, number of previous chemotherapy lines [0–1 vs. 2], and visceral disease) in multivariate cox/logistic regression models. Hazard ratios/odds ratios and their 95% CIs were derived.

Because of the early study termination, we tested whether the comparison of the 2 activity groups (6.0 vs. 7.4 GBq) would likely have held up in the originally proposed study population of 200 patients with a post hoc conditional power calculation simulation (*12*). This assumes that the additional patients required to complete the originally planned study cohort exhibit characteristics similar to those of the patients enrolled. The method applies random samples and 1,000 iterations to account for sampling variability. If this calculation yields around a conditional power calculation of 80% (i.e., $P < 0.05$ in 80% of the 1,000 simulations), then the difference in treatment regimen–associated outcomes would be statistically different.

Statistical analyses were performed using SPSS, version 22 (IBM) and STATA, version 15 (StataCorp LLC).

RESULTS

Enrollment and Baseline Characteristics

We enrolled 51 patients with progressive mCRPC between November 2017 and July 2018 (Supplemental Fig. 1). Eight of 51 (16%) patients were excluded after enrollment because of disease progression ($n = 4/8$, 50%), negative PSMA PET ($n = 2/8$, 25%), death ($n = 1/8$, 13%), or screen failure ($n = 1/8$, 13%). Forty-three of 51 (84%) patients received at least 1 cycle of ^{177}Lu-PSMA: 14 of 43 (33%) and 29 of 43 (67%) in the 6.0- and 7.4-GBq groups, respectively.

Baseline characteristics are provided in Table 1. In the overall study population, median baseline PSA levels and doubling times were 27.4 ng/mL (IQR 9.5–115.6) and 1.5 mo (IQR 1.0–2.3), respectively. Twenty-two of 43 patients (51%) had received ≥ 2 chemotherapy regimens, and 35 of 43 (82%) underwent treatment with both abiraterone and enzalutamide before ^{177}Lu-PSMA. Twenty-nine of 43 (67%) patients had > 20 metastasis on PSMA PET.

The cutoff date for follow-up was June 25, 2020. Median follow-up for patients who survived was 24.8 mo (IQR 22.9–28.8).

Efficacy Endpoints

PSA RRs. PSA RR after 2 cycles was available in 40 of 43 patients (93%). Overall PSA RR was 11 of 40 (28%; 95% CI 14.6–43.9) and 16 of 43 (37%; 95% CI 23.0–53.3) after 2 cycles (primary endpoint) and at any time, respectively (Fig. 1; Table 2). There was no difference of PSA RRs between the 2 treatment arms after 2 cycles ($P = 0.12$) or at any time ($P = 0.31$). The median time to best PSA response was 8.9 wk (IQR, 6.9–25.1) in all 43 patients and 28.8 wk (IQR, 15.2–36.2) in the 16 PSA responders.

Biochemical PFS. At the end of follow-up, 2 of 43 patients (5%) were alive without PSA progression. The median PSA PFS was 3.7 mo in the overall study population (95% CI 2.0–5.4). It was 2.9 mo (95% CI 0.0–9.0) and 3.7 mo (95% CI 1.9–5.6) in the 6.0- and the 7.4-GBq groups ($P = 0.25$), respectively (Fig. 2; Table 2; Supplemental Fig. 2).

Bone Pain PFS. The pain RR in evaluable patients was 12 of 18 (67%), 6 of 7 (86%), and 6 of 11 (55%) in the overall study population, the 6.0-GBq group, and the 7.4-GBq group, respectively ($P = 0.31$) (Table 2). Pain PFS was 8.2 mo (95% CI 3.9–12.5), 5.4 mo (95% CI not reached), and 8.2 mo (95% CI 2.3–14.1) in the overall study population, the 6.0-GBq group, and the 7.4-GBq group, respectively ($P = 0.94$) (Supplemental Fig. 3; Table 2).

OS. At the end of follow-up, 12 of 14 (86%) and 25 of 29 (87%) of patients had died in the 6.0- and 7.4-GBq arms, respectively. The median OS of the overall study population was 14.0 mo (95% CI 11.8–19.4). The injected activity was not associated with OS: 15.6 (95% CI 11.8–19.4) versus 13.5 mo (95% CI 10.0–17.0) in the 6.0- and the 7.4-GBq arms ($P = 0.87$), respectively (Fig. 2; Table 2; Supplemental Fig. 2). Patients who experienced a PSA decline ≥ 50% at any time (best response; $n = 16/43$, 37%) had a significantly longer OS than those who did not (27/43, 63%): median: 20.8 versus 10.8 mo; $P = 0.005$ (Fig. 3). However, no significant difference was observed when comparing the OS of patients who had a PSA decline ≥ 50% after 2 cycles only ($n = 11/40$, 28%) with those who did not ($n = 29/40$, 72%): median: 19.1 versus 13.7 mo; $P = 0.46$ (Fig. 3).

After adjusting for baseline factors (ECOG, number of previous chemotherapy regimen [0–1 vs. 2], visceral disease), the treatment activity (6.0 vs. 7.4 GBq) remained not associated with treatment outcomes (P values > 0.05, multivariate cox/logistic regression models, Supplemental Table 1).

The post hoc conditional power calculation simulation assumed a comparable demographic and disease distribution for 157 simulated patients (to obtain the initially planned population of 200 patients). Randomly sampling (with replacement) 86 patients from the 6.0-GBq cohort and 71 patients from the 7.4-GBq cohort and repeating this process 1,000 times yielded a significant difference ($P < 0.05$) between activity effects on outcome in only 47 of 1,000 simulations (4.7%).

DISCUSSION

This prospective randomized phase 2 study compared two ^{177}Lu-PSMA treatment activity levels in patients with mCRPC who progressed after conventional treatments. PSA RR, PSA PFS, pain RR, and OS did not differ between the 2 activity arms (6.0 vs. 7.4 GBq). This study is, to our knowledge, the first attempt to compare prospectively 2 activity regimens of ^{177}Lu-PSMA therapy. The results are in line with a retrospective study comparing 2 similar treatment activity levels of ^{177}Lu-PSMA (6.0 vs. 7.5 GBq) (*13*).

The primary efficacy endpoint (i.e., PSA RR after 2 cycles of ≥ 40% in the whole cohort) was not met, possibly because of premature study closure at 36% of the planned enrollment (71/200). This study closure was prompted by the IND sponsorship transfer to Endocyte Inc. and the opening of the phase 3 registration VISION trial (NCT03511664). The current PSA RR is lower than those reported in the Australian prospective phase 2 clinical trials, after 2 cycles (28% vs. 50% in the LuPSMA trial), and at any time point (38% vs. 64% in the LuPSMA trial and 66% in TheraP Trial) (*4*,*6*). More rigorous patient selection that included ^{18}F-FDG PET to exclude patients with hyperglycolytic but low PSMA-expressing lesions resulted in improved PSA RR. Dual-tracer PSMA/^{18}F-FDG PET phenotyping can improve patient selection to ^{177}Lu-PSMA therapy and this approach should be further implemented in future prospective trials. However, despite different PSA RRs, OS was similar (median: 14.0 vs. 13.7 mo in the LuPSMA trial) (*5*). Of note, the quality of life improvement previously reported was also observed in our cohort: pain levels improved in 67% of the evaluable patients (*4*–*6*). Further studies on patients reported outcomes are warranted.

A comparative metaanalysis suggested that ^{177}Lu-PSMA was less toxic, induced higher PSA RR (mean frequency 44% vs. 22%) and possibly improved OS (median of 14 vs 12 mo; $P = 0.33$) compared with other third-line treatments for mCRPC, such as enzalutamide and cabazitaxel (*14*). The multicenter prospective randomized

TABLE 1
Characteristics of Study Population at Baseline

Characteristic	Overall (n = 43)	6.0 GBq (n = 14)	7.4 GBq (n = 29)
Age (y)	74 (68–78)	76 (70–79)	72 (65–78)
Time since diagnosis of PCa (y)	7 (4–17)	8 (5–17)	7 (4–15)
Gleason grade group at diagnosis*			
≥4	25 (64%)	9 (69%)	16 (62%)
PSA (ng/mL)	27.4 (9.5–115.6)	31.3 (12.6–160.2)	26.1 (9.5–124.4)
PSA doubling time (mo)	1.5 (1.0–2.3)	1.3 (1.0–1.7)	1.8 (1.0–3.2)
Total alkaline phosphatase (U/l)	87 (67–125)	82 (60–175)	94 (69–117)
Hemoglobin (g/dL)	12.0 (10.9–13.2)	12.1 (11.2–12.9)	11.6 (10.8–13.3)
Platelets (10^3/mL)	208 (160–245)	207 (163–356)	208 (158–238)
ECOG performance status			
0	13 (30%)	8 (57%)	5 (17%)
1	21 (49%)	4 (29%)	17 (59%)
2	9 (21%)	2 (14%)	7 (24%)
Pain at baseline (BPI score)			
No pain	21 (49%)	4 (28%)	17 (58%)
Mild (*1–4*)	11 (26%)	5 (36%)	6 (21%)
Moderate to severe (*5–10*)	11 (26%)	5 (36%)	6 (21%)
Previous mCRPC systemic treatments			
Chemotherapy regimen lines			
0	11 (26%)	4 (29%)	7 (24%)
1	10 (23%)	4 (29%)	6 (21%)
2	12 (28%)	3 (21%)	9 (31%)
≥3	10 (23%)	3 (7%)	7 (24%)
Abiraterone	41 (95%)	13 (93%)	28 (97%)
Enzalutamide	37 (86%)	13 (93%)	24 (83%)
Abiraterone + enzalutamide	35 (82%)	12 (86%)	23 79%)
^{223}Ra	14 (33%)	4 (29%)	10 (35%)
Prior lines of mCRPC systemic treatment			
1	4 (9%)	1 (7%)	3 (10%)
≥2	39 (91%)	13 (93%)	26 (90%)
≥3	31 (72%)	10 (71%)	21 (72%)
≥4	25 (58%)	8 (57%)	17 (59%)
Extent of disease on PSMA-PET			
≤20 metastases	14 (33%)	4 (29%)	10 (34%)
2 metastases	29 (67%)	10 (71%)	19 (66%)
Sites of disease on PSMA PET			
Node only (N1 or M1a)	3 (7%)	1 (7%)	2 (7%)
Bone only (M1b)	9 (21%)	3 (21%)	6 (21%)
Node + bone (M1b and [N1 or M1a])	15 (35%)	7 (50%)	8 (28%)
Visceral (M1c with/without any other site)†	15 (35%)	3 (21%)	12 (41%)

*Data missing for 4 patients.
†Visceral includes lung, liver, rectum, pancreas, peritoneal, brain, and adrenal.
BPI = bone pain index.
Data are median, with IQR in parentheses, or *n* (%).

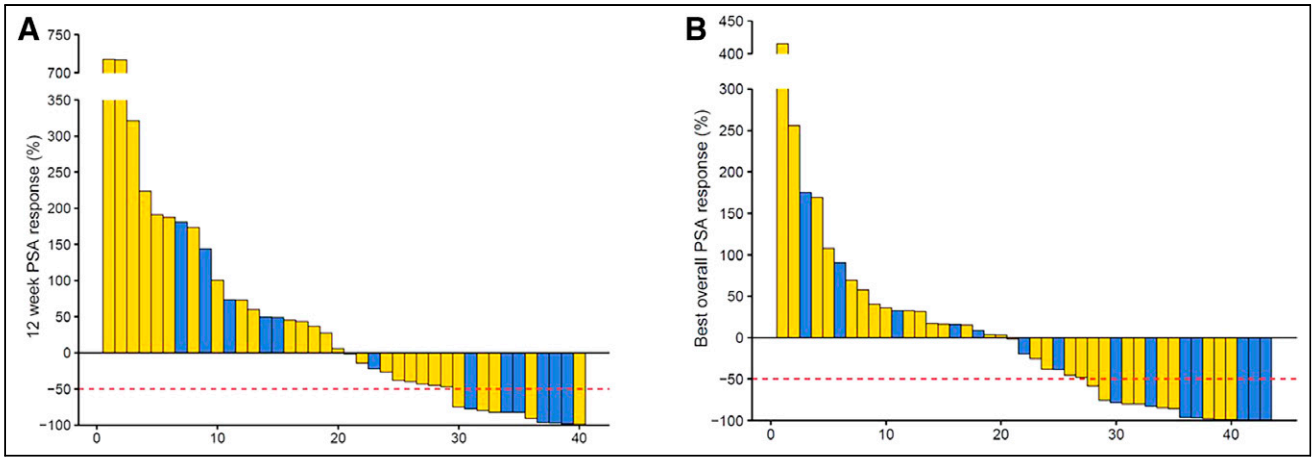

FIGURE 1. Waterfall plots showing PSA changes relative to baseline after 2 cycles of ^{177}Lu-PSMA (A) and any time during treatment (B).

TheraP trial comparing ^{177}Lu-PSMA with cabazitaxel confirmed these findings with higher PSA RR (66% vs. 44%) and less grade 3–4 adverse events (33% vs. 53%) in the ^{177}Lu-PSMA arm (*6*). Improvement of OS with ^{177}Lu-PSMA will be critical for regulatory approval, and the results of the VISION trial NCT03511664 (best supportive/standard care vs. ^{177}Lu-PSMA + best supportive/standard care) are awaited.

A significant association between best PSA RR and OS was observed, in line with prior reports (*3*,*5*), supporting further investigation of PSA RR as an intermediate surrogacy endpoint for OS.

Findings are limited by an early study closure before completing target enrollment (36%). This was beyond the control of the investigators and resulted in a small sample size. Consequently, the distribution between the 2 treatment groups was also altered (14 vs. 29) as 1:1 randomization was performed centrally for both sites. The premature study termination limits the comparison between the 2 treatment activity groups. However, due to the narrow difference in the 2 tested activities (~20%, 6.0 vs. 7.4 GBq) even the limited data suggest that there is likely no or only small differences in efficacy between these 2 activities. This is consistent with prior reports that found similar response and toxicity rates to comparable levels of injected activity (6.0 vs. 7.5 GBq) (*13*). To further test whether the current results of the comparison of the 2 activity groups (6.0 GBq vs. 7.4 GBq) in this cohort of 43 patients would likely have

TABLE 2
Primary and Secondary Endpoints Results

Outcome measure	Overall (n = 43)	6.0 GBq (n = 14)	7.4 GBq (n = 29)	Hazard ratio (95% CI)	P
Primary endpoint					
PSA response after 2 cycles					
No. of evaluable patients	40	13	27		
PSA decline ≥ 50% after 2 cycles	11 (28%, 95% CI 15–44)	6 (46%, 95% CI 19–75)	5 (19%, 95% CI 6–38)	—	0.12*
Secondary endpoint					
Best PSA response					
No. of evaluable patients	43	14	29		
Best PSA response ≥ 50%	16 (37%, 95% CI 23–53)	7 (50%, 95% CI 23–77)	9 (31%, 95% CI 15–51)	—	0.31*
Pain response					
No. of evaluable patients	18	7	11		
Patients with pain improvement (n)	12 (67%)	6 (86%)	6 (55%)	—	0.31*
Pain PFS					
Median (mo)	8.2 (95% CI 3.9–12.5)	5.4 (not reached)	8.2 (95% CI 2.3–14.1)	0.96 (0.35–2.66)	0.94
Post hoc analysis					
OS					
Median (mo)	14.0 (95% CI 10.1–17.9)	15.8 (95% CI 11.8–19.4)	13.5 (95% CI 10.0–17.0)	0.94 (0.46–1.92)	0.87

*P values compare the 6.0- and 7.4-GBq treatment arms using exact Fisher test.

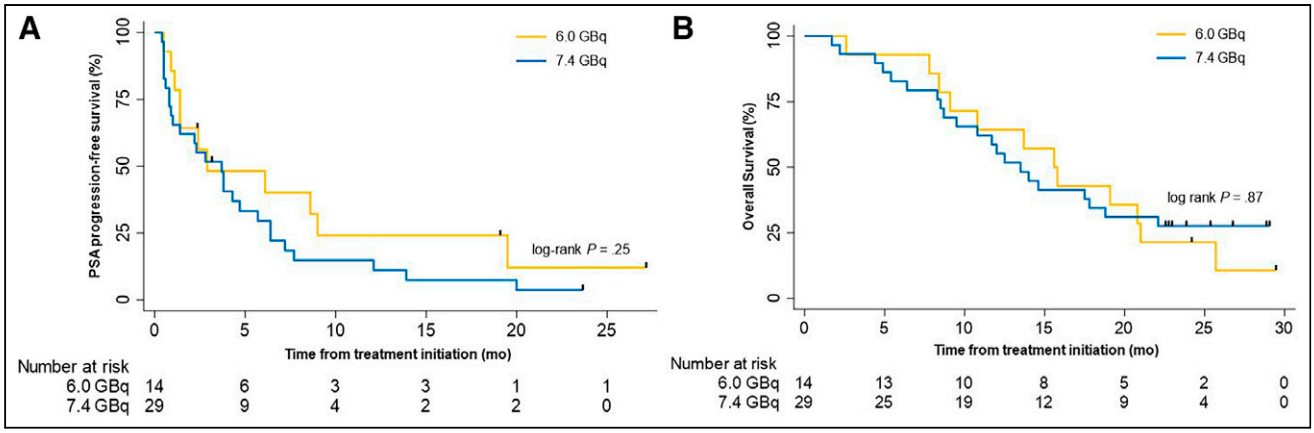

FIGURE 2. Survival Kaplan–Meier curves. Kaplan–Meier curves for PSA PFS (A) and OS (B) by treatment arm. Tick marks indicate censored data. The log-rank test is given with $P < 0.05$ considered significant.

held up in the originally proposed study population of 200 patients, we conducted a post hoc conditional power calculation simulation (*12*). After 1,000 simulations, only 47 of 1,000 simulations (4.7%) were significant ($P < 0.05$). Further calculation revealed that around 3,400 patients per group (6,800 total) would have been needed to show a significant difference in effectiveness of the 2-activity regimen (conditional power of 80%).

As another limitation, the study population was heterogeneous regarding prior treatment. The study was self-funded and patients were charged for the study drug (cost recovery, Title 21 CFR 312.8). For ethical reasons, the study therefore allowed various prior systemic therapies for inclusion. To correct for heterogeneity in treatment history and baseline characteristics, we conducted a standard covariate adjustment analysis (Supplemental Table 1). After adjusting for baseline factors including ECOG, number of previous chemotherapy regimen (0–1 vs. 2), and presence of visceral disease, the treatment activity was still not associated with treatment outcome. Thus, administered activity (6.0 vs. 7.4 GBq) did not appear to affect treatment outcome.

To reduce out-of-pocket costs, imaging follow-up modalities were selected by patients and referring oncologists. Thus, a variety of imaging modalities (CT, bone scan, MRI, PSMA, choline, fluciclovine, FDG) were used to assess radiographic progression, which may have increased variance of event data. For instance, PET imaging results in shorter time to progression when compared with conventional anatomic imaging. Because of the lack of standardization, effective conclusions could not be assured. The follow-up imaging analysis is provided in the supplemental material (Supplemental Tables 2 and 3 and Supplemental Fig. 4).

Finally, there was no central blinded review of the screening PSMA PET, and criteria to establish PSMA-target expression were not predefined and left to the discretion of the local investigators. Studies establishing optimal PSMA PET criteria for patient selection and therapy response assessment are warranted.

CONCLUSION

We report here the UCLA study site efficacy results of the prospective phase 2 study RESIST-PC of ^{177}Lu-PSMA for mCRPC after more than 2 y of follow-up. The study closed enrollment before reaching the cohort size because of IND sponsorship transfer to Endocyte Inc. The study population was heterogeneous. PSA RR after 2 cycles and at any time were 28% and 38%. Pain RR was 67%, and the median OS was 14 mo. There was no difference in PSA RR between administration of 6.0 and 7.4 GBq of ^{177}Lu-PSMA. Results justify confirmation with real-world data analysis and further trials to refine and optimize the

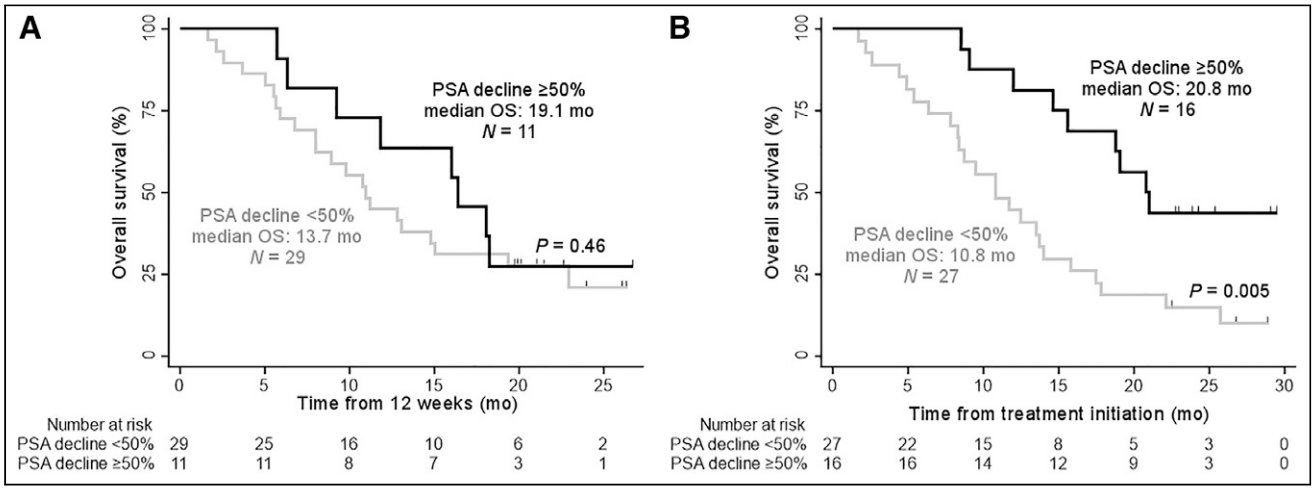

FIGURE 3. Kaplan–Meier curves for OS by PSA response after 2 cycles (A) and at any time (B). Tick marks indicate censored data. The log-rank test is given with $P < 0.05$ considered significant.

^{177}Lu-PSMA therapy administration scheme to improve tumor radiation dose delivery and efficacy.

DISCLOSURE

Jeremie Calais is the recipient of grants from the Prostate Cancer Foundation (2020 Young Investigator Award, 20YOUN05), the Society of Nuclear Medicine and Molecular imaging (2019 Molecular Imaging Research Grant for Junior Academic Faculty), the Philippe Foundation Inc. (NY, USA), and the ARC Foundation (France) (International Mobility Award SAE20160604150) and reports prior consulting activities outside of the submitted work for Advanced Accelerator Applications, Blue Earth Diagnostics, Curium Pharma, GE Healthcare, IBA Radiopharma, Janssen, Progenics, POINT Biopharma, Radiomedix, and Telix Pharmaceuticals. Andrei Gafita was the recipient of the Jonsson Comprehensive Cancer Center Fellowship award and the Dr. Christiaan Schiepers postdoctoral fellowship award. Matthias Eiber was a consultant for ABX, Blue Earth Diagnostics, and Progenics and has patent rights on rhPSMA outside of the submitted work. David Ranganathan is an employee and equity holder of RadioMedix. Ken Herrmann received funding from the German Research Foundation (Deutsche Forschungsgemeinschaft grant HE 5247/4-1) and was a consultant for Advanced Accelerator Applications, Amgen, Bayer, Curium Pharma, GE Healthcare, IPSEN, Janssen Pharmaceuticals, BTG, Sirtex, Novartis, ROTOP, and Bain Capital outside of the submitted work. In addition, Ken Herrmann is a board member of and holds equity in Sofie Biosciences; intellectual property is patented by the University of California and licensed to Sofie Biosciences. Ebrahim Delpassand reports equity ownership at Excel Nuclear Oncology Center and RadioMedix. Wolfgang P. Fendler received financial support from the German Research Foundation (Deutsche Forschungsgemeinschaft, DFG, grants FE1573/1-1/807122 and FE1573/3-1/659216 and DFG Research Training Group 1739); was a consultant for Endocyte and BTG; and received fees from RadioMedix, Bayer, and Parexel outside of the submitted work. Johannes Czernin was supported by the Prostate Cancer Foundation (2019 and 2017 Challenge Award, 19CHAL09, 17CHAL02) and by the Johnson Comprehensive Cancer Center NIH-NCI Cancer Center Support Grant (P30 CA016042) and was a consultant for Endocyte Inc. (VISION trial steering committee), Actinium Pharmaceuticals, and Point Biopharma outside of the submitted work. In addition, Johannes Czernin is a founder and board member of and holds equity in Sofie Biosciences and Trethera Therapeutics; intellectual property is patented by the University of California and licensed to Sofie Biosciences and Trethera Therapeutics. No other potential conflict of interest relevant to this article was reported.

ACKNOWLEDGMENTS

We thank all the patients and their referring physicians whose willingness to participate made this study possible. We thank the whole staff team of the UCLA Nuclear Medicine and Theranostics Division whose hard work made this study possible.

KEY POINTS

QUESTION: What is the efficacy profile of 2 activity regimens of ^{177}Lu-PSMA therapy (6.0 GBq vs. 7.4 GBq) in patients with mCRPC?

PERTINENT FINDINGS: In this prospective randomized phase 2 study that included 43 patients with progressive mCRPC, ^{177}Lu-PSMA therapy resulted in biochemical response in 38%, and the median OS was 14 mo. There was no difference in efficacy between administration of 6.0 and 7.4 GBq of ^{177}Lu-PSMA.

IMPLICATIONS FOR PATIENT CARE: ^{177}Lu-PSMA therapy using and 6.0 and 7.4 GBq is a therapeutic option for patient with mCRPC with a good efficacy.

REFERENCES

1. Rahbar K, Ahmadzadehfar H, Kratochwil C, et al. German multicenter study investigating ^{177}Lu-PSMA-617 radioligand therapy in advanced prostate cancer patients. *J Nucl Med.* 2017;58:85–90.
2. Yadav MP, Ballal S, Sahoo RK, Dwivedi SN, Bal C. Radioligand therapy with ^{177}Lu-PSMA for metastatic castration-resistant prostate cancer: a systematic review and meta-analysis. *AJR.* 2019;213:275–285.
3. Heck MM, Tauber R, Schwaiger S, et al. Treatment outcome, toxicity, and predictive factors for radioligand therapy with ^{177}Lu-PSMA-I&T in metastatic castration-resistant prostate cancer. *Eur Urol.* 2019;75:920–926.
4. Hofman MS, Violet J, Hicks RJ, et al. [^{177}Lu]-PSMA-617 radionuclide treatment in patients with metastatic castration-resistant prostate cancer (LuPSMA trial): a single-centre, single-arm, phase 2 study. *Lancet Oncol.* 2018;19:825–833.
5. Violet J, Sandhu S, Iravani A, et al. Long-term follow-up and outcomes of retreatment in an expanded 50-patient single-center phase II prospective trial of ^{177}Lu-PSMA-617 theranostics in metastatic castration-resistant prostate cancer. *J Nucl Med.* 2020;61:857–865.
6. Hofman MS, Emmett L, Sandhu S, et al. [^{177}Lu]Lu-PSMA-617 versus cabazitaxel in patients with metastatic castration-resistant prostate cancer (TheraP): a randomised, open-label, phase 2 trial. *Lancet.* 2021;397:797–804.
7. Vickers AJ. How to randomize. *J Soc Integr Oncol.* 2006;4:194–198.
8. Cleeland CS, Ryan KM. Pain assessment: global use of the Brief Pain Inventory. *Ann Acad Med Singapore.* 1994;23:129–138.
9. Mathias SD, Crosby RD, Qian Y, Jiang Q, Dansey R, Chung K. Estimating minimally important differences for the worst pain rating of the Brief Pain Inventory-Short Form. *J Support Oncol.* 2011;9:72–78.
10. Scher HI, Morris MJ, Stadler WM, et al. Trial design and objectives for castration-resistant prostate cancer: updated recommendations from the prostate cancer clinical trials working group 3. *J Clin Oncol.* 2016;34:1402–1418.
11. Danila DC, Morris MJ, de Bono JS, et al. Phase II multicenter study of abiraterone acetate plus prednisone therapy in patients with docetaxel-treated castration-resistant prostate cancer. *J Clin Oncol.* 2010;28:1496–1501.
12. Walter SD, Han H, Guyatt GH, et al. A systematic survey of randomised trials that stopped early for reasons of futility. *BMC Med Res Methodol.* 2020;20:10.
13. Seifert R, Kessel K, Schlack K, Weckesser M, Bögemann M, Rahbar K. Radioligand therapy using [^{177}Lu]Lu-PSMA-617 in mCRPC: a pre-VISION single-center analysis. *Eur J Nucl Med Mol Imaging.* 2020;47:2106–2112.
14. von Eyben FE, Roviello G, Kiljunen T, et al. Third-line treatment and ^{177}Lu-PSMA radioligand therapy of metastatic castration-resistant prostate cancer: a systematic review. *Eur J Nucl Med Mol Imaging.* 2018;45:496–508.

Safety of PSMA-Targeted Molecular Radioligand Therapy with ^{177}Lu-PSMA-617: Results from the Prospective Multicenter Phase 2 Trial RESIST-PC (NCT03042312)

Jeremie Calais[1–3], Johannes Czernin[1–3*], Pan Thin[1], Jeannine Gartmann[1], Kathleen Nguyen[1], Wesley R. Armstrong[1], Martin Allen-Auerbach[1–3], Andrew Quon[1–3], Shadfar Bahri[1–3], Pawan Gupta[1], Linda Gardner[1], Magnus Dahlbom[1], Beilei He[4], Rouzbeh Esfandiari[5], David Ranganathan[6], Ken Herrmann[7], Matthias Eiber[8], Wolfgang P. Fendler[7], and Ebrahim Delpassand[5,6*]

[1]*Ahmanson Translational Theranostics Division, Department of Molecular & Medical Pharmacology, University of California Los Angeles, Los Angeles, California;* [2]*Institute of Urologic Oncology, University of California Los Angeles, Los Angeles, California;* [3]*Jonsson Comprehensive Cancer Center, University of California Los Angeles, Los Angeles, California;* [4]*Advanced Accelerator Applications, a Novartis Company, Geneva, Switzerland;* [5]*Excel Diagnostics and Nuclear Oncology Center, Houston, Texas;* [6]*RadioMedix, Inc., Houston, Texas;* [7]*Department of Nuclear Medicine, University of Duisburg-Essen and German Cancer Consortium (DKTK)-University Hospital Essen, Essen, Germany; and* [8]*Department of Nuclear Medicine, Technical University Munich, Klinikum rechts der Isar, Munich, Germany*

The purpose of this analysis was to report the safety evaluation of ^{177}Lu-PSMA-617 derived from the cohort of 64 patients exposed to ^{177}Lu-PSMA-617 in the RESIST-PC trial NCT03042312. **Methods:** RESIST-PC was a prospective multicenter phase 2 trial. Patients with progressive metastatic castration-resistant prostate cancer after ≥ 1 novel androgen-axis drug, either chemotherapy naïve or postchemotherapy, with sufficient bone marrow reserve, normal kidney function, sufficient PSMA expression by PSMA PET, and no PSMA-negative soft-tissue lesions were eligible. Patients were randomized (1:1) into 2 activity groups (6.0 or 7.4 GBq per cycle) and received up to 4 cycles every 8 wk. The primary safety endpoint was assessed by collecting and grading adverse events using the Common Terminology Criteria for Adverse Events. Patients were followed until disease progression, death, serious or intolerable adverse events, study termination by sponsor, patient withdrawal, lost to follow-up, or 24 mo after the first cycle. **Results**: The study was closed at enrollment of 71 of 200 planned patients because of sponsorship transfer. A total of 64 (90.1%) patients received at least 1 cycle of ^{177}Lu-PSMA-617: 28 (36%) in arm 1 (6.0 GBq) and 41 (64%) in arm 2 (7.4 GBq). There were 10 (43.5%), 19 (46.5%), and 29 (45.3%) patients who completed 4 cycles of ^{177}Lu-PSMA-617 in the 6.0-GBq arm, 7.4-GBq arm, and overall, respectively. The most common treatment-emergent adverse events (TEAEs) of any grade in the 6.0-GBq arm, the 7.4-GBq arm and overall, were dry mouth (47.8%; 63.4%; 57.8%, respectively), fatigue (56.5%; 51.2%; 53.1%, respectively), nausea (52.2%; 43.9%; 46.9%, respectively), and diarrhea (13.0%; 31.7%; 25.0%, respectively). Frequencies of all other TEAEs were comparable among the 2 groups (within 10% difference). Serious possibly drug-related TEAEs were reported for 5 (7.8%) patients overall (none were considered as probably or definitely related to treatment): 1 subdural hematoma grade 4, 1 anemia grade 3, 1 thrombocytopenia grade 4, 1 gastrointestinal hemorrhage grade 3, and 1 acute kidney injury grade 3. There were no clinically significant changes in vital signs in electrocardiograms in the 2 treatment groups. No trend to creatinine increase or increasing frequency of shifts from normal to abnormal over time for any hematologic parameter was noted. **Conclusion:** ^{177}Lu-PSMA-617 was safe and well-tolerated at 6.0 and 7.4 GBq per cycle given at 8-wk intervals with side effects easily managed with standard medical support. With established safety, further clinical trials applying individualized dosimetry and testing different ^{177}Lu-PSMA-617 administration schemes (activity levels, time intervals) are needed to optimize tumor dose delivery and treatment efficacy.

Key Words: metastatic castration-resistant prostate cancer; radionuclide therapy; molecular radiotherapy; prostate-specific membrane antigen; ^{177}Lu, RESIST-PC; prospective randomized phase 2 trial; theranostics; safety

J Nucl Med 2021; 62:1447–1456
DOI: 10.2967/jnumed.121.262543

Targeted molecular radioligand therapy (RLT) offers the possibility to treat cancer lesions in a specific and tumor-selective manner by targeting cell surface proteins expressed on malignant cells. RLT targeting somatostatin receptor using ^{177}Lu-DOTATATE gained regulatory approval in 2018 in patients with metastatic neuroendocrine tumors based on the results on an industry-sponsored randomized phase 3 trial (*1*) and is now an established therapy. The prostate-specific membrane antigen (PSMA) is a target for prostate cancer (PCa) therapy because it is highly expressed in PCa (*2*). PSMA-617 is a small molecule that clears rapidly from plasma and binds with high affinity to the extracellular domain of PSMA (*3*). It can be labeled with lutetium-177 (^{177}Lu) for RLT. β-particles emitted from ^{177}Lu have a short-range of approximately 1 mm, enabling delivery of high doses of radiation to tumors while minimizing damage to surrounding normal tissues.

The RESIST-PC trial was designed in 2017 to assess the efficacy and safety of ^{177}Lu-PSMA-617 using 2 commonly used activity regimen (6.0 and 7.4 GBq per cycle) in patients with progressive metastatic castration-resistant prostate cancer (mCRPC). The administration scheme of ^{177}Lu-PSMA-617 (amount of injected peptide or ligand [nmol], amount of injected activity [GBq – mCi], time interval between each cycle or fractionation, number of

Received May 5, 2021; revision accepted Jul. 7, 2021.
For correspondence or reprints, contact Jeremie Calais (jcalais@mednet.ucla.edu).
Guest Editor: Todd Peterson, Vanderbilt University.
*Contributed equally to this work.
Published online July 16, 2021.

cycles) derives mostly from prior empiric compassionate use of ^{177}Lu-PSMA-617 in Germany (*4–6*) and prospective trials using other established molecular radionuclide therapy agents (^{177}Lu-DOTATATE, ^{223}Ra, ^{90}Y-ibritumomab-tiuxetan) (*1*,*7*,*8*). The selected 8-wk interval between treatment cycles was based on established hematologic safety considerations (blood count Nadir at 3–6 wk after molecular radionuclide therapy administration) reported in the above-mentioned randomized prospective phase 3 trials (*1*,*7*,*8*). The 6.0- and 7.4-GBq activity regimens were chosen based on dosimetry data (*9*,*10*) and the NETTER-1 trial experience (*1*).

RESIST-PC was an investigator-initiated trial (IIT) but was switched to a sponsored study after the acquisition of the development rights of PSMA-617 by Endocyte (see the "Materials and Methods" section) and subsequently closed before reaching the target enrollment in 2018. Because of the early study termination and limited data availability, the efficacy endpoints were not analyzed as initially planned. The efficacy outcome results of the University of California Los Angeles (UCLA) study cohort were published separately (*11*). Here we report the safety evaluation of the study drug derived from the multicenter prospective cohort of 64 patients exposed to ^{177}Lu-PSMA-617.

MATERIALS AND METHODS

Study Design

RESIST-PC was a prospective, randomized, open-label, multicenter phase 2 study conducted at University of California Los Angeles (UCLA; Los Angeles, CA) and Excel Diagnostics Nuclear Oncology Center (Houston, TX). The primary objective of the study was to assess the efficacy and safety of 2 ^{177}Lu-PSMA-617 activity regimens (6.0 GBq and 7.4 GBq per cycle) in patients with mCRPC. It was initially an IIT cosponsored by the principal investigators under a U.S. Food and Drug Administration (FDA) Investigational New Drug (IND) application. The study was approved by the UCLA institutional review board (IRB# 17-000330) and registered on ClinicalTrials.gov (NCT03042312). After the acquisition of the worldwide rights to develop and commercialize PSMA-617 in 2017, the U.S. IND sponsorship was transferred to Endocyte. As the company initiated the prospective international multicenter registration trial (VISION; NCT03511664), the RESIST-PC trial, subsequently identified as PSMA-617-02, was not consistent with the overall company strategy. Thus, the study was closed before all 200 planned patients were enrolled in 2018. Here we report the safety evaluation in the patients exposed to the study drug ($n = 64$).

Patients

Patients with progressive mCRPC after abiraterone or enzalutamide, chemotherapy-naive or chemotherapy-treated (regardless the number of prior chemotherapy regimens) were eligible. Patients who had received PSMA-targeted radionuclide therapy were excluded. Pretreatment PSMA PET was required for eligibility (see the "Procedures" section below). Sufficient bone marrow reserve (hemoglobin $\geq$ 9.9 g/dL, platelet count $\geq 100 \times 10^9$/L, white blood cell count [WBC] $\geq 2.5 \times 10^9$/L, and absolute neutrophil count $\geq 1.5 \times 10^9$/L) and Eastern Cooperative Oncology Group Performance Score of 0–2 were required inclusion criteria. Patients with diffuse bone involvement by bone scintigraphy (superscan), impaired kidney function (glomerular filtration rate [GFR] $<$ 40 mL/min, serum creatinine $>$ 1.5$\times$upper limit of normal [ULN], urinary tract obstruction or marked hydronephrosis), or impaired liver function (aspartate aminotransferase [AST] and alanine aminotransferase [ALT] $>$5$\times$ULN) were excluded.

Patients were referred specifically to this trial and continued care with their treating medical oncologist or urologist in close coordination with the study site investigators. They traveled to the trial sites per protocol. Patients were prescreened based on their prostate cancer history before initial consultation visit. Informed written and oral consent was obtained from all patients during the initial consultation visit.

Procedures

Screening PSMA PET. PSMA PET performed within 3 mo before randomization was required for eligibility. Local study-site investigators visually determined sufficient target expression (majority of lesions with uptake equal to or above liver uptake) and absence of PSMA-negative lesions visible on anatomic imaging modalities (CT, MRI). No semiquantitative thresholds were applied. OsiriX software (Pixmeo) was used for visual assessment (*12*).

Randomization. Patients were randomized (1:1 ratio) to receive either 6.0 ($\pm$10%, arm 1) or 7.4 GBq ($\pm$10%, arm 2) of ^{177}Lu-PSMA-617 per treatment cycle. Randomization (1:1 ratio) was performed in accordance with Vickers et al. (*13*). Randomization was not stratified for any variable. A list of random allocations for patients 1 to 200 was created, concealed, and stored at the investigator's site without modification. A clinical research coordinator who was not involved in clinical management assigned the randomized allocation. There was no blinding of patients or physicians.

Treatment Intervention. ^{177}Lu-PSMA-617 was radiolabeled with carrier-free ^{177}Lu (RadioMedix, Inc.). The labeled product was produced, tested, released, and delivered under good-manufacturing-practice conditions as a sterile, ready-to-use solution for infusion. ^{177}Lu-PSMA-617 was intravenously applied over approximately 15–30 min using an infusion pump at 8 $\pm$ 1 wk intervals up to a maximum of 4 cycles. Salivary glands were cooled using icepacks (started 30 min before injection of ^{177}Lu-PSMA-617 and maintained for 4 h after injection). Treatment cycles continued until disease progression, severe toxicity occurred (see the "Safety Assessments" section below), patient withdrawal, or per investigator decision. Patients were permitted to receive concurrent radiotherapy or other non-chemotherapy treatments.

Safety Assessments. Physical examination, vital signs, and 12-lead electrocardiogram were performed at each site visit. Laboratory tests (comprehensive metabolic panel [CMP], estimated GFR [eGFR], complete blood count [CBC]) were performed at baseline (within 72 h of the first treatment dose) and every 2 wk ($\pm$3 d) after the first dose of study medication, continued until 12 wk after the last dose, and every 3 mo ($\pm$1$\times$wk) thereafter until discontinuation from the study. The CBC, eGFR, and CMP within 2 wk of each subsequent treatment cycle were used to assess the eligibility for the corresponding treatment cycle. Telephone follow-up was performed 7 $\pm$ 3 d after each treatment cycle, and for the follow-up phase in 3 $\pm$ 1 mo intervals until study termination.

Serious AEs (SAEs) were graded according to the Common Terminology Criteria for Adverse Events (CTCAE), version 4.0, whereas AEs were described by severity (i.e., mild, moderate, severe) by the local investigators. Severity was used to describe the intensity of a specific event, which can be of relatively minor medical significance (such as a grade 3 headache). SAE is based on patient/event outcome or action criteria and was used for events that posed a threat to the patient's life or ability to function. Seriousness (not intensity/severity) serves as a guide for defining regulatory reporting obligations.

In the case of occurrence of grade 3–4 SAEs or severe AEs, treatment administration was suspended until resolution (defined as CTCAE grade $\leq$ 2) up to 12 wk after the last cycle. Patients were discontinued from the study in the case of grade 4 hematologic SAE during $>$ 3 wk, grade 3 renal SAE during $>$ 3 wk, or any other grade 3–4 SAEs during $>$ 12 wk.

In the case of a patient experiencing the same event more than once, the maximum toxicity grade was presented. Multiple occurrences of the same AEs occurring in 1 individual were counted only once. The local investigators assessed whether AEs were study drug–related as follows: not, unlikely, possibly, probably or definitely related. A treatment-emergent adverse event (TEAE) was defined as an AE that was not

present before the first dose of ^{177}Lu-PSMA-617 but appeared after treatment, or was present at treatment initiation but worsened during treatment. An AE that was present at treatment initiation but resolved and then reappeared while the patient was on treatment was a TEAE (regardless of the intensity of the AE when the treatment was initiated). The treatment-emergent period was defined as the period from the date of initiation of randomized treatment up to 30 d after date of last administration of study treatment or the day before the initiation of subsequent anticancer treatment, whichever occurred first.

Kidney dosimetry was required by the FDA to be performed in the initial versions of the study protocol with a discontinuation rule using a maximum threshold dose to the kidneys of 23 Gy. Dosimetry data obtained after the first cycle for the first 20 patients (16 from UCLA and 4 from Excel Diagnostics) were analyzed. The estimated cumulated radiation dose after 4 cycles did not exceed the permitted renal dose of 23 Gy in any patient, demonstrating overall favorable renal dosimetry. Thus, dosimetry was no longer required per protocol (protocol PSMA-617-02 amendment 4, June 2018). Final dosimetry analysis will be reported separately.

Study Duration

Patients were followed until disease progression, death, serious or intolerable AE (that in the opinion of the investigator required the patient's discontinuation), study termination by sponsor, patient withdrawal, lost to follow-up, or 24 mo after the first treatment cycle.

Data Management and Quality

Designated investigator staff entered the data into an electronic data/electronic Case Report Form (OpenCLinica eDC). The contract research organization responsible for site monitoring was Pharmtrace. PrimeVigilance was responsible for the pharmacovigilance safety database once Endocyte became the sponsor for this study.

Statistical Analysis

The primary endpoints were the efficacy and the safety of ^{177}Lu-PSMA-617. Safety was assessed by collecting and grading AEs using the CTCAE, version 4.0. Efficacy (assessed by baseline to 12-wk decline in tumor marker level [prostate-specific antigen, PSA $\geq$ 50%] (*14*)) is not reported here due to premature study termination after only 71of 200 patients enrolled. As the power of the predefined test could not be ensured, no formal statistical test for overall response $\geq$ 50% was performed. The actual sample size was insufficient to perform the analyses that would allow for appropriate evaluation of effectiveness. Therefore, no statistical test for comparing the 2 groups was performed. No interim analysis was planned. Missing data were not replaced. We used descriptive statistics including mean, SD, median and interquartile range (Q1–Q3), and range (minimum–maximum) for continuous variables, and number and percentage for categoric variables. Data were analyzed using SAS, version 9.4 (SAS Institute Inc.).

Role of the Funding Source

RESIST-PC was initially an investigator-sponsored trial. Patients were charged for the drug under Title 21 of the Code of Federal Regulation Section (CFR) 312.8. After the sponsorship transfer, site monitoring, pharmacovigilance, and data analysis was supported by Endocyte/Novartis. The corresponding author had complete data access and had final responsibility to submit for publication.

RESULTS

Patient Enrollment

Between July 5, 2017, and June 22, 2018, a total of 71 patients (51 at UCLA and 20 at Houston) signed informed consent and were randomized (ITT population): 28/71 (39%) in arm 1 (6.0 GBq) and 43/71 (61%) in arm 2 (7.4 GBq). There were 7/71 patients (9.9%) randomized but not treated: 2 with PSMA-negative liver lesions (screen failure), 2 were too weak for treatment, 1 with low platelets (34×10^9/L), 1 withdrew consent, and 1 died. A total of 64/71 (90.1%) patients received at least 1 cycle of ^{177}Lu-PSMA-617 (safety population): 23/64 (36%) in arm 1 (6.0 GBq) and 41/64 (64%) in arm 2 (7.4 GBq). The last visit of the last subject was on January 15, 2020, and the study completion date was January 8, 2021. Seven of 71 (9.9%) deaths were reported during the study from enrollment through the 24-mo follow-up: 4 of 28 (14.3%) and 3 of 43 (7.0%) in the 6.0-GBq and 7.4-GBq treatment arms, respectively (patient disposition [ITT population] in Supplemental Table 1; supplemental materials are available at http://jnm.snmjournals.org).

Protocol Deviations

Fifty seven/71 subjects (80.3%) experienced protocol deviations (Supplemental Table 2). Most of these included procedures done outside the protocol required timing. In 40 of 71 (56.3%) patients, the pretherapy baseline PSA was performed after the randomization and was not included for analysis.

Baseline Characteristics and Prostate Cancer Treatment History (ITT Population, *n* = 71)

The demographic and baseline disease characteristics were comparable across the 2 treatment groups and are presented in Table 1. Fifty-four/71 (80.6%) patients had a PSA doubling time $\leq$ 6 mo. Fifty-eight/71 (81.7%) patients underwent at least 1 round of chemotherapy for PCa before study enrollment. Fifty-seven/71 (80.3%) patients underwent at least 1 prior taxane regimen; 54/71 (76.1%) patients had docetaxel and 26/71 (36.6%) had cabazitaxel therapy. Sixty-seven/71 (94.4%) patients were treated with abiraterone and 55/71 (77.5%) patients with enzalutamide.

Screening PSMA PET Findings (ITT Population, *n* = 71)

A summary of the screening PSMA PET staging of the ITT population is provided in Supplemental Table 3. Three patients did not undergo the screening PSMA PET scan because of poor clinical status/disease progression (withdrawal). PSMA PET was performed using ^{68}Ga-PSMA-11 in 66 of 68 (97%) and ^{18}F-DCFPyL in 2 of 68 (3%) patients. Two patients were excluded from the study because of PSMA-negative liver lesions (screen failure). Overall, 4 of 68 patients (6%) had nodal disease only (N1 or M1a), 62 of 68 (91%) had bone disease (M1b), and 25 of 68 (37%) had visceral metastasis.

Treatment Exposure (Safety Population, *n* = 64)

There were 10/23 (43.5%), 19/41 (46.5%), and 29/64 (45.3%) patients who completed 4 cycles of ^{177}Lu-PSMA-617 in the 6.0-GBq arm, 7.4-GBq arm, and overall, respectively (Table 2). The mean $\pm$ SD cumulative activity was 16.9 ± 7.6, 21.4 ± 8, and 19.8 ± 8.1 GBq in the 6.0-GBq arm, 7.4 GBq, arm and overall, respectively (Table 2).

There were 13/23 (56.5%), 27/41 (65.9%), and 40/64 (62.5%) patients with at least 1 other concurrent systemic therapy for mCRPC during the study (Table 3): hormonal therapy in 12/23 (52.2%), 25/41 (61%), 37/64 (57.8%); abiraterone in 3/23 (13%), 5/41 (12.2%), 8/64 (12.5%); enzalutamide in 2/23 (8.7%), 7/41 (17.7%), 9/64 (14.1%); and other in 10/23 (43.5%), 16/41 (39%), 26/64 (40.6%) in the 6.0-GBq arm, 7.4-GBq arm, and overall, respectively. Two patients received concurrent radiotherapy: 1 bone lesion (6.0-GBq arm 1) and 1 local recurrence (7.4-GBq arm 2).

TABLE 1
Baseline Characteristics (ITT Population)

Characteristic	6.0 GBq arm (n = 28)	7.4 GBq arm (n = 43)	Overall (n = 71)
Age (y)			
Mean (SD)	72.1 (8.39)	69.1 (8.62)	70.3 (8.60)
Minimum; maximum	55; 95	54; 84	54; 95
<65 y (n)	4 (14.3%)	13 (30.2%)	17 (23.9%)
≥65 y (n)	24 (85.7%)	30 (69.8%)	54 (76.1%)
Race/ethnicity (n)			
Asian	1 (3.6%)	1 (2.3%)	2 (2.8%)
Black/African American	0	1 (2.3%)	1 (1.4%)
Hispanic/Latino	0	1 (2.3%)	1 (1.4%)
White	26 (92.9%)	40 (93.0%)	66 (92.9%)
Other	1 (3.6%)	0	1 (1.4%)
Time since initial prostate cancer diagnosis (y)			
Mean (SD)	8.06 (7.323)	8.06 (7.152)	8.06 (7.156)
Minimum; maximum	0.7; 27.2	0.3; 25.9	0.3; 27.2
Initial Gleason score, categorized (n)			
4–7	7 (25.0%)	13 (30.2%)	20 (28.2%)
8–10	20 (71.4%)	26 (60.5%)	46 (64.8%)
Unknown	1 (3.6%)	4 (9.3%)	5 (7.0%)
Baseline PSA doubling time (mo)			
n	26	41	67
Mean (SD)	4.35 (7.131)	3.89 (3.977)	4.07 (5.376)
Median	1.91	2.46	2.07
Q1; Q3	1.18; 3.38	1.41; 4.90	1.22; 4.90
Minimum; maximum	0.0; 31.4	0.0; 20.7	0.0; 31.4
≤6 (n)	21 (80.8%)	33 (80.5%)	54 (80.6%)
>6 (n)	5 (19.2%)	8 (19.5%)	13 (19.4%)
Baseline PSA (ug/L)			
n	12	19	31
Mean (SD)	208.86 (391.804)	287.92 (830.231)	257.32 (686.578)
Median	46.03	19.34	23.66
Q1; Q3	11.28; 99.35	5.34; 68.00	5.59; 93.20
Minimum; maximum	0.6; 1166.0	1.9; 3499.0	0.6; 3499.0
Number of prior chemotherapies per patient			
n	22 (78.6%)	36 (83.7%)	58 (81.7%)
Median	2.0	2.0	2.0
Q1; Q3	1.0; 3.0	1.0; 3.0	1.0; 3.0
Minimum; maximum	1; 7	1; 5	1; 7
Type of prior chemotherapies per patient (n)			
Cabazitaxel	9 (32.1%)	17 (39.5%)	26 (36.6%)
Docetaxel	21 (75.0%)	33 (76.7%)	54 (76.1%)
Other	9 (32.1%)	18 (41.9%)	27 (38.0%)
Type of other prior systemic treatment (n)			
Abiraterone	26 (92.9%)	41 (95.3%)	67 (94.4%)
Enzalutamide	21 (75.0%)	34 (79.1%)	55 (77.5%)
Hormonal therapy	22 (78.6%)	39 (90.7%)	61 (85.9%)
Standard ADT	19 (67.9%)	22 (51.2%)	41 (57.7%)
^{223}Ra	5 (17.9%)	14 (32.6%)	19 (26.8%)
Other	20 (71.4%)	31 (72.1%)	51 (71.8%)

TABLE 2
Randomized Treatment Exposure, Summary of Cycles (Safety Population)

	6.0 GBq (n = 23)	7.4 GBq (n = 41)	Overall (n = 64)
Duration of study treatment (mo)			
Mean (SD)	3.49 (2.37)	3.66 (2.01)	3.60 (2.13)
Median	3.71	3.71	3.71
Q1; Q3	1.87; 5.75	1.87; 5.55	1.87; 5.55
Minimum; maximum	0.0; 6.3	0.0; 7.7	0.0; 7.7
Number of cycles started by patient			
Mean (SD)	2.8 (1.23)	3.0 (1.07)	2.9 (1.12)
Median	3.0	3.0	3.0
Q1; Q3	2.0; 4.0	2.0; 4.0	2.0; 4.0
Minimum; maximum	1; 4	1; 4	1; 4
Number of cycles started by patient categories (n)			
1 cycle	5 (21.7%)	3 (7.3%)	8 (12.5%)
2 cycles	4 (17.4%)	15 (36.6%)	19 (29.7%)
3 cycles	4 (17.4%)	4 (9.8%)	8 (12.5%)
4 cycles	10 (43.5%)	19 (46.3%)	29 (45.3%)
Dose per cycle (GBq/cycle)			
Mean (SD)	5.909 (0.2953)	7.245 (0.5241)	6.765 (0.7891)
Median	6.031	7.363	7.111
Q1; Q3	5.696 ; 6.142	7.134 ; 7.486	6.048 ; 7.410
Minimum; maximum	5.07 ; 6.31	4.91 ; 7.84	4.91 ; 7.84
Cumulative dose (GBq)			
Mean (SD)	16.913 (7.6668)	21.404 (8.0335)	19.790 (8.1376)
Median	18.583	22.287	19.917
Q1; Q3	11.392; 24.169	14.711; 29.454	14.297; 28.394
Minimum; maximum	5.07; 24.91	6.92; 30.59	5.07; 30.59

Results given as xx (xx.x) where xx = number of patients, (xx.x) = percentage of patients.
Duration of study treatment (months) = (treatment end date − treatment start date + 1)/30.4375.

Safety Evaluation (Safety Population, n = 64)

A summary overview of TEAEs that occurred in the study is presented in Supplemental Table 4. Main TEAEs are described in Table 4. In general, incidence of any AE was comparable between the groups: 22/23 (95.7%), 39/41 (95.1%), and 61/64 (95.3%) in the 6.0-GBq group, the 7.4-GBq group, and overall, respectively. The most frequently occurring TEAEs were dry mouth, fatigue, and nausea: 37/64 (57.8%), 34/64 (53.1%), and 30/64 (46.9%), respectively (Table 4). Notably, none of these events was reported to be severe, except 1 event of nausea in the 7.4-GBq treatment group (but did not require tube feeding, parenteral nutrition, or hospitalization). Dry mouth (47.8% vs. 63.4%) and diarrhea (13.0% vs. 31.7%) occurred more frequently in the 7.4-GBq group than in the 6.0 GBq group. Frequencies of all other TEAEs were comparable among the 2 groups (within 10% difference). There were no differences in AEs between patients aged ≥ 65 y (n = 48) and patients aged < 65 y (n = 16).

Anemia, thrombocytopenia, and leukopenia were reported overall in 8/64 (12.5%), 1/64 (1.6%), and 1/64 (1.6%), respectively. Mild decreases in mean white blood cell count, red blood cell count, and platelets (all components) were observed during treatment. However, during follow-up, the mean values tended to increase again. This was observed for the overall patient population, with no relevant differences between the groups. No trend to creatinine increase was observed during the study. There were 4 patients with grade 3 AST or ALT levels above the reference ranges that were primarily explained by liver metastases and were not considered to be related to the study treatment. Alkaline phosphatase (ALP) mean values over time during treatment had no substantial change, but individual patients had variable increase or decrease of ALP that was compatible with the disease. These overall laboratory findings for the patient population showed no relevant differences between the groups. The data must be interpreted with caution due to the small number of patients with available information at some of the time points.

There were no clinically significant changes in vital signs (systolic blood pressure [mm Hg], diastolic blood pressure [mm Hg], heart rate [bpm], temperature [°C], and respiratory rate [breaths per min]). There were no clinically significant abnormalities reported of electrocardiogram interpretations.

TEAEs leading to the reduction of ^{177}Lu-PSMA-617 were reported for 2/41 (4.9%) patients in the 7.4-GBq arm; both events

TABLE 3
Concurrent Therapies (Population: Safety Population)

	6.0 GBq (n = 23)	7.4 GBq (n =41)	Overall (n = 64)
Number of patients with at least 1 other treatment	13 (56.5)	27 (65.9)	40 (62.5)
Type of other treatments			
Abiraterone	3 (13.0)	5 (12.2)	8 (12.5)
Enzalutamide	2 (8.7)	7 (17.1)	9 (14.1)
Hormonal therapy	12 (52.2)	25 (61.0)	37 (57.8)
Other	10 (43.5)	16 (39.0)	26 (40.6)
Standard ADT	1 (4.3)	2 (4.9)	3 (4.7)
Bone metastasis RT	1 (4.3)	0	1 (1.6)
Prostate local recurrence RT	0	1 (2.4)	1 (1.6)
Number of other treatments			
n	13	27	40
Mean (SD)	2.8 (1.42)	2.4 (1.39)	2.5 (1.40)
Median	2.0	2.0	2.0
Q1; Q3	2.0; 3.0	1.0; 3.0	1.5; 3.0
Minimum; maximum	1; 6	1; 6	1; 6

Results given as xx (xx.x) where xx = number of patients, (xx.x) = percentage of patients. Data in parentheses are percentages, unless otherwise indicated.

ADT = Androgen deprivation therapy; RT = radiation therapy.

were anemia. The only TEAE that led to the discontinuation of ^{177}Lu-PSMA-617 was abdominal pain (grade 3 severity) reported in 1 patient in the 7.4-GBq group who had diffuse liver metastases and only received 1 cycle (unlikely related to treatment).

Serious drug-related TEAEs were reported for 5/64 (7.8%) patients overall: 1/23 (4.3%) in the 6.0-GBq group; and 4/41 (9.8%) in the 7.4-GBq group (Table 5). None was considered as *probably* or *definitely* related to treatment by the investigators, and all were reported as *possibly* related to treatment.

There was 1 acute kidney injury reported (grade 3 severity) in the 7.4-GBq arm. The nephrologist concluded that the creatinine elevation was likely related to concomitant medication with meloxicam. However, it could not be excluded that additional renal toxicity was caused by ^{177}Lu-PSMA-617. The investigator considered the acute kidney injury as possibly related to the treatment.

Of the 7 deaths reported, there was 1 death in the 7.4-GBq group determined to be possibly related to treatment due to hemotoxicity and gastrointestinal hemorrhage (72 d after last dose, grade 3 severity) and 1 death (94 d after last dose) in the 6.0-GBq group determined to be possibly related to treatment due to a subdural hematoma. Four deaths were reported as unrelated adverse events (death > 30 d after last dose of ^{177}Lu-PSMA-617, brain metastasis (n = 3), liver metastasis (n = 1)), and 1 death occurred in a patient before he received his first dose of ^{177}Lu-PSMA-617.

No patients developed myelodysplasia during the follow-up period.

DISCUSSION

This randomized phase 2 study compared 2 ^{177}Lu-PSMA-617 treatment activity levels in 64 patients with mCRPC who progressed after conventional therapies. ^{177}Lu-PSMA-617 was well tolerated irrespective of the activity regimen (6.0 vs. 7.4 GBq per cycle, in average 3 cycles per patient), in line with a prior retrospective study comparing similar activity levels (*15*). The most frequently occurring TEAEs were dry mouth, fatigue, and nausea in 57.8%, 53.1%, and 46.9% of the population, respectively. None of these events was reported to be severe. Serious TEAEs classified as possibly drug-related occurred in only 7.8% patients overall. The safety profile of ^{177}Lu-PSMA-617 in this study was as anticipated based on the mechanism of action and is generally consistent with previous ^{177}Lu-PSMA-617 experiences as documented in literature in similar populations of patients with mCRPC. The low toxicity profile of ^{177}Lu-PSMA-617 is attributed to the high binding affinity to the PSMA target protein and rapid renal excretion, limiting toxicity to nontarget organs.

Because ^{177}Lu-PSMA-617 is predominantly excreted by the kidneys, potential nephrotoxicity represents the main safety concern. In our cohort, the renal safety profile was excellent, with only 1 of 64 (1.5%) acute kidney injury recorded (grade 3) that was reversible and very likely related to concomitant medication. This is in line with prior reports. In an Australian retrospective cohort study reporting renal outcomes of ^{177}Lu-PSMA-617 therapy (mean cumulative activity 18.86 ± 6.7 GBq) after 8 mo of median follow-up, only 5 of 110 (4.5%) patients experienced grades 1–2 nephrotoxicity, with the main risk factor being prior chronic kidney disease (relative risk 4.2) (*16*). In the retrospective German multicenter study, grade 1–2 renal failure was reported in 12% (*5*). In the phase 2 LuPSMA trial, grade 1–2 renal toxicity was reported in 10% (*17*). In the TheraP trial, grade 1–2 creatinine increase occurred in 4 of 98 (4%), and 1 (1%) grade 3 acute kidney injury was reported (*18*). In the VISION trial, renal AEs of any grade were observed in 46 of 529 (9%) and of grade 3–5 in 18 of 529 (3.4%) (*19*).

TABLE 4
Main Treatment-Emergent Adverse Events (More Than 5% of Patients in Either Treatment Arm, and Blood and Kidney Laboratory Tests) (Safety Population)

	6.0 GBq (n = 23)		7.4 GBq (n = 41)		Overall (n = 64)	
Adverse event	All severity (n)	Severe (n)	All severity (n)	Severe (n)	All severity (n)	Severe (n)
Any event	22 (95.7)	2 (8.7)	39 (95.1)	7 (17.1)	61 (95.3)	9 (14.1)
Dry mouth	11 (47.8)	0	26 (63.4)	0	37 (57.8)	0
Fatigue	13 (56.5)	0	21 (51.2)	0	34 (53.1)	0
Nausea	12 (52.2)	0	18 (43.9)	1 (2.4)	30 (46.9)	1 (1.6)
Diarrhea	3 (13.0)	0	13 (31.7)	0	16 (25.0)	0
Constipation	6 (26.1)	0	9 (22.0)	0	15 (23.4)	0
Vomiting	4 (17.4)	0	8 (19.5)	1 (2.4)	12 (18.8)	1 (1.6)
Taste disorder	4 (17.4)	0	7 (17.1)	0	11 (17.2)	0
Pain	3 (13.0)	0	6 (14.6)	1 (2.4)	9 (14.0)	1 (1.6)
Decreased appetite	1 (4.3)	0	5 (12.2)	0	6 (9.4)	0
Arthralgia	3 (13.0)	0	2 (4.9)	0	5 (7.8)	0
Hemorrhage/hematoma	1 (4.3)	1 (4.3)	3 (7.3)	1 (2.4)	4 (6.3)	2 (3.1)
Infection	1 (4.3)	0	3 (7.3)	1 (2.4)	4 (6.3)	1 (1.6)
Headache	2 (8.7)	0	2 (4.9)	0	4 (6.3)	0
Dry eye	1 (4.3)	0	3 (7.3)	0	4 (6.3)	0
Back pain	2 (8.7)	0	1 (2.4)	0	3 (4.7)	0
Dyspnea	0	0	3 (7.3)	1 (2.4)	3 (4.7)	1 (1.6)
Key laboratory tests events						
Anemia	4 (17.4)	0	4 (9.8)	1 (2.4)	8 (12.5)	1 (1.6)
Thrombocytopenia	0	0	1 (2.4)	1 (2.4)	1 (1.6)	1 (1.6)
Leukopenia	0	0	1 (2.4)	0	1 (1.6)	0
Lymphopenia	0	0	1 (2.4)	0	1 (1.6)	0
Acute kidney injury	0	0	1 (2.4)	1 (2.4)	1 (1.6)	1 (1.6)
GFR decreased	1 (4.3)	0	0	0	1 (1.6)	0

Results given as xx (xx.x) where xx = number of patients with AEs, (xx.x) = percentage of patients. Every patient was counted a single time for each applicable specific AE. All AE tables are coded using MedDRA, version 22.1. Preferred terms are sorted in descending frequency of 'All severity' column, as reported in the 'Overall' column. Data in parentheses are percentages, unless otherwise indicated.

Bone marrow toxicity was rare, reversible, and manageable. Two patients delayed their subsequent cycle because of anemia. Thrombocytopenia and leukopenia were each reported only in 1 patient (1.6%). Hemorrhage/hematoma and infections were both reported in 4 patients (6.3%). The relationship to study drug in this population of advanced mCRPC patients with multiple bone metastasis at risk of having impaired bone marrow function from the disease is uncertain. Of note, the incidence of hematologic side effects in our study is slightly lower than that reported in the retrospective German multicenter study (grade 3–4 anemia 10%, thrombocytopenia 4%, leukopenia 3%)(*5*), the phase 2 LuPSMA trial (grade 3–4 anemia 10%, thrombocytopenia 10%, neutropenia 6%) (*17*), the TheraP trial (grade 3–4 anemia 8%, thrombocytopenia 11%, leukopenia 1%) (*18*), and the VISION trial (grade 3–4 anemia 13%, thrombocytopenia 8%, leukopenia 3%) (*19*). One reason may be that bone marrow may have been involved less frequently or less extensively in our cohort.

Because of the high uptake of PSMA radioligands in the salivary glands, xerostomia is a known side effect of ^{177}Lu-PSMA-617. Dry mouth occurred in 63.4% in the 7.4-GBq arm and 47.8% in the 6.0-GBq arm (57.8% overall) but was never graded as severe or irreversible, in line with the phase 2 LuPSMA trial (mean injected activity 7.5 GBq, grade 1–2 xerostomia in 66%, no grade 3–4) (*17*), the TheraP trial (injected activity 8.5 GBq, grade 1–2 xerostomia in 60%, no grade 3–4) (*18*), and the VISION trial (injected activity 7.4 GBq, grade 1–2 xerostomia in 39%, no grade 3–4) (*19*). Early reports underestimated this side effect (8% in the retrospective German multicenter study, mean injected activity 5.9 GBq) probably because of the absence of systematic data collection (*5*). Other symptoms such as taste disorder/dysgeusia (17% in our cohort, 12% in TheraP) or decreased appetite (9% in our cohort, 21% in VISION) are likely related to the salivary gland toxicity. Of note, we performed cooling of the salivary glands at the time of ^{177}Lu-PSMA-617 administration but without any tangible effect, as previously described (*20*,*21*).

Frequent, non–life-threatening but unpleasant side effects are important to know to adequately inform and, when possible, premedicate patients. Early reports significantly underestimated

TABLE 5
Serious Drug-Related TEAEs (Safety Population)

System organ class, preferred term	6.0 GBq (n = 23)	7.4 GBq (n = 41)	Overall (n = 64)
Any Serious Drug Related TEAE	1 (4.3)	4 (9.8)	5 (7.8)
Blood and lymphatic system disorders			
Anemia (grade 3, possibly related)	0	1 (2.4)	1 (1.6)
Thrombocytopenia (grade 4, possibly related)	0	1 (2.4)	1 (1.6)
Gastrointestinal disorders			
Gastrointestinal hemorrhage (grade 3, possibly related)	0	1 (2.4)	1 (1.6)
General disorders			
Death (grade 5, possibly related)	0	1 (2.4)	1 (1.6)
Injury complications			
Subdural hematoma (grade 4 possibly related)	1 (4.3)	0	1 (1.6)
Renal and urinary disorders			
Acute kidney injury (grade 3, possibly related)	0	1 (2.4)	1 (1.6)
Respiratory, thoracic and mediastinal disorders			
Pleural effusion (grade 3, possibly related)	0	1 (2.4)	1 (1.6)

Results given as xx (xx.x) where xx = number of patients with serious, drug-related TEAEs, (xx.x) = percentage of patients. Every patient was counted a single time for each applicable specific serious, drug-related AE with highest severity. A patient with multiple serious, drug-related TEAEs within a system organ class (SOC) was counted a single time for that SOC with the highest severity. None of the Serious drug-related TEAEs were considered as probably or definitely related to treatment by the investigators and all were reported as possibly related to treatment. Data in parentheses are percentages.

important side effects: the retrospective German multicenter study reported mild/moderate nausea in 6% and no intestinal transit disorder (*5*). Nausea and vomiting occurred in 46.9% (1.6% severe) and 18.8% (1.6% severe) of our study population, respectively. These numbers are in line with the phase 2 LuPSMA trial (nausea 48% and vomiting 22%) (*17*), the TheraP trial (nausea 41% and vomiting 13%) (*18*), and the VISION trial (nausea 35% and vomiting 19%) (*19*). Premedication with antiemetic medication (ondansetron or equivalent) is recommended and side effects usually do not last more than 24–48 h. Finally, diarrhea was reported in 31.7% of the 7.4-GBq arm and 13.0% of the 6.0-GBq arm (25% overall) and constipation in 23.4% overall. For comparisons, diarrhea was reported in 19.4 and 18.9% and constipation in 38% and 20.2% in the *TheraP and VISION* trials, respectively (*18*,*19*).

Overall, ^{177}Lu-PSMA-617 administered at 6.0 and 7.4 GBq per cycle and 8-wk interval appears to be better tolerated than available chemotherapy options which are associated with potentially life-threatening complications. Grade $\geq$ 3 neutropenia occurred in 45% of patients receiving cabazitaxel in the CARD trial and was reported in 32% to 47% of mCRPC patients receiving docetaxel (*22–24*). In the randomized TheraP trial that prospectively compared 98 patients receiving ^{177}Lu-PSMA-617 with 85 patients receiving cabazitaxel for progressing mCRPC, the toxicity profile was more favorable for ^{177}Lu-PSMA-617 than for cabazitaxel, with fewer grade 3–4 AEs (33% vs. 53%), except thrombopenia (11% vs. 0%). Of note, severe neutropenia and diarrhea occurred 3 times less: 4% versus 13% and 19% versus 56%, respectively.

The amount of injected activity (GBq – mCi) has been tailored to meet the dose limits used in external-beam radiation therapy (*25*). However, these dose limits are potentially overly conservative due to the low dose rate exposure from molecular radionuclide therapy compared with high dose rate of external-beam radiation. Higher activity regimen were safely administered in the German compassionate-use studies (up to 9.7 GBq [range 2–9.7 GBq]) (*5*) and the Australian clinical trials (up to 8.7 GBq per [range 4.4–8.7 GBq]) (*18*,*26*,*27*). Of note, in the phase I dose-escalation study NCT03042468, up to 22.2 GBq per cycle was safely administered with promising early efficacy and tolerability signals (*28*).

Due to IND sponsorship transfer to Endocyte Inc. and the early study closure before completion of the target enrollment (36%), the study findings are limited by the smaller sample size than the initially planned 200 patients. Thus, efficacy endpoints could not be analyzed as the power of the predefined test was insufficient for reliable statistical analysis. Consequently, the distribution between the 2 treatment groups was also altered (i.e., 40% patients assigned to the 6.0-GBq group and 60% assigned to the 7.4-GBq group) and the actual sample size cannot ensure formal statistical testing for comparing the 2 groups. However, due to the small difference in the 2 tested activities ($\sim$20%, 6.0 vs. 7.4 GBq) even the limited data suggest that there are likely no or only small differences in toxicity between these 2 activities. This is consistent with prior reports that found similar toxicity rates for comparable levels of injected activity (6.0 vs. 7.5 GBq) (*15*). The prematurely terminated randomization also makes it impossible to completely exclude differences in baseline characteristics or other possible confounders.

As another limitation, the study population was heterogeneous regarding prior treatments. Because the study was self-funded and patients were charged for the study drug (cost recovery, Title 21 CFR 312.8), the common denominator for inclusion was mCRPC disease. This reflects the clinical reality of a multitude of treatment options in advanced prostate cancer. Thus clinical selection for ^{177}Lu-PSMA-617 may be independent of prior treatments.

In addition, because patients were recruited from all across the United States, strict adherence to protocols was difficult to achieve.

Patients were seen at the study site most frequently for treatment only. They were managed by their off-site medical oncologist or urologist who often scheduled study procedures locally when possible. The required protocol procedures were completed locally when possible by treating physicians or, alternatively, completed locally at the trial site when patients were seen for treatments. Therefore, rigid adherence to predefined schedules was frequently not feasible. All study procedures falling outside the predefined protocol time windows (before randomization) were not considered for the analysis. This affected mostly the serum PSA measurements for the efficacy endpoint. It is deemed that protocol deviations did not have an impact on the safety results of this study but the data must be interpreted with caution due to the small number of patients with available data at some of the time points.

Finally, AEs were defined as occurring during the treatment period for only up to 30 d after the last cycle of ^{177}Lu-PSMA-617, which precludes assessments of any potential longer term toxicity.

CONCLUSION

In the prospective phase 2 multicenter trial RESIST-PC, 2 activity levels of ^{177}Lu-PSMA-617 were safely administered to 64 patients. There were no efficacy conclusions in this study due to early study termination. Overall, ^{177}Lu-PSMA-617 administered at up to 4 cycles at 8-wk intervals was safe and well tolerated at 6.0 and 7.4 GBq per cycle. Side effects were easily managed with standard medical support.

With established safety, further clinical trials applying individualized dosimetry and testing different ^{177}Lu-PSMA-617 administration schemes (activity levels, time intervals) are needed to optimize tumor dose delivery and treatment efficacy.

DISCLOSURE

Jeremie Calais is the recipient of grants from the Prostate Cancer Foundation (2020 Young Investigator Award, 20YOUN05), the Society of Nuclear Medicine and Molecular imaging (2019 Molecular Imaging Research Grant for Junior Academic Faculty), the Philippe Foundation Inc. (NY, USA) and the ARC Foundation (France) (International Mobility Award SAE20160604150). In addition, Jeremie Calais reports prior consulting activities outside of the submitted work for Advanced Accelerator Applications, Blue Earth Diagnostics, Curium Pharma, GE Healthcare, Janssen, IBA Radiopharma, POINT Biopharma, Progenics, Radiomedix, and Telix Pharmaceuticals. Johannes Czernin was supported by the Prostate Cancer Foundation (2019 and 2017 Challenge Award, 19CHAL09, 17CHAL02) and from the Johnson Comprehensive Cancer Center NIH-NCI Cancer Center Support Grant (P30 CA016042). Johannes Czernin is also a founder of and holds equity in Sofie Biosciences and Trethera Therapeutics. Intellectual property is patented by the University of California and licensed to Sofie Biosciences and Trethera Therapeutics. In addition, Johannes Czernin was a consultant for Endocyte Inc. (VISION trial steering committee), Actinium Pharmaceuticals, and Point Biopharma outside of the submitted work. David Ranganathan is an employee and equity holder of RadioMedix. Ken Herrmann received funding from the German Research Foundation (Deutsche Forschungsgemeinschaft grant HE 5247/4-1); he is a board member and holds equity in Sofie Biosciences. Intellectual property is patented by the University of California and licensed to Sofie Biosciences. In addition, Ken Herrmann was a consultant for Advanced Accelerator Applications, Amgen, Bayer, Curium Pharma, GE Healthcare, IPSEN, Janssen Pharmaceuticals, BTG, Sirtex, Novartis, ROTOP, and Bain Capital outside of the submitted work. Matthias Eiber was a consultant for ABX, Blue Earth Diagnostics, and Progenics and has patent rights on rhPSMA outside of the submitted work. Wolfgang P. Fendler received financial support from the German Research Foundation (Deutsche Forschungsgemeinschaft, DFG, grants FE1573/1-1/807122 and FE1573/3-1/659216 and DFG Research Training Group 1739), was a consultant for Endocyte and BTG, and received fees from RadioMedix, Bayer, and Parexel outside of the submitted work. Ebrahim Delpassand reports equity ownership at Excel Nuclear Oncology Center and RadioMedix. No other potential conflict of interest relevant to this article was reported.

ACKNOWLEDGMENTS

We thank all the patients and their referring physicians whose willingness to participate made this study possible. We thank the whole staff team of the UCLA Nuclear Medicine and Theranostics Division whose hard work made this study possible. We thank Dr. Lassman (University of Wurzburg, Germany) for his work on the dosimetry analysis.

KEY POINTS

QUESTION: What is the safety profile of 2 activity regimens of ^{177}Lu-PSMA-617 therapy in patients with mCRPC?

PERTINENT FINDINGS: In this prospective multicenter randomized phase 2 study that included 64 patients with progressive mCRPC, 2 activity regimens of ^{177}Lu-PSMA-617 therapy (6.0 and 7.4 GBq per cycle) were well tolerated. There was no difference in toxicity between administration of 6.0 and 7.4 GBq of ^{177}Lu-PSMA-617 per treatment cycle.

IMPLICATIONS FOR PATIENT CARE: ^{177}Lu-PSMA-617 therapy is a therapeutic option for patients with mCRPC with a good safety profile.

REFERENCES

1. Strosberg J, El-Haddad G, Wolin E, et al. Phase 3 trial of ^{177} Lu-DOTATATE for midgut neuroendocrine tumors. *N Engl J Med.* 2017;376:125–135.
2. Ghosh A, Heston WDW. Tumor target prostate specific membrane antigen (PSMA) and its regulation in prostate cancer. *J Cell Biochem.* 2004;91:528–539.
3. Benešová M, Schafer M, Bauder-Wust U, et al. Preclinical evaluation of a tailor-made DOTA-conjugated PSMA inhibitor with optimized linker moiety for imaging and endoradiotherapy of prostate cancer. *J Nucl Med.* 2015;56:914–920.
4. Ahmadzadehfar H, Eppard E, Kürpig S, et al. Therapeutic response and side effects of repeated radioligand therapy with ^{177}Lu-PSMA-DKFZ-617 of castrate-resistant metastatic prostate cancer. *Oncotarget.* 2016;7:12477.
5. Rahbar K, Ahmadzadehfar H, Kratochwil C, et al. German multicenter study investigating ^{177}Lu-PSMA-617 radioligand therapy in advanced prostate cancer patients. *J Nucl Med.* 2017;58:85–90.
6. Kratochwil C, Giesel FL, Stefanova M, et al. PSMA-targeted radionuclide therapy of metastatic castration-resistant prostate cancer with ^{177}Lu-labeled PSMA-617. *J Nucl Med.* 2016;57:1170–1176.
7. Witzig TE, Gordon LI, Cabanillas F, et al. Randomized controlled trial of Yttrium-90–labeled ibritumomab tiuxetan radioimmunotherapy versus rituximab immunotherapy for patients with relapsed or refractory low-grade, follicular, or transformed B-cell non-Hodgkin's lymphoma. *J Clin Oncol.* 2002;20:2453–2463.
8. Parker C, Nilsson S, Heinrich D, et al. Alpha emitter radium-223 and survival in metastatic prostate cancer. *N Engl J Med.* 2013;369:213–223.
9. Kabasakal L, AbuQbeitah M, Aygün A, et al. Pre-therapeutic dosimetry of normal organs and tissues of ^{177}Lu-PSMA-617 prostate-specific membrane antigen (PSMA) inhibitor in patients with castration-resistant prostate cancer. *Eur J Nucl Med Mol Imaging.* 2015;42:1976–1983.

10. Delker A, Fendler WP, Kratochwil C, et al. Dosimetry for ^{177}Lu-DKFZ-PSMA-617: a new radiopharmaceutical for the treatment of metastatic prostate cancer. *Eur J Nucl Med Mol Imaging.* 2016;43:42–51.
11. Calais J, Gafita A, Eiber MR, et al. Prospective phase 2 trial of PSMA-targeted molecular RadiothErapy with 177Lu-PSMA-617 for metastatic Castration-reSISTant Prostate Cancer (RESIST-PC): Efficacy results of the UCLA cohort. *J Nucl Med.* May 20, 2021 [Epub ahead of print].
12. Rosset A, Spadola L, Ratib O. OsiriX: an open-source software for navigating in multidimensional DICOM images. *J Digit Imaging.* 2004;17:205–216.
13. Vickers AJ. How to randomize. *J Soc Integr Oncol.* 2006;4:194–198.
14. Scher HI, Morris MJ, Stadler WM, et al. Trial design and objectives for castration-resistant prostate cancer: updated recommendations from the prostate cancer clinical trials Working Group 3. *J Clin Oncol.* 2016;34:1402–1418.
15. Seifert R, Kessel K, Schlack K, Weckesser M, Bögemann M, Rahbar K. Radioligand therapy using [^{177}Lu]Lu-PSMA-617 in mCRPC: a pre-VISION single-center analysis. *Eur J Nucl Med Mol Imaging.* 2020;47:2106–2112.
16. Gallyamov M, Meyrick D, Barley J, Lenzo N. Renal outcomes of radioligand therapy: experience of 177lutetium—prostate-specific membrane antigen ligand therapy in metastatic castrate-resistant prostate cancer. *Clin Kidney J.* 2019;13:1049–1055.
17. Violet J, Sandhu S, Iravani A, et al. Long-term follow-up and outcomes of retreatment in an expanded 50-Patient single-center phase II prospective trial of ^{177}Lu-PSMA-617 theranostics in metastatic castration-resistant prostate cancer. *J Nucl Med.* 2020;61:857–865.
18. Hofman MS, Emmett L, Sandhu S, et al. [^{177}Lu]Lu-PSMA-617 versus cabazitaxel in patients with metastatic castration-resistant prostate cancer (TheraP): a randomised, open-label, phase 2 trial. *Lancet.* 2021;397:797–804.
19. Sartor O, de Bono J, Chi KN, et al. Lutetium-177–PSMA-617 for metastatic castration-resistant prostate cancer. *N Engl J Med.* June 2021:NEJMoa2107322.
20. van Kalmthout LWM, Lam MGEH, de Keizer B, et al. Impact of external cooling with icepacks on ^{68}Ga-PSMA uptake in salivary glands. *EJNMMI Res.* 2018;8:56.
21. Yilmaz B, Nisli S, Ergul N, Gursu RU, Acikgoz O, Çermik TF. Effect of external cooling on ^{177} Lu-PSMA uptake by the parotid glands. *J Nucl Med.* 2019; 60:1388–1393.
22. Maia MC, Pereira AAL, Lage LV, et al. Efficacy and safety of docetaxel in elderly patients with metastatic castration-resistant prostate cancer. *J Glob Oncol.* 2018;4: 1–9.
23. Tannock IF, de Wit R, Berry WR, et al. Docetaxel plus prednisone or mitoxantrone plus prednisone for advanced prostate cancer. *N Engl J Med.* 2004;351: 1502–1512.
24. de Wit R, de Bono J, Sternberg CN, et al. Cabazitaxel versus abiraterone or enzalutamide in metastatic prostate cancer. *N Engl J Med.* 2019;381:2506–2518.
25. Emami B, Lyman J, Brown A, et al. Tolerance of normal tissue to therapeutic irradiation. *Int J Radiat Oncol Biol Phys.* 1991;21:109–122.
26. Yadav MP, Ballal S, Sahoo RK, Dwivedi SN, Bal C. Radioligand therapy with ^{177} Lu-PSMA for metastatic castration-resistant prostate cancer: a systematic review and meta-analysis. *AJR.* 2019;213:275–285.
27. Hofman MS, Violet J, Hicks RJ, et al. [^{177}Lu]-PSMA-617 radionuclide treatment in patients with metastatic castration-resistant prostate cancer (LuPSMA trial): a single-centre, single-arm, phase 2 study. *Lancet Oncol.* 2018;19:825–833.
28. Tagawa ST, Osborne JR, Hackett A, et al. Preliminary results of a phase I/II dose-escalation study of fractionated dose ^{177}Lu-PSMA-617 for progressive metastatic castration resistant prostate cancer (mCRPC). *Ann Oncol.* 2019;30:v329–v330.

Head-to-Head Comparison of ^{68}Ga-NOTA (^{68}Ga-NGUL) and ^{68}Ga-PSMA-11 in Patients with Metastatic Prostate Cancer: A Prospective Study

Minseok Suh[1,2], Hyung-Jun Im[2,3], Hyun Gee Ryoo[1,2], Keon Wook Kang[1], Jae Min Jeong[1], Sneha Prakash[4], Sanjana Ballal[4], Madhav P. Yadav[4], Chandrasekhar Bal[4], Chang Wook Jeong[5], Cheol Kwak[5], and Gi Jeong Cheon[1,6,7]

[1]Department of Nuclear Medicine, Seoul National University College of Medicine, Seoul, Korea; [2]Department of Molecular Medicine and Biopharmaceutical Sciences, Graduate School of Convergence Science and Technology, Seoul National University, Seoul, Korea; [3]Department of Applied Bioengineering, Graduate School of Convergence Science and Technology, Seoul National University, Seoul, Korea; [4]Department of Nuclear Medicine, AIIMS, New Delhi, India; [5]Department of Urology, Seoul National University College of Medicine, Seoul, Korea; [6]Cancer Research Institute, Seoul National University, Seoul Korea; and [7]Institute of Radiation Medicine, College of Medicine, Seoul National University, Seoul, Korea

^{68}Ga-NOTA Glu-Urea-Lys (NGUL) is a novel prostate-specific membrane antigen (PSMA)–targeting tracer used for PET/CT imaging. This study aimed to compare performance in the detection of primary and metastatic lesions and to compare biodistribution between ^{68}Ga-NGUL and ^{68}Ga-PSMA-11 in the same patients with prostate cancer. **Methods:** Eleven patients with metastatic prostate cancer were prospectively recruited. The quantitative tracer uptake was determined in normal organs and in primary and metastatic lesions. **Results:** ^{68}Ga-NGUL showed significantly lower normal-organ uptake and rapid urinary clearance. The number and sites of detected PSMA-positive primary and metastatic lesions were identical, and no significant quantitative uptake difference was observed. ^{68}Ga-NGUL showed a relatively lower tumor-to-background ratio than ^{68}Ga-PSMA-11. **Conclusion:** In a head-to-head comparison with ^{68}Ga-PSMA-11, ^{68}Ga-NGUL showed lower uptake in normal organs and similar performance in detecting PSMA-avid primary and metastatic lesions. ^{68}Ga-NGUL could be a valuable option for PSMA imaging.

Key Words: prostate-specific membrane antigen; ^{68}Ga-NGUL; ^{68}Ga-PSMA-11; biodistribution

J Nucl Med 2021; 62:1457–1460
DOI: 10.2967/jnumed.120.258434

Prostate-specific membrane antigen (PSMA), a transmembrane protein overexpressed in prostate cancer, has been one of the most highlighted targets for imaging and therapy of prostate cancer (*1*,*2*). Among many PSMA PET tracers, ^{68}Ga-PSMA-11 is the most extensively investigated and well-established tracer (*3*). ^{68}Ga-PSMA-11 is superior to conventional imaging modalities in staging and detection of biochemical failure in patients with prostate cancer (*4*–*7*).

We recently developed a novel PSMA-targeting tracer named ^{68}Ga-NOTA-Glu-Urea-Lys (NGUL), based on Glu-Urea-Lys derivatives conjugated with NOTA chelator via a thiourea-type short linker (*8*). In our previous study, ^{68}Ga-NGUL showed a higher tumor-to-background ratio and substantially lower kidney uptake than ^{68}Ga-PSMA-11 in PSMA-positive tumor-xenografted mice (*8*).

To further investigate the clinical feasibility of ^{68}Ga-NGUL, we have conducted a prospective head-to-head comparison study between ^{68}Ga-NGUL and ^{68}Ga-PSMA-11 PET/CT. The specific aims of this study were to compare the detection efficacy and biodistribution between ^{68}Ga-NGUL and ^{68}Ga-PSMA-11 in the same patients with metastatic prostate cancer.

MATERIALS AND METHODS

Subjects

Patients with metastatic prostate cancer were prospectively recruited into this study. Each patient underwent ^{68}Ga-NGUL and ^{68}Ga-PSMA-11 PET/CT. The quality of the tracer was assessed before administration, and ^{68}Ga-NGUL showed high purity and stability (Supplemental Fig. 1; supplemental materials are available at http://jnm.snmjournals.org). This study was approved by the Institutional Review Board. All patients gave written informed consent to undergo 2 consecutive PSMA-targeted PET/CT scans. All procedures performed in this study were in accordance with the ethical standards of the institutional research committee and with the 1964 Helsinki declaration and its later amendments or comparable ethical standards.

Image Acquisition and Analysis

The PET/CT scans were obtained at 60 min after tracer injection. Any focal accumulation of ^{68}Ga-NGUL and ^{68}Ga-PSMA-11 not explained by physiologic uptake was defined as a pathologic lesion. Lesion numbers and lesion uptake, as SUV_{max}, were compared (Supplemental Fig. 2A). Tracer uptake was quantified in normal organs, including salivary glands, liver, spleen, and kidney, and blood-pool activity was measured in the inferior vena cava (Supplemental Fig. 2B). The normal-organ distribution of both tracers was quantified as SUV_{mean}. In addition, 3 patients underwent dynamic PET/CT scanning (60 min) of the pelvic region to evaluate the urinary clearance.

Statistical Analysis

Statistical analyses were performed using Prism, version 5.0 (GraphPad Software), and the MedCalc statistical packages, version 14.8 (MedCalc Statistical Software). Shapiro–Wilk testing was used to

Received Oct. 20, 2020; revision accepted Jan. 28, 2021.
For correspondence or reprints, contact Gi Jeong Cheon (larrycheon@gmail.com).
Published online February 26, 2021.

evaluate data normality. The 2 tracers were compared using the Wilcoxon signed-rank test, linear regression, and Bland–Altman analysis.

RESULTS

Eleven patients were prospectively enrolled into the study. Their characteristics are summarized in Supplemental Table 1. The interval between ^{68}Ga-NGUL and ^{68}Ga-PSMA-11 PET/CT was 1–4 d, and no patient received any treatment between the scans. Quantitative data are expressed as the median and interquartile range (IQR).

Normal-Organ Distribution

Overall, the 2 scans showed similar distribution patterns, with the highest uptake in the kidneys (Fig. 1). An intrapatient quantitative comparison revealed significant differences in organ uptake between the 2 scans. The SUV_{mean} in the kidneys, salivary glands, spleen, and liver was significantly lower for ^{68}Ga-NGUL than for ^{68}Ga-PSMA-11 (Supplemental Table 2; Fig. 1). Linear correlation and agreement between ^{68}Ga-NGUL and ^{68}Ga-PSMA-11 are demonstrated in Supplemental Table 2 and Supplemental Fig. 3.

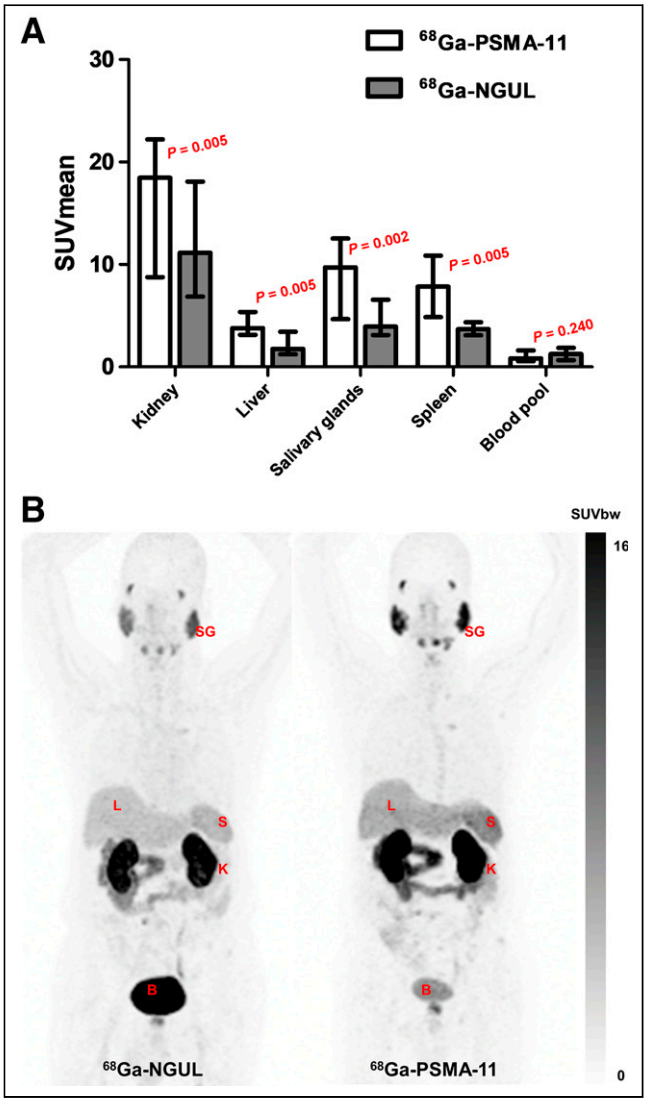

FIGURE 1. (A) SUV_{mean} of normal organs for ^{68}Ga-PSMA-11 and ^{68}Ga-NGUL. Median with interquartile range as error bar is plotted on bar chart. Wilcoxon signed-rank test for paired data was used for statistical comparison. (B) Representative image showing normal-organ distribution of ^{68}Ga-PSMA-11 and ^{68}Ga-NGUL. B = bladder; K = kidney; L = liver; S = spleen; SG = salivary glands; SUVbw = SUV body weight.

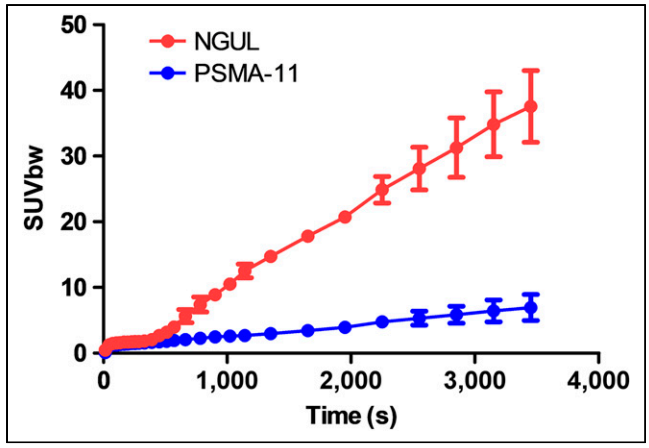

FIGURE 2. Time–activity curve of both ^{68}Ga-PSMA-11 and ^{68}Ga-NGUL derived from bladder region of interest.

From the dynamic PET imaging, the time–activity curve of the bladder was obtained for both tracers (Fig. 2). Over time, higher bladder retention was observed for ^{68}Ga-NGUL, reflecting more rapid urinary clearance than for ^{68}Ga-PSMA-11.

Analysis of Primary and Metastatic Lesions

^{68}Ga-NGUL and ^{68}Ga-PSMA-11 could detect primary lesions in all patients (n = 11). There was no significant difference in the SUV_{max} of primary tumors (Fig. 3A; Supplemental Table 2).

In a total of 11 patients, 161 nodal and 59 bone PSMA-avid metastases were identified. All lesions were detected identically by both tracers, and none of the lesions was detected by only ^{68}Ga-NGUL or only ^{68}Ga-PSMA-11 (Supplemental Table 3). Quantitative uptake was evaluated in a total of 36 lesions (20 lymph nodes and 16 bone metastases); a maximum of 2 lesions per organ and a total of 5 lesions were selected in each patient. No significant differences in lymph node or bone metastasis uptake were observed between ^{68}Ga-NGUL and ^{68}Ga-PSMA-11 (Fig. 3A; Supplemental Table 2). Linear correlation and agreement between ^{68}Ga-NGUL and ^{68}Ga-PSMA-11 are demonstrated in Supplemental Table 2 and Supplemental Fig. 4. The median tumor-to-background ratio of ^{68}Ga-NGUL tended to be lower than that of ^{68}Ga-PSMA-11 in primary tumors (37.5 [IQR, 26.8–62.8] vs. 58.3 [IQR, 33.5–90.4]; P = 0.067) and lymph node metastases (29.7 [IQR, 18.5–55.9] vs. 48.1 [IQR, 12.5–99.1]; P = 0.114), and the difference was statistically significant in the case of bone metastases (48.7 [IQR, 29.1–61.9] vs. 81.0 [IQR, 25.7–97.8]; P = 0.007) (Fig. 3B).

DISCUSSION

We found that ^{68}Ga-NGUL showed lower uptake in the normal organs, including the kidneys, salivary glands, spleen, and liver. ^{68}Ga-NGUL also showed more rapid clearance through the urinary system than did ^{68}Ga-PSMA-11. There was no significant difference in absolute lesion uptake; however, tumor-to-background ratio tended to be lower for ^{68}Ga-NGUL than for ^{68}Ga-PSMA-11.

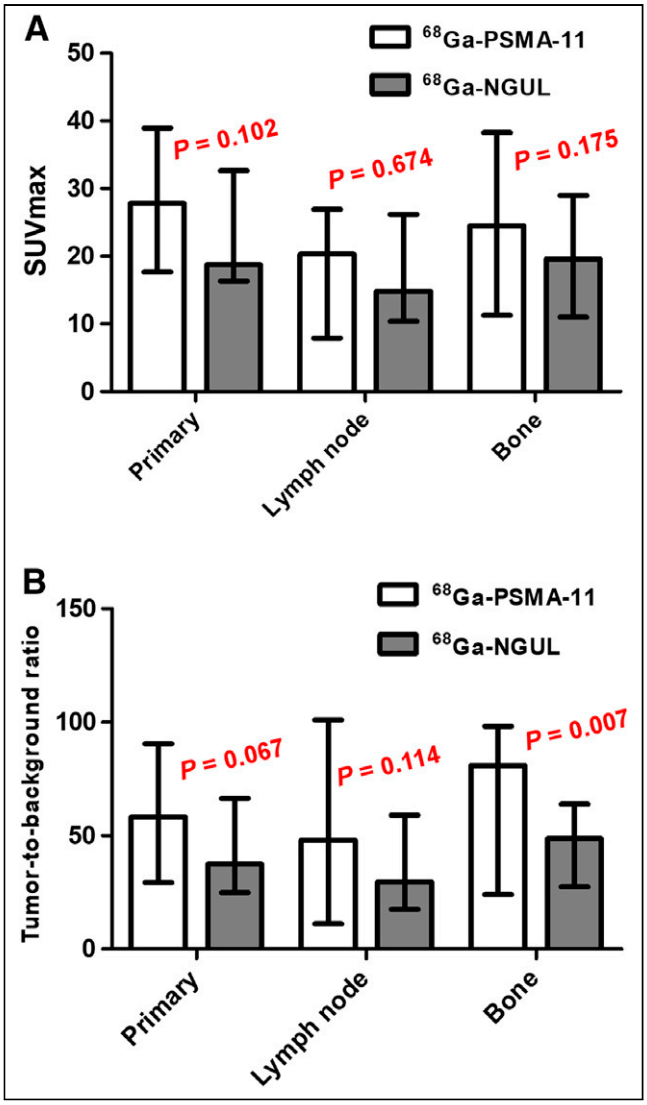

FIGURE 3. (A) SUV_{max} of primary tumor, lymph node, and bone metastases for ^{68}Ga-PSMA-11 and ^{68}Ga-NGUL. (B) Tumor-to-background ratio of primary tumor, lymph node, and bone metastases for ^{68}Ga-PSMA-11 and ^{68}Ga-NGUL. Median with interquartile range as error bar is plotted on bar chart. Wilcoxon signed-rank test for paired data was used for statistical comparison.

Still, the ability to detect primary and metastatic lesions was identical between ^{68}Ga-NGUL and ^{68}Ga-PSMA-11.

Several biodistribution studies of ^{68}Ga-PSMA-11 have demonstrated well the cellular expression of PSMA throughout the body: in parts of the lacrimal glands and major salivary glands, liver, spleen, kidneys, and intestines (*9*,*10*). In this study, ^{68}Ga-NGUL showed a distribution pattern visually similar to that of ^{68}Ga-PSMA-11. However, clearance via the urinary tract was more rapid for ^{68}Ga-NGUL than for ^{68}Ga-PSMA-11. Also, normal-organ uptake of ^{68}Ga-NGUL in the kidney, liver, salivary glands, and spleen was significantly lower than that of ^{68}Ga-PSMA-11. Several factors, including hydrophilicity, small molecular size, and low protein-binding properties, could explain the rapid clearance of ^{68}Ga-NGUL (*11*,*12*). NGUL has a lower molecular weight (769.82 vs. 947 g/mol) and higher hydrophilicity (log P = −3.3 vs. −3.9) than PSMA-11 (Supplemental Fig. 5). Indeed, as a diagnostic imaging agent, ^{68}Ga-NGUL may interfere with the detection of lesions adjacent to the urinary tract because of early clearance through the kidney to the bladder. To overcome this limitation, proper hydration and a postvoiding delayed scan should be considered in future imaging protocols for ^{68}Ga-NGUL.

Despite the faster clearance of ^{68}Ga-NGUL, there was a trend toward a lower tumor-to-background ratio. In our previous study, the binding affinity of ^{68}Ga-NGUL was 18.3 nM (*8*), which is relatively lower than that of ^{68}Ga-PSMA-11, reported to be 24.3 nM (*13*). Thus, it is speculated that the fraction of unbound ^{68}Ga-NGUL is relatively higher than that of ^{68}Ga-PSMA-11 and the amount taken up by normal organs or tumor is relatively lower. As a result, the difference in the tumor-to-background ratio becomes more pronounced.

Some limitations should be noted. First, because of a small number of patients, we cannot draw a generalized conclusion. However, as a head-to-head comparison study, the difference between the distribution of the 2 compounds seems to be solid. Nonetheless, further studies with a larger number of patients are needed to validate our findings. Second, our cohort does not have whole-body PET data on multiple time points. As a result, we could not assess the clinical dose difference between the 2 agents. However, the effective dose measured from the animal experiments was 0.019 mSv/MBq (Supplemental Table 4), which is similar to the dosimetry data provided by ^{68}Ga PSMA-11 clinical studies. Lastly, the PSA level was not considered comprehensively. Because the PSMA-avid tumor burden correlates significantly with PSA level, it is considered to be a good indicator of tumor status at each scanning time point (*4*,*14*). However, since the interval between 2 scans was short, within 4 d, we speculate that the difference in tumor status between imaging time points is negligible.

CONCLUSION

A head-to-head comparison of ^{68}Ga-NGUL and ^{68}Ga-PSMA-11 revealed lower uptake of ^{68}Ga-NGUL in the normal organs, including the kidneys, salivary glands, spleen, and liver, and more rapid clearance through the urinary system. Although ^{68}Ga-NGUL showed a trend toward low tumor-to-background ratios, its ability to detect primary and metastatic lesions was the same as that of ^{68}Ga-PSMA-11. Therefore, ^{68}Ga-NGUL could be a valuable option for PSMA PET/CT imaging.

DISCLOSURE

This work was supported by a National Research Foundation of Korea grant funded by the Korean government (MSIT) (NRF-2020R1A2C2011428 and NRF-2020M2D9A1093988), by the Korea Health Technology R&D Project through the Korea Health Industry Development Institute (HI18C1916, HI19C0339), and by the Creative-Pioneering Researchers Program through Seoul National University. This work was supported by the Technology Innovation Program (20001235, Development of Novel Radiopharmaceutical for Prostate Cancer Targeted Imaging Diagnosis) funded by the Ministry of Trade, Industry, and Energy (Korea). The NGUL kit vial was provided by Cellbion Co., Ltd. Hyung-Jun Im, MD, PhD, is a consultant for Cellbion. No other potential conflict of interest relevant to this article was reported.

KEY POINTS

QUESTION: How does ^{68}Ga-NGUL PET/CT compare with ^{68}Ga-PSMA-11 in patients with metastatic prostate cancer?

PERTINENT FINDINGS: Compared with ^{68}Ga-PSMA-11, ^{68}Ga-NGUL showed lower uptake in the normal organs and more rapid clearance and tended to show a lower tumor-to-background ratio. Still, the ability to detect primary and metastatic lesions was identical between ^{68}Ga-NGUL and ^{68}Ga-PSMA-11, and no significant difference with respect to lesion uptake was observed.

IMPLICATIONS FOR PATIENT CARE: ^{68}Ga-NGUL can be a valuable option for imaging and theranostics in patients with metastatic prostate cancer.

REFERENCES

1. Iravani A, Violet J, Azad A, Hofman MS. Lutetium-177 prostate-specific membrane antigen (PSMA) theranostics: practical nuances and intricacies. *Prostate Cancer Prostatic Dis.* 2020;23:38–52.
2. Siva S, Udovicich C, Tran B, Zargar H, Murphy DG, Hofman MS. Expanding the role of small-molecule PSMA ligands beyond PET staging of prostate cancer. *Nat Rev Urol.* 2020;17:107–118.
3. Eder M, Schafer M, Bauder-Wust U, et al. ^{68}Ga-complex lipophilicity and the targeting property of a urea-based PSMA inhibitor for PET imaging. *Bioconjug Chem.* 2012;23:688–697.
4. Ceci F, Uprimny C, Nilica B, et al. ^{68}Ga-PSMA PET/CT for restaging recurrent prostate cancer: which factors are associated with PET/CT detection rate? *Eur J Nucl Med Mol Imaging.* 2015;42:1284–1294.
5. Fendler WP, Eiber M, Beheshti M, et al. ^{68}Ga-PSMA PET/CT: joint EANM and SNMMI procedure guideline for prostate cancer imaging: version 1.0. *Eur J Nucl Med Mol Imaging.* 2017;44:1014–1024.
6. Eiber M, Maurer T, Souvatzoglou M, et al. Evaluation of hybrid ^{68}Ga-PSMA ligand PET/CT in 248 patients with biochemical recurrence after radical prostatectomy. *J Nucl Med.* 2015;56:668–674.
7. Hofman MS, Lawrentschuk N, Francis RJ, et al. Prostate-specific membrane antigen PET-CT in patients with high-risk prostate cancer before curative-intent surgery or radiotherapy (proPSMA): a prospective, randomised, multicentre study. *Lancet.* 2020;395:1208–1216.
8. Moon SH, Hong MK, Kim YJ, et al. Development of a Ga-68 labeled PET tracer with short linker for prostate-specific membrane antigen (PSMA) targeting. *Bioorg Med Chem.* 2018;26:2501–2507.
9. Afshar-Oromieh A, Malcher A, Eder M, et al. PET imaging with a [^{68}Ga]gallium-labelled PSMA ligand for the diagnosis of prostate cancer: biodistribution in humans and first evaluation of tumour lesions. *Eur J Nucl Med Mol Imaging.* 2013;40:486–495.
10. Prasad V, Steffen IG, Diederichs G, Makowski MR, Wust P, Brenner W. Biodistribution of [^{68}Ga]PSMA-HBED-CC in patients with prostate cancer: characterization of uptake in normal organs and tumour lesions. *Mol Imaging Biol.* 2016;18:428–436.
11. Di L. Strategic approaches to optimizing peptide ADME properties. *AAPS J.* 2015;17:134–143.
12. Varma MV, Feng B, Obach RS, et al. Physicochemical determinants of human renal clearance. *J Med Chem.* 2009;52:4844–4852.
13. Kelly J, Amor-Coarasa A, Nikolopoulou A, et al. Synthesis and pre-clinical evaluation of a new class of high-affinity ^{18}F-labeled PSMA ligands for detection of prostate cancer by PET imaging. *Eur J Nucl Med Mol Imaging.* 2017;44:647–661.
14. Schmidkonz C, Cordes M, Schmidt D, et al. ^{68}Ga-PSMA-11 PET/CT-derived metabolic parameters for determination of whole-body tumor burden and treatment response in prostate cancer. *Eur J Nucl Med Mol Imaging.* 2018;45:1862–1872.

Rational Linker Design to Accelerate Excretion and Reduce Background Uptake of Peptidomimetic PSMA-Targeting Hybrid Molecules

Ann-Christin Eder[1–3], Martin Schäfer[1], Jana Schmidt[1], Ulrike Bauder-Wüst[1], Mareike Roscher[1], Karin Leotta[4,5], Uwe Haberkorn[4,5], Klaus Kopka*[1,6], and Matthias Eder*[2,3]

[1]*Division of Radiopharmaceutical Chemistry, German Cancer Research Center (DKFZ), Heidelberg, Germany;* [2]*Department of Nuclear Medicine, University Medical Center Freiburg, Faculty of Medicine, University of Freiburg, Freiburg, Germany;* [3]*Division of Radiopharmaceutical Development, German Cancer Consortium (DKTK), partner site Freiburg, Freiburg, Germany and German Cancer Research Center, Heidelberg, Germany;* [4]*Department of Nuclear Medicine, Heidelberg University Hospital, Heidelberg, Germany;* [5]*Clinical Cooperation Unit Nuclear Medicine, German Cancer Research Center (DFKZ), Heidelberg, Germany; and* [6]*German Cancer Consortium (DKTK), Heidelberg, Germany*

The evolution of peptidomimetic hybrid molecules for preoperative imaging and guided surgery targeting the prostate-specific membrane antigen (PSMA) significantly progressed over the past few years, and some approaches are currently being evaluated for further clinical translation. However, accumulation in nonmalignant tissue such as kidney, bladder, spleen, or liver might limit tumor-to-background contrast for precise lesion delineation, particularly in a surgical setting. To overcome these limitations, a rational linker design aims at the development of a second generation of PSMA-11–based hybrid molecules with an enhanced pharmacokinetic profile and improved imaging contrast. **Methods:** A selection of rationally designed linkers was introduced to the PSMA-targeting hybrid molecule Glu-urea-Lys-HBED-CC-IRDye800CW, resulting in a second-generation peptidomimetic hybrid molecule library. The biologic properties were investigated in cell-based assays. In a preclinical proof-of-concept study with the radionuclide ^{68}Ga, the impact of the modifications was evaluated by determination of specific tumor uptake, pharmacokinetics, and fluorescence imaging in tumor-bearing mice. **Results:** The modified hybrid molecules carrying various selected linkers revealed high PSMA-specific binding affinity and effective internalization. The highest tumor-to-background contrast of all modifications investigated was identified for the introduction of a histidine- (H) and glutamic acid (E)–containing linker ($(HE)_3$-linker) between the PSMA-binding motif and the chelator. In comparison to the parental core structure, uptake in nonmalignant tissue was significantly reduced to a minimum, as exemplified by an 11-fold reduced spleen uptake from 38.12 ± 14.62 percentage injected dose (%ID)/g to 3.47 ± 1.39 %ID/g (1 h after injection). The specific tumor uptake of this compound (7.59 ± 0.95 %ID/g, 1 h after injection) was detected to be significantly higher than that of the parental tracer PSMA-11. These findings confirmed by PET and fluorescence imaging are accompanied by an enhanced pharmacokinetic profile with accelerated background clearance at early time points after injection. **Conclusion:** The novel generation of PSMA-targeting hybrid molecules reveals fast elimination, reduced background organ enrichment, and high PSMA-specific tumor uptake meeting the key demands for potent tracers in nuclear medicine and fluorescence-guided surgery. The approach's efficacy in improving the pharmacokinetic profile highlights the strengths of rational linker design as a powerful tool in strategic hybrid-molecule development.

Key Words: PSMA; hybrid molecules; prostate cancer; guided surgery; pharmacokinetic profile

J Nucl Med 2021; 62:1461–1467
DOI: 10.2967/jnumed.120.248443

Surgical resection of tumor tissue represents one of the main curative treatment options in the clinical management of prostate cancer (*1*). The precise detection and comprehensive resection of malignancies is thereby of high significance for patient survival and therapy success. During resection, several difficulties are limiting the therapeutic outcome. Although malignant tissue can be precisely localized preoperatively using diagnostic radiopharmaceuticals, the translation to the operating theater often remains challenging. This increases the risk that tumor tissue will be missed by the surgeon (*2*,*3*). Additionally, a close proximity of lesions to essential healthy structures such as the urinary bladder or nerves impedes a wide dissection in the lower pelvis, resulting in positive surgical margins (*4*). These difficulties cause an increased possibility of cancer recurrence and subsequent treatment failure (*5*). Consequently, template-based extended lymphadenectomies, for example, are performed to diminish the risk of left-behind lesions (*6*,*7*). Besides malignant tissue, a considerable amount of healthy tissue is removed during this surgical strategy, causing increased morbidity. Hence, there is a strong medical need for advances in the field of intraoperative navigation to precisely delineate tumor tissue from surrounding healthy tissue.

To overcome these issues, novel approaches have been developed over the past few years comprising the detection of malignant tissue supported by both a γ-probe and a fluorescent dye. A combination of these 2 modalities in so-called hybrid or dual-labeled approaches compensates for their respective disadvantages, thereby merging the strengths of both technologies. In a clinical scenario, these novel approaches provide preoperative imaging (e.g., PET/CT) for planning of the surgery, combined with subsequent intraoperative navigation. The first clinical proof-of-concept studies with the indocyanine green–based hybrid sentinel

Received May 1, 2020; revision accepted Jan. 13, 2021.
For correspondence or reprints, contact Ann-Christin Eder (ann-christin.eder@uniklinik-freiburg.de).
*Contributed equally to this work.
Published online March 19, 2021.

lymph node tracer indocyanine green–^{99m}Tc-nanocolloid demonstrated the feasibility of dual-modality approaches to improve surgical accuracy in different cancer types (*8–10*). Because nontargeted approaches have their limitations in precisely detecting tumor tissue, recent advances have focused on the design of targeted dual-modality probes.

For the specific targeting of prostate cancer, the prostate-specific membrane antigen (PSMA) has been identified as an excellent target structure. PSMA is a transmembrane carboxypeptidase that is selectively overexpressed in most prostate carcinomas, including local lesions, malignant lymph nodes, and bone metastases (*11–14*). The first PSMA-targeting dual-modality antibodies and small-molecule peptidomimetic inhibitors have recently demonstrated the feasibility of hybrid detection in preclinical studies (*15–18*). Besides high and specific tumor uptake of targeted hybrid probes, a favorable pharmacokinetic profile with, for example, a low accumulation in off-target tissue, fast clearance, and a resulting high imaging contrast at early time points after injection is crucial for further clinical translation.

With the development of dual-modality low-molecular-weight PSMA inhibitors based on the clinically established PET tracer ^{68}Ga-PSMA-11, a versatile platform was designed tolerating the conjugation of a fluorescent dye combined with a radiolabel moiety (*18–20*). Our theranostic dual-modality platform is thus characterized by high and fast PSMA-specific tumor uptake along with rapid background clearance allowing preoperative imaging combined with intraoperative guidance (*18*). The advantageous effect of introducing spacer moieties comprising histidine (H) and glutamic acid (E) on the biodistribution profile of Affibody (Affibody AB) molecules was originally reported by Hofstrom et al. (*21*). Further work from our group successfully established (HE)$_3$ linker modifications to PSMA-11 leading to significantly enhanced tumor-to-background contrast and reduced uptake in dose-limiting background organs (*22*). Because of the high clinical relevance, we introduced charged spacer moieties to our theranostic dual-modality platform, leading to a second generation of hybrid probes with improved imaging contrast. The insights investigated in this pharmacokinetic proof-of-concept study demonstrate a valuable progression aiming at clinical translation for better management of prostate cancer patients.

MATERIALS AND METHODS

Chemical Synthesis, Radiolabeling, Determination of Lipophilicity, and Serum Stability

The synthesis of the variants of Glu-urea-Lys-HBED-CC-IRDye800CW comprising a series of amino acid linker modifications was performed according to previously published protocols (*18*,*22–25*) (the supplemental materials available at http://jnm.snmjournals.org provide details on the synthesis and chemical structures of the compounds). $^{68}Ga^{3+}$ (half-life, 68 min; β^+, 89%; maximum $E_{\beta+}$, 1.9 MeV) was obtained from a ^{68}Ge/^{68}Ga generator based on a pyrogallol resin support, with details of compound characterization (radiolabeling, determination of lipophilicity, serum stability studies) provided in the supplemental materials (*26*).

In Vitro Evaluation

PSMA-positive LNCaP cells (CRL-1740; ATCC) and PSMA-negative PC-3 cells (CRL-1435; ATCC) were cultured in RPMI medium supplemented with 10% fetal calf serum and 2 mM L-glutamine (all from PAA). Cells were grown at 37°C in humidified air with 5% CO_2 and were harvested using trypsin-ethylenediaminetetraacetic acid (0.25% trypsin, 0.02% ethylenediaminetetraacetic acid; Invitrogen). Cell line authentication is regularly performed, and the LNCaP and PC-3 cell lines were authenticated on March 6, 2020. The competitive cell binding assay and internalization experiments were performed as described previously (*19*,*25*).

Biodistribution and Preclinical Proof of Concept

For the experimental tumor models, 5×10^6 cells of LNCaP or PC-3 (in 50% Matrigel; Becton Dickinson) were subcutaneously inoculated into the flank of 7- to 8-wk-old male BALB/c *nu/nu* mice (Charles River). For biodistribution studies, the ^{68}Ga-labeled compounds were injected into a tail vein (1–3 MBq [60 pmol, $n = 3$] and 30–50 MBq [500 pmol, $n = 3$]). At 1 and 2 h after injection, respectively, the animals were sacrificed. Organs of interest were dissected, blotted dry, and weighed. The radioactivity was measured using a γ-counter and calculated as percentage injected dose [%ID]/g. Optical imaging was performed with the Odyssey CLx system (excitation wavelength, 800 nm; LI-COR Biosciences). In an additional preclinical proof of concept ($n = 1$), mice were anesthetized (2% sevoflurane; Abbvie) and 0.5 nmol of the ^{68}Ga-labeled compound in 0.9% NaCl (pH 7) were injected into the tail vein. Preoperative PET imaging was performed with a PET scanner (Inveon PET; Siemens). For subsequent optical imaging to identify the tumor by fluorescence, mice were sacrificed after PET imaging and dissected tissue analyzed using the Odyssey CLx system (the supplemental materials provide details on the imaging protocol, software, image reconstruction, and procedure). All animal experiments were approved by the regional authorities *Regierungspräsidium Karlsruhe* and *Regierungspräsidium Freiburg* and complied with the current laws of the Federal Republic of Germany.

Statistical Aspects

Experiments were performed at least in triplicate, except for the proof-of-concept study ($n = 1$). Quantitative data are expressed as mean ± SD. The n values are given in the respective figure or table captions. If applicable, means were compared using the Student t test (Prism, version 8; GraphPad Software, Inc.). P values of less than 0.05 were considered statistically significant.

RESULTS

Synthesis, Radiolabeling, and Serum Stability

For this pharmacokinetic proof-of-concept study, Glu-urea-Lys-HBED-CC-IRDye800CW (tumor uptake 1 h after injection, 13.66 ± 3.73 %ID/g) was selected as an exemplary model core structure for our theranostic dual-modality platform for 2 main reasons. First, this compound has been preclinically proven to perform comparably to or even to outperform successfully established molecules such as PSMA-11 (tumor uptake 1 h after injection, 4.89 ± 1.34 %ID/g) or PSMA-617 (tumor uptake 1 h after injection, 8.47 ± 4.09 %ID/g) (*18*,*22*,*27*). Second, the choice of the structure previously comprising the bulky clinically relevant near-infrared dye IRDye800CW simplifies further clinical translation of the findings, since small molecules' biologic properties are typically strongly influenced when conjugated to a fluorescent dye. In a first step, charged linker moieties found to be favorable with respect to pharmacokinetic properties in previous studies were introduced combining solid-phase and classic organic synthesis strategies (Supplemental Figs. 1 and 2) (*18*,*22*). As the most promising candidate in former studies, the $(HE)_3$-motif was additionally inserted between the chelator and the fluorescent moiety to investigate the influence of linker positioning within the molecule (Supplemental Fig. 2) (*23*,*28*). The dye was conjugated to the precursor molecules as IRDye800CW-NHS-ester in the last step. A detailed description of

TABLE 1
Cell Binding and Internalization Data of Compounds

Compound	Specifically cell surface–bound*	Specifically internalized*	IC_{50} (nM)† Free ligands	$^{69/71}$Ga-labeled compounds
Glu-urea-Lys-$(HE)_1$-HBED-CC-IRDye800CW	3.00 ± 1.42	3.27 ± 1.83	28.41 ± 14.39	35.57 ± 22.83
Glu-urea-Lys-$(WE)_1$-HBED-CC-IRDye800CW	6.47 ± 3.69	13.77 ± 8.50	43.70 ± 14.12	56.80 ± 17.10
Glu-urea-Lys-$(HE)_3$-HBED-CC-IRDye800CW	8.30 ± 3.93	6.45 ± 3.36	51.29 ± 11.84	69.98 ± 22.88
Glu-urea-Lys-HBED-CC-$(HE)_3$-IRDye800CW	6.26 ± 1.49	3.70 ± 0.51	41.74 ± 18.26	52.21 ± 7.33

*^{68}Ga-labeled compounds. Specific cell uptake was determined by blockage using 500 μM 2-PMPA. Data are percentage applied radioactivity bound to 10^5 cells.

†Radioligand: ^{68}Ga-PSMA-10 (dissociation constant, 3.8 ± 1.8 nM (25); $c_{radioligand}$, 0.75 nM [c = concentration]).

Data are expressed as mean ± SD (n = 3). Affinity to PSMA and internalization properties of compounds were determined in vitro using PSMA-positive cells (LNCaP). For all compounds, PSMA-specific internalization was detected, as well as high binding affinity to PSMA (in low nanomolar range) not significantly dependent on complexation.

the synthetic strategies is provided in the supplemental materials. The final products were obtained in greater than 98% purity and their analytic data are summarized in Supplemental Figures 3 and 4 and Supplemental Tables 1 and 2. Lipophilicity, determined as log$D$ at pH 7.4 in n-octanol/phosphate-buffered saline, was found to be in the same range as the respective Glu-urea-Lys-HBED-CC-IRDye800CW reference compound with a $\log D_{pH\ 7.4}$ value of −2.21 ± 0.36 (Supplemental Table 1) (*18*). Radiolabeling with ^{68}Ga resulted in radiochemical yields greater than 99%, and the molar activities of the ^{68}Ga-labeled compounds were detected to be around 80–120 GBq/μmol (Supplemental Figs. 5–7). ^{68}Ga-Glu-urea-Lys-$(HE)_3$-HBED-CC-IRDye800CW was found to be stable in mouse and human serum up to 2 h.

PSMA-Specific Binding and Internalization Properties

High and specific affinity to PSMA in the nanomolar range was revealed for all tested compounds in competitive binding studies, and this affinity was not significantly complexation-dependent (Table 1; Supplemental Fig. 8). The introduction of $(HE)_1$- or tryptophane (W)-containing $(WE)_1$ motifs between the PSMA-binding motif and the chelator or of the $(HE)_3$ motif between the chelator and the fluorescent dye had no impact on binding properties as compared with the reference Glu-urea-Lys-HBED-CC-IRDye800CW (*18*). Interestingly, the $(HE)_3$ motif inserted between PSMA-binding unit and chelator moiety significantly reduced the affinity to PSMA (P = 0.024). Specific cell surface binding was detected for all tested dual-labeled probes (Table 1; Supplemental Fig. 9). Incorporating the $(WE)_1$ (P = 0.482) or $(HE)_3$ motif (P = 0.053) near the PSMA-binding motif resulted in the most pronounced specifically internalized fractions not significantly differing from the reference (*18*). In contrast, changing the intramolecular $(HE)_3$ motif position by inserting the linker between the chelator and the dye (P = 0.021) or introducing $(HE)_1$ as a linker structure next to the PSMA-binding motif (P = 0.021) revealed significantly reduced internalization properties (Table 1).

Specific Enrichment in Xenograft Tumors with Enhanced Contrast to Background Tissue

The impact of the introduction of charged amino acid linker motifs to Glu-urea-Lys-HBED-CC-IRDye800CW on in vivo specific PSMA targeting and accompanying background organ enrichment was further evaluated in biodistribution studies. ^{68}Ga-Glu-urea-Lys-$(HE)_3$-HBED-CC-IRDye800CW revealed a significantly increased, PSMA-specific tumor uptake in LNCaP xenograft tumors (7.59 ± 0.95 %ID/g, $P < 0.05$), compared with the incorporation of other motifs or intramolecular positioning of the $(HE)_3$ motif near the fluorescent dye at 1 h after injection (Figs. 1A and 1B; Supplemental Figure 10; Supplemental Tables 3–5). Although in comparison to the core structure, tumor uptake was significantly reduced for ^{68}Ga-Glu-urea-Lys-$(HE)_3$-HBED-CC-IRDye800CW (P = 0.031), it proved to be significantly increased when compared with ^{68}Ga-PSMA-11 (P = 0.047) or ^{68}Ga-PSMA-I&F (P = 0.045) and identical to ^{68}Ga-PSMA-617 (P = 0.735) (*17*,*22*,*27*). In addition, tracer uptake of ^{68}Ga-Glu-urea-Lys-$(HE)_3$-HBED-CC-IRDye800CW in nonmalignant tissue was significantly reduced to a minimum, with striking effects on spleen uptake, for example, which could be reduced from 38.12 ± 14.62 %ID/g to 3.47 ± 1.39 %ID/g (Fig. 1A; Supplemental Table 3) (*18*). From the series presented here, the introduction of the $(HE)_3$ motif near the PSMA-binding motif led to the highest tumor-to-background contrast. Noticeably, this compound even outperforms the core structure Glu-urea-Lys-HBED-CC-IRDye800CW with regard to tumor-to-background ratio (Supplemental Table 4). For all compounds, the renal pathway was identified to be the most likely elimination mechanism.

Additionally, to finalize the analysis of the pharmacokinetic properties of the favored compound ^{68}Ga-Glu-urea-Lys-$(HE)_3$-HBED-CC-IRDye800CW, biodistribution studies at 2 h after injection were conducted (Figs. 1C and 1D; Supplemental Table 6). Specific tumor accumulation was significantly reduced after injection of 60 pmol (3.10 ± 1.17 %ID/g) as compared with 1 h after injection (7.59 ± 0.95 %ID/g) (P = 0.007). Contemporaneously, the compound was strongly excreted from background tissue, resulting in remaining high tumor-to-background ratios up to 2 h after injection (Supplemental Table 6). Administration of higher doses of ^{68}Ga-Glu-urea-Lys-$(HE)_3$-HBED-CC-IRDye800CW (500 pmol) mainly confirmed the findings and even resulted in higher tumor-to-background ratios for muscle at 1 and 2 h after injection (Figs. 1C and 1D; Supplemental Tables 7 and 8).

Small-Animal PET and Optical Imaging

Subsequent small-animal PET studies with ^{68}Ga-Glu-urea-Lys-$(HE)_3$-HBED-CC-IRDye800CW confirmed strong tumor uptake in the LNCaP xenograft model accompanied by rapid clearance

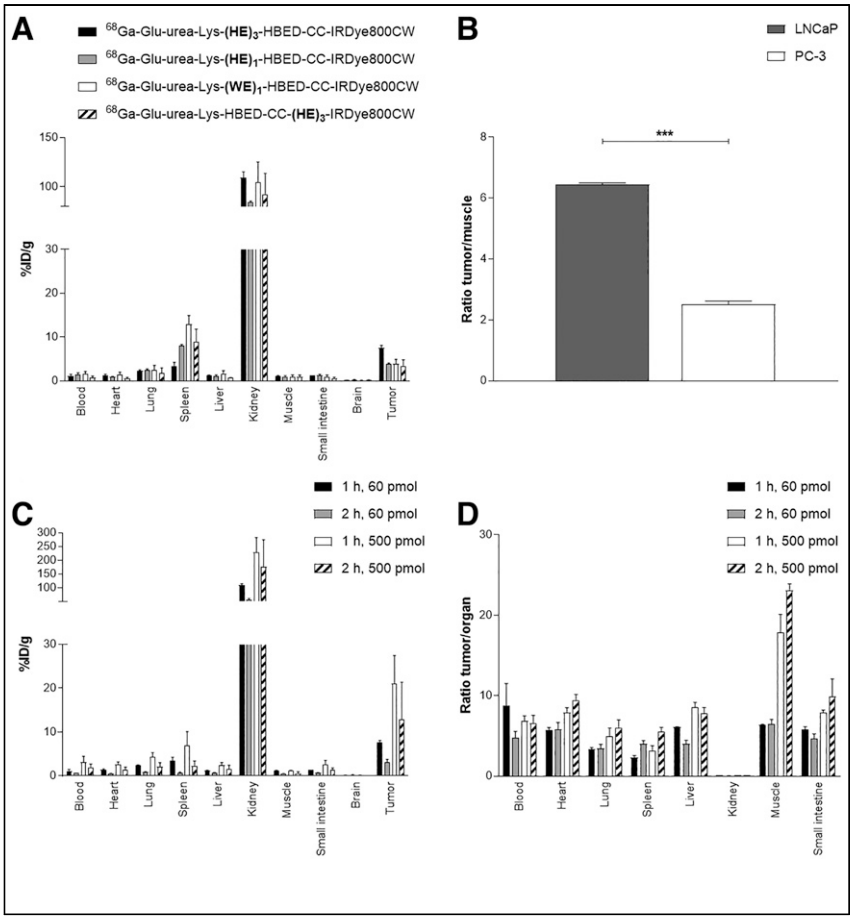

FIGURE 1. (A) Organ distribution of 60 pmol of ^{68}Ga-labeled compounds at 1 h after injection (LNCaP), with statistics shown in Supplemental Figure 10. (B) LNCaP in comparison to PC-3 tumor-to-muscle ratio of 60 pmol of ^{68}Ga-labeled Glu-urea-Lys-$(HE)_3$-HBED-CC-IRDye800CW 1 h after injection (***$P < 0.001$). (C and D) Organ distribution (C) and tumor-to-organ ratios (D) of 60 and 500 pmol of ^{68}Ga-labeled Glu-urea-Lys-$(HE)_3$-HBED-CC-IRDye800CW at 1 and 2 h after injection in LNCaP tumor–bearing BALB/c *nu/nu* mice. Data are expressed as mean %ID/g tissue ± SD ($n = 3$).

from nonmalignant tissue, resulting in high imaging contrasts at early time points after injection (Figs. 2A–2D). High PSMA specificity was proven in vivo because no measurable uptake was observed in PSMA-negative PC-3 xenografts (Fig. 2B). The corresponding time–activity curves of the dynamic PET scan up to 60 min after injection demonstrate rapid clearance from off-target tissue (muscle, liver, heart) but continuous accumulation in bladder and kidney due to the renal pathway of excretion (Fig. 2C).

In fluorescence imaging, ^{68}Ga-labeled Glu-urea-Lys-$(HE)_3$-HBED-CC-IRDye800CW obtained high tumor uptake, resulting in excellent tumor visualization and strong tumor-to-background contrast (Fig. 3; Supplemental Figs. 11 and 12). Additionally, the renal excretion pathway and the significantly reduced spleen uptake based on radioactivity was fluorescently confirmed.

DISCUSSION

The development of dual-modality probes for preoperative imaging and intraoperative guidance (radioguidance or fluorescence guidance) specifically targeting PSMA represents a promising new strategy in the diagnosis and therapy of PCa. The improved detection of tumor tissue supported by both a γ-signal and a fluorescent dye might overcome current surgical limitations. Therefore, a novel class of dual-labeled low-molecular-weight PSMA inhibitors has recently been developed, thereby successfully demonstrating their feasibility for clinical translation in preclinical proof-of-concept studies (*16–18*). In particular, a specific and sufficiently high tumor uptake combined with a fast pharmacokinetic profile resulting in high tumor-to-background contrast at early time points after injection challenges low-molecular-weight hybrid tracer development. ^{68}Ga-Glu-urea-Lys-HBED-CC-IRDye800CW was the first PSMA-targeting low-molecular-weight hybrid probe characterized by a 3-fold increased tumor uptake compared with the parental molecule PSMA-11 while preserving a fast pharmacokinetic profile.

Nevertheless, like other peptidomimetic PSMA inhibitors, this dual-modality approach results in excretion via the renal pathway and accumulation in nonmalignant tissue (spleen). Probe enrichment close to the surgical field might hamper specific lesion detection, particularly when close to the urinary system. Additionally, nonmalignant accumulation might be of concern regarding toxicity issues during clinical translation of this approach.

To address this limitation, our study found a rational hybrid molecule design to be a promising tool to accelerate the pharmacokinetic profile while preserving high tumor uptake. In particular, introduction of spacer moieties comprising (HE) proved favorable to modulate the biodistribution profile of Affibody molecules and peptidomimetic inhibitors, thereby improving tumor-to-background contrast and potential uptake in dose-limiting nonmalignant tissue (*21–23*).

In this study, rational linker design was applied to the peptidomimetic hybrid molecule Glu-urea-Lys-HBED-CC-IRDye800CW, the current lead of our theranostic dual-modality platform. Because of its favorable characteristics (high specific tumor uptake, fast pharmacokinetic properties) and successfully incorporated clinically relevant near-infrared dye (simplified clinical translation of pharmacokinetic study findings), it was designated for a further proof-of-concept pharmacokinetic modulation (*18*). The chemical motifs $(HE)_1$, $(HE)_3$, and $(WE)_1$ found to be beneficial in previous studies were selected for this approach (*21–23*).

The binding affinities of all second-generation compounds resulting from the present study were in the low-nanomolar range, indicating the selected linker motifs to have a negligible functional impact. Nevertheless, inserting the (HE) motif as a triplicate between the PSMA-binding motif and the chelator slightly reduces PSMA affinity. Although a single charged or lipophilic motif is tolerated in terms of affinity, motif repetitions might hamper the advantageous interactions of the chelator HBED-CC with the arene-binding side of the PSMA-binding pocket (*29*). Specific internalization of all modifications was observed to be highest for the

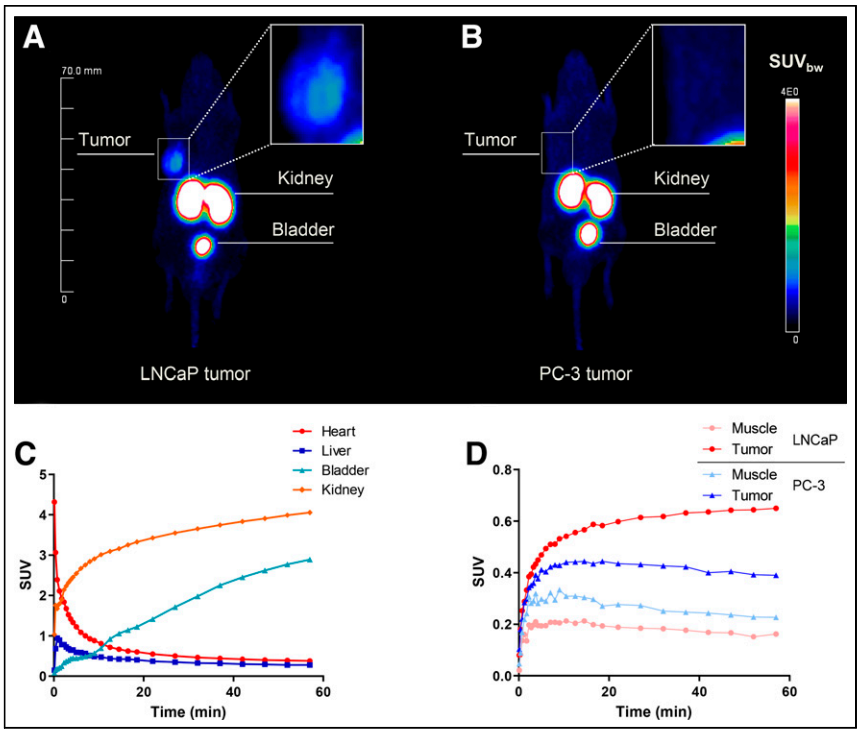

FIGURE 2. (A and B) Whole-body maximum-intensity projections with tumor magnifications of 0.5 nmol of ^{68}Ga-labeled Glu-urea-Lys-$(HE)_3$-HBED-CC-IRDye800CW (~50 MBq) in LNCaP (A) and PC-3 (B) tumor–bearing BALB/c *nu/nu* mice (right flank) 120 min after injection obtained from small-animal PET imaging (n = 1; 1 animal was used for each cell line LNCaP and PC-3, respectively). (C and D) Corresponding time–activity curves for background organs (C) and for tumor and muscle (D).

tryptophan-containing motif located close to the PSMA-binding motif, hypothetically exploiting supportive lipophilic interactions in the PSMA funnel (*30*).

However, the determined advantageous in vitro properties of $(HE)_1$ and $(WE)_1$ motif introduction did not result in an increased tumor uptake. Although $(HE)_1$ and $(WE)_1$ located between the PSMA-binding unit and the radiometal chelator significantly enhanced tumor uptake in previous findings (*22*), the effect could not be demonstrated in this study. Strikingly, including the $(HE)_3$ motif at the same intramolecular location resulted in a strongly improved background organ enrichment profile of the hybrid molecule at early time points after injection (1 h after injection). In particular, spleen uptake was reduced by a factor of 11 when compared with the parental structure ^{68}Ga-Glu-urea-Lys-HBED-CC-IRDye800CW, matching findings of earlier studies (*22*). In addition, this modification revealed the highest tumor-to-background ratios to relevant nonmalignant tissue of all tested compounds, including the parental structure. The resulting tumor uptake was significantly higher than for any of the other modified variants of this study, and previously reported compounds such as PSMA-11 and PSMA-I&F—not, however, exceeding the core structure Glu-urea-Lys-HBED-CC-IRDye800CW and PSMA-617 (*17*,*19*,*27*). Accordingly, it can be concluded that the novel compound features superior characteristics in terms of tumor uptake and tumor-to-background contrast warranting further investigation.

Thus, the exact intramolecular position of $(HE)_3$ was found to be highly crucial, because an introduction on a different location in the molecule results in significantly reduced or even negative effects on background organ enrichment and tumor uptake. The introduction of $(HE)_3$ near the PSMA-binding motif was found to noticeably influence the spleen uptake, for instance, as is in line with previous studies (*22*).

The improved background organ enrichment profile of the novel hybrid molecule ^{68}Ga-Glu-urea-Lys-$(HE)_3$-HBED-CC-IRDye
800CW was accompanied by a significantly accelerated excretion via the renal pathway by means of reduced kidney enrichment as compared with the parental structure ^{68}Ga-Glu-urea-Lys-HBED-CC-IRDye800CW, leading to high tumor-to-background-contrast as early as 1 h after injection, which proved persistent up to 2 h after injection (*18*). Surprisingly, at 1 h after

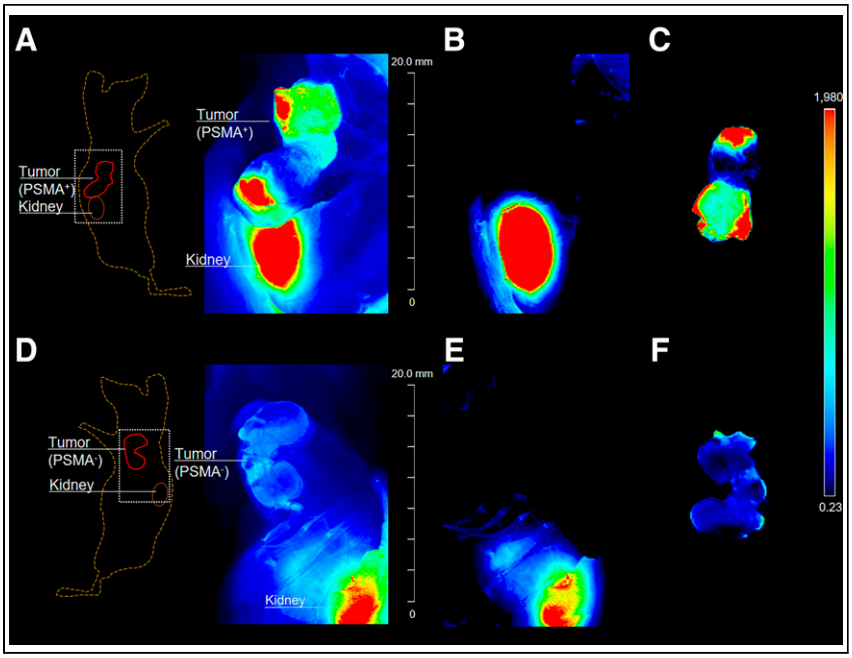

FIGURE 3. Optical imaging after injection of 0.5 nmol of ^{68}Ga-labeled Glu-urea-Lys-$(HE)_3$-HBED-CC-IRDye800CW in LNCaP (A–C) and PC-3 (D–F) tumor–bearing BALB/c *nu/nu* mice (n = 1; 1 animal was used for each cell line LNCaP and PC-3, respectively). Mice were sacrificed 2 h after injection after PET imaging, and fluorescence was detected with Odyssey CLx system (excitation wavelength, 800 nm). Fluorescence intensity is presented in heat-map coloring. (A and D) Skin covering subcutaneous xenograft tumors was removed, and imaging was performed to locate tumor. (B and E) Tumor tissue was resected and another scan performed to ensure complete tumor tissue removal. (C and F) Fluorescence signal of resected tumors is presented. Tissue lying on surface of imaging system during fluorescence detection explains small artifacts in fluorescence images.

injection, the high tumor-to-background contrast manifested about 60 min earlier for the pharmacokinetic-improved compound than for the parental compound. This earlier manifestation is caused by a dramatically minimized enrichment in nonmalignant tissue leading to a 2.0-fold higher tumor-to-blood ratio and a 1.6-fold higher tumor-to-muscle ratio at early time points after injection of 60 pmol. Consequently, increased contrast in the surgical field can be expected from these data, encouraging further clinical translation. Since other dyes are also being discussed in terms of stability, brightness, or tissue penetration, for example, further studies might identify the ideal combination finally representing the lead second-generation PSMA-targeting hybrid probe.

CONCLUSION

This study found rational linker design to be a powerful tool in hybrid molecule development, leading to a novel generation of PSMA-targeting peptidomimetic hybrid molecules with a significantly improved pharmacokinetic profile. With fast elimination and subsequent reduced enrichment in nonmalignant tissue, this approach addresses the highly disruptive factor of background accumulation during surgical resection while preserving a high PSMA-specific tumor uptake. The pharmacokinetic modification strategy uncovered in this study offers extensive utility in the future discovery and development of targeted peptidomimetic hybrid agents.

DISCLOSURE

Financial support was received through the VIP+ grant VP00130, Federal Ministry of Education and Research (BMBF), Germany. Martin Schäfer, Ulrike Bauder-Wüst, Uwe Haberkorn, Matthias Eder, Klaus Kopka, and Ann-Christin Eder hold patent rights on dual-labeled PSMA inhibitors. No other potential conflict of interest relevant to this article was reported.

KEY POINTS

QUESTION: Is the tool of rational linker design suitable to improve the pharmacokinetic profile and elimination rate in peptidomimetic hybrid molecule development?

PERTINENT FINDINGS: This preclinical proof-of-concept study found rational linker design to be a valuable tool to selectively affect the pharmacokinetic profile and elimination rate of PSMA-targeting peptidomimetic hybrid molecules. Introduction of a designated sequence of amino acids significantly reduced enrichment in nonmalignant tissue to a minimum, thereby also enhancing the elimination profile while preserving a high specific tumor uptake.

IMPLICATIONS FOR PATIENT CARE: Background-organ accumulation of novel hybrid molecules in, for example, the surgical field represents one of the main challenges in hybrid molecule development. The study findings introduce a tool to overcome these limitations and further advance discovery in novel image-guided surgery approaches for clinical translation.

REFERENCES

1. Cornford P, van den Bergh RCN, Briers E, et al. EAU-EANM-ESTRO-ESUR-SIOG guidelines on prostate cancer. Part II-2020 update: treatment of relapsing and metastatic prostate cancer. *Eur Urol.* 2021;79:263–282.
2. Weckermann D, Dorn R, Trefz M, Wagner T, Wawroschek F, Harzmann R. Sentinel lymph node dissection for prostate cancer: experience with more than 1,000 patients. *J Urol.* 2007;177:916–920.
3. Mattei A, Fuechsel FG, Bhatta Dhar N, et al. The template of the primary lymphatic landing sites of the prostate should be revisited: results of a multimodality mapping study. *Eur Urol.* 2008;53:118–125.
4. Yossepowitch O, Briganti A, Eastham JA, et al. Positive surgical margins after radical prostatectomy: a systematic review and contemporary update. *Eur Urol.* 2014;65:303–313.
5. Stephenson AJ, Eggener SE, Hernandez AV, et al. Do margins matter? The influence of positive surgical margins on prostate cancer-specific mortality. *Eur Urol.* 2014;65:675–680.
6. Munbauhal G, Seisen T, Gomez FD, et al. Current perspectives of sentinel lymph node dissection at the time of radical surgery for prostate cancer. *Cancer Treat Rev.* 2016;50:228–239.
7. Kiss B, Thoeny HC, Studer UE. Current status of lymph node imaging in bladder and prostate cancer. *Urology.* 2016;96:1–7.
8. van der Poel HG, Buckle T, Brouwer OR, Valdes Olmos RA, van Leeuwen FW. Intraoperative laparoscopic fluorescence guidance to the sentinel lymph node in prostate cancer patients: clinical proof of concept of an integrated functional imaging approach using a multimodal tracer. *Eur Urol.* 2011;60:826–833.
9. Brouwer OR, Buckle T, Vermeeren L, et al. Comparing the hybrid fluorescent-radioactive tracer indocyanine green-^{99m}Tc-nanocolloid with ^{99m}Tc-nanocolloid for sentinel node identification: a validation study using lymphoscintigraphy and SPECT/CT. *J Nucl Med.* 2012;53:1034–1040.
10. KleinJan GH, van den Berg NS, de Jong J, et al. Multimodal hybrid imaging agents for sentinel node mapping as a means to (re)connect nuclear medicine to advances made in robot-assisted surgery. *Eur J Nucl Med Mol Imaging.* 2016;43:1278–1287.
11. Silver DA, Pellicer I, Fair WR, Heston WD, Cordon-Cardo C. Prostate-specific membrane antigen expression in normal and malignant human tissues. *Clin Cancer Res.* 1997;3:81–85.
12. Wright GL Jr, Haley C, Beckett ML, Schellhammer PF. Expression of prostate-specific membrane antigen in normal, benign, and malignant prostate tissues. *Urol Oncol.* 1995;1:18–28.
13. Sweat SD, Pacelli A, Murphy GP, Bostwick DG. Prostate-specific membrane antigen expression is greatest in prostate adenocarcinoma and lymph node metastases. *Urology.* 1998;52:637–640.
14. Minner S, Wittmer C, Graefen M, et al. High level PSMA expression is associated with early PSA recurrence in surgically treated prostate cancer. *Prostate.* 2011;71:281–288.
15. Lütje S, Rijpkema M, Franssen GM, et al. Dual-modality image-guided surgery of prostate cancer with a radiolabeled fluorescent anti-PSMA monoclonal antibody. *J Nucl Med.* 2014;55:995–1001.
16. Banerjee SR, Pullambhatla M, Byun Y, et al. Sequential SPECT and optical imaging of experimental models of prostate cancer with a dual modality inhibitor of the prostate-specific membrane antigen. *Angew Chem Int Ed Engl.* 2011;50:9167–9170.
17. Schottelius M, Wurzer A, Wissmiller K, et al. Synthesis and preclinical characterization of the PSMA-targeted hybrid tracer PSMA-I&F for nuclear and fluorescence imaging of prostate cancer. *J Nucl Med.* 2019;60:71–78.
18. Baranski AC, Schafer M, Bauder-Wust U, et al. PSMA-11-derived dual-labeled PSMA inhibitors for preoperative PET imaging and precise fluorescence-guided surgery of prostate cancer. *J Nucl Med.* 2018;59:639–645.
19. Eder M, Schafer M, Bauder-Wust U, et al. ^{68}Ga-complex lipophilicity and the targeting property of a urea-based PSMA inhibitor for PET imaging. *Bioconjug Chem.* 2012;23:688–697.
20. Hope TA, Aggarwal R, Chee B, et al. Impact of ^{68}Ga-PSMA-11 PET on management in patients with biochemically recurrent prostate cancer. *J Nucl Med.* 2017;58:1956–1961.
21. Hofstrom C, Orlova A, Altai M, Wangsell F, Graslund T, Tolmachev V. Use of a HEHEHE purification tag instead of a hexahistidine tag improves biodistribution of Affibody molecules site-specifically labeled with ^{99m}Tc, ^{111}In, and ^{125}I. *J Med Chem.* 2011;54:3817–3826.
22. Baranski AC, Schafer M, Bauder-Wust U, et al. Improving the imaging contrast of ^{68}Ga-PSMA-11 by targeted linker design: charged spacer moieties enhance the pharmacokinetic properties. *Bioconjug Chem.* 2017;28:2485–2492.
23. Eder M, Löhr T, Bauder-Wüst U, et al. Pharmacokinetic properties of peptidic radiopharmaceuticals: reduced uptake of (EH)3-conjugates in important organs. *J Nucl Med.* 2013;54:1327–1330.
24. Eder M, Wangler B, Knackmuss S, et al. Tetrafluorophenolate of HBED-CC: a versatile conjugation agent for ^{68}Ga-labeled small recombinant antibodies. *Eur J Nucl Med Mol Imaging.* 2008;35:1878–1886.

25. Schafer M, Bauder-Wust U, Leotta K, et al. A dimerized urea-based inhibitor of the prostate-specific membrane antigen for ^{68}Ga-PET imaging of prostate cancer. *EJNMMI Res.* 2012;2:23.
26. Schuhmacher J, Maier-Borst W. A new Ge-68/Ga-68 radioisotope generator system for production of Ga-68 in dilute HCl. *Int J Appl Radiat Isot.* 1981;32:31–36.
27. Benešová M, Schafer M, Bauder-Wust U, et al. Preclinical evaluation of a tailor-made DOTA-conjugated PSMA inhibitor with optimized linker moiety for imaging and endoradiotherapy of prostate cancer. *J Nucl Med.* 2015;56:914–920.
28. Liolios C, Schafer M, Haberkorn U, Eder M, Kopka K. Novel bispecific PSMA/GRPr targeting radioligands with optimized pharmacokinetics for improved PET imaging of prostate cancer. *Bioconjug Chem.* 2016;27:737–751.
29. Zhang AX, Murelli RP, Barinka C, et al. A remote arene-binding site on prostate specific membrane antigen revealed by antibody-recruiting small molecules. *J Am Chem Soc.* 2010;132:12711–12716.
30. Mesters JR, Barinka C, Li W, et al. Structure of glutamate carboxypeptidase II, a drug target in neuronal damage and prostate cancer. *EMBO J.* 2006;25:1375–1384.

Utility of ^{211}At-Trastuzumab for the Treatment of Metastatic Gastric Cancer in the Liver: Evaluation of a Preclinical α-Radioimmunotherapy Approach in a Clinically Relevant Mouse Model

Huizi Keiko Li[1], Yukie Morokoshi[1], Satoshi Kodaira[2], Tamon Kusumoto[2], Katsuyuki Minegishi[3], Hiroaki Kanda[4], Kotaro Nagatsu[3], and Sumitaka Hasegawa[1]

[1]*Radiation and Cancer Biology Group, National Institutes for Quantum and Radiological Science and Technology, Chiba, Japan;*
[2]*Radiation Measurement Research Group, National Institutes for Quantum and Radiological Science and Technology, Chiba, Japan;*
[3]*Targetry and Target Chemistry Group, National Institutes for Quantum and Radiological Science and Technology, Chiba, Japan; and*
[4]*Department of Pathology, Saitama Cancer Center, Saitama, Japan*

A liver metastasis from a primary gastric cancer (LMGC) is relatively common and results in an extremely poor prognosis due to a lack of effective therapeutics. We here demonstrate in a clinically relevant mouse model that an α-particle radioimmunotherapy approach with ^{211}At-labeled trastuzumab has efficacy against LMGCs that are positive for human epidermal growth factor receptor 2 (HER2). **Methods:** ^{211}At was produced in a cyclotron via a ^{209}Bi (α,2n) ^{211}At reaction. ^{211}At-trastuzumab was subsequently generated using a single-step labeling method. NCI-N87 cells (HER2-positive human gastric cancer cells) carrying a luciferase gene were intrasplenically transplanted into severe combined immunodeficiency mice to generate an HER2-positive LMGC model. A biodistribution study was then conducted through the intravenous injection of ^{211}At-trastuzumab (1 MBq) into these LMGC xenograft mice. In parallel with this experimental therapy, phosphate-buffered saline, intact trastuzumab, or ^{211}At-nonspecific human IgG (1 MBq) was injected into control groups. The therapeutic efficacy was evaluated by monitoring tumor changes by chemiluminescence imaging. Body weights, white blood cell counts, and serum markers of tissue damage were monitored at regular intervals. Microdosimetry using a CR-39 plastic detector was also performed. **Results:** The biodistribution analysis revealed an increased uptake of ^{211}At-trastuzumab in the metastasized tumors that reached approximately 12% of the injected dose per gram of tissue (%ID/g) at 24 h. In contrast, its uptake to the surrounding liver was about 4 %ID/g. The LMGCs in the mouse model reduced dramatically at 1 wk after the single systemic injection of ^{211}At-trastuzumab. No recurrences were observed in 6 of 8 mice treated with this single injection, and their survival time was significantly prolonged compared with the control groups, including the animals treated with ^{211}At-nonspecific antibodies. No severe toxicities or abnormalities in terms of body weight, white blood cell number, liver function, or kidney parameters were observed in the ^{211}At-trastuzumab group. Microdosimetric studies further revealed that ^{211}At-trastuzumab had been delivered at an 11.5-fold higher dose to the LMGC lesions than to the normal liver. **Conclusion:** α-radioimmunotherapy with ^{211}At-trastuzumab has considerable potential as an effective and safe therapeutic option for LMGC.

Key Words: cancer metastasis; gastric cancer; HER2; α-RIT

Received May 8, 2020; revision accepted Jan. 13, 2021.
For correspondence or reprints, contact Sumitaka Hasegawa (hasegawa.sumitaka@qst.go.jp).
Published online February 5, 2021.

J Nucl Med 2021; 62:1468–1474
DOI: 10.2967/jnumed.120.249300

Gastric cancer (GC) is the fifth most frequently diagnosed cancer and the third leading cause of cancer-related death worldwide (*1*). Significantly, 35% of GC patients develop a distant metastasis at the time of diagnosis, with 4%–14% of GCs developing a liver metastasis (liver metastasis from a primary GC, or LMGC) (*2*). No satisfactory therapeutics have yet been established for LMGCs, and the prognosis is therefore dismal, with a 5-y survival rate of 0%–10%. Human epidermal growth factor receptor 2 (HER2) has shown promise as a therapeutic target for GC, as HER overexpression is observed in 7%–34% of patients (*3*). Of note in this regard, previous studies have reported a higher HER2 positivity in LMGCs (37.2%) and a correlation of this overexpression with the poor prognosis in these patients (*4*,*5*). Indeed, a recombinant humanized monoclonal antibody targeting the HER2 protein, trastuzumab, has now been clinically used for HER2-overexpressing GCs (*6*). However, despite the clinical benefits of this drug in combination with chemotherapy, the long-term survival of LMGC patients remains unsatisfactory (*7*).

α-particle radioimmunotherapy (α-RIT) is a targeted radionuclide treatment regimen that uses monoclonal antibodies for the specific delivery of radionuclide-emitting α-particles (*8*). ^{211}At is one of the currently attractive α-particle emitters in terms of clinical use because it has an appropriate half-life (7.2 h) and can be manufactured using a cyclotron (*9*). Our prior preclinical studies in mouse models have provided evidence that ^{211}At-labeled antibodies are effective against several cancers without severe toxic effects (*10*,*11*). The therapeutic effectiveness of ^{211}At-labeled trastuzumab has been reported (*12*,*13*). Furthermore, the benefit of single-domain antibody fragments targeting HER2 has been studied (*14*).

We hypothesized that a targeted delivery of α-particles using a cancer-specific antibody would have therapeutic efficacy against LMGC. We thus investigated the use of ^{211}At-trastuzumab against HER2-overexpressing LMGCs in a preclinical mouse model.

MATERIALS AND METHODS

Cells and Reagents

The human NCI-N87 (N87) cell line was purchased from ATCC and was transfected with RediFect Red-FLuc-Puromycin lentiviral particles to establish N87 cells carrying luciferase genes (N87/Luc), as described previously (*13*). The MKN45-Luc (MKN45/Luc) cells were obtained from the Japanese Collection of Research Bioresources Cell Bank. Cells were cultured in RPMI-1640 medium, supplemented with 10% fetal bovine serum and 1% penicillin-streptomycin (Wako), and maintained in a humidified atmosphere of 5% CO_2 at 37°C. The anti-HER2 monoclonal antibody trastuzumab and human IgG (HuIgG) were purchased from Chugai Pharmaceutical and Invitrogen, respectively. *N*-succinimidyl-3-(trimethylstannyl)benzoate was obtained from Santa Cruz Biotechnology and stored at −30°C. *N*-chlorosuccinimide was purchased from Tokyo Chemical Industry.

Antibodies and Radiochemistry

^{211}At was produced in a cyclotron via a ^{209}Bi (α,2n)^{211}At reaction at the National Institute of Radiologic Sciences of the National Institutes for Quantum and Radiologic Science and Technology, as described previously (*15*). The ^{211}At labeling of antibodies was also performed in accordance with a previously described method (*10*). Briefly, antibodies (3–5 mg/mL in 0.2 M sodium carbonate buffer, pH 8.5) were conjugated with *N*-succinimidyl-3-(trimethylstannyl)benzoate, and this immunoconjugated preparation was isolated in phosphate-buffered saline using a Sephadex 50 spin column (GE Healthcare). The tin concentration of the immunoconjugates was determined by inductively coupled plasma mass spectrometry using an Agilent 7500a device (Yokogawa Analytic Systems) (*16*). Briefly, the protein solutions (100 μL, 232.8–296.5 μg of protein) were digested with 0.5 mL of nitric acid (Tama Chemicals) at 90°C for 30 min using a microwave oven, diluted with ultrapure water. Under our experimental conditions, the quantitation limit of tin was 0.042 ng/g. The tin levels of trastuzumab or HuIgG without *N*-succinimidyl-3-(trimethylstannyl)-benzoate in the solvent were below this quantitation limit. The immunoconjugate was then adjusted to pH 5.5 by adding citric acid before labeling. ^{211}At (55–90 MBq) was dissolved with a 0.04 mg/mL solution of *N*-chlorosuccinimide in methanol supplemented with 1% acetic acid for labeling. The immunoconjugate (2–3 mg/mL) was added to ^{211}At and reacted for 1 min, followed by another 1-min reaction with a 2 mg/mL solution of *N*-chlorosuccinimide. Finally, sodium ascorbate (50 mg/mL) was added to stop the reaction. ^{211}At-labeled antibodies (^{211}At-trastuzumab and ^{211}At-HuIgG) were isolated in phosphate-buffered saline using a Sephadex 50 spin column and verified by high-performance liquid chromatography.

Animal Experiments

All animal experiments were approved by the Animal Care and Use Committee of the National Institute of Radiological Sciences at the National Institutes for Quantum and Radiological Science and Technology and complied with the institutional guidelines on animal care and handling.

LMCG Xenograft Mouse Model

N87/Luc or MKN45/Luc cells (2×10^6 cells in 50 μL of medium) were intrasplenically transplanted into C.B17/Icr-scid/scidJcl mice (CLEA Japan, Inc.) under anesthesia to form liver metastases via the splenic vein. The spleen was resected after transplantation to avoid tumor formation in the spleen.

Biodistribution and Dose Estimation

Biodistribution studies were performed as described previously (*10*). Briefly, ^{211}At-trastuzumab or ^{211}At-HuIgG (1 MBq/100 μL) was intravenously injected into the LMGC xenograft mice. At 1, 3, and 24 h after injection, a group of 4–5 mice was euthanized and tumor and tissues were dissected. The activities in each tissue were measured using a γ-counter (Aloka) to calculate the percentage injected dose (%ID)/g. The absorbed dose of tumor and tissues were estimated as described previously (*17*). Briefly, the doses were estimated using the area under the curve on the basis of the biodistribution data (the trapezoidal method) and the mean energy emitted per transition of ^{211}At and a daughter nuclide ^{211}Po with a correction for the branching ratio (*18*). A radiation weighting factor of 5 was used (*19*).

Experimental Therapy

The experimental therapy was performed by giving an injection of ^{211}At-trastuzumab (1 MBq) intravenously to the LMGC xenograft mice. Phosphate-buffered saline, intact trastuzumab, or ^{211}At-HuIgG (1 MBq) was also injected into control groups. All protein doses were adjusted to the equivalent amount (10 μg) by adding intact antibody. The therapeutic efficacy was evaluated by monitoring tumor changes via chemiluminescence imaging. Body weights, white blood cell counts, and serum markers of tissue damage were monitored at regular intervals to evaluate the toxicity of the treatment. Mice were euthanized when the chemiluminescence intensity of the tumor reached 1×10^6 or at 120 d after injection.

Immunohistochemistry and Histologic Analysis

The HER2 expression level in the LMGCs was confirmed by immunohistochemical staining using a Histofine HER2 kit (Nichirei Biosciences) in accordance with the manufacturer's instructions. Histologic analysis was performed as described previously (*10*). Briefly, LMGC xenograft tissues were sampled from the mice at 1, 3, and 24 h after injection of ^{211}At-trastuzumab, fixed with 10% (v/v) formalin, and embedded in paraffin for sectioning. After sectioning, sequential samples were used for HER2 and hematoxylin and eosin staining.

Microdosimetry

α-particle detection and microdosimetry were performed as described previously (*20*,*21*). Briefly, LMGC xenograft tissues containing a normal liver region were dissected at 24 h after the intravenous injection of ^{211}At-trastuzumab (1 MBq), filled with optimal-cutting-temperature compound, and sectioned at an 8-μm thickness using a cryotome (Leica Biosystems). Sectioned samples were then placed on a CR-39 plate and exposed for 8 h at room temperature. During the exposure, the same sections were stained with hematoxylin and eosin, and histologic images were acquired using a scanning microscope with a ×20 objective lens. At 8 h after placement on CR-39, the samples were removed and the CR-39 plate was chemically etched for 2 h in 7 M sodium hydroxide solution at 70°C. Microscope images of the α-particle tracks were captured under an FSP-1000 microscope (Seiko Time Systems Inc.) and analyzed with track analysis software (PitFit) (*22*).

Statistical Analysis

Statcel 3 software (OMS) was used for all statistical analysis. Tumor volumes and survival data were analyzed using 2-way repeated measures ANOVA and the Kaplan–Meier method, respectively. A P value of less than 0.05 was considered significant.

RESULTS

Radiochemistry

The number of tin groups per antibodies measured using inductively coupled plasma mass spectrometry were 5.2 ± 0.1 (n = 3) and 2.6 ± 0.5 (n = 3) for trastuzumab and HuIgG immunoconjugates, respectively. The labeling yield and specific activity of our test molecules were 51.6% ± 9.1% and 95.2–453.0 kBq/μg for ^{211}At-trastuzumab and 56.2% ± 9.7% and 19.9–521.7 kBq/μg for

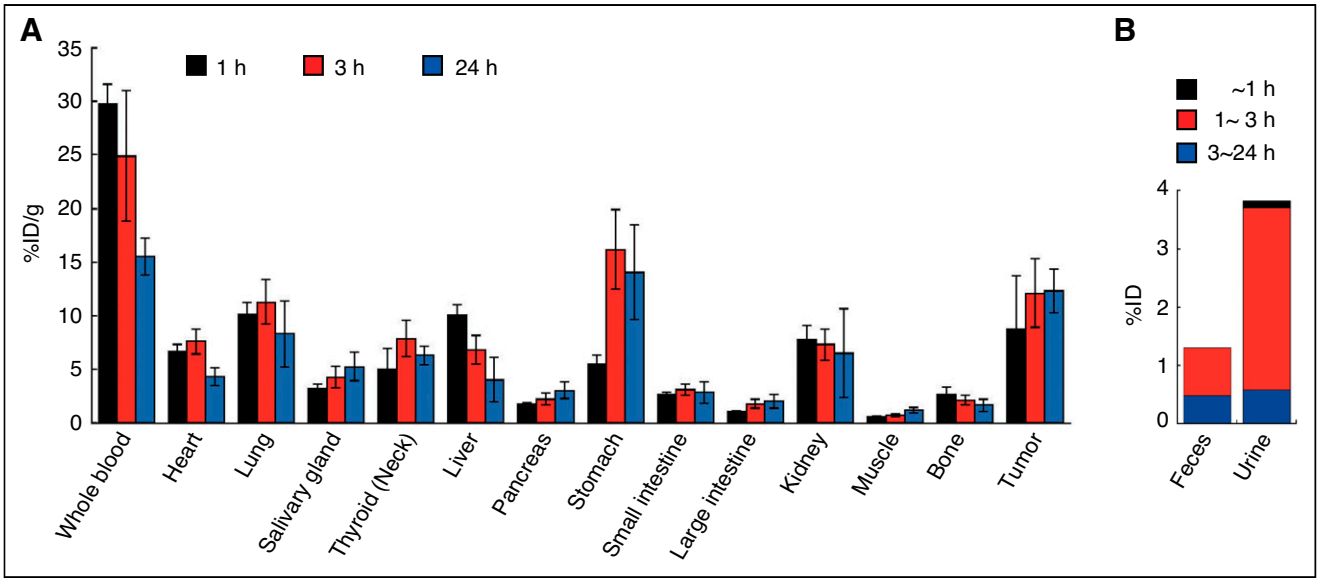

FIGURE 1. Biodistribution of ^{211}At-trastuzumab in LMGC mouse model. (A) %ID/g for ^{211}At in blood, organs, and tumor tissues at 1, 3, and 24 h after intravenous injection of ^{211}At-trastuzumab (1 MBq). Data represent mean ± SD (n = 5 for each time point). (B) %ID of ^{211}At in feces and urine of mice. Five animals were used at each time point. Data represent mean (n = 5).

^{211}At-HuIgG, respectively. The radiochemical purities of these agents were consistently measured above 95%.

Establishment of LMGC Mouse Model

An LMGC mouse model was established by transplanting N87/Luc or MKN45/Luc cells via the splenic vein into C.B17/Icr-scid/scidJcl mice (Supplemental Figs. 1 and 2; supplemental materials are available at http://jnm.snmjournals.org). LMGC lesions in this mouse model were confirmed both by chemiluminescence and visually (Supplemental Figs. 1A–1D). Immunohistochemical analyses confirmed the overexpression of HER2 in the LMGC lesions containing N87/Luc cells (Supplemental Figs. 1E and 1F).

Biodistribution and Absorbed Dose of ^{211}At-Trastuzmab in LMGC Mouse Model

Because the in vitro cell binding of ^{211}At-trastuzumab to N87 cells and resulting cytotoxicity were reported previously (*13*), we investigated the biodistribution of this agent in our LMGC mice after the splenic vein implantation of N87/Luc cells into these animals. We measured longitudinal changes in the ^{211}At uptake in each tissue and tumor after the mice received an intravenous injection of ^{211}At-trastuzumab (1 MBq) (Fig. 1A). The tumor uptake was 8.8 ± 5.0 %ID/g at 1 h after injection and increased over time up to 12.3 ± 2.0 %ID/g at 24 h after injection. Because of its systemic administration, ^{211}At uptake in the blood (29.8 ± 1.8 %ID/g), heart (6.7 ± 0.7 %ID/g), lung (10.2 ± 1.1 %ID/g), and liver (10.1 ± 0.9 %ID/g) was relatively higher than in other tissues at 1 h but then gradually decreased (15.6 ± 1.7, 4.3 ± 0.9, 8.3 ± 3.1, and 4.0 ± 2.1 %ID/g, respectively). Higher uptake in the thyroid and stomach (6.3 ± 0.9 and 14.1 ± 4.4 %ID/g, respectively, at 24 h) was observed, likely because of free ^{211}At. We further observed that ^{211}At-trastuzumab was excreted mainly in the urine (3.8 %ID up to 24 h, Fig. 1B). The absorbed dose by each tissue was calculated from the biodistribution data (Table 1). The absorbed dose at the tumor was estimated to be 4.58 Gy up to 24 h after injection. The tumor–to–normal-liver ratio was 1.59, calculated from the biodistribution data. The ^{211}At uptake decreased in the tumor at 24 h after the injection of ^{211}At-trastuzumab, compared with a reduction after only 1 or 3 h in another LMGC model generated using MKN45/Luc cells that have a significantly lower HER2 expression level than N87/Luc cells (Supplemental Fig. 2). In addition, ^{211}At uptake was found in our analysis to be decreased in the tumor at 24 h after the injection of ^{211}At-HuIgG, compared with at only 1 or 3 h in the N87/Luc LMGC model (Supplemental Fig. 3).

Therapeutic Efficacy of ^{211}At-trastuzumab Against LMGC in Mouse Model

We next evaluated the therapeutic efficacy of α-RIT using ^{211}At-trastuzumab to treat LMGCs in our mouse model (Figs. 2 and

TABLE 1
Absorbed Doses at 24 Hours after Intravenous Injection of ^{211}At-Trastuzumab (1 MBq)

Tissue	Absorbed dose (Gy)
Whole blood	10.11
Heart	2.96
Lung	4.39
Salivary glands	1.61
Thyroid (neck)	2.95
Liver	2.88
Pancreas	0.85
Stomach	5.79
Small intestine	1.20
Large intestine	0.66
Kidney	2.90
Muscle	0.27
Bone	0.87
Tumor	4.58

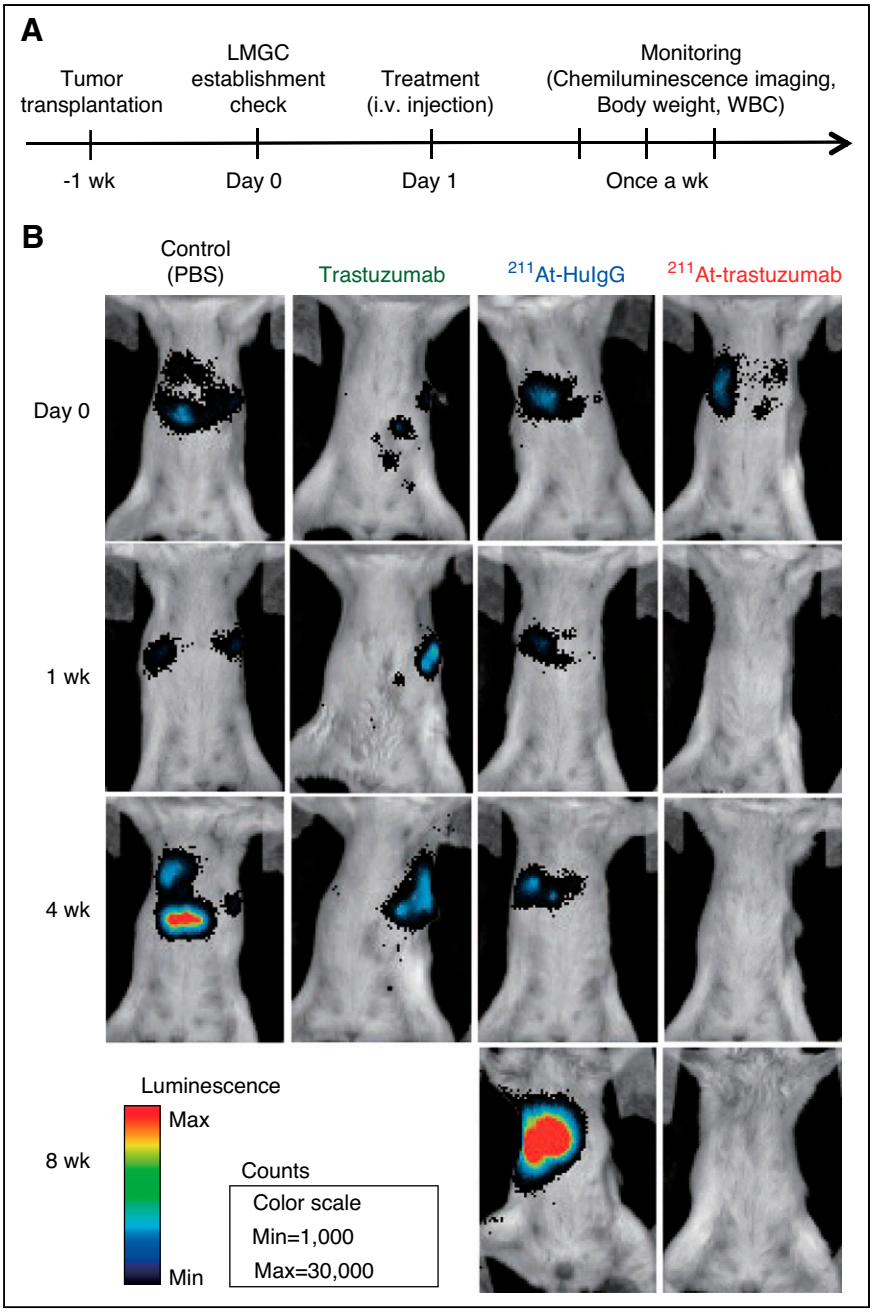

FIGURE 2. α-RIT with ^{211}At-trastuzumab in LMGC mouse model. (A) Treatment schema. (B) Representative chemiluminescence images of LMGC lesions in model mice on day before (day 0) and 1, 4, and 8 wk after treatment. Mice were treated with phosphate-buffered saline (PBS), trastuzumab (10 μg), ^{211}At-HuIgG (1 MBq, 10 μg), or ^{211}At-trastuzumab (1 MBq, 10 μg). Color scale indicates chemiluminescence intensity per pixel. i.v. = intravenous; WBC = white blood cell.

3). Chemiluminescence imagery revealed that a single injection of ^{211}At-trastuzumab eradicated the LMGC lesions in the mice that received it, whereas these tumors grew aggressively in the animals that received control injections of phosphate-buffered saline, unlabeled trastuzumab, or ^{211}At-HuIgG (Fig. 2B). The tumor changes at 28 d after treatment (Fig. 3A) and the relative chemiluminescence intensity of the LMGCs (Fig. 3B) indicated that these lesions were well controlled by the systemic injection of ^{211}At-trastuzumab. No recurrences were observed in 6 of 8 mice treated with a single injection of ^{211}At-trastuzumab during the period of observation. ^{211}At-trastuzumab also significantly prolonged the survival of the LMGC mice (Fig. 3C) compared with the control treatment groups. Histopathologic studies revealed necrotic lesions in both untreated and ^{211}At-trastuzumab–treated LMGCs (Fig. 3D). However, the percentage of necrotic lesions in the tumors was higher in the ^{211}At-trastuzumab–-treated group.

Toxicity

We evaluated the toxicity levels of ^{211}At-trastuzumab in the mouse model by monitoring body weight and conducting biochemical examinations of liver and kidney function. Body weight decreased immediately and started to recover about 1 wk after injection of either ^{211}At-HuIgG or ^{211}At-trastuzumab (Fig. 4A). No obvious leukocytopenia was observed during the period of observation (Fig. 4B). Biochemical examinations indicated no significant changes in the glutamic oxaloacetic transaminase, glutamic pyruvate transaminase, blood urea nitrogen, or creatinine levels before and after treatment (Fig. 4C). No atrophy, apoptosis, or noticeable damage was observed histopathologically in either the liver or the stomach at 3 h after α-RIT treatment (Fig. 4D).

Microdosimetry

Figure 5 shows an intensity map of the α-particle tracks emitted from ^{211}At on the metastatic tumors in an LMGC mouse liver at 24 h after injection of ^{211}At-trastuzumab. We extracted the tumor region of interest (Fig. 5A, dark pink) from a frozen section that included metastatic tumors by binarization by setting band-pass thresholds for the 24-bit color levels (red, 255; green, 163; blue, 173), and the number of α-tracks located in the tumor region of interest in the tissue sample was counted in a binarized image (Fig. 5A). High-density α-tracks were compared between the tumor region and the normal-tissue region; the numbers of α-tracks per unit area of tumor and normal liver were 49,849 ± 975/cm^2 and 5,125 ± 126/cm^2, respectively. The mean absorbed doses per section in the tumor and normal-tissue regions at 24 h were 54.1 ± 1.1 and 4.7 ± 0.1 mGy, respectively, suggesting that the tumor region received an 11.5-fold higher dose than the normal liver (Fig. 5B). This dosimetry was performed on an 8-μm-thick tissue sample from which we visualized a very localized dose distribution in the section that distinguished the area in which the α-particles were concentrated in the tumor.

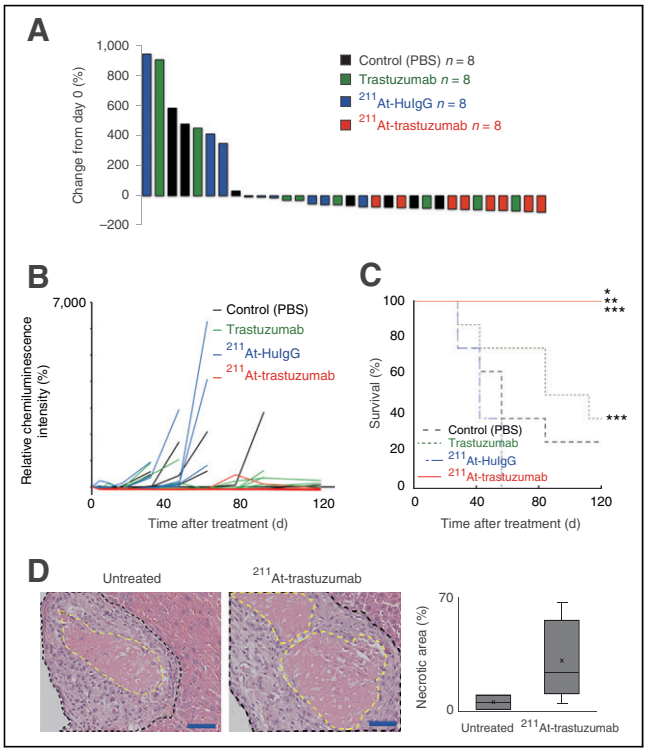

FIGURE 3. Results of ^{211}At-trastuzumab α-RIT in LMGC mouse model. (A) Waterfall plot of percentage tumor chemiluminescence intensity change in each mouse at 28 d after treatment. Tumor chemiluminescence intensity at day 0 was set as baseline (n = 8 in each group). (B) Relative chemiluminescence intensity of tumor in each mouse. Chemiluminescence intensity at day 0 was considered to be 100% (n = 8 in each group). (C) Kaplan–Meier survival curves for LMGC mice. *$P < 0.05$ vs. control. **$P < 0.05$ vs. trastuzumab. ***$P < 0.05$ vs. ^{211}At-HuIgG (n = 8 in each group). (D) Histopathologic analysis by hematoxylin and eosin staining of LMGC lesions that were untreated and were treated for 3 h with α-RIT. Scale bars = 50 μm. Percentages of necrosis in tumors are shown at right. Two (for untreated) or 5 (for treated with ^{211}At-trastuzumab) mice were used. Data represent mean ± SD. PBS = phosphate-buffered saline.

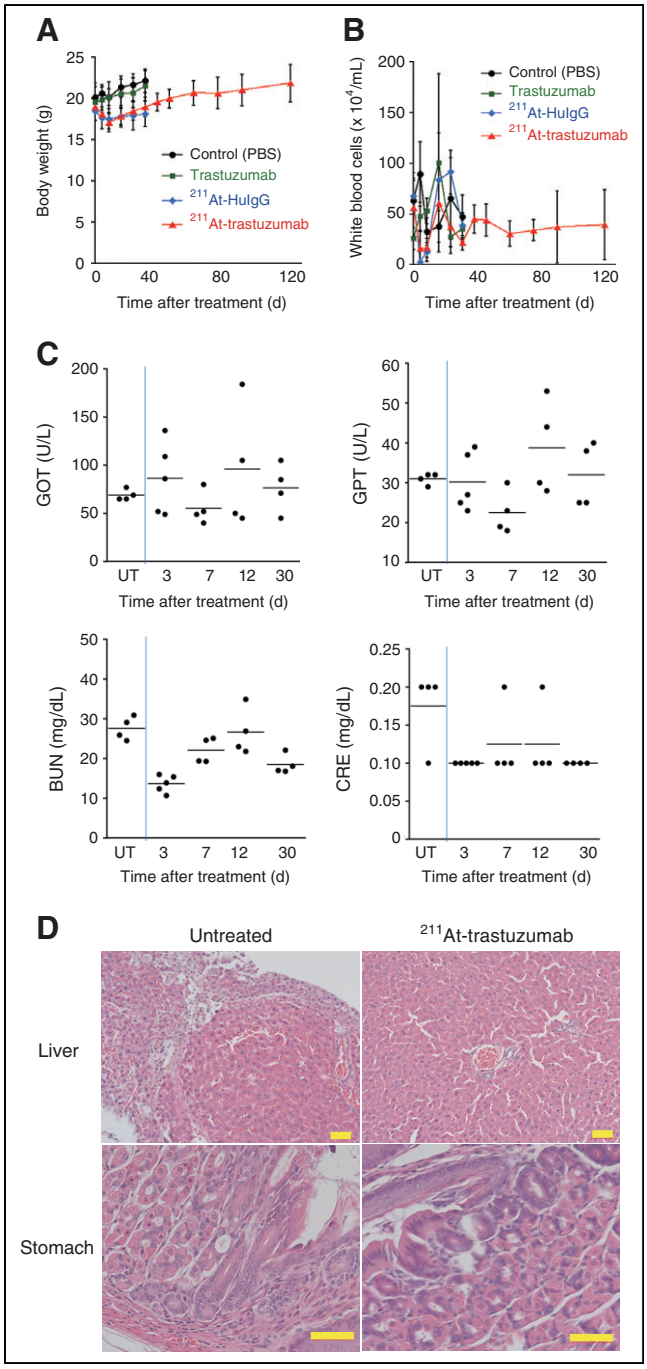

FIGURE 4. Toxicity evaluation of ^{211}At-trastuzumab α-RIT in LMGC mouse model. (A and B) Body weights (A) and white blood cell counts (B) of LMGC mice after treatment are shown. Plots are interrupted if mouse reached endpoint. Data represent mean ± SD. (C) Glutamic oxaloacetic transaminase (GOT), glutamic pyruvate transaminase (GPT), blood urea nitrogen (BUN), and creatinine (CRE) levels measured up to 30 d after ^{211}At-trastuzumab α-RIT. Data for each mouse are shown in graph. (D) Histopathologic analysis by hematoxylin and eosin staining of mouse liver and stomach in animals that were untreated or treated with ^{211}At-trastuzumab for 3 h with α-RIT, respectively. Scale bars = 50 μm. PBS = phosphate-buffered saline; UT = untreated mice.

DISCUSSION

The results of our present analysis indicate that a systemic injection of ^{211}At-trastuzumab achieves dramatic tumor control in a clinically relevant mouse model of HER2-overexpressing LMGCs. In the mice treated with ^{211}At-trastuzumab, the LMGCs were eradicated without recurrence during the monitored period in 6 of 8 animals. Previous studies have indicated that α-particles induce huge clusters of irreparable DNA double-strand breaks and thereby cause targeted cancer cell death (*10*,*11*). Consistent with these findings, we found in our present analyses that broad necrotic legions arise in LMGCs treated with ^{211}At-trastuzumab. The survival of LMGC mice treated with ^{211}At-trastuzumab was also significantly prolonged compared with the control-treated animals. These findings are particularly relevant because despite the continuing improvements in chemotherapy regimens, current treatments for LMGC patients are still limited in terms of extending survival, and the prognosis in these cases thus remains dismal. Hepatic resection and radiofrequency ablation are recommended in these cases if the metastasis is limited to the liver, but patients with LMGC often have multiple metastatic tumors in the liver and further metastases in the peritoneum, lymph nodes, and adjacent organs (*23*–*25*). Hence, our current therapeutic strategy holds promise for the future management of LMGCs that are positive for HER2.

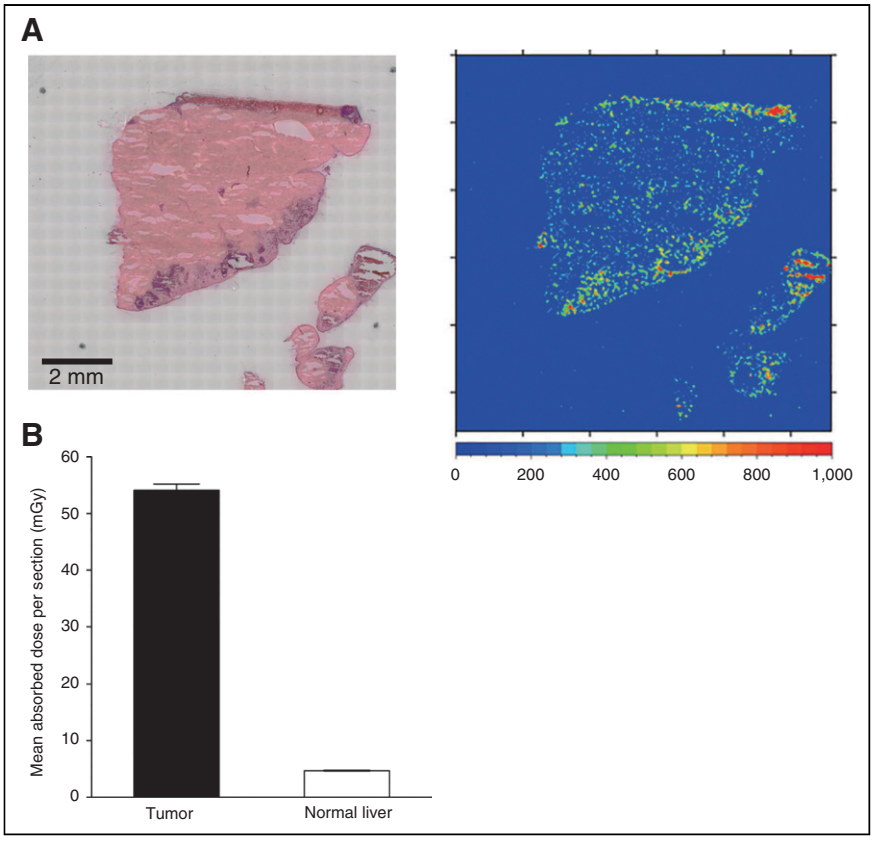

FIGURE 5. Microdosimetry. (A) Microscopic images of sectioned sample of mouse liver tissue, including metastasized tumors, and contour map of α-particle track density at binned positions (ΔX, ΔY) with 50-μm intervals at 24 h after treatment. Scale bars = 2 mm. (B) Estimated local absorbed dose per frozen section at tumor and normal liver regions at 24 h after treatment.

Targeting α-particle therapy or α-RIT using ^{211}At has been shown to be therapeutically effective for HER2-positive cancers in various mouse xenograft systems. For example, ^{211}At-trastuzumab has been shown to be therapeutically effective in a mouse model of radioresistant ovarian cancer (*12*). A previous study reported the effectiveness of single-domain antibody fragments as an attractive platform for ^{211}At delivery targeting HER2 because of their prolonged tumor targeting and rapid clearance from normal tissues (*14*). In addition, α-emitters other than ^{211}At are also used for α-RIT against cancer. ^{227}Th-labeled trastuzumab has shown significant therapeutic effects in a HER2-positive ovarian cancer xenograft (*26*). Recently also, α-RIT using ^{213}Bi has been shown to be effective for experimental pancreatic ductal adenocarcinoma (*27*).

Since α-particles are highly cytotoxic, the safety of the α-RIT approach is an important consideration for possible clinical applications. Damage to normal liver tissues will be one of the top issues of concern if this treatment approach is being tested for metastatic tumors in the liver. Hence, an effective and accurate dose estimation in the normal liver and metastatic tumors is of particular importance. We have here estimated the appropriate radiation dose for the normal liver and metastatic tumors using 2 different approaches: a biodistribution-based dose estimation and microdosimetry using a CR-39 plastic detector that we have previously reported (*21*). The tumor-to-liver ratios in the absorbed dose at 24 h after injection were 1.6 and 11.5 in the biodistribution-based dose estimation and the microdosimetry, respectively (Table 1; Fig. 5B). LMGCs were carefully dissected to separate them from normal liver in the former approach, but normal liver tissues were inevitably mixed in with the LMGC samples measured, which would affect the result. Notably, ^{211}At or ^{211}At-trastuzumab would be expected to be localized in tissues with a nonhomogeneous distribution. Our microdosimetric analyses revealed that a 10-fold higher dose had been given to the tumor than to the normal liver, suggesting that the α-particles had been successfully targeted using the antibody and that our strategy minimized the damage to the surrounding normal tissue (Fig. 5). This finding is highly relevant to the established and continuing concerns about systemic drug administration, including hematologic toxicity levels, damage to excretion pathways (liver and kidney), and the accumulation of free ^{211}At in normal tissues.

Although a transient but recoverable loss of body weight was observed in our α-RIT–treated LMGC mice, no apparent toxicities were evident over the monitoring period. Moreover, higher uptakes of ^{211}At-trastuzumab were observed in the stomach (Fig. 1A), but we found no apparent histopathologic abnormalities (Fig. 4D). These data support the safety of ^{211}At-trastuzumab for translation to clinical use.

There were some limitations to this study. Although our LMGC model is highly relevant to the clinical manifestations of LMGC, the severe combined deficiency mice we used have, of course, severely defective immunity, and the effects of the immune system in tumor eradication via ^{211}At-trastuzumab are unknown. Tumor-bearing mouse models with a functional immune system may be desirable for future studies of this treatment approach. In addition, we used only a single injection of ^{211}At-trastuzumab in our current mouse experiments, but because ^{211}At has a short half-life, this agent could conceivably be administrated via multiple injections to improve its efficacy. Further studies would be needed to evaluate the therapeutic efficacy and toxicity associated with a multiinjection approach.

CONCLUSION

α-RIT using ^{211}At-trastuzumab is efficacious in a clinically relevant mouse model of LMGC lesions that overexpress HER2. We propose that this strategy holds promise as a therapeutic option for LMGC in human patients.

DISCLOSURE

This work was supported in part by the Japan Society for the Promotion of Science (JSPS) (KAKENHI 17K10462 to Sumitaka

Hasegawa, 17J02307 to Huizi Keiko Li, 17H05093 to Satoshi Kodaira, JP16H06276 [AdAMS] to Sumitaka Hasegawa), and a research grant from the Astellas Foundation for research on metabolic disorders (to Sumitaka Hasegawa). No other potential conflict of interest relevant to this article was reported.

ACKNOWLEDGMENTS

We thank Atsushi Tsuji for advice about biodistribution-based dose estimation, Shino Homma-Takeda for the inductively coupled plasma mass spectrometry measurements, Hisashi Suzuki for radioisotope production, Takashi Murakami (Saitama Medical University) for the MKN45/Luc cells, Masumi Abe for encouragement with this present research, and the members of the Radiation and Cancer Biology Group for helpful discussions and technical assistance.

KEY POINTS

QUESTION: What is the potential of ^{211}At-trastuzumab for treating HER2-positive LMGC?

PERTINENT FINDINGS: A single intravenous injection of ^{211}At-trastuzumab significantly inhibited growth of LMGC in mice.

IMPLICATIONS FOR PATIENT CARE: ^{211}At-trastuzumab has potential as a future LMGC treatment in humans.

REFERENCES

1. Bray F, Ferlay J, Soerjomataram I, Siegel RL, Torre LA, Jemal A. Global cancer statistics 2018: GLOBOCAN estimates of incidence and mortality worldwide for 36 cancers in 185 countries. *CA Cancer J Clin.* 2018;68:394–424.
2. Sun Z, Zheng H, Yu J, et al. Liver metastases in newly diagnosed gastric cancer: a population-based study from SEER. *J Cancer.* 2019;10:2991–3005.
3. Bang YJ, Van Cutsem E, Feyereislova A, et al. Trastuzumab in combination with chemotherapy versus chemotherapy alone for treatment of HER2-positive advanced gastric or gastro-oesophageal junction cancer (ToGA): a phase 3, open-label, randomised controlled trial. *Lancet.* 2010;376:687–697.
4. Dang HZ, Yu Y, Jiao SC. Prognosis of HER2 over-expressing gastric cancer patients with liver metastasis. *World J Gastroenterol.* 2012;18:2402–2407.
5. Jiang H, Li Q, Yu S, et al. Impact of HER2 expression on outcome in gastric cancer patients with liver metastasis. *Clin Transl Oncol.* 2017;19:197–203.
6. Carter P, Presta L, Gorman CM, et al. Humanization of an anti-p185HER2 antibody for human cancer therapy. *Proc Natl Acad Sci USA.* 1992;89:4285–4289.
7. Guner A, Yildirim R. Surgical management of metastatic gastric cancer: moving beyond the guidelines. *Transl Gastroenterol Hepatol.* 2019;4:58.
8. Carlin S. Penetrating the barriers to successful alpha-radioimmunotherapy. *J Nucl Med.* 2018;59:934–936.
9. Zalutsky MR, Pruszynski M. Astatine-211: production and availability. *Curr Radiopharm.* 2011;4:177–185.
10. Li HK, Sugyo A, Tsuji AB, et al. Alpha-particle therapy for synovial sarcoma in the mouse using an astatine-211-labeled antibody against frizzled homolog 10. *Cancer Sci.* 2018;109:2302–2309.
11. Li HK, Hasegawa S, Nakajima NI, Morokoshi Y, Minegishi K, Nagatsu K. Targeted cancer cell ablation in mice by an alpha-particle-emitting astatine-211-labeled antibody against major histocompatibility complex class I chain-related protein A and B. *Biochem Biophys Res Commun.* 2018;506:1078–1084.
12. Palm S, Back T, Claesson I, et al. Therapeutic efficacy of astatine-211-labeled trastuzumab on radioresistant SKOV-3 tumors in nude mice. *Int J Radiat Oncol Biol Phys.* 2007;69:572–579.
13. Li HK, Morokoshi Y, Nagatsu K, Kamada T, Hasegawa S. Locoregional therapy with alpha-emitting trastuzumab against peritoneal metastasis of human epidermal growth factor receptor 2-positive gastric cancer in mice. *Cancer Sci.* 2017;108:1648–1656.
14. Choi J, Vaidyanathan G, Koumarianou E, Kang CM, Zalutsky MR. Astatine-211 labeled anti-HER2 5F7 single domain antibody fragment conjugates: radiolabeling and preliminary evaluation. *Nucl Med Biol.* 2018;56:10–20.
15. Nagatsu K, Minegishi K, Fukada M, Suzuki H, Hasegawa S, Zhang MR. Production of ^{211}At by a vertical beam irradiation method. *Appl Radiat Isot.* 2014;94:363–371.
16. Homma-Takeda S, Nishimura Y, Terada Y, Ueno S, Watanabe Y, Yukawa M. Tin accumulation in spermatozoa of the rats exposed to tributyltin chloride by synchrotron radiation x-ray fluorescence (SR-XRF) analysis with microprobe. *Nucl Instrum Methods Phys Res B.* 2005;231:333–337.
17. Sudo H, Tsuji AB, Sugyo A, et al. Preclinical evaluation of the acute radiotoxicity of the alpha-emitting molecular-targeted therapeutic agent ^{211}At-MABG for the treatment of malignant pheochromocytoma in normal mice. *Transl Oncol.* 2019;12:879–888.
18. Eckerman KF, Endo A. *MIRD: Radionuclide Data and Decay Schemes.* 2nd ed. Society of Nuclear Medicine and Molecular Imaging; 2008:616, 624.
19. Sgouros G, Roeske JC, McDevitt MR, et al. MIRD pamphlet no. 22 (abridged): radiobiology and dosimetry of alpha-particle emitters for targeted radionuclide therapy. *J Nucl Med.* 2010;51:311–328.
20. Kodaira S, Li HK, Konishi T, Kitamura H, Kurano M, Hasegawa S. Validating alpha-particle emission from ^{211}At-labeled antibodies in single cells for cancer radioimmunotherapy using CR-39 plastic nuclear track detectors. *PLoS One.* 2017;12:e0178472.
21. Kodaira S, Morokoshi Y, Li HK, Konishi T, Kurano M, Hasegawa S. Evidence of local concentration of alpha-particles from ^{211}At-labeled antibodies in liver metastasis tissue. *J Nucl Med.* 2019;60:497–501.
22. Yasuda N, Namiki K, Honma Y, et al. Development of a high speed imaging microscope and newsoftware for nuclear track detector analysis. *Radiat Meas.* 2005;40:311–315.
23. Makino H, Kunisaki C, Izumisawa Y, et al. Indication for hepatic resection in the treatment of liver metastasis from gastric cancer. *Anticancer Res.* 2010;30:2367–2376.
24. Kim HR, Cheon SH, Lee KH, et al. Efficacy and feasibility of radiofrequency ablation for liver metastases from gastric adenocarcinoma. *Int J Hyperthermia.* 2010;26:305–315.
25. Luo Z, Rong Z, Huang C. Surgery strategies for gastric cancer with liver metastasis. *Front Oncol.* 2019;9:1353.
26. Heyerdahl H, Abbas N, Sponheim K, Mollatt C, Bruland O, Dahle J. Targeted alpha therapy with ^{227}Th-trastuzumab of intraperitoneal ovarian cancer in nude mice. *Curr Radiopharm.* 2013;6:106–116.
27. Jiao R, Allen KJH, Malo ME, et al. Evaluation of novel highly specific antibodies to cancer testis antigen Centrin-1 for radioimmunoimaging and radioimmunotherapy of pancreatic cancer. *Cancer Med.* 2019;8:5289–5300.

Identification of a PET Radiotracer for Imaging of the Folate Receptor-α: A Potential Tool to Select Patients for Targeted Tumor Therapy

Patrycja Guzik[1], Hsin-Yu Fang[1], Luisa M. Deberle[1], Martina Benešová[1,2], Susan Cohrs[1], Silvan D. Boss[2], Simon M. Ametamey[2], Roger Schibli[1,2], and Cristina Müller[1,2]

[1]*Center for Radiopharmaceutical Sciences, Paul Scherrer Institute, Villigen-PSI, Switzerland; and* [2]*Department of Chemistry and Applied Biosciences, ETH Zurich, Zurich, Switzerland*

The aim of this study was to identify a folate receptor-α (FRα)–selective PET agent potentially suitable for the selection of patients who might profit from FRα-targeted therapies. The 6*R* and 6*S* isomers of ^{18}F-aza-5-methyltetrahydrofolate (MTHF) were assessed regarding their binding to FRα and FRβ, expressed on cancer and inflammatory cells, respectively, and compared with ^{18}F-AzaFol, the folic acid–based analog. **Methods:** FR selectivity was investigated using FRα-transfected (RT16) and FRβ-transfected (D4) CHO cells. The cell uptake of ^{18}F-folate tracers was investigated, and receptor-binding affinities were determined with the nonradioactive analogs. In vitro autoradiography of the ^{18}F-folate tracers was performed using RT16 and D4 tissue sections. Biodistribution studies and PET/CT imaging of the radiotracers were performed on mice bearing RT16 and D4 xenografts. **Results:** The uptake of ^{18}F-6*R*-aza-5-MTHF was high when using RT16 cells (62% ± 10% of added activity) but much lower when using D4 cells (5% ± 2%). The FRα selectivity of ^{18}F-6*R*-aza-5-MTHF was further demonstrated by its approximately 43-fold higher binding affinity to FRα (half-maximal inhibitory concentration [IC_{50}], 1.8 ± 0.1 nM) than to FRβ (IC_{50}, 77 ± 27 nM). The uptake of ^{18}F-6*S*-aza-5-MTHF and ^{18}F-AzaFol was equal in both cell lines (52%–70%), with similar affinities to FRα (IC_{50}, 2.1 ± 0.4 nM and 0.6 ± 0.3 nM, respectively) and FRβ (0.8 ± 0.2 nM and 0.3 ± 0.1 nM, respectively). The autoradiography signal obtained with ^{18}F-6*R*-aza-5-MTHF was 11-fold more intense for RT16 than for D4 tissue sections. Biodistribution data showed high uptake of ^{18}F-6*R*-aza-5-MTHF in RT16 xenografts (81% ± 20% injected activity per gram [IA]/g 1 h after injection) but significantly lower accumulation in D4 xenografts (7.3% ± 2.1% IA/g 1 h after injection), which was also visualized using PET. The uptake of ^{18}F-6*S*-aza-5-MTHF and ^{18}F-AzaFol was similar in RT16 (53% ± 10% IA/g and 45% ± 2% IA/g, respectively) and D4 xenografts (77% ± 10% IA/g and 52% ± 7% IA/g, respectively). **Conclusion:** This study demonstrated FRα selectivity for ^{18}F-6*R*-aza-5-MTHF but not for ^{18}F-6*S*-aza-5-MTHF or ^{18}F-AzaFol. This characteristic, together with its favorable tissue distribution, makes ^{18}F-6*R*-aza-5-MTHF attractive for clinical translation to enable detection of FRα-positive cancer while preventing undesired accumulation in FRβ-expressing inflammatory cells.

Key Words: folate receptor (FR); 5-MTHF; PET; ^{18}F; FRα selectivity

J Nucl Med 2021; 62:1475–1481
DOI: 10.2967/jnumed.120.255760

Received Oct. 17, 2020; revision accepted Jan. 13, 2021.
For correspondence or reprints, contact Cristina Müller (cristina.mueller@psi.ch).
Published online January 15, 2021.

The folate receptor-α (FRα) is a cell membrane–associated protein that has been used for targeted therapies in oncology (*1*). The FRα-expressing malignancies are mainly gynecologic cancers, such as ovarian, endometrial, and cervical tumors, but non–small cell lung cancer, triple-negative breast cancer, and kidney cancer were also reported to be frequently positive for FRα (*2–6*).

The use of folic acid–based radiotracers for nuclear imaging was proposed for diagnosis of FR-positive cancer and for the selection of patients who would profit from FR-targeted tumor therapies (*7–10*). ^{111}In-DTPA-folate and ^{99m}Tc-EC20 suitable for SPECT were the first two folate radioconjugates tested in patients (*8,11,12*). Folic acid–based radiotracers bind to both FRα and FRβ, which have distinct tissue expression profiles (*13,14*). The FRα is present in malignant tissue (*15*), whereas FRβ is expressed mainly on activated macrophages involved in inflammatory diseases (*16*). As a result, folic acid–based radiotracers accumulate not only in tumors but also at sites of inflammation, which may result in false-positive findings due to coexisting inflammatory conditions in cancer patients.

6*S*/6*R*-5-methyltetrahydrofolates (MTHF) are reduced folate forms, in contrast to folic acid, which is the synthetic, oxidized version of folate vitamins. It was previously reported that the physiologic 6*S*-5-MTHF, but not the 6*R*-5-MTHF, binds with approximately 50-fold higher affinity to FRα than to FRβ (*17,18*). In a proof-of-concept study published by Vaitilingam et al., a dimethylated reduced version of ^{99m}Tc-EC20 was prepared to achieve FRα selectivity (*19*). Indeed, it was experimentally demonstrated that ^{99m}Tc-DMTHF, a reduced form of ^{99m}Tc-EC20, accumulated much more in tumors of mice than at sites of inflammation (*19*).

In view of a clinical application, folate radiotracers for PET imaging would be clearly favored (*20,21*). ^{18}F-based radiotracers profit from the favorable decay characteristics of ^{18}F (half-life, 110 min; average $E\beta^+$, 250 keV) and the option of quantifying the accumulated activity using standard protocols that are also used for interventions with ^{18}F-FDG (*22*).

Among a large number of developed ^{18}F-folate tracers (*21*) only two were used in clinics. Verweij et al. reported on the use of ^{18}F-polyethylene glycol folate for macrophage imaging in patients with rheumatoid arthritis (*23*), whereas ^{18}F-AzaFol has recently been tested in a clinical phase I trial in ovarian and lung cancer patients in Switzerland (NCT0342993) (*24,25*). A tumor-selective ^{18}F-folate tracer for PET that targets solely FRα and not FRβ would be essential to unambiguously identify patients who could profit from FRα-targeted therapies.

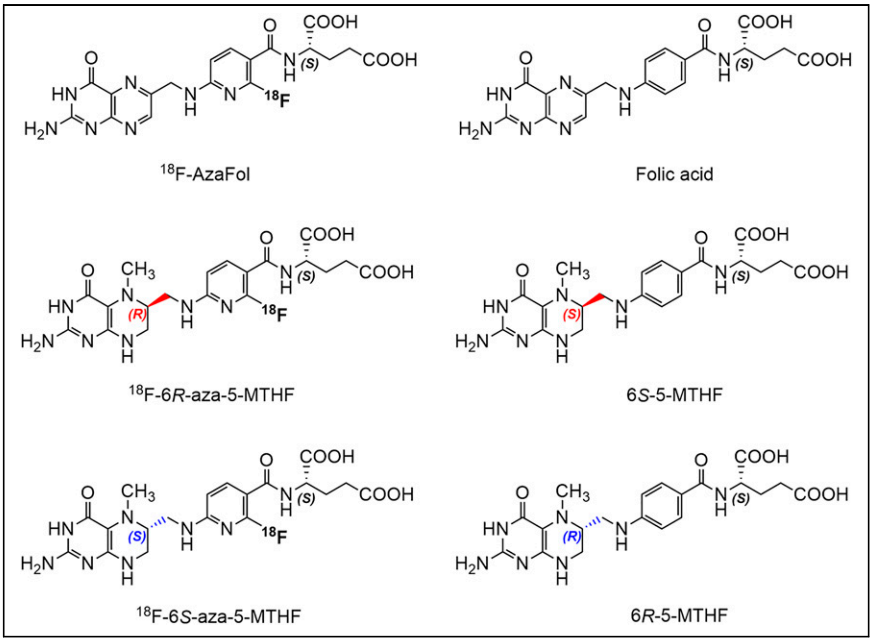

FIGURE 1. Chemical structures of ^{18}F-AzaFol, ^{18}F-6*R*-aza-5-MTHF, and ^{18}F-6*S*-aza-5-MTHF, as well as folic acid, 6*S*-5-MTHF, and 6*R*-5-MTHF (*26*). Stereochemical nomenclature of corresponding isomers of nonfluorinated and fluorinated 5-MTHFs are inversed because of change in substituents' priority at stereogenic center.

We have previously developed radiotracers based on 6*S*- and 6*R*-5-MTHF as a targeting agent (*26*), in which the ^{18}F-label was integrated in the folate backbone as was the case for ^{18}F-AzaFol (Fig. 1) (*26*). These 5-MTHF–based ^{18}F-tracers accumulated to a higher extent in tumor xenografts of mice than did ^{18}F-AzaFol, and the 6*R* isomer even showed a favorable excretion profile. The goal of the present study was, therefore, to investigate ^{18}F-6*R*-aza-5-MTHF and ^{18}F-6*S*-aza-5-MTHF with regard to their binding affinity to FRα and FRβ, in order to assess the potential of using them for tumor-selective PET imaging.

MATERIALS AND METHODS

Folate Derivatives

The precursors (6*R*- or 6*S*-N^2-acetyl-3'-aza-2'-chloro-5-MTHF di-*tert*-butylester and N^2-acetyl-3'-aza-2'-chlorofolic acid di-*tert*-butylester) for the radiofluorination and the nonradioactive 6*S*-5-MTHF (physiologic form) and 6*R*-5-MTHF (nonphysiologic form) were provided by Merck & Cie. Folic acid was obtained from Sigma-Aldrich. The nonradioactive fluoro-folates, as well as 6*R*-3'-aza-2'-^{18}F-5-MTHF (^{18}F-6*R*-aza-5-MTHF), 6*S*-3'-aza-2'-^{18}F-5-MTHF (^{18}F-6*S*-aza-5-MTHF), and 3'-aza-2'-^{18}F-folic acid (^{18}F-AzaFol), were synthesized at ETH Zurich according to a previously reported method (*24,26*). The molar activity of the radiotracers was in the range of 20–250 GBq/μmol, with commonly higher values for ^{18}F-AzaFol than for the 5-MTHF–based radiotracers (*24,26*). ^{3}H-folic acid was obtained from Moravek Biochemicals, Inc.

Cell Culture

CHO cells transfected with FRα (designated as RT16) or FRβ (designated as D4) were kindly provided by Prof. Larry H. Matherly of Wayne State University (*27*). The cells were cultured in folate-free minimal essential medium-α. KB cells (FR-positive human cervical carcinoma cell line, ACC-136) were obtained from the German Collection of Microorganisms and Cell Cultures (DSMZ GmbH) and cultured in folate-deficient RPMI medium. PC-3 cells (FR-negative human prostate cancer cell line, ACC-465) were also obtained from DSMZ but cultured in normal RPMI 1640 medium. The cell culture media were supplemented with 10% fetal calf serum, L-glutamine, and antibiotics.

Western Blot

Expression of FRα and FRβ in RT16 and D4 cells, respectively, was verified by Western blot analysis, whereas FRα -expressing KB and FR-negative PC-3 tumor cells were used as positive and negative controls, respectively. Cell protein extracts (30 μg/well) were separated by sodium dodecyl sulfate–polyacrylamide gel electrophoresis and transferred to a polyvinylidene difluoride membrane. After blocking with 5% bovine serum albumin (BSA) solution, the membrane was incubated with a primary anti-FRα antibody (1:625 rabbit monoclonal antibody PA5-42004; Invitrogen) or anti-FRβ antibody (1:1,000 rabbit monoclonal antibody GTX105822; GeneTex) overnight at 4°C. For signal detection, a secondary antirabbit IgG antibody functionalized with horseradish peroxidase was used together with chemiluminescent substrate. Detection of β-actin served as a loading control (anti-β-actin antibody: 1:2,000 mouse monoclonal antibody 3700 [Cell Signaling Technology] and 1:5,000 horseradish peroxidase–conjugated antimouse IgG 7076S [Cell Signaling Technology]). The expression of FRα and FRβ on RT16 and D4 cells, respectively, was assessed by comparison of the signal with that of KB cells and shown on one representative Western blot.

Cell Internalization of ^{18}F-6*R*/6*S*-Aza-5-MTHF and ^{18}F-Azafol

Cell uptake of ^{18}F-6*R*-aza-5-MTHF, ^{18}F-6*S*-aza-5-MTHF, and ^{18}F-AzaFol was determined as previously reported (*26,28*). In brief, RT16 and D4 cells were seeded in poly-L-lysine–coated 12-well plates to form confluent monolayers overnight. The cells were incubated with the ^{18}F-folate radiotracer (~200 kBq; 25 μL) with or without excess folic acid (~100 μM) for 3 h at 37°C. The results were expressed as percentage of total added activity. The statistical significance was assessed using a two-way ANOVA with a Tukey multiple comparisons posttest using GraphPad Prism software (version 7.0). A P value of less than 0.05 was considered statistically significant.

FRα- and FRβ-Binding Affinity (Half-Maximal Inhibitory Concentration [IC_{50}] Values)

The IC_{50} values for FRα and FRβ were determined in displacement experiments using nonradioactive fluoro-folates (^{19}F-6*R*-aza-5-MTHF, ^{19}F-6*S*-aza-5-MTHF, and ^{19}F-AzaFol) and ^{3}H-folic acid as previously reported (*24*). The binding affinities of the corresponding nonfluorinated analogs (6*R*-5-MTHF, 6*S*-5-MTHF, and folic acid) were determined for comparison. The folate derivatives of interest were applied in a concentration range of 5 pM–50 μM (Supplemental Table 1; supplemental materials are available at http://jnm.snmjournals.org). The FR-bound fraction of ^{3}H-folic acid was measured using a β-counter (Packard Bioscience Cobra II). The IC_{50} values were determined by nonlinear regression analysis of displacement curves obtained from at least three independent experiments, using GraphPad Prism software. For comparison, the relative affinities of ^{19}F-6*S*-aza-5-MTHF and ^{19}F-

6*R*-aza-5-MTHF were presented as a percentage of the binding affinity determined for ^{19}F-AzaFol (set as 100%). The receptor-binding affinities of 6*R*-5-MTHF and 6*S*-5-MTHF were expressed relative to the determined binding affinity of folic acid (set as 100%).

Autoradiography Studies

Autoradiography studies were performed using tissue sections of RT16, D4, KB, and PC-3 xenografts as previously reported (*29*). The sections were incubated in Tris-HCl buffer containing 0.25% BSA. After removal of the buffer, the sections were incubated for 1 h at room temperature with the ^{18}F-folate radiotracers (150 kBq/100 μL) in Tris-buffer containing 1% BSA with or without addition of excess folic acid (100 μM). Autoradiographic images were obtained using a storage phosphor system (Cyclone Plus; Perkin Elmer) and quantified using OptiQuant software (version 5.0). The signals obtained from RT16, D4, and PC-3 xenograft sections were normalized to the signal obtained from a KB xenograft section (set as 100%). The resulting values of ^{18}F-6*R*-aza-5-MTHF and ^{18}F-6*S*-aza-5-MTHF were expressed relative to the signal of ^{18}F-AzaFol, which was set as 100%. Representative images were prepared using ImageJ (version 1.52d).

Immunohistochemistry

After deparaffinization, rehydration, and antigen retrieval of the xenograft sections (RT16, D4, and KB), the slides were treated with 3.5% hydrogen peroxide, followed by endogenous biotin blockade using avidin solution (avidin/biotin blocking kit SP-2001; Vector Laboratories) in an aqueous solution of 3% BSA and normal 5% goat serum. The sections were incubated with an anti-FRα antibody (PA5-42004; Invitrogen) and an anti-FRβ antibody (GTX105822; GeneTex) diluted 1:800 and 1:400, respectively, in biotin solution mixed with 3% BSA at 4°C overnight. Afterward, the sections were incubated with the secondary antibody (goat antirabbit IgG, BA-1000; Vector Laboratories) diluted 1:1,000 and 1:500 in phosphate-buffered saline containing 3% BSA. Signal was visualized using reagents of commercial kits (Vectostain Elite ABC-horseradish peroxidase kit, peroxidase PK-6100, and 3,3′-diaminobenzidine substrate kit peroxidase (horseradish peroxidase) SK-4100; Vector Laboratories), followed by counterstaining using hematoxylin. After tissue dehydration, the sections were fixed with xylene and images were taken using a light microscope (Axio Lab.A1; Zeiss).

In Vivo Studies

All applicable international, national, and institutional guidelines for the care and use of laboratory animals were followed. The studies were performed according to the guidelines of the Swiss Regulations for Animal Welfare after ethical approval by the Cantonal Committee of Animal Experimentation and permission by the responsible authorities. Female severe combined immunodeficient CB17 mice were purchased from Charles River Laboratories. All animals were fed with a folate-deficient rodent diet (ssniff Spezialdiäten GmbH). The mice were inoculated with RT16 cells (6×10^6 cells in 100 μL of phosphate-buffered saline) on the right shoulder and D4 cells (6×10^6 cells in 100 μL of phosphate-buffered saline) on the left shoulder. Biodistribution and PET/CT imaging studies were performed 8–10 d later.

Biodistribution Studies

The respective ^{18}F-folate radiotracer (~5 MBq, 100 μL, ~0.2 nmol) was injected into the lateral tail vein, and the mice were sacrificed at 1 or 3 h after injection. Selected tissues and organs were collected and weighed, and the activity was measured using a γ-counter (Wallac Wizard 1480; Perkin Elmer). The results for 3–4 mice per time point were listed as a percentage of the injected activity (IA) per gram of tissue mass, using counts of a standard solution (5% IA) measured at the same time. The datasets were analyzed for significance using a one-way ANOVA with a Tukey multiple comparison posttest using GraphPad Prism software. A P value of less than 0.05 was considered statistically significant.

PET/CT Imaging Studies

PET/CT scans were performed using a small-animal PET/CT scanner (G8; Perkin Elmer (*30*)) as previously reported (*26*). After emptying the urinary bladder of the mice, they were anesthetized with a mixture of isoflurane (1.5%–2.0%) and oxygen for PET/CT acquisitions. Static whole-body PET scans of 10-min duration were obtained at 1 and 3 h after intravenous injection of ^{18}F-folate radiotracers (5 MBq, ~0.2 nmol, 100 μL), followed by a CT scan of 1.5 min. The acquisition of the data and their reconstruction was performed using the G8 PET/CT scanner software (version 2.0.0.10). The images show one representative example for each radiotracer, prepared using VivoQuant postprocessing software (version 3.5; inviCRO Imaging Services and Software).

RESULTS

Uptake of ^{18}F Radiotracers in FRα-Positive RT16 and FRβ-Positive D4 Cells

Western blot analysis unambiguously confirmed FRα expression on RT16 cells and FRβ expression on D4 cells by detection of the bands at 38 and 29 kDa, respectively (Fig. 2A). The quantified signal for FRα on RT16 cells and FRβ on D4 cells was in the range of 20%–45% of the FRα signal of KB cells. Only a weak signal of 6%–7% was obtained for FRα on D4 cells and FRβ on RT16 cells. This was in the same range as the signal for PC-3 cells (5%–6%), which are FR-negative (Supplemental Fig. 1) (*31*).

The uptake of ^{18}F-6*R*-aza-5-MTHF (62% ± 10% of total added activity) and ^{18}F-6*S*-aza-5-MTHF (64% ± 15%) into RT16 cells was in the same range as for ^{18}F-AzaFol (52% ± 4%) after a 3-h incubation period ($P > 0.05$). The internalized fractions of all three radiotracers were in the range of 11%–13% of total added activity ($P > 0.05$). FRα-specific uptake was confirmed by complete blockade of radiotracer uptake in cell samples preincubated with excess folic acid (Fig. 2B). Experiments performed on D4 cells showed significantly lower uptake of ^{18}F-6*R*-aza-5-MTHF (5% ± 2%; $P < 0.05$) than of ^{18}F-6*S*-aza-5-MTHF (70% ± 7%) or ^{18}F-AzaFol (61% ± 14%), which were both in the same range ($P > 0.05$). Coincubation of D4 cells with excess folic acid reduced the uptake of all radiotracers to background levels (<0.1%) (Fig. 2B).

FRα and FRβ Binding Affinities

The binding affinity of ^{19}F-6*R*-aza-5-MTHF to FRα was approximately 40-fold higher (IC_{50} value, 1.8 ± 0.1 nM) than that to FRβ (77 ± 27 nM). In contrast, the binding affinity of ^{19}F-6*S*-aza-5-MTHF to both FR isoforms was similar (2.1 ± 0.4 nM and 0.8 ± 0.2 nM, respectively), and the same held true also for ^{19}F-AzaFol (0.6 ± 0.3 nM and 0.3 ± 0.1 nM, respectively). These findings corresponded well with the determined values of the respective nonfluorinated analogs, demonstrating an approximately 70-fold higher binding of 6*S*-5-MTHF to FRα than to FRβ but equal binding affinities to both FR isoforms for 6*R*-5-MTHF and folic acid (Table 1; Supplemental Fig. 2).

Determination of the FRα-binding affinity of ^{19}F-6*R*-aza-5-MTHF and ^{19}F-6*S*-aza-5-MTHF relative to ^{19}F-AzaFol (set as 100%) revealed a lower value for the reduced folates (29%–34%), which was in line with the results obtained for nonfluorinated 6*S*-5-MTHF and 6*R*-5-MTHF relative to folic acid (28%–44%). The relative binding affinity to FRβ was 300-fold lower for ^{19}F-6*R*-aza-5-MTHF than for ^{19}F-AzaFol, whereas the FRβ-binding affinity of ^{19}F-6*S*-aza-5-MTHF was only slightly reduced, which

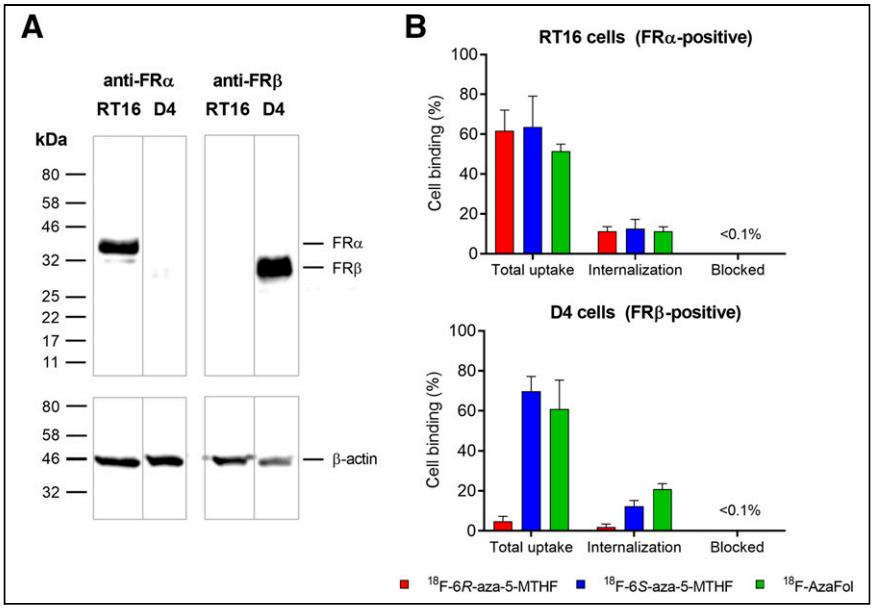

FIGURE 2. (A) Western blot analysis of FRα expression in RT16 cell lysates and FRβ expression in D4 cell lysates (top panel). β-Actin staining as loading control (bottom panel). (B) Cell uptake and internalization of ^{18}F-6*R*-aza-5-MTHF, ^{18}F-6*S*-aza-5-MTHF, and ^{18}F-AzaFol in RT16 and D4 cells after 3 h of incubation at 37°C. Unspecific binding of radiotracers (blocked) was determined by coincubation of cells with folic acid (100 μM). Results are presented as average ± SD (n = 3).

corresponded well with the binding affinities of the nonfluorinated folates to FRβ relative to folic acid (Table 1).

Autoradiography Studies Using ^{18}F-Folate Tracers

In vitro autoradiography studies revealed a similar signal intensity on RT16 xenograft sections for ^{18}F-6*R*-aza-5-MTHF (74% ± 28%) and ^{18}F-6*S*-aza-5-MTHF (89% ± 33%), which was comparable to the signal of ^{18}F-AzaFol (set as 100%) (Fig. 3). A similar binding pattern was obtained with FRα-positive KB xenograft sections (Supplemental Fig. 3). The images obtained with D4 xenograft sections demonstrated, however, an over 10-fold lower signal for ^{18}F-6*R*-aza-5-MTHF (7% ± 4%; $P < 0.05$) than for ^{18}F-6*S*-aza-5-MTHF (81% ± 36%) relative to ^{18}F-AzaFol (set as 100%). Coincubation of ^{18}F-folates with excess folic acid to block the FR-specific binding resulted in only background signals, comparable to those obtained for FR-negative PC-3 tissue (Supplemental Fig. 3).

The expression of FRα on RT16 (and KB as a positive control) and FRβ on D4 xenograft sections was verified by a positive immunohistochemical staining result using an anti-FRα antibody and anti-FRβ antibody. The nonspecific binding was determined in the absence of the primary antibody (Supplemental Fig. 4).

Biodistribution of ^{18}F-Folate Tracers

Biodistribution studies were performed on RT16/D4 xenograft-bearing mice. At 1 and 3 h after injection of ^{18}F-6*R*-aza-5-MTHF, the uptake into FRα-positive RT16 xenografts ranged from 81% to 94% IA/g and was significantly higher than the uptake into FRβ-positive D4 xenografts (7.3%–7.6% IA/g; $P < 0.05$) (Fig. 4). The accumulation of ^{18}F-6*S*-aza-5-MTHF was in the same range for both xenograft types (RT16: 53%–122% IA/g; D4: 77%–149% IA/g), which was also the case for ^{18}F-AzaFol (RT16: 26%–45% IA/g; D4: 28%–52% IA/g) (Fig. 4). The increased uptake of 5-MTHF–based ^{18}F-folate tracers in FRα-positive RT16 xenografts, compared with the uptake of ^{18}F-AzaFol, was in line with previous data obtained from KB tumor–bearing nude mice (*26*).

The presented data, obtained for severe combined immunodeficient CB17 mice, showed a 3-fold lower renal retention of ^{18}F-6*R*-aza-5-MTHF (11%–25% IA/g) than of ^{18}F-6*S*-aza-5-MTHF (31%–41% IA/g) or ^{18}F-AzaFol (35%–58% IA/g), as previously observed in nude mice (Supplemental Tables 2–4) (*26*).

PET/CT Imaging Studies Using ^{18}F-Folate Tracers

Mice bearing RT16 and D4 xenografts on the right and left shoulders, respectively, were imaged at 1 and 3 h after injection of

TABLE 1
FR-Binding Affinities of Fluorinated and Nonfluorinated (Aza)-5-MTHF Derivatives Relative to ^{19}F-Azafol or Folic Acid, Respectively (Set as 100%), Determined with FRα-Expressing RT16 Cells and FRβ-Expressing D4 Cells

Compound	Relative affinity to FRα	Relative affinity to FRβ
^{19}F-AzaFol	100% (0.6 ± 0.3 nM)	100% (0.3 ± 0.1 nM)
^{19}F-6*R*-aza-5-MTHF	34% (1.8 ± 0.1 nM)	0.3% (77 ± 27 nM)
^{19}F-6*S*-aza-5-MTHF	29% (2.1 ± 0.4 nM)	32% (0.8 ± 0.2 nM)
Folic acid	100% (0.4 ± 0.2 nM)	100% (0.3 ± 0.1 nM)
6*S*-5-MTHF*	44% (0.9 ± 0.3 nM)	0.4% (64 ± 10 nM)
6*R*-5-MTHF*	28% (1.4 ± 0.5 nM)	34% (0.8 ± 0.4 nM)

*Stereochemical nomenclature of corresponding isomers of nonfluorinated 5-MTHFs are inversed because of different priority of substituents at the stereogenic center.

Data in parentheses represent the absolute binding affinities.

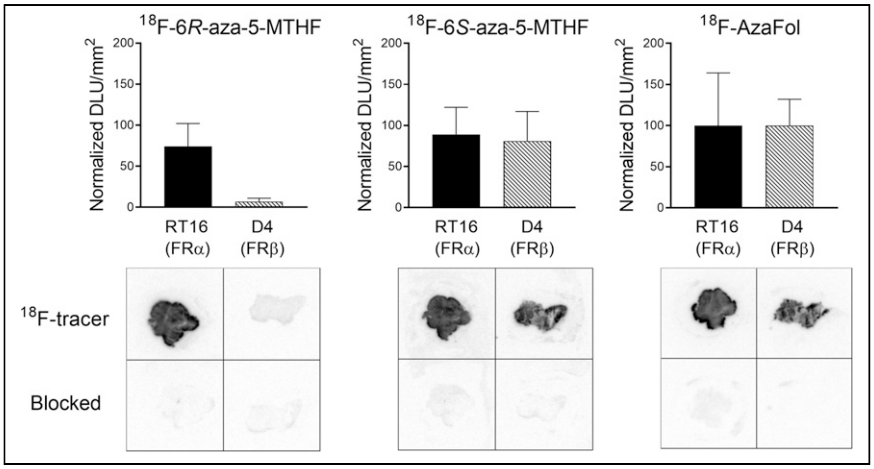

FIGURE 3. Signal intensities (normalized digital light units [DLU] per area [mm^2]) of ^{18}F-6*R*-aza-5-MTHF, ^{18}F-6*S*-aza-5-MTHF, and ^{18}F-AzaFol (set as 100%) quantified on the basis of RT16 (left) or D4 (right) autoradiography images. Bottom panel demonstrates FR blockade performed with excess folic acid.

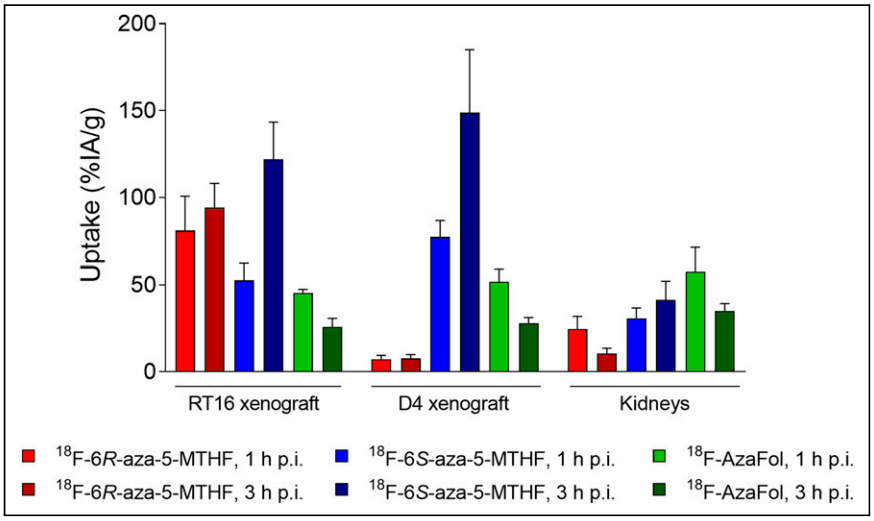

FIGURE 4. Graph representing uptake of ^{18}F-6*R*-aza-5-MTHF (red), ^{18}F-6*S*-aza-5-MTHF (blue), and ^{18}F-AzaFol (green) in RT16 and D4 xenografts and in kidneys at 1 and 3 h after injection of ^{18}F-folate radiotracers (5 MBq/mouse). p.i. = after injection.

the ^{18}F-folate radiotracers using preclinical PET/CT (Fig. 5). In agreement with the biodistribution data, a selective accumulation of ^{18}F-6*R*-aza-5-MTHF in the RT16 xenograft was readily visualized on PET/CT images. This finding was in clear contrast to the images obtained after injection of ^{18}F-6*S*-aza-5-MTHF and ^{18}F-AzaFol, which accumulated equally in RT16 and D4 xenografts. The PET images further confirmed the previously published data that showed much lower kidney retention of ^{18}F-6*R*-aza-5-MTHF than of ^{18}F-6*S*-aza-5-MTHF or ^{18}F-AzaFol (*26*). The RT16 xenograft-to-kidney ratios were, thus, considerably higher for the 6*R* isomer than for the 6*S* isomer, whereas the opposite held true for the xenograft-to-liver ratios.

DISCUSSION

FR-targeted cancer therapies, including folic acid–drug conjugates (e.g., vintafolide (*32,33*)), FRα -targeted antibodies (e.g., farletuzumab (*34*)), or FRα antibody–drug conjugates (e.g., mirvetuximab soravtansine (*35*)), hold promise for the treatment of patients with FRα -positive tumors (*1,8*). The response to these therapies will, however, critically depend on the patient inclusion criteria, which should consider only those cases in which most lesions are FRα -positive (*36*). Although ^{18}F-AzaFol visualizes FR-positive tissue on PET images (*25*), false-positive results may occur because of concomitant accumulation of the radiotracer in FRβ-expressing macrophages involved at sites of inflammation. Having a means at hand to provide a full picture of FRα-positive lesions in an individual patient would thus present an essential step toward the success of any FRα-targeted cancer therapy concept (*1,8*).

In this study, we have demonstrated that ^{19}F-6*R*-aza-5-MTHF displayed significantly higher affinity to FRα than to FRβ, indicating the anticipated FRα selectivity. These findings agree with those obtained from the corresponding nonfluorinated versions of 5-MTHF, confirming the original observation of Wang et al., who reported 6*S*-5-MTHF to have an approximately 50-fold higher affinity to FRα than to FRβ (*17,18*). However, folic acid and the nonphysiologic 6*R*-5-MTHF, as well as their fluorinated analogs, showed equal binding to both FR isoforms.

The fact that only the 6*R* isomer—not the 6*S* isomer—of the novel aza-5-MTHF–based ^{18}F-folate tracers bound with higher affinity to FRα than to FRβ is an essential finding. It indicates the need for diastereomerically pure folate radiotracers other than previously proposed by the development of a racemic mixture of ^{99m}Tc-DMTHF (*19*).

The in vivo evaluation of tumor-specific folate radiotracers in the presence of inflammation is challenging in mice, since the number of activated macrophages is commonly low and, hence, the expected signal from inflammatory sites is lower than the signal from the tumor tissue. This situation may complicate the interpretation of the results with regard to FRα selectivity. To unambiguously determine whether the ^{18}F-folate radiotracers accumulated specifically in FRα -expressing tissue, we have established a mouse model using RT16 and D4 cells to grow xenografts of comparable volumes. Using these mice enabled the determination of FRα-selective uptake of ^{18}F-6*R*-aza-5-MTHF in RT16 xenografts, whereas the accumulation in D4 xenografts was significantly lower. In contrast, ^{18}F-6*S*-aza-5-MTHF and ^{18}F-AzaFol showed comparable accumulation in both xenografts.

It is important to recognize that in addition to the FRα-selective accumulation of ^{18}F-6*R*-aza-5-MTHF, this radiotracer also showed the most favorable clearance from background tissues, including the kidneys as previously demonstrated by Boss et al., who

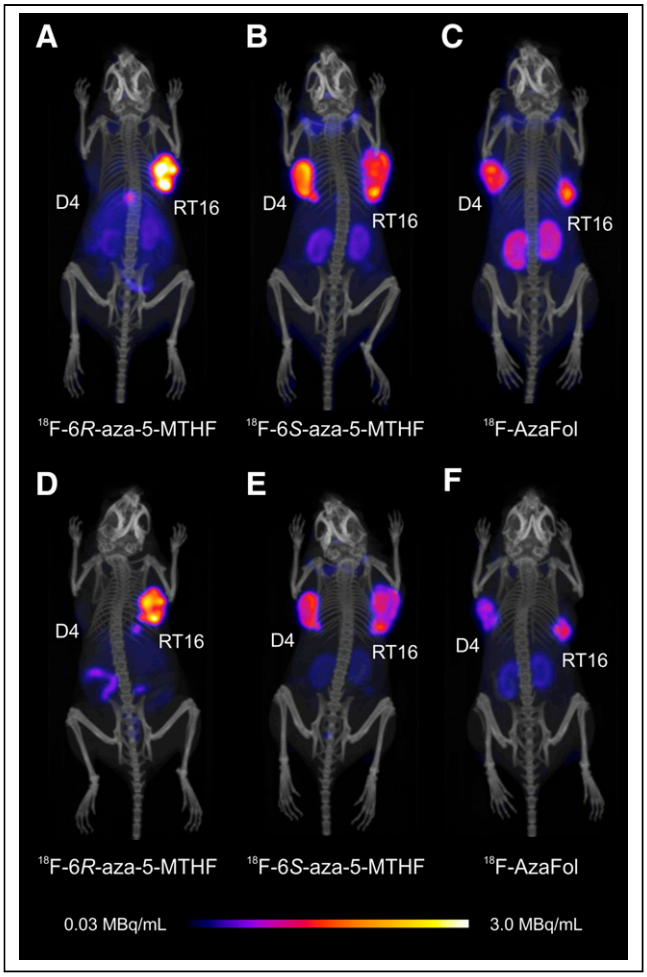

FIGURE 5. PET/CT images of mice bearing RT16 and D4 xenografts 1 h (A–C) and 3 h (D–F) after injection of ^{18}F-folate radiotracers (5 MBq/mouse) shown as maximum-intensity projections.

used KB tumor–bearing nude mice (*26*). The somewhat decreased FRα-binding affinity of the 5-MTHF–based ^{18}F radiotracers, as compared with the affinity of ^{18}F-AzaFol, is in line with the common knowledge that reduced folates display lower FR-binding affinity than does folic acid (*15,17,18*). Although the high FR-binding affinity of folic acid was postulated as a particular advantage of FR-targeting agents, we believe that 5-MTHF–based ^{18}F radiotracers may be favorably used for this purpose as they may be more efficiently released from FR after internalization (*37*). This could explain the higher uptake of ^{18}F-6*R*-aza-5-MTHF and ^{18}F-6*S*-aza-5-MTHF than of ^{18}F-AzaFol in RT16 and KB xenografts (*26*).

CONCLUSION

In this study, we have identified ^{18}F-6*R*-aza-5-MTHF as a novel PET agent that accumulated in FRα-positive RT16 xenografts but not in FRβ-positive D4 xenografts grown in the same mouse. The favorable tissue distribution profile of ^{18}F-6*R*-aza-5-MTHF, together with the herein-determined FRα selectivity, means a breakthrough in the field. PET imaging using ^{18}F-6*R*-aza-5-MTHF might serve as a way to unambiguously identify patients who can profit from FRα-targeted therapies; thus, ^{18}F-6*R*-aza-5-MTHF's potential for clinical translation deserves the highest attention.

DISCLOSURE

A patent application for ^{18}F-based folate radiotracers has been filed by Merck & Cie, Inc., whereby Roger Schibli, Simon M. Ametamey, Silvan D. Boss, and Cristina Müller are coinventors. The project was financially supported by Merck & Cie, Inc. (Schaffhausen, Switzerland), and by the Swiss National Science Foundation (grants 310030_156803 and 310030_188968). Patrycja Guzik was financially supported by a Swiss Government Excellence Scholarship. No other potential conflict of interest relevant to this article was reported.

ACKNOWLEDGMENTS

We thank Anna Becker, Raffaella Schmid, and Fan Sozzi-Guo for technical assistance with the experiments, and we thank Annette Krämer for producing the ^{18}F-based radiotracers at ETH Zurich.

KEY POINTS

QUESTION: Are 5-MTHF–based PET agents specific for the tumor-associated FRα?

PERTINENT FINDINGS: The data from this preclinical study confirm that ^{18}F-6*R*-aza-5-MTHF binds specifically to FRα, which makes this radiotracer useful as a tumor-specific PET agent.

IMPLICATIONS FOR PATIENT CARE: A PET imaging agent such as ^{18}F-6*R*-aza-5MTHF for the unambiguous identification of FRα-expressing tumor types will be essential for the selection of patients who might profit from FRα-targeted therapies.

REFERENCES

1. Scaranti M, Cojocaru E, Banerjee S, Banerji U. Exploiting the folate receptor alpha in oncology. *Nat Rev Clin Oncol.* 2020;17:349–359.
2. Parker N, Turk MJ, Westrick E, Lewis JD, Low PS, Leamon CP. Folate receptor expression in carcinomas and normal tissues determined by a quantitative radioligand binding assay. *Anal Biochem.* 2005;338:284–293.
3. Low PS, Kularatne SA. Folate-targeted therapeutic and imaging agents for cancer. *Curr Opin Chem Biol.* 2009;13:256–262.
4. Assaraf YG, Leamon CP, Reddy JA. The folate receptor as a rational therapeutic target for personalized cancer treatment. *Drug Resist Updat.* 2014;17:89–95.
5. Zhang Z, Wang J, Tacha DE, et al. Folate receptor alpha associated with triple-negative breast cancer and poor prognosis. *Arch Pathol Lab Med.* 2014;138:890–895.
6. Norton N, Youssef B, Hillman DW, et al. Folate receptor alpha expression associates with improved disease-free survival in triple negative breast cancer patients. *NPJ Breast Cancer.* 2020;6:4.
7. Pribble P, Edelman MJ. EC145: a novel targeted agent for adenocarcinoma of the lung. *Expert Opin Investig Drugs.* 2012;21:755–761.
8. Teng L, Xie J, Teng L, Lee RJ. Clinical translation of folate receptor-targeted therapeutics. *Expert Opin Drug Deliv.* 2012;9:901–908.
9. Xu L, Bai Q, Zhang X, Yang H. Folate-mediated chemotherapy and diagnostics: an updated review and outlook. *J Control Release.* 2017;252:73–82.
10. Farran B, Pavitra E, Kasa P, Peela S, Rama Raju GS, Nagaraju GP. Folate-targeted immunotherapies: passive and active strategies for cancer. *Cytokine Growth Factor Rev.* 2019;45:45–52.
11. Siegel BA, Dehdashti F, Mutch DG, et al. Evaluation of ^{111}In-DTPA-folate as a receptor-targeted diagnostic agent for ovarian cancer: initial clinical results. *J Nucl Med.* 2003;44:700–707.
12. Fisher RE, Siegel BA, Edell SL, et al. Exploratory study of ^{99m}Tc-EC20 imaging for identifying patients with folate receptor-positive solid tumors. *J Nucl Med.* 2008;49:899–906.
13. Low PS, Henne WA, Doorneweerd DD. Discovery and development of folic-acid-based receptor targeting for imaging and therapy of cancer and inflammatory diseases. *Acc Chem Res.* 2008;41:120–129.
14. Müller C. Folate based radiopharmaceuticals for imaging and therapy of cancer and inflammation. *Curr Pharm Des.* 2012;18:1058–1083.

15. Antony AC. Folate receptors. *Annu Rev Nutr.* 1996;16:501–521.
16. Yi YS. Folate receptor-targeted diagnostics and therapeutics for inflammatory diseases. *Immune Netw.* 2016;16:337–343.
17. Wang X, Shen F, Freisheim JH, Gentry LE, Ratnam M. Differential stereospecificities and affinities of folate receptor isoforms for folate compounds and antifolates. *Biochem Pharmacol.* 1992;44:1898–1901.
18. Maziarz KM, Monaco HL, Shen F, Ratnam M. Complete mapping of divergent amino acids responsible for differential ligand binding of folate receptors a and b. *J Biol Chem.* 1999;274:11086–11091.
19. Vaitilingam B, Chelvam V, Kularatne SA, Poh S, Ayala-Lopez W, Low PS. A folate receptor-alpha-specific ligand that targets cancer tissue and not sites of inflammation. *J Nucl Med.* 2012;53:1127–1134.
20. Müller C. Folate-based radiotracers for PET imaging: update and perspectives. *Molecules.* 2013;18:5005–5031.
21. Boss SD, Ametamey SM. Development of folate receptor-targeted PET radiopharmaceuticals for tumor imaging: a bench-to-bedside journey. *Cancers (Basel).* 2020;12:1508.
22. Almuhaideb A, Papathanasiou N, Bomanji J. ^{18}F-FDG PET/CT imaging in oncology. *Ann Saudi Med.* 2011;31:3–13.
23. Verweij NJF, Yaqub M, Bruijnen STG, et al. First in man study of [^{18}F]fluoro-PEG-folate PET: a novel macrophage imaging technique to visualize rheumatoid arthritis. *Sci Rep.* 2020;10:1047.
24. Betzel T, Müller C, Groehn V, et al. Radiosynthesis and preclinical evaluation of 3'-aza-2'-[^{18}F]fluorofolic acid: a novel PET radiotracer for folate receptor targeting. *Bioconjug Chem.* 2013;24:205–214.
25. Gnesin S, Müller J, Burger IA, et al. Radiation dosimetry of ^{18}F-AzaFol: a first in-human use of a folate receptor PET tracer. *EJNMMI Res.* 2020;10:32.
26. Boss SD, Müller C, Siwowska K, et al. Diastereomerically pure 6R- and 6S-3'-aza-2'-^{18}F-fluoro-5-methyltetrahydrofolates show unprecedentedly high uptake in folate receptor-positive KB tumors. *J Nucl Med.* 2019;60:135–141.
27. Deng Y, Wang Y, Cherian C, et al. Synthesis and discovery of high affinity folate receptor-specific glycinamide ribonucleotide formyltransferase inhibitors with antitumor activity. *J Med Chem.* 2008;51:5052–5063.
28. Müller C, Mindt TL, de Jong M, Schibli R. Evaluation of a novel radiofolate in tumour-bearing mice: promising prospects for folate-based radionuclide therapy. *Eur J Nucl Med Mol Imaging.* 2009;36:938–946.
29. Müller C, Forrer F, Schibli R, Krenning EP, de Jong M. SPECT study of folate receptor-positive malignant and normal tissues in mice using a novel ^{99m}Tc-radiofolate. *J Nucl Med.* 2008;49:310–317.
30. Gu Z, Taschereau R, Vu NT, et al. Performance evaluation of G8, a high-sensitivity benchtop preclinical PET/CT tomograph. *J Nucl Med.* 2019;60:142–149.
31. Siwowska K, Schmid RM, Cohrs S, Schibli R, Müller C. Folate receptor-positive gynecological cancer cells: in vitro and in vivo characterization. *Pharmaceuticals (Basel).* 2017;10:72.
32. Lorusso PM, Edelman MJ, Bever SL, et al. Phase I study of folate conjugate EC145 (vintafolide) in patients with refractory solid tumors. *J Clin Oncol.* 2012;30:4011–4016.
33. Luyckx M, Votino R, Squifflet JL, Baurain JF. Profile of vintafolide (EC145) and its use in the treatment of platinum-resistant ovarian cancer. *Int J Womens Health.* 2014;6:351–358.
34. Sato S, Itamochi H. Profile of farletuzumab and its potential in the treatment of solid tumors. *Onco Targets Ther.* 2016;9:1181–1188.
35. Moore KN, Martin LP, O'Malley DM, et al. A review of mirvetuximab soravtansine in the treatment of platinum-resistant ovarian cancer. *Future Oncol.* 2018;14:123–136.
36. Morris RT, Joyrich RN, Naumann RW, et al. Phase II study of treatment of advanced ovarian cancer with folate-receptor-targeted therapeutic (vintafolide) and companion SPECT-based imaging agent (^{99m}Tc-etarfolatide). *Ann Oncol.* 2014;25:852–858.
37. Kamen BA, Smith AK. A review of folate receptor alpha cycling and 5-methyltetrahydrofolate accumulation with an emphasis on cell models in vitro. *Adv Drug Deliv Rev.* 2004;56:1085–1097.

PSMA-Targeted Therapeutics: A Tale About Law and Economics

TO THE EDITOR: Without any doubt, the breakthrough in radiopharmaceuticals targeting prostate-specific membrane antigen (PSMA) has stirred up nuclear medicine and radiopharmaceutical research and ultimately boosted industrial engagement in the entire field. The first-in-humans application of the ^{68}Ga-labeled PET tracer ^{68}Ga-PSMA-11 in 2011 (hence its present name; initially referred to as ^{68}Ga-HBED-PSMA) (1) galvanized the community and led to a fierce race toward the matching ^{177}Lu-therapeutics. To the best of our knowledge, this games' first goal was scored by ^{177}Lu-PSMA I&T, being the first radiometal-based PSMA ligand that was successfully applied for therapy of metastatic castration-resistant prostate carcinoma (2). Shortly thereafter, one novel compound after another appeared, aiming primarily at therapeutic applications (e.g., ^{177}Lu-PSMA-617) (3) and purely imaging applications (e.g., ^{18}F-PSMA-1001) (4). Interestingly, the commercial interest also led to unexpected short squeezes in some supply chains. For example, PSMA-617 became widely unavailable one fine day as a result of a change in ownership of the patent rights, leaving many clinical radiopharmacies at odds on how to settle their respective requirements.

At this point, it is interesting to note that no patents were filed for PSMA-11 and PSMA I&T, most likely because the tremendous commercial success of this class of radiopharmaceuticals was not foreseeable at that time. As a result, PSMA-11 was widely used and became a global de facto standard for PSMA PET in an incredibly short time. Because it is sold by numerous manufacturers worldwide and is available as a labeling kit, it is still one of the most frequently used PSMA tracers, despite other agents that might arguably be more potent. In principle, the same used to be true for PSMA I&T. For quite a time, many departments were relying on it for their clinical routine. However, the market situation for this compound also took an interesting turn when a fairly old chelator patent entered the stage.

PSMA I&T features a particular flavor of DOTA as the chelator moiety (5), namely, a tetraazacyclododecane with 3 acetic acids and 1 glutaric acid side arm—hence its acronym DOTAGA (6). This bifunctional chelator structure was developed more than 20 y ago by Helmut Mäcke et al., and a patent application was filed for it on May 11, 2001 (7). The patent slumbered for quite a while but eventually was licensed from Basel University by CheMatech, a company that codeveloped and marketed DOTAGA anhydride (8), a valuable building block for making DOTAGA-functionalized compounds. By February 2019, parts of the same patent, covering the use of DOTAGA in all its conjugates, allegedly were sublicensed to another player in the field in order to gain property rights for PSMA I&T (9). As a countermove, others have announced that any applicable license fees for PSMA I&T, made from a stock of DOTAGA anhydride purchased from CheMatech before February 2019, have inherently been settled by originally purchasing the DOTAGA used for making PSMA I&T from a licensee (i.e., CheMatech), and thus, the PSMA I&T produced therewith may nonetheless be purchased and used without infringing any law (10).

Whether this is true shall not be commented on here, since this legal skirmish just became history anyway. It remains to be asked to what extent the expiry of the DOTAGA patent (by May 11, 2021) bears the potential to change the game of thrones that is being played in the field of PSMA theranostics. The fact that a powerful therapeutic PSMA radioligand, ^{177}Lu-PSMA I&T, may be manufactured and used without any patent restrictions from May 11 onward will probably have an impact on future development, availability, and pricing of similar agents. To all researchers in the field, this tale might be a lesson—and a warning—to secure their intellectual property in sufficient time to save themselves from late regrets.

REFERENCES

1. Eder M, Schäfer M, Bauder-Wüst U, et al. ^{68}Ga-complex lipophilicity and the targeting property of a urea-based PSMA inhibitor for PET imaging. *Bioconjug Chem.* 2012;23:688–697.
2. Weineisen M, Schottelius M, Šimeček J, et al. ^{68}Ga- and ^{177}Lu-labeled PSMA I&T: optimization of a PSMA-targeted theranostic concept and first proof-of-concept human studies. *J Nucl Med.* 2015;56:1169–1176.
3. Benešová M, Bauder-Wüst U, Schäfer M, et al. Linker modification strategies to control the prostate-specific membrane antigen (PSMA)-targeting and pharmacokinetic properties of DOTA-conjugated PSMA inhibitors. *J Med Chem.* 2016;59:1761–1775.
4. Cardinale J, Schäfer M, Benešová M, et al. Preclinical evaluation of ^{18}F-PSMA-1007, a new prostate-specific membrane antigen ligand for prostate cancer imaging. *J Nucl Med.* 2017;58:425–431.
5. Weineisen M, Šimeček J, Schottelius M, Schwaiger M, Wester HJ. Synthesis and preclinical evaluation of DOTAGA-conjugated PSMA ligands for functional imaging and endoradiotherapy of prostate cancer. *EJNMMI Res.* 2014;4:63.
6. Eisenwiener KP, Powell P, Mäcke HR. A convenient synthesis of novel bifunctional prochelators for coupling to bioactive peptides for radiometal labelling. *Bioorg Med Chem Lett.* 2000;10:2133–2135.
7. Maecke H, Eisenwiener K, Powell P, inventors; University Hospital Basel, assignee. Prochelators of radiometal labeled molecules. European patent EP1289571 (B1). July 21, 2004.
8. Bernhard C, Moreau M, Lhenry D, et al. DOTAGA-anhydride: a valuable building block for the preparation of DOTA-like chelating agents. *Chemistry.* 2012;18:7834–7841.
9. PSMA I&T. ATT Scintomics website. https://sci-att.com/psma-it-2/. Accessed August 23, 2021.
10. PSMA. ABX Advanced Biochemical Compounds website. https://www.abx.de/Information/Index/?viewId=Pro_tracer. Accessed August 23, 2021.

Johannes Notni
Technische Universität München
München, Germany
E-mail: johannes.notni@tum.de

Published online March 31, 2021.
DOI: 10.2967/jnumed.121.262308

Reply: PSMA-Targeted Therapeutics: A Tale About Law and Economics

Johannes Czernin
David Geffen School of Medicine at UCLA
Los Angeles, California
E-mail: jczernin@mednet.ucla.edu

Published online May 20, 2021.
DOI: 10.2967/jnumed.121.262566

REPLY: I thank Dr. Notni for his recent letter in which he provides his perspective on one part of the success story of PSMA-targeted theranostics. Success stories often come with conflicts and intellectual ownership discussions.

Dr. Notni makes important points. He acknowledges the pivotal role of the inventors of ^{177}Lu-PSMA I&T in shaping the field (1). He also emphasizes our obvious responsibility to honor patent protection. I would like to highlight that both patented and unpatented compounds can be successful and become market drivers. It is important to allow free market forces to compete for business. For instance, one company is currently initiating a phase 3 clinical trial with the nonpatented compound ^{177}Lu-PSMA I&T in patients with castration-resistant prostate cancer (2). As another example, the U.S. Food and Drug Administration recently granted a new-drug application for the non–patent-protected ^{68}Ga-PSMA-11 for a wide range of indications in patients with prostate cancer (3). This development further establishes the high clinical relevance and impact of PSMA-targeted PET imaging in the care of prostate cancer patients (4). Reimbursement will set the stage and prepare the market for several soon-to-be-approved compounds with comparable diagnostic performance. Then the market will decide which ones are most conveniently used clinically. It is thus important to recognize that both patented and nonpatented compounds can address unmet clinical needs, improve patient outcomes, and create significant revenues while following very different business models. I would, however, urge caution regarding exploiting the lack of patent protection for rebranding long-established compounds. Such measures would simply create market and customer confusion.

Theranostics are rapidly growing and have generated substantial interest from industry. Both protected and unprotected compounds will have their place in the clinic and in research. Non–patent-protected compounds could greatly facilitate translational research, addressing (independent of Big Pharma) resistance to PSMA-targeted therapeutics, for instance.

Protected and nonprotected compounds will give rise to larger and smaller companies, all aiming to become fiscally solid despite very different business models.

They all are part of the new nuclear medicine ecosystem, make important contributions to patient care, and will shape the further development of our discipline. We should therefore appropriately appreciate the outstanding contributions that have given nuclear medicine an immense boost over the past 15 years.

REFERENCES

1. Weineisen M, Schottelius M, Šimeček J, et al. ^{68}Ga- and ^{177}Lu-labeled PSMA I&T: optimization of a PSMA-targeted theranostic concept and first proof-of-concept human studies. *J Nucl Med.* 2015;56:1169–1176.
2. POINT Biopharma announces phase 3 prostate cancer trial. Intrado GlobeNewswire website. https://www.globenewswire.com/news-release/2020/05/12/2031731/0/en/POINT-Biopharma-Announces-Phase-3-Prostate-Cancer-Trial.html. Published May 12, 2020. Accessed August 23, 2021.
3. Sartor O, Hope TA, Calais J, Fendler WP. Oliver Sartor talks with Thomas A. Hope, Jeremie Calais, and Wolfgang P. Fendler about FDA approval of PSMA. *J Nucl Med.* 2021;62:146–148.
4. Sonni I, Eiber M, Fendler WP, et al. Impact of ^{68}Ga-PSMA-11 PET/CT on staging and management of prostate cancer patients in various clinical settings: a prospective single-center study. *J Nucl Med.* 2020;61:1153–1160.

^{18}F-FDG–Avid Axillary Lymph Nodes After COVID-19 Vaccination

TO THE EDITOR: In a recent patient with a left-side parotid malignancy (biopsy-proven mammary analog secretory carcinoma), ^{18}F-FDG PET/CT was obtained during the workup (Fig. 1). The findings showed ^{18}F-FDG avidity in the left axillary lymph nodes with an overall SUV_{max} of 4.5 and an ^{18}F-FDG–avid left supraclavicular lymph node. This result prompted an ultrasound-guided biopsy of the lymph nodes before surgery. Pathologic examination of both subsites revealed lymphocytes consistent with a benign lymph node. Around the time of the biopsy, the patient recalled that she had received the first dose of the Moderna Therapeutics messenger RNA-1273 vaccine 10 d beforehand in her left deltoid. After vaccination, she had injection site soreness and some mild fatigue and general malaise for about 4 h. She then underwent successful superficial parotidectomy, with margin-negative and node-negative resection of the left parotid mammary analog secretory carcinoma.

Shortly after the aforementioned patient was seen, 3 mo post-treatment PET imaging was obtained as part of oncologic surveillance for a patient with a history of oral cavity/oropharyngeal squamous cell carcinoma. On physical examination 3 d before her PET study, laryngoscopy revealed findings concerning for recurrence in the previous surgical bed. Both sides of the neck were palpated, and no lymphadenopathy was appreciated. On PET, the left axillary and left supraclavicular nodes had ^{18}F-FDG avidity, with an SUV_{max} of 5.1. Because of our previous experience with the other patient, this second patient was questioned specifically regarding coronavirus disease 2019 (COVID-19) vaccination. She was able to recall that she had received the first dose of the COVID-19 vaccine 14 d beforehand, though she could not recall the manufacturer. The patient reported minimal symptoms after vaccination and was asymptomatic at the time of the PET scan. She was taken to the operating room for direct laryngoscopy, and biopsy of the concerning area revealed mild dysplasia with no evidence of carcinoma.

^{18}F-FDG uptake is not tumor-specific and can be seen in infection, inflammation, and granulomatous disease (1). Axillary lymph node ^{18}F-FDG avidity has been reported in patients receiving several types of vaccines, including vaccinations to influenza, H1N1, and the human papillomavirus vaccine, but has not been reported in association with the COVID-19 vaccine (2–4). Ultrasound-guided fine-needle aspiration is generally a low-morbidity procedure, though no procedure is without risk. Biopsy of her axillary node could likely have been avoided if the correlation between her recent history of vaccination and her left axillary ^{18}F-FDG–avid lymph nodes had been determined. Limited data on mammary analog secretory carcinoma shows a 5.5% rate of cervical nodal metastasis, but biopsy of a

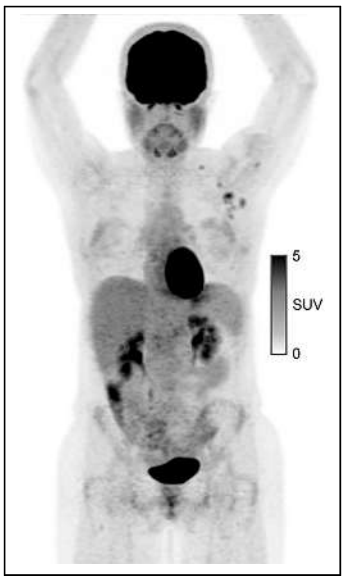

FIGURE 1. ^{18}F-FDG PET/CT showing left axillary and left supraclavicular avidity. Maximum-intensity-projection image with SUV scale at right.

supraclavicular node with ^{18}F-FDG uptake is prudent in the setting of an ipsilateral parotid malignancy (5).

As vaccination against the 2019 novel coronavirus becomes more widespread, it will be important to consider vaccination history, especially in patients who undergo ^{18}F-FDG PET/CT for cancer staging or surveillance. Reporting the vaccine history and injection location before obtaining PET imaging may help with interpretation of these studies. Further study could reveal what percentage of patients have ^{18}F-FDG–avid lymph nodes after vaccination and elucidate the time required after vaccination to allow for resolution of uptake in regional lymph nodes. This information may be able to guide recommendations on the timing of PET imaging and COVID-19 vaccination.

REFERENCES

1. Rahman WT, Wale DJ, Viglianti BL, et al. The impact of infection and inflammation in oncologic ^{18}F-FDG PET/CT imaging. *Biomed Pharmacother.* 2019;117:109168.
2. Focosi D, Caracciolo F, Galimberti S, Papineschi F, Petrini M. False positive PET scanning caused by inactivated influenza virus vaccination during complete remission from anaplastic T-cell lymphoma. *Ann Hematol.* 2008;87:343–344.
3. Iyengar S, Chin B, Margolick JB, Sabundayo BP, Schwartz DH. Anatomical loci of HIV-associated immune activation and association with viraemia. *Lancet.* 2003;362:945–950.
4. Panagiotidis E, Exarhos D, Housianakou I, Bournazos A, Datseris I. FDG uptake in axillary lymph nodes after vaccination against pandemic (H1N1). *Eur Radiol.* 2010;20:1251–1253.
5. Anderson JL, Haidar YM, Armstrong WB, Tjoa T. Analysis of clinical features of mammary analog secretory carcinoma using the Surveillance, Epidemiology, and End Results database. *JAMA Otolaryngol Head Neck Surg.* 2019;145:91–93.

B. Jake Johnson*
Kathryn M. Van Abel
Daniel J. Ma
Derek R. Johnson
**Mayo Clinic*
Rochester, Minnesota
E-mail: johnson.brian@mayo.edu

Published online March 19, 2021.

DOI: 10.2967/jnumed.121.262108

Specific and Nonspecific Uptake in Quantitative ^{89}Zr-Immuno-PET

TO THE EDITOR: In a recent review, van Dongen et al. illustrated why ^{89}Zr-immuno-PET has become an important tool for the in vivo characterization of novel biologic drugs and their targets (*1*). A technical "State of the Art" article summarized PET quantification of ^{89}Zr-tracer uptake, stressing that total tissue uptake results from a target-specific and a nonspecific contribution. The latter involves a first, so-called reversible, part related to free tracer in blood and interstitium, quantified by the Patlak *y*-intercept (V_t). The second, irreversible, part is related to ^{89}Zr residualization after monoclonal antibody (mAb) uptake and degradation by antigen-negative cells, quantified by the Patlak uptake-rate constant (K_i). This description is fully in line with a previous study coauthored by van Dongen, using Patlak analysis in normal tissues (kidney, liver, lung, and spleen) without known target expression for 4 ^{89}Zr-labeled mAbs, respectively (*2*). van Dongen et al. thus suggested that future quantitative ^{89}Zr-immuno-PET studies should consider multiple-time-point acquisitions to assess nonspecific uptake versus time, with at least 3 late time points, and that sophisticated modeling strategies should be developed (*1*,*2*).

We believe that this suggestion warrants further comments that might be helpful for anticipating quantitative ^{89}Zr-immuno-PET studies in tumors, designed for assessing in vivo target engagement. First, the nonspecific-irreversible uptake should be quantitatively compared with the total-tumor uptake, in order to actually determine whether it might be significant or negligible (*1*,*2*). To justify this proposal, let us consider recent results about ^{89}Zr-anti-PD-L1, designed for monitoring in vivo chemotherapy-mediated modulation of tumor-PD-L1 expression (*3*). After extracting tracer input function and tumor data showing irreversible uptake (using the Web-Plot-Digitizer software in Jung et al.'s Figures 2B and 3B, respectively (*3*)), Patlak analysis provides a total-tumor K_i of 0.0289 $mL \cdot g^{-1} \cdot h^{-1}$ ($R^2 = 0.9993$). For comparison, combining 4 ^{89}Zr-labeled mAbs, the baseline value of the nonspecific K_i in the kidney, liver, lung, and spleen was previously found to be 0.0007, 0.0011, 0.0002, and 0.0005 $mL \cdot g^{-1} \cdot h^{-1}$, respectively (*2*). The total tumor K_i value of the ^{89}Zr-anti-PD-L1 random example thus appears to be between 26- and 145-fold higher than the nonspecific K_i values of normal tissues. Even assuming that the nonspecific contribution might vary depending on tumors and patients, unlike for normal tissues across patients, we do suggest this first issue deserves consideration.

Second, we suggest that the principle of a 3-time-point method, previously described for quantitative ^{64}Cu-immuno-PET, might be adapted to ^{89}Zr-immuno-PET (*4*). Rather than the 3 late time points suggested by van Dongen et al., 3 time points are needed at early (after reaching equilibrium), mid, and late imaging, for assessing K_i, V_t, and a release-rate constant (k_R). Indeed, we believe the Patlak assumption of irreversible uptake cannot be justified in an arbitrary tissue, including tumors, as evidenced by ^{64}Cu-NOTA-RamAb in VEGFR-2–positive HCC4006 tumors: $K_i = 0.0314$ $mL \cdot g^{-1} \cdot h^{-1}$, $k_R = 0.0387$ h^{-1}, and $V_t = 0.2075$ $mL \cdot cm^{-3}$ (without a RamAb blocking dose) (*4*). Noteworthy, this method cannot differentiate between specific and nonspecific uptake, and the actual meaning of the 3 kinetic parameters should be specified under each situation. However, it should be emphasized that a kinetic modeling analysis able to differentiate between specific and nonspecific uptake may probably increase the number of parameters involved in fitting 3-time-point PET data, which is contrary to the Akaike criteria (*5*).

Finally, if nonspecific uptake has proven quantitatively negligible compared with specific uptake, or, alternatively, if differentiating between them has proven unrealistic in current clinical practice, we suggest that a single time point for optimal quantitative ^{89}Zr-immuno-PET might be probed (under the irreversible-trapping condition) (*6*).

REFERENCES

1. van Dongen GAMS, Beaino W, Windhorst AD, et al. The role of ^{89}Zr-immuno-PET in navigating and derisking the development of biopharmaceuticals. *J Nucl Med.* 2021; 62:438–445.
2. Jauw YWS, O' Donoghue JA, Zijlstra JM, et al. ^{89}Zr-immuno-PET: toward a noninvasive clinical tool to measure target engagement of therapeutic antibodies in vivo. *J Nucl Med.* 2019;60:1825–1832.
3. Jung KH, Park JW, Lee JH, Moon SH, Cho YS, Lee KH. ^{89}Zr-labeled anti-PD-L1 antibody PET monitors gemcitabine therapy-induced modulation of tumor PD-L1 expression. *J Nucl Med*. 2021;62:656–664.
4. Laffon E, Marthan R. A three-time-point method for assessing kinetic parameters of ^{64}Cu-labeled ramucirumab trapping in VEGFR-2 positive lung tumors. *Phys Med.* 2017;43:1–5.
5. Akaike H. A new look at the statistical model identification. *IEEE Trans Automatic Control.* 1974;19:716–723.
6. Laffon E, Marthan R. Is there a relevant imaging time for optimal quantitative ^{89}Zr-DFO-daratumumab PET imaging? *Radiology*. 2021;299:E285.

Eric Laffon[*]
Roger Marthan
[*]*Hôpital Haut-Lévèque*
Pessac, France
E-mail: elaffon@u-bordeaux.fr

Published online February 26, 2021.
DOI: 10.2967/jnumed.121.262065

JUST ANNOUNCED!

Sam Gambhir Trailblazer Award

The new Sam Gambhir Trailblazer Award honors outstanding achievement and excellence in transformative research (either basic science, translational science, or clinical science) and exceptional mentorship for mid-career professionals. Award recipients will be acknowledged at the SNMMI Annual Meeting during the Wagner Highlights Lecture. This new award is named after Sanjiv "Sam" Gambhir, MD, PhD, an internationally recognized pioneer in molecular imaging. Gambhir dedicated his career to developing methods of early disease detection, ushering in a new era of molecular imaging to flag signals of disease in its nascent stages.

Applications Open October 1, 2021.

For more information to apply:
www.snmmi.org/GambhirAward

SNMMI Value Initiative
SOCIETY OF NUCLEAR MEDICINE & MOLECULAR IMAGING

The most powerful words you'll ever hear.

"Thank You."

With your contribution, our profession can continue efforts leading to critical advances in cancer treatments and care.

The **Value Initiative Transformative Leadership Campaign** is the cornerstone for making these efforts a reality for patients of all ages.

The world needs more "thank you's."

Help improve the life of a patient. Lend your support today.

www.snmmi.org/TransformativeLeadership

SNMMI is a 501 (c)(3) tax id 36-2496678. Your donation is tax deductible as per current IRS regulations. Please remember SNMMI in your estate plans.

SNMMI | Value Initiative

SOCIETY OF NUCLEAR MEDICINE & MOLECULAR IMAGING

MIRION TECHNOLOGIES

Network Ready with Remote Connectivity

CRC®-PC SMART CHAMBER

- Connects to network infrastructure so that display can be viewed from any network PC (remote viewing)
- Direct interface to Nuclear Medicine Management Systems – no readout required
- Ethernet Communications
- Automated QC
- Software upgrade via Ethernet interface
- Built-in database to store QC, Moly and User Log
- Power over Ethernet or USB port
- User adjustable threshold for faster response times
- Small footprint

Available in two fill pressures

The new CRC-PC Smart Chamber combines the well-known and highly reliable measurement Capintec™ chamber with an innovative web-based user interface to meet today's business requirements. Remote connectivity and network ready interface set the Smart Chamber apart as the most advanced in dose calibration.

Call 1-800-631-3826
for more information

CAPINTEC, INC.
Part of Mirion Technologies

www.capintec.com

OPS-2215 – 11/2020

10/21

The Journal of Nuclear Medicine

October 2021 ▪ Vol. 62 ▪ Pages 1323–1485